Solid State Chemistry: A Contemporary Overview

Published on June 1, 1980 on http://pubs.acs.org | doi: 10.1021/ba-1970-0186.fw001

Solid State Chemistry: A Contemporary Overview

Smith L. Holt, EDITOR
University of Georgia

Joseph B. Milstein, EDITOR
Solar Energy Research Institute

Murray Robbins, EDITOR
Bell Telephone Laboratories

Based on a symposium sponsored by the Solid State Subdivision of the ACS Division of Inorganic Chemistry at the Summer Symposium on Solid State Chemistry, Laramie, Wyoming, July 31–August 4, 1978.

ADVANCES IN CHEMISTRY SERIES **186**

AMERICAN CHEMICAL SOCIETY
WASHINGTON, D. C. 1980

Library of Congress CIP Data

Solid state chemistry.
(Advances in chemistry series; 186 ISSN 0065–2393)

Includes bibliographies and index.

1. Solid state chemistry—Congresses.
I. Holt, Smith L., 1938– II Milstein, Joseph B., 1944– III. Robbins, Murray, 1931– IV. American Chemical Society. Division of Inorganic Chemistry. Solid State Subdivision. V. Summer Symposium on Solid State Chemistry, 1st, University of Wyoming, 1978. VI. Series.

QD1.A355 no. 186 [QD478] 540S [541'.0421] 80–17185
ISBN 0–8412–0472–1 ADCSAJ 186 1–437 1980

PRINTED IN THE UNITED STATES

Advances in Chemistry Series

M. Joan Comstock, *Series Editor*

Published on June 1, 1980 on http://pubs.acs.org | doi: 10.1021/ba-1970-0186.fw001

FOREWORD

ADVANCES IN CHEMISTRY SERIES was founded in 1949 by the American Chemical Society as an outlet for symposia and collections of data in special areas of topical interest that could not be accommodated in the Society's journals. It provides a medium for symposia that would otherwise be fragmented, their papers distributed among several journals or not published at all. Papers are reviewed critically according to ACS editorial standards and receive the careful attention and processing characteristic of ACS publications. Volumes in the ADVANCES IN CHEMISTRY SERIES maintain the integrity of the symposia on which they are based; however, verbatim reproductions of previously published papers are not accepted. Papers may include reports of research as well as reviews since symposia may embrace both types of presentation.

PREFACE

As our society becomes more technologically anchored, the role of solid state chemistry in solving problems is seen clearly. While in the past man has witnessed the growth of the electronics industry, based on the ability of solid state chemists to prepare desired materials of high purity, in the future he undoubtedly will see solid state chemists designing and producing materials that contribute in such varied fields as energy conversion, storage, and transmission, information storage and processing, and resource management. Indeed, this process is already under way. From the academic point of view, solid state chemistry is a mature discipline in Europe, but it is still in its infancy in the United States. With these realizations in mind, a conference entitled "The First Summer Symposium on Solid State Chemistry" was held at the University of Wyoming at Laramie, WY in 1978.

The purpose of this meeting was to allow chemists and physicists to interact on a broad range of subjects, most of which would perforce be distinct from the area of research of any one participant. One consequence of such a format is that attendees are obliged to consider subjects that are new to them; hopefully, the examination of problems from different perspectives will lead to fruitful insights and exchanges, or to novel approaches to difficult problems. As a result of this intention, the chapters in this volume cover many topics. The chapters are presented under three general headings: Applications of Physical Techniques to Solid State Chemistry; Materials for Energy Conversion, Storage, and Transmission; and Preparation and Properties of Diverse Solids.

The chapters in the first section discuss less commonly used physical techniques for analysis and/or characterization of solids. The second section has a heavy emphasis on the exploitation of solar energy, but includes such topics as catalysis, hydrogen storage, and novel conducting materials as well. The last segment deals with the more traditional topics of preparation and properties, but the materials studied and/or the methods used are generally of an unusual nature.

It is expected that similar broadly constituted conferences will be held in the future, and it is hoped that the present volume will be useful and of interest to the solid state community.

The editors wish to thank all of the contributors, without whose efforts this volume would have been impossible. They also gratefully acknowledge the financial support of the National Science Foundation and the Petroleum Research Fund.

Department of Chemistry
University of Georgia
Athens, GA 30602

SMITH L. HOLT

Solar Energy Research Institute
Golden, CO 80401

JOSEPH B. MILSTEIN

Bell Telephone Laboratories
Murray Hill, NJ 07974

MURRAY ROBBINS

September 28, 1979

Muon Spin Rotation: An Exotic Probe of the Atomic Environment

ARTHUR B. DENISON

Department of Physics and Astronomy, University of Wyoming, Laramie, WY 82071

The muon, through its magnetic moment, acts as a probe of the magnetic environment in a solid on the atomic scale. The purpose of this review is to elucidate the type of information that may be obtained. The muon may remain as a free particle as in all metallic conductors, or as in some insulators and semiconductors, it may combine with an electron to form muonium. In ferromagnetic metals the various components of the local field have been studied and interpreted. The behavior of muonium in solids is varied depending on the nature of the bound electron, which may be either localized or diffuse over a number of lattice neighbors.

The mu meson ($\mu^{\pm}$), or muon, is a sensitive and delicate probe of matter on the atomic scale. This particle, which carries either a plus or a minus charge, may mimic the behavior of the proton or electron in matter and thus finds itself involved in a variety of probe situations ranging from chemical reactions to static and dynamic magnetic behavior in solids.

Due to the nonconservation of parity (*1*), the $\pi^{\pm} \rightarrow \mu^{\pm} + \nu$ decay produces muons with their spins opposite to the linear momentum (π is a pi meson and ν is neutrino). With proper momentum definition a polarized beam of muons may be obtained. The polarized muons stop in matter and reflect the local magnetic environment through the Larmor precession frequency. The positive muon may remain free as μ^{+}, but in many cases it may combine with an electron (e^{-}) to form muonium ($\mu^{+} - e^{-}$). At the end of the muon lifetime (about 2.2×10^{-6} sec), the decay ($\mu^{\pm} \rightarrow e^{\pm} + \nu + \bar{\nu}$) produces a positron (electron), which is emitted preferentially in the direction of the muon spin. The precession frequency of the muon (and therefore the local magnetic field) can be

0-8412-0472-1/80/33-186-003$05.75/1

measured with positron detectors in a given solid angle. Another important quantity is the depolarization time. This characteristic time reveals the dynamic environment of the muon through dephasing of the spins originally in phase in the beam. This dephasing time is closely related to the T_2 relaxation time often measured in magnetic resonance experiments to obtain information concerning the interatomic motions and correlations.

In the following text the muon spin rotation (μSR) method will be described in more detail. The formation and quantum description of muonium will be considered. A survey of the kinds of studies that may be done with μSR is given. This survey, although not meant to be exhaustive, should give the reader a good idea of what is now being done in the field. The field currently is very active and new ideas and types of measurements are being generated constantly. Several excellent review articles currently exist (*2, 3*) and are recommended to the reader for broader and more detailed information.

Method of Measurement

Figure 1 lists some of the important properties of the muon. The muon, a lepton with spin 1/2, is produced from pion decay in a nuclear accelerator. Several high-flux meson facilities (or meson factories) exist today. The primary sites used for μSR work are the Los Alamos Meson Physics Facility (LAMPF) in New Mexico, the Tri-University Meson Facility (TRIUMF) in Vancouver, British Columbia, the Schweizerisches Institut für Nuklearforschung (SIN) in Villigen, Switzerland, and the Russian Institute for Nuclear Studies at Dubna. Due to the type of interaction that acts during the pion decay (*1*), the muon magnetic moment is directed in the opposite sense to the muon momentum. By selecting muons within a given momentum range, one may obtain a highly polarized muon beam (about 90%). The mass of the muon is 206.8 times the mass of the electron, which means it is about one-ninth the mass of the proton. Both positive and negative muons may be produced. The lifetime of the muon is short (about 2.2×10^{-6} sec), so the experiments must be designed to obtain the relevant information within just a few lifetimes. The magnetic moment is the key to the μSR technique, as the Larmor precession frequency is measured to obtain the magnetic field at the site of the muon in the sample under study. For the free muon the Larmor precession frequency (f_L) is $f_L = 13.55$ kHz/G $\times$ B (G), where B is the magnetic field strength.

The method of detection of the precession of the muon magnetic moment again relies on the fact that parity is not conserved in the weak decay mode of the muon. The positive muon decays into a positron (e^+)

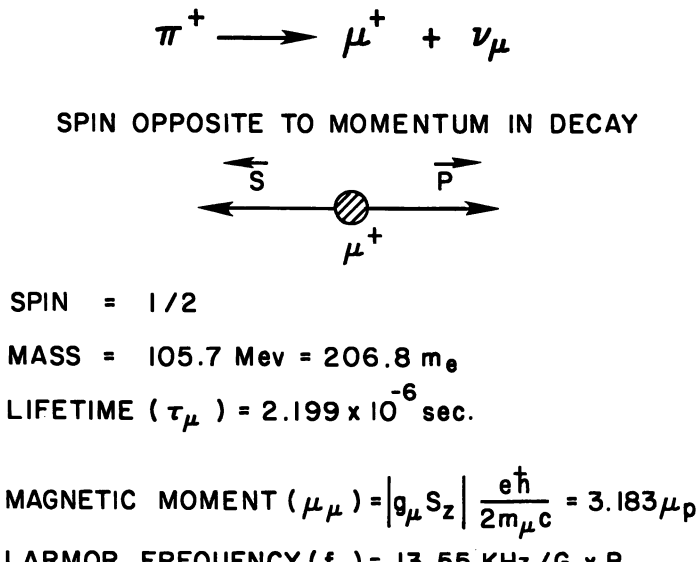

Figure 1. Properties of the muon

and two neutrinos ($\mu^+ \rightarrow e^+ + \nu_e + \bar{\nu}_\mu$) in such a way that the positron is emitted in a preferential direction with respect to the muon magnetic moment. If y is the energy of decay normalized to the maximum possible energy (52.8 MeV), then

$$N(y, \Theta) = 2y^2\{(3 - 2y) + P(2y - 1)\cos\Theta\} \quad (1)$$

gives the distribution of positrons of energy y ejected at an angle Θ from the muon moment, where P is the initial polarization. If one integrates over the allowed energy spectrum, the total asymmetry for the decay positrons is given by

$$N(\Theta) = N_0\left[1 + \left(\frac{1}{3}\right) P\cos\Theta\right] \quad (2)$$

This preferential forward direction of decay positrons with respect to the muon spin can be used to follow the muon precession with positron detectors in a given solid angle with respect to the sample target.

Figure 2 shows an idealized experimental setup. A polarized beam of muons is directed into a sample target. The muons slow down and essentially stop in that target. For most of the materials studied, the slowing-down process does not destroy the initial muon polarization. As the muon enters the target, a count in scintillator counter S_1 is registered. If the muon stops in the target, no count will be observed in S_2. We denote a stopped muon as $S_1\overline{S_2}$, where $\overline{S_2}$ is an anti-S_2. With this event a clock is started. If the muon decays when its magnetic moment is pointed in the direction of S_3, the positron will pass through S_3. When the positron is detected in S_3, the clock is stopped and the total event is stored as a count in the correct time bin of a multichannel analyzer. As many events are recorded, a time histogram is built up, which shows the time-modulated decay of the precessing muon, as shown in Figure 3.

The signal can be represented as

$$N(t) = N_0\, e^{-t/\tau_\mu}[1 + A(t)\, \cos(\omega t + \phi)] + \mathrm{BG} \qquad (3)$$

for muons that have decayed at the same chemical site (t represents time). The initial number of muons decaying at $t \equiv 0$ is given by N_o, τ_μ is the muon lifetime, ω is the Larmor frequency or frequency of the wiggles in the decay histogram, ϕ gives the phase of the first wiggle with respect to counter's zero time, and BG is the background signal. The function $A(t)$, the so-called depolarization function, carries the information about dynamical aspects of the chemical environment. This function describes the dephasing of the precessing muons due to the distribution of local magnetic fields and the time-modulated atomic environment. Often the function can be simply represented as $A(t) = A_0 \exp(-t/t_{dep})$, where t_{dep} plays the same role as T_2, the reciprocal of the line width in magnetic resonance measurements. We will have more to say about the information that can be obtained from this function as we treat actual experiments. It is possible, of course, that the muon may stop in several unequivalent sites, which would then give a more complicated time histogram, showing beats. The frequency information can be obtained as the power spectrum or Fourier transform of the histogram.

Muonium

Before discussing the type of chemical or physical information that can be obtained from μSR experiments, it is necessary to consider the exotic atom muonium (*4*). This atom, consisting of a positive muon and an electron, has many features of the hydrogen atom. The important

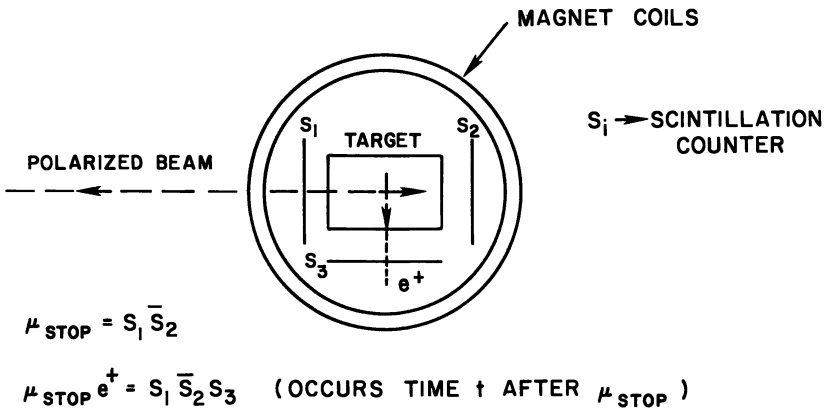

Figure 2. Schematic for experimental setup. The magnetic field is directed perpendicular to the incoming beam and the initial polarization

μ SR HISTOGRAM

$$N(t) = N_0 e^{-t/\tau_\mu} \left\{ 1 + A e^{-t/T} \cos(\omega^\mu t + \phi) \right\} + BG$$

τ_μ = MUON LIFETIME (2.2 μ sec.)

- A = INITIAL POLARIZATION OF "STOPPED" MUON
- T = DEPOLARIZATION TIME
- $\omega^\mu = 2\pi f_L$ = PRECESSION FREQUENCY OF μ^+

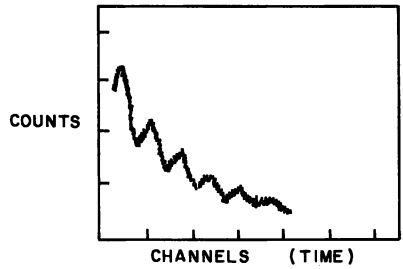

Figure 3. The measured signal (time histogram) obtained in the μSR experiment

point for our discussion is that muonium is quickly formed in many insulators and semiconductors so that the muon decay histogram has the spectral features of this coupled two-spin system. The interaction Hamiltonian for muonium in an external magnetic field H is given as

$$\mathcal{H} = \mathcal{A}\mathbf{I} \cdot \mathbf{S} + g_\mu \beta_\mu \mathbf{H} \cdot \mathbf{I} + g_e \beta_e \mathbf{H} \cdot \mathbf{S} \quad (4)$$

which gives rise to the familiar Breit-Rabi energy diagram shown in Figure 4. The muonium hyperfine interaction has a strength given by $\mathcal{A}/h = \omega_0/2\pi = 4463$ MHz where h is Planck's constant. At low magnetic fields the spins interact strongly with one another and the external field acts only as a perturbation. The opposite extreme occurs at high fields as the spins decouple and line up with the external field. The two field regions are best described with two different quantum representations, (F, m_F) at low field and (I, S, m_μ, m_e) at high fields. The diagram

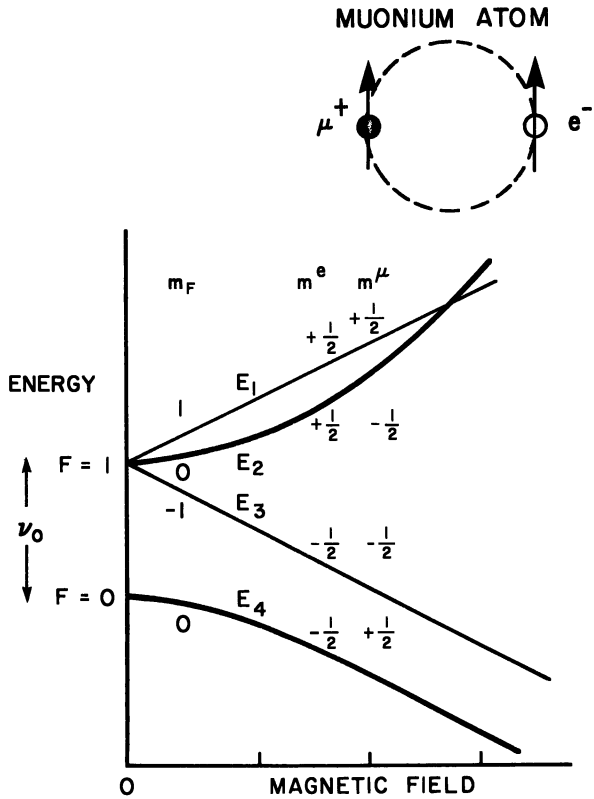

Figure 4. Breit–Rabi diagram for the muonium atom. The energies E_i *are given analytically in the text. Magnetic field is given in kilogauss units;* $\nu_0 = 4463$ *MHz.*

in Figure 4 shows the energy levels and the relative projections of the spins. The states at any magnetic field are described in the high-field representation as (E_i is the energy)

$$
\begin{aligned}
|E_1> &= |++>_{||} \\
|E_2> &= s|+->_{||} + c|-+>_{||} \\
|E_3> &= |-->_{||} \\
|E_4> &= c|+->_{||} - s|-+>_{||}
\end{aligned}
\tag{5}
$$

with

$$
c = \frac{1}{\sqrt{2}}\left[1 + \frac{x}{(1+x^2)^{1/2}}\right]^{1/2}, \quad s = \frac{1}{\sqrt{2}}\left[1 - \frac{x}{(1+x^2)^{1/2}}\right]^{1/2}
$$

and

$$
x = \frac{(g_e\beta_e - g_\mu\beta_\mu)\ |\mathbf{H}|}{h\omega_0}
$$

Experimentally one looks for the muonium precession frequencies. The observed frequencies depend on the magnitude of the applied field and its direction relative to the initial muon polarization. Muonium is formed with the initial polarization direction of the muon preserved so that the electron is captured in a state either parallel, $|+,+>$, or antiparallel, $|+,->$, to the muon projection. The general situation with respect to arbitrary magnetic field orientation is complicated, but one can examine some simple cases. In the case of a weak transverse field, the states $|+,+>$ and $|+,->$ are not really eigen states since the axis of quantization (external magnetic field) is perpendicular to the initial muon polarization. Nevertheless, the situation is not so complicated, since the coupled(triplet) spin state will precess in the magnetic field in a direction dominated by the electron moment. The wiggles on the time histogram will occur with a frequency $f_L^{Mu} = 1/2(f_L^e + f_L^\mu) = (1.4\ \text{MHz} \cdot \text{G}^{-1})$. At higher fields the correct calculation must be made (5) to obtain the frequencies corresponding to the $\Delta m = 1$ transitions between the states shown in Figure 4. The resulting histogram will show beats that may be analyzed by Fourier transforms to obtain the desired frequencies.

For muonium in a longitudinal field, the states $|+,+>$ and $|+,->$ are formed with 50% of the total muonium population in each state. However, the state $|+,->$ is not pure in the sense that it is a superposition of states E_2 and E_4, that is, $|+,-> = s|E_2> + c|E_4>$. Such a mixed state will oscillate in time between $|+,->$ and $|-,+>$ with the

frequency ω_{24}. At low external magnetic fields, $\omega_{24} = \omega_0$ and this frequency is too high to resolve with current apparatus, so half the available polarization is lost. As the field is increased, however, one can show that the polarization of the $|+,-\rangle$ state oscillates between $+1$ and $P_{\min}$, where $P_{\min} = (x^2 - 1)/(x^2 + 1)$, with $x = \omega/\omega_0$. The resulting muon polarization as a function of magnetic field is then given by

$$P(x) = \frac{1}{2} + \left(\frac{1}{2}\right)\left[\frac{x^2}{(1 + x^2)}\right] \tag{6}$$

Muonium in Insulating Solids: Depolarization Studies. The behavior of muonium in an external magnetic field, described in the preceding section, is for muonium in a vacuum in the absence of perturbing effects. Deviations from such behavior for muonium in solids provides information about the material under study. Much of the current theory of depolarization, as well as early measurements, was done by the Russian group (*5, 6, 7, 8*). Depolarization from the atomic environment comes from several causes, the most important of which is the so-called proper muonium mechanism (*8*). The muonium electron is strongly coupled to the environment and through spin interactions relaxes rapidly. The muon that is coupled to the electron through the hyperfine interaction also depolarizes rapidly. As an external longitudinal field is applied above the critical field, the spins are decoupled and the muonium polarization restored. Figure 5 shows the restoration of polarization of muonium in quartz. The fit to the data is excellent when using Equation 6 which describes the ideal case for muonium in a vacuum. Quartz (SiO_2) appears neutral to muonium in many respects. It is possible, using Equation 6 and the definition of $x = (\omega/\omega_0)$, to find the effective hyperfine constant $\mathcal{A}$ of the muonium in a given substance by fitting the data obtained from depolarization as a function of magnetic field. In quartz, as expected, the vacuum value of the hyperfine coupling constant is obtained.

A modification of this process occurs when the electron associated with the muonium is chemically active. If the electron enters into a chemical bond, the muon will be free for a time before attaching to another electron. The muon becomes rapidly depolarized (in low field) while it is in muonium but not so rapidly as a free muon. Examining this process in detail (*9*), one finds that the depolarization follows

$$P = 1 - \frac{(\omega\tau)^2\,(1 + 2\nu\tau)}{2[\,(\omega\tau)^2(1 + \nu\tau + x^2) + (1 + 2\nu\tau)^2]} \tag{7}$$

where x has its usual definition, ν is the flipping frequency of the electron in muonium, and τ is the lifetime of the muonium configuration. Figure

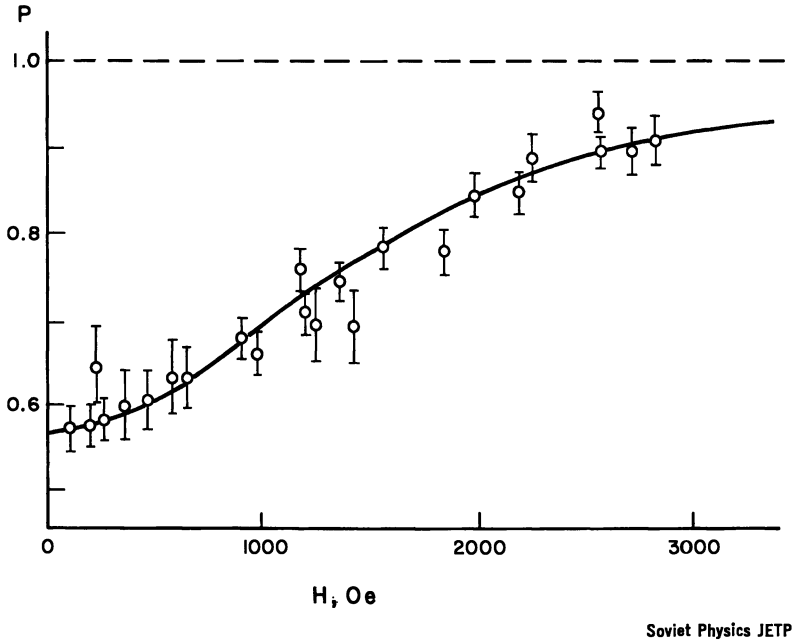

Figure 5. The residual polarization for muonium in quartz (SiO_2) as a function of magnetic field. The external magnetic field is perpendicular to the beam polarization (8). (Solid line predicted by Equation 6 in text.)

6 shows the close agreement with the prediction for muonium in KCl as a function of magnetic field. It was impossible to obtain ν and τ separately, although the product $\nu\tau$ was determined ($\nu\tau = 1.81 \pm 0.10$). Feasible bounds on the separate quantities are discussed in the original paper. Additional discussion of the mechanism of depolarization of the muon also is given there, which points up the importance of impurities in the sample. Impurities such as those found in KCl give rise to local magnetic fields, which depolarize the mu meson. Again, by examining the external field dependence on this extra depolarization, one may estimate the magnitude of the local field. These authors report a calculated local field on the order of 50 G.

Muonium in Insulating Solids: Precession Measurements. Recall that through the Fourier analysis of a time histogram taken from muonium precession in a transverse field, the frequencies corresponding to the $\Delta m = 1$ transitions in the Breit-Rabi diagram (Figure 4) may be obtained. Figure 7 shows the power spectrum resulting from the Fourier transform of the histogram of muonium in SiO_2 (quartz) and in p-doped Si. The two frequencies so obtained for SiO_2 are ω_{12} and ω_{34}. From these measured frequencies at a known magnetic field, one can readily calculate the muonium hyperfine coupling constant. As mentioned previously, the

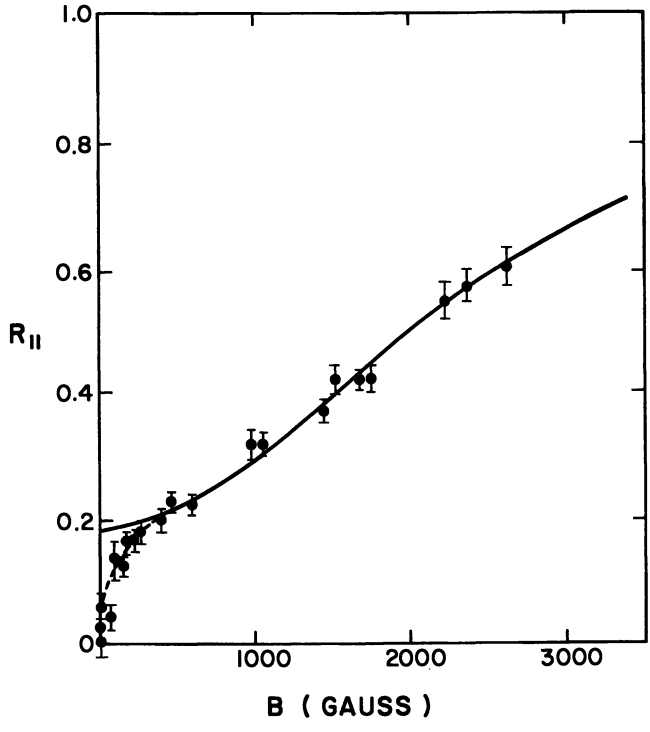

Soviet Physics JETP

Figure 6. The residual polarization as a function of magnetic field in KCl. The effects of forming and reforming the muon atom in the chemical environment give rise to the curve above 200 G. Additional depolarization due to local magnetic fields is evident at low fields (9). (Solid line predicted by Equation 7 in text.)

hyperfine constant is the same as that for muonium in a vacuum. In other words, the muonium in SiO_2 has found a spacious enough site to accommodate itself essentially unperturbed. Such unperturbed muonium is found in a number of materials (*2*).

In contrast to this vacuumlike behavior are the results for the semiconductors Si and Ge. In fact, the behavior of muonium in these materials is currently one of the most interesting problems in μSR. Gurevich (*5*) observed muonium in Ge that showed the hyperfine frequency $\omega_{hyp}(Ge) \approx 0.56\ \omega_0(vac)$. Brewer et al. (*10*) published their results in 1973 for p-doped Si (*see* Figure 7). For muonium in the interstitial site they observed $\omega_{hyp}(Si) \approx 0.405\ \omega_0(vac)$. The muonium behaves as though it is somewhat swollen in the site in which it finds itself. Such muonium in which the muon and electron are essentially localized, albeit swollen, is called deep-donor muonium. If one assumes that the hyperfine interaction follows the contact interaction $|\psi(0)|^2 \propto (1/r^3)$, where $|\psi(0)|^2$ is

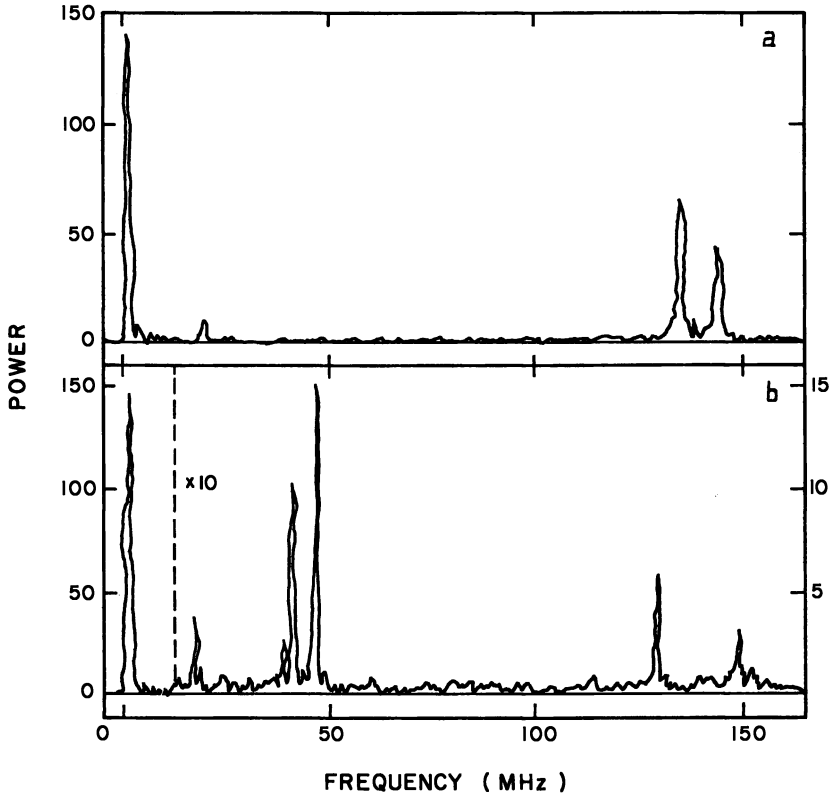

Physical Review Letters

Figure 7. (a) The power spectrum from the time histogram for muonium in quartz (SiO_2). The two frequencies near 130 MHz represent the transitions ν_{12} and ν_{34} in the Breit-Rabi diagram (10). (b) The power spectrum from muonium in Si. The upper frequencies come from a swollen muonium in Si and the lower two frequencies have their origin in a shallow donor muonium (10).

proportional to the electron density at the muon site, then the radius can be calculated to have expanded by roughly 20%. Wang and Kittel (*11*) interpreted the swelling as due to shielding by the valence band electrons. Coker, Lee, and Das (*12*) have attempted to predict the observed hyperfine shift by using a self-consistent, charge-extended Hückel model with a cluster of 31 atoms. Reasonable agreement is found for both the models above for the deep-donor muonium.

Another set of frequencies has been observed, however, that are anisotropic with respect to crystal orientation in the external field. These lines, the so-called anamolous lines, were difficult to interpret and produced g and $\mathcal{A}$ values that were hard to explain. The Swiss group

[Patterson et al. (*13*)] found that by rotating the crystal about various axes, they could predict frequencies quite well, using an anisotropic spin Hamiltonian.

$$\mathcal{H}_{Mu}{}^{*} = \mathcal{A}_{\perp}\,(I_x S_x + I_y S_y) + \mathcal{A}_{||} i_Z S_z - g_e\beta_e\,\mathbf{S}\cdot\mathbf{H} - g_\mu\beta_\mu\,\mathbf{I}\cdot\mathbf{H} \qquad (8)$$

It was found that this anisotropic hyperfine interaction had an axis of symmetry ($\mathcal{A}$) about any one of the <111> directions. This description, which is not uncommon in electron spin resonance work, allowed a much simpler interpretation with the reasonable parameters

$$|\mathcal{A}_{\perp}| = 92.1 \pm 0.3\ \text{MHz}$$

$$|\mathcal{A}_{||}| = 17.1 \pm 0.3\ \text{MHz}$$

$$g_\mu = 2.01 \pm 0.01$$

$$g_e = 2.2 \pm 0.2$$

Further work is presently being done to elucidate the nature of the site with this symmetry. Several possible models are put forward in the original paper.

Positive Muons in Metal

The muon (μ^+) remains as a free muon in conductors, where the metallic electrons are correlated and act to screen the μ^+ charge rather than contributing an electron to make the muonium atom. Two general types of problems have been studied that have proved most exciting: (1) the study of muon diffusion in metals and (2) the study of magnetic interactions in materials. Both studies require knowledge of the whereabouts of the muon and therefore deal with the physics of interstitial sites, defects, and trapping.

Diffusion. Information concerning the diffusion and trapping of muons in metals is obtained through the depolarization time. This depolarization time depends on temperature and local environmental factors, such as the magnetic surroundings and the mechanism of trapping. Several metals have been examined. The results show that the behavior of the muon is by no means uniform for different materials. It is becoming clear that even for a given metal sample the experimental results can be quite different, depending on the number of impurities in the sample. The results are sensitive to the method of preparation and

annealing, which may influence structural defects and dislocations. Many new results are appearing in the literature (*see*, for example, *14–22*), and communication with various laboratories shows the lively activity in this field, with new and puzzling results appearing constantly. Rather than a complete survey of all the materials examined to date, a discussion of the general approach to understanding the results with some specific examples will be given here.

In Equation 3 the term $A(t)$ carries the depolarization information. Recall that the depolarization time is the characteristic dephasing time of the muons due to dynamic relaxation effects from the sample itself. It has been known for a long time in the field of magnetic resonance relaxation that the relaxation times are determined by the power spectrum of the time-modulated local magnetic environment. Theories that quantitatively predict the relaxation times use a correlation time τ, characteristic of the period of the local magnetic fluctuations. Reasonable success in both magnetic resonance and muon depolarization has been obtained by using the function (*21*)

$$A(t) = A_0 \exp\{-2\sigma_S^2 \tau^2[\exp(-t/\tau) - 1 + t/\tau]\} \qquad (9)$$

where τ is the characteristic magnetic fluctuation time (often the muon hop time) and σ_S^2 represents a lattice sum over the neighboring nuclear dipoles. This function reduces to a Gaussian ($A_0 e^{-\sigma_S^2 t^2}$) for slow diffusion ($\tau \to \infty$) and to an exponential ($e^{-2\sigma_S^2 \tau t}$) for fast diffusion ($\tau \to 0$). As mentioned, the experiments are done as a function of temperature for any given sample, and the quantity in the exponential of $A(t)$ is measured.

As an example of the results obtained as a function of temperature, the data of Gauster et al. (*14*) are shown in Figure 8. The data for Cu were fit by using the general expression (Equation 9), with a value for σ^2 of 0.257 ± 0.003 s^{-1}. This value of σ^2 assumes the muon is trapped at an octahedral interstitial site. The results on Al, on the other hand, show a surprising lack of trapping, even at very low temperatures. This lack of trapping in Al can be partially rationalized if one assumes that the concentration of trapping sites is low, so that a muon cannot find vacancies in its lifetime or, alternatively, that such sites are not deep traps, so that detrapping occurs quickly. The explanation for this large difference between these two materials with similar face-centered cubic (FCC) lattices is not complete at this time.

The basic model of diffusion given is further substantiated in Cu by a beautiful set of experiments done by Camani et al. (*22*) as interpreted by Hartmann (*23*). The copper nucleus, in addition to possessing a magnetic dipole moment, has a reasonably large quadrupole moment.

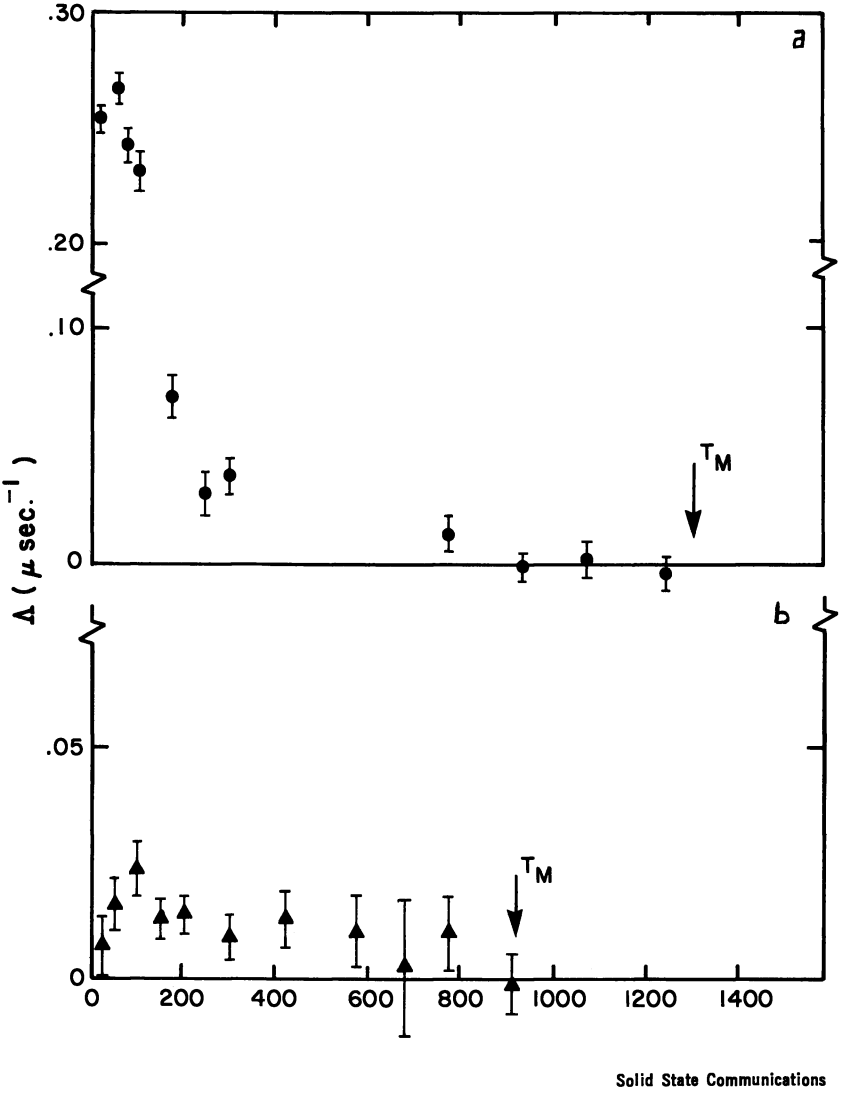

Figure 8. The depolarization rate of the diffusing μ^+ in (a) Cu and (b) Al as a function of temperature (14)

In the case of muon diffusion in Cu the muon distorts the site at which it sits. Such a distortion produces an electric field gradient different from zero, which will interact with the neighboring nuclear quadrupole moments. The orientation of the neighboring nuclei, and therefore the resulting dipole sum σ^2, depends on the interaction of the quadrupole moment with the induced electric field gradient and the interaction of the nuclear magnetic dipole moment with any magnetic field present.

The depolarization of the muon spins was measured as a function of an applied external magnetic field. The results so obtained, using a single crystal of Cu oriented in a known way in the external magnetic field, are shown in Figure 9. These results, which depend on the competition between the nuclear orientation due to the electric field gradient and the external magnetic field, agree extremely well with the theory. In addition, the amount of distortion due to the presence of the muon has been measured. Figure 10 shows the results of depolarization measured as a function of external field and as a function of crystal orientation. A best fit to the data occurs for an assumed expansion of the lattice site of about 5%.

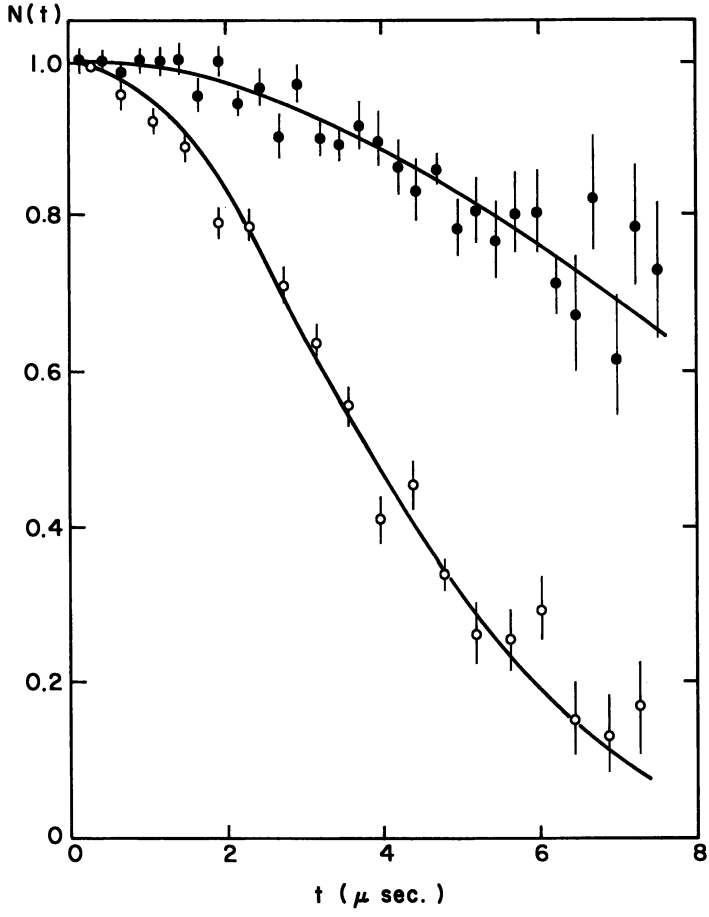

Figure 9. Measured asymmetry N(t) *in Cu(111) at 80 K as a function of magnetic field strength and direction: (●), 4800 G; (○), 3500 G (22).*

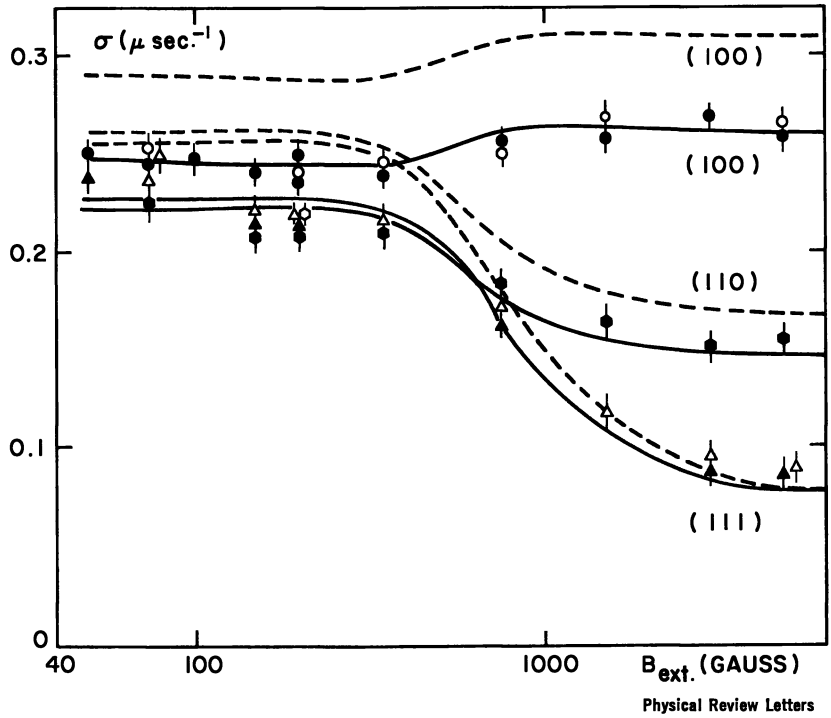

Figure 10. Depolarization rate of the μ^+ in a single crystal of Cu as a function of magnetic field strength and direction: (– – –), the predicted values for undistorted site; (——), the predicted values for a dilation of the site by 5%. Cu(100): (●), 80 K; (○), 20 K. Cu(110): (⬢), 80 K; (⬡), 20 K. Cu(111): (▲), 80 K; (△), 20 K (22).

Recent results on niobium and vanadium (*17, 18, 19, 20*) show more complicated behavior of the depolarization exponential as a function of temperature. Figure 11 illustrates the general behavior of the depolarization function. The feature of concern is the dip corresponding to a decrease in depolarization rate at particular temperatures. Such dips are very dependent on the purity of the samples used. The current interpretation can be qualitatively mentioned here, although the details of the theory are still being worked out (*15, 17, 19*), and it is clear that more data are required. In the high-temperature region (D) multiphonon processes occur that essentially keep the muon untrapped, resulting in an averaging of the local magnetic environment, giving small depolarization. As the temperature goes down (C), traps do become effective, so that the muon finds itself stationary in the vicinity of nuclear magnetic dipoles, which quickly dephase the muon spins. In the region of the dip (B) two models are currently used. For this effect in Ni, Grebinnik

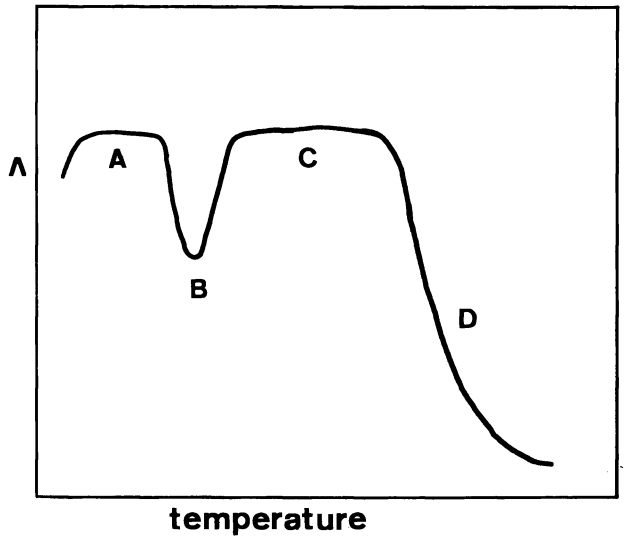

Figure 11. General behavior of the depolarization rate of muons in the body-centered cubic metals Nb and V

et al. (*15*) have proposed a kind of quantum tunneling as a mechanism for diffusion, which actually increases as the temperature decreases. This model treats the region at very low temperature (A) as being effective in allowing the muon to diffuse readily and find traps. The opposing theory (*19*) argues that in region B the muon diffusion in a classical sense has slowed to the point where it is difficult to find a depolarizing trap and yet is fast enough that motional averaging, as mentioned above, is still effective. In this latter model at very low temperatures, the muon is slowed to the point that the motional averaging disappears.

The diffusion experiments do relate to some fundamental questions about the behavior of a muon in matter. Is the muon localized or is it spread out in the quantum mechanical sense? How does this character change as a function of temperature? The muon and its resulting strain field, a polaron, may move together through a crystal but again change character as a function of temperature. The future should bring some answers to these questions.

Magnetism. The muon has been used as a probe in a variety of magnetic materials. Work has been done in the metal ferromagnets as well as in both metallic and nonmetallic antiferromagnets. Several different aspects of magnetization and the origin of magnetism have been examined looking at both static and dynamic effects. Perhaps the simplest and cleanest type of measurement is to monitor the change in the local magnetization above and below the critical temperature. Figures 12(a) and

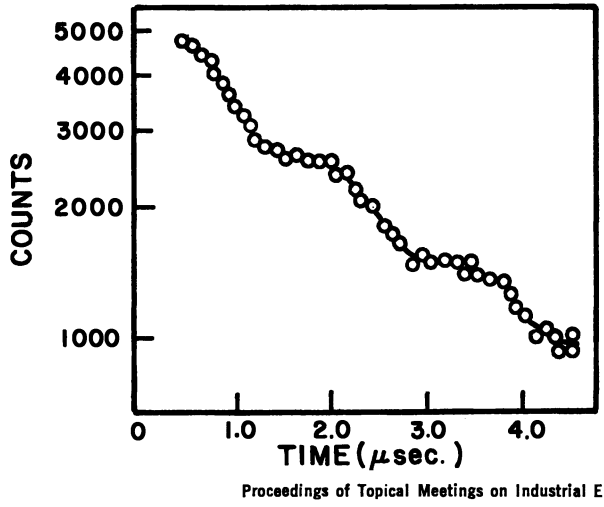

Figure 12a. Time histogram in paramagnetic Ni, to be compared with Figure 12b (27)

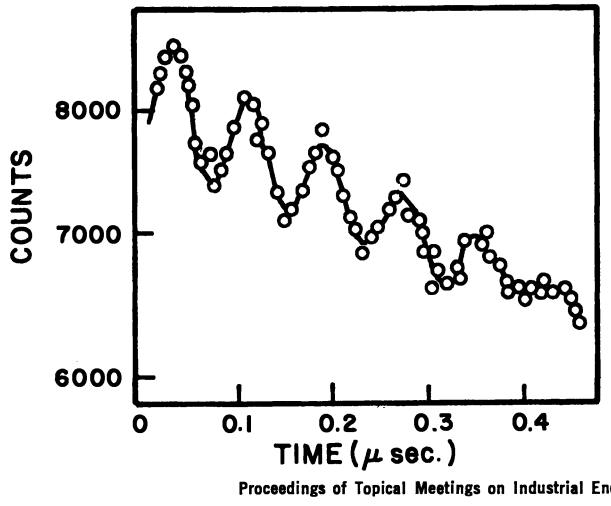

Figure 12b. Ni in the ferromagnetic phase (27).

12(b) show the dramatic change in local magnetization in Ni in the paramagnetic and ferromagnetic state. Figure 12(c) shows the general growth of magnetization and the closeness to the familiar Brillouin function.

Measurements have been made in ferromagnetic Ni, Fe, and Co and in Gd [*see* Review by A. Schenck (*24*)] as well as antiferromagnetic Dy

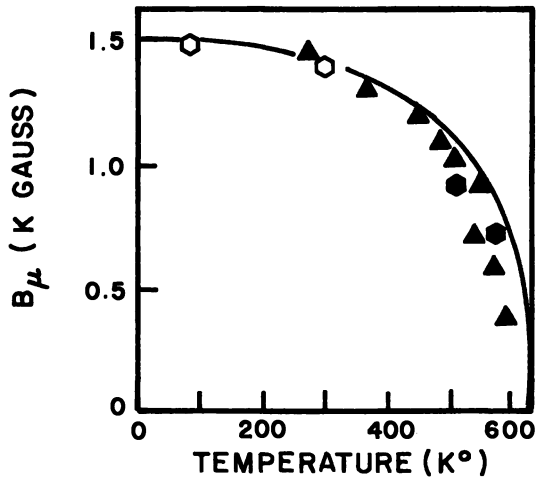

Figure 12c. The local magnetic field at the stopped muon site as a function of the applied magnetic field: (▲), (●), polycrystal, μ^+; (⬡), single crystal, μ^+.

and Ho (Dy has both an antiferromagnetic and ferromagnetic phase as the temperature is lowered). These studies become quickly nontrivial when the origin of the observed field is questioned in detail. The internal (site) field is given generally as

$$B_{\text{tot}} = B_{\text{ext}} - B_{\text{dem}} - B_{\text{L}} + B_{\text{dip}} + B_{\text{hyp}}$$

where B_{ext} is the externally applied field; B_{dem} is the demagnetization field (generally dependent on the shape of the sample); B_{L} is the Lorentz field; B_{dip} is the field contributed from the surrounding nuclear (or electronic) dipoles; and B_{hyp} is the field due to the overlap of the conduction electron wave function with the muon (the so-called contact hyperfine field). Physically, the most interesting quantities are B_{dip} and B_{hyp}. The dipole field is important in determining the site of the stopped muon. These fields are not zero in Co and Gd. The positive muon, which finds itself generally at an interstitial site, is a positively charged impurity and as such modifies the electron density in its vicinity. The hyperfine field results from the unpaired electron spin density at the site of the muon, which depends on electron density and electron polarization. As such the muon acts as a probe of its own disturbing influence on the conduction band. Once the perturbing effects are removed, however, the behavior of the conduction electrons at the interstitial site can be interpreted in the normal site.

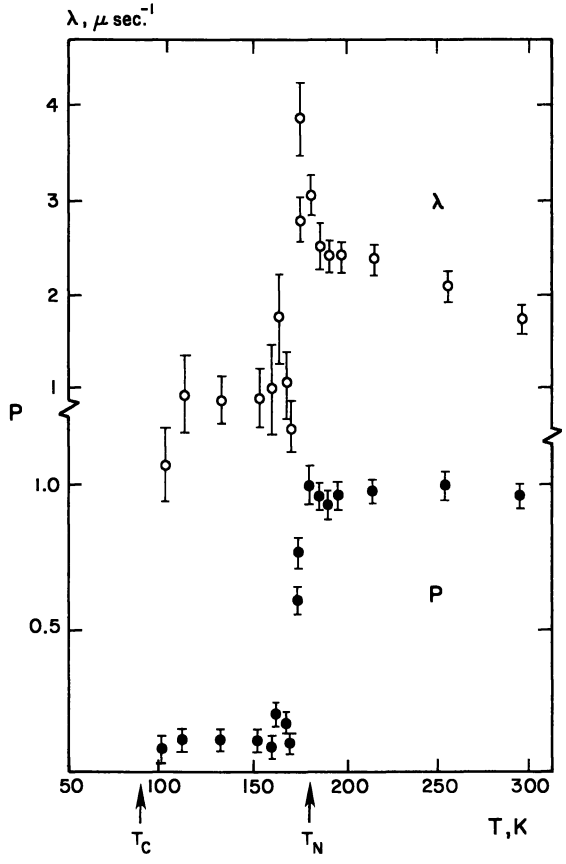

Figure 13. Measured values of depolarization rate (λ) and residual polarization (P) in Dysprosium as a function of temperature. T_N is the Neel temperature (29).

A few comments about the results should be made. In all four of these ferromagnets the local magnetic field arising from the contact interaction with the conduction electrons is negative, that is, in the opposite direction to the applied field. In Ni the hyperfine field is quite small based on what one might expect from increased spin density due to charge redistribution around the positive muon. In the case of Co and Ni the muon may stop in two sites with different symmetry. It is inferred from the precession data and calculation of B_{dip} that the muon stops at an octahedral site. For Gd, which is a hexagonal close-packed (hcp) crystal, all stopping sites have a nonzero dipole contribution. From the data and the calculated dipole sum, it is inferred that the muon stops in the octahedral site.

Antiferromagnetic Dy and Ho have been examined by using μSR. Figure 13 shows the depolarization rate and asymmetry A_0 measured as a function of temperature by Gurevich et al. (*25*). Dy has both a ferromagnetic and antiferromagnetic transition. The results for Ho are similar, showing a discontinuity of both the depolarization rate and initial asymmetry near T_N. These measurements were made at 306 G. Hofmann et al. (*26*) used the μSR technique to measure the local magnetic field at the site of the positive muon in Dy (Figure 14). A single precession frequency was seen in both the ferromagnetic and antiferromagnetic states, showing that the muon must be stationary.

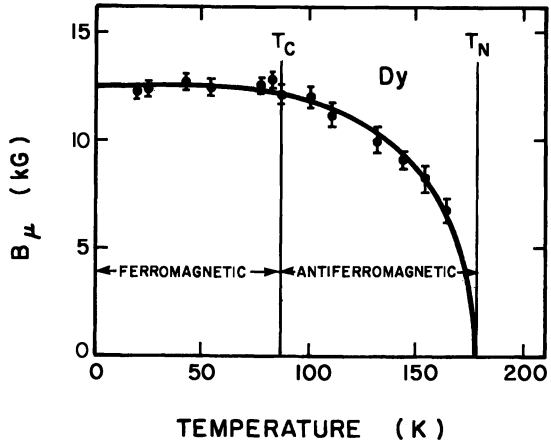

Figure 14. Local magnetic field at the site of the stopped muon in Dy as a function of temperature (26)

Conclusion

In summary, the muon, either free or combined with an electron to form muonium, shows interesting effects brought about by the interactions occurring in solids at the atomic level. The positive muon is sensitive to the electron density and chemical environment. Both static and fluctuating local magnetic fields can be measured through the precession frequency and depolarization times. The general study of the interactions of the muon and muonium in matter gives information both about the material under study and the nature of the muon in matter, with new experiments often showing unexpected or surprising results. As time progresses, the nature of the muon in matter will become clearer. Perhaps one can compare μSR with the growth of the field of magnetic resonance. The early resonance experiments were of an exploratory nature, albeit exciting, yet as the subject became better understood, the technique became powerful as an analytic tool in chemistry.

Glossary of Symbols

$e^{\pm}$ = electron (+ or −)
$\mu^{\pm}$ = muon (+ or −)
ν = neutrino
t = time
ω = frequency, in radians per second; $\omega = 2\pi f = 2\pi\nu_i$, where f and ν_i are in hertz
f_L = Larmor precession frequency of free muon
y = energy of decay positron (normalized to 52.8 MeV)
P = initial polarization of muon
$P(x)$ = polarization as a function of applied magnetic field
A_0 = effective initial polarization of muons stopped in sample
$A(t)$ = depolarization function (as function of time)
$\mathbf{B}, \mathbf{H}$ = magnetic field strength (in gauss); B_i normally is used to mean contribution to local field in the solid
$\mathcal{H}$ = Hamiltonian operator
g = spectroscopic splitting factor (Lande g factor for free muonium)
$\beta = (e\hbar/2mc)$ Bohr magneton (electron or muon)
$\mathcal{A}$ = hyperfine coupling constant ($\|$ or $\perp$), parallel or perpendicular to an axis of symmetry
$\mathbf{I}$ = muon spin quantum operator
$\mathbf{S}$ = electron spin quantum operator
$\mathbf{F} = \mathbf{I} + \mathbf{S}$
$|E_i>$ = wave function of state at energy E_i
$|I, S>$ = wave function for coupled $\mathbf{I}$ and $\mathbf{S}$ spin system obtained for the case of an externally applied field parallel to the initial muon polarization
τ_μ = natural lifetime of muon (about 2.2×10^{-6} sec)
τ = characteristic fluctuation time of magnetic environment
σ_S^2 = parameter representing the strength of the interaction of the muon with neighboring magnetic dipole moments
μSR = muon spin rotation
S_i = scintillation counter i
hcp = hexagonal close-packed

Literature Cited

1. Garwin, R. L.; Lederman, L. M.; Weinrich, M. *Phys. Rev.* **1957**, *105*, 1415.
2. Brewer, J. H.; Crowe, K. M.; Gygax, F. N.; Schenck, A. In "Muon Physics III;" Hughes, V. W.; Wn, C. S., Eds.; Academic: New York, 1975.
3. Schenck, A. "Nuclear and Particle Physics at Intermediate Energies;" Warren, B. J., Ed.; Plenum: New York, 1976.
4. Hughes, V. W. *Phys. Rev. A* **1970**, *1*, 595.

5. Gurevich, I. I.; Ivanter, I. G.; Meleshko, E. A.; Nikol'skii, B. A.; Selivanov, V. I.; Smilga, V. P.; Sokolov, B. V.; Shestakov, V. D. *Sov. Phys.—JETP (Engl. Transl.)* **1971**, *33*, 253.
6. Ivanter, I. G.; Smilga, V. P. *Sov. Phys.—JETP (Engl. Transl.)* **1968**, *27*, 301.
7. Ivanter, I. G. *Sov. Phys.—JETP (Engl. Transl.)* **1972**, *36*, 990.
8. Minaichev, E. V.; Myasishcheva, G. G.; Obukhov, Yu. V.; Roganov, V. S.; Savel'ev, G. I.; Firsov, V. G. *Sov. Phys.—JETP (Engl. Transl.)* **1970**, *31*, 849.
9. Ivanter, I. G.; Minaichev, E. V.; Myasishcheva, G. G.; Obukhov, Yu. V.; Roganov, V. S.; Savel'ev, G. I.; Smilga, V. P.; Firsov, V. G. *Sov. Phys.—JETP (Engl. Transl.)* **1972**, *35*, 9.
10. Brewer, J. H.; Crowe, K. M.; Gygax, F. N.; Johnson, R. F.; Patterson, B. D. *Phys. Rev. Lett.* **1973**, *31*, 143.
11. Wang, J. S.; Kittel, C. *Phys. Rev. B* **1973**, *7*, 713.
12. Coker, A.; Lee, T.; Das, T. P. *Hyperfine Interact.* **1978**, *4*, 821.
13. Patterson, B. D.; Hintermann, A.; Kündig, W.; Meier, P. F.; Waldner, F.; Graf, H.; Recknagel, E.; Weidinger, A. Wichert, Th. *Phys. Rev. Lett.* **1978**, *40*, 1347.
14. Gauster, W. B.; Hefnner, R. H.; Huang, C. Y.; Hutson, R. L.; Leon, M.; Parkin, D. M.; Schillaci, M. E.; Trifthauser, W.; Wampler, W. R. *Solid State Commun.* **1977**, *24*, 619.
15. Grebinnik, V. G.; Gurevich, I. I.; Zhukov, V. A.; Klimov, A. I.; Mayoror, V. N.; Manych, A. P.; Mel'nikov, Ye. V.; Nikol'skii, B. A.; Piragor, A. V.; Panomarer, A. N.; Selivanor, V. I.; Suyekin, V. A. *Pisma Zh. Eksp. Teor. Fiz.* **1977**, *25*, 322.
16. Kossler, W. J.; Fiory, A. T.; Murnick, D. E.; Stronach, G. E.; Lankford, W. F. *Hyperfine Interact.* **1977**, *3*, 287.
17. Lankford, W. F.; Birnbaum, H. K.; Fiory, A. T.; Minnich, R. P.; Lynn, K. G.; Stronach, G. E.; Bieman, L. H.; Kossler, W. J.; Lindemuth, J. *Hyperfine Interact.* **1978**, *4*, 833.
18. Birnbaum, H. K.; Camani, M; Fiory, A. T.; Gygax, F. N.; Kossler, W. J.; Rüegg, W.; Schenck, A.; Schilling, H. *Phys. Lett. A* **1978**, *65*, 435.
19. Fiory, A. T.; Lynn, K. G.; Parkin, D. M.; Kossler, W. J.; Lankford, W. F.; Stronach, C. E. *Phys. Rev. Lett.* **1978**, *40*, 968.
20. Borghini, M.; Niinikoski, T. O.; Soulie', J. C.; Hartmann, O.; Karlsson, E.; Norlin, L. O.; Pernestal, K.; Kehr, K. W.; Richter, D.; Walker, E. *Phys. Rev. Lett.* **1978**, *40*, 1723.
21. Abragam, A. "Principles of Nuclear Magnetism;" Oxford University Press: New York, Chapter 10.
22. Camani, M.; Gygax, F. N.; Rüegg, W.; Schenck, A.; Schilling, H. *Phys. Rev. Lett.* **1977**, *39*, 836.
23. Hartmann, O. *Phys. Rev. Lett.* **1977**, *39*, 832.
24. Schenck, A. *Hyperfine Interact.* **1978**, *4*, 301.
25. Gurerich, I. I.; Klimov, A. I.; Maiorov, V. N.; Nikoliskii, B. A.; Roganov, V. S.; Selivanov, V. I.; Suetin, V. A. *Sov. Phys.—JETP Lett.* **1976**, *23*, 310.
26. Hofmann, W.; Kündig, W.; Meier, P. F.; Patterson, B. D.; Rüegg, K.; Echt, O.; Graf, H.; Recknagel, E.; Weidinger, A.; Wichert, T. *Phys. Lett. A* **1978**, *65*, 343.

RECEIVED September 21, 1978.

Some Uses of High-Resolution Electron Microscopy in Solid State Chemistry

LEROY EYRING

Department of Chemistry and the Center for Solid State Science, Arizona State University, Tempe, AZ 85281

The principles of electron microscopy are briefly sketched to permit an evaluation of the potential use and limitations of high-resolution techniques to solid state chemistry. The ReO_3-related systems have been extensively studied and are very selectively reviewed and illustrated. Compositions in the interval MO_3 to M_2O_5 are described, including the formation and destruction of point and extended defects. The intergrowth of regular structural elements with defects and the ordering of the latter into new phases are observed. These phases include oxygen deficient MO_3, tetragonal tungsten bronzes of variable composition, and also the block structures such as H–Nb_2O_5 of varied composition. Fluorite-related phases representative of the larger class of less ideally suited materials for high-resolution transmission electron microscopy (HRTEM) study have been investigated. The results on these ordinary materials are described and illustrated, including structure determination where conventional methods have failed, new phases, various forms of extended defects, and phase transformations.

Solid state chemistry is comprehensive in its concern. It deals, at the molecular level, with composition, structure, bonding, reaction characteristics, and thermodynamic properties of solids, as is typical of the chemistry of gases and solutions. In addition, and in particular, it is concerned with the properties of materials that derive from their solidness. For these materials three-dimensional structure and structural defects are at the root of their composition and properties. The range of

0–8412–0472–1/80/33–186–027$09.00/1

chemical variation is greatly enlarged in the solid state because of the relaxation of stoichiometry requirements, and hence from this fact is derived the possibility of infinite compositional variability and anisotropic reaction alternatives.

It would be difficult to overestimate the importance of exhaustive structural characterization. No one needs to be convinced of the value of an X-ray or neutron diffraction investigation, which reveals the repeating unit, hence the long-range order, in crystalline materials—this is the beginning of almost any study. However, the intimate details of the structure of real solids, including their defects and imperfections, greatly influence their chemical properties. Classical diffraction methods give limited information from such small regions of space; therefore, we must look elsewhere for a technique that yields this structural information.

Most chemists feel less at home in reciprocal space, since their view of structure involves the spatial configuration of atoms described in terms of the length and directions of chemical bonds or of displaced or moving atoms. In these terms the composition, structure, stability, reactivity, or mechanism of reaction are conceived in terms of literal models of atoms in fixed or transient positions. To the extent that this is true, an instrument that would magnify a region of space sufficiently and in a time frame compatible to human observation (so that individual atoms could be identified and located in space and followed as chemical changes occur) would be the ultimate instrument of chemical analysis. The high-resolution electron microscope (HREM) has this audacious potential. It is our purpose here to sketch, of necessity superficially, the present state of these techniques as they are used to illuminate solid state chemistry.

The advantage of direct visualization of the structure of real solids, including their defects, becomes apparent when one reviews the torturous path by which indirect methods yield uncertain identification of the principal defects in any material. One must not oversell HREM as a direct means of following the course of chemical reaction in solids, but the value of being able to visualize the types of defects and their juxtaposition in any material is enormous. The impact of HREM on our knowledge of structure and mechanism in solid state chemistry has been profound.

It has been more than a score of years since Menter (*1*) anticipated the elucidation of structure based on lattice imaging. His dream has been realized in large measure today when two-dimensional images capable of point-to-point intuitive interpretation at a resolution of 3.5 Å or better are being taken. The technique is flourishing both in practice and theory, expanding daily its range of application to solids. We will now qualitatively examine the methods of this technique in order to assess their

usefulness and limitations. This will be followed by a glimpse of diverse types of studies of interest to the solid state chemist. Finally, an attempt will be made to see directions the field might take in the immediate future.

HREM Imaging

Under favorable circumstances it is possible to image a crystal in two dimensions with a point-to-point resolution of about 2 Å. It has been possible to image crystals at a resolution of about 3.5 Å for the past several years using relatively inexpensive, commercially available instruments. It is to be hoped that within the next decade it will be routine to image crystals at about 1.5 Å. This means that, whereas now details of structure, including defects, are revealed microscopically at the subunit cell level (say, the level of coordination polyhedra), it should be possible to observe solids at the atomic level. Clearly these advances in technique have unfathomed significance for solid state chemistry.

For a thorough discussion of electron microscope imaging of crystal structures, the book "Diffraction Physics" by John M. Cowley is suggested (*2*). More abbreviated sources, such as Cowley (*3*), Allpress (*4*), Allpress and Sanders (*5*), Allpress et al. (*6*), and O'Keefe et al. (*7, 8*), should be consulted for references to the primary literature and for the detailed mathematical, experimental, and calculational details of microscopic imaging.

At present, most of the work being done is with conventional fixed beam high-resolution transmission electron microscopy (HRTEM) operating at 100 keV. These microscopes are direct analogues of optical microscopes: particles from an electron gun are accelerated and concentrated on the sample to be imaged. The effective size of the source is normally a few microns in diameter (*2*).

The resolution and contrast of the image are largely determined in the initial stage of magnification by the objective lens. Spherical aberration, which depends on phase retardation, increases very rapidly for beams diffracted at increasing Bragg angles. Lenses in common use have a spherical aberration constant of 1–3 mm, limiting the resolution to a few angstroms. This, rather than high-voltage or lens-current instabilities, is the principal limitation to resolution (*2*). Electromagnetic stigmators are adjusted to correct any astigmatism.

Electron microscopy is enhanced because of the ease with which both selected area electron diffraction and an image of the same region of a crystal can be recorded. Figure 1 illustrates both modes of operation of a typical three-lens magnifying system, using the symbolism of geometric optics. The region of the specimen to be viewed is bathed by the nearly parallel electron beam after it has passed through the condenser lens system. The scattered electrons from the specimen are

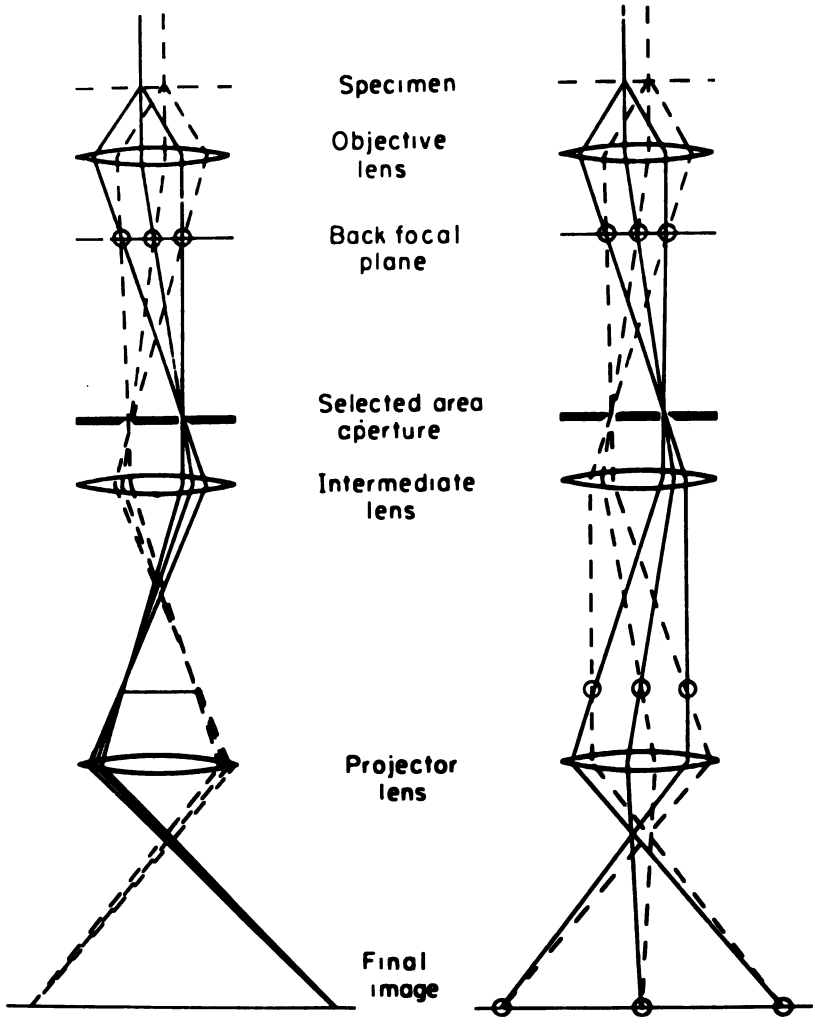

Figure 1. The ray paths in an electron microscope used (a) to produce a high-magnification image or (b) to produce a diffraction pattern of a selected area of the specimen.

focused on the back focal plane of the objective lens to produce the diffraction pattern. This is the first Fourier transform of the object. These electrons interfere again in the Gaussian image plane to produce an image. The amplitude distribution in the image is a Fourier transform of that in the back focal plane.

The focal length of the intermediate lens may be changed [as in Figure 1(b)] so that instead of the image plane the back focal plane of

the objective is imaged at the object plane of the projector lens, where it may be viewed on a fluorescent screen or photographed.

A small aperture placed in the image plane of the objective lens will select only part of the image to be magnified. Since a switch in the intermediate lens will not change the area selected in the aperture, the diffraction pattern produced in the diffraction mode will represent only the selected area. This selected area electron diffraction capability is of immense importance, especially with crystalline specimens, since it permits correlation of the diffraction pattern with the same region of contrast observed in the image. The minimum area selected is limited by the spherical aberration of the lens to regions about 0.5 μm in diameter at 100 keV.

The Formation of the Image. As indicated above, the image is formed by interference of the electron beams in the image plane of the objective lens. An objective aperture is used to select the diffracted beams that will be used to form the image. The aperture is important for two fundamental reasons. First, because the phase retardation of a diffracted beam varies as the fourth power of the angle of traversal of the lens (*5*), it is advanatgeous to limit the beams to those scattered at lower angles. Second, since there is a finite resolution of the microscope, contrast is improved if those beams are removed that are from interplanar spacings less than the resolution of the microscope and hence would simply contribute to the background.

If only one diffracted beam is included with the direct beam, interference will produce simply a set of fringes, which under suitable conditions will correspond to the set of planes in real space that give rise to the diffraction spot. More often, many beams are used with the direct beam to form a bright-field, two-dimensional image (*2*). In some instances it may be desired to exclude the direct beam and obtain an image only from interference of the diffracted beams producing a dark-field image. In this case a higher resolution has been observed (*9*).

Other Experimental Conditions. It is necessary to reduce contamination of the specimen as much as possible. This is accomplished by providing surfaces cooled to liquid nitrogen temperatures in the vicinity of the specimen. In some cases it is necessary to improve the vacuum, and this automatically reduces the rate of contamination.

In order to have images that can be interpreted intuitively, it is necessary to have specimens less than 100 Å thick. This is accomplished in any of several ways. Metals may be prepared in thin, evaporated, or sputtered films. Brittle, nonmetallic specimens may be prepared by grinding—sometimes at liquid nitrogen temperatures—producing fragments thin enough to be imaged. In any case, ion thinning may be used, and if the structural features of interest are not affected by this treatment, suitably thin specimens may be obtained.

The specimens are supported frequently on holey carbon grids, where a thin edge of suitable characteristics is found projecting over a hole in the support film.

For high-resolution imaging of crystals it is necessary to have a double-tilting specimen holder that can orient the crystal along any of several zone axes as desired.

In order to have good contrast in an image which is also interpretable, the correct aperture and thinness of crystal must be combined with a carefully adjusted focus. Usually this requires an underfocus of about 900 Å (*10*). Absorption produces no contrast in the Gaussian image plane if the aperture is unrestricted (*5*).

The Calculation of Images. In order for HRTEM to be useful in the determination of structure, the images produced, which are an array of light and dark spots, must be interpretable in terms of the type and location of the atoms in the specimen. Ideally the image would simply be a two-dimensional projection of the atomic arrangement, enabling the contrast to be interpreted intuitively (Figure 2). Under carefully controlled conditions of specimen and microscope, this has been found to be possible (*10*).

Satisfying all these conditions is more limiting than is desirable, and one would like to be able to use image contrast where these stringent requirements are not fully met. Such images are not interpretable with confidence in terms of atom positions unless they can be shown to agree with calculated images over a range of conditions (*8*). Therefore, it is necessary to calculate images that correspond to the orientations and thicknesses of the specimen of known or postulated structure and compare these with those observed. In order to make the calculations the conditions of focus of the microscope must have specified values, and the beam divergence, aperture size, and spherical aberration constant must be known (*8*). Even if the details of structure cannot be determined with assurance, the characteristics of the image allow unequivocal identification with a particular phase. For most chemical studies this information is enough, and it cannot be obtained in other ways.

Computer packages now have been developed that enable image calculations to be made based on *n*-beam multislice dynamical theory (*8, 11*). These calculated images are necessary to the interpretation of observed images, as will be illustrated below.

High-Voltage HRTEM. The optimum resolution of a microscope is given by the equation

$$d = 0.6\lambda^{3/4}C_s^{1/4}$$

where d is the half-width of the spread function, λ is the wavelength of the electron, and C_s is the spherical aberration coefficient (*2, 3*). Good,

M. C. Escher's Eight Heads,
Escher Foundation—Gemeentemuseum—The Hague

Figure 2. A print by M. C. Escher showing about one and a half unit cells. Light and dark patches are intuitively interpretable in terms of the elements of the structure. Even out of focus, the relative distances and symmetries are preserved. The more perverse will find satisfaction in viewing it upside down (31).

stable, high-voltage supplies now can be made and used with very stable lens currents, so that it should be possible to increase the resolution by decreasing λ, that is, by going to high-voltage electrons. At 500 keV one expects to obtain 1.7 Å point-to-point resolution.

There are several advantages to using high-voltage microscopes such as the ability to study specimens three or four times as thick with the same ease of interpretation as in 100-keV machines. Contrast will be enhanced by a factor of two or three, with the same clarity and with less damage due to inelastic scattering. The principal advantage for the chemist, however, will be the possibility of fitting controlled atmosphere specimen stages in the much larger microscope lens channels. The more penetrating electron beam will be less affected by the thin gaseous environment provided for the specimen at equilibrium. A resolution of atoms

conjures up the not impossible feat of observing the transport of atoms in crystals. This should also advance the capability of determining structure by direct imaging.

The results of 1-MeV microscope studies of several materials and the instrument itself have been described by Horiuchi and his co-workers (*12, 13, 14*). The resolution improvement over 100-keV instruments is dramatic. With a 2-Å resolution, one can virtually resolve the atoms at the tetrahedral sites between the crossed shear planes in the block structure $Nb_{12}O_{29}$. However, these instruments are extremely expensive and will require a great deal of development before they become as practically useful as the 100-keV instruments.

Applications of HRTEM to Solid State Chemistry

The development of the field of electron microscopy is of enormous significance to the solid state chemist. It is amazing to contemplate that all the high-resolution studies ever made have examined only about 1 mm^2 of specimen area with a mass of about 0.2 μg of material. There is a lot more to be seen! Even with this small mass, studies have included the observation of ultrastructure and defects in a great variety of mineral specimens (*15*), carbon in many forms including diamond, graphite, and even single-atom-thick sheets (*16*), and a wide range of crystalline and noncrystalline inorganic solids (*17*).

We will discuss here only two types of studies on crystalline oxides. The first includes examination of many structural types and defects in ReO_3-based crystals (most work has been done on these almost ideally suited materials) and the second includes studies of the fluorite-related binary rare earth oxides to illustrate the value of the technique in a more ordinary but less well suited crystal type.

Structures Based on the ReO_3 Structure Type—Region of Crystallographic Shear. The ReO_3 structure is one of the easiest to visualize. It consists of metal atoms octahedrally coordinated with oxygen in which all corners of the coordination octahedra are shared in three directions. This cubic network has the same appearance projected along any of the principal axes—that is, metal-filled octahedra in square outline with alternate squares unfilled in a checkerboard fashion. The unfilled squares are elements of square tunnels in all three directions. The unit cells of these related structures are one coordination octahedron thick (about 4.8 Å) and frequently quite large in the other directions; hence they are almost ideal subjects for high-resolution study.

The investigations we will discuss involve reduced WO_3 sometimes containing Mo or Nb. Nb is the most common metal in the highly reduced materials investigated. The oxides near MO_3 in composition

have defects called crystallographic shear (CS). Those of intermediate composition have defects involving octahedra that have sheared in a cylindrical fashion, providing pentagonal tunnels along the axis of shear. The most reduced oxides are sheared in two directions. All these materials preserve the octahedral coordination of the metal atoms by increasing edge sharing of the coordination octahedra as the metal-to-oxygen ratio is increased by reduction.

CS in WO_3 has been studied by Iijima (*18*) and is idealized in Figures 3(b) and 3(c). Figure 3(b) shows a projection of ReO_3 along the *c*-axis. Imagine removal of all oxygens in a (210) plane and closing the structure to regain the same oxygen structure by a shearing action 1/2 [110]. Such an operation is represented by $(210)1/2[1\bar{1}0]$. This is the creation of a Wadsley defect (*19*). Figure 3a is a high resolution micrograph of such a Wadsley defect (*18*). The main features are unmistakable even though the real edge-sharing octahedra are considerably distorted. Iijima found that under other than optimum imaging conditions, the detail is not so evident. Nevertheless, the defects are easily recognized, and their formation and deployment in this structure can be observed.

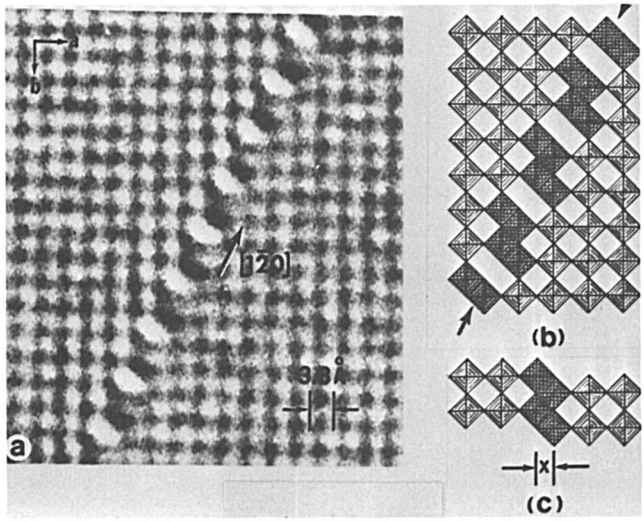

Figure 3. (a) High-resolution electron micrograph of a $WO_{3-\delta}$ crystal obtained with the electron beam incident parallel to the c*-axis. A prominent feature of the contrast shows the $(2\bar{1}0)$ CS plane, across which square arrays of the dark dots (indicating W atom positions) are shifted. The contrast distributions are in good accordance with the idealized model of the (210) CS plane (b). However, the image showed that edge-sharing octahedra (shaded) are considerably distorted, so that the distance* X *of (c) is much larger than in the ideal model* (18).

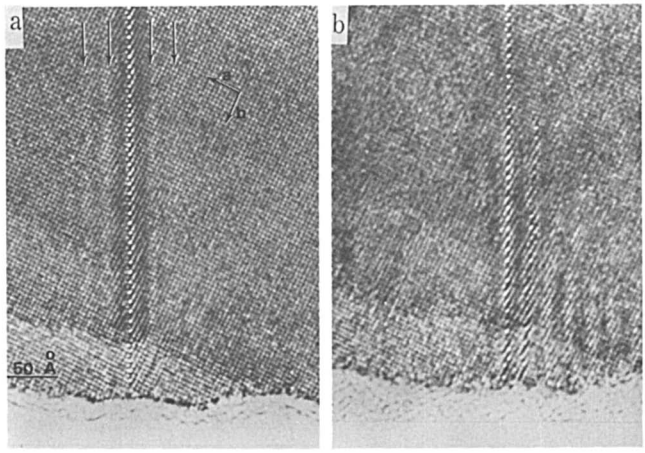

Journal of Solid State Chemistry

Figure 4. (a) Oscillatory dark and light contrast bands running parallel to the CS plane on both sides. (b) With further electron beam irradiation, new CS planes develop with the same periodicity as that of the oscillatory contrast in (a) (18).

There is a clear premonitory behavior before the CS planes develop during electron irradiation [Figure 4(a)]. This manifests itself as waves of contrast variation of a regular spacing, which then develop into CS defects parallel to an original defect [Figure 4(b)]. This appearance of linear parallel lines of blotches of contrast along the [102] direction indicates early stages of development of the shear planes. These dark strain fields disappear when the shear occurs. As Wadsley defects increase in concentration, they tend to become parallel and to purge themselves of kinks, which appear frequently in the early stages.

This behavior is consistent with aggregation of oxygen vacancies on a disk, surrounded by partial dislocations, which can expand and move longitudinally as suggested by Anderson and Hyde (*20*).

Iijima observed only (210) and ($2\bar{1}0$) CS planes in material reduced at 1022°C. There were no planes observed in the [010] zone. On the other hand, during electron beam heating, CS occurs on (201) and ($20\bar{1}$). This anisotropic behavior is considered to be due to the distortion of monoclinic WO_3 structures from the cubic ReO_3. The distortion is a function of temperature, as are the preferred directions of shear. In no case were (102) planes preferred.

THE REGION OF THE TETRAGONAL TUNGSTEN BRONZE TYPE OF STRUCTURES. Iijima and Allpress (*21, 22*) clarified the nature of structures and defects in WO_3 containing pentavalent cations (Nb) in considerable concentration, together with the concomitant oxygen deficiency.

In these structures, as in ReO_3, only corner sharing of coordination octahedra occurs, but columns of four or more strings of octahedra shear cylindrically along *c* such that when corner sharing is reestablished, triangular and pentagonal tunnels have been created along the periphery of the shear surface. The tunnels can be filled by strings of —Nb—O—Nb— in ordered ways to generate a variety of superstructures. Figure 5 illustrates these phenomena in tetragonal tungsten bronze (TTB), $4Nb_2O_5 \cdot 9WO_3$ and $2Nb_2O_5 \cdot 7WO_3$.

The various TTB-like elements may occur individually as extended defects, be ordered into a definite structure, or be intergrown with the WO_3 matrix to accommodate any composition. This is observed as clearly shown in Figure 6, where regions of $4Nb_2O_5 \cdot 9WO_3$ are separated by

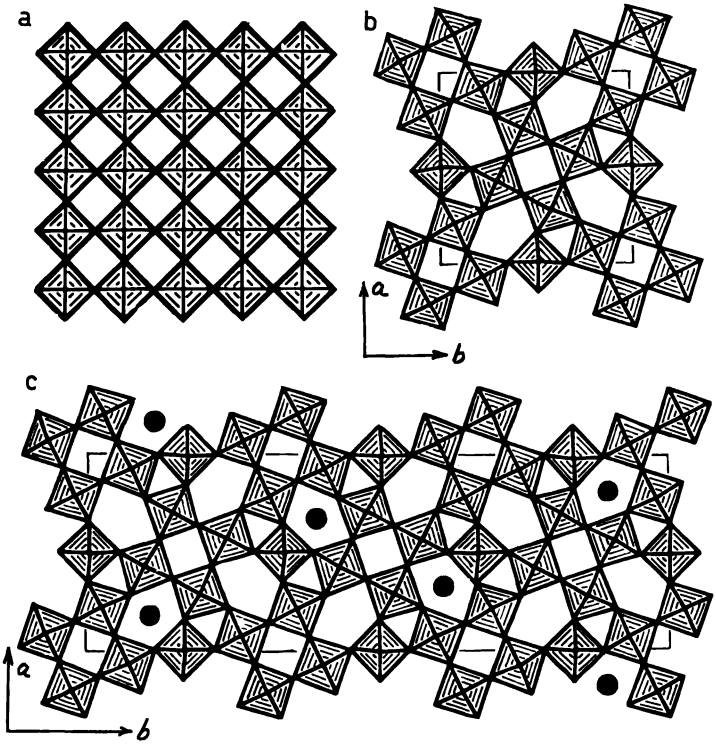

Acta Crystallographica

Figure 5. Structural elements encountered in the binary system $Nb_2O_5 \cdot WO_3$. Each hatched square represents an MO_6 octahedron, which shares its corner oxygen atoms with neighboring octahedra to form a lattice of composition MO_3. (a) The cubic ReO_3 structure. (b) The host lattice of the tetragonal tungsten bronze (TTB). (c) The structure of $4Nb_2O_5 \cdot 9WO_3$ contains three TTB subcells, and the superlattice is a consequence of the ordered occupation of one-third of the pentagonal tunnels by –O–M–O–M–O– strings parallel to c *(filled circles)* (21).

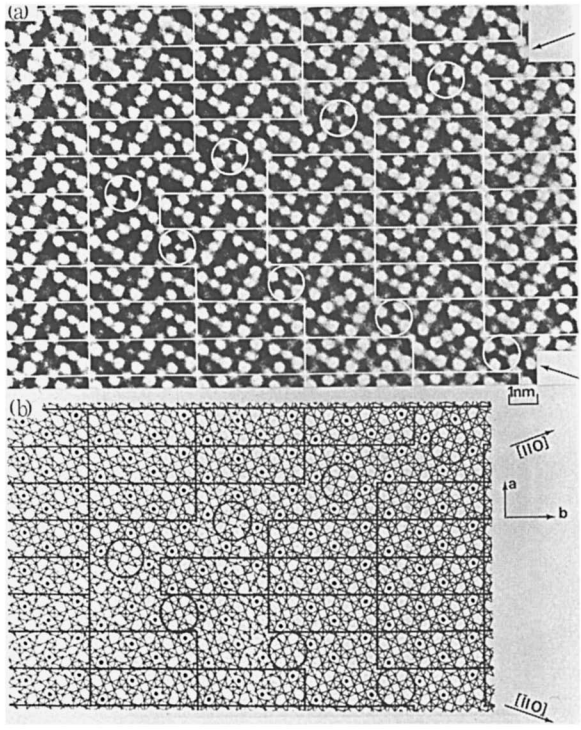

Acta Crystallographica

Figure 6. (a) Lattice image from a crystal of $4Nb_2O_5 \cdot 9WO_3$ containing a zigzag, out-of-phase boundary (marked with arrows). Rectangles outline the unit cells of the ordered structure, and circles within the boundary mark TTB subcells in which all four pentagonal tunnels are empty. The presence of the boundary causes a displacement of 1/3 [010] in the ordered structure. (b) Model of the boundary structure, derived from the contrast in (a). The host lattice of the corner-shared octahedra is continuous, but the pattern of occupied tunnels (full circles) is interrupted at the boundary (21).

a zigzag, out-of-phase boundary. The correlation between the thin crystal image contrast and the structure is clearly shown.

It has been possible from these studies to explore the composition limits of each phase by observing directly the occupancy of the tunnels when phase separation occurred. It has been possible to see a variety of intergrowth patterns, and it has been possible to determine new structures by direct observation.

The Block Structures. If the oxygen deficiency is further increased by continued increase of Nb^{5+} ions, the ReO_3-related structures switch once more into a different regime. .In this case the crystallographic shear characteristic of the moderately reduced WO_3 occurs in two directions

to give infinite columns of ReO_3 structure of small dimensions in two directions shifted with respect to each other along the column such that edge sharing occurs at their boundaries.

Figure 7 (23) gives a schematic representation of the idealized block structure of the polymorph H–Nb_2O_5 both as a projection of edge- and corner-sharing octahedra and as an abstract representation showing only the blocks and the columns of tetrahedrally coordinated Nb atoms. Notice that 3 × 4 octahedral columns are regularly interspersed with 3 × 4 columns sheared and shifted one-half an octahedral distance to permit edge sharing.

In Figure 8 (23) a thin crystal, which is primarily of the H–Nb_2O_5 structure, is interrupted by a fault in which two 3 × 4 columns are intergrown. This is similar to a stacking fault of layers of atoms. Notice that the apparent reduction resulting in increased edge sharing has been accommodated in a most ingenious way, preserving the octahedral coordination of most of the metal atoms.

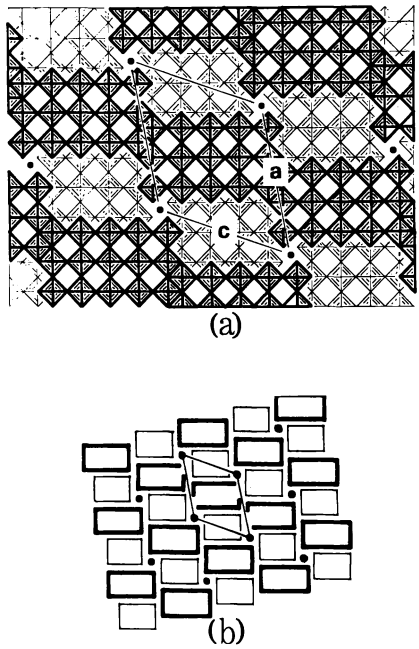

Acta Crystallographica

Figure 7. (a) Idealized model of the structure of H–Nb_2O_5 and (b) its simple representation. The darker and lighter squares, which form 3 × 5 and 3 × 4 blocks by their corner sharing, are centered about the two levels perpendicular to the b*-axis and are 1.9 Å apart. The black circles represent the tetrahedrally coordinated Nb atoms. The unit cell is outlined (*a = 21.2, b = 3.8, c = 19.4 Å *and* $\beta = 120°$*) (23).*

Published on June 1, 1980 on http://pubs.acs.org | doi: 10.1021/ba-1970-0186.ch002

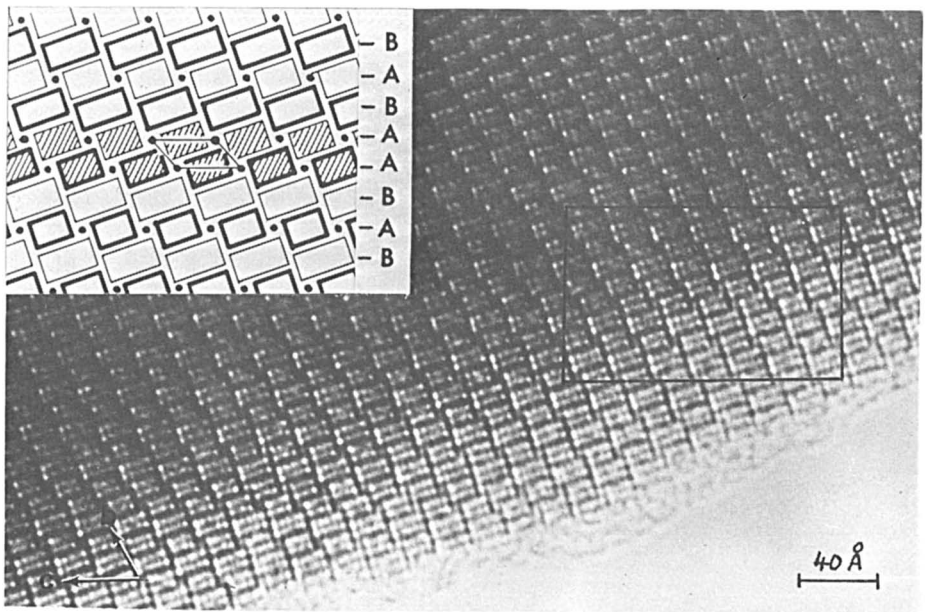

Acta Crystallographica

Figure 8. Two-dimensional lattice image of $H–Nb_2O_5$ showing defects parallel to the c*-axis. Inset corresponds to the enclosed area* (23).

The studies so far illustrated have established that when a suitable crystal is viewed in a high-resolution microscope with the appropriate orientation and with the correct adjustment of the electron optics and physical choice of reflections, an image is obtained that can be interpreted intuitively in terms of the two-dimensional projected potential of the crystal. Furthermore, this high-resolution image reveals defects when they occur beyond the point-to-point resolution, which is usually 3.5 Å or better in microscopes presently available.

Beyond the rather two-dimensional defects just discussed, it has been possible to observe point defects in some of these block structures. Such defects have been described, for example, by Iijima et al. (*24*). In Figure 9(a) a point defect is clearly shown in the 3 × 4 block structure of $Nb_{12}O_{29}$, where a white spot indicating one of the square tunnels is replaced by a black spot, resulting from a shift in the atomic positions. Figure 9(b) gives their interpretation of the anatomy of the defect—two displaced interstitial metal atoms and two excess oxygen atoms. Figure 9(c) shows the locations of the displaced metal atoms in the perfect structure, suggesting that the defects could be annealed out (or produced in rare cases) by heating with the electron beam. That this is true is illustrated in Figure 10, where in the sequence (a), (b), (c), defects appear and, more often, disappear as a function of time irradiated in the electron beam. STATES OF AMERICA

The point defects are thought to be due to only a few atoms and not to a few columns of atoms. Furthermore, the defects could be ascribed

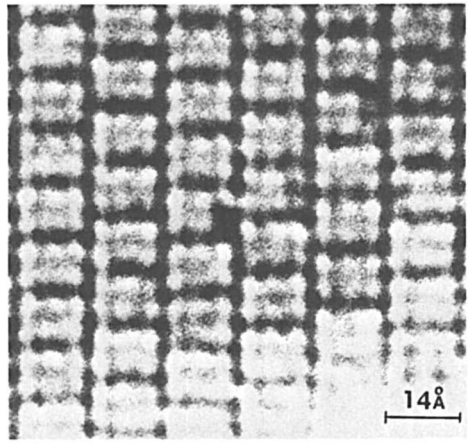

Acta Crystallographica

Figure 9a. Enlarged image of the black spot appearing in Figure 10(c). The position of the spot corresponds to one of the 2 × 3 channels in a block (24).

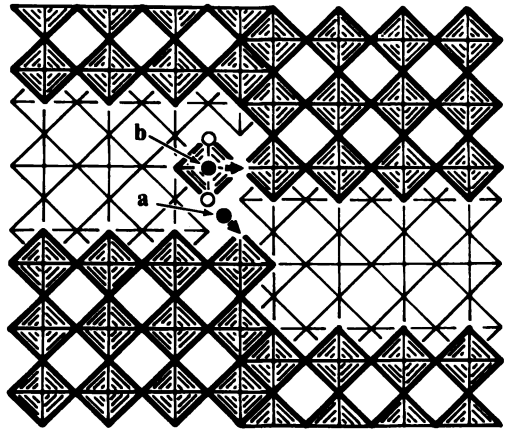

Figure 9b. A proposed model for the point defect derived from the image of Figure 9a. The point defect is a complex composed of two interstitial metal atoms (indicated by a and b) and two oxygen atoms (○) (24).

entirely to the oxygen excess in the original crystal; hence, as the oxygen is lost by heating in the microscope, the defects disappear. Detailed calculations should be made to bolster such more or less intuitive interpretations of the nature of observed defects. Such calculations were made by Skarnulis et al. (25) for the contrast in the vicinity of the rows of tetrahedral metal atoms in the block structures, with quite unexpected results. They found that dark contrast in the tetrahedral positions does not necessarily imply an excess of metal there but rather small shifts of atoms in adjacent octahedral positions.

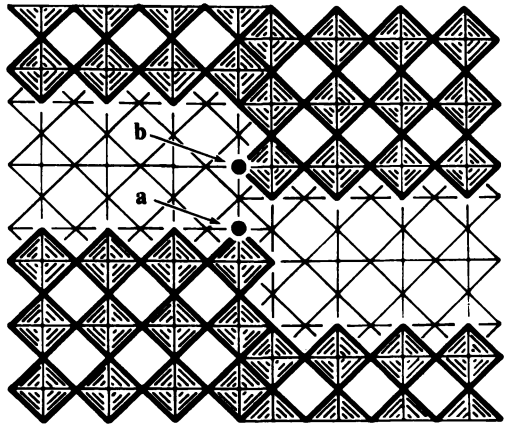

Figure 9c. Perfect structure corresponding to the one in Figure 9b (24)

HRTEM on Fluorite-Related Structures. As has been pointed out, HRTEM techniques are best applied to crystals whose interesting structural relationships are shown in projection when viewed along a very short axis. This is true both in theory and practice. The systems of ReO_3-related structures discussed so far are nearly ideal in this respect, and they have revealed the intimate details of their structural relationships and imperfections in a shameless way. We now demonstrate the use of HRTEM on a more common type of structure, which does not have a very short axis in one direction with large dimensions in the other two and hence strains the assumptions of the present calculational abilities and the capabilities of the microscope. For this purpose we review work done on the rare earth oxides, which are fluorite-related systems.

The structures of intermediate phases in the fluorite-related rare earth oxides had been studied by conventional diffraction means and by indirect means, such as electrical conductivity and the pressure dependence of composition, for many years without approaching a satisfactory understanding of the structural basis of the homologous series of intermediate phases. For an understanding of the chemistry of any material, the structural principle relating distinct phases and the nature of the

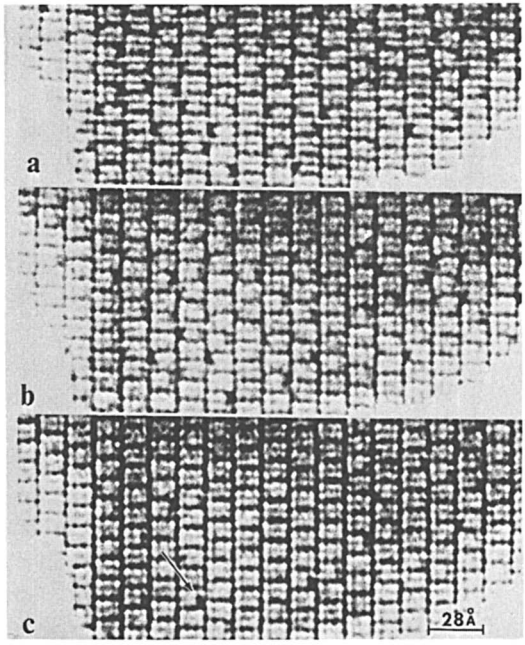

Acta Crystallographica

Figure 10. (a, b, c) Series of pictures taken at several-minute intervals, showing the effect of electron irradiation on the black spots (24)

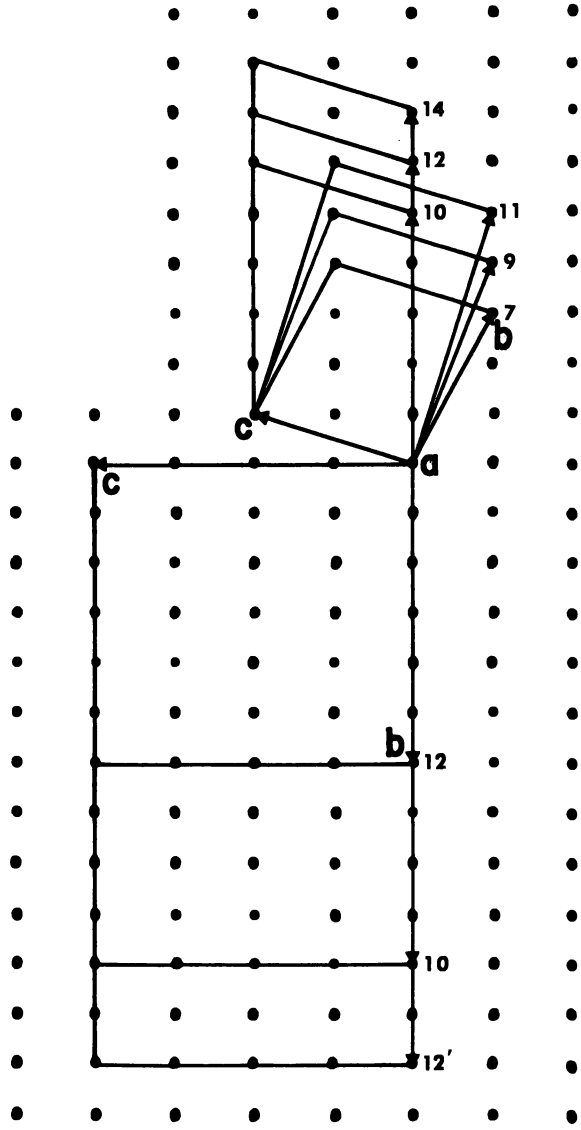

Journal of Solid State Chemistry

Figure 11. Projections of the unit cells of the fluorite-related homologous series of the rare earth oxides along the common a*-axis,* $[2\bar{1}1]_F$. *Notice that the unit cell of monoclinic 12 is obtained by twinning the primitive 12 about (110) and that 12′ is formed when 12 is further twinned about (011). The monoclinic unit cell of 10 is formed analogously to 12′ from the primitive 10. The monoclinic unit cells all have a common* ac *plane, different from that common to the primitive unit cells* (26).

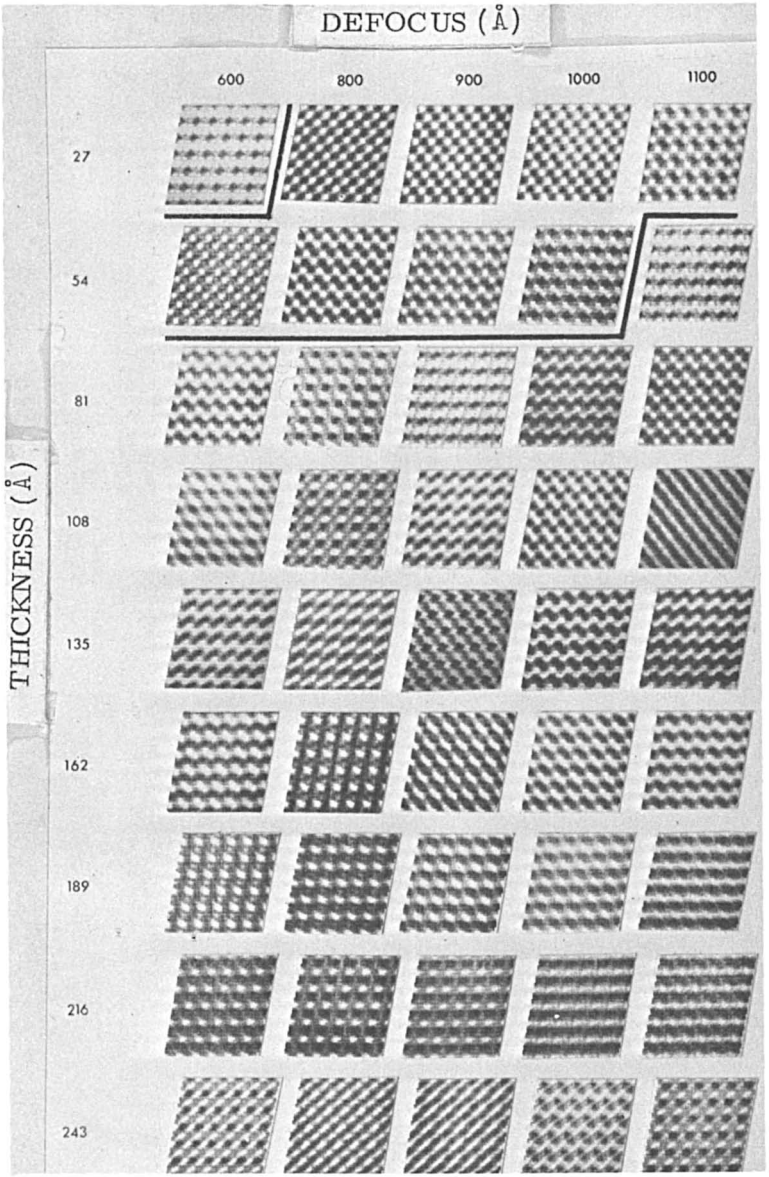

Journal of Solid State Chemistry

Figure 12. Calculated n*-beam crystal structure images for the* $\langle 100 \rangle_7$ *zone of* Pr_7O_{12}*. Calculations were made with atomic-scattering factors (6 × 6 unit cells). Notice that the image at 27-Å thickness and 900-Å underfocus is a projection of the actual arrangement of two columns of oxygen vacancies per unit cell. A similar image recurs at about 135-Å thickness. The other most prevalent image has one spot per unit cell and, although unequivocably recognizable, does not correspond to the projected potential* (11).

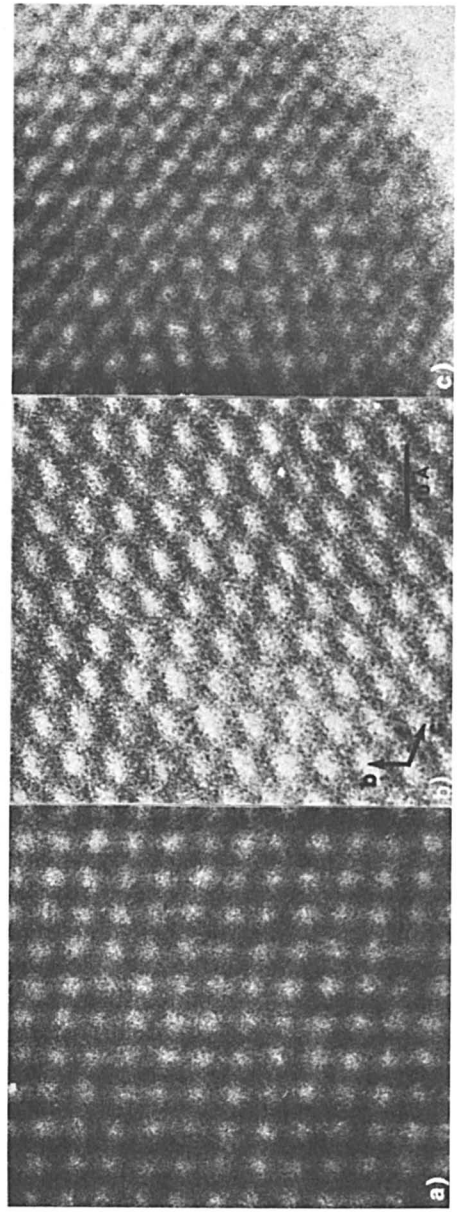

Journal of Solid State Chemistry

Figure 13. Observed $\langle 100 \rangle_7$ image of Pr_7O_{12} and $Zr_3Sc_4O_{12}$. (a) A typical image of Pr_7O_{12} with one spot per unit cell. (b) A thick image of Pr_7O_{12}. (c) A thin-crystal image of $Zr_3Sc_4O_{12}$, showing the vacancy arrangement on the right-hand side (11).

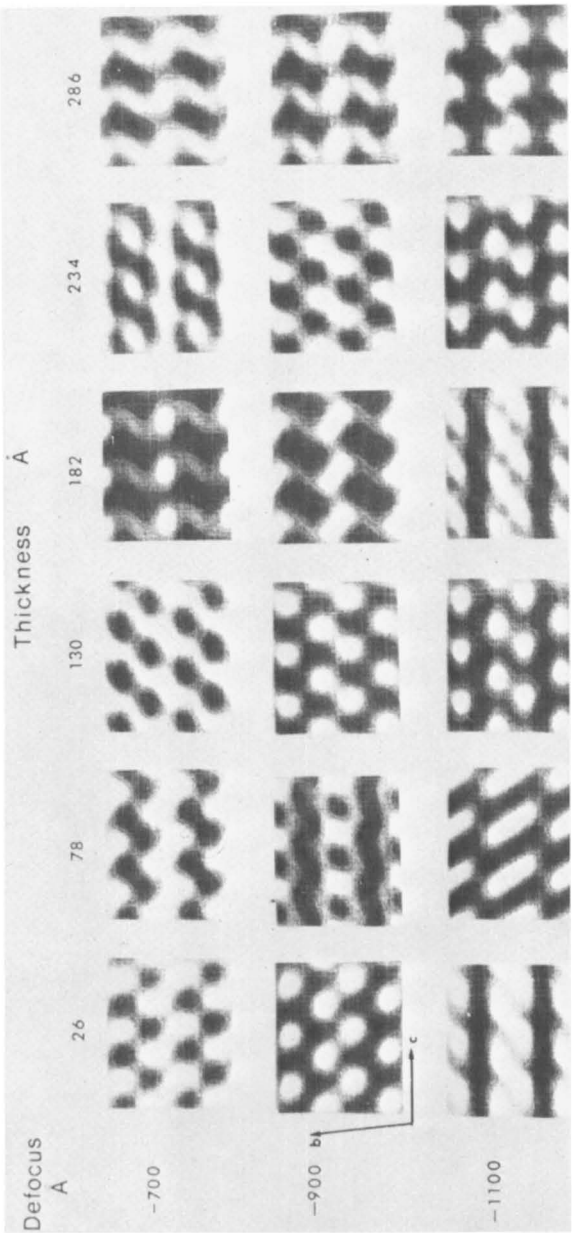

Figure 14. Calculated n*-beam crystal structure images of the proposed model of zeta-phase Pr_9O_{16}. At 900-Å underfocus the images at 26-Å and 130-Å thickness correspond to the projected potential (28).*

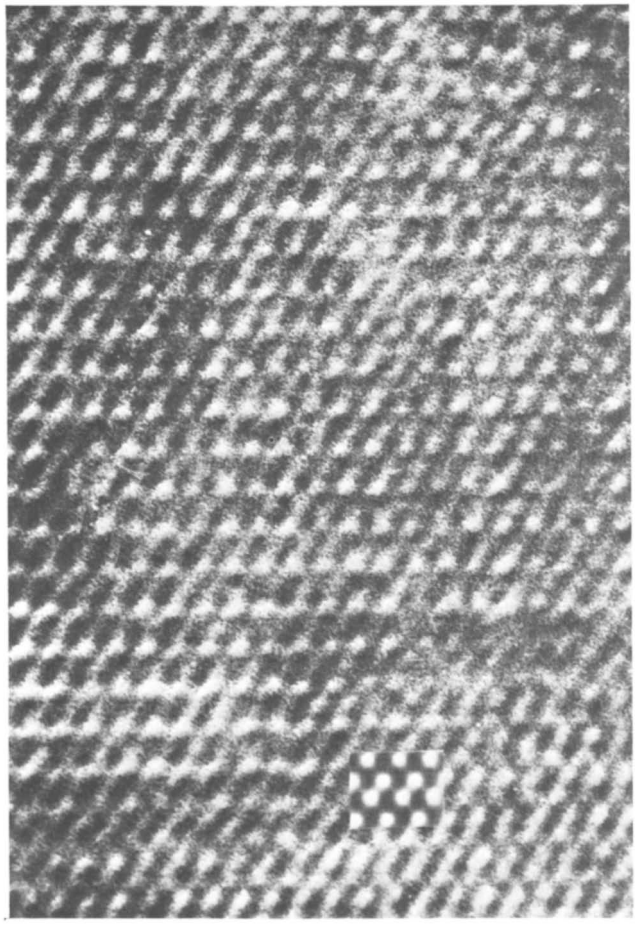

Figure 15. Observed $\langle 100 \rangle_9$ image of Pr_9O_{16}. Inset shows the correspondence of the image to that calculated for a thin crystal (28).

isolated defects involved in any associated chemical change must be delineated. Sustained efforts to get this information had been only marginally successful before HRTEM was applied.

THE INTERMEDIATE PHASES. Compositionally, the higher oxides of the rare earths (Ce, Pr, and Tb) had been shown to belong to a homologous series R_nO_{2n-2}, with R meaning rare earth, and n an integer, $4 \leq n \leq \infty$ ($n = 4, 7, 9, 10, 11, 12, \infty$ known). Except for hexagonal Ce_4O_6 and Pr_4O_6 (high temperature), all the phases were known to be fluorite-related, but determination of their true unit cells had been impossible. The problem stemmed mainly from the difficulty in growing single crystals of suitable size and perfection without unmanageable

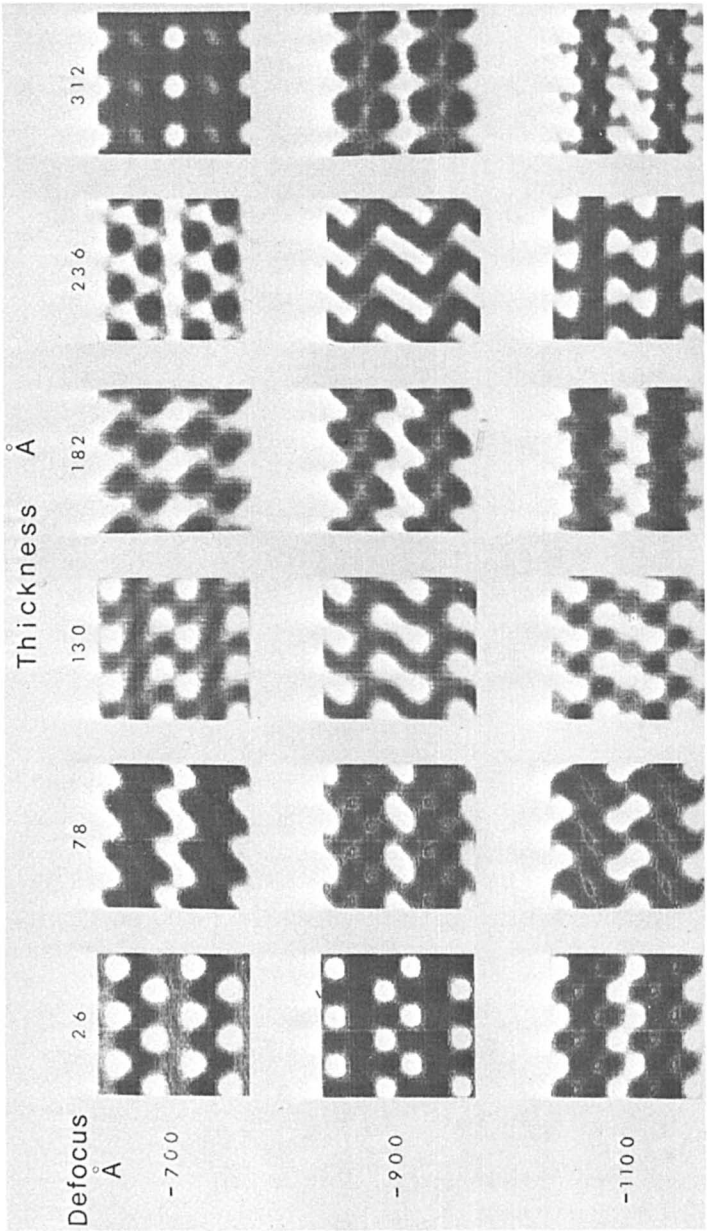

Figure 16. Calculated n*-beam crystal structure images of the proposed model of delta-phase* $Tb_{11}O_{20}$. *The image at a thickness of 26 Å at 900-Å underfocus corresponds to the projected potential of the proposed structure* (28).

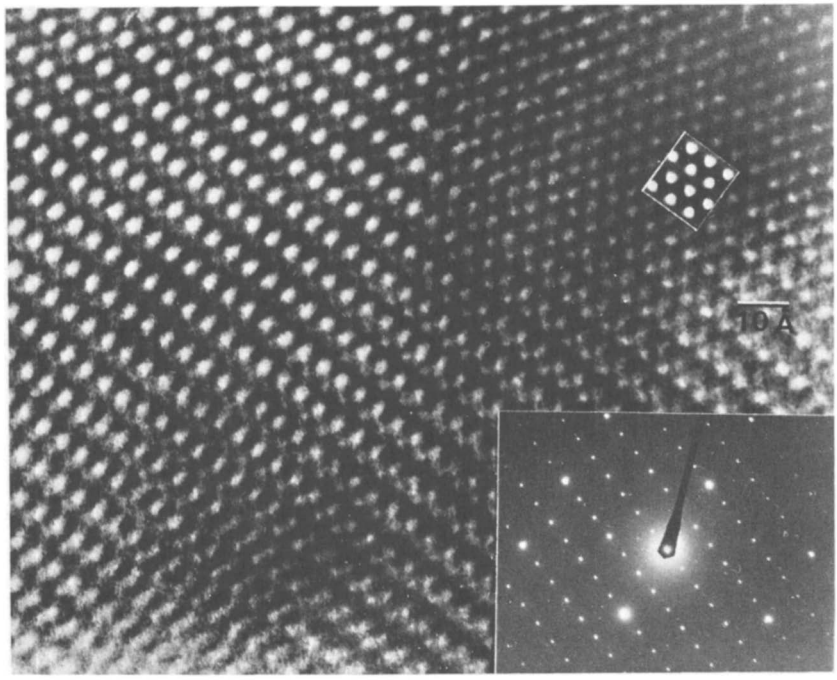

Figure 17. Observed image of $Tb_{11}O_{20}$. There are clearly two spots per unit cell corresponding closely to the proposed structure (inset is calculated thin-crystal image) (28).

twinning. The electron microscope is quite capable of examining thin crystals 1 μ^2 in area, which are typically untwinned and quite suitable for observation.

A study of all the then-known phases in the PrO_x and TbO_x systems were made by Kunzmann and Eyring (*26*), using electron optical techniques. This study revealed the unit cells of all the established phases and suggested a structural principle for the odd members of the series. The researchers found that if the crystals were viewed down their *a*-axis (in the $\langle 21\bar{1} \rangle_F$ zone, where F stands for fluorite indices), they exhibited a regularly varying projection profile, as illustrated in Figure 11. This indicates that the *a*-axis is common to all the homologous series, and in that limited sense it is the largest fluorite defect feature that all phases have in common.

Further examination reveals, however, that the series is dichotomous with the odd-*n* group characterized by a common *ac* plane and the even members also with a common but different *ac* plane. That is, the odd members also have a *c*-axis in common, and the even members a common but different *c*-axis. Indeed, the even members are formed by

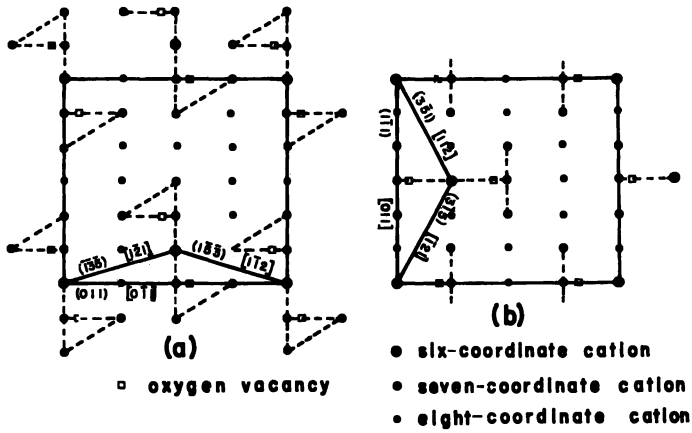

Figure 18. Projection in $\langle 21\bar{1} \rangle_F$ *of two possible structures of* $Pr_{24}O_{44}$ (n = 12). *(a) Model with P1 symmetry. (b) Model with Pm symmetry* (29).

twinning a primitive cell, related to the odd members (and shown in Figure 11), at the unit cell level, giving a folded defect feature whose folds are related to the *ac* planes of the odd members. This *ac* plane is characterized by having all the metal atoms it contains six- (rather than seven- or eight-) coordinated with the two vacant oxygen positions across the body diagonal of their coordination cube at an angle of 73° to the *ac* plane. Therefore, the largest feature in common to all the phases is this *ac* plane, which, in the even members, is folded in a zigzag way.

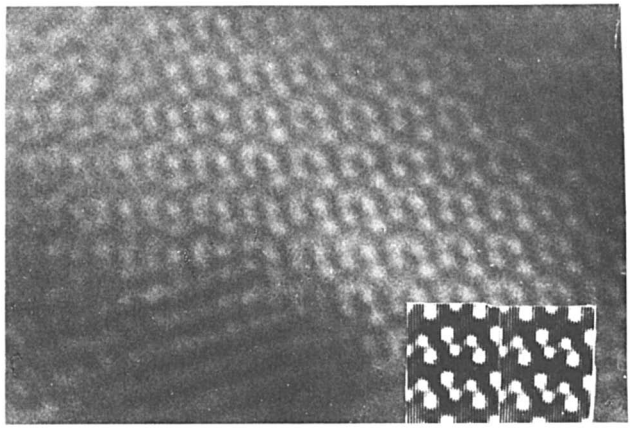

Figure 19. Crystal structure image in $\langle 21\bar{1} \rangle_F$ *of a thin crystal of* $Pr_{24}O_{44}$. *The inset is a calculated image from the P1 structural mole, Figure 18* (29).

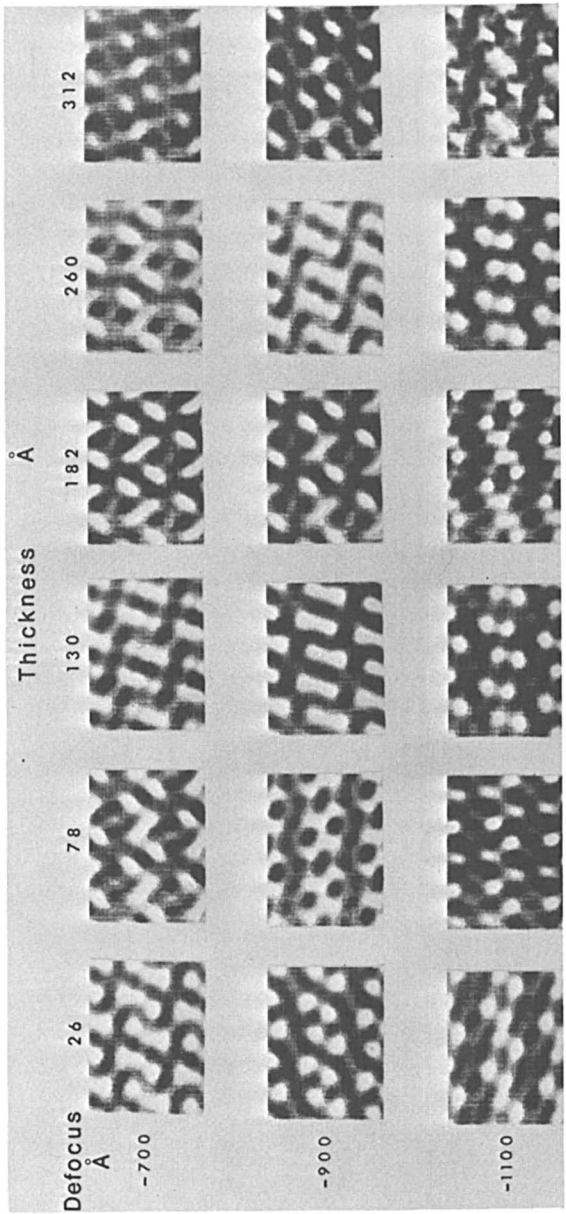

Figure 20. Calculated image for $Tb_{24}O_{44}$, a polymorph of $Pr_{24}O_{44}$. Notice the shift in the rows of undulating oxygen vacancy pairs in the images at a thickness of 26 A and a 900-A underfocus with respect to the inset of Figure 19 (28).

The structure of Pr_7O_{12} has been determined by total profile analysis of neutron powder diffraction data. This has served as the basis of prediction of metal atom shifts in the trial structures (*27*).

From observed and calculated high-resolution images, it has been possible to determine structures for the odd members Pr_7O_{12}, Pr_9O_{16}, $Tb_{11}O_{20}$ ($Pr_{11}O_{20}$ is observed to have a quite different and very large unit cell). The calculated and observed images are given in Figures 12–17. The study of Pr_7O_{12} was done by Skarnulis et al. (*11*), while that of Pr_9O_{16} was made by Tuenge and Eyring (*28*), and $Tb_{11}O_{20}$ was studied by Kunzmann and Eyring (*26*) and Tuenge and Eyring (*28*). In the case of Pr_7O_{12}, whose structure is known (*27*), the resolution of the microscope is not quite sufficient to separate the rows of vacancy spots that are calculated for thin crystals and that recur at greater thicknesses. These rows of vacancies are clearly resolved, however, in the higher members, and there is satisfactory agreement between calcu-

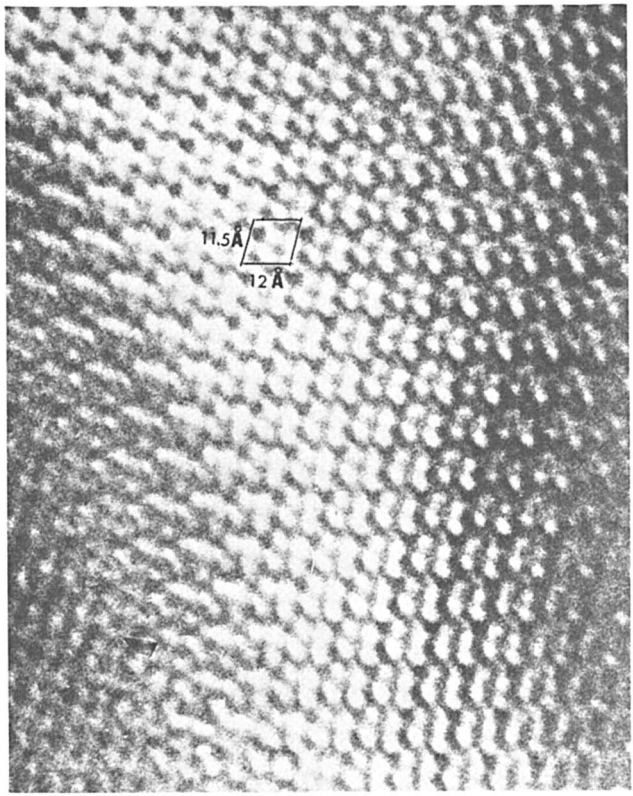

Figure 21. Observed crystal structure image of $Tb_{24}O_{44}$, calculated in Figure 20 (28)

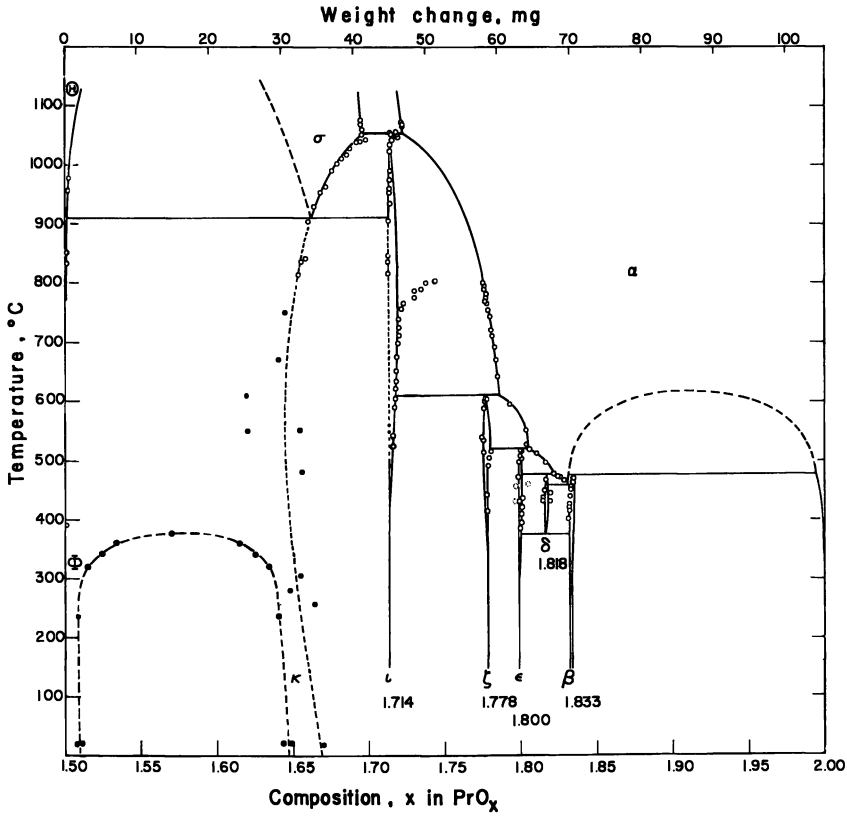

Figure 22. Phase diagram of the PrO_x–O_2 system. Prominent features are the homologous series R_nO_{2n-2}, $4 \leq n \leq \infty$, and two nonstoichiometric phases α and σ.

lated and observed images. There remains little doubt that the proposed structures of the odd members are correct.

The proposed projected structure of the even member phases may be suggested by that for β phase ($Pr_{24}O_{44}$). The proposed structure is shown in Figure 18 (29), in which the folded planes similar to those for the odd members are apparent. Figure 19 (29) shows an observed image with the calculated image as an inset; the agreement is rather good. The structures for the $n = 12$ members for $Tb_{12}O_{22}$, of which there are several, are different. One of them, calculated and observed, is shown in Figures 20 and 21 (28). Notice that there is only a subtle difference between these two structures. They have the same volume and hence the same vacancy density. The vacancies occur in undulating pairs along the $[110]_F$ direction, but in one case one sheet is shifted along $(110)_F$ with respect to the next.

It should be repeated that in the past it had not been possible to sort out these structures by using the conventional methods of X-ray and neutron diffraction, but HRTEM has yielded a great deal of very specific information. The complexity of the system is remarkable. Virtually all the higher oxides belong to the compositional homologous series RE_nO_{2n-2}, and apparently all with $n \geq 7$ have very similar defect structures, differing only by the spacing of planar defect features, yet the only isomorph in the three series is R_7O_{12}. For example, for $n = 12$ the one polymorph seen so far in the PrO_x system is different from any of the three or more seen in the TbO_x system.

HRTEM in the Study of Phase Reactions. It is clear by now that HRTEM can be used to get structural information on a variety of phases. In this case the specimen and microscope conditions must be known and controlled very carefully. In many other cases, however, where the structures are known, unknown, or immaterial, the phases, phase relationships, and the intergrowth characteristics are clearly identifiable by the cell parameters or symmetry characteristics, which are revealed by the intensity distribution in the image but which do not correspond to the array of the charge density of the crystal. It is probable that the contribution of HRTEM to solid state chemistry will be greatest in these

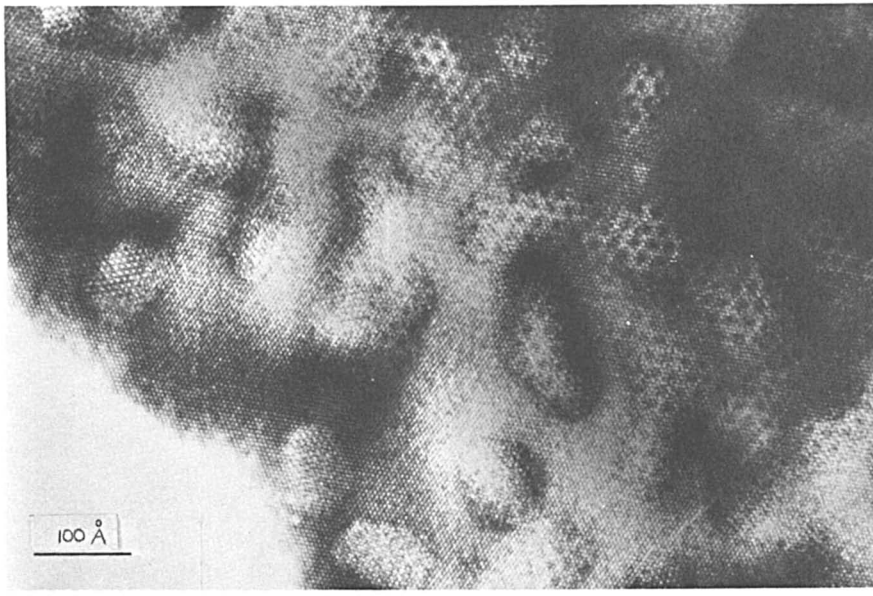

Figure 23. Image of $Zr_{0.29}Sc_{0.71}O_{1.64}$ in the $\langle 111 \rangle_F$ zone. Notice domains of the n = 4 phase about 70 Å across imbedded in a matrix of an n = 7 phase. The large hexagonal pattern is due to an overlay of the two phases in perfect register.

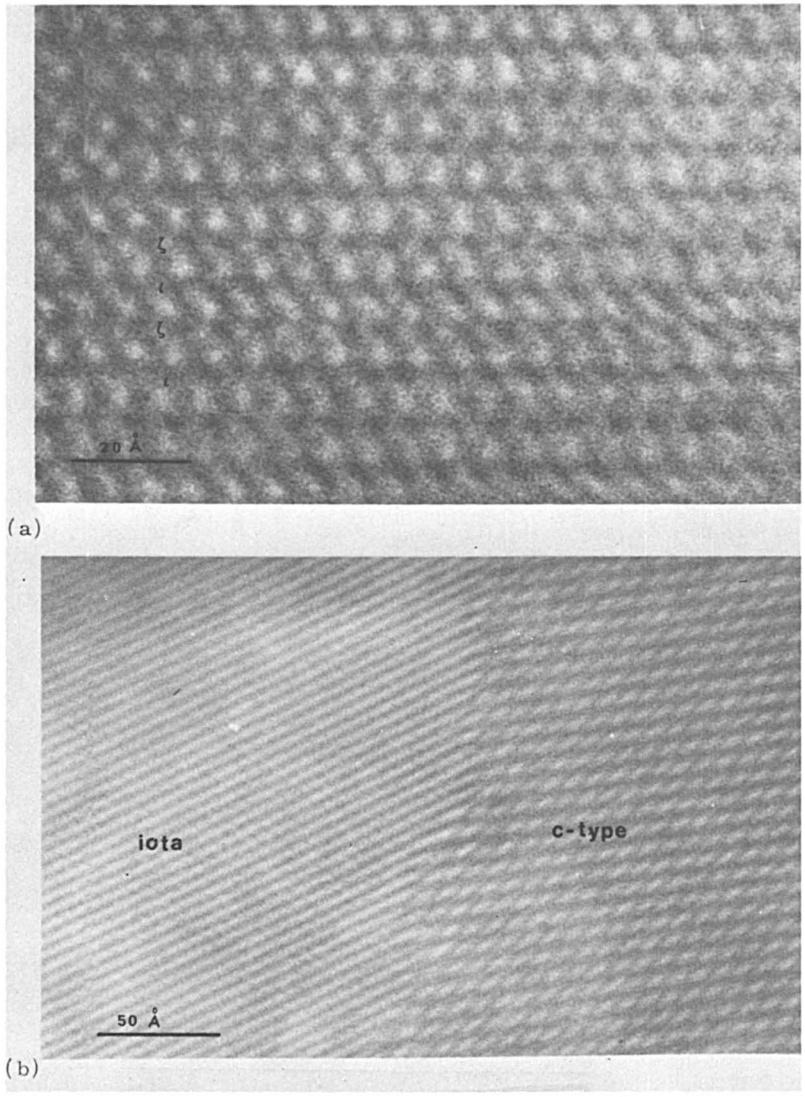

Figure 24. Image of intergrowths of members of the homologous series. (a) Lattice image from $\langle 100 \rangle_9$, showing intergrowth with iota. Domains of n = 4 *with* n = 7 *phase. Notice the thinness of the interface between these phases of different structures. (b) $\langle 111 \rangle_F$ lattice image, showing a domain of Pr_9O_{12} in a crystal that is largely sigma phase. An intimate intergrowth between* n = 7 *and* n = 9 *phases. These phases are perfectly coherent, having the same* ac *planes at the interface and differing only in the width of the slab—in this case, one unit cell wide for a few cycles (32).*

Published on June 1, 1980 on http://pubs.acs.org | doi: 10.1021/ba-1970-0186.ch002

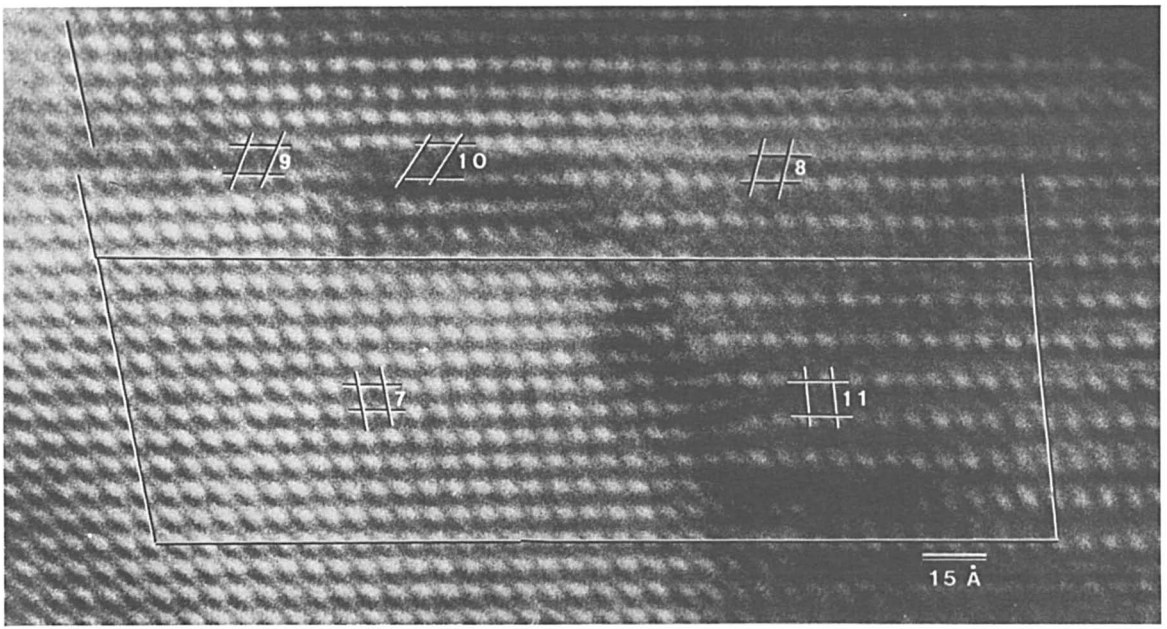

Figure 25. An image of multiple-phased TbO_x down $[21\bar{1}]_F$. The specimen was prepared by reduction of $Tb_{11}O_{20}$ in the microscope. Integers indicate n *in Tb_nO_{2n-2} for cell projections in the various parts. Strain fields are apparent in the* $n = 7$, $n = 11$ *phase interface* (28).

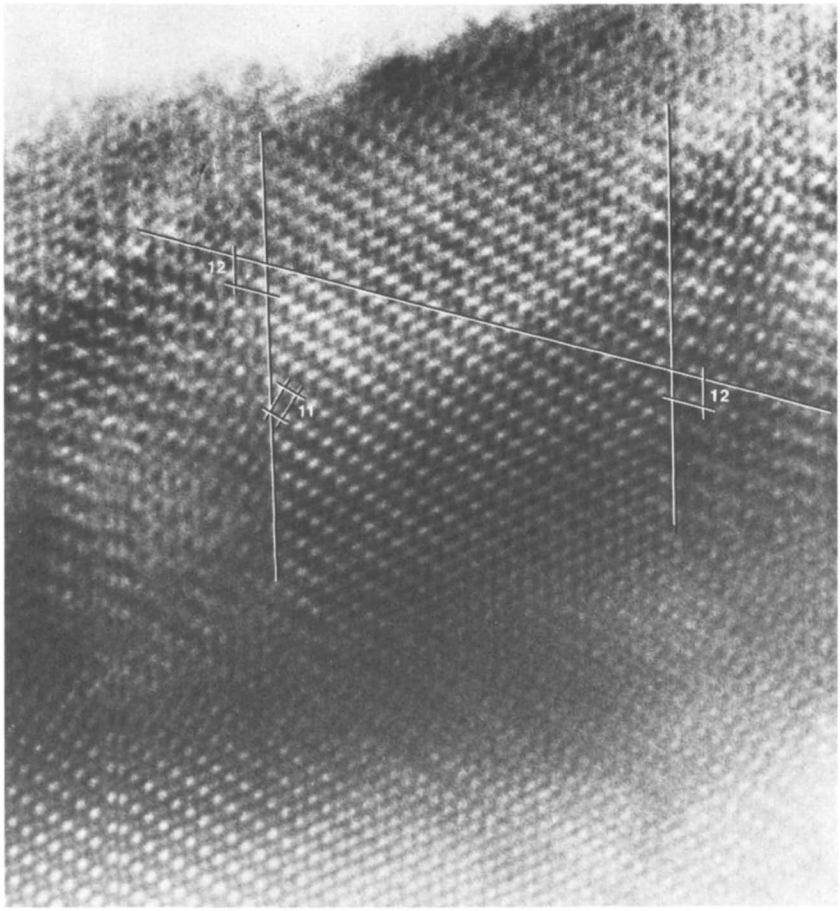

Figure 26. An image of intergrown slabs of n = *12 and* n = *11 phases in highly oxidized* TbO_x. *In this projection the body diagonal of* n = *11 is the same length as the edge of* n = *12, permitting almost perfect coherence (28).*

latter cases where reaction information, if not structural information, is given directly. Chemical reaction in the solid state is accompanied by the redistribution of material, and this is recorded directly by HRTEM.

The use of HRTEM to give information about the individual defects in solids, which are the agents of chemical change, have been repeatedly mentioned in the paragraphs above where the REO_3-related structures were discussed. We close our discussion with some examples of crystals of the fluorite-related materials undergoing change.

The phase diagram of the PrO_x system is shown in Figure 22. Of interest here are images of transformation events in the two-phased

regions. In Figure 23 the intergrowth of the $n = 4$ and $n = 7$ phases in the related system $Zr_xSc_yO_z$ are observed in the $\langle 111 \rangle_F$ zone; we see here the perfect topotaxial relationship and the coherence of the two phases. There is a matrix of R_7O_{12} in which domains of R_4O_6 of about 70-Å diameter are dispersed. These two phases are different enough in structure that they do not seem to intergrow at the unit cell level. Micrographs of pure PrO_x in this composition region are similar [*see* Figure 24(b)].

In Figure 24(a) the intergrowth of the $n = 7$ and $n = 9$ phases is observed. In these cases the structures are very similar, differing only

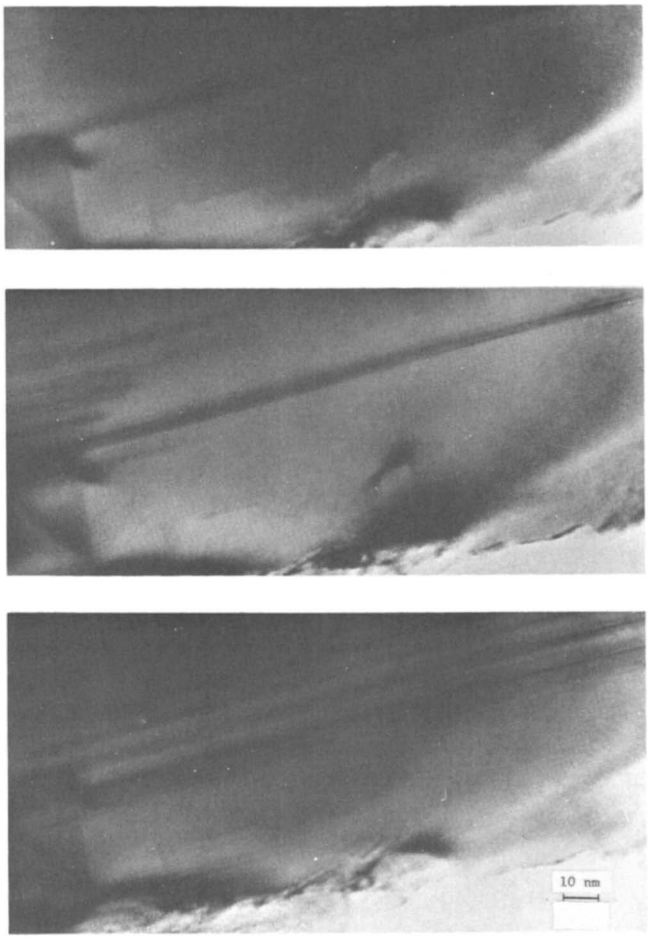

Figure 27. Sequential images from a $\langle 21\bar{1} \rangle_F$ zone, showing nucleation and growth of sheets of n = 7 *into an* n = 9 *phase of PrO_x. Time between images about 2 min (30).*

by a small variance in the *b*-axis, and have intergrowth of variable thickness across the common *ac* planes. Images resemble structures with frequent stacking faults. The alternating of $n = 7$ and $n = 9$, one unit cell thick, can be readily discerned for a short distance.

In the TbO_x–O_2 system, the principle two-phase region is between $n = 7$ and $n = 11$. Figure 25 shows a region of intergrowth of these two phases. Between lines of good register, one can observe 11 rows of $n = 7$ and 7 rows of $n = 11$, with the region between clearly marked by dark strain fields. Figure 26 shows a region of intergrowth of $n = 12$ and $n = 11$, where the projected body diagonal of $n = 11$ equals the cell edge of $n = 12$.

In certain cases chemical change can be followed as it occurs at high resolution. Figure 27 (*30*) gives a sequence of images taken only a few minutes apart (the exposure time is about 7 sec) during the decomposition of a crystal of $n = 9$, showing dramatically the nucleation and rapid growth of the $n = 7$ phase occurring along the *ac* plane. There is much slower growth along *b*.

Conclusion

The technique and use of HRTEM in broad studies of the more or less ideal structural systems, based upon the ReO_3 structure, has been illustrated. In this case individual extended and point defects have been seen in splendid detail, including formation and destruction; regions of coherent intergrowth of component parts have been observed at the level of resolution of coordination octahedra; and the individual phases have been displayed with images faithful to the charge density projection to a resolution of 3.5 Å. In some cases new structures have been directly indicated.

In addition, similar studies of an ordinary system not so ideally suited to HRTEM, the fluorite-related system, have been described. In this case we note that the best structural information available for the intermediate phases is obtained by direct observation of image contrast. Also, the details of phase reactions are shown to be revealed directly by HRTEM images. In this case, too, new phases are observed and characterized for the first time.

Computer packages for the calculation of images are available to make monitoring of results possible, and microscopes are being improved and invented. There should be a bright future for the application of this technique to the study of solid state problems. The number of cases studied so far is miniscule compared to the obvious applications.

Glossary of Symbols

HRTEM = high-resolution transmission electron microscopy
HREM = high-resolution electron microscope
d = half width of the spread function
λ = wavelength of the electron
C_s = spherical aberration coefficient
keV = volts $\times 10^{-3}$
MeV = volts $\times 10^{-6}$
$[uvw]$ = indices of a direction in the direct lattice (zone axis)
$\langle uvw \rangle$ = indices of a "form" of zone axis
(hkl) = indices of a set of parallel planes
CS = crystallographic shear
a, b, c = unit-cell vectors
n = an integer marking a member of a homologous series
R = rare earth element
$\iota = R_7O_{12}$, $n = 7$
$\zeta = R_9O_{16}$, $n = 9$
$\epsilon = R_{10}O_{18}$, $n = 10$
$\delta = R_{11}O_{20}$, $n = 11$
$\beta = R_{12}O_{22}$, $n = 12$

Literature Cited

1. Menter, J. W. *Proc. R. Soc. London, Ser. A* **1956**, *236*, 119.
2. Cowley, J. M. "Diffraction Physics"; North-Holland: Amsterdam, 1975; Chapters 13, 17, 18.
3. Cowley, J. M. *Annu. Rev. Phys. Chem.* **1978**, *29*, 251.
4. Allpress, J. A. *Nat. Bur. Stand. (U.S.) Spec. Publ.* **1972**, *364*, 87.
5. Allpress, J. A.; Sanders, J. V. *J. Appl. Crystallogr.* **1973**, *6*, 165.
6. Allpress, J. A.; Hewat, E. A.; Moodie, A. F.; Sanders, J. V. *Acta Crystallogr., Sect. A* **1972**, *28*, 528.
7. O'Keefe, M. A. *Acta Crystallogr., Sect. A* **1973**, *29*, 322.
8. O'Keefe, M. A.; Buseck, P. R.; Iijima, S. *Nature* **1978**, *274*, 322.
9. Pierce, L.; Buseck, P. R. *Science* **1974**, *186*, 1209.
10. Iijima, S. *J. Appl. Phys.* **1971**, *42*, 5891.
11. Skarnulis, A. J.; Summerville, E.; Eyring, L. *J. Solid State Chem.* **1978**, *23*, 59.
12. Horiuchi, S.; Matsui, Y.; Bando, Y. *Jpn. J. Appl. Phys.* **1976**, *15*, 2483.
13. Horiuchi, S.; Kikuchi, T.; Goto, M. *Acta Crystallogr., Sect. A* **1977**, *33*, 701.
14. Horiuchi, S.; Matsui, Y.; Bando, Y.; Sekikawa, Y.; Sakaguchi, K. *Proc. Intern. Conf. High-Voltage Microscopy, 5th, Kyoto, 1977.*
15. Veblen, D. R.; Buseck, P. R.; Burnham, C. W. *Science* **1977**, *198*, 359.
16. Millward, G. R.; Jefferson, D. A.; Thomas, J. M. *J. Microscopy* **1978**, *113*, 1.
17. Cowley, J. M. *Annu. Rev. Mater. Sci.* **1976**, *6*, 53.
18. Iijima, S. *J. Solid State Chem.* **1975**, *14*, 52.
19. Andersson, S. "The Chemistry of Extended Defects in Nonmetallic Solids"; Eyring, L.; O'Keeffe, M., Eds.; North-Holland: Amsterdam, 1970.

20. Anderson, J. S.; Hyde, B. G. *J. Phys. Chem. Solids* **1967**, *28*, 1393.
21. Iijima, S.; Allpress, J. A. *Acta Crystallogr., Sect. A* **1974**, *30*, 22.
22. Ibid., 29.
23. Iijima, S. *Acta Crystallogr., Sect. A* **1973**, *29*, 18.
24. Iijima, S.; Kimura, S.; Goto, M. *Acta Crystallogr., Sect. A* **1973**, *29*, 632.
25. Skarnulis, A. J.; Iijima, S.; Cowley, J. M. *Acta Crystallogr., Sect. A* **1976**, *32*, 799.
26. Kunzmann, P.; Eyring, L. *J. Solid State Chem.* **1975**, *14*, 229.
27. Von Dreele, R. B.; Eyring, L.; Bowman, A. L.; Yarnell, J. L. *Acta Crystallogr., Sect. B* **1975**, *31*, 971.
28. Tuenge, R. T.; Eyring, L. *J. Solid State Chem.* **1979**, *29*, 165.
29. Summerville, E.; Tuenge, R. T.; Eyring, L. *J. Solid State Chem.* **1978**, *24*, 21.
30. Inaba, H.; Lin, S. H.; Eyring, L., unpublished data.
31. Escher, M. C. *Eight Heads;* Escher Foundation, Haags Gemeentemuseum: The Hague, Grauenhage, Denmark.
32. Goodenough, J. B.; Whittingham, M. S., Eds. In "Solid State Chemistry of Energy Conversion and Storage," *Adv. Chem. Ser.* **1977**, *163*.

RECEIVED September 18, 1978.

Electron Resonance in ABX_3 Linear Chain Systems

BARRY B. GARRETT

Florida State University, Tallahassee, FL 32306

Despite the many theoretical and experimental studies of electron resonance line shapes for linear chain antiferromagnets in the paramagnetic state, there are still qualitatively new observations to be made for these systems. The line width anisotropy of TMMC and several related compounds has been described as proportional to $|Y_2^0|^n$. *The one-dimensional case should give* $n = 4/3$, *but we find* $n = 1.8$ *from the curvature of the anisotropy and* $n = 2$ *from a fit of the anisotropy for* $[(CH_3)_4N]MnCl_3$ *(TMMC),* $[(CH_3)_4N]MnBr_3$ *(TMMB), and* $CsMnBr_3$ *(CMB). To fit the line width anisotropies and the frequency dependence of the line widths, nonsecular components of the dipole–dipole interaction must be included in the relaxation mechanism. Three-dimensional* $CsMnCl_3$ *has a line width anisotropy accurately described by* $(1 + \cos^2\theta)$.

The use of electron resonance line widths to monitor spin correlations in the paramagnetic state of one-dimensional magnetic systems has been common for several years. Much theoretical interest has centered on the diffusive behavior of the spin correlations, the non-Lorentzian line shape, and the problems of deconvoluting four-spin correlation functions that arise in the description of electron resonance line widths (*1–5*). Experimental studies have focused more on the angular dependence of the line width and the line broadening that occurs on approaching the three-dimensional ordering temperature of an antiferromagnet from above (*6–11*). An oversimplified description of the contributions to the electron resonance line width is that an exchange-narrowed line is

0-8412-0472-1/80/33-186-063$05.00/1

broadened by dipole–dipole interactions between nearest neighbors in a linear chain. The spin correlations for this dipolar interaction dissipate more slowly than might be expected because the correlations must diffuse away primarily along the chain. In the long correlation time limit the angular dependence of the dipolar interaction $(3 \cos^2 \theta - 1) = Y_2^0$ is projected into the line width anisotropy. As the temperature is lowered toward the ordering temperature, the spin correlation lengths—and hence the correlation times—become longer; thus the line becomes broader as an ordered state is approached.

These low-dimensional features were observed in the prototypical one-dimensional systems $CsMnCl_3 \cdot 2H_2O$ = CMC (cesium manganese trichloride dihydrate) (*7, 8*) and $[(CH_3)_4N]MnCl_3$ = TMMC (tetramethylammonium manganese trichloride) (*5, 9*) with line width minima for external field orientations near 55° from the chain axis, a strong broadening at low temperatures, and supposedly frequency-independent line widths. While these features have been cited as characteristic of one-dimensional spin coupling, two-dimensional magnetic systems exhibit similar line width anisotropy due to dominant dipole–dipole interactions with a symmetric set of neighbors in a plane (*10, 11*). The angular dependance of the line width for TMMC was fitted by $|Y_2^0|^{4/3}$ in accordance with diffusive models (*1, 9*) by ignoring the width at the 55° orientation, and line shape was shown to be non-Lorentzian for angles at which the diffusive terms is dominant.

A recent theoretical treatment of spin relaxation in one dimension (*5*) partially avoids the four-spin correlation problem while developing a full treatment of frequency, temperature, and angular dependence of the line width. While this treatment does not account fully for the high-temperature line width—nor does it fit the angular anisotropy very well for TMMC—it does develop the nonsecular contributions to the line width, including their anisotropies. The secular term varies as $|3 \cos^2 \theta - 1|^n$, and the nonsecular terms vary as $10 \sin^2 \theta \cos^2 \theta$ and $\sin^4 \theta$; in the long correlation time limit only the secular term contributes to the line width, while for short correlation times the three terms have equal weights and the anisotropy reduces to $1 + \cos^2 \theta$. The latter anisotropy corresponds to the usual result for an axial antiferromagnet with three-dimensional connectivity (*12*). The nonsecular terms give Lorentzian line shapes.

Experiments

This paper presents a summary of our experimental studies of the temperature dependence of the angular anisotropy for several linear chain $AMnX_3$ systems [A = Rb^+, Cs^+, or $[(CH_3)_4N^+]$ and X = Cl or Br]. All these materials have hexagonal structures with linear chains of face-

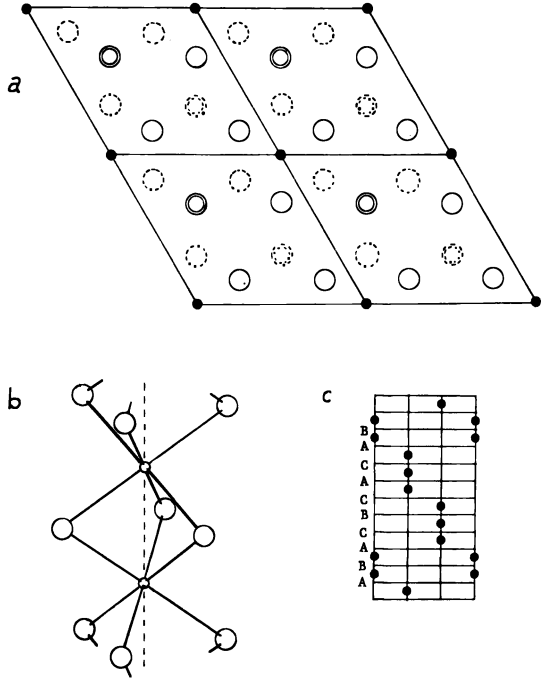

Figure 1. ABX_3 structures: (a) four unit cells viewed down the c-axis; (⊙), A; (○), X; at 1/4, 3/4 (dashed lines); (●), B; at 0, 1/2; (b) perspective view of the chain; (c) hexagonal layer stacking pattern in $CsMnCl_3$.

shared $MnCl_6$ octahedra except $CsMnCl_3$ and $RbMnCl_3$. $CsMnCl_3$ has a related structure consisting of face-shared trimer units that corner-share with three other trimers on each end; $RbMnCl_3$ has dimer units with similar three-dimensional connectivity. The structures are illustrated in Figure 1. Samples for electron resonance were obtained from larger crystals prepared for optical studies in S. L. Holt's Laboratories (*13, 14, 15, 16*). Very small crystals were cleaved off the larger samples and mounted, using a polarizing microscope, with the *c*-axis normal to the axis of a quartz rod for positioning in the electron paramagnetic resonance (EPR) cavity. Care was taken to ensure that the samples were small enough not to disturb the cavity tuning. All Q band spectra were taken with crystal mountings verified with X band data and all crystal mountings were verified with at least two separate crystals. All line width data are peak-to-peak derivative widths in gauss.

Results

Cesium manganese trichloride, $CsMnCl_3$, is a good three-dimensional analog of the linear chain manganese compounds. In view of the

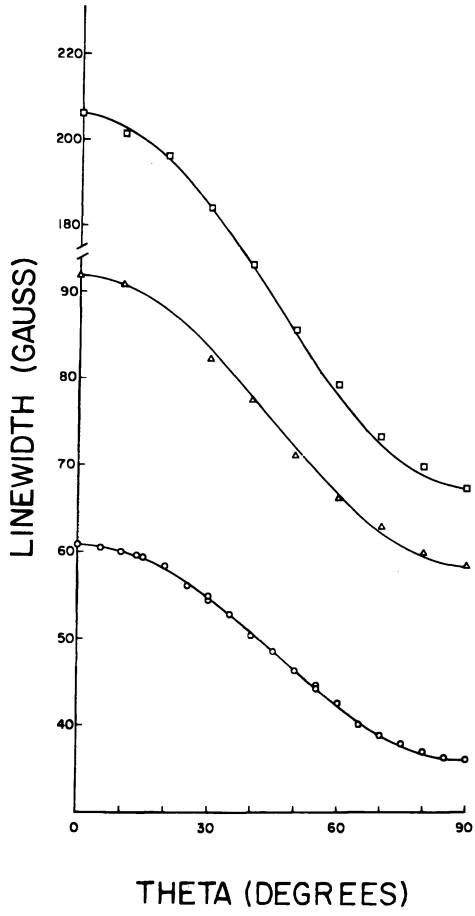

Figure 2. Line width anisotropy for $CsMnCl_3$ fitted by $\Delta H_{pp} = [A(1 + \cos^2 \theta) + B]$; σ = rms deviation: (○), 295 K, 9.27 GHz, A = 24.8, B = 11.3, σ = 0.26; (△), 295 K, 34.99 GHz, A = 32.8, B = 25.7, σ = 0.6; (□), 78 K, 9.23 GHz, A = 118.7, B = 4.1, σ = 1.5.

numerous demonstrations that a three-dimensional antiferromagnetically coupled paramagnet should have $[1 + \cos^2 \theta]$ line width anisotropy, it was surprising to find very little experimental verification in the literature. For that reason it seemed worthwhile to make such a verification. The line widths for $CsMnCl_3$ are well represented by $A(1 + \cos^2 \theta) + B$, as shown in Figure 2, with root mean square (rms) deviations about 1% of the line width. The coefficients A and B are both dependent on frequency and temperature. The line shapes for $CsMnCl_3$ were in every case Lorentzian and superimposable with scaling. A similar line width anisotropy was obtained for $RbMnCl_3$, but the conchoidal fracture and

moisture sensitivity of the crystals caused us to cease further measurements once the form of the anisotropy was established.

Linear chain rubidium and cesium–manganese tribromides show similar line width properties, but much more extensive data were taken on the cesium salt. The X band 295-K data for these salts, Figures 3 and 4, are well represented by $A \cos^4 \theta + B$, with no evidence for a 55° minimum and having much too rapid a line width decrease away from the c-axis to be represented by $(1 + \cos^2 \theta)$. Lowering the temperature gave no essential variation of the line width anisotropy, and the line shapes were all Lorentzian. Such results were quite surprising because these salts were known to have one-dimensional, linear chain properties from optical and magnetic studies (*14, 15*). Thus it was both a relief and

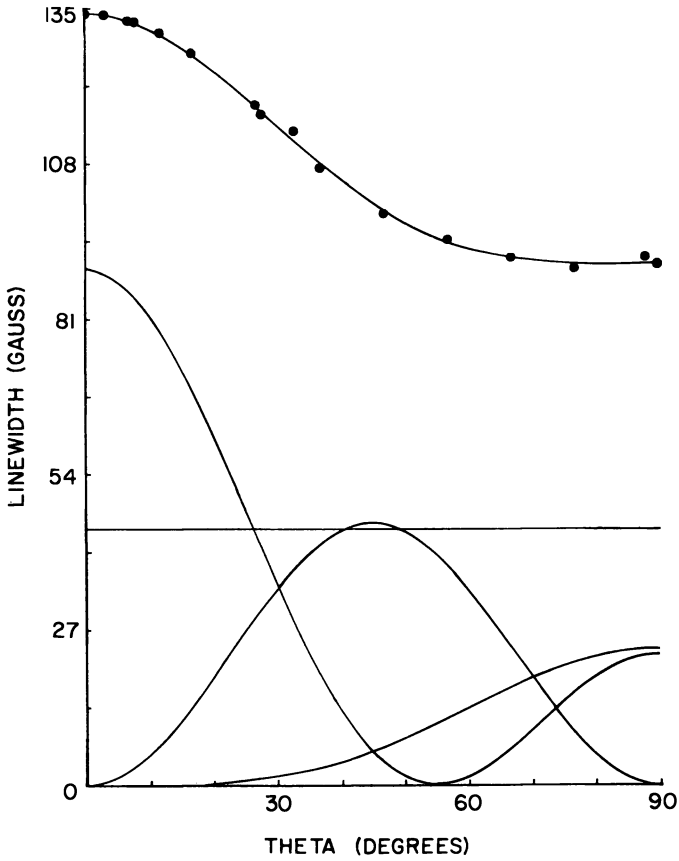

Figure 3. Line width anisotropy for $RbMnBr_3$ at 295 K and 9.27 GHz: (●), data. The curve through the data is fitted with $\sigma = 0.66$ G. Components of the fit, $22.93\ |Y_2^0|^2 + 181.45 \sin^2 \theta \cos^2 \theta + 23.62 \sin^4 \theta + 44.40$, are shown below.

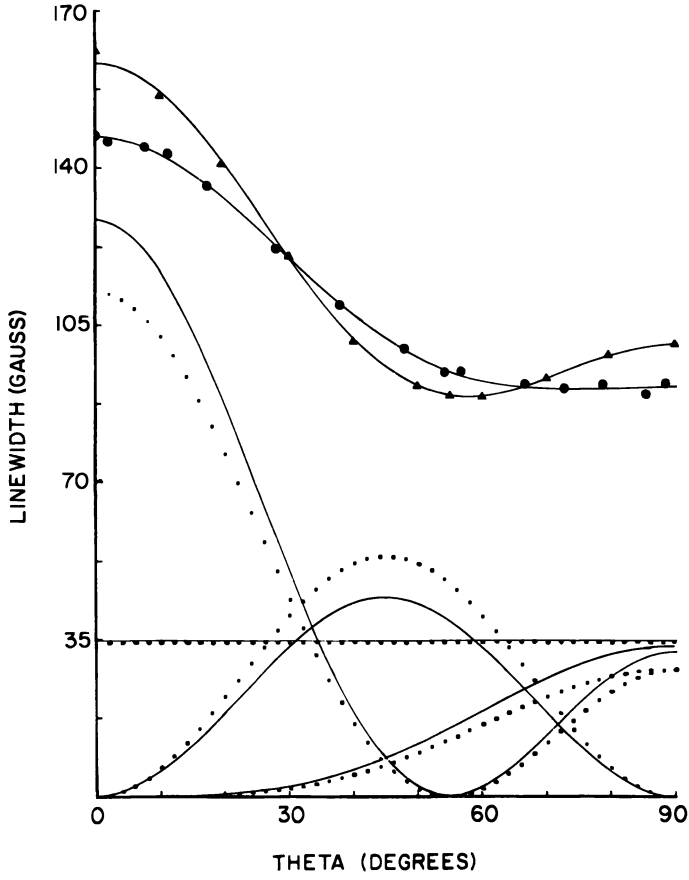

Figure 4. Line width anisotropy for $CsMnBr_3$ at 295 K and 9.26 GHz: (●), data. The solid curve through the X band data is fitted with $\sigma = 0.91$ G. Components of the fit, 28.11 $|Y_2^0|^2 + 214.5 \sin^2\theta \cos^2\theta + 28.43 \sin^4\theta + 34.57$, are shown as dotted lines. 34.99 GHz: (▲), data. The solid curve through the Q band data is fitted with $\sigma = 0.72$ G. Components of the fit, 34.14 $|Y_2^0|^2 + 177.7 \sin^2\theta \cos^2\theta + 33.51 \sin^4\theta + 34.83$, are shown as continuous curves below.

a second surprise to find a 55° minimum in the Q band line width anisotropy for $CsMnBr_3$ (cesium manganese tribromide) (CMB). This demonstrates that the 55° line width minimum is not a necessary consequence of one-dimensional magnetism and that the correlation times for this system are accessible in the usual EPR frequency range. It is also interesting that the line shapes are Lorentzian in the absence of the 55° minimum but non-Lorentzian shapes appear for angles other than $\theta = 55°$ when the line width minimum is present. Comparison of X band and Q band anisotropies for $CsMnBr_3$ in Figure 4 shows that they do not

differ by a single additive component because each curve lies well below the other over a significant range of angles, and there can be no negative contributions to a line width.

The fact that the qualitative features of the line width anisotropy are frequency-dependent indicates that the correlation time is in that intermediate region where nonsecular terms are not averaged away; thus it is appropriate to attempt a description of the line width anisotropy with a linear combination of the secular dipolar term $|Y_2^0|^n$ and the nonsecular terms $\sin^2\theta\cos^2\theta$ and $\sin^4\theta$ together with a constant. The results of a least-squares fitting for the $RbMnBr_3$ and $CsMnBr_3$ data are shown in Figures 3 and 4. The experimental anisotropies are obviously well represented by such a fitting with rms deviations of less than 1%. The two frequency data for $CsMnBr_3$ are represented by the same constant term and slightly different relative weights of the secular and nonsecular terms as is appropriate for the case of an intermediate correlation time. The fitting of the $RbMnBr_3$ data is similar to that for $CsMnBr_3$ at X band. In each case the relative coefficients of the secular and nonsecular terms are close to those that will give a net $(1 + \cos^2\theta)$ anisotropy, with the primary deviation being the small coefficient of the $\sin^2\theta\cos^2\theta$ term.

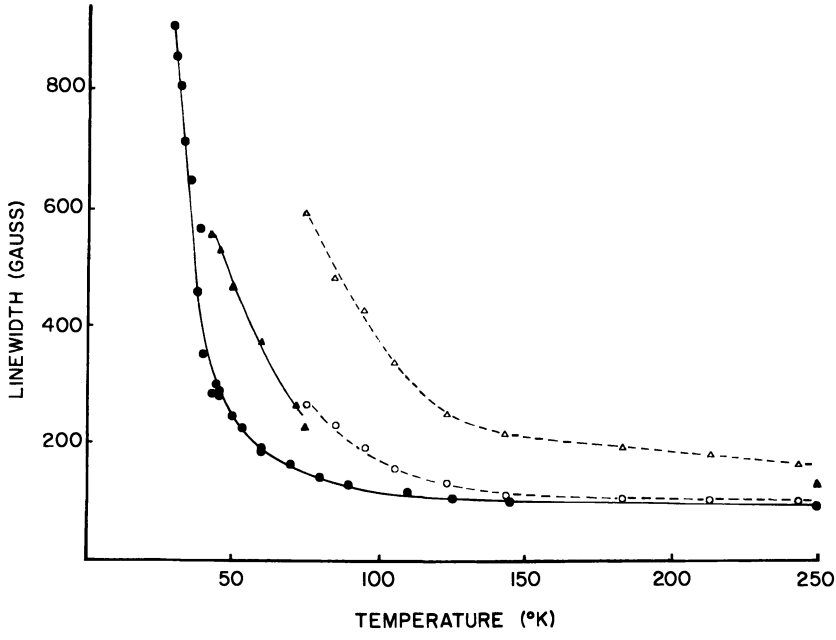

Figure 5. Temperature dependence of line widths. $RbMnBr_3$: (▲), $\theta = 0°$; (●), $\theta = 90°$. $CsMnBr_3$: (△), $\theta = 0°$; (○), $\theta = 90°$.

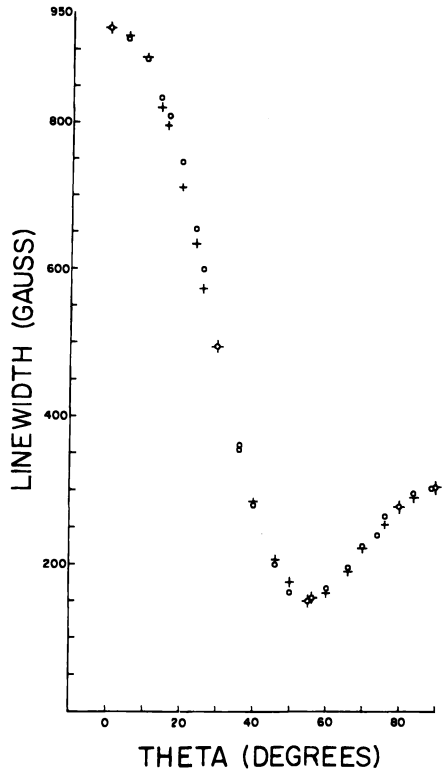

Figure 6. Line width anisotropy at 295 K and 9.27 GHz: (○), TMMC; (+), TMMB. The TMMB data is scaled 3.39 [ΔH − ΔH_{55}] + ΔH_{55} (TMMC).

The temperature dependences of the parallel and perpendicular X band line widths for both $CsMnBr_3$ and $RbMnBr_3$ are shown in Figure 5. In view of the fittings and frequency dependence described above, it is surprising that both of these salts appear to be approaching high-temperature limiting line widths at room temperature. It is also notable that $CsMnBr_3$ exhibits a much more gradual line broadening with a higher-temperature onset of such broadening than does $RbMnBr_3$. In neither case have we been able to correlate the broadening curve with the three-dimensional ordering at lower temperatures.

Shifting attention now to the best-known one-dimensional magnetic system, TMMC, and its bromide analogue, $[(CH_3)_4N]MnBr_3$ = TMMB (tetramethylammonium manganese tribromide), we also find some unusual frequency and temperature effects on the electron resonance line widths. Figure 6 shows a superposition of X band angular-dependent line widths for TMMC and TMMB, which clearly shows that these salts

have the same line width anisotropy at room temperature. (Note that the TMMB line width in excess of the 55° width is multiplied by 3.39 for this comparison.) TMMC has been reported to have a frequency-independent line width, but a careful comparison of X band and Q band line widths for one single crystal mounting, shown in Figure 7, illustrates that there is a nontrivial frequency dependence of the line width anisotropy. TMMB has a similar if not identical frequency dependence at room temperature. Fitting the TMMB and TMMC room temperature data in the same manner as done in Figures 3 and 4 yields fit with about four-to-one dominance of the secular $(Y_2^0|^2$ term over the nonsecular terms. No reasonable fits of the data could be obtained with $|Y_2^0|^n$, $n = 4/3$, as previously suggested (9). In fact, all fittings of TMMC and TMMB data with $n < 2$ required nonphysical, negative line width contributions even though an analysis of the curvature of the line width anisotropies yielded $n = 1.8$ for single-term fittings.

Studies of the temperature dependence of TMMB line widths revealed a sudden disappearance of the 55° minimum between 145 K and 140 K, as shown in Figure 8. This transition is also observable in the

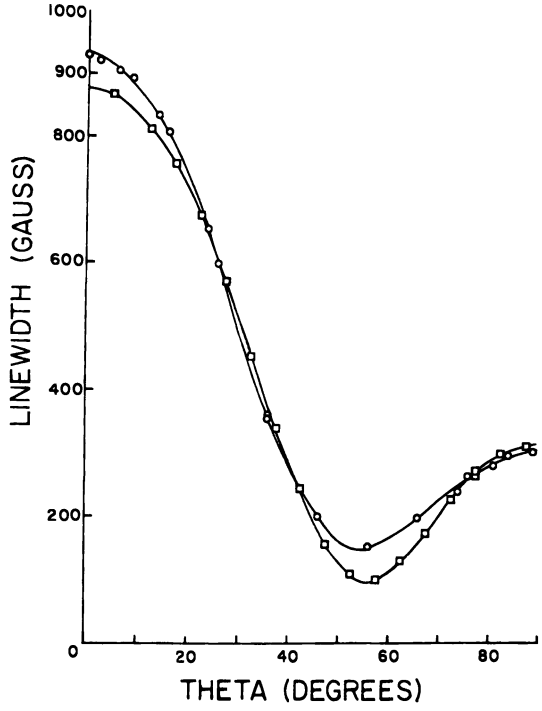

Figure 7. Frequency dependence of line width anisotropy for TMMC: (○), 9.2 GHz; (□), 34.99 GHz.

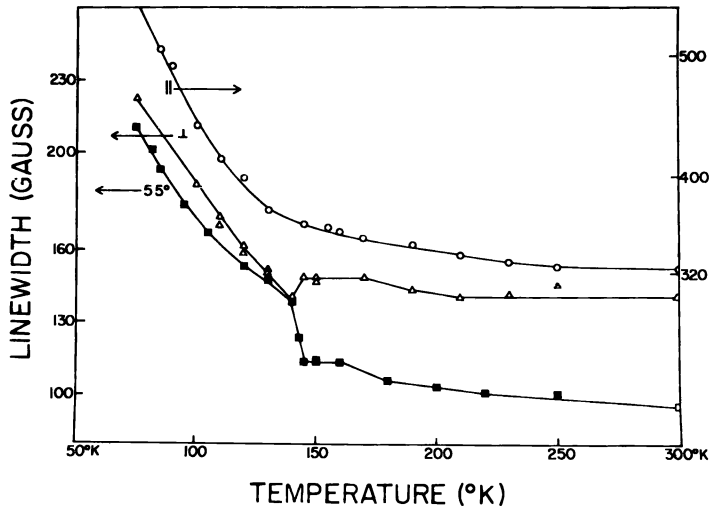

Figure 8. Temperature dependence of TMMB line widths: (○), θ = 0°; (△), θ = 90°; (□), θ = 55°.

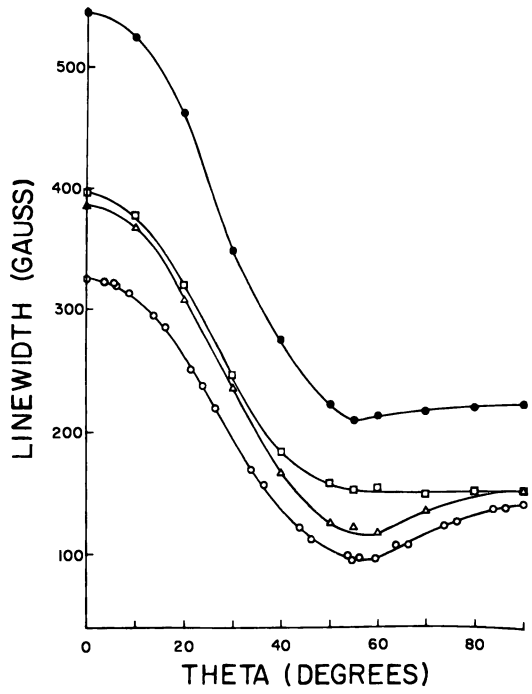

Figure 9. Temperature dependence of line width anisotropy for TMMB: (○), 293 K; (△), 150 K; (□), 139 K; (●), 75 K.

perpendicular line width but appears to have no immediate effect on the parallel line width. Examination of the line width anisotropy above and below the 140-K transition, Figure 9, shows that the primary effect is added width in the region of the 55° minimum. A small 55° minimum is reestablished as TMMB is cooled to 75 K. At lower temperatures the anisotropy becomes more complicated and has not been completely analyzed.

The transition in TMMB was subsequently observed to manifest itself by increasing the magnitude of the trigonal splittings in the optical spectrum (*16*). All these results suggested that the 140-K transition could be due to an ordering of the methyl groups in the tetramethylammonium cation similar to that observed by Morosin (*17*) in TMMC at 128 K. This supposition was recently verified in a low-temperature X-ray study by Alcock and Holt (*18*). Thus it appeared worthwhile to reexamine TMMC line widths near the 128-K transition. As can be seen in Figure 10, there is no evidence in the epr line widths for any change near 128 K. Interestingly, the X-ray evidence suggests larger changes in TMMC than in TMMB at the transition (*18*), but optical (*16, 19*) and epr studies can only detect a transition in TMMB.

At lower temperatures the line width for TMMC begins to broaden rapidly at 45 K, corresponding to the development of long correlation

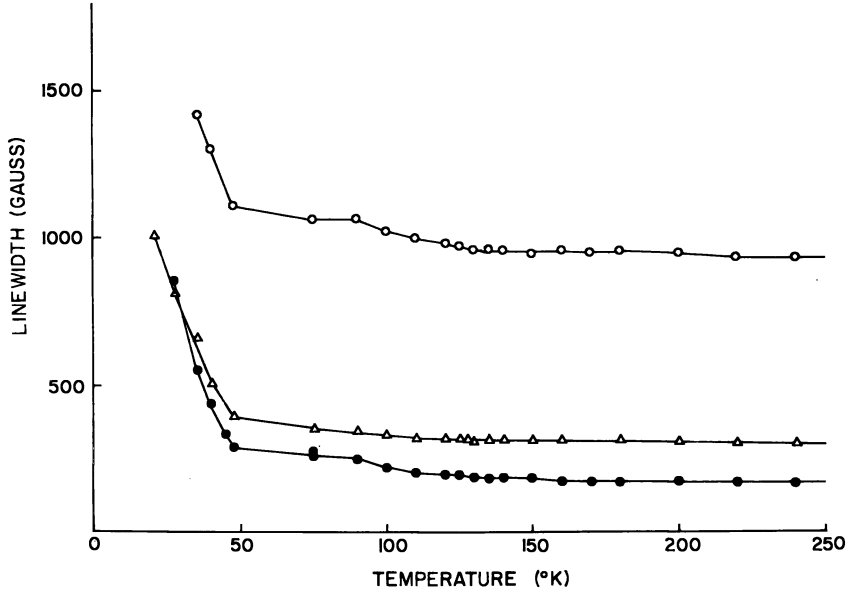

Figure 10. Temperature dependence of TMMC line widths: (○), θ = 0°; (△), θ = 90°; (●), θ = 55°.

lengths and times in the chains. The 55° minimum disappears at about 30 K and the line becomes too broad to observe at around 20 K. A very weak line becomes observable near 20 K and narrows to an isotropic 700-G-wide line below 11 K. This weak line probably is not caused by manganese ions participating in linear chain correlations but rather is caused by spins that are only weakly coupled into the correlated spin system. These weakly coupled ions could be manganese ions at surfaces or near defects or possibly even impurity ions. Such weakly coupled spins could be very useful probes of spin dynamics near or in the ordered state.

Literature Cited

1. Gulley, J. E.; Hone, D.; Scalapino, D. J.; Silbernagel, B. G. *Phys. Rev. B* **1970**, *1*, 1020.
2. Hone, D. "17th Conference on Magnetism and Magnetic Materials," *AIP Conf. Proc.* **1971**, 5.
3. Hennessy, M. J.; McElwee, C. D.; Richards, P. M. *Phys. Rev. B* **1973**, *1*, 930.
4. Lagendijk, A. *Physica (Utrecht)* **1976**, *83*, 283.
5. Cheung, T. T. P.; Soos, Z. G.; Dietz, R. E.; Merritt, F. R. *Phys. Rev. B* **1978**, *17*, 1266.
6. Kedzie, R. W.; Shane, R. J.; Kestigan, M.; Croft, W. J. *J. Appl. Phys.* **1965**, *36*, 1195.
7. Ajiro, Y.; VanderVen, N. S.; Friedberg, S. A. "17th Conference on Magnetism and Magnetic Materials," *AIP Conf. Proc.* **1971**, *5*.
8. Tazuke, Y.; Nagata, K. *J. Phys. Soc. Jpn.* **1975**, *38*, 1003.
9. Dietz, R. E.; Merritt, F. R.; Dingle, R.; Hone, D.; Silbernagel, B. G.; Richards, P. M. *Phys. Rev. Lett.* **1971**, *26*, 1186.
10. Richards, P. M.; Mueller, K. A.; Boesch, H. R.; Waldner, F. *Phys. Rev. B* **1974**, *10*, 4531.
11. Benner, H. *Phys. Rev. B* **1978**, *18*, 319.
12. Huber, D. L. *J. Phys. Chem. Solids* **1971**, *32*, 2145.
13. Ackerman, J. F.; Cole, G. M.; Holt, S. L. *Inorg. Chim. Acta* **1974**, *8*, 323.
14. Cole, G. M.; Putnik, C. F.; Holt, S. L. *Inorg. Chem.* **1975**, *14*, 2219.
15. Putnik, C. .; Cole, G. M.; Holt, S. L. *Inorg. Chem.* **1976**, *15*, 2001.
16. Putnik, C. F.; Cole, G. M.; Holt, S. L. *Inorg. Chem.* **1976**, *15*, 2135.
17. Peercy, P. S.; Morosin, B. *Phys. Lett. A* **1971**, *36*, 409.
18. Alcock, N. W.; Holt, S. L. *Acta Crystallogr.* **1978**, *B34*, 1970.
19. Day, P.; Dubicki, L. *J. Chem. Soc., Faraday Trans. II* **1973**, *69*, 363.

RECEIVED September 13, 1978.

Design of a Time-of-Flight Single-Crystal Diffractometer for the Argonne Prototype Pulsed-Neutron Source

S. W. PETERSON, A. H. REIS, JR., A. J. SCHULTZ, and P. DAY

Chemistry Division, Argonne National Laboratory, Argonne, IL 60439

The prototype pulsed-neutron source, zero-gradient synchrotron intense neutron generator prototype prime (ZING P'), and its expected successors, intense pulsed neutron system I (IPNS I) and IPNS II, at Argonne National Laboratory will supply neutrons at 30 or 60 Hz and peak flux levels of 10^{14}–10^{16} $n \cdot cm^{-2} \cdot sec^{-1}$. *These user-oriented facilities will be available to the scientific community on a proposal basis. A time-of-flight (TOF) single-crystal diffractometer based on the Laue technique and utilizing a broad thermal neutron spectrum (0.7–5 Å) is being designed to take full advantage of the high instantaneous flux. The design of a first-stage instrument is based on the use of a* ^{3}*He-filled, multiwire, position-sensitive area detector of the Borkowski–Kopp type. The 20 × 20-cm active area of the detector has a 100 × 100 multiwire double-cathode grid, which can provide about 2-mm spatial resolution; the third data parameter, TOF, is resolvable into 1000 channels. The initial microprocessor data memory will limit the product of* x, y, *and time resolution to* 10^6 *bytes. Data collection will involve simultaneous measurement of* 10^2–10^3 *reflections in the Laue mode with stationary crystal and detector. A strategy for collecting a complete sphere of data with a minimum number of fixed crystal and counter positions is being developed. Angular movements of crystal and detector are provided by means of a four-circle diffractometer; provision also is made for a detector translation. Crystal orienta-*

0–8412–0472–1/80/33–186–075$05.00/1

tion procedures similar to those used in current four-circle instruments are being devised. Data collection rates are expected to be greater than 10^4 reflections per day at IPNS II.

For the exploration of new areas of solid state chemistry, instrumentation must develop at the same pace and level of sophistication as the evolving research areas. Condensed-matter neutron diffraction experiments have proved to be essential to the understanding of the structure of materials. Only three high-flux (about 10^{15} n · cm^{-2} · sec^{-1}) reactors exist worldwide at which state-of-the-art neutron-scattering studies can be accomplished. Although two of them are in the United States, their availability to the general research community has been quite restricted (*1*).

In the future, more intense neutron fluxes (10^{16} n · cm^{-2} · sec^{-1} or greater) are needed to study more complex condensed-matter systems, which are increasingly becoming concerns of the solid state, chemical, and biological communities. In addition, high-flux sources would allow the use of smaller sample sizes, thereby greatly extending the range of materials that can be investigated. Such fluxes are beyond the current design capabilities of steady state fission reactors. However, new high-flux pulsed-neutron sources with peak fluxes that may approach 10^{16} are already under development. One of these is a pulsed reactor; the others make use of high-energy pulsed beams from particle accelerators (*2*). For example, high-energy protons from a synchrotron source can be injected into a heavy metal target, dislodging large numbers of high-energy neutrons, which, when moderated, yield pulsed thermal (and epithermal, $E > 0.15$ eV) neutron beams whose peak flux can be much

Table I. Pulsed-Neutron

Name	*Location*
Tohoku Linac[a]	Tohoku, Japan
Harwell Linac II[a]	Harwell, UK
ORLEA[a] (with multiplier)	Oak Ridge, US
WNR[a]	Los Alamos, US
KENS[b]	Tsukuba, Japan
NIMROD[b] (modified)	Rutherford, UK
IPNS I[b]	Argonne, US
IBR-2[b]	Dubna, USSR

[a] Existing.

higher than that available in steady state reactors. A partial listing of proposed and existing pulsed sources is shown in Table I.

The Argonne National Laboratory IPNS program as developed over the past six years is shown in Table II. The second, or ZING P′, stage is currently in operation; however, construction of IPNS phase I will start in October, 1978, and operation is scheduled to begin in April, 1981. Development of neutron-scattering and diffraction instrumentation that takes advantage of TOF measurements inherent in pulsed-beam operation is an integral part of the Argonne program. Six instruments—four of which are already, or shortly to be, in operation—are planned for the ZING P′ phase and are listed in Table III. The small-angle and single-crystal diffractometers are currently in design and early construction stages.

The Argonne pulsed-neutron facilities are planned and will be operated to encourage extensive use by the entire scientific community. Within this concept, the prototype TOF single-crystal neutron diffraction system described below is being developed.

TOF Neutron Techniques

Thermal neutrons make very suitable probes for condensed matter because of their favorable wavelength, energy, and velocity properties. Thermal neutron wavelengths (1.8 Å nominal) are comparable in magnitude to interatomic distances and to commonly available X-ray wavelengths. This fact led to the development of monochromatic neutron techniques for structural research even though neutrons lack the intense characteristic radiation common to x-rays. In the case of crystalline powder samples the conventional technique uses a fixed wavelength and the intensity, I, of the diffracted beam is measured as a function of the

Source Projects Worldwide

Method	*Frequency (Hz)*	*Peak Thermal Flux* $(n \cdot cm^{-2} \cdot sec^{-1})$
(e^-, λ, n)	110	10^{12}
(e^-, λ, n)	150	1.5×10^{13}
(e^-, λ, n) and fission	800	1.5×10^{14}
Spallation	120	10^{14}
Spallation	15	10^{14}
Spallation	53	4×10^{15}
Spallation	30	10^{15}
Fission	5	10^{16}

[b] Design and construction stage.

Table II. Argonne National Laboratory

Facility	*Proton Accelerator*	*Frequency (Hz)*	*Protons/Pulse*
ZING P	ZGS[a] booster I	10	2.5×10^{10}
ZING P′	ZGS booster II	30	1×10^{12}
IPNS, Phase I	ZGS booster II	30	5×10^{12}
IPNS II, phase II	HIS[b]	60	5×10^{13}

[a] Zero-gradient synchrotron.

scattering angle 2θ. Whenever the Bragg equation $\lambda = 2d \sin \Theta$ is satisfied, a maximum is observed in I versus 2θ (λ is the neutron wavelength, d is the lattice spacing, and Θ is the Bragg scattering angle). In the more recently developed TOF method for neutrons, the roles of λ and θ are reversed, and neutrons of variable wavelength are used to measure the diffracted beam intensities at a fixed angle 2θ. This method (*3, 4, 5*) is very powerful for powder diffraction, in part because of its utilization of the broad energy distribution associated with thermalized neutrons.

TOF techniques have been extended to single-crystal diffraction, and the methods (*6*) developed are quite similar to the well-known X-ray Laue technique. In the X-ray case polychromatic radiation is diffracted from a stationary single crystal, and the diffraction pattern is recorded on a photographic film. Figure 1 shows X-ray Laue patterns of monoclinic decamethylferrocene–tetracyanoquinodimethane (TCNQ), a charge transfer compound with interesting solid state properties. These patterns are obtained with a stationary crystal, using white radiation produced from an Mo X-ray tube, and they indicate the pattern and density of spots that are characteristic of the method. The fatal flaw in this otherwise useful method is that all the orders ($n = 1 \rightarrow l$) of a Bragg plane, where n is an integer and l is one of the Miller Indices hkl, diffract wavelengths λ_1/n (λ_1 is the first order) at precisely the same angle. The

Table III. ZING P′ Instruments

A. Powder Diffractometers
   1. High Resolution,[a] $\Delta Q/Q \approx 0.3\%$
   2. High Intensity, $\Delta Q/Q \approx 1\%$

B. Single-Crystal Diffractometer, unit cells less than **25 Å**

C. Small-Angle Diffractometer

D. Inelastic Spectrometers
   1. Crystal Analyzer, $E < 30$ meV, ΔE 2–10 meV
   2. Chopper Spectrometer, $E < 1$ eV, $\Delta E/E \approx 0.05$

[a] $Q = 4\pi \sin \Theta/2$.

Pulsed-Neutron Source Program

Proton Energy (MeV) and Target	*Neutrons/ Proton*	*No. of Neutron Beams*	*Peak Thermal Neutron Flux ($n \cdot cm^{-2} \cdot sec^{-1}$)*	*Operation*
200 Pb	2	2	5×10^{11}	January 1974
500	8	5	10^{14}	October 1977
500 ^{238}U	20	12	7.5×10^{14}	April, 1981
800 ^{238}U	30	12	10^{16}	

[b] High-intensity synchrotron.

measured intensity is a sum over all the orders. This property effectively has blocked the development of the X-ray Laue method for structure analysis. In the neutron case the overlapping orders are separated in time, and TOF measurements easily permit resolution of the orders allowing individual *hkl* values to be obtained readily. Figure 2 shows a diagram of the Argonne single-crystal instrument (under construction) designed to operate in the Laue mode. The design (7) uses the well-known four-circle geometry for orienting the crystal and rotating the detector in a horizontal plane and also provides a detector translation along the 2θ arm. The key to rapid data collection is the position-sensitive area detector, which, when operated in a TOF mode, provides a three-dimensional grid with two space and one time coordinates. A large detector of this type will easily permit simultaneous measurement of 10^2–10^3 diffraction peaks.

Description of the TOF Pulsed-Neutron Single-Crystal Diffractometer

Source, Chopper, and Beam Line. The basic layout of the neutron source, ZING P′, is shown in Figure 2. H^- particles are injected from a 50-MeV linear accelerator into a 500-MeV synchrotron. The H^- particles are stripped of their electrons to form H^+. A kicker magnet directs the protons onto a tungsten target where each proton reacts to produce about 8 neutrons. A polyethylene moderator, a Be reflector, and a large shield complete the assembly. The ZING P′ prototype source is expected to operate at a 30-Hz repetition rate, yield 1×10^{12} protons per pulse, and give a peak thermal neutron flux of approximately 10^{14} $n \cdot cm^{-2} \cdot sec^{-1}$. The resulting thermal neutron spectrum is shown in Figure 3.

The single-crystal instrument will be placed 8.5 m from the moderator on a beam line that tapers from a 10×10-cm beam size at the moderator to 0.5×0.5 cm at the sample. The flight path and beam divergence are chosen so as to give the best possible trade-off between time resolution and intensity requirements.

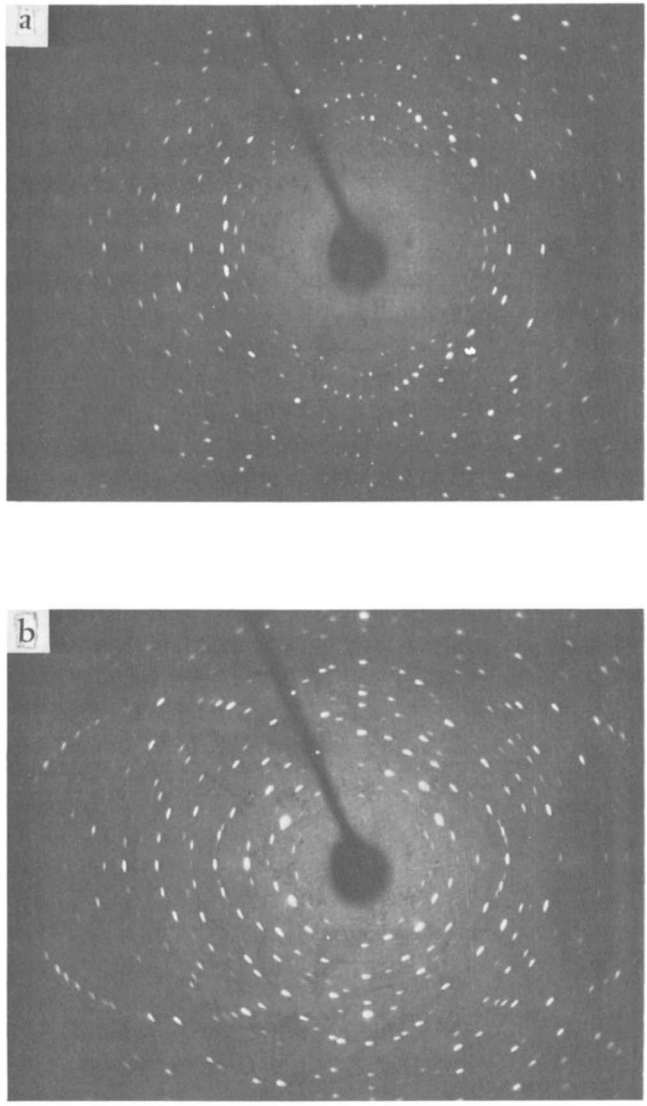

Figure 1. Laue diffraction photographs of a monoclinic crystal of decamethylferrocene–TCNQ mounted along the b*-axis; the X-ray beam is oriented parallel to the* c*-axis and* a*-axis, respectively.*

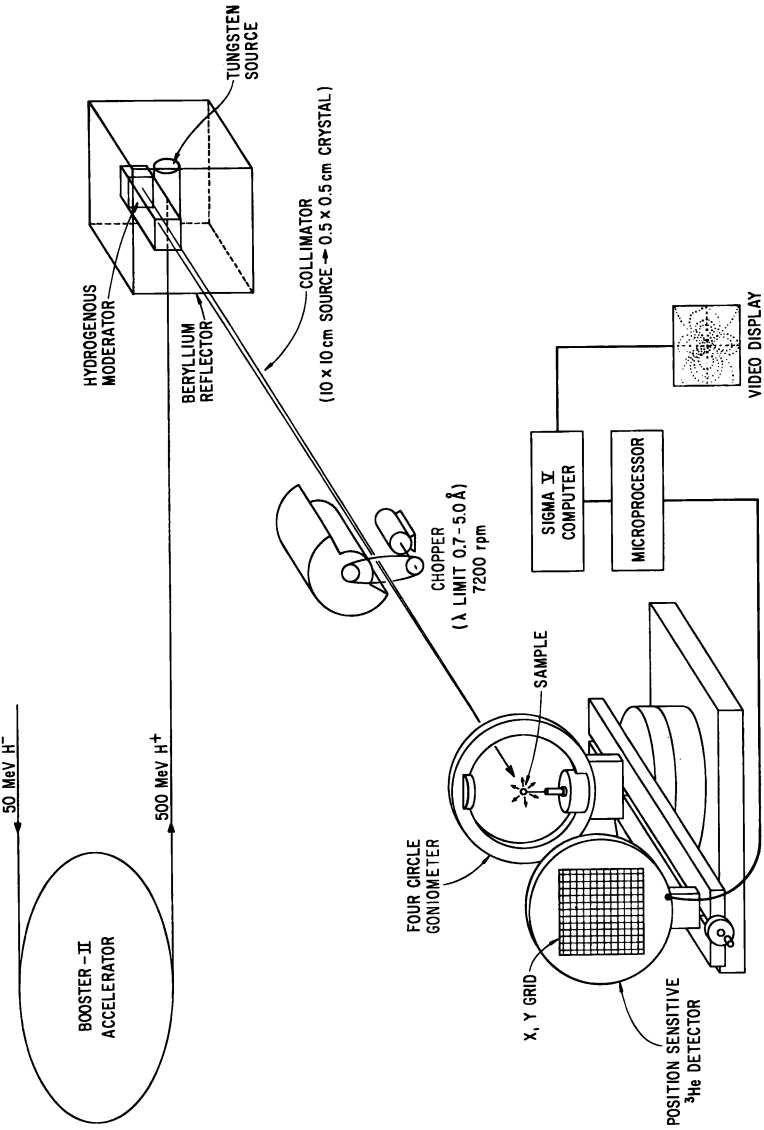

Figure 2. Diagramatic description of the TOF pulsed-neutron single-crystal diffractometer

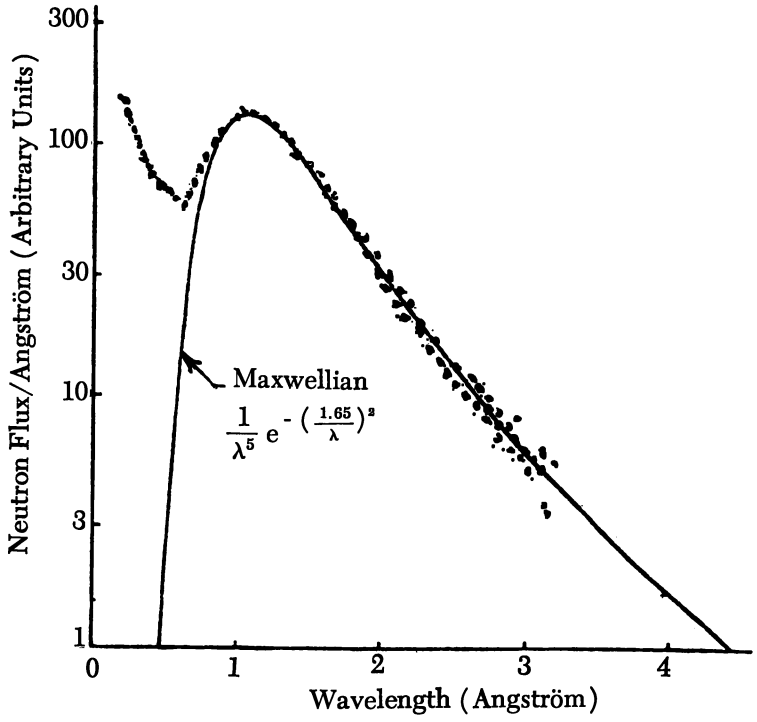

Figure 3. The thermal neutron source spectrum of ZING P'

Since neutrons produced in the target and partially thermalized in the hydrogenous moderator appear in bursts at 1/30-sec intervals, their time of arrival at the detector, after scattering by the sample, can be timed readily. The time t is given by $t = l/v$, where l is the flight path length and v is the neutron velocity. The neutron wavelength λ is given by the De Broglie expression $\lambda = h/mv$, where h is Planck's constant and m is the neutron mass. Thus the wavelength is proportional to TOF and is easily obtained. Every neutron arriving at a position-sensitive detector with TOF measurement capability can be characterized with x and y position coordinates and a t or λ coordinate. The precision of these coordinates is limited by the time resolution, given largely by the neutron pulse width (about 15 μsec for 1-Å neutrons), which is proportional to wavelength, and the flight path length and by the spatial resolution of the detector and the data storage system.

With a flight path of 9 m (source-to-sample = 8.5 m, sample-to-detector = 0.5 m) and a 30-cycle repetition rate, neutrons for which $\lambda > 14.7$ Å will be overtaken by the much faster neutrons of the succeeding pulse. This frame overlap condition, if present, would result in assign-

ment of incorrect wavelengths and must be eliminated. The addition of a chopper to the system allows selection of a limited wavelength band, eliminating both very short and very long wavelength neutrons, which may be undesirable. Specifications of such a chopper are given in Table IV.

Detector System

As we have seen above, a stationary crystal can produce several hundred simultaneous Laue reflections when irradiated by a polychromatic beam. When a pulsed polychromatic beam is used, these reflections are separated in time, and an appropriate position-sensitive area detector can determine the position coordinates and wavelength associated with each reflection, as well as the intensity. The detector adopted for the current instrument is a ^{3}He-filled, multiwire proportional counter of the Borkowski–Kopp type (*8*). The anode–cathode assembly is shown in Figure 4, and a simplified diagram is given in Figure 5. The detector is filled to 5 atm pressure with 3 atm of ^{3}He and 2 atm of Xe gas. The neutron reaction within the detector is $^1n + {}^3He \rightarrow {}^3H + {}^1p + 0.77$ MeV. The Xe gas is added to shorten the path lengths of the reaction products, a proton and a triton. The energetic triton and proton generate, by collision, electrons that flow toward the anode and positive ions that flow toward the cathodes. The positive ions move very slowly, hence

Table IV. Design of Chopper for Single-Crystal Diffractometer/ZING P′: Horizontal Axis

Specifications:
- Source-to-chopper entrance: 4.0 m
- Source-to-chopper exit: 4.5 m
- Chopper length: 0.5 m
- Chopper radius: 0.2 m
- Chopper velocity: 7200 rpm (120 Hz)
- Wavelength range (full intensity): 0.7–5.0 Å
- Wavelength range (opening and closing): 0.5–5.2 Å
- Beam size at entrance: 5 cm in diameter

4.0 m: Front Chopper Face
- 0.7 Å; $v = 5.6505 \times 10^3$ m · sec^{-1}; $t = 0.7079 \times 10^{-3}$ sec;
- 30.58° = opening angle
- 5.0 Å; $v = 0.7910 \times 10^3$ m · sec^{-1}; $t = 5.0568 \times 10^{-3}$ sec;
- 218.46° = closing angle

4.5 m: Back Chopper Face
- 0.7 Å; $v = 5.6505 \times 10^3$ m · sec^{-1}; $t = 0.7963 \times 10^{-3}$ sec;
- 34.40° = opening angle
- 5.0 Å; $v = 0.7910 \times 10^3$ m · sec^{-1}; $t = 5.6890 \times 10^{-3}$ sec;
- 245.77° = closing angle

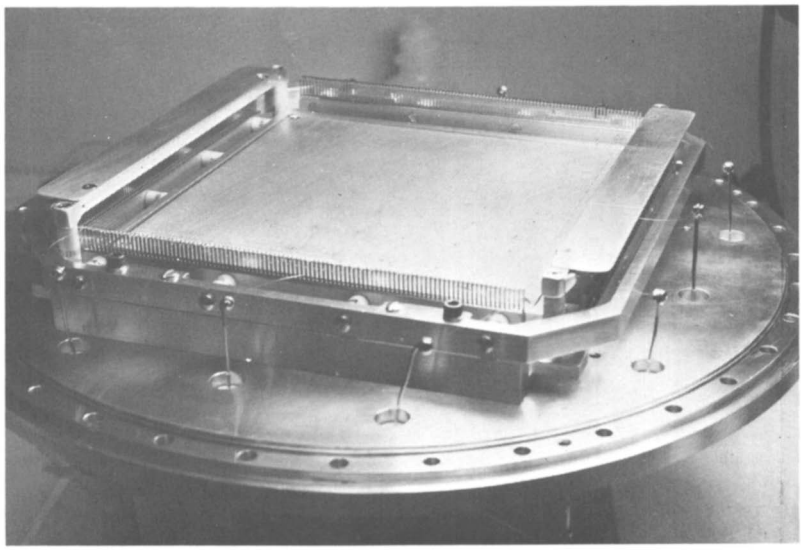

Figure 4. Anode–cathode assembly for a multiwire, two-dimensional, position-sensitive proportional counter

the pulse detected at the cathodes is primarily an induced charge effect due to the electron avalanche near the anode. The difference in the rise times of the current pulse generated in the two cathode circuits and measured at the two ends of each circuit is used to determine the x and y coordinates of the location of the event. The two cathode grids are orthogonal and strung continuously from single wires in the pattern shown in Figure 5. The resulting grids have 2-mm separations in both x and y (100 turns per 20-cm counter dimension), and the expected spatial resolution is approximately equal to the wire spacing.

Data Storage and Microprocessor Requirements. The rate of data collection that becomes possible by matching high-flux pulsed sources with efficient multidetectors is rather large, and this creates a formidable data-handling and storage problem. The magnitude of the problem is apparent when one considers that a single multidetector can accept data at about 50,000 events per second and each event must be coded to an address with a resolution of 100×100 channels for spatial information and 1000 channels for time, giving a total of 10^7 potential storage locations. The electronic detection system that is being designed for this purpose actually provides for 256×256 channels of position information and a 4096-channel time base, which is an even larger matrix.

The data acquisition task is solved by using a local microprocessor and a remote Sigma 5 computer. Located next to the instrument is a

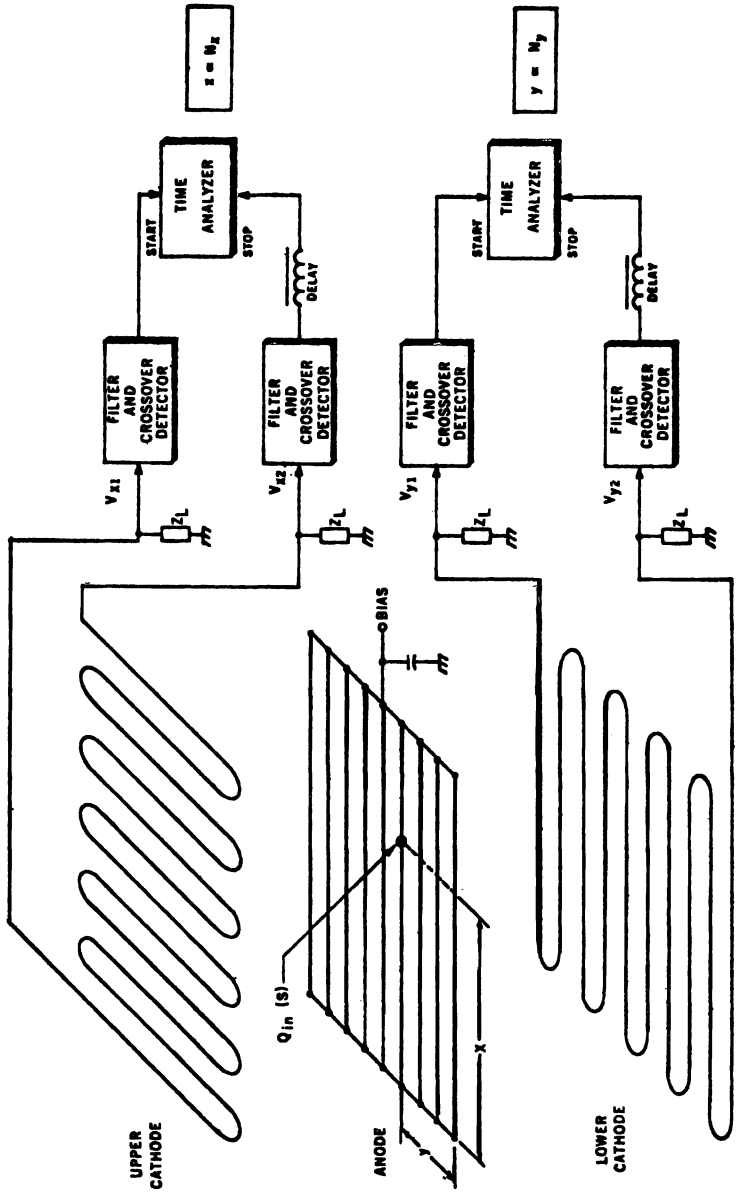

Figure 5. Simplified diagram of the multiwire proportional counter and signal processing circuits of the Borkowski–Kopp type (3).

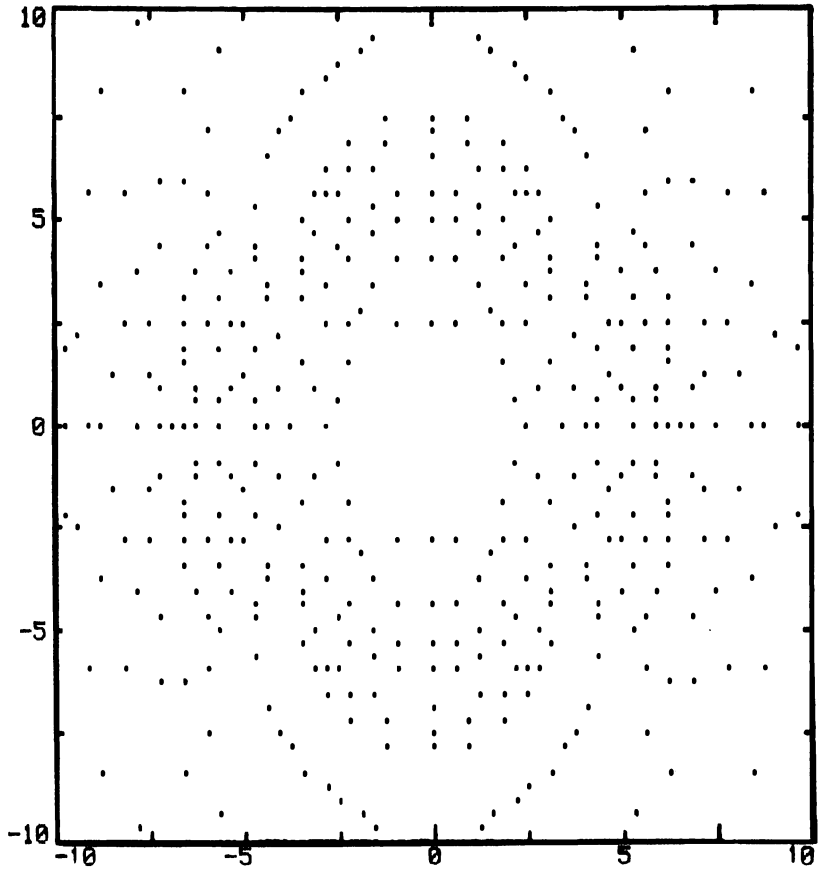

Figure 6. Simulated Laue patterns of a two-dimensional proportional counter. The histogram is for the same crystal orientation as that for the X-ray Laue pattern of Figure 1(a). The units of the ordinate and abscissa are in centimeters. Each asterisk represents a set of hkl *values with no order separation in time.*

microprocessor with 512 64-bit words of writable control store (a new control program can be loaded in a few seconds) and 10^6 bytes (8 bits) of data memory. The microprocessor will position the crystal and detector, read the x, y, and time analog to digital convertors (ADC's), buffer the events in data memory, and transmit [at 10 kilobauds (kBd)] the addresses of overflowed buffer locations to a Sigma 5 computer (1 mi distant). The Sigma will build three-dimensional histograms and store them on disk memory for display and manipulation by the user at the experimental site. The Sigma 5 provides sufficient storage and computational capacity (it supports 26 other unrelated experiments) to support user

and/or automatic control of the experiment, interactive spectral simulation, manipulation and analysis of the collected histograms, and partial structure determination. Since adequate buffering (256:1) for the initial data rates will require 8-bit buffers, the present microprocessor data memory (expandable to 2×10^6 bytes) will limit the product of the x, y, and time resolutions to 10^6 bytes ($64 \times 64 \times 256$ being a typical choice).

A simulation program has been developed to generate sample histograms of neutron Laue patterns. In Figure 6 is shown a simulated histogram of neutron Laue data for decamethylferrocene-TCNQ, which may be compared with the X-ray Laue pattern, Figure 1(a). This pattern gives an impression of the number of simultaneous reflections that can be recorded by a system with sufficient resolution.

User-Oriented Software

A software package for the TOF single-crystal instrument is being developed with the needs of the occasional outside user in mind; that is, the software will prompt the user when inputs are required. The goal of the software development is to provide a system for automatic crystal orientation and determination of unit cell and crystal symmetry, automatic collection of a unique data set, and reduction of the data to a form suitable for structure analysis. Since the Laue technique is essentially novel, new or substantially modified versions of older diffractometer programs are being prepared for all the necessary software.

The system is being designed so that a crystal can be mounted on the two-circle Huber goniometer (Figure 2) in a general orientation. The orientation matrix, unit cell parameters, and Laue symmetry then can be determined from the Laue histogram generated with the crystal set in its initial orientation. The flow diagram of Figure 7 illustrates the process. N strong reflections are selected from the initial histogram and stored in a reflection file. The program LBLIND, (BL) (*9*), an automatic indexing program, operates on these to determine initial cell constants, symmetry, initial orientation matrix, and reflection indices; LS, a least-squares refinement program, refines the unit cell and matrix by least-squares procedures; THRE, a crystal orientation program using data for three reflections, generates an orientation matrix and unit cell and may be used in place of LBLIND when three indexed reflections are known. HRES, a program for determining Laue spot coordinates, allows high-resolution determination by a process involving allocation of the buffer memory to a limited region of the detector; and NEWH, a reflection indexing program, allows the indexing of a set of reflections by placing an orientation matrix in core.

In the data collection portion the experimental parameters, along with the reciprocal lattice limits, are fed into GEN, a reflection indexing

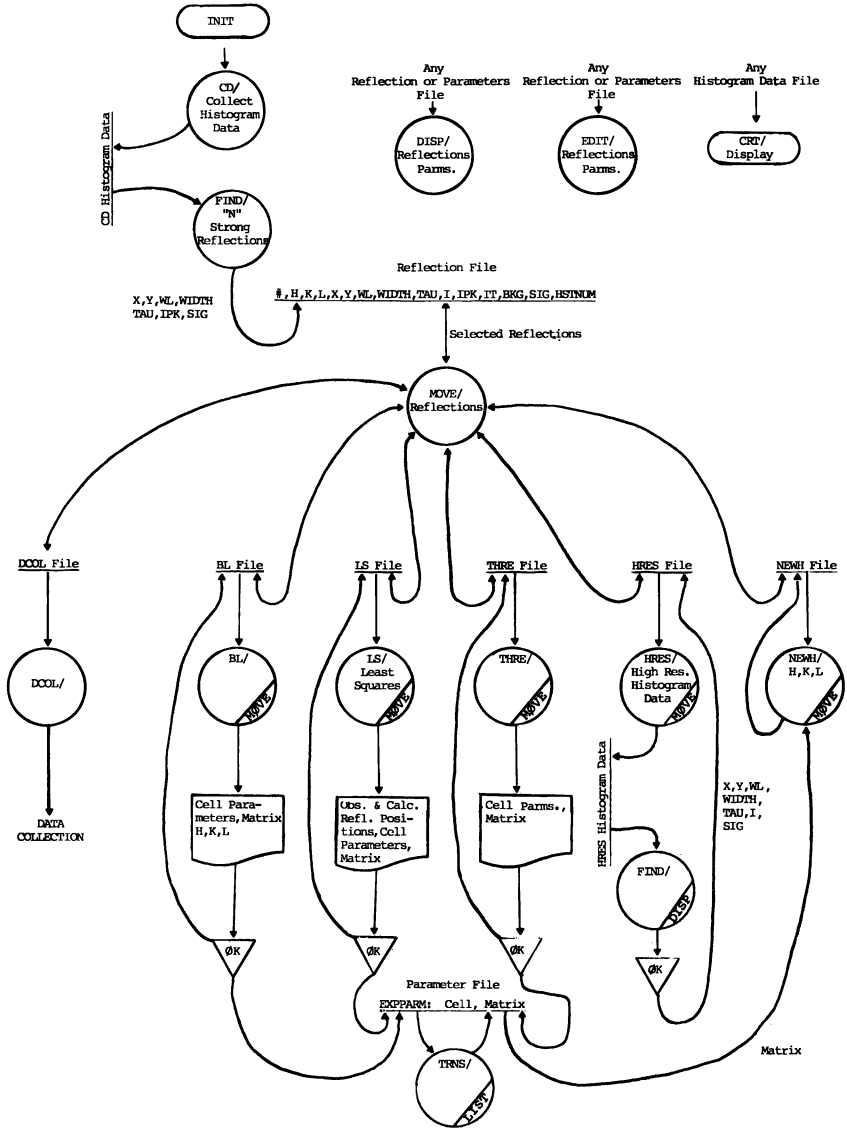

Figure 7. The crystal alignment and unit cell determination software flow diagram: (#), reflection number; x *= coordinate of peak position on detector in horizontal direction;* y *= coordinate of peak position on detector in vertical direction; WL = wavelength; width = peak width at half height; TAU = (sin θ)/λ;* I *= IT − BKG; IPK = peak height; IT = total intensity; BKG = background under peak; SIG = standard deviation of* I*; HSTNUM = histogram number designation. The various programs that may be run are shown in circles.*

Table V. Number of Simultaneous Reflections

2θ (degrees)	d_{min} (Å)	d_{max} (Å)	N[a, b]
30	3.3	16.8	20
90	1.2	6.1	1100
180	0.83	4.2	4400

[a] N = number of reflections = $(8\ A_{det}/3\ R_{det}^2)\ (\sin\theta)^4\ V_{unit\ cell}\ [(1/\lambda_{min}^3) - (1\lambda_{max}^3)]$ with $V_{unit\ cell} = (25\ Å)^3$; R_{det} = crystal-to-detector distance = 30 cm; A_{det} = detector area = (20×20) cm^2; $\lambda_{max} - \lambda_{min} = 6$ Å, where λ is the neutron wavelength; $\lambda_{min} = 1$ Å, 2θ = the mean scattering angle in the horizontal plane.

[b] Data rate for IPNS II is about 50,000 reflections per degree; or, alternatively, X-ray-sized samples of about 0.2-mm edge would give 250 reflections per degree.

program, which generates an *h,k,l* file for data collection. The program PNSET is used to determine the number of crystal orientations and detector angles required to collect a complete data set. This mapping of reciprocal space will be accomplished in an orderly way, but adjacent histograms will inevitably overlap, thus providing, incidentally, adequate scaling between reflections. The data are collected in a stationary crystal mode, and, depending on the detector and crystal positions, the number of reflections N collected at each setting may vary greatly. Table V indicates the number of simultaneous reflections that may be collected at a certain θ and a wavelength range from 1 Å to 7 Å. As θ is increased, smaller d spacings are detectable and N increases. The program CD provides for setting the chi, phi, omega, and 2θ angles to predetermined values and for collecting a set of reflection intensities that constitute the desired histogram. During data collection the developing histogram can be viewed on a Textronix video display unit.

In the data reduction phase each histogram, which has been stored on a Sigma 5 computer—transferred from the microprocessor to a Sigma 5 disk at each overflow of an address location—will be integrated to

Table VI. Advantages and Disadvantages of a TOF Pulsed-Neutron Single-Crystal Instrument

Advantages:

1. No scanning required—λ integration
2. Spectrum rich in $\lambda < 1$ Å (small d_{hkl}'s measurable)
3. λ^4 factor favors large λ's
4. Simultaneous measurement of many (10^2–10^3) *hkl*'s
5. Each *hkl* easily measured at several λ's allowing correction for extinction and multiple diffraction
6. Smaller sample size with increased flux

Disadvantages:

1. Source spectrum must be accurately known
2. Extinction and absorption have a wavelength dependence
3. Detector uniformity and stability are critical

determine peak intensities and backgrounds. Corrections then will be applied for source spectrum, wavelength variation of scattering efficiency, and absorption and extinction. Finally, reflections will be sorted and averaged, with various statistical error estimates applied to the final data set.

Summary

A TOF pulsed neutron single-crystal diffraction system is being developed for the ZING P′ and IPNS facilities at Argonne National Laboratory. The advantages and distances of this instrument are summarized in Table VI. We feel that the disadvantages can be dealt with experimentally, and the advantages of the system outweigh those of comparable non-TOF types of instruments. The instrument is intended for use by a national user community and is being designed accordingly.

Acknowledgments

In a program of this magnitude, there are many people involved. We acknowledge the help from these various groups and especially the following people: J. M. Carpenter and R. K. Crawford, IPNS program; M. K. Kopp, Oak Ridge National Laboratory; F. J. Lynch and R. Brenner, Electronics Division, detector design and fabrication; R. Kleb, Solid State Science Division, beam line design; R. A. Jacobson (Iowa State University), J. M. Kolenko, C. B. Morgan, R. W. Broach, C. Willi, and P. Rogan, Chemistry Division, software design; J. M. Williams, Chemistry Division, user group development; F. R. Lenkszus, Electronics Division, microprocessor design and development. Work was performed under the auspices of the Division of Basic Energy Sciences of the U.S. Department of Energy.

Glossary of Symbols

A_{det} = detector area
CHM = Chemistry Division
d = lattice spacing
EL = Electronics Division
h = Planck's constant
I = intensity
IPNS = intense pulsed neutron system
l = flight path length
m = neutron mass
n = neutron

N = number of reflections
$Q = 4\pi \sin \Theta/\lambda$
R_{det} = crystal-to-detector distance
SCD = single crystal diffractometer
SSS = Solid State Science Division
t = time (sec)
TOF = time of flight
v = neutron velocity
ZGS = zero-gradient synchrotron
ZING P′ = zero-gradient synchrotron intense neutron generator prototype prime
λ = neutron wavelength
Θ = Bragg scattering angle
E = neutron energy
θ = Bragg angle
TCNQ = tetracyanoquinodimethane
h,k,l = Miller indices
ADC = analog to digital converter

Literature Cited

1. "Neutron Research on Condensed Matter: A Study of the Facilities and Scientific Opportunities in the United States"; National Research Council, National Academy of Science: Washington, D.C., 1977.
2. Carpenter, J. M. *Nucl. Instr. and Meth.* **1977**, *145*, 91.
3. Buras, B.; Leciejewic, T. *Nukleonika* **1963**, *8*, 75.
4. Buras, B.; Leciejewicz, T. *Phys. Stat. Sol.* **1964**, *4*, 349.
5. Buras, B. Reactor Centrum Nederland Report, 234, 1975, p. 307.
6. Buras, B.; Mikke, K.; Lebech, B.; Leciejewicz, J. *Phys. Stat. Sol.* **1965**, *11*, 567.
7. Meister, H.; Carpenter, J. M.; Peterson, S. W. IPNS Argonne Report No. 4, December 15, 1978.
8. Borkowski, C. J.; Kopp, M. K. *Rev. Sci. Instrum.* **1975**, *46*, 951.
9. Jacobson, R. Department of Chemistry, Iowa State University.

RECEIVED September 13, 1978.

Some Recent Progress in Solid State Chemistry of Electronic Materials

R. A. LAUDISE

Bell Laboratories, Murray Hill, NJ 07974

The electronic materials community provides a driving force for much research and development in solid state chemistry. Recent progress in five areas is described: (1) intercalation compounds for storage batteries; (2) new titanate microwave dielectrics; (3) the reactions of oxygen in semiconductor silicon; (4) amorphous dielectrics; and (5) imperfections in quartz.

Electronic materials are the bricks and mortar of solid state devices, which in turn are the sine qua non of electronic systems. Progress in telecommunications, automata, computers, and related fields is critically dependent on improving the properties of existing electronic materials and discovering new materials with better properties. Solid state chemistry plays a central role in electronic materials research and development. Many of the goals of solid state chemistry are identical to those of electronic materials research. Indeed, often the general goals of solid state chemistry are best pursued by using electronic materials as the vehicle. For example, we believe some important goals of solid state chemistry are the following:

1. To understand the connection between chemical bonding and structure in solids and their properties. In electronic materials the foundations of understanding that the physicists have built for electronic properties often give the solid state chemist a solid base from which to begin activities.
2. To understand the genesis of imperfections in solids, their equilibria, and their role in determining properties. Here electronic properties often provide a unique probe that the solid state chemist may exploit for determining the nature and concentration of imperfections.

0-8412-0472-1/80/33-186-095$05.00/1

3. To improve and understand preparative methods so as to have the power to prepare a variety of solids. Here the goals of electronic materials and solid state chemistry are completely consistent, and the economic driving forces for useful electronic materials often have resulted in subtle, difficult, and expensive preparative techniques and equipment being routinely available.
4. To discover new solids with interesting properties. Here electronic materials scientists would probably define "interesting" as "ultimately useful." Semantic nuances aside, most would agree that solid state chemistry and electronic materials are again in resonance and that "interesting" can cover a great deal of territory in modern electronics.

In the remainder of this paper we will give brief reviews of some recent solid state chemistry activities in Bell Laboratories, which we believe illustrate, to a considerable degree, the fulfillment of many of these goals and show the synergy between solid state chemistry and electronic materials. Examples could just as well have been chosen from the work of many other laboratories in electronic materials. The subjects considered are these: intercalation compounds as storage battery electrodes. (Here we submit that the motivating forces include the fulfillment of goals 1, 3, and 4); new titanate dielectrics (goals 1 and 4); oxygen precipitation in dislocation-free Si (goal 2); new amorphous dielectrics (goals 1, 3, and 4); and imperfections in quartz (goals 2 and 3).

Our overviews of each of the subjects will, of necessity, be cursory and we recommend perusal of the original papers for those wishing more complete (and rigorous) descriptions.

Intercalation Compounds as Storage Battery Electrodes

Layered compounds have been available since antiquity, mica and graphite being prime examples. Following the availability of X-ray crystallographic structural information, it became apparent that the unique properties of such compounds (cleavability in mica, slipperiness in graphite) were caused by a layered configuration at the atomic level, with strong chemical bonds within the layers and weak bonds between them. Interest in solids with interactions in less than three dimensions, such as linear chain conductors and layered compounds, is presently high because they often provide tests of our understanding of the relationship between bonding, structure, and properties. One family of compounds of high research interest since the late 1960s has been the layered transition metal chalcogenides. As an example, study of these compounds did much to untangle the connections between bonding and properties and showed that they were the first materials to exhibit the phenomenon of charge density waves (*1, 2*).

A charge density wave (CDW) is a coupled periodic distortion both of the conduction electron density and the lattice, with the wavelength of the distortion determined by the Fermi surface. Since one- and two-dimensional solids have Fermi surfaces with sections that are parallel or nesting, CDW often exist. In three-dimensional solids such features may infrequently occur by accident, while in solids of less than three dimensions they will be likely to occur. The Fermi surface delineates the distribution of momentum of electrons in the conduction band and hence is related to the distribution of bonds in the solid. Solids with a nonisotropic bond distribution thus possess quite asymmetric Fermi surfaces. At the onset temperature of the CDW its wavelength is incommensurate with the lattice spacing, so that while, for example, M^+ ions move toward regions of high negative charge, no superlattice occurs. At a lower temperature the CDW wavelength can often be a multiple of lattice spacing, producing a superlattice structure. Some of the phase changes thought to limit electrical storage capacity as more lithiums are intercalated into transition metal chalcogenides are believed to be associated with CDW-like behavior. Alloying of Fe, for example, which was previously shown to inhibit CDWs, has been used to extend the capacity of practical electrodes.

It is possible to introduce atoms (intercalate) between the layers of many-layered materials, especially when the bonding between layers is as weak as van der Waals forces. For instance, in VS_2, Li may be introduced between the layers (Figure 1) without substantially perturbing the structure.

Research on intercalation compounds for energy storage has been conducted by Murphy, DiSalvo, Trumbore, Broadhead and their colleagues (*3, 4, 5, 6*) at Bell Laboratories and by Whittingham and colleagues (*7, 8*) at Exxon. We will review here some of the recent Bell Laboratories activities. It became apparent to D. W. Murphy and F. J. DiSalvo (*3, 4*) and their colleagues (*5, 6*) that Li-intercalated chalcogenides might be attractive as battery materials for several reasons:

1. The structure was little perturbed by intercalation, suggesting that an electrode could survive many charge–discharge cycles without deterioration.
2. The reduction potential of the Li^0/Li^+ couple is high, indicating a battery with a high voltage might be possible.
3. The atomic weight of Li is low, indicating that a battery in which each gram of Li discharged could produce many coulombs might be possible. Such a battery would have a very favorable charge storage density per kilogram of electrode, that is, many watt hours per kilogram of electrode could be stored.

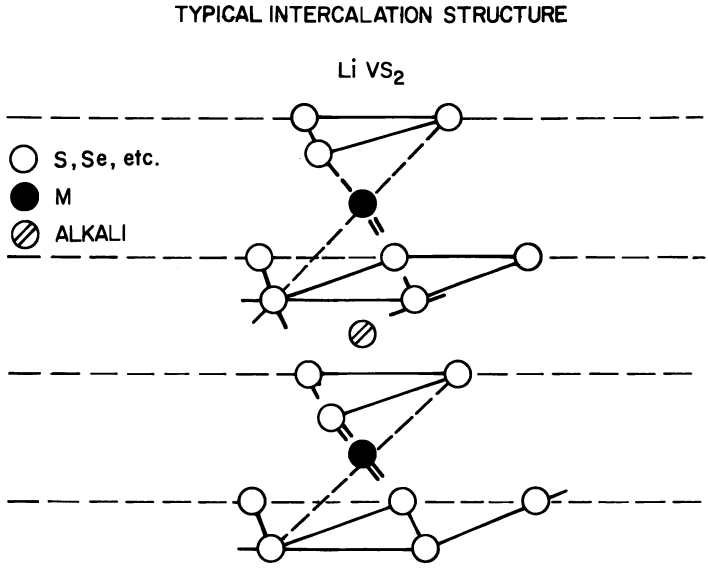

Figure 1. Schematic of Li intercalation in transition metal dichalcogenides

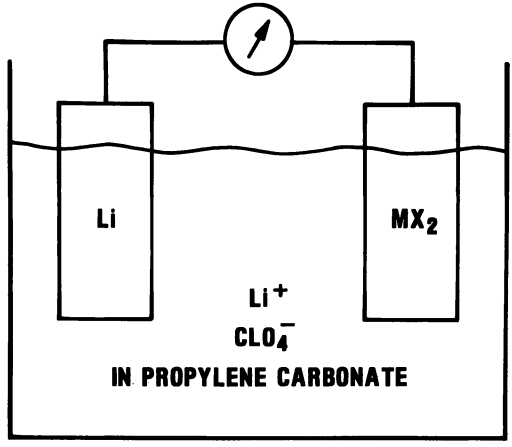

DISCHARGE

$$Li \longrightarrow Li^+ + e^-$$

$$Li^+ + VS_2 + e^- \longrightarrow LiVS_2$$

Figure 2. Cell configuration for intercalation electrode storage battery

Investigation of a variety of possible materials for electrodes required that new synthetic techniques for layered chalcogenides be devised. These have been discussed in the literature and will not be reviewed here (*9, 10, 11*). As a result of these studies, several compounds were characterized and their optimization for electrode materials has proceeded a considerable distance.

A typical cell configuration that resulted from these studies is shown in Figure 2, a room temperature cell using $LiClO_4$ in propylene carbonate as the electrolyte. The theoretical storage density of a variety of electrodes is summarized (*3, 4*) in Figure 3. As can be seen, greater-than-a-factor-of-two improvement over Pb acid and Ni–Cd batteries is possible. Cells have been cycled many times. Much solid state chemistry and development remains to be done, but the contributions of solid state chemistry are already apparent.

CELL	POWER DENSITY IN WATT-HOURS/KG
Li/TiS_2	480
Li/VS_2	510
$Li/V_{1-x}M_xS_2$ (M = Fe,Cr)	510-550
Ni/Cd	240
Pb ACID BATTERY	247

Figure 3. Power storage density for battery electrodes

New Titanate Dielectrics

An important field in solid state chemistry of electronic materials is molecular engineering. Obviously, real materials are developed through a large amount of empiricism. However, as much as possible, modern researchers attempt to design useful materials from first principles—to make use of our basic atomic and molecular knowledge to devise materials with optimum engineering properties for real devices, that is, to molecularly engineer materials. Solid state chemistry, which addresses the basic properties of materials and attempts to understand the connection between bonding and structure and properties, provides perhaps a unique viewpoint toward engineering real materials.

An example of materials that have been engineered to have unique useful properties are the titanium-rich barium titanates, which have been designed to have a high dielectric constant, a unique low dielectric

loss, and a temperature stability at microwave frequencies so that they can replace large, expensive metallic resonant cavities. In microwave circuitry it is important to control precisely the carrier frequencies. This is accomplished by the use of carefully sized air-filled metal cavities or by the use of dimensionally controlled ceramic dielectrics. In each case the dimensions and the dielectric constant fix the resonant frequency of the device and thus set the frequency that is passed or stopped. Since ceramics have a higher dielectric constant than air, smaller devices are possible. However, for practical devices the loss and temperature stability for a ceramic-based system must be comparable with that for a metal cavity system.

For a copper cavity at 4 GHz, typical specifications are loss tan $< 1.5 \times 10^{-4}$ and a temperature coefficient of resonant frequency less than or equal to 17 ppm per degree. (The temperature coefficient is controlled by the thermal expansion of Cu, resulting in a decrease in resonant frequency when temperature increases.) For an appropriate ceramic device these requirements must be met, and, in addition, for the size decrease to be attractive, the dielectric constant (K) of the material should be greater than 30.

H. M. O'Bryan and his coworkers (*12, 13*) showed that in searching for an appropriate material it is logical to consider the dielectric constant requirement first. High-polarizability materials would be expected to have a large K. Polarizability arises from electric and ionic contributions. For $K > 30$ an electronic contribution alone would be insufficient. Therefore, one must consider materials with high ionic polarizabilities. High ionic polarizability arises in solids with small, highly charged cations that are easily moved relative to the anion lattice when an electric field is applied. Promising classes would include oxides containing cations such as Ti^{4+}, Zi^{4+}, Hf^{4+} or $V^{3+,5}$, $Nb^{3+,5}$, $Ta^{3+,5}$ and so on. If the dielectric constant is greater than 100, the small size of the device and the resultant very small dimensional control will be economically unattractive. Therefore, very high K compounds such as ferroelectrics are ruled out.

Typical dielectric materials with $K > 30$ have negative temperature coefficients of their dielectric constant (approximately -300 ppm per degree, leading to an approximately 150-ppm temperature coefficient for the resonant frequency). This effect is the direct result of the decrease in the number of polarizable entities per volume as temperature increases and the lattice expands. There is a subclass of materials for which, as the temperature increases, an increase in polarization per entity compensates for the volume expansion. That is, in some solids the ionic polarizability per Ti^{4+} increases in a way to compensate for the decrease in Ti^{4+} per unit volume as the solid expands. This effect can occur in certain perovskite materials, because the angle of tilt of the oxygen

octahedra changes with temperature in a way to make cation movement easier. Typical compounds exhibiting this effect include $CaZrO_3$, $SiZrO_3$, $Ba_2Ti_9O_{20}$, and $BaTi_4O_9$, where the temperature coefficients are substantially closer to zero than for normal dielectrics.

Dielectric loss will be enhanced in conductive materials so that electric conductivity via impurities or oxidation state changes is avoided. Lattice imperfections such as vacancies, second phases, foreign ions, and grain boundaries all interfere with ionic motion in the oscillating electric field and increase loss in the microwave region, so these are to be avoided or minimized also.

Based on the considerations above, O'Bryan and co-workers (*12, 13*) engineered a compound, $Ba_2Ti_9O_{20}$. In the ceramic form, which is required for cost effectiveness, it was particularly important to control the microstructure and purity. The properties of this material are $K = 40$, temperature coefficient of resonant frequency 2 ppm/°C, and loss tan 1×10^{-4}.

Figure 4 shows a device with a ceramic resonator ($d = 1/2$) in) exposed. This device replaces a Cu cavity whose dimensions are 8×2 in. This device is being considered for use in a new digital radio system designed to serve as a major communications link in metropolitan

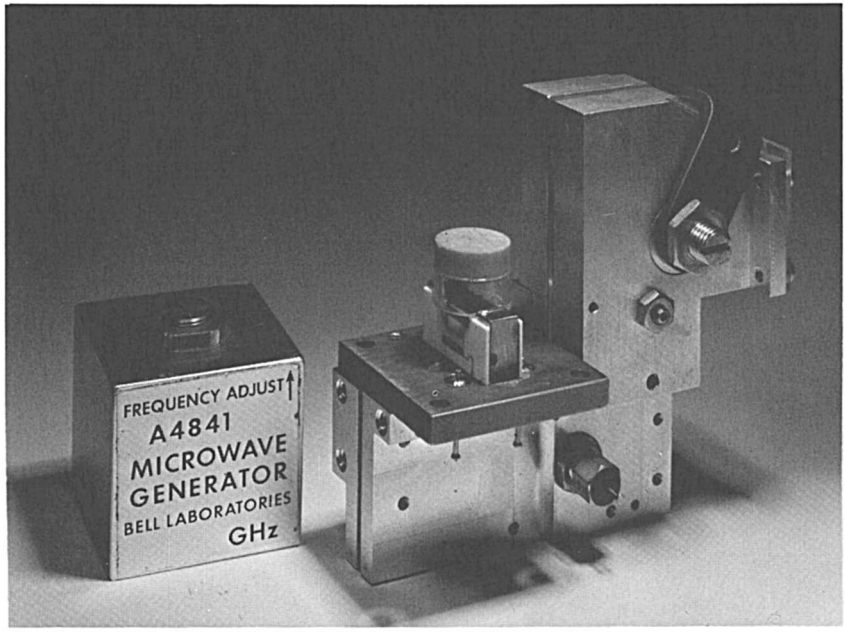

Figure 4. Digital radio microwave filter using $Ba_2Ti_9O_{20}$ dielectric

areas. Dubbed DR-18, for digital radio at 18 GHz, the system will carry up to 28,224 simultaneous telephone conversations and is critically dependent on the molecularly engineered titanate dielectric we have described.

Oxygen Precipitation in Dislocation-Free Si

Semiconductor materials, because of their purity and perfection and because of their well-understood electronic properties, provide an ideal medium to study the genesis of imperfections and their interactions and equilibria with impurities. The need for higher-performance and smaller-feature-size devices and the need for understanding how to avoid and control imperfections and secure desired dopant profiles make such studies technologically essential. Space does not permit reviewing the long listing of such work. We will discuss here some recent studies of Patel, Jackson, and Reiss (*14, 15*) on the precipitation of oxygen initially present in dislocation-free Si and the kinetics of the formation of the stacking fault loops that are caused by this precipitation.

Among the defects known to be produced when oxygen containing dislocation-free Si is heated are stacking faults, which have been shown to be always associated with precipitates or precipitation colonies at their center. It is generally assumed that these precipitates are some form of SiO_2. In the work of Patel, Jackson, and Reiss (*14, 15, 16*) dislocation-free crystals containing approximately 8×10^{17} cm^{-3} of oxygen were heated for various times in the temperature range 1000°–1200°C, where the fault sizes (1–10^3 μm) could be conveniently observed by X-ray topography and optical microscopy. Samples were preannealed at 700°C before the higher-temperature treatment. The formation of stacking faults (Figure 5) as revealed by X-ray topography and etching was not observed at 1200°C unless the samples had previously been also annealed at 700°C. This occurred in spite of the fact that, for oxygen $(c/c_s) \approx 1.2$ at 1200°C, where c is the oxygen concentration and c_s is the equilibrium solubility at 1200°C. Clearly, oxygen precipitation at 1200°C requires a nucleation center of some sort that is produced by the 700°C anneal (*15, 16*).

Quantitative optical and X-ray topographic measurements were used to determine fault sizes. These stacking faults were shown [Maher et al. (*17*), Figure 6] to be associated with a central precipitate and dislocations. Because of the large coherency strains associated with oxygen precipitation, the precipitate particle is always associated with dislocations. The large volume change accompanying precipitation also requires displacement of silicon from the particle per matrix interface:

$$2O_i + 2Si_{Si} \rightarrow SiO_2 \downarrow + Si_i$$

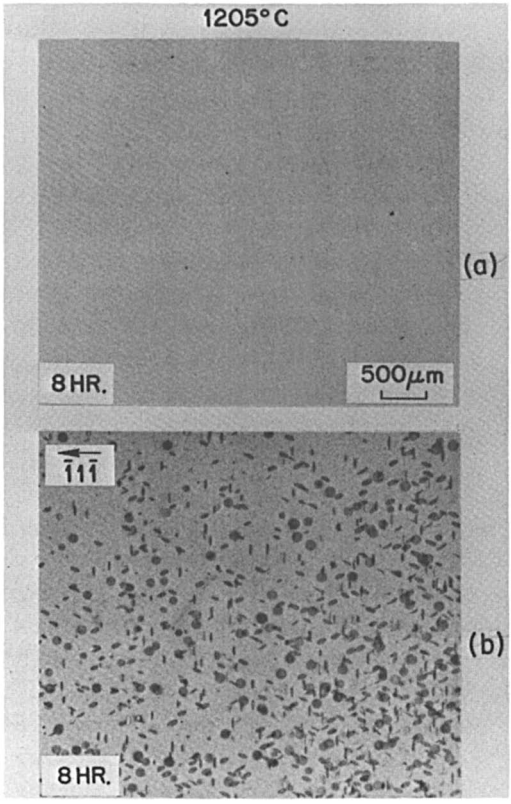

Journal of Applied Physics

Figure 5. X-ray topographs AgKα_1: (top) As-grown Czochralski Si, approximately 8 × 10^{17} cm^{-3} oxygen, heated at 1205°C for 8 hr; (bottom) identical crystal heated at 700°C for 2 hr prior to 1200°C 8-hr treatment (14).

The excess interstitial silicons (Si_i) diffuse away and collapse to form an interstitial Frank type of extrinsic fault. As pointed out by Maher, Mahajan, et al. (*16, 17*), TEM observation cannot distinguish between this mechanism and one in which a Shockley partial and a Frank partial dislocation are formed by dissociation of a perfect dislocation. The Shockley partial would then glide away, leaving the Frank partial surrounding a stacking fault. Growth occurs by oxygen diffusing to that central precipitate and interstitials formed at the precipitate in turn migrating to the fault edge, causing it to grow. Once the partial interstitial loop is formed, precipitate growth can be visualized to proceed by the following:

1. Diffusion of oxygen to a spherical surface of radius R_1 concentric with a growing particle of radius R, where R_1 is approximately a lattice distance

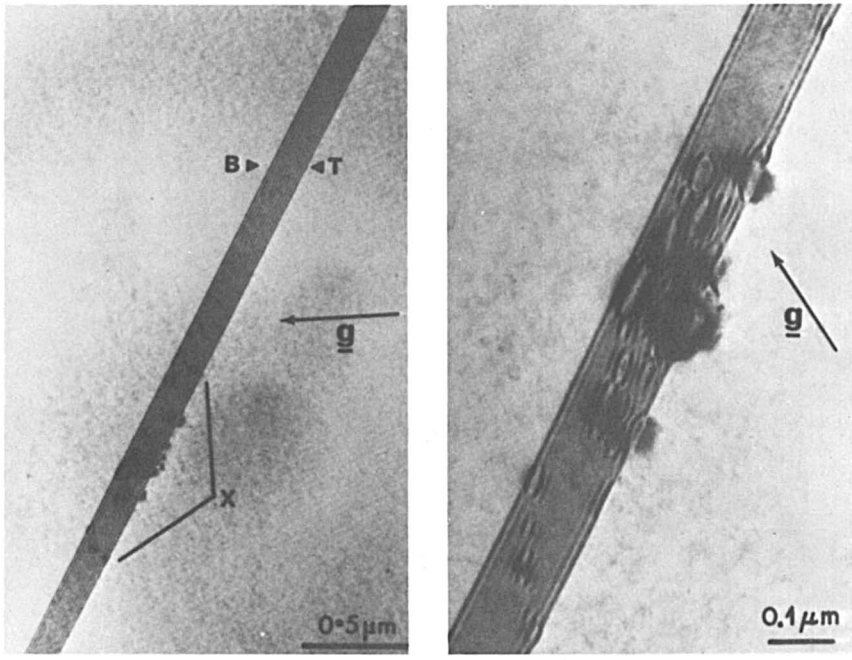

Journal of Applied Physics

Figure 6. Stacking fault generated after 45 hr at 1000°C. Note the clearly defined central precipitate colony and the trace of the earlier position of the Frank partial (17).

2. A reversible jump from a site on a shell of radius R_1 to the surface of the particle
3. A net transfer of oxygen on the surface to a growing edge and a net flux of silicon from the particle to the edge of the stacking fault

The model leads to an expressions for the growth of the diameter of the fault with time, leading to the dependence

$$d \propto t^{3/4}$$

The $t^{3/4}$ dependence arises because the model above predicts a $t^{1/2}$ dependence of the growth of the particle radius R. Hence $R \approx Kt^{1/2}$, where K is a constant involving the coefficient of self-diffusion. From this we find that the particle volume at any time t is $4/3\ \pi R^3 \approx 4/3\ \pi(Kt)^{3/2}$. If we now assume that the volume of material in the stacking fault $[(\pi D^2/4)b]$ is proportional to the particle volume, we can show that $D \approx K^{3/4}t^{3/4}$. Figure 7 shows that the $t^{3/4}$ dependence is well obeyed.

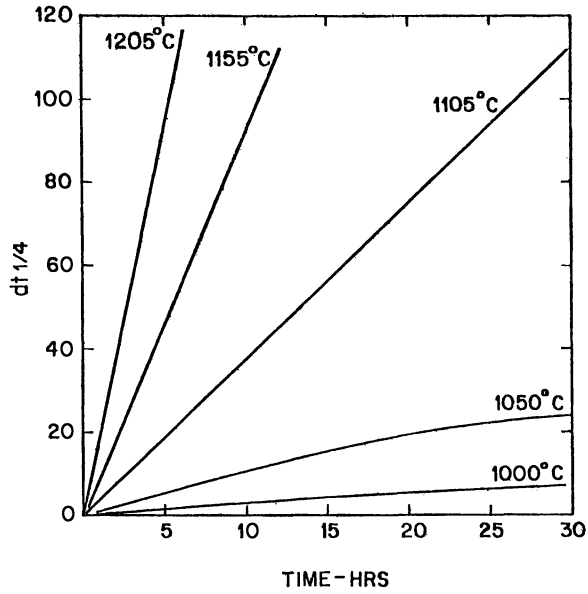

Figure 7. Plot of $dt^{1/4}$ *vs. time for the growth of precipitate diameter* (d) *in Si* (14)

Appropriate studies of the temperature dependence of the growth rate give energies of activation consistent with the energies of activation for the self-diffusion of silicon.

Thus careful solid state chemical studies have given a reasonably complete picture of the genesis and growth of oxygen precipitates and their associated physical imperfections in Si. The studies even suggest processing regimes (temperatures and times) that will minimize undesired imperfections in Si.

New Amorphous Dielectrics

Materials that form glasses easily have high viscosity melts, so that they cannot order even when cooled rather slowly. It has been known for a long time that rapid quenching can freeze in the disordered state of liquids, producing amorphous solids.

Many materials can be formed as amorphous solids by cooling at rates of 10^5–10^6 °C · sec^{-1}, using apparatus such as splat coolers and techniques pioneered by Duwez, Willens, and Klement (*18, 19*). The problem with such methods, where an almost explosive gas blast splats a spray of small liquid droplets onto a high-thermal-conductivity surface, is that the samples produced are small and consequently hard to charac-

terize and are often in a morphology (relatively finely divided particulates) that is technologically uninteresting. The work of Chen, Miller, and others (*20, 21, 22*) has resulted in the availability of techniques for producing very long ribbon geometries of rapidly quenched materials. A typical arrangement of Miller's and Chen's apparatus is shown in Figure 8. A jet of molten material melted by resistance or radio frequency heating in the tube reservoir is directed at a cambered, high-thermal-conductivity spinning wheel. The material is quenched (10^5–10^6 °C · sec^{-1}), often resulting in the formation of a glass. Centrifugal force holds the ribbon formed in contact with the wheel while it is cooled, but the camber angle is such that the ribbon is later cast off the wheel. This apparatus and its relative, the roller quencher, have been used to make amorphous metallic alloys with high strengths (*23, 24, 25*) (probably due to the absence of grain boundaries and crystallographic slip planes present in polycrystalline materials of the same composition) and with unusual magnetic properties (*26, 27*). If the alloy composition is chosen appropriately, almost ideal soft magnetic materials can be formed (*26*). Such materials have very low coercive forces. They magnetize and demagnetize very easily, because domain walls in an amorphous material can move easily since no grain boundaries are present.

Recently Glass and Nassau (*28*) have used the roller quencher to prepare a number of new amorphous dielectrics. In particular, they have succeeded in preparing amorphous a-$LiNbO_3$ and a-$LiTaO_3$. These materials exhibit dielectric maxima (Figure 9) at a temperature lower than their crystalline Curie temperature and show positive tests for pyroelectricity after poling. M. E. Lines (*29*) developed a theory (pre-

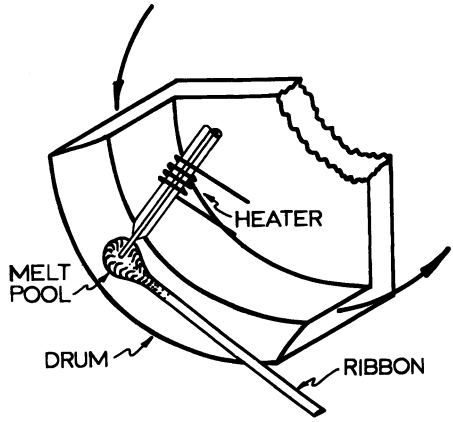

Figure 8. Schematic of spin-quenching apparatus for preparing amorphous materials

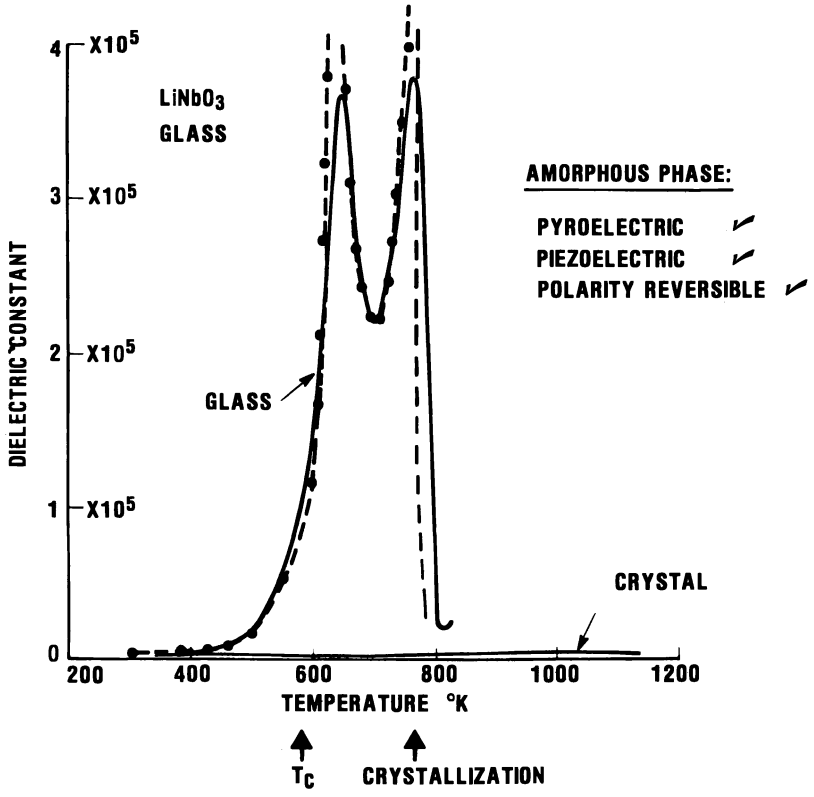

Figure 9. Dielectric constant of crystalline and amorphous $LiNbO_3$: lower temperature peak due to dipole effects; higher temperature peak due to crystallization.

ceding the experimental work) that predicts that ferroelectricity can exist in amorphous materials. A qualitative representation of one feature of this theory is shown in Figure 10. As can be seen, provided local dipoles are preserved (in the case of niobates and tantalates, the local NbO_6 and TaO_6 polyhedra are preserved to some degree), then in the presence of an applied field some net dipole alignment is permitted. Simple geometric arguments suggest that quantities dependent on dipole alignment could still have finite magnitudes in the glass, though reduced over their crystal values, since the local MO_6 groups are randomly oriented to any particular direction of field application.

Glass, Nassau, and Negran (*30*) have investigated, also very recently, the ionic conductivity of a-$LiNbO_3$ and a-$LiTaO_3$. They realized that some of the problems with crystalline, high-ionic-conductivity solid electrolytes arise from the fact that while the conductivity in single crystals is high, this is only so when the crystallography allows the motion

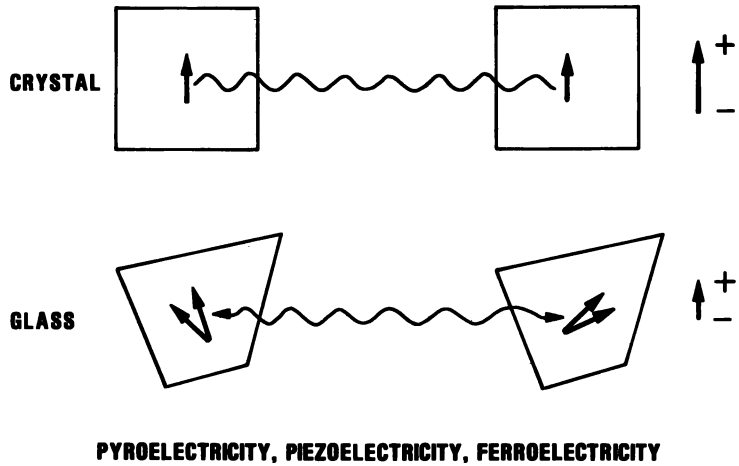

Figure 10. Schematic of alignment of electric dipoles in an amorphous dielectric and in a crystal in an applied electric field

of small ions such as alkalis along specific crystallographic axes. Optimum materials have a high density of weakly bonded ionic species as well as a high degree of disorder in the mobile ion sublattice. These structural requirements are rather stringent, and few crystalline materials meet them. In addition, practical batteries usually require polycrystalline materials in which the discontinuity of mobile ion channels at grain boundaries usually reduces conductivity. In glasses the structural requirements are not so severe, since they are disordered to begin with. Thus it is not surprising that, for instance, Na^+ ion mobility is high in tetrahedrally coordinated silicate glasses. The conductivity is, of course, isotropic, and grain boundary problems are nonexistent.

Already Glass et al. (*30*) have shown that niobate and tantalate glasses can exhibit room temperature conductivities as high as 10^5 $(\Omega \cdot cm)^{-1}$. In the case of a-$LiNbO_3$ this is 10^{20} times the conductivity of the single crystal. Thus conductivities 10^{-1} times those of ceramic Liβ-Al_2O_3 already have been obtained. Understanding so far is qualitative, and by no means have all the relevant systems and variables been explored. It is not unfair to say that amorphous dielectrics are a new state of matter awaiting the further understanding and exploration of solid state chemists.

Imperfections in Quartz

Quartz is probably the second most important material in electronics, at least in terms of volume produced. Probably close to 500,000 lb · $year^{-1}$

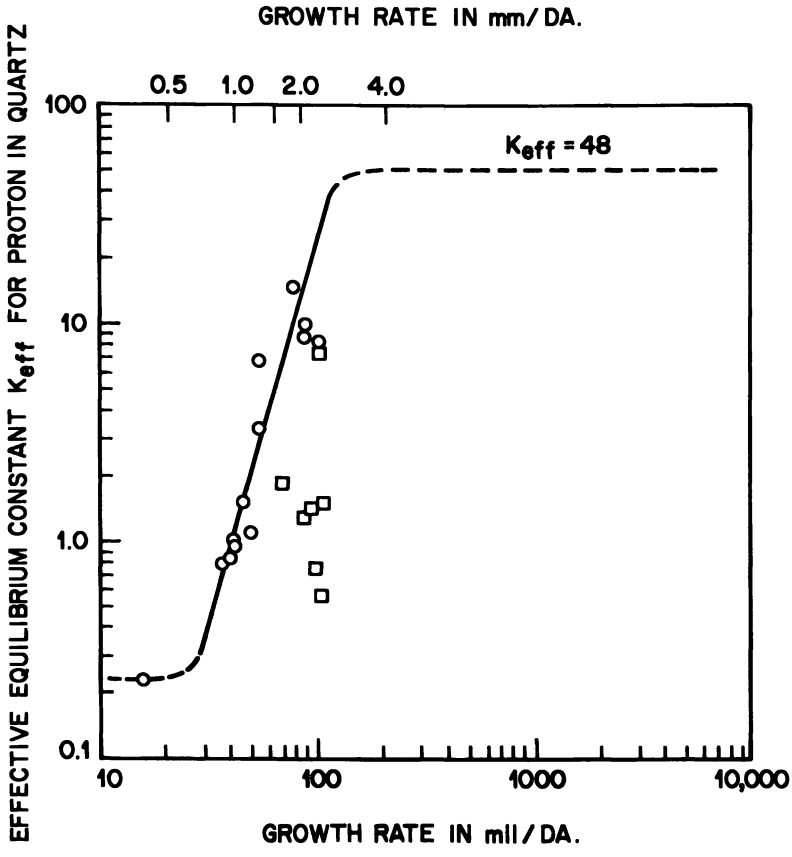

Figure 11. Partition of impurities as a function of quartz growth rate [effective equilibria constant = (M^{3+} · H^+) in solid per (M^{3+}) in solution (OH^-) in solution]. Crystallization temperatures: (○), 350°C; (□), 360°–375°C.

of hydrothermally grown quartz are produced in the world. We (*31, 32*) have studied the partition of impurities in quartz and have shown that the charge compensation reaction

$$M^{3+}(aq) + H^+(aq) \rightarrow M_{Si}^{3+} + H_i^+$$

where $M^{3+}(aq)$ is Fe^{3+} (from corrosion of the steel autoclave wall in which the quartz is grown) or Al^{3+} (an impurity in the small-particle natural quartz feedstock that is recrystallized) and $H^+(aq)$ enters the lattice as OH^- from the aqueous OH^- solutions used to get high enough solubility for crystallization at the condition of growth (25,000 psi, 1*M* NaOH, about 400°C). M^{3+} ions go to Si^{4+} lattice sites and are charge-compensated by interstitial H^+ (which easily fits into the large channels

in the quartz lattice parallel to the *c* direction). The H^+ ions strongly associate with lattice $O^=$ ions so that their presence and concentration can be measured by infrared absorption. In addition, OH causes an acoustic loss, which limits the usefulness of piezoelectric filters and oscillators (*31, 32*). We have shown that the distribution constant for H^+ depends upon growth rate via the Burton–Prim–Slichter equation (Figure 11) and have devised ways to minimize OH and improve the piezoelectric usefulness of quartz (*33*).

Lately we have studied methods for preparing dislocation-free quartz. Figure 12 shows dislocation-free and highly dislocated specimens of hydrothermal quartz that we have grown (*33*). Dislocation-free material

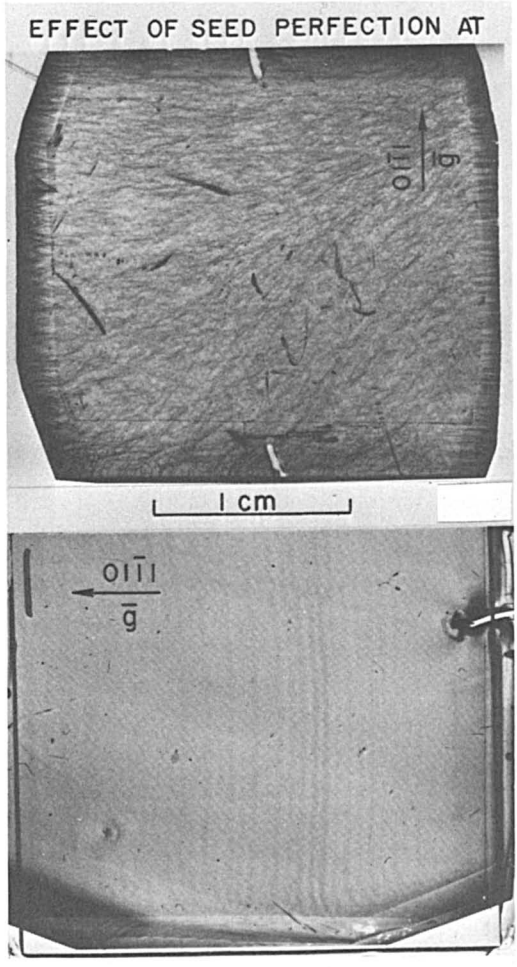

Figure 12. Specimens of synthetic quartz: (top) *highly-dislocated;* (bottom) *dislocation-free.*

can be readily grown provided carefully etched (damage-free) dislocation-free seeds are used. Dislocations can be initiated if particulate inclusions are grown into the quartz. When quartz growth is from an Fe-containing vessel, these inclusions are usually $Fe_6^{2+}Fe_9^{3+}H_9Na_{12}(Si_3O_8)_{15}$, the mineral Tuhualite. Such inclusions can be minimized if growth is from noble metal–lined autoclave. The analogies between these studies and those made on Si are obvious, though quartz is more complicated chemically and nowhere nearly as well understood. Nevertheless, the need and usefulness of the solid state chemical viewpoint in understanding and improving this important material is paramount.

Conclusions

We have tried to give several examples of recent work where solid state chemistry has played a role in accomplishing electronic materials research and development. We hope we also have been able to show that as a result of these studies, where electronic materials were the learning medium, the science and technology of solid state chemistry have been advanced.

Acknowledgments

We would like to thank D. M. Murphy and F. J. DiSalvo, H. M. O'Bryan, K. A. Jackson, J. R. Patel, H. S. Chen, G. Y. Chin, A. M. Glass, K. Nassau, J. H. Wernick and E. D. Kolb for discussions, for providing material, and for allowing us to describe their work.

Literature Cited

1. Wilson, J. A.; DiSalvo, F. J.; Mahajan, S. *Phys. Rev. Lett.* **1974**, *32*, 882.
2. Wilson, J. A.; DiSalvo, F. J.; Mahajan, S. *Adv. Phys.* **1975**, *24*, 117.
3. Murphy, D. W.; Carides, J. N.; DiSalvo, F. J.; Cros, C.; Waszczak, J. V. *Mater. Res. Bull.* **1977**, *12*, 825.
4. Murphy, D. W.; Trumbore, F. A. *J. Cryst. Growth* **1977**, *39*, 185.
5. Broadhead, J. "Power Sources 4"; Collins, D. H., Ed.; Oriel Press: 1973; 469.
6. Broadhead, J.; Trumbore, F. A. "Power Sources 5"; Collins, D. H., Ed.; Academic: New York, 1975; 661.
7. Whittingham, M. S. *Prog. Solid State Chem.* **1977**, *12*, 1.
8. Whittingham, M. S.; Gamble, F. R. *Mater. Res. Bull.* **1975**, *10*, 363.
9. Murphy, D. W.; DiSalvo, F. J.; Hull, G. W., Jr.; Waszczak, J. V. *Inorg. Chem.* **1976**, *15*, 17.
10. Murphy, D. W.; Trumbore, F. A. *J. Electrochem. Soc.* **1976**, *123*, 960. **1976**, *123*, 960.
11. Murphy, D. W.; Trumbore, F. A.; Carides, J. N. *J. Electrochem. Soc.* **1977**, *124*, 325.
12. O'Bryan, H. M., Jr.; Thompson, J. J., Jr.; Plourde, J. K. *J. Am. Ceram. Soc.* **1974**, *57*, 450.
13. Plourde, . K.; O'Bryan, H. M., Jr.; Thompson, J. J., Jr. *J. Am. Ceram. Soc.* **1975**, *58*, 418.

14. Patel, J. R.; Jackson, K. A.; Reiss, H. *J. Appl. Phys.* **1977**, *48*, 5279.
15. Reiss, H.; Patel, J. R.; Jackson, K. A. *J. Appl. Phys.* **1977**, *48*, 5247.
16. Mahajan, S.; Rozgonyi, G. Z.; Brasen, D. *Appl. Phys. Lett.* **1977**, *30*, 73.
17. Maher, D. M.; Staudinger, A.; Patel, J. R. *J. Appl. Phys.* **1976**, *47*, 3813.
18. Klement, W., Jr.; Willens, R. H.; Duwez, P. *Nature* **1960**, *187*, 869.
19. Duwez, P.; Willens, R. H.; Klement, W., Jr. *J. Appl. Phys.* **1960**, *31*, 1136.
20. Chen, H. S.; Miller, C. E. *Mater. Res. Bull* **1976**, *11*, 49.
21. Liebermann, H. H.; Graham, C. D., Jr. *IEEE Trans. Magn.* **1976**, *MAG-12*, 921.
22. Chen, H. S.; Miller, C. E. *Rev. Sci. Instrum.* **1970**, *41*, 1237.
23. Leamy, H. J.; Chen, H. S.; Way, T. T. *Metall. Trans.* **1972**, *3*, 69.
24. Masumoto, T.; Maddin, R. *Mater. Sci. Eng.* **1975**, *29*, 1.
25. Davis, L. A. In "Metallic Glasses"; Gilman, J. J., Leamy, H. J., Eds.; ASM: Metals Park, OH, 1978; 191.
26. Sherwood, R. C.; Gyorgy, E. M.; Chen, H. S.; Ferris, S. D.; Norman, G.; Leamy, H. J. *AIP Conf. Proc.* **1974**, *24*, 745.
27. Gyorgy, E. M. In "Metallic Glasses"; Gilman, J. J.; Leamy, H. J., Eds.; AMS: Metals Park, OH, 1978; 275.
28. Glass, A. M.; Lines, M. E.; Nassau, K.; Shiever, J. W. *Appl. Phys. Lett.* **1977**, *31*, 249.
29. Lines, M. E., submitted for publication in *Phys. Rev.*
30. Glass, A. M.; Nassau, K.; Negran, T. J., in press.
31. Ballman, A. A.; Laudise, R. A.; Rudd, D. W.; *Appl. Phys. Lett.* **1966**, *8*, 53.
32. Lias, N. C.; Grudenski, E. E.; Kolb, E. D.; Laudise, R. A. *J. Cryst. Growth* **1973**, *18*, 1.
33. Barns, R. L.; Freeland, P. E.; Kolb, E. D.; Laudise, R. A.; Patel, J. R., submitted for publication in *J. Cryst. Growth.*

RECEIVED September 13, 1978.

6

Photo Responses of Pure and Doped Rutile

JOHN B. GOODENOUGH

Inorganic Chemistry Laboratory, South Parks Road,
Oxford OX1 3QR England

Photoconductivity, photosensitized electron spin resonance (ESR), and photosensitized electrochemical reactions of pure and doped rutile are summarized. The first two measurements have revealed the energies of metastably occupied, localized states—both native-defect and impurity $3d^n$ states —relative to the band edges. Electrochemical studies suggest the general shape of the density of donor surface states in reduced rutile; they also reveal both a fast ($t_{1/2} < 0.1$ sec) anodic and a slow ($t \approx 10$ sec) cathodic photocurrent in rutile photosensitized with $[Ru(bipy)_3]Cl_2$. The data are related to the questions of localized versus itinerant 3d electrons in oxides, the possible formal valence states of transition metal ions, and the design of a suitable anode for the photoelectrolysis of water with sunlight.

Over the past 50 years remarkable developments have occurred in our control and use of metals, polymers, glasses, and electronic materials. Metallurgists have been primarily concerned with the mechanical properties of solids; solid state chemists have largely formed their identities within the context of electronic materials. In these technologies the solid state physicists have mediated between the chemist–metallurgist and the engineer; they have also built the conceptual foundations for our description and control of the mechanical and electronic properties of crystalline materials.

As the century of inexpensive oil draws to a close, the technical community turns increasingly toward the problems of energy collection, storage, and utilization. In these technologies chemical engineering plays a significant role, and mediation between energy engineers and those who prepare and characterize materials will require a much greater chemical

0-8412-0472-1/80/33-186-113$06.25/1

component than has traditionally been brought to materials problems by the physicists. Chemists trained in the concepts of solid state physics are already in too short supply for industrial demand, and the problem is destined to become more acute in the near future.

For this chapter I have chosen a restricted topic—some photo responses in pure and doped rutile—that nevertheless has windows in four directions: our descriptions of electrons in solids, solar energy utilization and catalysis, materials characterization, and electrochemistry.

Bulk and Surface Electron States

In oxides, outer s and p electrons primarily responsible for chemical bonding are *itinerant*: they are described by one-electron band theory in which each electron is considered to be shared equally by all like atoms on equivalent lattice positions. Oxides have a large ionic component in their binding energies, and the electrostatic Madelung energy stabilizes filled, primarily O^{2-}:$2p^6$ bands a finite energy below any empty, primarily cationic s and p bands. The energy gap $E_g = (E_c - E_v)$ between the top of the filled O^{2-}:$2p^6$ valance bands (E_v) and the bottom of the empty cation —s, p bands (E_c) is generally so large in oxides of the main group elements that shallow donor or acceptor centers associated with these bands are thermodynamically unstable relative to the formation of native defects. (Heavy posttransition elements may form oxides capable of supporting shallow donors or acceptors.)

Common native defects in oxides are anion and cation vacancies. An isolated anion vacancy, V_0, creates a positive crystal field potential that stabilizes below the conduction band edge E_c localized states centered at V_0; they are symmetrized, near-neighbor cation orbitals lowered out of the conduction band. They correspond to the well-known color centers encountered in alkali halides. In oxides an isolated V_0 center traps one electron at an energy about $2e^2/R \sim 0.8$ eV below E_c, where R is the distance from the V_0 center to a nearest-neighbor cation and e is the electron charge. These centers may trap one, two, or three electrons; vacancy clustering and vacancies near the surface trap electrons at somewhat different energies. As a result, anion vacancies provide a distribution of donor states extending about 1 eV below E_c. Similarly, cation vacancies create a distribution of acceptor states above the valance band edge E_v formed from symmetrized, near-neighbor anion orbitals raised out of the valence band.

Outer 4f electrons at rare earth cations are *localized*: they are well described by crystal field theory, and interatomic interactions can be treated by perturbation theories (superexchange, double exchange, or indirect exchange). Localized electrons in a partially filled shell are charac-

terized by discretely separated energy levels for different occupancies, in this case for different values of n in the $4f^n$ manifold. The energy separaitons U are due to the electrostatic coulomb interactions between electrons of that shell.

Outer d electrons at transition metal cations in oxides may be itinerant or localized (*1*); in some cases itinerant and localized d electrons coexist at the same cation (*2*). Whether electrons are itinerant or localized depends upon the relative magnitudes of the intraatomic energies U and the interatomic energies. Interatomic energies are measured by the tight-binding bandwidth $w_b = 2zb$, where z is the number of like nearest neighbors and b is the nearest-neighbor resonance (or electron transfer) integral

$$b_{ij} = (\psi_i, \mathcal{H}'\psi_j) \tag{1}$$

in which $\mathcal{H}'$ is the perturbation of one-electron potential at site $\boldsymbol{R}_j$ due to a like atom at $\boldsymbol{R}_i$ and ψ_i, ψ_j are one-electron atomic wave functions at these sites. ($\boldsymbol{R}_i$ is the vectorial distance from a chosen origin to the ith lattice site.) The bandwidth $w_b = 2zb$ follows directly from first-order tunneling theory and the assumption $U = 0$. If $w_b << U$, the electrons are localized; if $w_b >> U$, the electrons are itinerant. Where $w_b \sim U$, conventional band theory must be modified by the introduction of strong correlation energies and electron–lattice coupling.

The locations of the d^n and f^n energies relative to E_c and E_v determine what formal valence states are available to transition metal or rare earth cations. The rare earth oxides have 5d bands that overlap the 6s and 6p bands, so E_c may be the edge of a 5d rather than a 6s band. Such is the case in EuO, for example (*3*). If the energy of a $4f^n$ manifold lies within the energy gap $E_g = (E_c - E_v)$, then two formal valence states are possible for the rare earth cation; they correspond to the configurations $4f^n$ *and* $4f^{n-1}$. In EuO the Eu^{2+}:$4f^7$ energy level lies about 1.1 eV below E_c, and oxidation to create Eu^{3+}:$4f^6$ configurations is possible. On the other hand, the energies U for 4f electrons are generally $U > E_g$, and commonly no $4f^n$ configuration has an energy within E_g. In this case only ine $4f^n$ configuration can be obtained. For example, only the Gd^{3+}:$4f^7$ core configuration is found. Substitution of gadolinium for europium in $Eu_{1-x}Gd_xO$ results in the Gd configuration $4f^75d^1$, where the $5d^1$ state is a shallow donor state just below E_c. (In this oxide shallow donor states are possible because E_c is at the bottom of a 5d band). On the other hand, the Gd^{3+}:$4f^7$ level lies well below E_v, so it is impossible to oxidize Gd_2O_3 so as to create a Gd^{4+}:$4f^6$ level.

The free ion energies U for transition metal d^n configurations are smaller than those for rare earth $4f^n$ configurations, and in a crystal, coval-

ent mixing with neighboring ligands produces a larger reduction of a transition metal U from its free ion value. Therefore, a transition metal $U < E_g = (E_c - E_v)$ is common, especially where E_c is the bottom of a cation s band. Consequently, at least one, and perhaps several, d^n configuration has its energy within a given E_g. This situation makes multiple formal valence states possible. In the case of vanadium, for example, the oxides VO, V_2O_3, VO_2, and V_2O_5 are all known, which implies energy separations of the V^{2+}:d^3, V^{3+}:d^2, and V^{4+}:d^1 configurations that are less than 3 eV. Since these ions can have d electron bandwidths approaching 2 eV in oxides, the condition $U \sim w_b$ is fulfilled. The peculiar chemical and physical properties of vanadium oxides reflect this situation (*1*).

If two transition metal ions are present in the same crystal, the relative energies of their d^n manifolds determine the formal valence states on the cations. For example, $FeVO_3$ could be $Fe^{2+}V^{4+}O_3$ or $Fe^{3+}V^{3+}O_3$. With the first set of valence states, ordering of cations within the corundum subarray is expected to give the ilmenite structure of $FeTiO_3$. In fact, the ions remain disordered and Mössbauer spectroscopy confirms an Fe^{3+}:d^5 configuration (*4*).

A knowledge of the energies of localized electron manifolds and the energies U that separate them, of the positions of the band edges E_c and E_v, and of the energy distribution of bulk states associated with native defects is necessary for any systematic design of solid state electronic devices. In addition, the device engineer may need to control surface states. In elemental semiconductors these have energies near the center of the gap $E_c - E_v$ unless active in chemisorption; in polar compounds the surface states for each species tend to be displaced above (cationic) or below (anionic) the center of the gap. Chemisorption occurs where surface state orbitals interact with atomic or molecular orbitals of a chemical species adsorbed on the surface; the interaction produces a chemical bond between the solid and the adsorbate. Chemical activity at the surface depends on the positions of the surface states relative to the bulk states and their electron occupancy before and after chemisorption or physisorption.

This chapter summarizes some experiments designed to provide information about bulk and surface states in TiO_2. Rutile has been extensively studied as a possible anode for the photoelectrolysis of water by sunlight, a topic dealt with in another chapter of this volume (*5*).

Dopant $3d^n$ Configurations

Rutile crystallizes in a tetragonal structure with Ti^{4+} ions in simple strings of edge-shared octahedra parallel to the *c*-axis that are connected by sharing common octahedral site corners; *see* Figure 1. Each O^{2-} ion is bridging in one string and nonbridging in the other; each has three

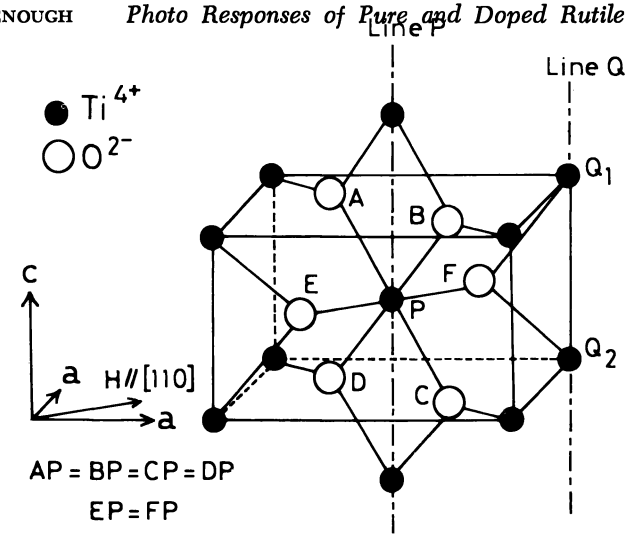

Figure 1. Tetragonal structure of TiO_2

coplanar, nearest-neighbor cations and a p_π orbital directed perpendicular to the plane toward a vacant octahedral site. This structure gives rise to energy bands having E_v as the top of the O^{2-}:$2p_\pi^2$ band and E_c as the bottom of the empty Ti^{4+}:3d bands; *see* Figure 2. The cubic component of the crystalline fields splits the fivefold-degenerate 3d orbitals into three more stable t_{2g} and two less stable e_g orbitals. The Ti^{4+}—O^{2-}—Ti^{4+} interactions are strong enough to transform the e_g orbitals into one-electron σ^* orbitals and two of the t_{2g} orbitals into one-electron π^* orbitals; Ti^{4+}—Ti^{4+}

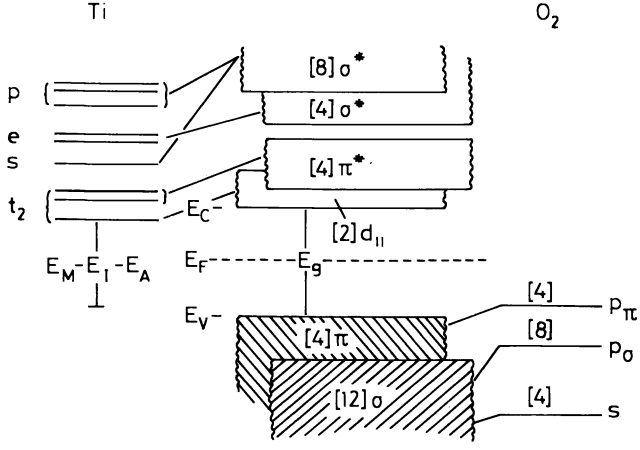

Figure 2. Schematic energy band diagram for TiO_2

interactions parallel to the *c*-axis transform the remaining t_{2g} orbital into a one-dimensional band allowing conductivity along the *c*-axis. The photoconductivity of single-crystal TiO_2 exhibits a large anisotropy at threshold, $E_g = (E_c - E_v) = 3.0$ eV; the conductivity along the *c*-axis is more than two orders of magnitude larger than that in the basal plane (*6*), which places E_c at the bottom of the one-dimensional 3d band, as illustrated in Figure 2.

Electrochemical measurements locate the H^+/H_2 level of an aqueous solution of pH = 1 at 4.5 eV below the vacuum level, and measurements of the flat-band potential of *n*-type TiO_2 relative to the H^+/H_2 level in such a solution suggest an electron affinity $\chi \sim 4$ eV (*7*). (A Fermi energy E_F about 0.4 eV below E_c is estimated in these experiments, where E_F was about optimal for the photoelectrolysis of water.) This measurement, together with E_g, provides absolute energies for E_c and E_v in TiO_2, a neutral adsorbed layer at the surface occurring for pH = 5.7 (*8*).

Initial attempts to measure the energies of $3d^n$ manifolds of several transition metal cations substituted into TiO_2 relied heavily on semiempirical arguments (*9*). In these experiments the intensities of the electron spin resonance (ESR) signals associated with different $3d^n$ configurations were monitored as a function of the concentration of interstitial lithium. Unfortunately, it was not possible to determine accurately the position of the Fermi energy in the band gap as a function of the Li^+ ion concentration. Therefore, a combination of photoconductivity and photosensitive ESR measurements was made at the University of Tokyo to overcome this difficulty (*10*).

Surface photocurrent versus wavelength λ ($\Delta\lambda \sim 10$ nm) of the incident light, chopped at 300 Hz for improved detection, was measured at 77 K (to reduce dark currents) on as-sliced or oxidized samples. Figure 3(a) shows the results before and after exposure to an intense white light for a crystal slab as sliced from an original, undoped ingot. Electrons excited by the white light at 77 K become trapped in metastable states having energies within E_g; these are interpreted to be primarily surface states. A room temperature anneal returns the sample to its equilibrium distribution. The strong absorption below 415 nm is due to excitation across the 3.0 eV band gap. Figure 3(b) shows typical results for similar experiments on oxidized crystal slabs substitutionally doped with V, Cr, Mn, and Fe. Doping to 0.001–0.01% levels was accomplished by heating single-crystal slabs of TiO_2 with the transition metal powder at 400°–800°C for 1 hr in a sealed tube and subsequently oxidizing in oxygen at 850°–1000°C for 1 day. The results were insenitive to the dopant ion; the increased densities of states appear to be bulk states associated with cation vacancies created by oxidation (*see* discussion of polarized light experiments below). As expected, the density of deep acceptor states associated

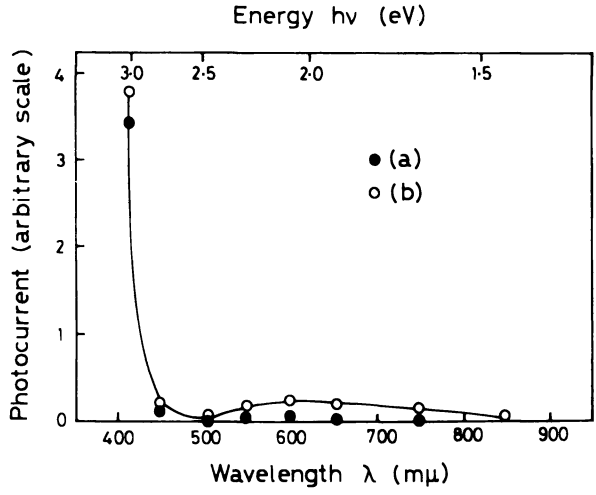

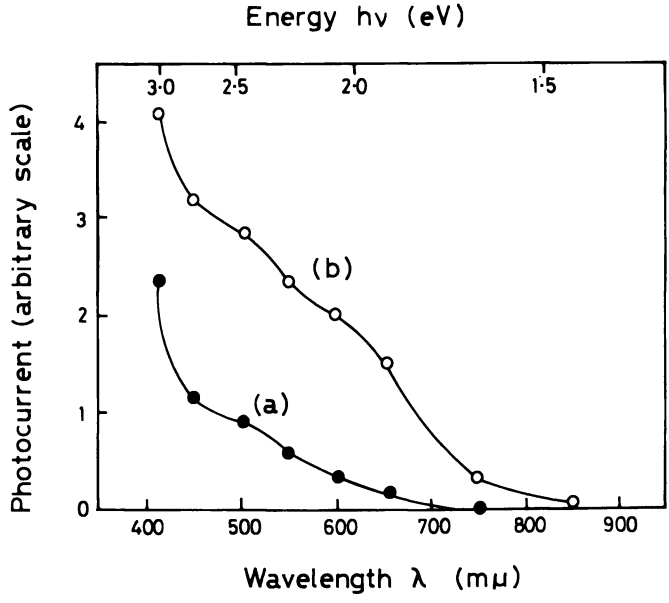

Figure 3. Surface photocurrent at 77 K vs. wavelength λ of incident monochromatic light (Δλ ≃ 10 nm): (●) before; (○), after exposure to intense white light for (a) as-sliced and (b) doped, followed by oxidation single-crystal TiO_2 (10).

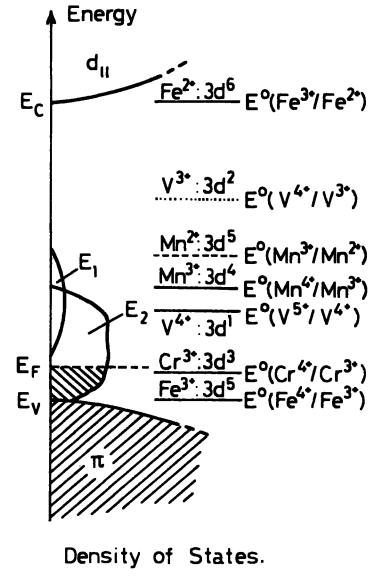

Figure 4. Schematic summary of band gap states metastably occupied at 77 K as revealed by surface photoconductivity and photosensitive ESR measurements

with cation vacancies extends about 1 eV above E_V. Before irradiation with white light, few of the acceptor states are occupied by electrons, consistent with a fermi energy E_F near E_V.

After exposure of the doped samples to white light, the photocurrent was monitored as a function of the time of exposure to the monochromatic light. The photocurrent decreased with time for $\lambda \geqslant 500$ nm, as might be expected if the monochromatic light returns the electron distribution toward equilibrium. However, for $\lambda \leqslant 450$ nm the photocurrent increases with time, which indicates that the monochromatic radiation is either pumping electrons out of acceptor states that are being repopulated thermally by electrons or increasing the surface mobility of the electrons by populating surface traps with electrons excited from the bulk. Both phenomena can be expected for bulk acceptor states below E_F, which would place E_F within 0.3 eV of E_V in the oxidized samples.

In summary, the photocurrent measurements confirm a band gap of $E_g \approx 3.0$ eV, and they reveal a narrow band of low density of states (designated E_1 states in Figure 4) extending from the center of the band gap to about 0.5 eV above E_V, and in oxidized samples a density of acceptor states extending a full 1 eV above E_V with an E_F about 0.3 eV above E_V. The E_1 states are assumed to be surface states that are primarily of anionic character; the bulk acceptor states (designated E_2 in Figure 4) appear to be centered at cation vacancies.

In contrast to the photoconductivity measurements, photosensitive ESR spectra at 77 K, observed with a conventional X band spectrometer,

were dopant-ion specific. Figure 5 illustrates three types of experiments that were performed: (a) the constant-intensity dark signal undergoes a change ΔI that varies with the time t_1 after exposure to monochromatic light; (b) the ΔI from a dark signal that has been changed by previous white light exposure at 77 K is monitored as a function of the time t_2 after exposure to monochromatic light; and (c) the ΔI from a dark signal that has been changed by exposure at 77 K to white light followed by 415-nm light is monitored as a function of the time t_3 after exposure to monochromatic light. Figures 6 and 7 show ΔI versus λ for $t_1 = 2$ min and $t_2 =$

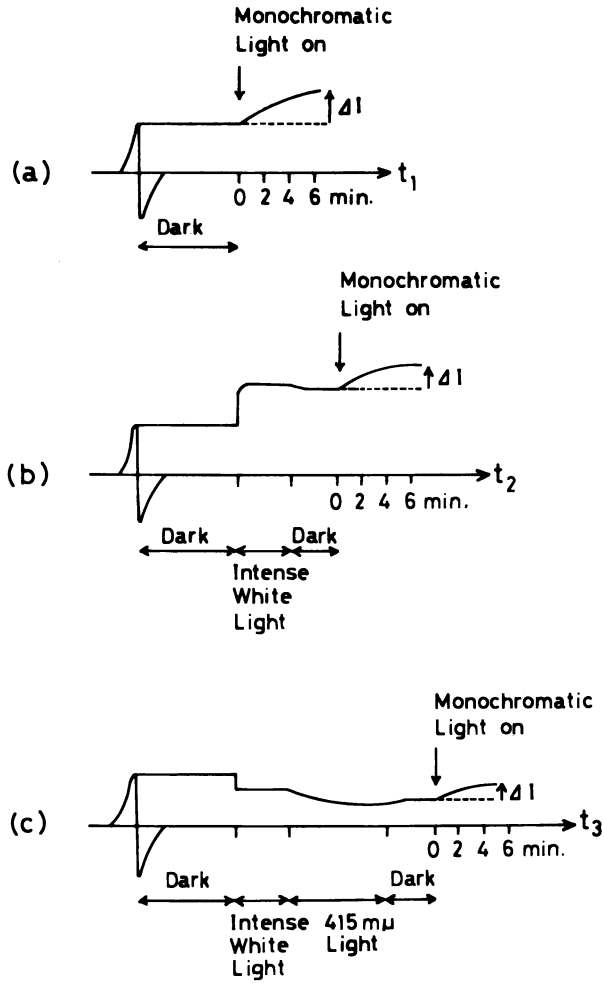

Figure 5. Definition of experimental times (a) t_1, (b) t_2, and (c) t_3, and schematic representation of typical variations of ESR signal intensity with times at 77 K (10). (Differential peak ∝ intensity)

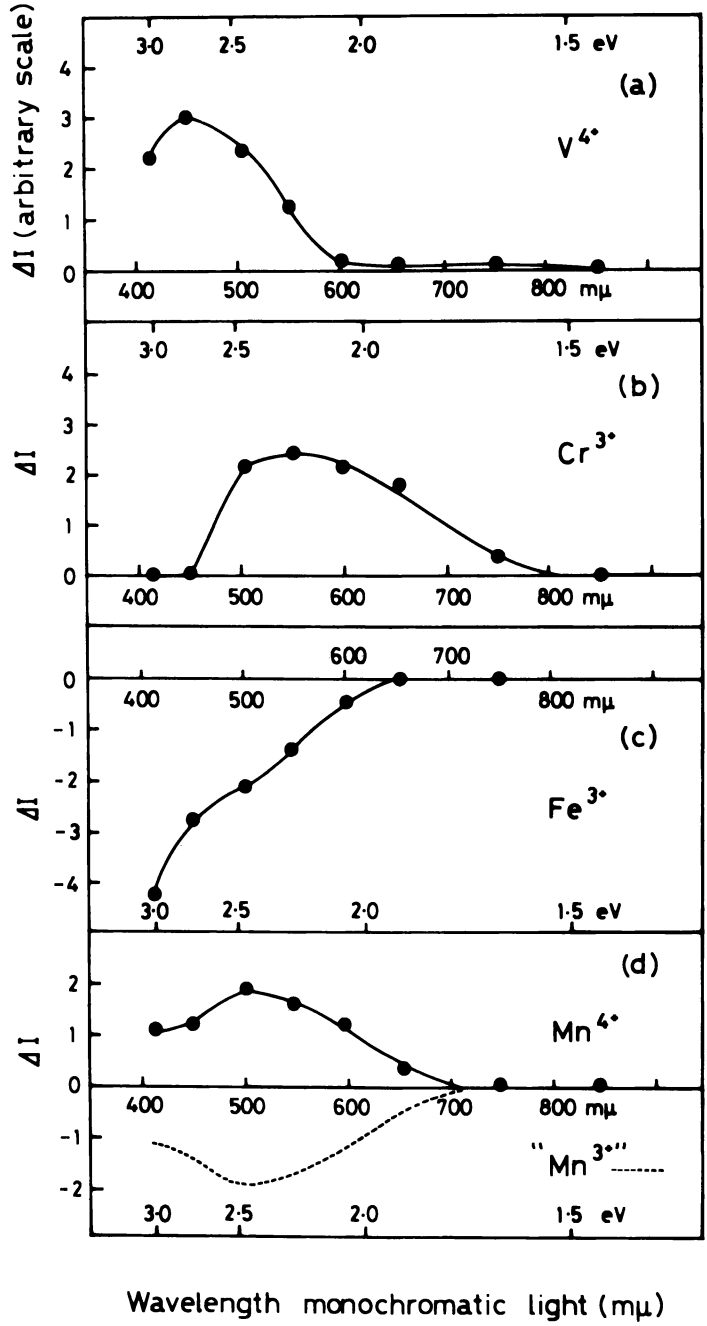

Figure 6. Spectra at 77 K of the change ΔI in ESR signal intensity from $t_1 = 0$ *to* $t_1 = 2$ *min for four impurity cations in* TiO_2*: (a–c) oxidized; (d) reduced* (10).

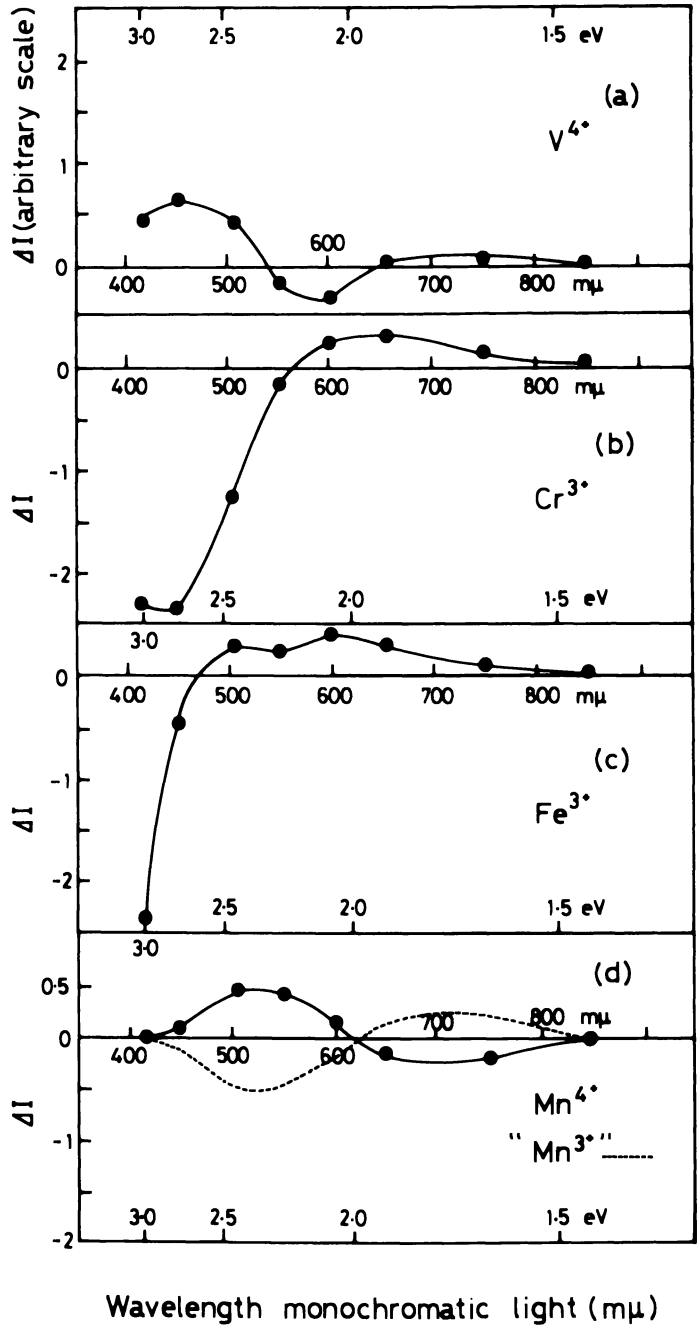

Figure 7. Spectra at 77 K of the change ΔI in ESR signal intensity from $t_2 = 0$ *to* $t_2 = 2$ *min for the same impurity–cation states in the same* TiO_2 *crystals as in Figure 6: (a–c) oxidized; (d) reduced* (10).

2 min, respectively. All signals were normalized to the intensity of the monochromatic light, and between each measurement the influence of the previous exposure to monochromatic light was removed by either a room temperature anneal (Figure 6) or a reirradiation by white light (Figure 7).

For each dopant an ESR signal is associated with a given formal valence state $M^{m+}:3d^n$; the intensity of the signal depends upon the number of dopant ions in the M^{m+} state. Changes in the $3d^n$ population are caused by light-induced electron transfer to or from the M^{m+} ions:

$$M^{m+}:3d^n + 1e \rightarrow M^{(m-1)+}:3d^{n+1} \quad (2)$$

$$M^{m+}:3d^n - 1e \rightarrow M^{(m+1)+}:3d^{n-1} \quad (3)$$

$$M^{m+} + M^{m+} \rightarrow M^{(m-1)+} + M^{(m+1)+} \quad (4)$$

The E_1 and E_2 states as well as the valence band may serve as sources or sinks for electrons, and electron or hole transfer through the crystal occurs via the conduction and valence bands, respectively. As indicated in Figures 6 and 7, the ESR signals monitored were from the $V^{4+}:3d^1$, the $Cr^{3+}:3d^3$, the $Fe^{3+}:3d^5$, and the $Mn^{4+}:3d^3$ ions.

Interpretation of the spectra of Figures 6 and 7 is based on the assumption that electrons, once excited from E_1, E_2, or $3d^n$ states to the conduction band by monochromatic light of wavelength λ, can move through the crystal either to become retrapped at a distant, localized electron center or to recombine with a valence band hole. Moreover, monochromatic light having $\lambda < 450$ nm may create mobile valence band holes either indirectly—by exciting electrons from an E_2 state that becomes thermally repopulated from the valance band—or directly if $\lambda <$ 415 nm. Metastable electrons can be trapped at E_1, E_2, or d^n centers.

In oxidized TiO_2:V most of the vanadium ions have the formal valence $V^{5+}:3d^0$. The ESR signal from a $V^{4+}:3d^1$ ion is sharp and easily monitored. The V^{4+}/V^{5+} ratio is so low in oxidized samples that any V^{3+} ion population can be ignored and any changes ΔI versus t_1 in the ESR signal represent an increase in the V^{4+} ion population from its equilibrium value. The spectrum of Figure 6(a) shows $\Delta I > 0$ only for $\lambda < 600$ nm. From Figure 3(b) the density of occupied states for the virgin dark state is negligible for $\lambda > 700$ nm, and we would expect a two-way exchange of electrons between $3d^n$ configurations and E_1 or E_2 states where the energy $h\nu \approx [E_c - E(V^{4+})]$. However, a $\Delta I > 0$ can be expected for $h\nu > [E_c - E(V^{4+})]$, since a metastable electron distribution becomes possible under these conditions. This reasoning places the $V^{4+}:3d^1$ level about 2.1 eV below E_c, an assignment that appears to be confirmed by Figure 7(a). After exposure to white light, the $V^{4+}:d^1$ population is

nearly doubled, and monochromatic light tends to return this population to its equilibrium value, making $\Delta I < 0$, if $h\nu \approx [E_c - E(V^{4+})]$. The maximum ΔI at about 450 nm for both t_1 and t_2 reflects electron transfer from V^{4+} ions to mobile holes created by thermal excitation to E_2 states near E_V.

In oxidized TiO_2:Cr, the Cr^{3+}/Cr^{4+} population ratio is much larger than the V^{4+}/V^{5+} ratio in oxidized TiO_2:V. This observation indicates that the Cr^{3+}:$3d^3$ level lies distinctly below the V^{4+}:$3d^1$ level at 2.1 eV below E_c. From Figures 6(b) and 7(b), reasoning similar to that for TiO_2:V places the Cr^{3+}:$3d^3$ level about 2.7 eV below E_c. A large crystal-field splitting places the high-spin Cr^{2+}:$3d^4$ level well above E_c, so this valence state need not be considered.

In the case of oxidized TiO_2:Fe, essentially all the iron ions are in the Fe^{3+}:$3d^5$ state at equilibrium, and any ΔI at t_1 must be negative. The existence of the ilmenite phase $Fe^{2+}Ti^{4+}O_3$ indicates that the Fe^{2+}:$3d^6$ level may lie below E_c in TiO_2, at least if occupied, so a $\Delta I < 0$ can be produced either by excitations from E_1 or E_2 states to Fe^{2+}:$3d^6$ levels near E_c or by the reaction

$$2Fe^{3+} \xrightarrow{h\nu} Fe^{2+} + Fe^{4+} \tag{5}$$

if the empty Fe^{3+}:$3d^5$ level lies above E_V. As seen in Figure 6(c), failure to observe at $\Delta I < 0$ until $\lambda < 650$ nm seems to place the empty Fe^{2+}:$3d^6$ level about 0.1 eV above E_c. However, lattice relaxation about an occupied Fe^{2+}:$3d^6$ level would stabilize this by about 0.3 eV, thereby placing the occupied level about 0.2 eV below E_c and allowing formation of Fe^{2+}:$3d^6$ ions in the presence of Ti^{4+} ions. This deduction appears to be confirmed by the observation of ΔI at t_2, Figure 7(c), and at t_3 (*10*). As $\lambda \rightarrow 415$ nm, Reaction 5 appears to produce a sharp increase in $|\Delta I|$. It also is enhanced for $\lambda < 450$ nm by thermal excitation of valence band electrons to emptied E_2 states with subsequent hole capture at an Fe^{3+}:$3d^5$ level. Although the occupied Fe^{3+}:$3d^5$ level appears to be at, or just below, E_V, the empty level is lifted above E_V by lattice relaxation about the Fe^{4+}:$3d^4$ ion. Thus the filled Fe^{3+}:$3d^5$ level appears to lie just below E_V in TiO_2 and the empty Fe^{2+}:$3d^6$ level just above E_c, so octahedral site iron in oxides has an energy

$$U = E(Fe^{2+}) - E(Fe^{3+}) \approx 3 \text{ eV} \tag{6}$$

Since this marks addition of the first electron after the half-filled, high-spin 3d shell, it is a relatively large free-ion U. Such a small value for the crystalline U is quite consistent with the relatively high superexchange interactions between Fe^{3+} ions in oxides (*1*).

Since $FeVO_3$ contains Fe^{3+} and V^{3+} ions rather than Fe^{2+} and V^{4+} ions, we must place the octahedral site V^{3+}:$3d^2$ level below the Fe^{2+}:$3d^6$ level, and hence below E_c in TiO_2. This deduction implies that for octahedral site vanadium in oxides,

$$U = E(V^{3+}) - E(V^{4+}) \leq 2 \text{ eV} \tag{7}$$

which is consistent with the observation of a semiconductor–metal transition in VO_2 characteristic of a $U \approx w_b$ (*1*).

In the case of TiO_2:Mn, oxidized samples contain nearly all the manganese ions in the Mn^{4+}:$3d^3$ state, indicating a Mn^{3+}:$3d^4$ level in the vicinity of the V^{4+}:$3d^1$ level, which is 2.1 eV below E_c. The existence of the ilmenite $Mn^{2+}Ti^{4+}O_3$ indicates that the Mn^{2+}:$3d^5$ level also lies below E_c. Because the rate of decay of a metastable Mn^{3+} ion to a Mn^{4+} state in oxidized TiO_2:Mn is too rapid for convenient monitoring of the ESR signal from Mn^{4+}:$3d^3$ ions, the photosensitive ESR signals shown in Figures 6(d) and 7(d) are for reduced TiO_2:Mn. In reduced TiO_2:Mn the fermi energy E_F lies close to E_c, and very few of the manganese ions are Mn^{4+}:$3d^3$. This finding is also consistent with a Mn^{3+}:$3d^4$ level at least 2 eV below E_c. In the spectra of Figures 6(d) and 7(d), a positive ΔI for the measured Mn^{4+} ESR signal represents a negative ΔI for the Mn^{3+} ions, where the Mn^{2+} ion population must be included in the Mn^{3+} ion population. Raising E_F above the Mn^{3+}:$3d^4$ level in reduced TiO_2:Mn also reduces the concentration of cation vacancies and may introduce anion vacancies. Therefore, the density of E_2 states should be smaller, and a corresponding density of donor states below E_c may be introduced. However, there is no evidence for a metastable capture of electrons in cationic states.

Since the population of Mn^{4+} ions is very small in reduced TiO_2:Mn, only a $\Delta I > 0$ can occur for t_1. The reaction

$$2Mn^{3+} \xrightarrow{h\nu} Mn^{4+} + Mn^{2+} \tag{8}$$

should introduce at $\Delta I > 0$ for t_1, where $h\nu \approx [E_c - E(Mn^{3+})]$, which places the Mn^{3+}:$3d^4$ level about 1.9 eV below E_c. After exposure to white light, the metastable electron distribution leaves a larger population of Mn^{4+} ions—and presumably of Mn^{2+} ions as well. Therefore, $\Delta I < 0$ for t_2 is possible $h\nu < [E_c - E(Mn^{3+})]$, and Figure 7(d) is consistent with placement of the Mn^{3+}:d^4 level about 1.9 eV below E_c. Absence of a $\Delta I < 0$ for t_2 at 850 nm seems to place the Mn^{2+}:$3d^5$ level at least 1.5 eV below E_c, which gives, for octahedral site Mn in oxides, an energy of

$$U = E(Mn^{2+}) - E(Mn^{3+}) \leq 0.5 \text{ eV} \tag{9}$$

in the absence of a static Jahn–Teller distortion at the Mn^{3+} ion. This deduction is consistent with the observation of a spontaneous disproportionation reaction $2Mn^{3+} \rightarrow Mn^{2+} + Mn^{4+}$, but only for a few special cases where the structure accommodates the two valence states in anion interstices of distinctly different size.

The use of polarized monochromatic radiation adds another dimension to the experiment. In Figure 1 we see two inequivalent strings of edge-shared octahedra running parallel to the *c*-axis. Labeled P and Q strings in Figure 1, they are distinguished by a 90° rotation about the *c*-axis. If the magnetic field is parallel to the *c*-axis, ESR signals from the P and Q strings are equivalent. If the field is parallel to a [110] axis, the two signals are resolved. The principal site axis in the basal plane is [110] for the P strings and $[1\bar{1}0]$ for the Q strings. We define Signal I as that from cations having their principal basal-plane axis parallel to the magnetic field **H** (P cations if **H** || [110]) and Signal II as that from cations with this axis perpendicular to the magnetic field (Q cations if **H** || [110]).

With the electric-field vector **E** of the monochromatic radiation polarized parallel to the *c*-axis and the magnetic field **H** parallel to the [110] axis, the spectra for Signals I and II were essentially identical and similar to those found for unpolarized light. With the monochromatic **E** vector parallel to the external magnetic field along the [110] axis, the spectra for Signals I and II became clearly different for $\lambda < 600$ nm, the energy domain populated by E_2 states. There is no anisotropy associated with the energy domain populated by E_1 states. For V^{4+} ions the spectra corresponding to Figure 7 have $\Delta I > \Delta I_o$ for Signal I and $\Delta I < \Delta I_o$ for Signal II, where ΔI_o is the isotropic signal of Figure 7. For Fe^{3+} ions Signal I has $\Delta I < \Delta I_o$ and Signal II has $\Delta I > \Delta I_o$ just the reverse (*10*). These anisotropies impose severe constraints on any model of the bulk native defect responsible for the E_2 states.

The observed anisotropies reflect different valence state populations at P and Q cations after photoexcitation by the polarized monochromatic light. Essentially one-dimensional electron transfer along the *c*-axis is possible because E_c is at the bottom of a one-dimensional 3d band; *see* Figure 2. The observed anisotropies are consistent with a preferential charge transfer from E_2 defects to P cations (Signal I), since the V^{4+}:$3d^1$ level lies above the E_2 band and the Fe^{3+}:$3d^5$ level lies below it. Photoexcitation of an electron from an E_2 state below $E(V^{4+})$ may be followed by a V^{4+} ion decay, a direct charge transfer to that E_2 state from a neighboring V^{4+} ion. In this case photoexcitation makes $\Delta I > 0$ and decay makes $\Delta I < 0$. Preferential photoexcitation from E_2 states to a P line, but equal decay from P and Q lines, would produce a $\Delta I > \Delta I_o$ for Signal I and a $\Delta I < \Delta I_o$ for Signal II. In the case of TiO_2:Fe photo-

excitation of E_2 electrons to the Fe^{2+}:$3d^6$ level diminishes the population of Fe^{3+} ions, and the situation is just opposite that for TiO_2:V.

Cation vacancy acceptor states would have an energy band with the same relation to the valence band as the observed E_2 states. Irradiation with monochromatic light polarized along the [110] axis would excite an electron in a P vacancy to a Q string Ti:3d conduction band via an anion E or F in Figure 1. Electrons trapped at a Q vacancy would be excited via the same anions to a P string conduction band. If the absorptivity of the light is determined by the anion–cation charge transfer rather than the polarizability of the electrons within a cation vacancy, the transition probability for electron transfer from a Q vacancy to a P string is greater than from a P vacancy to a Q string; *see* Figure 1. This is the preferential charge transfer required to account for the anisotropies of Signals I and II. We therefore conclude that the E_2 states are associated, at least in large part, with cation vacancies introduced by sample oxidation.

Thus far we have found that low-temperature measurements of the surface photoconductivity of oxidized samples provides information about the density distribution of localized states capable of trapping metastable electrons. In the as-sliced specimens a band of E_1 states was identified extending 1 eV below the center of the band gap; these are tentatively interpreted to be anionic surface states. Oxidized samples exhibit a denser band of E_2 states extending about 1 eV above E_V; and with the aid of polarized light in photosensitized ESR measurements, they are identified as primarily cation vacancy acceptor states. Photosensitized ESR measurements also permit placement of localized $3d^n$ manifold energies associated with substitutional dopants. These findings are summarized in Figure 4. In order to obtain information about cationic surface states and anion-vacancy states, which do not appear to capture metastable electrons at 77 K, we may turn to electrochemical measurements on reduced TiO_2.

Electrochemical Studies

Hydrogen is an important chemical feedstock now obtained from fossil fuels, except where abundant hydropower is available. Moreover, it is itself a fuel representing convenient long-term energy storage. Utilization of solar energy, which has a large seasonal variation in most latitudes, is plagued by the need for long-term storage. Therefore, the conversion of solar energy into hydrogen via the electrolysis of water must be a high-priority technical objective.

Future hydrogen production from water with solar energy will probably utilize photovoltaic cells coupled to a conventional electrolysis plant. The cost of efficient photovoltaic cells will come down by at least

an order of magnitude in the next 10 years, and better oxygen electrodes for electrolysis cells now appear feasible. The advantages of such a dual system are flexibility, allowing multiphoton processes via series connection of cells, and greater efficiency of energy concentration. Nevertheless, the announcement by Fujishima and Honda (*11*) of one-photon photoelectrolysis of water with ultraviolet (UV) light and a working anode of n-type TiO_2 has stimulated investigation of the direct photoelectrolysis of water by sunlight, especially after it was shown that polycrystalline films of TiO_2 are as effective as single crystals (*12*). The solar spectrum peaks at about 2.5 eV, and the electrolysis of water under ambient conditions requires 1.23 eV at the power levels of solar insolation. The optimum voltage from a photovoltaic cell is about $0.6E_g$, where E_g is the band gap of the working semiconductor electrode. Therefore, an $E_g \geqslant$ 2.1 eV is needed for single-photon electrolysis of water; but 2.1 eV is still an attractive match to the solar spectrum.

A water electrolysis cell consists of two metallic electrodes connected by a power source and immersed in an aqueous electrolyte. In a photoelectrolysis cell the electrodes are connected directly, and the power source is (solar) radiation incident on a semiconductor electrode. One or both electrodes may be illuminated and semiconducting. The oxygen anode must be an n-type semiconductor, the hydrogen cathode a p-type semiconductor. Since existing hydrogen electrodes are better than oxygen electrodes, most initial work has concentrated on an n-type semiconductor anode with a platinum hydrogen electrode.

The ideal energy diagram for the electrodes and electrolyte of such a cell are shown schematically in Figure 8. Light of energy $h\nu > E_g$

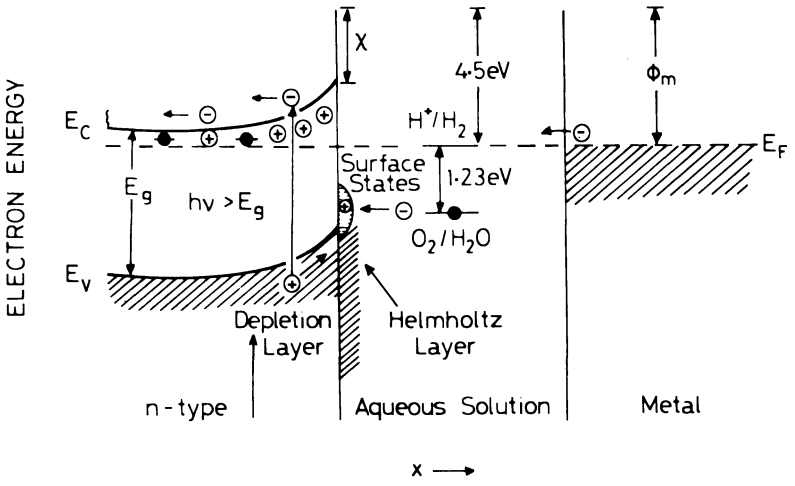

Figure 8. One-electron energies versus distance x *for the semiconductor–liquid–metal interfaces of a photoelectrolysis cell*

incident on the semiconducting electrode creates a hole–electron pair. If light is absorbed in the depletion layer near the liquid–solid interface, separation of the electrons and holes can be accomplished by the internal electric field—proportional to dE_c/dx, or the band bending—before electron–hole recombination occurs. The band bending shown in Figure 8 has a sign that drives holes to the semiconductor–liquid interface and electrons away from it to the platinum–liquid interface. At the platinum electrode, electrons combine with H^+ ions to cause the evolution of H_2. For this to occur the Fermi energy E_F—common to both shorted electrodes —must be at the H^+/H_2 level in the liquid, which is 4.5 eV below vacuum at pH = 1. If E_F is 0.3–0.4 eV below E_c, band bending of the correct sign requires an electron affinity $\chi < 4.2$ eV. For efficient hole–electron separation a $\chi < 3.8$ eV is needed. The light-generated holes, on the other hand, enter the band of semiconductor surface states. There they accept electrons from the O_2/H_2O level to cause the evolution of gaseous O_2. If holes collect in the O^{2-}:$2p^6$ band, chemical instability should result. Therefore, E_V should be below the O_2/H_2O level, which is 5.73 eV below vacuum at pH = 1. A $\chi < 3.8$ eV and an E_V below the O_2/H_2O level requires a semiconductor with $E_g > 2.0$ eV, in good agreement with our initial estimate.

Even if E_V is deeper than the O_2/H_2O level, chemical instability of the semiconductor anode can be a problem. A $\chi < 3.8$ eV means that preparation of an n-type material requires fairly severe reducing conditions. Evolution of oxygen at the surface of such an n-type semiconductor without reoxidation of the solid is only possible because the band bending drives electrons away from the surface, which is itself oxidized. But under these conditions an internal field exists to drive positively charged particles to the surface and negatively charged particles into the bulk. These particles may be ions as well as holes and electrons. If the ions in the solid are mobile at room temperature, the electrode will be chemically unstable. This constraint places severe limitations on the range of semiconducting materials that can be used, especially if the electrodes must have lifetimes of 20 years.

Three strategies can be pursued to circumvent these problems:

1. Start with a stable electrode of large energy gap and appropriate χ, such as $SrTiO_3$, and introduce localized manifolds in the gap at an energy 2.0–2.2 eV below E_c. Substitution of Sn^{2+} ions for Sr^{2+} ions, for example, would appear promising. Substitution of $2Pr^{3+}$ ions for $3Sr^{2+}$ ions would probably give too small an extinction coefficient. Substitutions for Ti^{4+} ions would perturb the narrow Ti:3d bands. Whatever the strategy, it must leave the system chemically stable, retain an itinerant 3d electron conduction band (if titanates are used), and introduce a level-to-band transition of sufficient oscillator strength that most of the

light is absorbed within the depletion layer. This is a difficult set of constraints to satisfy.

2. Obtain a good oxygen electrode and use a p-type semiconductor for a working cathode.

3. Start with a stable working anode of large energy gap and appropriate χ, such as $SrTiO_3$, and photosensitize with a dye molecule attached to the surface. This strategy requires absorption of a major fraction of the incident light within a film of dye that is thin enough for charge transfer from an excited state of the molecule to the solid to be much more probable than a return to the ground state, as illustrated schematically in Figure 9.

Clark and Sutin (*13*) reported efficient charge transfer to TiO_2 from a photoexcited RuL_3^{2+} ion, where L = 2,2′-bipyridyl, and the nitrogen atoms form an octahedral interstice for the ruthenium. The ground state 4d electron configuration at a Ru^{2+} ion is low-spin $t_{2g}^6e_g^0$; the first excited state, $*Ru^{2+}:t_{2g}^5e_g^1$, is about 2.1 eV above it and has a long lifetime. At pH = 1 the $*RuL_3^{2+}$ level is above E_c at the surface of TiO_2, so charge transfer to the TiO_2 conduction band is possible; *see* Figure 9. Moreover, the RuL_3^{3+} ion left behind after the charge transfer has a narrow, empty RuL_3^{2+} level that overlaps the O_2/H_2O level at pH = 1; the occupied levels are somewhat lower than the unoccupied. Therefore, RuL_3^{3+} ions accept electrons from the O_2/H_2O level to return to the RuL_3^{2+} state with the evolution of gaseous O_2.

At Oxford, attempts to reproduce the experiments of Clark and Sutin gave quite different results, and interpretation of the experiment has provided indirect information about charge transfer processes to and from surface states in reduced TiO_2 (*14*).

The working electrode of the experimental cell was a single-crystal slice of TiO_2 having an (001) face exposed to light from a 1000-W Mazda high-pressure xenon lamp directed through either a monochromator or a 450-nm interference filter of 20-nm bandwidth. The TiO_2 slices were reduced under H_2 at 600°C for 2 hr, and the exposed face was subsequently polished with diamond or alumina paste and etched with concentrated nitric acid or CP-4 etchant to produce an extremely flat surface, as determined by scanning electron microscopy. These slices were mounted with an electrochemically inert silicone–rubber glue, and contact was made at the back of the sample with evaporated indium. A platinum-mesh counter electrode was placed in a separate compartment of the cell, and a standard Ag/AgCl electrode (SSE) was connected to the cell by a salt bridge. The base electrolyte used conductivity water and was always 0.5*M* Aristar-grade H_2SO_4 and Na_2SO_4. Deoxygenation of the electrolyte was done with nitrogen or argon purified by passage through copper turnings at 120°C. The $[RuL_3]Cl_2$ added was made by

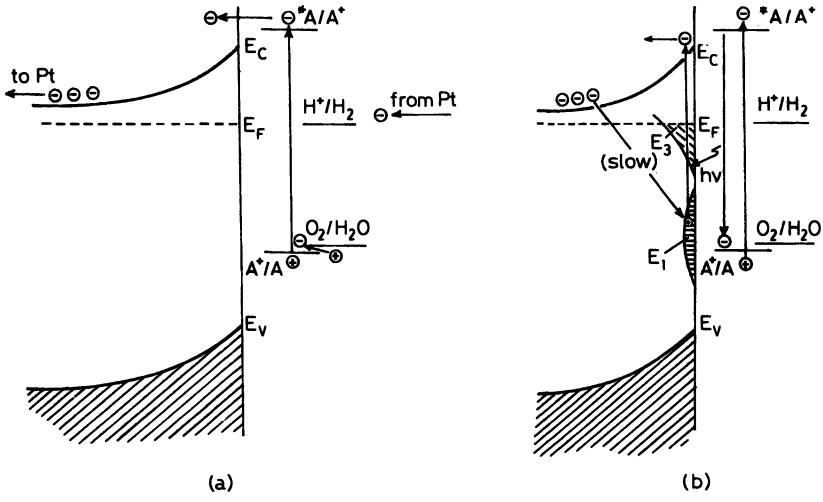

Figure 9. Schematic representation of photosensitized semiconductor electrode: (a) photoelectrolysis (anodic photocurrent); (b) energy transfer modifying cathodic current.

direct recombination followed by multiple recrystallization from deionized water. Preelectrolysis of the solutions did not change the electrode kinetics.

The flat-band potentials of the TiO_2 electrodes were determined from measurements of both Mott–Schottky capacitances and photocurrent appearance potentials.

Figure 10 is the energy level diagram for the working electrode–electrolyte interface. In this diagram $E^0(A^{m+}/A^{(m-1)+})$ is the energy of intersection of the two narrow energy densities of states for the couple indicated in parentheses if the populations of each couple are equal. The more oxidized partner is always at a higher energy. The energy splitting reflects different ligand bond lengths for different electron occupation, as in the discussion above of $Fe^{3+}:3d^5$ and $Fe^{2+}:3d^6$ levels in TiO_2. The level $E^0(*RuL_3^{2+}/RuL_3^{+} - t_{2g})$, neglected in the energy diagrams of Clark and Sutin, corresponds to the energy at which an electron is transferred to the empty t_{2g} orbital of the excited $*Ru^{2+}:t_{2g}^5e_g^1$ ion to form $Ru^+:t_{2g}^6e_g^1$. The $E^0(RuL_3^{2+}/RuL_3^{+})$ level for e_g-electron transfer is higher in energy by the photoexcitation $E^0(RuL_3^{2+}/*Ru_3^{2+})$-$E^0(RuL_3^{3+}/RuL_3^{2+})$, which is the crystal-field splitting. Two sets of band gap states are shown: E_1 and E_3 states. The E_1 states appear to be anionic surface states; the E_3 states are sensitive to surface preparations and perhaps also to the reduction method. The flat-band potential was −0.3 V with respect to SSE in the electrolyte specified.

Wilson (*15*) has shown that the density of donor states near the surface, the E_3 states of Figure 10, can be inferred from a plot of the photocurrent versus cell potential under band gap illumination in the absence of any sensitizer such as $[RuL_3]Cl_2$. In his model the electric field distribution is assumed to be unperturbed by the photoexcitation, and any hole generated in the depletion layer is assumed to reach the surface. At the surface the holes either recombine with surface electrons or produce a current in the cell by accepting electrons from the liquid. Electron–hole recombination at the surface represents a loss. The quantum efficiency for charge transfer to the liquid is obtained by normalizing the charge transfer flux (given by the current in the external circuit) to the incident photon flux. The independent variable is the voltage across the depletion layer, which is given by the voltage across the cell measured from the flat-band potential. The shape of the quantum-efficiency- (or photocurrent) versus-voltage curve varies with the surface density of

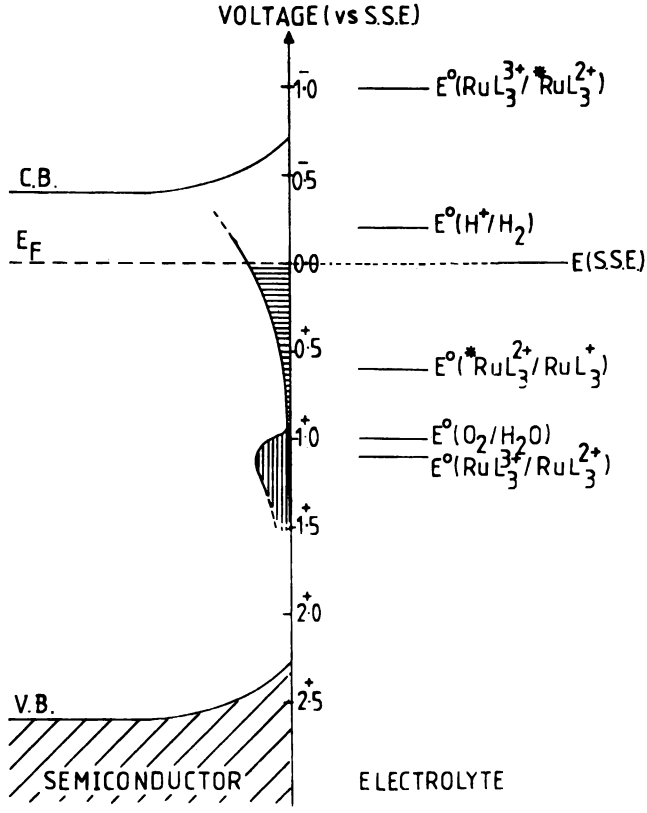

Figure 10. Surface state energy densities and electrolyte energies relative to the band edges of n-type TiO_2 (14)

donor states, and the Wilson analysis gives a reasonable fit to the data if the donor states are assumed to have an exponential decrease in density on moving from E_c into the energy gap. This exponential decrease is indicated schematically in Figure 10. If the E_3 states are primarily anion vacancy trap states, the shape of the surface density of states might decrease on moving into the gap, more like the distribution of E_2 states revealed by Figure 3(b). Such a distribution would also give a reasonable fit in the Wilson analysis.

With or without $[RuL_3]Cl_2$, the cell showed a cathodic dark current at electrode potentials negative of +0.5 V with respect to the flat-band potential. A cathodic current means a net electron transfer from the solid to the electrolyte, presumably from E_3 states to the H^+/H_2 level.

The $RuL_3^{2+} \rightarrow {}^*RuL_3^{2+}$ transition is excited by 450-nm radiation, which has a photon energy $h\nu < E_g$. A photocurrent was observed if 450-nm radiation was applied in the presence of $[RuL_3]Cl_2$. At the light intensities and dye concentrations used, the total photocurrent was always a small fraction of the dark current. It had two principal characteristics: (a) at voltages more positive than about +0.4 V with respect to flat-band conditions, a small *anodic* photocurrent with fast ($t_{1/2} < 0.1$ sec) rise time was observed; (b) at all voltages less than +0.5 V with respect to the flat-band potential, a *cathodic* photocurrent with slow ($t_{1/2} \approx 10$ sec) rise time was observed. The cathodic photocurrent had a steady-state value substantially greater than that of the anodic photocurrent; it was reduced by about 50% when oxygen was rigorously purged from the system for several hours with purified argon.

The model proposed by Clark and Sutin (*13*) for the anodic photocurrent has the general form

$$A \underset{h\nu}{\overset{k_g}{\rightleftharpoons}} B \overset{\text{diffusion}}{\sim\sim\sim\rightarrow} \text{electrode} \overset{k}{\longrightarrow} O + e^- \qquad (10)$$

where $A = RuL_3^{2+}$, $B = {}^*RuL_3^{2+}$, $O = RuL_3^{3+}$, e^- is the electron transferred to the solid to give an anodic current, k_g is the rate of decay, and k is the electron transfer velocity. In such a model the concentration b of excited species B is governed by the equation

$$\frac{\partial b}{\partial t} = D\frac{\partial^2 b}{\partial x^2} - k_g b + \phi I e a \qquad (11)$$

where D is the diffusion constant, x is the distance from the electrode, and the last term gives the rate of generation of b by light of intensity I falling on species A in concentration a, for extinction coefficient ϕ. If a is taken to be constant and I to be independent of x, implying only light

observed close to the surface produces a B at the surface, integration of Equation 11 subject to the boundary conditions

$$b\ (x,0) = 0 \text{ and } D\frac{\partial b}{\partial x}_{x=0} = kb\,(0,t) \tag{12}$$

gives an anodic current that, for wide variations in the adjustable parameter k^2/Dk_g, rises to a maximum in the range $0 < k_g t < 10$. Given a $k_g \approx 5 \times 10^5$ sec^{-1}, the photocurrent reaches this maximum within a few milliseconds at most, consistent with the fast rise time observed. On the other hand, the analysis also shows that a similar model cannot be used to account for the slow rise time of the cathodic photocurrent.

A model capable of providing a quantitative interpretation of the cathodic photocurrent considers changes in the ongoing cathodic dark current as a result of electron loss from the surface. Electron transfer from a surface state to the conduction band can be accomplished in three ways (*see* Figure 10): (a) an E_3 electron transfer to the $^*RuL_3^{2+}/RuL_3^{+}$ level is followed by electron transfer back to the conduction band from the $RuL_3^{2+}/^*RuL_3^{+}$ level; (b) electron transfer to the conduction band from the RuL_3^{3+}/RuL_3^{2+} level is followed by an E_1 electron transfer to the RuL_3^{3+}/RuL_3^{2+} level; and (c) energy transfer from the $^*RuL_3^{2+} \rightarrow RuL_3^{2+}$ transition excites a surface state electron into the conduction band. In any of these processes no net charge transfer to or from the solid takes place. However, there is a change in the charge distribution at the surface due to transfer of electrons to the bulk. The buildup of positive charge at the surface is equivalent to shifting the applied voltage to a more negative value, which increases experimentally the ongoing dark current. The cathodic photocurrent thus represents a light modulation of the dark cathodic current. With this mechanism the time constant for establishing a steady state condition depends on the rate of recombination of the conduction band electron and the surface state hole created.

An important future step is to attach the sensitizer ion directly to the semiconductor surface to see how changes in the surface states and charge transfer processes alter the situation. Preliminary experiments are encouraging.

Glossary of Symbols

E_g = energy gap, equal to $(E_c - E_v)$
E_c = energy at bottom of the titanium 3d conduction band
E_v = energy at top of the oxygen valence band
E_1, E_2, E_3 = energies of bands of energy gap states: E_1 presumably refers to surface states, E_2 to cation vacancies, E_3 to anion vacancies

$E(d^n), E(f^n)$ = energies of localized d^n or f^n configurations
V_o = isolated anion vacancy
R = distance from a V_o center to a nearest-neighbor cation
e = magnitude of the electron charge
w_b = bandwidth
U = intraatomic coulomb energy splitting $E(d^n)$ from $E(d^{n+1})$ or $E(f^n)$ from $E(f^{n+1})$
χ = electron affinity, that is, separation of E_c from vacuum energies
b_{ij} = resonance (or electron transfer) integral between orbitals on neighboring like cations at positions $\mathbf{R}_i$ and $\mathbf{R}_j$
e_g, t_{2g} = one-electron d orbitals in a cubic crystalline field
t_1, t_2, t_3 = times defined by Figure 5
ΔI = change in intensity of X band ESR signal normalized to the intensity of the incident monochromatic light
$h\nu, \lambda$ = energy, wavelength of the incident monochromatic light
$\Delta\lambda$ = change in wavelength
Signal I, II = X band ESR signal from P and Q strings of cations (Figure 1) if external **H** || [110] and monochromatic light is polarized with **E** vector || **H**.
H = applied magnetic field
E = electric-field vector of monochromatic, polarized light
L = 2,2′-bipyridyl
$k_g(sec^{-1})$ = rate of decay from excited state $*RuL_3^{2+}$ to ground state RuL_3^{2+}
$k(cm \cdot sec^{-1})$ = electron transfer velocity from excited $*RuL_3^{2+}$ to the anode
$D(cm^2 \cdot sec^{-1})$ = diffusion coefficient for RuL_3 in the electrolyte
x = distance into electrolyte from the anode surface
a, b = concentrations of RuL_3^{2+} and $*RuL_3^{2+}$
ϕ = extinction coefficient for light absorbed by RuL_3^{2+}
z = number of like nearest neighbors
$\mathcal{H}'$ = perturbation of one-electron potential at site $\mathbf{R}_j$
E_F = fermi energy level
ESR = electron spin resonance
SSE = standard Ag/AgCl electrode 26

Acknowledgments

I would like to express my thanks to K. Mizushima, M. P. Dare-Edwards, and R. D. Wright for permission to discuss their experiments

before publication, and to A. Hamnett for discussion of his quantitative analyses of the photocurrent mechanisms occurring in photosensitized TiO_2.

Literature Cited

1. Goodenough, J. B. *Prog. Solid State Chem.* **1971**, *5*, 145.
2. Goodenough, J. B. *Mater. Res. Bull.* 1971, *6*, 967.
3. Goodenough, J. B. "Defects and Transport in Oxides"; Setzer, M. S., Jaffee, R. I., Eds.; Plenum: New York, 1974; 55.
4. Cox, D. E.; Takin, W. J.; Shirane, G. *J. Phys. Chem. Solids* **1962**, *23*, 863.
5. Wold, A. Chapter 4 in this book.
6. Parker, R. A.; Wasilik, J. H. *Phys. Rev.* **1960**, *120*, 1631.
7. Mavroides, J. G.; Kafalas, J. A.; Kolesar, D. F. *Appl. Phys. Lett.* **1976**, *29*, 10.
8. Butler, M. A.; Ginley, D. S. *J. Electrochem. Soc.* **1978**, *125*, 228.
9. Mizushima, K.; Tanaka, M.; Iida, S. *J. Phys. Soc. Jpn.* **1972**, *32*, 1519.
10. Mizushima, K.; Tanaka, M.; Asai, A.; Iida, S.; Goodenough, J. B. *J. Phys. Chem. Solids* **1979**, *40*, 1129.
11. Fujishima, A.; Honda, K. *Nature* **1972**, *238*, 37.
12. Mavroides, J. G.; Tchernev, D. I.; Kafalas, J. A.; Kolesar, D. F. *Mater. Res. Bull.* **1975**, *10*, 1023.
13. Clark, W. D. K.; Sutin, N. *J. Am. Chem. Soc.* **1977**, *99*, 4677.
14. Hamnett, A.; Dare-Edwards, M. P.; Wright, R. D.; Seddon, K. R.; Goodenough, J. B. *J. Phys. Chem.* **1979**, *83*, 3280.
15. Wilson, R. H. *J. Appl. Phys.* **1977**, *48*, 4292.

RECEIVED September 21, 1978.

Solid State Precursors: A Low-Temperature Route to Complex Oxides

J. M. LONGO, H. S. HOROWITZ, and L. R. CLAVENNA

Corporate Research Laboratories, Exxon Research and Engineering Company, Linden, NJ 07036

The atomic scale mixing of cations in solid solution precursors having the calcite structure results in the ability to synthesize fully reacted mixed-metal oxides at significantly lower temperatures and in shorter times than are required for conventional solid state synthesis techniques. These lower temperatures of reaction have yielded oxides with surface areas that are 10 to 100 times higher than the same oxides prepared by conventional methods. This synthesis technique also has been used to study phase relations in the manganese-rich portion of the Ca–Mn–O system at temperatures below 1000°C and has resulted in the assemblage of a new subsolidus phase diagram containing several low-temperature phases having the following compositions: $Ca_2Mn_3O_8$, $CaMn_3O_6$, $CaMn_4O_8$, *and* $CaMn_7O_{12}$.

Metal oxides containing more than one type of cation are of interest from both a practical and fundamental point of view. Complex oxides are able to stabilize unusual oxidation states, have significant nonstoichiometry, and contain unique structural arrangements. However, they are limited in several applications, especially catalytic applications, because of the low surface area that results from the high temperatures usually needed to obtain complete reaction.

The traditional ceramic approaches to these complex metal oxides involve repeated high-temperature firing of the component oxides with frequent regrindings. These harsh conditions are required to overcome the slow reaction kinetics that occur when two solids are brought together, as is illustrated in Figure 1. The reactant particles are schematic-

0–8412–0472–1/80/33–186–139$05.00/1

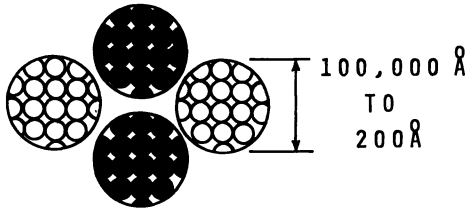

Figure 1. Conventional solid state reaction techniques give slow reaction kinetics.

ally illustrated to emphasize the fact that no matter what the particle size, each reactant particle contains only one type of cation. Severe reaction conditions are necessary to obtain a single-phase product because of the diffusional limitations of solid state reactions. Initial reaction is rapid, but further reaction goes slower and slower as the product layer builds up and diffusion paths become longer. A fine powder of approximately 10-μm particle size (100,000 Å) still represents diffusion distances on the order of 10,000 unit cell dimensions. The use of techniques such as freeze-drying (*1, 2*) or coprecipitation (*3, 4*) improves reactivity of the component oxides or salts because these methods can give initial crystallites on the order of only several hundred angstroms in diameter. But this still means diffusion must occur across 10 to 50 unit cells.

The severity of reaction conditions necessary to overcome these diffusional limitations naturally leads to crystalline, low-surface-area materials. Additionally, the high temperatures that must be utilized limit the ability to stabilize the higher valence states of transition metal elements.

Ideally, in order to achieve complete reaction in the shortest amount of time and at the lowest possible temperature, one would like to see mixing of the component cations on an atomic scale. Compound precursors (*5, 6*) will achieve this goal, but the stoichiometry of the precursor, unfortunately, often does not coincide with the stoichiometry of the desired product. The use of solid solution precursors (*7*) provides all the advantages of compound precursors but avoids the stoichiometry limitations.

A solid solution may be obtained by substitution (to a variable extent) of one element in a host lattice by another element, such that the crystallographic symmetry of the host lattice is not altered. For the purposes of this discussion, a solid solution may be considered to be the interpenetration on an atomic scale of two chemically different but structurally similar lattices. Conceptually, then, if one wants to prepare a complex oxide at low temperatures, one can form a solid solution between

two (or more) cations in the proper ratio, having an anion lattice that can be modified. Thus if a solid solution carbonate is synthesized, it can rapidly be decomposed to an oxide; likewise, if a solid solution oxide precursor is prepared, it can either be reduced or oxidized to the desired phase depending on the valence states of the cations. In each of these cases the cations are already mixed on an atomic scale in the single-phase precursor so that decomposition, oxidation, or reduction is rapid and complete at significantly lower temperatures and shorter times. Figure 2 schematically illustrates the solid solution precursor concept. Whereas the reactant cations may be 100,000 Å apart in conventional solid state reactions (Figure 1), in solid solution precursors they are on the order of 10 Å apart, regardless of particle size. Furthermore, the nature of the solid solution is such that it is possible to continuously vary the cation composition in the structure, and one is not limited to discrete compound precursors.

The solid solution precursor technique has, to date, been exploited in this laboratory primarily for the preparation of high-surface-area, mixed-metal oxides by decomposition of solid solutions of carbonates having the calcite structure. This technique has wide applicability since the carbonates of Ca, Mg, Zn, Mn, Fe, Co, Ni, and Cd all form the calcite structure and will, in general, form solid solutions with each other. In this paper we will describe our experience with the solid solution precursor method when applied to several of these mixed-metal systems.

The most obvious benefit of this synthesis technique is that it gives a route to higher-surface-area complex oxides. Just as important, however, is the approach provided by the solid solution precursor technique to the discovery of totally new materials that are not stable at the higher temperatures usually necessary for conventional solid state reaction between small particles.

The Ca–Mn–O system was chosen as a starting point in order to explore the potential of the solid solution precursor method for synthe-

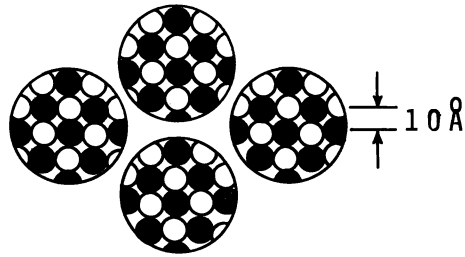

Figure 2. Solid solution precursor techniques give fast reaction kinetics

sizing new complex oxides. This system fulfills the primary requirement for such a study in that $CaCO_3$ and $MnCO_3$ are isostructural, each displaying the calcite crystal structure. Thus it is possible to prepare Ca–Mn carbonate solid solution precursors for subsequent reaction to Ca–Mn oxides. There are additional characteristics that make the Ca–Mn–O system a particularly versatile one for exploring the properties of new mixed-metal oxides. First of all, the Mn ion is a very flexible transition metal occurring in the solid state as the 2+ through the 7+ cations. When incorporated along with the electropositive Ca into a crystal structure, the higher valence states of Mn can be stabilized, especially at low temperature.

In this paper we describe previously unattainable low-temperature phase relations in the manganese-rich portion of the Ca–Mn–O system. This new low-temperature phase diagram (Figure 3) shows the complexity possible when a cation can have multiple valences and when there is sufficient reactivity to obtain equilibrium at low temperatures. The use of the extremely reactive solid solution precursors, $Ca_{1-x}Mn_xCO_3$, also has allowed us to monitor synthesis parameters that are usually obscured by conventional high-temperature reaction conditions. Accordingly, the influence of heating rate, oxygen partial pressure, particle morphology, temperature, and residual surface species on the final product will be discussed.

Experimental

Most materials syntheses referred to in this report were carried out by using the solid solution precursor method (7). Precursors were prepared by precipitating the carbonates from a weakly acidic solution of the appropriate cations in the desired stoichiometry. Ammonium carbonate was the precipitating agent. The solid solution precursors were reacted at temperatures ranging from 800° to 1000°C for times ranging from 0.5 to 150 hr. The reaction atmosphere was pure flowing O_2, unless otherwise specified. The conventional solid state reaction syntheses that were carried out were accomplished by hand-grinding, with an agate mortar and pestle, the calcium and manganese reagent-grade carbonates and then firing in oxygen at the specified temperatures. These firings were usually interrupted at frequent intervals for additional grinding in order to facilitate the reaction.

All reaction products and solid solution precursors were examined on a Phillips X-ray diffractometer to determine which phases were present. Oxygen content of all Ca–Mn oxide phases was established by using a Fisher Thermogravimetric Analyzer containing a Cahn electrobalance. Samples were reduced in H_2 and weight loss was attributed to manganese with oxidation states higher than 2+. The average manganese valence was also determined by wet chemical means (8). The method for experimentally measuring the cation stoichiometry, as well as the procedure for determining the decomposition temperature of the low-temperature Ca–Mn oxide phases, is detailed in Horowitz et al. (9).

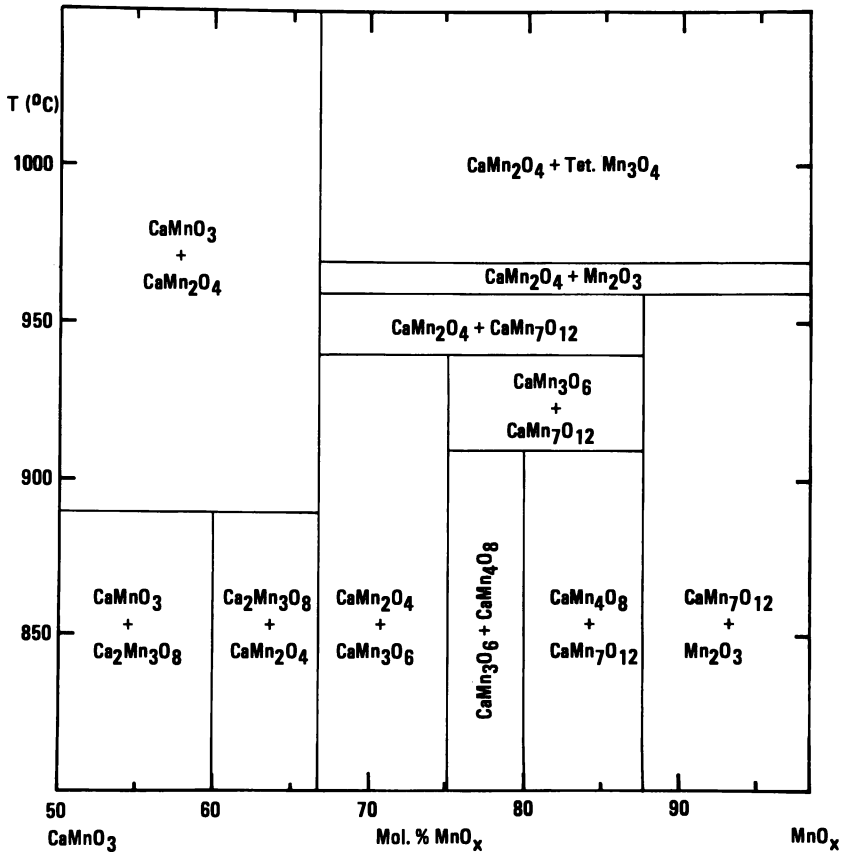

Figure 3. Isobaric (P_{O_2} = 1.0 atm) subsolidus phase relations in the manganese-rich portion of the Ca–Mn–O system

Specific surface areas were determined by the Brunauer–Emmett–Teller (BET) method, using nitrogen adsorption. Single-point determinations were used; these were found to agree within 5% of triple-point determinations.

Results

Following the experimental procedures outlined above, a series of carbonate precipitates was prepared. X-ray diffraction confirmed that the precipitates were single-phase solid solutions having the calcite crystal structure. Thus the homogeneous mixing of metal cations on an atomic scale (about 10 Å) was achieved. Table I lists the interplanar spacings of the major X-ray diffraction peaks for some of the mixed-metal

Table I.

Compound	(hkl) (104)	(hkl) (012)
$CaCO_3$	3.03	3.85
$[Ca_{0.67}Mn_{0.33}]CO_3$	2.99	3.80
$[Ca_{0.60}Mn_{0.40}]CO_3$	2.97	3.77
$[Ca_{0.50}Mn_{0.50}]CO_3$	2.94	3.75
$[Ca_{0.29}Mn_{0.71}]CO_3$	2.91	3.74
$[Ca_{0.25}Mn_{0.75}]CO_3$	2.90	3.71
$[Ca_{0.20}Mn_{0.80}]CO_3$	2.90	3.71
$[Ca_{0.125}Mn_{0.875}]CO_3$	2.88	3.70
$[Ca_{0.08}Mn_{0.92}]CO_3$	2.87	3.70
$MnCO_3$	2.85	3.67
$[Cd_{0.11}Mn_{0.89}]CO_3$	2.86	3.67
$[Cd_{0.125}Mn_{0.875}]CO_3$	2.87	3.70
$[Cd_{0.33}Mn_{0.67}]CO_3$	2.88	3.71
$[Cd_{0.50}Mn_{0.50}]CO_3$	2.91	3.74
$CdCO_3$	2.94	3.80
$CoCO_3$	2.74	3.55
$[Co_{0.67}Mn_{0.33}]CO_3$	2.80	3.61
$[Co_{0.40}Mn_{0.60}]CO_3$	2.83	3.65
$MnCO_3$	2.85	3.67

carbonate precursors prepared. The corresponding data for the end-member carbonates are also included for comparison.

As Table I shows, the systems described here (Ca–Mn, Cd–Mn, Co–Mn) adhere fairly closely to Vegard's law. Therefore, the monitoring of lattice parameters, or of a specific interplanar spacing, provides a convenient method for checking, to a first approximation, the composition of a single-phase precipitate. For compositional increments of the sizes that are seen in Table I, the changes in interplanar spacing are generally resolvable, and the precipitates of differing compositions can be roughly identified and distinguished from one another. When more precise estimates of composition are desired, this approach is unacceptable because the high-surface-area precipitates have X-ray diffraction patterns whose peaks are too broad to make precise lattice parameter determination possible. Because of this uncertainty in the composition of the precursor (the metal cation stoichiometry of the precursor was not always in exact agreement with the stoichiometry of the initial aqueous solution of metal cations), compositional analysis for metal cation stoichiometry was performed on the reacted mixed-metal oxides.

The importance of precursor particle size was minimized in our introduction to the solid solution precursor concept; however, it can still have an important effect on reaction kinetics. Although cations are mixed on an atomic scale within each reactant particle, the size of the

Interplanar Spacings

(hkl)				
(113)	*(202)*	*(110)*	*(116)*	*(024)*
2.27	2.09	2.49	1.87	1.90
2.25	2.07	2.46	1.84	1.89
2.24	2.05	2.45	1.84	1.86
2.23	2.05	2.44	1.83	1.86
2.21	2.03	2.43	1.81	1.86
2.21	2.03	2.42	1.80	1.86
2.20	2.02	2.42	1.79	1.86
2.19	2.01	2.41	1.78	1.85
2.19	2.01	2.40	1.78	1.84
2.17	2.00	2.40	1.77	1.83
2.19	2.01	2.40	1.77	1.84
2.19	2.01	2.40	1.78	1.84
2.19	2.02	2.42	1.79	1.85
2.21	2.04	2.43	1.81	1.87
2.25	2.07	2.46	1.84	1.89
2.11	1.95	2.33	1.70	1.78
2.15	1.99	2.37	1.75	1.81
2.16	1.99	2.38	1.75	1.82
2.17	2.00	2.40	1.77	1.83

reactant particle can still limit the extent of gas–solid contact and heat transfer through the particle.

Table II shows how the BET surface area of the solid solution precursor can be modified by minor adjustments to the precipitation procedure. Referring to Table II, one can see that a 1:1 Ca:Mn ratio solid solution precursor powder, which was recovered and dried immediately after precipitation, has a surface area of 9 $m^2 \cdot g^{-1}$. With the thought that the presence of residual electrolyte, in the form of ammonium carbonate, might be causing agglomeration of particles and thereby lowering the apparent surface area, another batch was prepared in which the normal precipitation was followed by a thorough water rinse procedure. After it was dried, the powder was much finer in appearance and more free flowing than the untreated powder, and its surface area

Table II. Surface Area of Precursors Can Be Modified

	Surface Area ($m^2 \cdot g^{-1}$)		
	No Treatment	*H_2O Rinse*	*H_2O + IPA Rinse*
$MnCO_3$	66	110	150
$CaMn(CO_3)_2$	9	32	74
$CaCO_3$	1	11	10

showed an increase to 32 $m^2 \cdot g^{-1}$. In order to further decrease agglomeration, we made an attempt to displace residual water with the lower-surface-tension isopropyl alcohol (IPA) by following precipitation with consecutive water and IPA rinses. The powder, which was again finer in appearance and more free flowing than the untreated precipitate, showed another increase in surface area to 74 $m^2 \cdot g^{-1}$.

Table II also indicates that additional batches of precipitates were prepared as controls. The $MnCO_3$ precipitate shows the same trend of increasing surface area with the water rinse and another increase with the water plus IPA rinse. The $CaCO_3$ shows a large increase in surface area for the water rinse and the water plus IPA rinse when compared to the untreated precipitate, but does not show a significant difference between the water and water plus IPA-rinsed powders.

These results are of preliminary nature and their implications are not fully understood. However, it does appear that real and significant improvements in surface area can be effected by relatively minor modifications in the precipitation procedure.

As mentioned before, magnesium, calcium, and most of the first-row divalent transition elements form the calcite structure. Theoretical crystal chemistry considerations would lead one to expect that it is possible to prepare, by the process described, single-phase solid solution calcite precipitates of almost all combinations of these elements. Experimental results with one such combination (nickel and manganese), however, revealed that the precipitate prepared in this case was not a single-phase calcite structure material but a precipitate consisting of $MnCO_3$ with a calcite structure and an amorphous Ni-containing phase. It is evident from the results of this experiment that the solid solution precursor concept is not as universal as it first appeared, and that the applicability of this method for any contemplated combination of elements must be experimentally determined.

After having prepared and characterized the solid solution calcite precursor, one may fire it at a preselected temperature (generally less than 1000°C) and for a time sufficient to yield the desired high-surface-area mixed-metal oxide. Since the cations are already homogeneously mixed on an atomic scale in the precursor, the decomposition of the calcite to the fully reacted, mixed-metal oxide takes place at significantly lower temperatures and in shorter times relative to synthesis by conventional solid state techniques.

In the Ca–Mn–O system, for example, the preparation of the perovskite, $CaMnO_3$, by standard solid state reaction requires heating of the component oxides or carbonates at 1300°C in an oxygen-containing atmosphere for several days with frequent regrinding. The resulting product is very crystalline and has a surface area of only 0.2 $m^2 \cdot g^{-1}$.

The same pure compound can be prepared by decomposing, under oxidizing conditions, a 1:1 Ca:Mn solid solution calcite precursor at 900°C for 30 min. The surface area of this fully reacted perovskite, $CaMnO_3$, is 11 $m^2 \cdot g^{-1}$.

The fully reacted perovskite-related oxide Ca_2MnO_4 has been prepared with a surface area of 17 $m^2 \cdot g^{-1}$ by reacting a 2:1 Ca:Mn solid solution calcite precursor at 800°C in air for 15 min. Standard solid state reaction of the same compound from the component carbonates (1300°C for several days with frequent regrindings) gives a surface area of only 0.8 $m^2 \cdot g^{-1}$.

In the Cd–Mn–O system the compound $Cd_2Mn_3O_8$ has been prepared at 500°C for 1 hr, in oxygen from a solid solution calcite precursor having a 2:3 Cd:Mn ratio. This compound has a surface area of 98 $m^2 \cdot g^{-1}$; the same compound prepared by conventional solid state reaction had a surface area of 3 $m^2 \cdot g^{-1}$.

In general, the solid solution precursor method gives improvements in surface area relative to conventional solid state techniques that range from a factor of 10 to 100.

An additional benefit that can be derived from the relatively low synthesis temperatures afforded by the solid solution precursor technique is the ability to synthesize totally new materials. Figure 3 shows that the low reaction temperatures made possible by the solid solution precursors reveals fairly complex subsolidus relations in the Ca–Mn–O system, including four compounds that are not stable at 1 atm O_2 above 1000°C.

The first compound to appear is $CaMn_7O_{12}$, which is also the most stable mixed-valence compound of the system. It contains six Mn^{3+} and one Mn^{4+} and has a structure related to perovskite (*10*), with three Mn^{3+} and a Ca^{2+} on the A site. This compound was first reported by Bochu et al. (*10*), who employed pressures of 80 kbar and reaction temperatures of 1000°C for its synthesis. Joubert, in a private communication, reports that they also have been able to prepare this phase without high pressure (*11*). Above 960°C, $CaMn_7O_{12}$ breaks down into $CaMn_2O_4$ and Mn_2O_3.

At lower temperatures ($T < 940$°C) another mixed-valence phase appears with a Ca/Mn ratio of 1/3. Thermogravimetric analysis in H_2 shows that one-third of the manganese is present as Mn^{4+} and therefore indicates a formula of $CaMn_3O_6$. Toussaint (*12*) reports a $CaMn_3O_7$ in his study, but his published X-ray pattern shows only the strong lines of $CaMn_4O_8$. He states that there were small amounts of the calcium-rich phase $CaMnO_3$ present in his preparation of $CaMn_3O_7$. Below 910°C a compound with a Ca/Mn ratio of 1/4 appears in the phase diagram. In this case thermogravimetric analysis shows that one-half of the manganese

is present as Mn^{4+}, leading to a formula of $CaMn_4O_8$. Toussaint (*12*) reports a phase $CaMn_4O_7$, but his X-ray data show it to be a mixture containing predominantly $CaMn_7O_{12}$. A thorough analysis of our own X-ray patterns for $CaMn_3O_6$ and $CaMn_4O_8$ is not complete, but it does appear that these two phases are related structurally. They can both be written as Ca_xMnO_2, where $x = 1/3$ for $CaMn_3O_6$ and $x = 1/4$ for $CaMn_4O_8$, suggesting that they are related to the A_xMnO_2 phases described by Fouassier et al. (*13*).

Below 890°C a compound having a Ca/Mn ratio of 2/3 becomes stable. Thermogravimetric analysis gives a formula of $Ca_2Mn_3O_8$ (*14*), which indicates that all manganese are 4+. $Ca_2Mn_3O_8$ is a layered structure consisting of infinite manganese oxide sheets held together by Ca^{2+} in trigonal prismatic coordination with oxygen (*15*).

The solid solution precursor technique was the only synthesis method found to yield the low-temperature Ca–Mn–O compounds in pure form. Conventional solid state reaction methods would yield these compounds only as constituents of multiphase mixtures, even after prolonged (several hundred hours) firings at 800°–900°C with numerous interruptions for regrindings. The low-temperature phases discussed above, along with $CaMnO_3$ and $CaMn_2O_4$, were the only phases encountered in the Mn-rich portion of the phase diagram, although syntheses from precursors of intermediate compositions were tried.

As might be expected from the presence of a number of mixed-valence phases, the reaction kinetics of the lower- (less than 1000°C) temperature phase diagram are very sensitive to several experimental variables. Subtle changes in the oxygen partial pressure during reaction have rather dramatic effects on the reaction kinetics. Such changes in the oxygen partial pressure may be brought about by the presence of residual surface species. For example, washing the solid solution precipitate precursor with a hydrocarbon can impede the attainment of single-phase products. Presumably during decomposition in the presence of hydrocarbons, a CO/CO_2 atmosphere is locally generated at reaction interfaces. The initial reducing atmosphere will favor formation of phases with Mn^{3+}, which must then react to form the equilibrium phase. In a similar manner, grinding the starting materials or intermediate products under acetone has a marked effect on the ability to attain equilibrium. In fact, grinding under acetone and then firing causes a sufficiently reducing atmosphere that $CaMn_4O_8$ (which has a high Mn^{4+} content relative to its decomposition products, $CaMn_3O_6$ and $CaMn_7O_{12}$) cannot be formed. This indicates that even though the reaction is carried out at the right temperature and oxygen partial pressure, the reaction kinetics for the formation of $CaMn_4O_8$ from $CaMn_3O_6$ and $CaMn_7O_{12}$ are very slow.

We have observed that the decomposition of the solid solution

precursor does not always directly lead to the desired product. For example, appropriate calcite precursors for $Ca_4Mn_3O_{10}$ and for $Ca_3Mn_2O_7$, upon decomposition in oxygen, lead to mixed-phase products, which consist predominantly of $CaMnO_3$ and Ca_2MnO_4. It is apparent that the unusually high stability of the perovskite (*16*) and perovskite-related structures of $CaMnO_3$ and Ca_2MnO_4, respectively, create large driving forces, which in turn create unfavorable kinetics for the formation of $Ca_4Mn_3O_{10}$ and $Ca_3Mn_2O_7$. The purity of reaction products can also be affected by the heating rate employed. Precursors should be introduced into a furnace that has already been preheated to the reaction temperature. Excessively slow heating rates are to be avoided, since they permit the formation of nonequilibrium phases. For example, $Ca_{1-x}Mn_xCO_3$ precursors will slowly decompose at low temperatures (about 500°C) to yield Mn oxides and Ca-rich carbonate.

The decomposition temperatures for the new low-temperature phases are very sensitive to the equilibrium oxygen pressure. Once the phases have been formed by control of temperature treatment at 1 atm O_2, they can be decomposed by switching to flowing air—or more dramatically by firing in stagnant air. For example, $CaMn_4O_8$, whose decomposition temperature in flowing O_2 is 910°C, will decompose if fired at 810°C in stagnant air. The effect on the structurally related $CaMn_3O_6$ is less pronounced, presumably because it contains a lower percentage of Mn^{4+}. A firing atmosphere of pure CO_2 destabilizes all the low-temperature phases ($Ca_2Mn_3O_8$, $CaMn_3O_6$, $CaMn_4O_8$, and $CaMn_7O_{12}$) to temperatures at least as low as 700°C.

For the compounds in the manganese-rich portion of the phase diagram there is a clear correlation between the percentage of Mn^{4+} and the decomposition temperature in 1-atm O_2. The one exception is $CaMnO_3$, which is an extremely refractory phase despite the fact that all its manganese is Mn^{4+}. This increased thermal stability can be understood in terms of the unique stability offered by the perovskite structure as well as its relatively high calcium content.

Conclusions

The solid solution precursor technique has been introduced as an effective method for mixed-metal-oxide synthesis. We have found that the atomic scale mixing of cations in solid solution precursors having the calcite structure results in the ability to synthesize fully reacted mixed-metal oxides at significantly lower temperatures and in shorter times then are required for conventional solid state synthesis techniques. These lower temperatures of reaction have yielded oxides with surface areas that are 10 to 100 times higher than the same oxides prepared by conventional methods.

Not only does the solid solution precursor synthesis route give higher-surface-area complex oxides, but it also provides an approach to the discovery of totally new materials that are not stable at the higher temperatures that usually characterize conventional solid state reactions. For example, the solid solution precursor technique has allowed us to assemble a new subsolidus Ca–Mn–O phase diagram containing several new low-temperature phases.

The solid solution precursor synthesis route is thought to have wide applicability since Mg, Ca, Cd, Mn, Fe, Co, Ni, and Zn carbonates all form the calcite structure. All the monoxides of these same elements, plus those of Sr and Ba, form the rock salt structure, thereby providing an alternate low-temperature synthesis route utilizing rock salt structure, solid solution precursors. These rock salt precursors may be obtained by decomposition, in inert or reducing atmospheres, of the appropriate calcite precursor. The aragonite group represents another collection of metal carbonates that can be effectively employed as solid solution precursors. Aragonite is a polymorph of calcite, and the cations that will crystallize with its structure include calcium, strontium, lead, and barium.

Acknowledgments

We gratefully acknowledge the assistance of H. J. Brady, J. T. Lewandowski, and G. Springston in the preparation and characterization of the materials mentioned in this study.

Literature Cited

1. Schnettler, F. J.; Monforte, F. R.; Rhodes, W. W. *Sci. Ceram.* **1968**, *4*, 79.
2. Kim, Y. S.; Monforte, F. R. *Am. Ceram. Soc. Bull.* **1971**, *50*, 532.
3. Stuijts, A. L. *Sci. Ceram.* **1970**, *5*, 335.
4. Sato, T.; Kuroda, C.; Saito, M. *Ferrites: Proc. Int. Conf. Jpn.* **1970**, 72.
5. Clabaugh, W. S.; Swiggard, E. M.; Gilchrist, J. *J. Res. Natl. Bur. Stand.* **1956**, *56*, 289.
6. Gallagher, P. K.; Johnson, D. W. *Thermochim. Acta* **1972**, *4*, 283.
7. Clavenna, L. R.; Longo, J. M.; Horowitz, H. S. U.S. Patent 4 060 500, 1977.
8. Pantony, D. A.; Siddiqi. *Talanta* **1962**, *9*, 811.
9. Horowitz, H. S.; Longo, J. M. *Mater. Res. Bull.* **1978**, *13*, 1359.
10. Bochu, B.; Chenevas, J.; Joubert, J. C.; Marezio, M. *J. Solid State Chem.* **1974**, *11*, 88.
11. Joubert, J. C., private communication.
12. Toussaint, H. *Rev. Chim. Miner.* **1964**, *1*, 141.
13. Fouassier, C.; Delmas, C.; Hagenmuller, P. *Mater. Res. Bull.* **1975**, *10*, 443.
14. Horowitz, H. S.; Longo, J. M. U.S. Patent 4 049 790, 1977.
15. Ansell, G. B.; Horowitz, H. S.; Longo, J. M. "International Conference of Crystallography, 11th," Poland, *1978*, 157.
16. Yoshimura, M.; Nakamura, T.; Sata, T. *Bull. Tokyo Inst. Technol.* **1974**, *120*, 13.

RECEIVED September 15, 1978.

Liquid-Junction Solar Cells Using Pressure-Sintered Polycrystalline CdSe and CdTe Semiconductors

MURRAY ROBBINS

Bell Laboratories, Murray Hill, NJ 07974

Liquid-junction solar cells, composed of a semiconducting electrode and counterelectrode immersed in a suitable oxidation–reduction (redox) electrolyte, can be used to convert solar energy to electrical energy. An advantage of this type of photoelectrochemical cell is that the substitution of polycrystalline for single-crystal electrodes should be possible without substantial efficiency losses. Pressure-sintered polycrystalline CdSe and CdTe have been prepared and annealed. Conversion efficiencies using polycrystalline CdSe and CdTe electrodes reached about 70% of that observed for cells containing single-crystal electrodes.

The cells to be discussed consist of a semiconductor electrode and a counterelectrode, immersed in a solution containing a suitable redox electrolyte. The *n*-type semiconductors, function as photo anodes. Upon illumination of the semiconductor, electrons are promoted from the valence band to the conduction band, creating an electron-hole pair at or near the semiconductor–liquid interface. Under the influence of the electric field in the space charge region, the holes migrate to the semiconductor–liquid interface and the electrons move through the bulk of the semiconductor to the external load and to the counterelectrode liquid interface. The hole at the semiconductor surface oxidizes the reduced half of the redox couple. The electron at the counterelectrode surface acts as a reducing agent, which can react with the oxidized

0–8412–0472–1/80/33–186–151$05.00/1

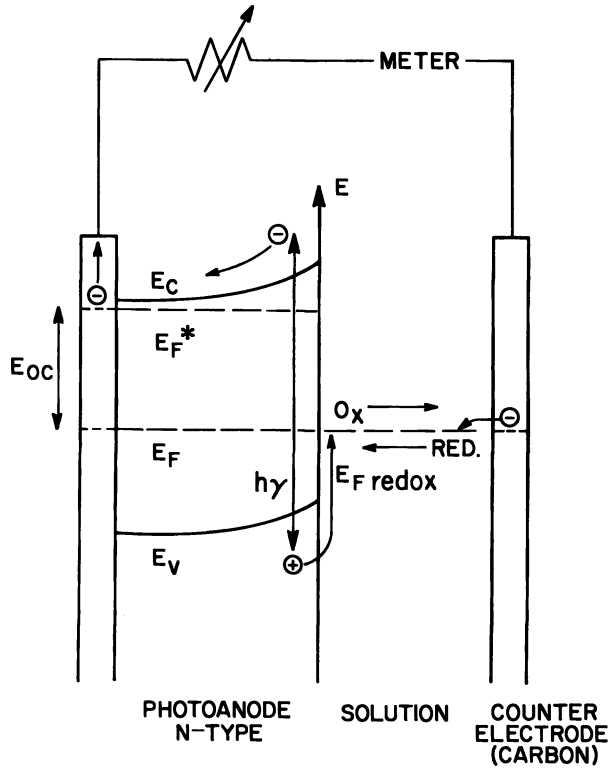

Figure 1. Schematic diagram of a liquid–junction solar cell

member of the redox couple (Figure 1). The electrode reactions for the sulfide–polysulfide couple are

$$\text{Photoanode:} \quad h^+ + S^= \rightarrow 1/2S_2^=$$

$$\text{Cathode:} \quad e^- + 1/S_2^= \rightarrow S^=$$

The equal and opposite reactions produce cells with no net chemical change.

The upper limit of the open-circuit photovoltage (E_{oc}), approached in an intensely illuminated liquid–junction solar cell, is approximately

$$E_{oc} = E_F^{(S)} - E_{redox}$$

where $E_F^{(S)}$ is the semiconductor Fermi level and E_{redox} is the redox potential of the electrolyte.

At the surface of the semiconductor anode the photo-generated hole can react in one of two ways:

$$MA^{(S)} + xh^+ \rightarrow M^{x+} + A^0 \quad (1)$$

$$R_{redox} + h^+ \rightarrow O_{redox} \quad (2)$$

In the first reaction the hole oxidizes the anion of the semiconductor (MA), leading to decomposition of the electrode, instead of oxidizing the reduced half of the redox couple (Equation 2). Electrode decomposition of this type was observed by Gerischer (*1*), who made the first liquid–junction solar cell by using an *n*-CdS photo anode in an aqueous solution of $K_4Fe(CN)_6/K_3Fe(CN)_6$ as the redox electrolyte.

Using a variety of binary semiconducting photo anodes (such as CdS or CdSe), researchers have shown (*2*) that semiconductor stability improves by using fast, reversible redox couples with increasingly reducing redox potentials. Redox couples that have been tested are S_2^{2-}/S^{2-}, Se_2^{2-}/S_e^{2-}, and Te_2^{2-}/Te^{2-} with redox potentials (E_{redox}) of -0.7, -0.9 and -1.1, respectively (*2*). As the E_{redox} becomes increasingly negative, the photovoltage decreases. It is evident, therefore, that semiconductor stability is achieved at the expense of cell efficiency. Of the three chalcogenide redox couples, S_2^{2-}/S^{2-} has been the first choice, as it has the most positive E_{redox}.

Semiconductor doping, purity and surface perfection are important factors in the preparation of photo anodes for liquid–junction cells for reasons similar to those operating in solid state photovoltaic devices.

Doping of semiconductors can be used to (1) produced the desired type of semiconductivity (*n* or *p*), (2) effect the conductivity of the semiconductors, (3) increase E_F in *n*-type semiconductors, and (*4*) control the thickness of the space charge region. Impurities and surface imperfections introduce recombination centers for electrons and holes. The purity of the semiconductor is controlled in the preparation of the material. Surface imperfections are created when samples are cut to size for cell use.

Polishing further damages the semiconductor surface, and it is necessary to etch the photo anodes before use. In Figure 2 the cell performance of etched and unetched single-crystal *n*-CdSe photo anodes, in S_2^{2-}/S^{2-} solution, are compared (*3*).

Table I shows the efficiencies observed for a variety of single-crystal, *n*-type semiconductor photo anodes. Heller et al. (*4*) found when CdSe photo anodes were used with S_2^{2-}/S^{2-} solution, the short-circuit photocurrent decayed as a function of time. The proposed mechanism for this decay involved the following reactions:

$$CdSe + 2h^+ \rightarrow Cd^{2+} + Se^0$$

$$Cd^{2+} + S^= \rightarrow CdS$$

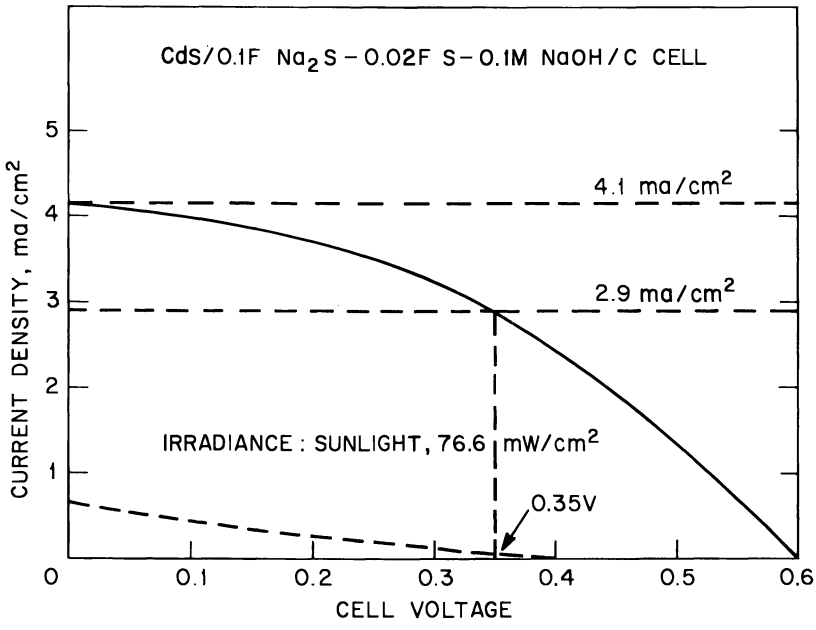

Figure 2. Current–voltage properties of liquid–junction cells using etched (——) and unetched (– – –) n-CdS photoanodes: I_{sc} = 4.1 mA · $(cm^2)^{-1}$; I_{max} = 2.9 mA · $(cm^2)^{-1}$; V_{max} = 0.35; and fill factor (ff) = $(I_{max} \times V_{max})/(I_{sc} \times V_{oc})$ (3).

The Cd^{2+} in solution is produced at the surface of the photo anode and remains in the vicinity of the semiconductor–liquid junction. Cd^{2+} and $S^{=}$ combine and form a CdS layer on the surface of the CdSe. This CdS film forms a blocking layer and prevents the photo-produced holes from migrating to the semiconductor–liquid interface. As shown in Figure 3, the addition of Se to the sulfur–polysulfide solution prevents this form

Table I. Cell Efficiencies (at 1 sun) Using Single-Crystal Photo Anodes

Cell	*Overall Conversion Efficiency (%)*	*Current Efficiency (%)*
n-CdTe | K_2Se–Se–KOH | C	8.4	65
n-CdSe | K_2S–S–KOH | C	7.5	80
n-GaAs | K_2Se–Se–KOH | C	12	70
n-InP | K_2Se–Se–KOH | C	unstable	
n-Si | K_2Se–Se–KOH | C	unstable	

of electrode degradation (*4*). The detailed mechanism by which the Se addition stabilizes the CdSe electrode is not known. One hypothesis involves the reaction of $Se^{=}$ with Cd^{2+} at the surface of the CdSe photo anode, thereby preventing the formation of a CdS blocking layer. The Se that has been added exchanges with the polysulfide electrolyte, darkening the color of the solution. Expected losses in cell efficiency caused by increased solution absorption of light were almost totally balanced by an increase in the open-circuit voltage (*4*). It was possible, therefore, to stabilize the CdSe photo anode with minimal loss of efficiency.

In *p-n* heterojunction cells there must be close matching of crystallographic parameters at the junction where efficiency losses in solid state photocells are a major problem in the use of polycrystalline semiconducting films. However, in the liquid–junction cell there are no crystallographic matching problems at the liquid–solid interface, and this ought not to be a source of loss upon shifting from single-crystal to polycrystalline electrodes.

With polycrystalline electrodes two important criteria must be met: (1) the grain size must exceed 1 μm for direct band gap semiconductors, so that all the incident light be absorbed in the first layer of grains as the grain boundaries act as traps for the minority carriers; (2) the space charge region must equal or exceed the absorption length so that the photo-excited carriers be separated by the field, thereby decreasing the

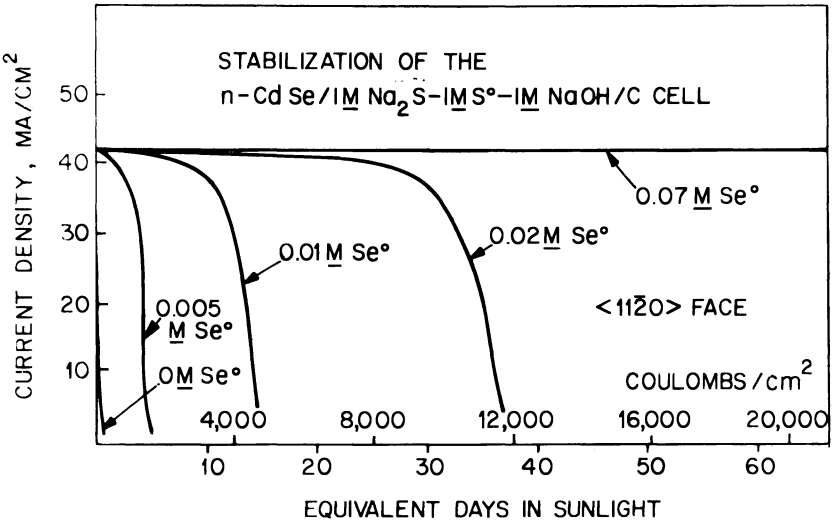

Figure 3. Stabilization of n-*CdSe photo anode by the addition of Se to* S_2^{2-}/S^2 *solution*

probability of recombination. In this work we report the preparation and performance of pressure-sintered, polycrystalline, *n*-CdSe and CdTe photo anodes.

Experimental

CdSe (99.999%) and CdTe (99.99%) powders (about 3 μm) were purchased from Alfa Products. The powders were pressed (5000 psi) at room temperature into pellets (0.75 in. diameter and 0.5 in. thick). The pellets were placed in a high-density alumina die with a 1-in. base. The pellet was surrounded by zirconia sand. The die was positioned in a kanthal-wound furnace between the platens of a Carver Co. bench press as shown schematically in Figure 4. The gas inlet at the bottom allows a flushing of the furnace interior with a neutral gas. A gas accumulator, yielding a 5-to-1 ratio of operating pressure to gas tank pressure, maintained a constant pressure on the press. A maximum tank pressure of 2000 lb allowed the author to maintain a maximum press pressure of 10,000 lb. The desired pressure was put on the die and the furnace temperature was maintained for 2 hr, followed by cooling at the rate of 75°C · hr^{-1} to room temperature. The slow heating and cooling cycles were necessary to avoid thermal shocking of the alumina die. The interior of the furnace was continuously flushed with N_2 or Ar. Table II gives pressure sintering conditions and the densities of CdSe and CdTe pellets produced. X-ray diffraction patterns were obtained to verify that no structural or gross chemical changes had taken place. Pellets of CdSe and CdTe were polished and thermally etched for 16 min at 600°C in the flowing A_N for microscopic study of the sample surface. In the pellets of CdSe and CdTe the average grain size was observed to be 20–30 μm. Hot, pressed pellets prepared in this manner were generally *p*-type, with resistances in excess of 200,000 Ω. In order to make the materials *n*-type and decrease the resistance, the pellets were annealed in Cd at a variety of temperatures and times. As the annealing temperature was increased, the resistivity of the samples decreased. In order to obtain the necessary time of annealing to yield uniform Cd doping, several pellets were sectioned to determine if the resistance was uniform throughout.

Annealed pellets were etched in 4/1 HCl/HNO_3 for 1 min, rinsed in water, immersed 1 min in a 10% KCN solution and rinsed for 1 min in H_2O. The resulting samples were In-wetted, Ag-epoxy-contacted, and mounted in epoxy for cell immersion. Table III shows the annealing conditions and cell performance of some of the *n*-CdSe polycrystalline electrodes in comparison to our best single-crystal CdSe electrode. A

Table II. Pressure-Sintering Conditions

Structure	T *(°C)*	*Pressure (lb)*
CdSe wurtzite	950	10,000
CdTe zinc blende	675	10,000

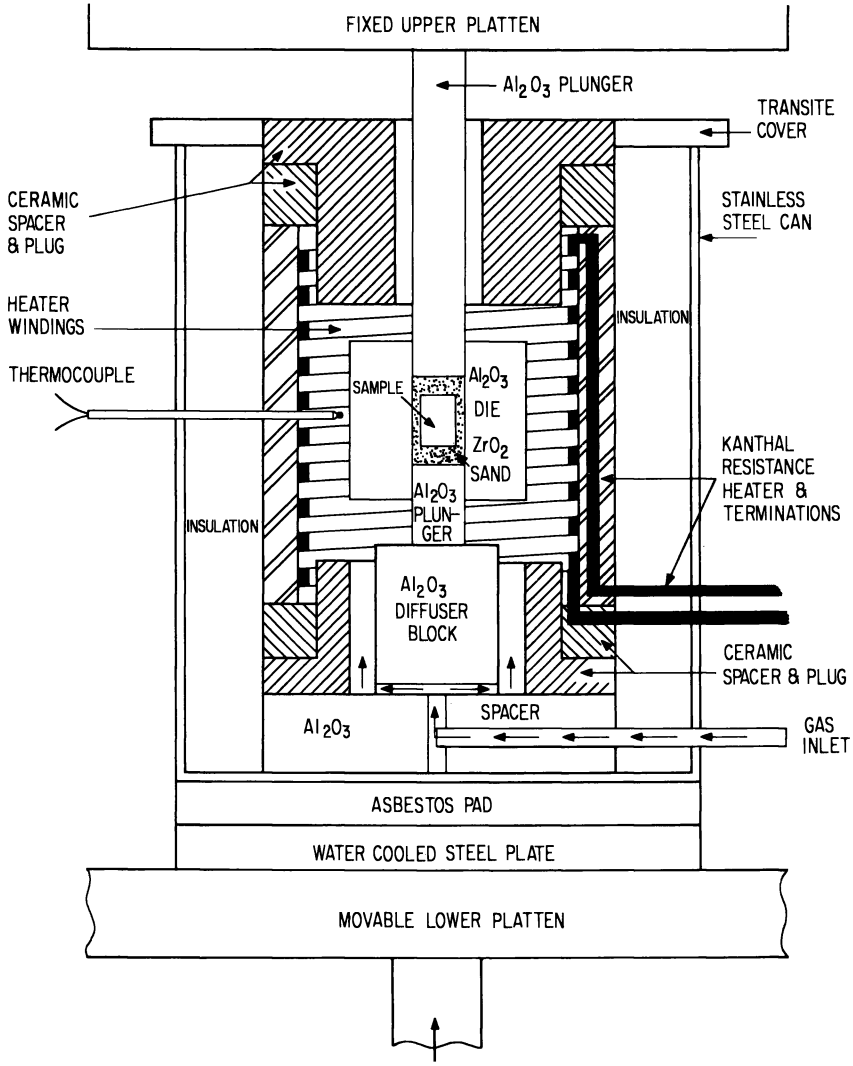

Journal of the Electrochemical Society

Figure 4. Schematic of pressure-sintering equipment

and Pellet Densities of CdSe and CdTe

Time (res)	*Pressed*	*Density, X-ray*	*% of X-ray Density*
2	5.37	5.66	95
2	5.75	5.85	99

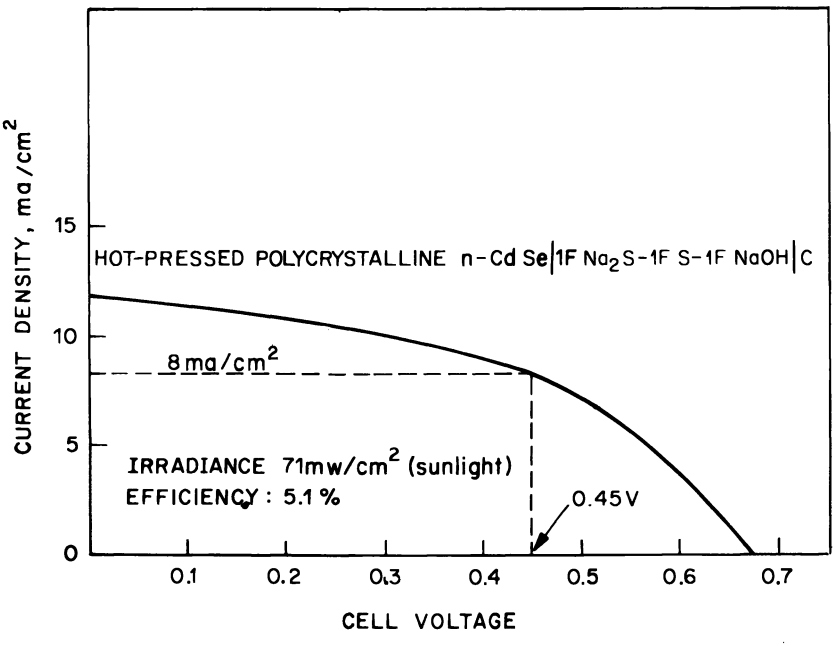

Figure 5. Properties of liquid–junction solar cell using a pressure-sintered polycrystalline n-CdSe photo anode (5)

solar conversion efficiency (5) of 5.1% (Figure 5), using an electrode similar to pellet 3, was measured.

Pressure-sintered CdTe was In-annealed and etched in a manner similar to that described for CdSe. CdTe photo anodes were prepared, and the liquid-junction solar cell output was compared, as in the case of CdSe, with CdTe single-crystal photo anodes, as shown in Figure 6.

Discussion

As seen in Table III, the efficiency of polycrystalline pressure-sintered photo anodes is not very dependent on the density of the pellet. It is

Table III. Annealing and Comparative

	Cd Anneal	
CdSe Sample	T (°C)	*Time (hr)*
Crystal		
Pressed pellet		
1	600	16
2	700	110

[a] Unit value corresponds to about 25 mA · $(cm^2)^{-1}$.

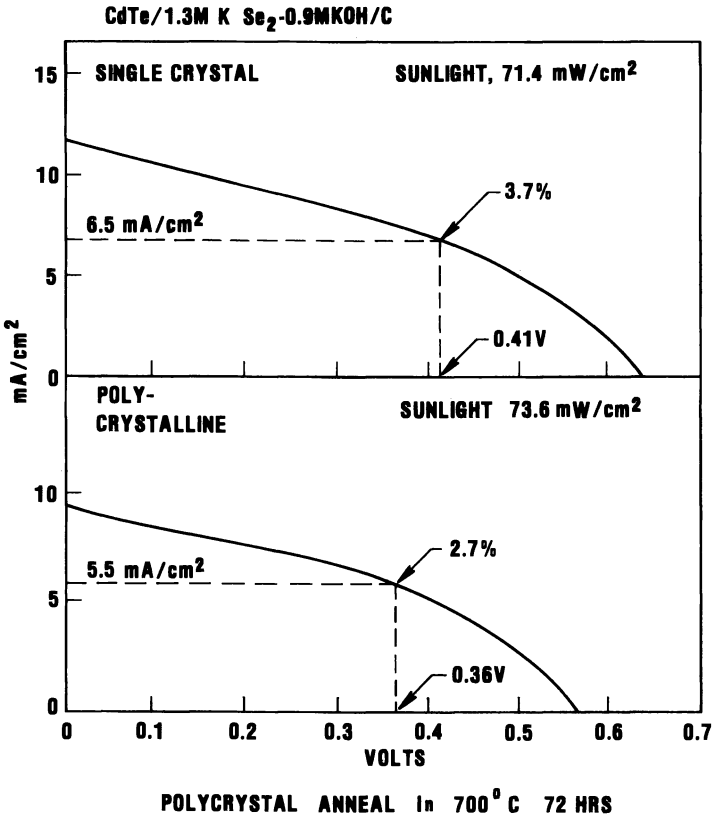

Figure 6. Properties of liquid–junction solar cells using single-crystal CdTe and pressure-sintered polycrystalline CdTe photo anodes

important that the pellet be sufficiently dense to exclude percolation of solution through the semiconductor to the conductor backing the anode. If such percolation occurs, the cell will be shorted and no photovoltaic effect will be observed.

Performance of Pressed CdSe Electrodes

Relative Current[a] (short circuit)	*Volts (open circuit)*	*Fill Factor*	*Relative Efficiency*
1.00	0.747	0.58	1.00
0.70	0.730	0.58	0.69
0.68	0.755	0.49	0.70

There is no difficulty in exceeding the 1-μm grain size necessary for light absorption in the first layer of grains.

Due to the difficulty in measuring carrier concentration in polycrystalline materials, the correct doping conditions (temperature and time) were arrived at empirically. Conditions were varied to produce samples for which the cell efficiency was maximized. When the best set of annealing conditions were attained, polycrystalline photo anodes with up to 70% of single-crystal efficiency for both CdSe and CdTe were obtained.

Conclusion

Liquid-junction solar cells using polycrystalline electrodes will operate at efficiencies that are commensurate with cells containing single-crystal electrodes. If this type of cell is ever to be of use in energy conversion, the ability to utilize polycrystalline electrodes will be an economic factor. Pressure sintering is a viable method of producing a variety of semiconducting photoelectrodes for study without the effort involved in growing single crystals.

Acknowledgment

The author thanks A. Heller and B. Miller, for their help in preparing this paper and in various other aspects of this work, and J. Thomson, Jr., and V. G. Lambrecht, Jr., for help with the pressure-sintering experiments.

Literature Cited

1. Gerischer, H. *J. Electroanal. Chem.* **1975**, *58*, 263.
2. Wrighton, M. S.; Bocarsly, A. B.; Bolts, J. M.; Ellis, A. B.; Legg, K. D. In "Semiconductor Liquid Junction Solar Cells," Conference Proceedings; Heller, A., Ed.; Electrochemical Society, Inc.: Princeton, NJ, 1977; p.138.
3. Heller, A.; Chang, K. C.; Miller, B. *J. Electrochem. Soc.* **1977**, *124*, 697.
4. Heller, A.; Schwartz, G. P.; Vadimsky, R. A.; Menezes, S.; Miller, B. *J. Electrochem. Soc.* **1978**, *125*, 1156.
5. Miller, B.; Heller, A.; Robbins, M.; Menezes, S.; Chang, K. C.; Thomson, J., Jr. *J. Electrochem. Soc.* **1977**, *124*, 1019.

RECEIVED November 10, 1978.

9

Oxyfluoride Photoelectrodes for the Photodecomposition of Water by Solar Energy

A. WOLD and K. DWIGHT

Department of Chemistry, Brown University, Providence, RI 02912

Several oxides—for example, TiO_2, $SrTiO_3$, SnO_2, and WO_3—have been used as anodes for the photoelectrolytic decomposition of water by solar energy. All these oxides must be made to conduct by the creation of oxygen defects. However, oxygen deficiencies undoubtedly are responsible for the long-term instability of the electrodes studied to date. An alternative method of enhancing conductivity is to use chemical substitution of oxygen by fluorine. The absence of oxygen vacancies should result in the formation of more stable electrodes toward oxygen in solution.

In most of the previous investigations that have dealt with *n*-type oxide electrodes for the photoelectrolysis of water, increased conductivity was achieved by the production of oxygen deficiencies. This early work on *n*-type anodes such as TiO_{2-x} indicated that the defect compounds were stable. However, recent evidence (*1, 2*) has shown that these compounds do not show long-term stability in the presence of oxygen at their surfaces. An alternative method of producing conducting electrodes is to substitute fluorine for oxygen rather than to create oxygen vacancies. Both methods result in the formation of $3d^1$ titanium, which would account for the relatively high conductivity obtained. In a recent publication Derrington et al. (*3*) reported on the photoelectrolytic behavior of $WO_{3-x}F_x$. Pure WO_3, prepared by completely oxidizing tungsten foil, could best be indexed on a triclinic system similar to the one reported by Roth and Waring (*14*). It transforms to a monoclinic phase upon the removal of small amounts of oxygen (*15*). Whereas the system WO_{3-x} ($O \leqslant x \leqslant 1$) is monoclinic throughout the entire range (*5*), the system $WO_{3-x}F_x$ prepared in the study of Derrington et al. (*3*) undergoes progressive structural modifications, which are summarized in Table I.

0-8412-0472-1/80/33-186-161$05.00/1

Table I. Structural

x	a (Å)	b (Å)
0	7.306(1)	7.527(1)
0.0079 ± 0.0005	7.301(1)	7.527(1)
0.0177 ± 0.001	7.311(1)	7.545(1)
0.0663 ± 0.005	7.369(1)	7.482(1)

The structure remains triclinic for very small ($x = 0.0079$) amounts of substituted fluorine in the system $WO_{3-x}F_x$. When the amount of substituted fluorine is 0.0177, the structure has undergone the transition to the monoclinic phase, and when $x = 0.0663$, the resulting phase is orthorhombic.

The resistivity of the pure WO_3 samples was approximately 10^6 Ω · cm. The resistivities of the WO_{3-x} samples ranged between 1.2×10^4 and 7×10^{-1} Ω · cm, and the resistivities of the $WO_{3-x}F_x$ samples ranged between 100 and 5 Ω · cm. Absorption measurements indicated that the band gap of WO_3 and all $WO_{3-x}F_x$ samples was 2.65 ± 0.10 eV. This is consistent with previous investigations (*3, 5–12*).

The photocurrents versus applied voltage are plotted in Figure 1 for several WO_{3-x} samples. Measurements were made with the electrolyte in equilibrium with air. As can be seen, the largest photocurrent is reached for the WO_{3-x} sample having the lowest resistance, with the photocurrents of the remaining samples decreasing as the resistance increases. These results are consistent, with the only effect being a change in the overall cell resistance.

The photocurrents for two triclinic samples of $WO_{3-x}F_x$ are shown versus applied bias in Figure 2, the measurements being made with the electrolyte in equilibrium with air. Although photocurrents were observed for all of the tungsten oxyfluorides studied, the monoclinic and orthorhombic compositions ($x \geqslant 0.0177$) show more complex behavior.

The spectral responses of the $WO_{3-x}F_x$ samples shown in Figure 3 were obtained with an applied bias of 0.5 V. The photocurrents plotted here were normalized for clarity by taking the ratio of the photocurrent at a given wavelength to the maximum photocurrent obtained (that is, at 400 nm). The actual photocurrents at 400 nm are for $x = 0.0079$, $I = 16.06$ μA · $(cm^2)^{-1}$, and for $x = 0.0083$, $I = 6.07$ μA · $(cm^2)^{-1}$. The colors of the materials varied from a light green for the $x = 0.0079$ sample to darker green for the $x = 0.0083$ sample.

The stability of the WO_{3-x} and $WO_{3-x}F_x$ samples was investigated by three procedures: stability against reoxidation, stability against hydrolysis or dissolution, and stability in a working cell arrangement. Figure 4 shows the results of the reoxidation experiments on samples of about 175 mg. While WO_{3-x} readily oxidizes at 250°–300°C, the $WO_{3-x}F_x$ sample

Properties of $WO_{3-x}F_x$

c	α	β	γ
3.854(1)	88°43′ ± 2′	90°17′ ± 2′	90°39′ ± 2′
3.856(1)	88°48′ ± 2′	90°17′ ± 2′	90°35′ ± 2′
3.851(1)	90°	90°51′	90°
3.848(1)	90°	90°	90°

is stable to 600°C, implying an increased stability to reoxidation. Also, the thermal gravimetric data shown in Figure 4 indicates that the composition of the oxyfluoride samples prepared in this study can be represented by the formula $WO_{3-x}F_x$. If the composition of the samples had been $WO_{3-x}F_y$ instead of $WO_{3-x}F_x$, then there would have been a gain in weight recorded equivalent to the value $x - y$. From Figure 4 we see that the sensitivity of this method is such that values of x (representing an oxygen deficiency) in the system WO_{3-x} can be determined, where values of x are less than 0.01.

Hydrolysis and dissolution experiments were made by placing samples of WO_{3-x} and $WO_{3-x}F_x$ in 0.2*M* H_2SO_4 and leaving these at 90°C for 350 hr. Neither sample showed any hydrolysis or dissolution.

Stability in a working cell, with the electrolyte in equilibrium with air, was determined by biasing the electrode at 0.5 V with respect to the

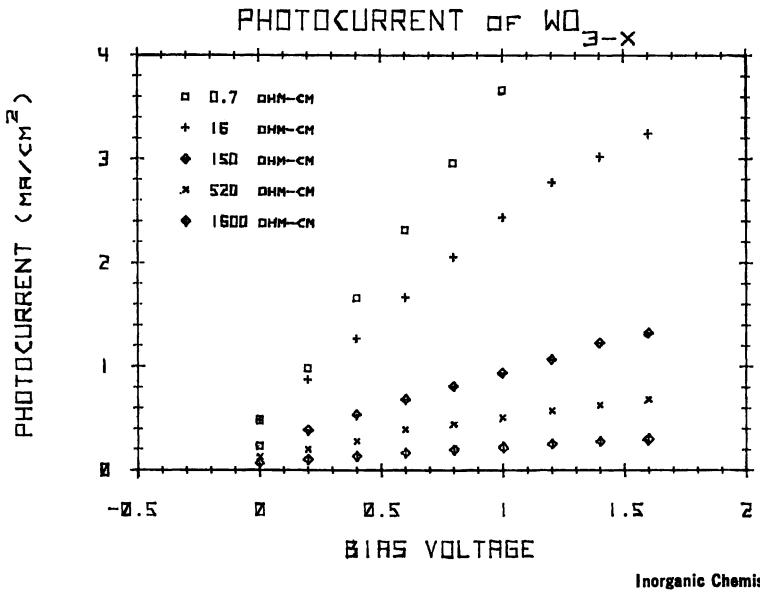

Inorganic Chemistry

Figure 1. Photocurrent versus applied bias for several WO_{3-x} samples in 0.2M $NaC_2H_3O_2$ (pH 7.8) (2)

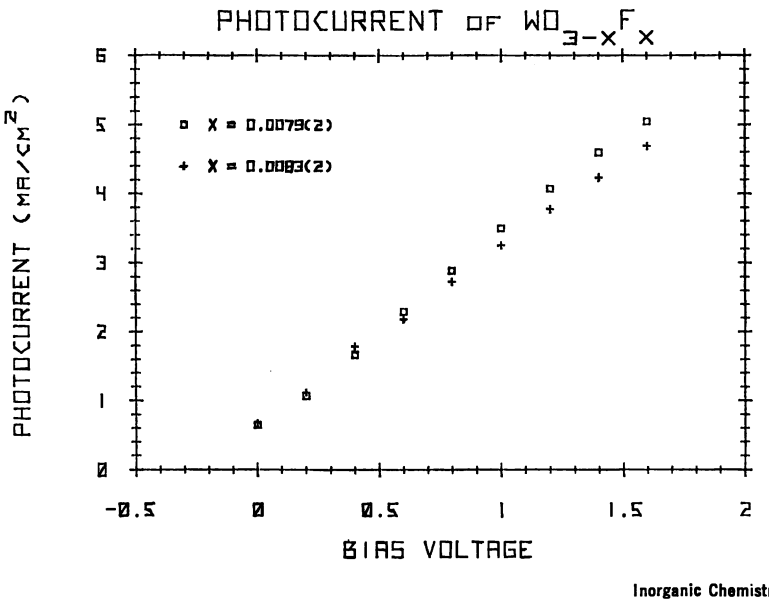

Figure 2. Photocurrent versus applied bias for several $WO_{3-x}F_x$ samples in 0.2M $NaC_2H_3O_2$ (pH 7.8) (2)

platinum cathode, illuminating then with the full output of a 150-W xenon lamp and monitoring the changes in photocurrent with time. While the slightly reduced WO_{3-x} films gave stable photocurrents, the more reduced samples were less stable. The most reduced sample ($x \approx 0.03$) was very unstable, with the photocurrent decreasing by 30% over a period of 2 hr. This is consistent with the results found by Hardee and Bard (*11*). On the other hand, the triclinic samples of $WO_{3-x}F_x$ gave stable photocurrents of 2 mA · $(cm^2)^{-1}$ for periods of up to 46 hr (about 700°C). In addition, there was no visible change on the surface of the electrode.

As a result of the work on the $WO_{3-x}F_x$ system, it was expected that members of the system $TiO_{2-x}F_x$ also would show increased stability over TiO_{2-x}, since all the anion sites would be occupied.

Samples of $TiO_{2-x}F_x$ were prepared by the fluorination of TiO_2 wafers (cut from single crystals obtained from National Lead), using a fluorinating system shown in Figure 5. Hydrogen fluoride was generated by the thermal decomposition of potassium bifluoride at 260°C. The TiO_2 wafer was positioned within a sample tube and centered with respect to the hot zone of a furnace. Figure 5 depicts the arrangement of the furnaces and gas train used for the preparation of the $TiO_{2-x}F_x$ samples. A gas mixture of 85% argon and 15% hydrogen was dried by passing it through a phosphorus pentoxide drying tube, flowing it over

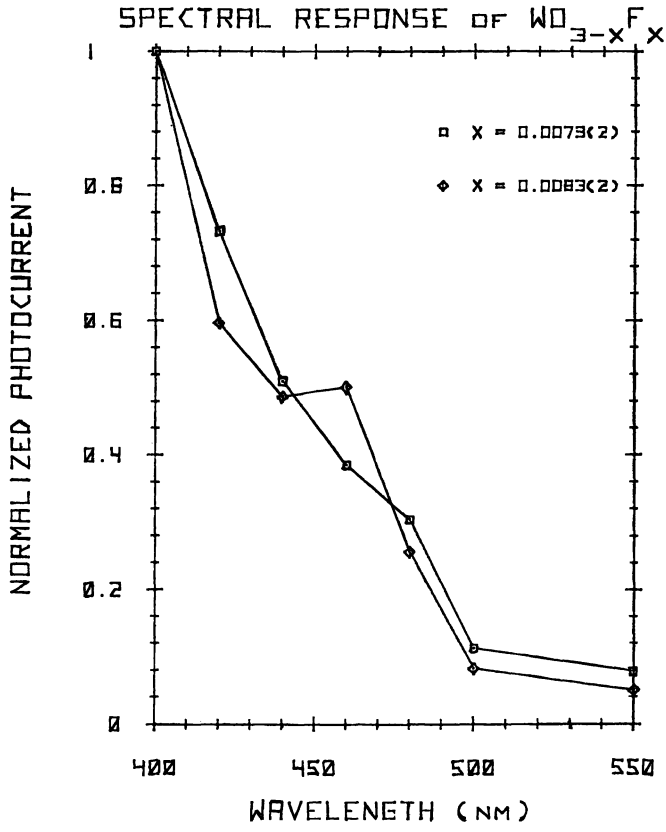

Figure 3. Normalized spectral reponse of $WO_{3-x}F_x$ in 0.2M $NaC_2H_3O_2$; Eg = optical band gap (2.7 eV) (2).

the potassium bifluoride (which was kept at 260°C), passing it over the sample, and finally exiting it through a sodium hydroxide bubbler. Samples were fluorinated at temperatures between 575° and 700°C. Attempts to fluorinate a TiO_2 wafer at 550° failed to yield a homogeneous product. The products prepared in this manner appeared pale blue to black in color. The darker colors resulted from higher-temperature preparations.

Samples of $TiO_{2-x}F_x$ were prepared for analysis by grinding a piece of each fluorinated wafer to give approximately 100 mg of sample. The finely divided powder was heated in an oxygen atmosphere from room temperature to 1000°C, and changes in the weight were recorded using a Cahn electrobalance (model RG) and a chart recorder. None of the samples in the series showed any measurable weight change, which

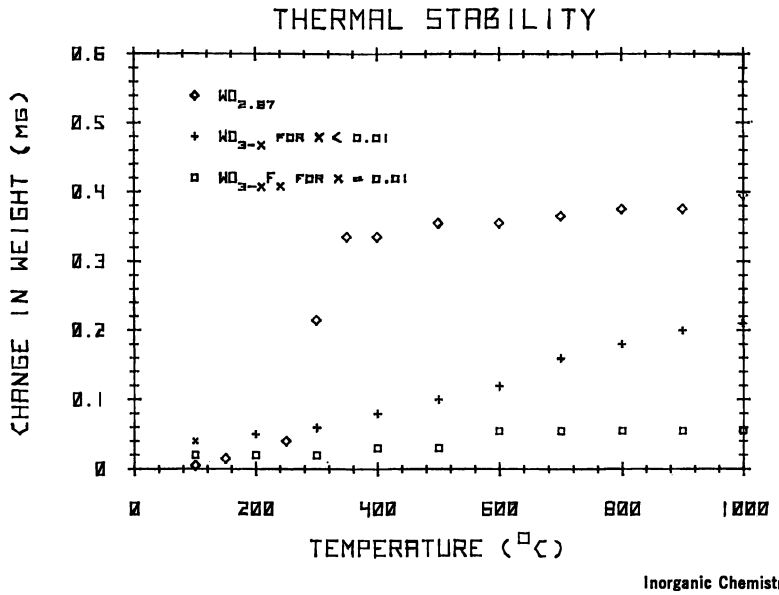

Figure 4. Stability against reoxidation for WO_{3-x} and $WO_{3-x}F_x$ in flowing oxygen (2)

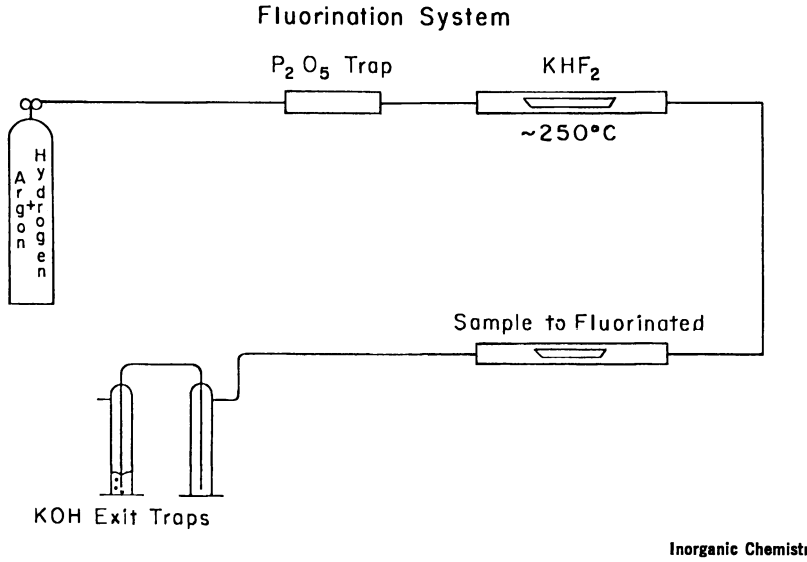

Figure 5. Schematic illustration of the fluorination apparatus (13)

indicated that the the fluorine had substituted for the oxygen and that, within the limits of the analysis (about 0.001), there were no measurable additional vacancies present in the compounds studied. The fluoride contents of the samples fluorinated at 700° and 600°C were determined with an Orion fluoride electrode (model 94-09). The fluoride content of the sample fluorinated at 700°C gave a value of x in $TiO_{2-x}F_x$ of 0.002, whereas that of the sample fluorinated at 600°C gave a value of $x = 0.0001$, which was the limit detectable by the fluoride electrode and is subject to some uncertainty, since the value of x in this material can be reported only within an accuracy equivalent to $\pm$ 0.0002.

A bar approximately 4 × 2 × 1 mm was cut from each of the fluorinated wafers in such a fashion that only the two large faces belonged to the outside surface of the sample. Each bar was further subdivided into three sections 4 × 2 × 0.25 mm in order to establish whether each fluorinated wafer was truly homogeneous. Thus the middle section was taken entirely from the interior of the wafer and made no contact with the outside surface. Indium leads were bonded ultrasonically to each section, and the standard Van der Pauw technique (*13*) was used to measure its resistivity. Excellent agreement, within experimental error, between the resistivity values for inside and outside sections was obtained for all the fluorinated wafers considered in this study. This result demonstrates that the fluorination process had penetrated uniformly throughout each sample. The measured resistivity values are shown as a function of fluorination temperature in Figure 6.

Electrodes were prepared by cutting pieces approximately 4 mm square from the fluorinated samples and evaporating a thin coating of copper onto the back of each to provide good electrical contacts. Anode assemblies were fabricated by using indium metal to solder these electrodes to platinum wires that had been sealed in small borosilicate glass tubes and then coating all but the front surface with an electrically insulating resin (Microstop, Michigan Chrome and Chemical Co.). Care was taken not to disturb the active photosurface. For measurement, these anodes were mounted in a small glass cell approximately 8 mm from the quartz window. A platinized platinum cathode (2.5 cm^2 in area) was mounted 2 cm behind and below with anode, and a saturated calomel reference electrode (SCE) 10 cm above it. The cell was filled with 100 mL of 0.2*M* sodium acetate electrolyte (pH $\approx$ 7.5), which was purged of dissolved oxygen by continuous bubbling of the 85% argon and 15% hydrogen gas. A cathode potential of approximately $-$ 0.64 V versus SCE was used as the criterion for completed purging.

A 150-W xenon arc was used to illuminate an aperture 5 mm in diameter, which was imaged onto the anode by means of a quartz lens.

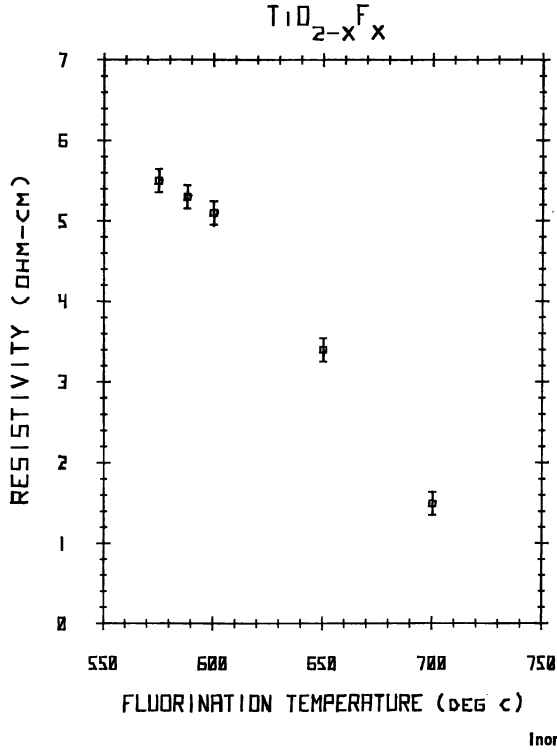

Figure 6. Variation of resistivity with the fluorination temperature of $TiO_{2-x}F_x$ electrodes (13)

This resulted in a reproducible area 2.25 mm in diameter irradiated with approximately 50 mW of total power. The instantaneous power was determined for each curve by using a calibrated Eppley thermopile (16-junction Coblentz-type). Anodic bias was applied via a voltage follower having an output impedance less than 0.1 Ω, and the resulting response was measured with a current amplifier, which inserted a negligible potential drop (less than 1 μV) in the external circuit.

The variation of photocurrent with anode potential (measured against SCE) is shown in Figure 7 for samples fluorinated at several temperatures (T_F) between 575° and 700°C. The indicated photocurrent densities have all been normalized to a total irradiation of 12.5 mW · $(mm^2)^{-1}$, corresponding to 50 mW incident over the illuminated area of 4 mm^2. It is evident that the saturation photocurrent (measured at an anode potential of 0.6 V) increases significantly with decreasing fluorination temperature over this range. The essentially linear nature of this relation-

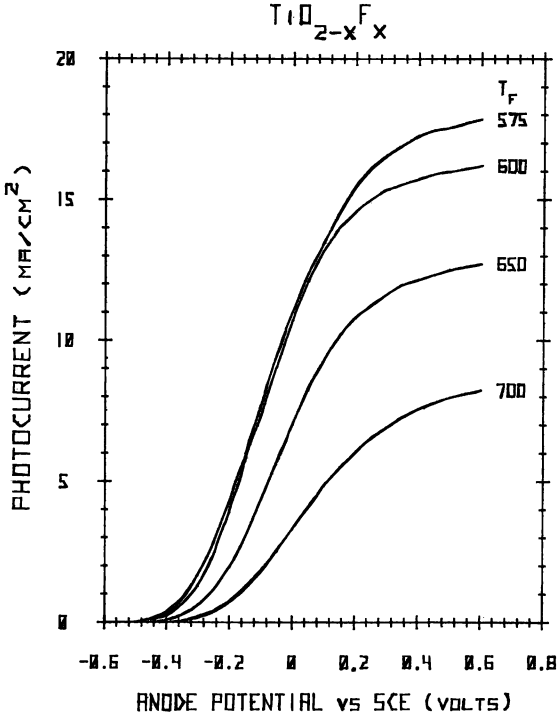

Inorganic Chemistry

Figure 7. Dependence of photocurrent upon anode potential (SCE reference) for $TiO_{2-x}F_x$ electrodes fluorinated at various temperatures T_F for white xenon arc irradiation of 1.25 W · $(cm^2)^{-1}$ (13)

ship can be seen in Figure 8. The peak photocurrent of 17.9 mA · $(cm^2)^{-1}$ obtained here is approximately twice the maximum [9.2 mA · $(cm^2)^{-1}$] found with unfluorinated TiO_{2-x} under similar conditions (*14*).

The lateral shift of the curves presented in Figure 7 results from a systematic variation of the flat-band potential (U_{fb}). Values for U_{fb} (measured against SCE) were obtained from the linear dependence of the square root of the photocurrent upon anode potential for small values of the current (values less than 0.5 mA · $(cm^2)^{-1}$ in Figure 7). They are shown plotted against fluorination temperature in Figure 9. The observed increase in flat-band potential corresponds to a decrease in its energy. This decrease in energy appears anomalous for an increase in carrier concentration, which would be expected to raise the Fermi level, but similar behavior has been reported elsewhere (*8*). The determining factor may well be a lowering of the valence band because of the greater electronegativity of the substituted fluorine (*10, 15*).

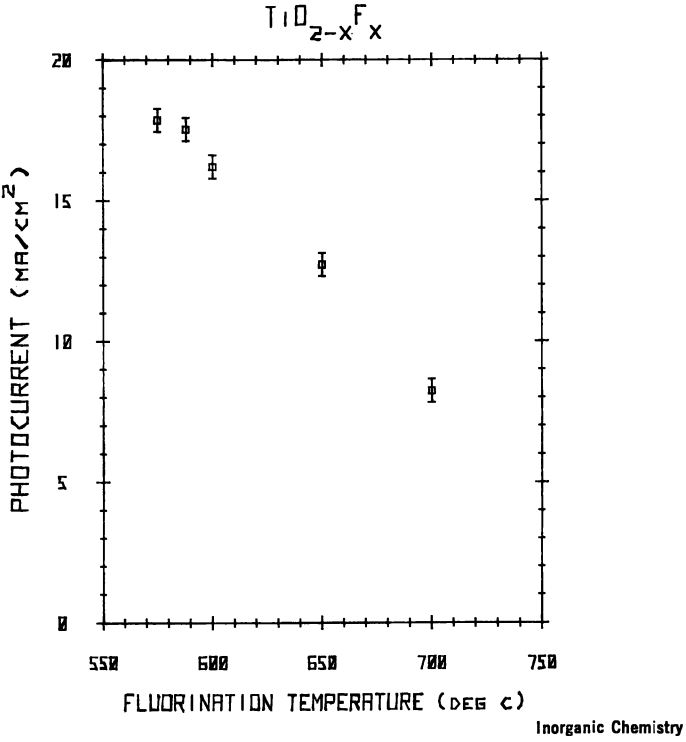

Figure 8. Variation of saturation photocurrent, measured at an anode potential of 0.6 V, with the fluorination temperature of $TiO_{2-x}F_x$ electrodes for white xenon arc irradiation of 1.25 W · $(cm^2)^{-1}$ (13)

The spectral photo response of the fluorinated electrodes was studied by inserting an Oriel monochrometer (model 7240) in place of the 5-mm aperture. The curves shown in Figure 10 were obtained at an anode potential of 0.6 V with a slit width of 0.5 mm, which gave a spectral resolution of 4 nm. The photocurrents have been normalized so as to yield integrated outputs corresponding to the values given in Figure 8. These data can also be expressed in terms of quantum efficiency (electrons per photon) by dividing the observed photocurrent (electrons per second) by the incident radiation (photons per second). The curves presented in Figure 11 have not been corrected for any absorption in the electrolyte or cell window, nor for reflection from the sample surface. From Figures 10 and 11 we see that the increase in observed photocurrent with decreasing fluorination temperature arises from increased responsivity at the longer wavelengths. These wavelengths penetrate more deeply into the electrodes, and their photo-generated electron-hole

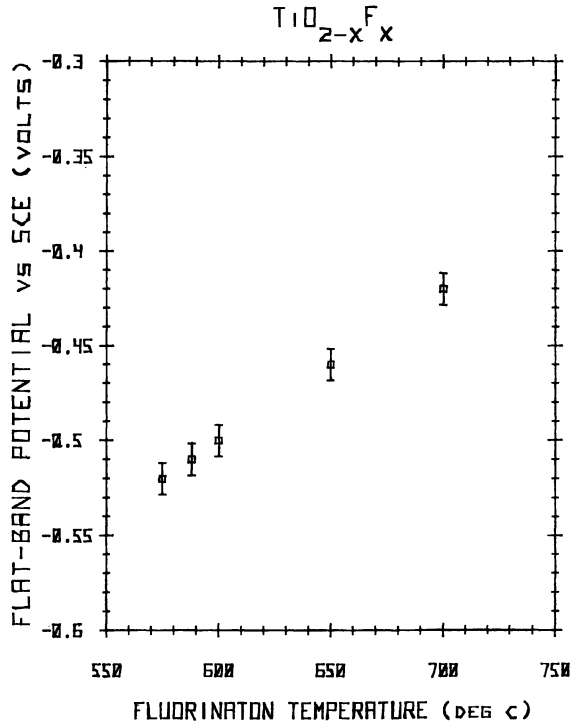

Figure 9. Variation of flat-band potential (SCE reference) with the fluorination temperature of $TiO_{2-x}F_x$ electrodes (13)

pairs will become separated only if this penetration is less than the width of the depletion layer. Thus the improved response observed at low T_F may be attributed to the increase in depletion layer width resulting from the increase in resistivity seen in Figure 6.

The spectral photo response of a sample of TiO_{2-x} reduced at 600°C also has been measured. The results, normalized to 9.2-mA·$(cm^2)^{-1}$ integrated output (*13*) are compared with those obtained for $TiO_{2-x}F_x$ in Figure 12. It is evident that the fluorinated material gives an appreciably greater response at the longer wavelengths, which effect can be attributed to an absence of vacancies in the fluorinated samples. The solar spectrum falls off much more rapidly below 400 nm than the xenon-arc spectrum. Thus the disparity between the outputs of fluorinated and reduced rutile would be greatly enhanced under solar irradiation.

The long-term stability of electrodes prepared from these same two samples has been determined under 12.5 mW · $(mm^2)^{-1}$ irradiation with an applied anodic bias of 1.5 V. The resulting decay of photocurrent with

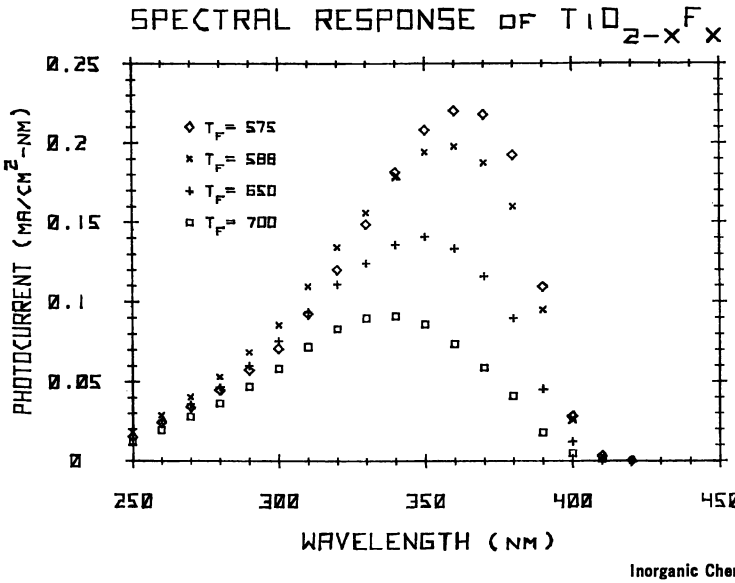

Figure 10. Spectral photo response of $TiO_{2-x}F_x$ for electrodes fluorinated at various temperatures T_F, normalized to white xenon arc irradiation of 1.25 W · (cm²)⁻¹ (13)

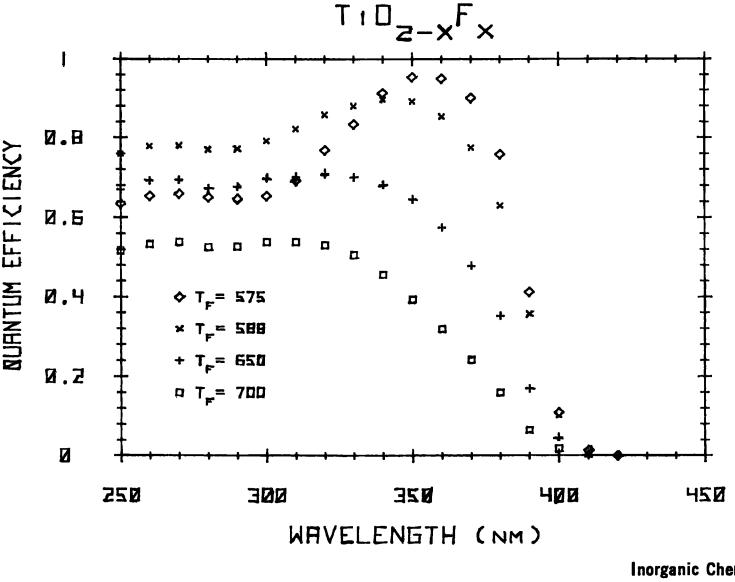

Figure 11. Quantum efficiency in electrons per photon as a function of excitation wavelength for $TiO_{2-x}F_x$ electrodes fluorinated at various temperatures T_F (13)

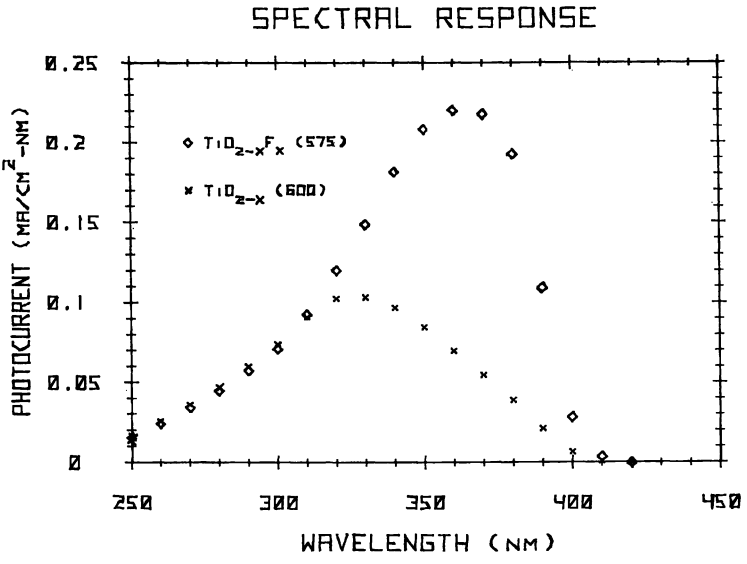

Figure 12. Comparison between the spectral photo response of $TiO_{2-x}F_x$ electrodes fluorinated at 575°C and that of TiO_{2-x} electrodes reduced at 600°C, normalized to white xenon arc irradiation of 1.25 W · $(cm^2)^{-1}$ (13)

time is shown in Figure 13. The fluorinated electrode was found to be appreciably less stable than the reduced electrode in 0.2*M* sodium acetate, presumably because of hydrolysis of the fluorine ions. Such hydrolysis should be suppressed by a sufficient concentration of fluoride ions in the electrolyte. Measurements were made in a lucite cell having a fluorite window 2 mm thick with a 0.2*M* solution of potassium bifluoride buffered to a pH of 6 with potassium hydroxide and with a 0.2*M* solution of unbuffered potassium bifluoride (pH = 3.5). As seen in Figure 13, the hydrolysis was partially and completely suppressed, respectively, by these two electrolytes. In the latter case the long-term stability was improved over that of unfluorinated rutile.

In summary, the substitution of small amounts of fluorine for oxygen in WO_3 increases the stability of the photo anode and in TiO_2 increases the photocurrent output, which arises from increased response at longer wavelengths. The improved response may be partially attributed to an increase in the width of the charge depletion layer. The increase in stability is a result of the lack of defects in the *n*-type oxyfluoride electrodes. Further work is necessary in order to determine if an oxyfluoride electrode can be prepared that combines increased stability with a sufficient photo response necessary for a suitable photo anode.

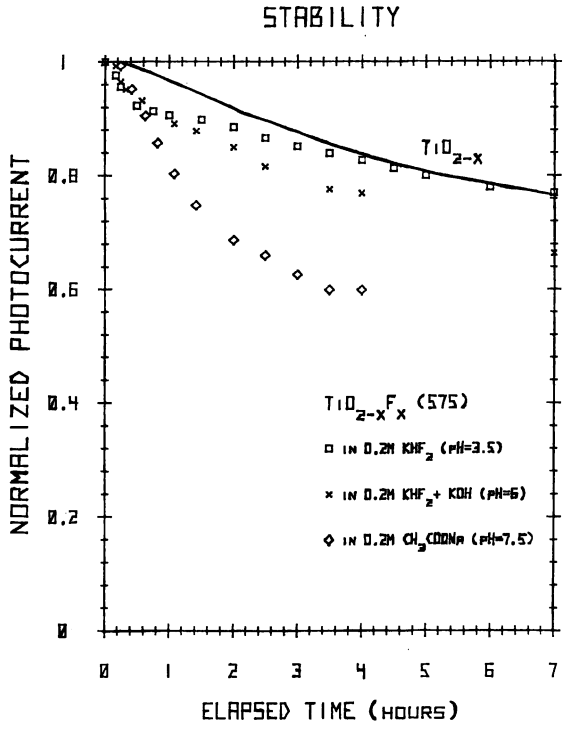

Inorganic Chemistry

Figure 13. Comparison between the decay of photocurrent with time for TiO_{2-x} electrodes in 0.2M sodium acetate and that for $TiO_{2-x}F_x$ electrodes fluorinated at 575°C in 0.2M potassium bifluoride, 0.2M potassium bifluoride buffered with potassium hydroxide, and 0.2M sodium acetate. Measurements were made with 1.5 V of anodic bias under white xenon arc irradiation of 1.25 W · $(cm^2)^{-1}$ (13).

Acknowledgment

The authors would like to acknowledge the Office of Naval Research, Arlington, VA, for their support of Kirby Dwight. Acknowledgment is also made to the National Science Foundation, Washington, D.C., No. GH 37104. In addition, the authors would also like to acknowledge the support of the Materials Research Laboratory Program at Brown University.

Literature Cited

1. Harris, L. A.; Wilson, R. H. *J. Electrochem. Soc.* **1976**, *123*, 1010.
2. Harris, L. A.; Gross, D. R.; Gerstner, M. E. *J. Electrochem. Soc.* **1977**, *124*, 839.
3. Derrington, C. E.; Godek, W. S.; Castro, C. A.; Wold, A. *Inorg. Chem.* **1978**, *17*, 977.

4. Roth, R. S.; Waring, J. L. *J. Res. Natl. Bur. Stand., Sec. A* **1966,** *70*(4), 281.
5. Gebert, E.; Ackermann, R. J. *Inorg. Chem.* **1966,** *5,* 136.
6. Butler, M. A.; Nasby, R. D.; Quinn, R. K. *Solid State Commun.* **1976,** *19,* 1011.
7. Deb, S. K. *Philos. Mag.* **1973,** *27,* 801.
8. DeWald, J. F. *J. Phys. Chem. Solids* **1960,** *14,* 155.
9. Gissler, W.; Memming, R. *Electrochem. Soc., Virginia Conf., Airlie, VA, May 1977.*
10. Gomes, W. P.; Cardon, F. "Proceedings of Conference on Electrochemistry and Physics of Semiconductor-Liquid Interfaces Under Illumination"; Heller, A., Ed.; Electrochem. Soc.: Princeton, NJ, 1977; 120.
11. Hardee, K. L.; Bard, A. J. *J. Electrochem. Soc.* **1977,** *124,* 215.
12. Hodes, G.; Cahen, D.; Manassen, J. *Nature (London)* **1786,** *26,* 312.
13. Van der Pauw, L. J. *Phillips Tech. Rev.* **1958,** *20,* 220.
14. Subbarao, S. N.; Yun, Y. H.; Kershaw, R.; Dwight, K.; Wold, A., unpublished data.
15. McCauldin, J. O.; McGill, T. C. "Electrochem. Soc. Monograph on Thin Films and Interfaces"; Mayer et al., Eds.; 1977; in press.

RECEIVED September 13, 1978.

10

Conducting Polymers: A Comparison of the Properties of Polythiazyl $(SN)_x$ and Polyacetylene $(CH)_x$ and Their Derivatives

G. B. STREET and T. C. CLARKE

IBM Research Laboratory, San Jose, CA 95193

The properties of the only two synthetic polymers known to exhibit metallic conductivity, $(SN)_x$ and doped $(CH)_x$, are discussed. Although pristine $(SN)_x$ is a semimetal and pristine $(CH)_x$ a low-band gap semiconductor, their behavior becomes intriguingly analogous after treatment with halogens. The effects of halogens and other dopants are discussed from a structural, electronic, and spectroscopic point of view.

The interest in synthetic metals, which had its origins in Little's theoretical work on room temperature superconductors (*1, 2*) has maintained its impetus, encouraged by systematic advances in materials resulting from the strongly interactive efforts of chemists and physicists. The earliest materials of interest were the Krogmann type of salts (*3*) and the organic charge transfer salts exemplified by TTF–TCNQ (*4*). Following these materials came $(SN)_x$ (*5–7*) and its halogen derivatives (*8–11*), the first polymeric metals and still the only examples of superconducting polymers. Most recently polyacetylene has been shown to exhibit a range of conductivity from semiconductor to metal when chemically treated with a variety of dopants (*12, 13*). As this class of synthetic metals has expanded, so has the possibility of achieving metallic and semiconducting properties in polymers while retaining the technologically desirable characteristics of plastics. In this paper we will examine the properties of $(SN)_x$ and its derivatives together with those of the metallic derivatives of $(CH)_x$. The chemistry (*6*) and physics

0–8412–0472–1/80/33–186–177$05.00/1

(*5, 7*) of $(SN)_x$ have been reviewed previously and its properties have been compared with those of the organic charge transfer salts (*14*). The polythiazyl halides have been the subject of a more recent review (*15*). The early work on linear and substituted polyacetylenes has been discussed by Meier (*16*).

History

Both $(SN)_x$ and $(CH)_x$ were well known in the chemical literature for many years prior to their relatively recent exploitation by the solid state community. It is pertinent to note that an appreciation of their most significant properties had to await extensive materials work to produce high-quality crystals of $(SN)_x$ and films of $(CH)_x$. Since 1953 $(SN)_x$ has been known to exhibit interesting electrical properties (*17*), but it was not until 1973 (*18*) that crystals of sufficient quality to demonstrate its intrinsic metallic properties were obtained. The difficulties with $(CH)_x$, which is prepared by polymerizing acetylene in presence of a Ziegler–Natta catalyst, were perhaps more severe. Crystals of $(CH)_x$ have not yet been prepared. Berets and Smith (*19*) discussed the problems of producing polyacetylene free from catalyst and oxygen. However, it was the extensive work of Shirikawa and his co-workers (*20, 21*) that finally led to the optimization of this process and the first highly pure polyacetylene, in the form of thin films. Nevertheless, Berets and Smith were able to show that the conductivity of compressed pellets of $(CH)_x$ powder could be varied over 7 orders of magnitude. The conductivity was increased by a factor of 10^3 by treatment with acceptors such as BF_3, whereas treatment with ammonia reduced the conductivity by a factor of 10^4. Chiang et al. (*13*) in conjunction with Shirakawa, using donors as well as acceptors, have varied the conductivity of polyacetylene films over 12 orders of magnitude. We have shown that certain transition metal salt solutions, for example, $AgClO_4$/toluene, are also effective in changing the conductivity of $(CH)_x$ films (*22*). Examination of these silver derivatives of $(CH)_x$ has been helpful in elucidating the mechanism by which other acceptors influence the conductivity of $(CH)_x$, and they will be discussed in some detail.

Structures and Bonding of $(SN)_x$ and $(CH)_x$

Though this review will be concerned largely with the properties of derivatives of $(SN)_x$ and $(CH)_x$ rather than the pristine materials, the similarities between the structures of $(SN)_x$ and $(CH)_x$ themselves deserve some attention and are also significant to the discussion of their

physical properties. Though $(SN)_x$ is formed via the solid state polymerization of S_2N_2, the resulting crystals are not highly perfect (*6*). They are fibrous and usually highly twinned besides containing a large number of defects (*23*). By contrast, even the best films of $(CH)_x$ are polycrystalline and not very ordered (*20*), showing only about 10 broad weak reflections in X-ray (*24*) and electron diffraction. The films are actually a mat of randomly aligned fibers packed with only 30% of theoretical density (*25*). Electron diffraction studies of individual fibers show preferred orientation even though the individual fibers are poorly crystalline (*26*). By combining the information from X-ray diffraction studies with the presumed geometry of the $(CH)_x$ chain and molecular-packing considerations, Baughman et al. (*24*) have proposed a structure for *cis*-polyacetylene. The structures of both $(SN)_x$ (*27*) and *cis*-$(CH)_x$ are given in Figure 1. $(SN)_x$ and $(CH)_x$ consist of essentially flat chains, the length of which is unknown. In the case of $(SN)_x$ the chains pack in parallel planes, whereas the chains in successive planes of $(CH)_x$ are rotated such that their π clouds are almost orthogonal, reducing the nonbonded electron interaction.

Obviously, it would be desirable to prepare $(CH)_x$ in the form of single crystals or even as oriented films in order to obtain a more complete understanding of many of the phenomena that are of interest in this material. Ito et al. (*20*) were able to partially align films by stretching. This technique has been significantly improved recently by Shirakawa and Ikeda (*28*) to give films that exhibit anisotropic properties. The similarity in the chain axis repeating unit of $(SN)_x$ and $(CH)_x$, as shown in Figure 1, encouraged us to attempt to grow $(CH)_x$ epitaxially on chain-aligned films of $(SN)_x$. However, the nature of the polymerization process is such that it occurs at the acetylene–catalyst solution interface, and no epitaxy took place. Attempts to grow oriented $(CH)_x$ films on stretched Mylar failed for similar reasons.

Intercalation of $(SN)_x$ and $(CH)_x$

The comparatively weak interchain bonding in $(SN)_x$ and $(CH)_x$ indicates that both materials might be subject to intercalation by appropriate guest molecules. The ready formation of adducts (*29, 30*) between S_4N_4 or S_2N_2 and Lewis acids, together with the observation that these types of molecules interact with $(CH)_x$ as we have described, suggests that they could intercalate in both chain structures. Exposing $(SN)_x$ to many such molecules gave no expansion characteristic of intercalation, except in the case of bromine (*31–40*). However, X-ray studies of $(CH)_x$ exposed to a variety of molecules, including bromine, showed that intercalation takes place readily in this system.

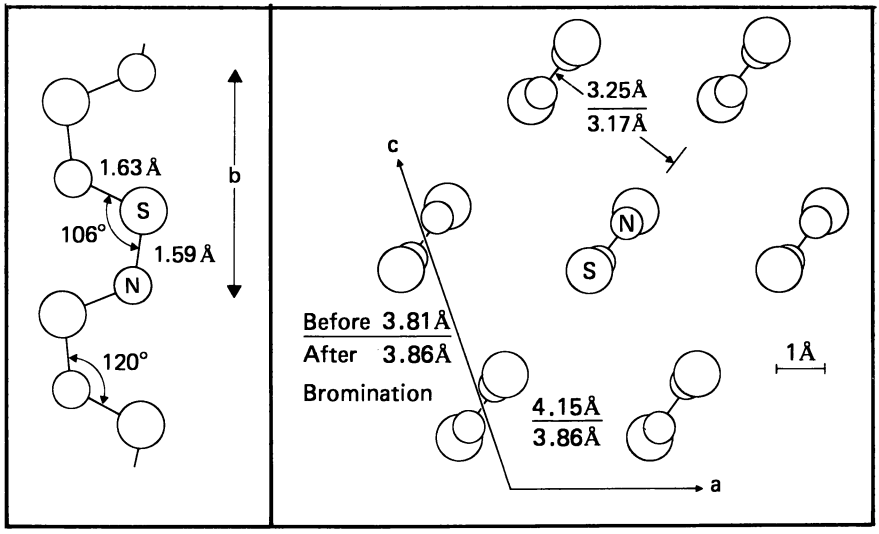

$(SN)_x$
Monoclinic $P2_1/C$

a = 4.153Å
b = 4.439Å β = 109.7°
c = 7.637Å

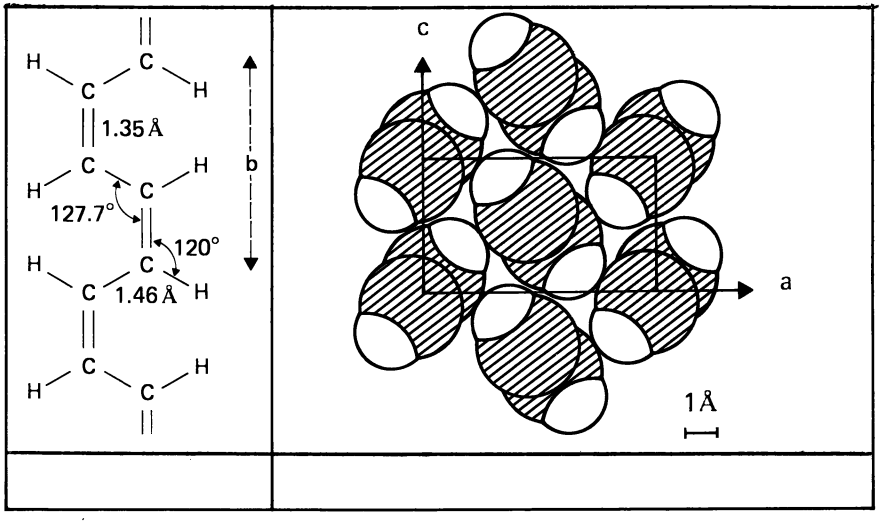

$(CH)_x$
Orthorhombic Pnma

a = 7.61Å
b = 4.47Å
c = 4.39Å

Figure 1. Comparison of the structures of $(SN)_x$ and cis-*$(CH)_x$ showing the chain configurations*

Bernard et al. (*31*) first reported that bromine could be intercalated into $(SN)_x$. Though the original shape of the $(SN)_x$ crystals is retained, at room temperature bromine vapor causes them to expand approximately 50% in volume perpendicular to the chain axis, to give a composition $(SNBr_{0.4})_x$. Despite this expansion in the volume of the crystals, the $(SN)_x$ unit cell volume contracts by 6% in directions perpendicular to the chain axis (*32*). Neither the crystals nor the unit cell show any change in dimensions along the chain axis. The fact that the separation between 102 planes decreases on bromination strongly suggests that the bromine is intercalating between the chains in the 102 plane and not between the 102 planes themselves.

Intercalation of $(CH)_x$ was first demonstrated by Baughman et al. (*24*). They showed from X-ray data that in the iodine-doped films reported by Chiang et al. (*11–13*) the iodine intercalates between the (100) planes. We have also prepared $(CHI_{0.2})_x$ by exposing $(CH)_x$ films to the room temperature vapor pressure of iodine overnight. In agreement with Baughman, our X-ray data (Table I) show that the iodine enters the $(CH)_x$ lattice such that it causes an expansion of the (100) plane spacing. The (100) peak, normally of zero intensity in pristine $(CH)_x$, becomes quite strong and shifts in value, owing to the iodine occupying the $(CH)_x$ chain sites in the (100) and (200) planes in an ordered fashion. Similar studies of $(CHBr_{0.47})_x$ (*22*) and $[CH(AsF_5)_{0.15}]_x$ indicate that these species intercalate in a fashion similar to iodine. In the case of $(CHI_{0.2})_x$ we were also able to measure the separation $d(002)$ and show that the volume of the unit cell had expanded by about 9.5%. From the data in Table I it is possible to calculate the van der Waals diameter, D, of the intercalant by using the formula

$$D(\text{Å}) = 2d^1(200) - 3.80$$

where $d^1(200)$ is the value of $d(200)$ after intercalation. The values obtained for iodine and bromine, 4.06 Å and 3.46 Å respectively, are in good agreement with the literature (*41*). The value obtained for AsF_5 is 4.98 Å, compared to 4.75 Å determined for an AsF_5–graphite intercalation compound (*42*). It is interesting to note that bromine causes a contraction in unit cell parameters for both $(SN)_x$ and $(CH)_x$.

Table I. X-ray Data for Pristine and Intercalated $(CH)_x$

	d*(100)* *(Å)*	d*(200)* *(Å)*	d*(002)* *(Å)*
$(CH)_x$	—	3.80	2.19
$(CHBr_{0.47})_x$	7.31	3.63	—
$(CHI_{0.2})_x$	7.96	3.93	2.30
$[CH(AsF_5)_{0.16}]_x$	8.83	4.39	—

Structure of the Intercalants

From X-ray diffraction, electron diffraction (*9, 34*), infrared (IR) (*37*), and Raman spectroscopy (*32–36*), magnetic susceptibility (*38*), and extended X-ray absorption fine structure (EXAFS) data (*39*), it appears that the bromine in $(SNBr_{0.4})_x$ is present as Br_3^- ions as well as neutral Br_2 molecules (*15*). Besides being intercalated in the 102 planes, the bromine species are also distributed in the interfibrillar regions. Because of the small diameter (30 Å) of the fibers of $(SN)_x$ after bromination (*9, 34*), the interfibrillar bromine may be as much as 90% of the total. Electron diffraction (*9*) and diffuse X-ray-scattering data (*40*) show that the bromine gives rise to a one-dimensional (1-D) commensurate superlattice oriented along the chain axis with a period of $2b$, twice that of the $(SN)_x$ chain. From geometrical considerations, it seems plausible that the $2b$ superlattice is due to Br_3^- oriented parallel to the $(SN)_x$ chains. In order to give rise to the 1-D superlattice, the Br_3^- must be attached to the $(SN)_x$ chain in a regular manner. As halogens are usually attached to sulfur atoms in polythiazyl halides, it seems likely that the Br_3^- ions order with their axes parallel to the $(SN)_x$ chains, in a manner that maximizes sulfur–bromine interactions, as shown in Figure 2. Similar principles would determine the arrangement of the Br_2 molecules.

Raman spectroscopy shows that the bromine intercalated into $(CH)_x$ also exists as Br_3^- ions (*22, 43*). From X-ray studies the axes of the Br_3^- ions would also appear to be parallel to the chain (*22*). However, in this case there is no evidence of any ordering of the Br_3^- ions along the chain direction, nor is there any significant amount of neutral Br_2. As the $(CH)_x$ fibers are about 200 Å in diameter, almost an order of magnitude larger than $(SN)_x$, the amount of bromine on the outside of the fibers is small compared with that intercalated between the chains. Despite these differences, the models of brominated $(SN)_x$ and $(CH)_x$ are remarkably similar. In both cases the bromine oxidizes the chain to give an extended polymeric cation, and the linear Br_3^- anions align parallel to the axis of the chains.

ICl, IBr, and I_2 all react with $(SN)_x$ (*8, 10, 45*), but the products are not simple intercalation compounds and they have not been extensively studied. These differences may relate to the larger size of iodine relative to bromine, but the lack of affinity of sulfur for iodine may be more significant. In the case of ICl both electron diffraction (*44*) and Raman studies (*33*) indicate that the ICl is absorbed primarily on the surface as the neutral molecule and that no oxidation of the chain takes place.

ICl, IBr, and I_2 all react with $(CH)_x$ also, and in the case of iodine the reaction is oxidative intercalation, as we have already discussed for

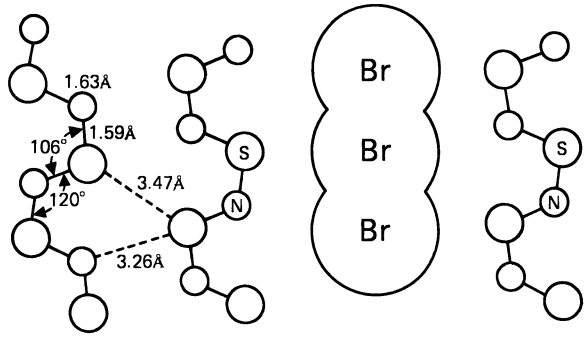

Figure 2. Model for brominated $(SN)_x$ showing possible orientation of Br_3^- relative to the $(SN)_x$ chain. The van der Waals dimensions of the Br_3^- ion are shown to scale with the $(SN)_x$ chain.

bromine. The iodine is present as I_3^- and also as a second species, either I_5^- or I_2 (*25*). Though AsF_5 does not react simply with $(SN)_x$, it does give an intercalation compound with $(CH)_x$. However, much less is known about the final state of the AsF_5 after intercalation. If the intercalation involves oxidation of the chain, as the electrical properties suggest and as is the case for bromine and iodine, the expected reaction would be

$$3AsF_5 + 2e \rightarrow 2AsF_6^- + AsF_3$$

(where e = electron). The experimental evidence in support of this mechanism is summarized elsewhere (*46*). EXAFS measurements suggst that this reaction also occurs in the intercalation of graphite by AsF_5 (*47*).

Spectroscopy

The IR (*48, 49*) and Raman spectra of $(SN)_x$ (*49, 50*) have been investigated several times; however, much of the early IR data (*51*) is complicated by the presence of impurities. Recent studies by Macklin et al. (*37*) show that on bromination the IR and Raman spectra change in a similar manner: the peaks broaden and shift somewhat in frequency. In addition, strong IR peaks appear in the Raman spectra and vice versa because of the loss of the inversion center relating the two chains in the unit cell of pristine $(SN)_x$. All these changes can be explained by the increase in disorder that takes place on bromination. After bromination, the difference between corresponding IR and Raman frequencies is reduced, reflecting the destruction of the vibrational association between the $(SN)_x$ chains. The 20–60-cm^{-1} shift in the IR peaks relative to pristine $(SN)_x$ is a measure of the strong interaction between the $(SN)_x$ lattice

and bromine. The observed increase in frequency of the SN stretching modes on bromination is consistent with the oxidation of the $(SN)_x$ chain by the bromine, which would remove antibonding π^* electrons. Although no new bands appear that can be related to S–Br or N–Br bonds, the presence of bromine as Br_3^- and Br_2 can be determined from bands in the region below 400 cm^{-1}. In the Raman (*33, 36*) the presence of Br_3^- is identified by its symmetric and asymmetric stretching frequencies at 150 and 190 cm^{-1} (*37*), respectively. A peak at 230 cm^{-1} is interpreted as Br_2 (*33, 37*). The large shift, from the value of 325 cm^{-1} observed for gaseous bromine, is a measure of the strength of its association with the $(SN)_x$ lattice.

Unlike $(SN)_x$, the $(CH)_x$ chain exists in both cis and trans forms. As prepared at − 78°C, the stable form has the cis geometry, but on heating to 200°C, it is converted to the thermodynamically more stable trans form (*20, 21*). These isomers are readily distinguishable by their characteristic IR and Raman spectra, as shown in Table II. These data were reported by Ito et al. (*21*). They reported a C–C stretch at 1100 cm^{-1} for the trans, but we have observed that this band is actually a doublet at 1080 cm^{-1} and 1120 cm^{-1} (*22*). Symmetry analysis (*52*) of the Raman and IR modes leads to assignment of cis-transoid and trans-transoid geometries for the cis and trans forms of polyacetylene, as shown in Figure 3.

On appropriate doping $(CH)_x$ becomes metallic and absorbs strongly in the IR (*12*); thus Raman techniques have provided most information about these metallic derivatives. However, in our experience as the amount of acceptor (Br_2, I_2, AsF_5, $AgClO_4$) increases, the Raman bands associated with pristine $(CH)_x$ becomes progressively weaker, and no new bands characteristic of the electron-depleted $(CH)_x$ chain appear

Table II. Infrared and Raman Spectra of *cis*- and *trans*-Polyacetylene

	Observed Frequency (cm^{-1})	
Assignment	*cis*	*trans*
C—H stretch	3057 (vw)	
	3044 (w)	3013 (m)
C—H in plane deformation	1329 (s)	1292 (vvw)
	1249 (w)	
C—H out of plane deformation	740 (vs)	1015 (vs)
C—C—C bond deformation	446 (vs)	
C=C stretch	1552[a]	1474[a]
C—C stretch	1262[a]	1080[a], 1120[a]
	920[a]	1016[a]

[a] Raman bands.

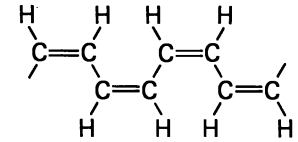

(a)

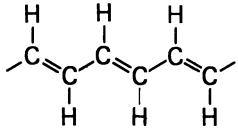

(b)

Figure 3. The cis-*transoid (a) and the trans-transoid (b) forms of* $(CH)_x$

(22). This may result from a screening effect associated with the free electron absorption of the metallic polymer. Doping mixed cis–trans films leads to interesting effects on the relative rates of disappearance of cis and trans bands. Doping with halogens or AsF_5 causes a decrease in the cis bands relative to trans, while the reverse effect is observed on treatment with silver perchlorate. This does not result from a cis–trans isomerization catalyzed by the dopant, because the absolute intensity of the trans bands does not actually increase on doping. Instead, the relative intensities of the cis and trans bands change; both gradually decrease with increasing dopant concentration. It appears more likely that this is a kinetic phenomenon, the *cis*-$(CH)_x$ reacting faster than trans with AsF_5 and the halogens, whereas the reverse is true for $AgClO_4$. This interpretation is reinforced by the observation that on treatment with ammonia the cis and trans Raman bands of both AsF_5- and $AgClO_4$-treated $(CH)_x$ films reappear with approximately the same relative and absolute intensities as in the undoped starting material.

The two C–C stretch bands of *trans*-$(CH)_x$ at 1080 and 1120 cm^{-1} also behave differently with different dopants. Treatment with silver perchlorate causes the 1120-cm^{-1} band to decrease more rapidly than the 1080-cm^{-1} band. Subsequent treatment with ammonia restores both bands to their original intensities. Bromine selectivity reduces the 1080-cm^{-1} band relative to the band at 1120 cm^{-1}. These results would seem to suggest the presence of two different types of trans environments, although the nature of this difference is not clear.

Bonding in $(SN)_x$ *and* $(CH)_x$

Before discussing the electrical properties of these polymers, it is instructive to discuss their bonding. From simple linear combination of atomic orbitals and molecular orbital (LCAO–MO) theory and from

elementary band theory, it is possible to rationalize their observed electrical properties. A more rigorous, but to many chemists less satisfying, treatment is obtained from detailed band structure calculations for $(SN)_x$ (*7*) and $(CH)_x$ (*53–55*).

In the simplest model for an isolated SN unit, both sulfur and nitrogen can be assumed to be sp^2 hybridized, with the remaining p orbital perpendicular to the plane of the chain. Eight electrons can be accommodated in the two bonding and one nonbonding sp^2 orbitals on each atom. Two electrons would then go into a π orbital formed by the p orbitals on the sulfur and nitrogen and one electron would reside in an unfilled π^* antibonding orbital. In a chain of such SN units the p orbitals form a delocalized π network along the chain, roughly corresponding to the π and π^* orbitals of the initial SN unit. The π band will be filled by two electrons per SN unit and the π^* level will remain half-filled, with one electron per (SN) unit. It is this half-filled π^* orbital that, in this simple model, is responsible for the metallic conductivity in $(SN)_x$. Band structure calculations reveal that $(SN)_x$ is actually a semimetal (*7*).

In the case of $(CH)_x$ each carbon of the basic CH unit may again be considered to be sp^2 hybridized, with one electron formally involved in each of the σ bonds to neighboring atoms and the fourth valence electron in the p orbital perpendicular to the plane of the chain. Within each basic C_2H_2 unit the p orbitals will then combine to form a filled π and an empty π^* orbital. In an extended polyolefin these molecular orbitals then give rise to a filled π band and an unfilled π^* band.

In the limit of complete electron delocalization and uniform carbon–carbon bond lengths, LCAO–MO theory predicts that the separation between the π and π^* bands would approach zero, causing $(CH)_x$ itself to exhibit metallic behavior. Both spectroscopic evidence (*56*) and theoretical predictions (*53–55*) suggest, however, that bond alternation and hence incomplete delocalization will be observed even in very long chain polyenes. This introduces a finite gap between the π and π^* bands, causing $(CH)_x$ to behave as a semiconductor, as is in fact observed experimentally.

Recent band structure calculations of Grant and Batra (*55*) confirm that bond-alternated $(CH)_x$ is a semiconductor. In case of *trans*-$(CH)_x$ the calculated band gap of 0.8 eV is caused by bond alternation. In the absence of such alternation the band structure of *trans*-$(CH)_x$ indicates that it would be a metal, in agreement with our simpler arguments. However, *cis*-$(CH)_x$, according to the band structure calculations, would have a band gap of about 1.0 eV, resulting from the crystal symmetry, even for the case of uniform bond lengths.

Chemical oxidation of $(CH)_x$ films to give a polyolefinic cation leads to removal of electrons from the filled π valence band and the observed

increase in conductivity. Similarly, chemical reduction to form a polyolefinic anion would lead to the introduction of electrons into the empty π^* conduction band, again giving rise to conductivity. To the extent that delocalization is increased in the ionic derivatives of $(CH)_x$, the width and separation of the π and π^* bands might also be expected to change on doping.

Electrical Properties of $(SN)_x$ and $(CH)_x$

The fact that $(CH)_x$ is a small-band gap semiconductor, whereas $(SN)_x$ is a semimetal, makes it much more sensitive to dopants. Indeed, the conductivity of $(CH)_x$ can be varied over 12 orders of magnitude, while that of $(SN)_x$ can be varied only by one order of magnitude. In addition, the reasons for the conductivity changes are not the same in both systems. In the case of $(CH)_x$ the observed changes can be explained in terms of changes in the number of carriers, while in $(SN)_x$ changes in the lifetime or the mobility of the carriers dominate the conductivity.

The increase in the conductivity of $(SN)_x$ on partial oxidation with bromine is shown in Figure 4(a) as a function of temperature (*9*). Similar changes in the conductivity, perpendicular and parallel to the $(SN)_x$ chains, have been reported by Chiang et al. (*11*). Even if all the bromine were present as Br_3^-, the number of carriers generated is not sufficient to explain the increase in conductivity. Grant (*57*) has calculated the shift of the Fermi level as a function of charge transfer, using a rigid band model for $(SN)_x$. A charge transfer, consistent with current estimates of the amount of Br_3^- in $(SNBr_{0.4})_x$, appears to remove the electron pocket in the band structure of $(SN)_x$ and hence eliminates electron-hole scattering. This type of scattering is believed to be the predominant mechanism responsible for limiting the conductivity of pristine $(SN)_x$. Suppression of electron-hole scattering process should be manifested by a change from a T^2 dependence of the resistivity (*58*) to a linear temperature (T) dependence. Although the observed temperature dependence is not linear, the trend toward smaller temperature exponents is apparent for the resistivity of brominated $(SN)_x$ (*11*). Furthermore, the thermopower, shown in Figure 4(b), becomes p-type on bromination, again consistent with the removal of the electron pocket. Thus the order-of-magnitude increase in conductivity on bromination is predominantly the result of an increase in the carrier lifetime rather than an increase in the number of carriers (*9*). Chemically, one can view the charge transfer as leading to the formation of an extended polythiazyl cation, with unit positive charge for every Br_3^-.

Greene et al. (*59*) have shown that the superconducting transition temperature of $(SN)_x$ increases by about 10% to 0.316 K on bromination,

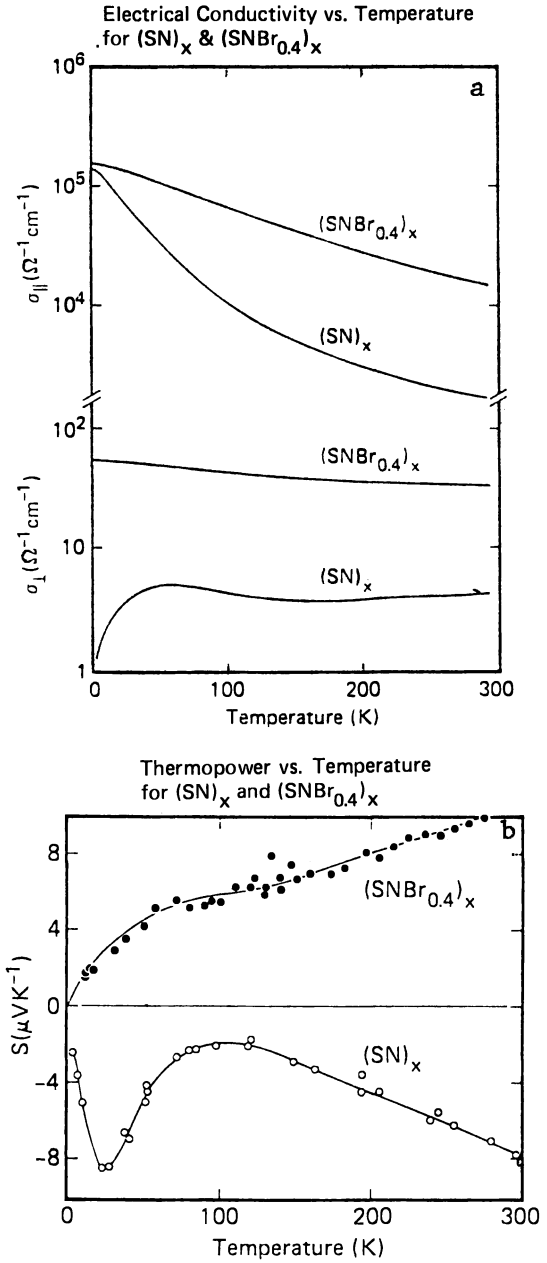

Figure 4. (a) Temperature dependence of the dc conductivities σ||b and σ⊥b; (b) absolute thermoelectric power Sb *for* $(SNBr_{0.4})_x$

and the width of the transition is reduced from 60 to 12 mK. In contrast to the temperature for $(SN)_x$ itself, the transition temperature after bromination decreases with pressure, as would be expected for a three-dimensional s–p superconductor. This behavior is consistent with the bromine causing an increase in the coupling between fibers or chains, as suggested by the reduction of the unit cell volume on bromination. The critical field anisotropy measurements and the Meissner effect measurements also indicate that $(SNBr_{0.4})_x$ is more three-dimensional than $(SN)_x$ (*59*).

$(CH)_x$ is similar to $(SN)_x$ in its reaction with bromine, but it also reacts with other acceptors and some donors. In a series of very interesting studies, Chiang, Heeger, MacDiarmid, Shirakawa, and their coworkers (*12, 13*) have shown that $(CH)_x$ can be chemically doped with donors or acceptors to yield n-type and p-type materials with electrical conductivities ranging over 12 orders of magnitude from insulator to metal. Stretching the films of $(CH)_x$ by a factor of three causes partial alignment of the fibers and leads, in the case of AsF_5 doping, to conductivities of 2000 $\Omega^{-1} \cdot cm^{-1}$, comparable to that of pristine $(SN)_x$ crystals (*60*). We have observed conductivities in the range of 1000 to 2000 $\Omega^{-1} \cdot cm^{-1}$ in unstretched films doped with 11–17% AsF_5. These same films exhibit a distinctly nonmetallic temperature dependence below 250 K, as shown in Figure 5(a) (*61*). The conductivity decreases by a factor of 1.5 on cooling from room temperature to 4.2 K. Over the small temperature range above 250 K that we have investigated, the conductivity is metallic. Thermopower studies imply that the fibers are intrinsically metallic over the whole temperature range. As shown in Figure 5(b), the thermopower is small (about 10 μV/K) and positive at 300 K with a linear temperature dependence, extrapolating to zero at 0 K. The sign of the thermopower is consistent with the AsF_5 acting as an acceptor, and the linear slope, with zero intercept, is typical of a metal. Presumably the activated conductivity observed for the film below 250 K is caused by poor interfiber coupling.

In order to account for the rather sharp increase in conductivity and infrared absorption that occurs around 1–2% dopant concentration, Chiang et al. (*12*) have proposed a model of $(CH)_x$ as a direct band gap, quasi-1-d semiconductor. The acceptor dopants give rise to hole states in the gap, which are localized at low concentration. As the concentration of dopant increases to a critical level of about 1–2%, the number of holes in the valence band becomes so large that they screen the bound states, and the transition to metallic conductivity takes place. However, we do not believe that doping creates states in the gap, though such states probably exist because of disorder. Instead, the acceptor molecule, for example, I_2, chemically oxidizes the $(CH)_x$ chain, and the

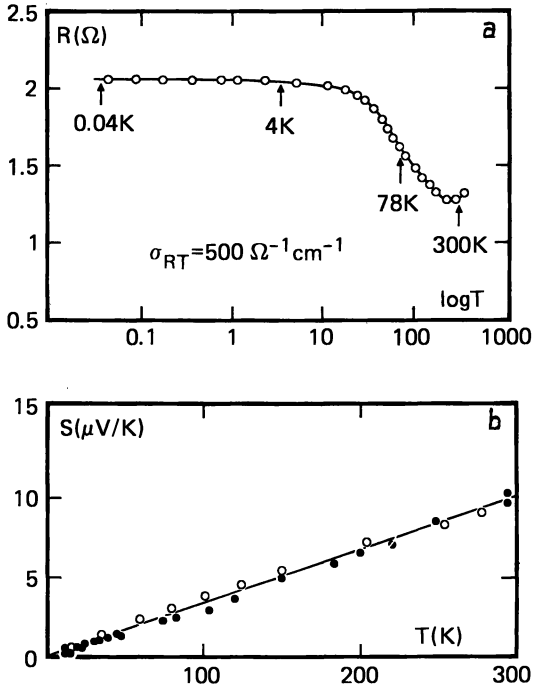

Figure 5. (a) Temperature dependence of the dc resistivity R (σ_{RT} = *conductivity at room temperature) (b) absolute thermopower* S *of* $[CH(AsF_5)_{0.12}]_x$.

acceptor level associated with a charged I_3^- acceptor state lies at some energy below the top of the valence band. As suggested by Chiang et al. (*12*), the charged acceptor localizes the hole at low dopant concentration.

We have found that treatment with certain metallic salt solutions also enhances the conductivity of $(CH)_x$ films (*22*). We will discuss these derivatives in some detail because they shed considerable light on the mechanism of the doping process. Dipping $(CH)_x$ films into appropriate silver perchlorate or tetrafluoroborate solutions in toluene gives films of composition $CH[AgClO_4]_{0.02}$, which show conductivities of 3 $\Omega^{-1} \cdot cm^{-1}$ at room temperature, very close to the conductivity of AsF_5-doped films at the same doping levels. Although silver salts are known to display ionic conductivity in other systems, the observed thermopower of 20 μV/degree is incompatible with ionic conductivity in this case (*62*). X-ray diffraction data for these films show that although the peaks corresponding to $(CH)_x$ itself remain unchanged and no silver perchlorate is observed, new peaks appear that can be attributed to free silver. The observed thermopower is too high to be attributable to free silver (1.5 μV/°C at 25°C) (*63*). Moreover, when the silver perchlorate–treated

films are exposed to ammonia vapor, the X-ray peaks corresponding to free silver remain unchanged, but the film conductivity decreases rapidly and permanently to levels comparable to those in untreated $(CH)_x$. Thus the enhanced conductivity in the doped films cannot be due to silver metal. The absence of conductivity associated with the free silver, both before and after exposure to ammonia, is explained by electron micrographs, which clearly show that the silver exists in discrete islands. The strong wavelength-independent absorption seen in the IR region after silver salt treatment, and attributed to metallic behavior, also disappears on ammonia exposure, allowing the observation of bands attributable to the perchlorate anion. These data suggest that the silver ions are acting as oxidants to give free silver and conducting polyolefinic cations with immobile perchlorate counterions (Equation 1).

$$(CH)_x + yAgClO_4 \rightarrow [(CH)_x^{y+}(ClO_4^-)_y] + yAg^\circ \quad (1)$$

We believe that other acceptors behave similarly, creating simple polyolefinic cations. Thus there is no need to invoke bromonium ions or similar π complexes.

Conclusions

The similarities and differences between $(SN)_x$ and $(CH)_x$ and their derivatives have been examined. The basic chain structures of both polymers are similar, but $(SN)_x$ is a semimetal whereas $(CH)_x$ is a semiconductor. After treatment with bromine, however, both materials exhibit metallic conductivity. Although the physics responsible for these increases in conductivity is not the same in both systems, the chemistry taking place upon bromination is quite similar. The chains are oxidized to polymeric cations and the bromine is reduced to Br_3^-. These linear Br_3^- ions are intercalated between the polymer chains, with their axes parallel. In the case of $(SN)_x$ this oxidation is limited to bromine, but $(CH)_x$ reacts with a variety of other acceptors as well as some donors. The physics and chemistry of these processes are believed to be similar to bromination, with the $(CH)_x$ forming a polyolefinic cation in the case of acceptors and a polyolefinic anion in the case of donors. The absence of similar donor complexes for $(SN)_x$ may reflect the fact that $(SN)_x$ already has one antibonding electron per SN unit in the highest occupied orbital.

The final stoichiometry of these intercalation compounds of $(SN)_x$ and $(CH)_x$ probably is determined by several factors. In the case of bromine, Br_2 enters the material and oxidizes the chains to a degree determined by the respective oxidation and reduction potentials and

Madelung energy, forming the polymeric cation and Br_3^- counter ions. If more bromine can fit into the lattice than can be reduced by the polymer, the excess will remain as neutral bromine. Such appears to be the case for $(SN)_x$, where both Br_3^- and Br_2 have been identified in $(SNBr_{0.4})_x$. In the case of $(CH)_x$, all the bromine is reduced to Br_3^-. A further factor that may also influence the stoichiometry as well as the electrical properties of these polymers is the metastability of these bromine complexes. $(SN)_x$ treated with bromine under less mild conditions tends to form $S_4N_3^+$ Br_3^-, and in the case of $(CH)_x$ bromine has a tendency to add across the ethylenic double bond.

The electrical properties of these conducting polymers offer many exciting possibilities. Progress toward achievement of their full potential should be encouraged by developments leading to more chemically and thermally stable materials.

Glossary of Symbols

D = van der Waals diameter
$d(hkl)$ = separation of the *hkl* planes
$d^1(hkl)$ = separation of the *hkl* planes after intercalation
EXAFS = extended X-ray absorption fine structure
mK = millidegrees Kelvin
R = resistance
S = thermopower
1-D = one-dimensional
μV = microvolts
Ω = ohms
TTF = tetrathiasulvalene
TCNQ = tetracyanoquinodimethane
IR = infrared
b = lattice constant in the chain direction for both $(SN)_x$ and $(CH)_x$
e = electron
NMR = nuclear magnetic resonance
LCAO = linear combination of atomic orbitals
MO = molecular orbital
T = temperature

Acknowledgments

We thank W. D. Gill, P. M. Grant, R. L. Greene, and J. B. Torrance for critically reading this manuscript and the Office of Naval Research for partial support.

Literature Cited

1. Little, W. A. *Phys. Rev. A* **1964**, *134*, 1416.
2. Davis, D.; Gutfreund, H.; Little, W. A. *Phys. Rev. B* **1976**, *13*, 4766.
3. Zeller, H. R. *Adv. Solid State Phys.* **1973**, *13*, 31.
4. Toombs, G. A. *Phys. Rep.* **1978**, *40*, 181.
5. Geserich, H. P.; Pintschovious, L. *Adv. Solid State Phys.* **1976**, *16*, 65.
6. Street, G. B.; Greene, R. L. *IBM J. Res. Dev.* **1977**, *99*, 21.
7. Greene, R. L.; Street, G. B. "Chemistry and Physics of One-Dimensional Metals"; Keller, H. J., Ed.; Plenum: New York, 1977; p. 167.
8. Street, G. B.; Gill, W. D.; Geiss, R. H.; Greene, R. L.; Mayerle, J. J. *J. Chem. Soc., Chem. Commun.* **1977**, 407.
9. Gill, W. D.; Bludau, W.; Geiss, R. H.; Grant, P. M.; Greene, R. L. Mayerle, J. J.; Street, G. B. *Phys. Rev. Lett.* **1977**, *38*, 1305.
10. Akhtar, M.; Kleppinger, J.; MacDiarmid, A. G.; Milliken, J.; Moran, M. J.; Chiang, C. K.; Cohen, M. J.; Heeger, A. J.; Peebles, D. L. *J. Chem. Soc., Chem. Commun.* **1977**, 473.
11. Chiang, C. K.; Cohen, M. J.; Peebles, D. L.; Heeger, A. J.; Akhtar, M.; Kleppinger, J.; MacDiarmid, A. G.; Milliken, J.; Moran, M. J. *Solid State Commun.* **1977**, *23*, 607.
12. Chiang, C. K.; Park, Y. W.; Heeger, A. J.; Shirakawa, H.; Louis, E. J.; MacDiarmid, A. G. *Phys. Rev. Lett.* **1977**, *39*, 1098.
13. Chiang, C. K.; Druy, M. A.; Gau, S. C.; Heeger, A. J.; Louis, E. J.; MacDiarmid, A. G.; Park, Y. W.; Shirakawa, H. *J. Am. Chem. Soc.* **1978**, *100*, 1013.
14. Grant, P. M.; Greene, R. L.; Gill, W. D.; Rudge, W. E.; Street, G. B. *Mol. Cryst. Liq. Cryst.* **1976**, *32*, 171.
15. Street, G. B.; Gill, W. D. "Molecular Metals"; Hatfield, W. E., Ed.; Plenum: New York, **1979**; p. 301.
16. Meier, H. "Organic Semiconductors"; Verlag Chemie: Weinheim, W. Germany, 1974.
17. Goehring, M.; Voigt, D. *Naturwissenschaften* **1953**, *40*, 482.
18. Walatka, V. V.; Labes, M. M.; Perlstein, J. H. *Phys. Rev. Lett.* **1973**, *31*, 1139.
19. Berets, D. J.; Smith, D. S. *Trans. Faraday Soc.* **1968**, 823.
20. Ito, T.; Shirakawa, H.; Ikeda, S. *J. Polym. Sci., Polym. Chem. Ed.* **1974**, *12*, 11.
21. Ito, T.; Shirakawa, H.; Ikeda, S. *J. Polym. Sci., Polym. Chem. Ed.* **1975**, *13*, 1943.
22. Clarke, T. C.; Geiss, R. H.; Kwak, J. F.; Street, G. B. *J. Chem. Soc., Chem. Commun.* **1978**, 489.
23. Baughman, R. H.; Chance, R. R. *J. Polym. Sci., Polym. Phys. Ed.* **1976**, *14*, 2019.
24. Baughman, R. H.; Hsu, S. L.; Pez, G. P.; Signorelli, A. J. *J. Chem. Phys.* **1978**, *68*, 5405.
25. Hsu, S. L.; Signorelli, A. J.; Pez, G. P.; Baughman, R. H. *J. Chem. Phys.* **1978**, *68*, 106.
26. Geiss, R. H.; Clarke, T. C.; Street, G. B., unpublished data.
27. Cohen, M. J.; Garito, A. G.; Heeger, A. J.; MacDiarmid, A. G.; Mikulski, C.M.; Saran, M. S. *J. Am. Chem. Soc.* **1976**, *98*, 3844.
28. Shirakawa, H.; Ikeda, S. *Synth. Metals* **1980**, *1*, 175.
29. Wynne, K. J.; Jolly, W. L. *Inorg. Chem.* **1967**, *6*, 107.
30. Patton, R. L.; Jolly, W. L. *Inorg. Chem.* **1969**, *8*, 1392.
31. Bernard, C.; Herold, A.; Lelaurain, M.; Robert, G. *Compt. rend. (c)* **1976**, *283*, 625.
32. Iqbal, Z.; Baughman, R. H.; Kleppinger, J.; MacDiarmid, A. G. *Ann. N.Y. Acad. Sci.* **1978**, *313*, 775.

33. Iqbal, Z.; Baughman, R. H.; Kleppinger, J.; MacDiarmid, A. G. *Solid State Commun.* **1978**, *25*, 409.
34. Street, G. B.; Etemad, S.; Geiss, R. H.; Gill, W. D.; Greene, R. L.; Kuyper, J.; Smith, R. D. *Ann. N.Y. Acad. Sci.* **1978**, *313*, 737.
35. Temkin, H.; Fitchen, D. B.; Gill, W. D.; Street, G. B., submitted for publication in *Ann. N. Y. Acad. Sci.*
36. Temkin, H.; Street, G. B. *Solid State Commun.* **1978**, *25*, 455.
37. Macklin, J.; Gill, W. D.; Street, G. B. *J. Chem. Phys.* **1979**, *70*, 2425.
38. Scott, J. C.; Kulick, J. D.; Street, G. B., unpublished data.
39. Morawitz, H.; Gill, W. D.; Grant, P. M.; Sayers, D. E.; Street, G. B., unpublished data.
40. Comes, R. *Bull. Am. Phys. Soc.* **1978**, *23*, 424.
41. Bondi, A. *J. Phys. Chem.* **1964**, *68*, 441.
42. Falardeau, E. R.; Hanlon, L. R.; Thomson, T. E. *Inorg. Chem.* **1978**, *17*, 301.
43. Lefrant, S.; Lichtmann, L. S.; Temkin, H.; Fitchen, D. B.; Miller, D. C.; Whitwell II, G. B.; Burlitch, J. M. *Solid State Commun.* **1979**, *29*, 191.
44. Thomas, J.; Geiss, R. H.; Street, G. B., unpublished data.
45. Philipp, A; Seeger, K., unpublished data.
46. Clarke, T. C.; Street, G. B. *Synth. Metals* **1980**, *1*, 119.
47. Bartlett, N.; Biagioni, R. N.; McQuillan, B. W.; Robertson, A. S.; Thompson, A. C. *J. Chem. Soc., Chem. Commun.* **1978**, 200.
48. Wendel, H. *J. Physics C* **1977**, *10*, L1.
49. Stolz, H. J.; Wendel, H.; Otto, A.; Pintschovius, L.; Kahlert, H. *Phys. Status Solidi B* **1976**, *78*, 277.
50. Temkin, H.; Fitchen, D. B. *Solid State Commun.* **1976**, *19*, 1181.
51. Chapman, D.; Warn, R. J. *Trans. Faraday Soc.* **1964**, *60*, 294.
52. Shirakawa, H.; Ito, T.; Ikeda, S. *Polym. J.* **1973**, *4*, 460.
53. Kuhn, H. *J. Chem. Phys.* **1949**, *17*, 1198.
54. Dewar, M. J. S. *J. Chem. Soc.* **1952**, 3544.
55. Grant, P. M.; Batra, I. *Solid State Commun.* **1979**, *29*, 225.
56. Hudson, B.; Kohler, B. *Annu. Rev. Phys. Chem.* **1974**, *25*, 437.
57. Grant, P. M., unpublished data.
58. Chiang, C. K.; Cohen, M. J.; Garito, A. F.; Heeger, A. J.; MacDiarmid, A. G.; Mikulski, C. M. *Solid State Commun.* **1976**, *18*, 1451.
59. Kwak, J. F.; Greene, R. L.; Fuller, W. W. *Phys. Rev. B* **1979**, *20*, 2658.
60. Park, Y. W.; Druy, M. A.; Chiang, C. K.; MacDiarmid, A. G.; Heeger, A. J.; Shirakawa, H.; Ikeda, S. J. *Polym. Sci., Polym. Lett. Ed.* **1979**, *17*, 195.
61. Kwak, J. F.; Clark, T. C.; Street, G. B.; Greene, R. L. *Solid State Commun.* **1979**, *31*, 355.
62. Magistris, A.; Pezzati, E.; Sinistria, C. *Z. Naturforsch Teil A* **1972**, *27*, 1379.
63. Pearson, W. B. *Solid State Phys.* **1961**, 3, 1411.

RECEIVED September 13, 1978.

Mixed Phenazine-*N*-Methylphenazinium-7,7,8,8-Tetracyano-*p*-Quinodimethanide: A Quasi-One-Dimensional Metallike System with Variable Band Filling

JOEL S. MILLER

Occidental Research Corporation, Irvine, CA 92713

ARTHUR J. EPSTEIN

Xerox Webster Research Center, Xerox Corporation, Rochester, NY 14644

A new series of highly conducting, one-dimensional (1-D) organic complexes based on the replacement of N-*methylphenazinium (NMP*$^+$*) with neutral phenazine (Phen) in (NMP*$^+$*)(TCNQ*$^-$*) (TCNQ*$^-$ *= 7,7,8,8-tetracyano*-p-*quinodimethane) is reported. The series of complexes was characterized by solution absorption spectra, X-ray diffraction, and differential scanning calorimetry (DCS). Up to 50% replacement of NMP*$^+$ *with phenazine has been achieved. Thus an isomorphous series of highly conducting organic complexes permitting the study of the physical properties of 1-D substances as a controlled function of band filling (Fermi energy) and disorder has been realized. Conductivity results show a semiconducting behavior, with charge carriers activated to extended states with a large, strongly temperature dependent mobility. The energy gap is found to decrease with decreasing band filling, varying as the square. The inconsistency of these results with various disorder models is also indicated.*

Recent studies of quasi-1-D substances have focused primarily upon the design of new materials and detailed analysis of the electrical, optical, and magnetic properties (*1–17*). However, a thorough under-

0-8412-0472-1/80/33-186-195$05.00/1

standing of the salient features of such 1-D materials has not as yet been achieved. We felt that new insights into the physical processes associated with 1-D systems could be made if we tailor-made an isomorphous series of complexes, which, to a first approximation, differed only in the degree of band filling, and we subsequently studied the physical properties as a function of Fermi energy.

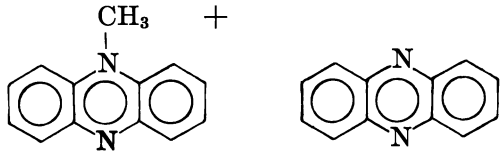

NMP⁺ Phenazine

1 2

The prototype system chosen (*18*) for modification was based on $(NMP^+)(TCNQ^-)$ (*19*). It seemed reasonable to assume that, if the TCNQ chain provides a driving force for the stabilization of the 1-D structure, removal of NMP^+ (and the electron associated with its $TCNQ^-$ moiety) would reduce the average charge per TCNQ, that is, $TCNQ^{z-}$ ($z < 1$). Removal of the cation would destroy the unit cell; however, substitution of the NMP^+ cation with a neutral molecule of comparable size, shape, and polarizability should stabilize the structure.

With these assumptions, and knowing that the crystal structure (*20*) of the disordered phase of (NMP)(TCNQ) contains randomly oriented methyl groups (*21*) (• in Figure 1) and that the methyl group is small in comparison with the ring systems and does not exhibit preferential orientations, one may predict that neutral phenazine, Phen, *2*, might substitute for the NMP^+, *1*, in (NMP)(TCNQ), forming an isomorphous complex.

Through Reactions A, B, C, or D, outlined in Scheme I, complexes of $(NMP^+)_x(Phen)_{1-x}(TCNQ^-)_x(TCNQ^0)_{1-x} \equiv (NMP^+)_x(Phen)_{1-x}(TCNQ)$, *3*, stoichiometry with $1 \geq x > 0.5$ could be isolated as dark, reflecting needle crystals. Visual appearance and crystallographic, elemental composition and DSC measurements, as well as temperature dependence of the conductivity and magnetic susceptibility, indicate that these crystals resemble but are not identical with $(NMP^+)(TCNQ^-)$.

Scheme I

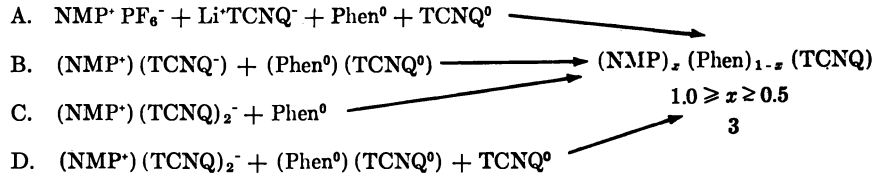

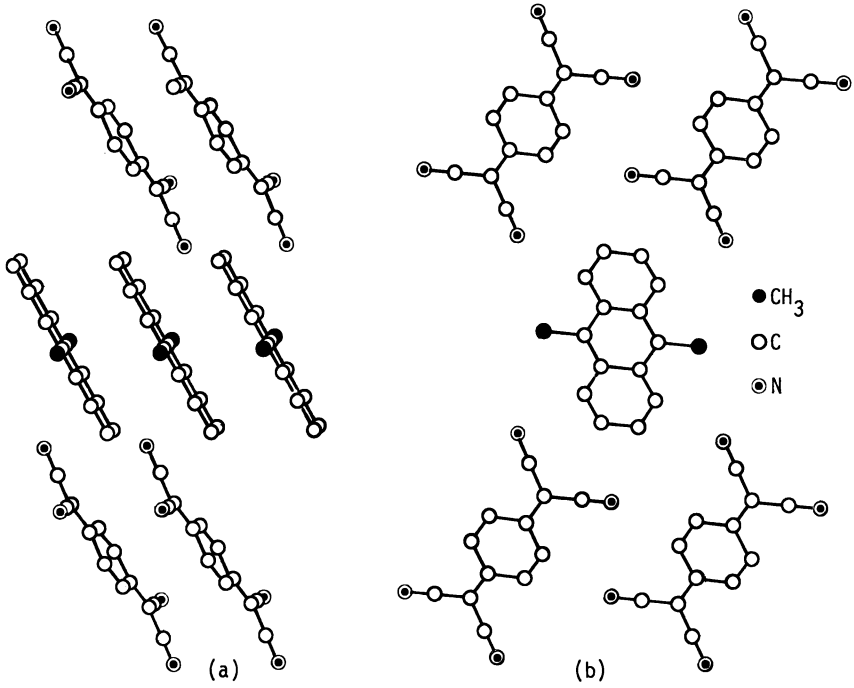

Figure 1. Structure of (NMP)(TCNQ). Replacement of NMP⁺ with neutral phenazine should increase disorder in the system without altering the gross structural features significantly. (a) Projection in ac *plane; (b) projection in* bc *plane. The TCNQ molecules stack parallel to the* a*-axis.*

Unit cell determinations were obtained on $3(x = 0.24 \pm 0.01$ and $0.46 \pm 0.01)$; *see* Table I. The results of the X-ray study show that $3(x = 0.24$ and $0.46)$ is not equivalent but isomorphous to the (NMP)-(TCNQ) structure previously reported by Fritchie (*20*), and exhibits

Table I. Unit Cell Parameters[a] for $(NMP)_x(Phen)_{1-x}TCNQ$

	(NMP)-(TCNQ)[b]	*$(NMP)_{0.74}$-$(Phen)_{0.26}$-TCNQ*	*$(NMP)_{0.54}$-$(Phen)_{0.46}$-TCNQ*
x	1.00	0.74	0.54
a (Å)	3.8682 (4)	3.890 (8)	3.865 (7)
b (Å)	7.7807 (8)	7.799 (3)	7.611 (32)
c (Å)	15.735 (2)	15.706 (6)	16.329 (51)
α	91.67 (1)	91.75 (6)	93.73 (49)
β	92.67 (1)	92.96 (13)	91.53 (31)
γ	95.38 (1)	95.45 (2)	94.65 (20)
V (Å³)	470.7	473.4	477.4

[a] Molecular Structure Corporation, College Station, Texas.
[b] *See* Fritchie (*20*).

large standard deviations, which are characteristic of the small crystals studied and the crystallographic disorder imposed upon the system by random replacement of the NMP^+ with Phen.

The solution absorption data, Figure 2, clearly shows that 3 [Figure 2(*e*)] contains phenazine, NMP^+, and neutral and anionic TCNQ and is

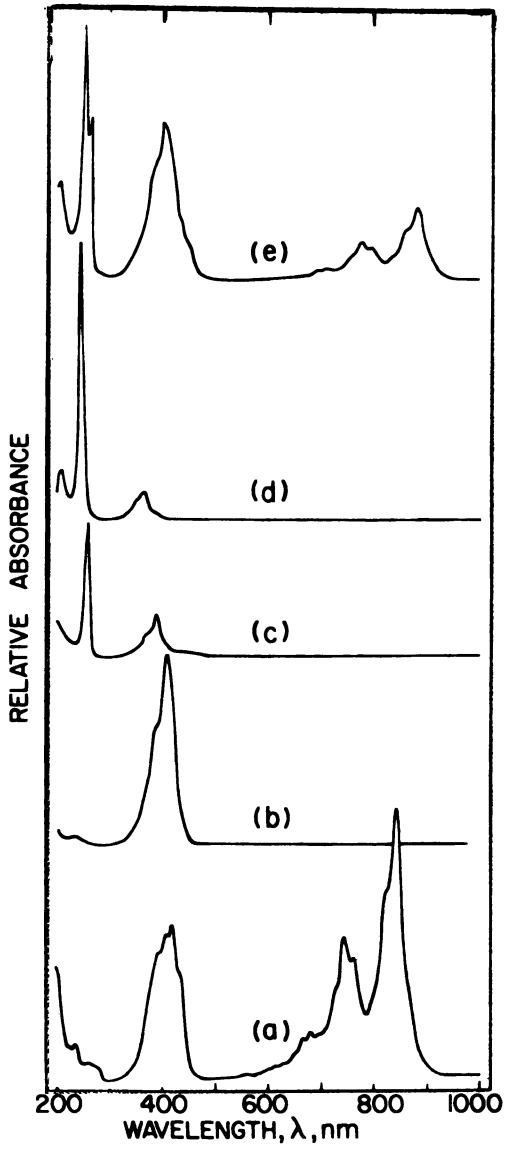

Figure 2. Absorption spectra: (a) Li^+TCNQ^-; (b) $TCNQ^0$; (c) $NMP^+PF_6^-$; (d) phenazine; (e) $(NMP)_{0.54}(Phen)_{0.46}(TCNQ)$. The ordinate is arbitrary.

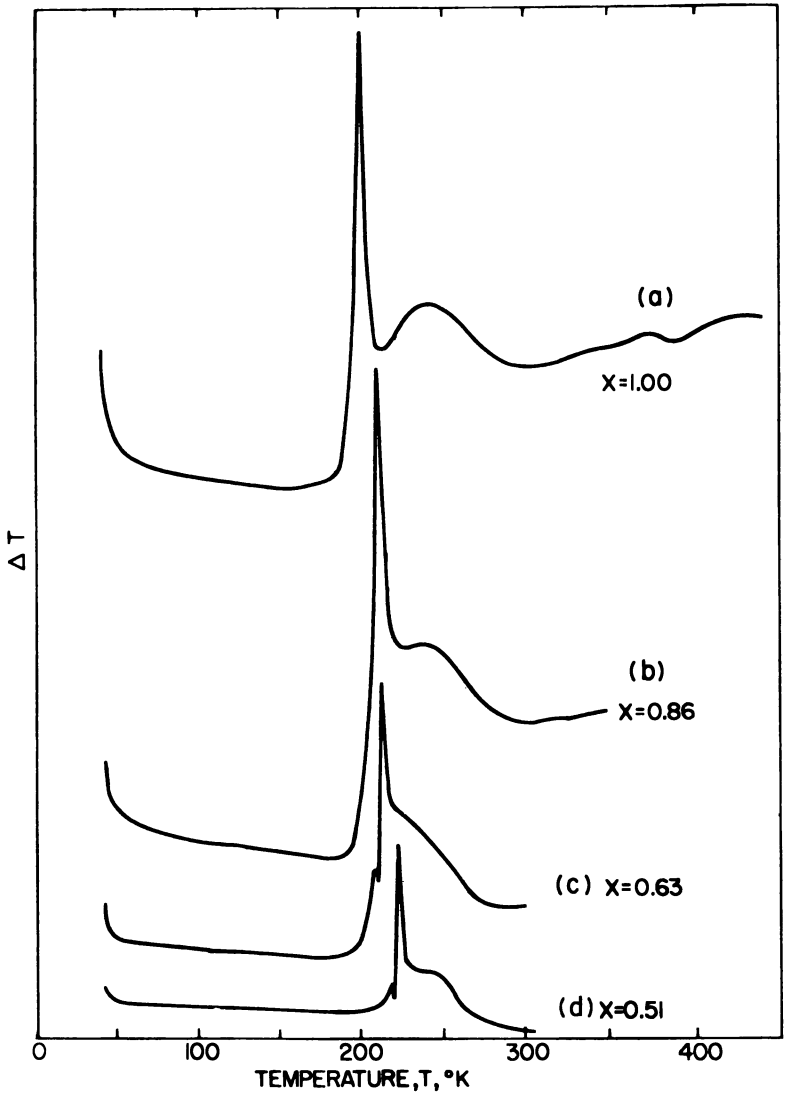

Figure 3. Differential scanning calorimetry traces of $(NMP)_x(Phen)_{1-x}TCNQ$ as a function of x

used to evaluate (*18*) the composition of 3, that is, x. The DSC traces are characteristic of exothermic (NMP)(TCNQ) and qualitatively dissimilar to endothermic (Phen)(TCNQ) (*23*) and $(NMP)(TCNQ)_2$ (*24*). Complex *3* exhibits an exothermic decomposition greater than 200°C. For larger x the decomposition exotherm occurs at higher temperatures. A new exothermic feature at 5°–15°C temperatures lower than the exotherm also appears with a magnitude that increases with x; *see* Figure 3.

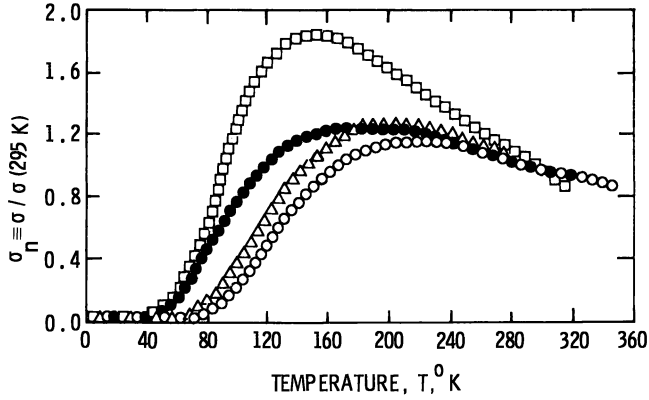

Figure 4. Normalized four-probe a-axis conductivity versus temperature for some representative $(NMP)_x(Phen)_{1-x}(TCNQ)$ samples. The solid lines are computer fits to Equation 1 with values given in Table II: (○), x = 1.00; (△), x = 0.94; (□), x = 0.81; (●), x = 0.63.

The dc electrical conductivity σ of 3 along the stacking direction is also similar but not equivalent to that of $(NMP^+)(TCNQ^-)$ (*18, 25*); *see* Figure 4. The metallike behavior, that is, $d\sigma/dT < 0$ (T = temperature), is observed for all the samples measured near room temperature. The differences in the room temperature conductivity values, given in Table II, are not significant due to the errors involved in measuring the cross-sectional areas of the small samples (about $1 \times 0.03 \times 0.02$ mm). The temperature for the maximum conductivity, T_m, is lower in $Phen^0$-replaced samples than in (NMP)(TCNQ) (*26*). The low-temperature behavior of these four samples is shown in Figure 5. While the conductivity decreases monotonically for $T < T_m$, the normalized conductivity, $\sigma_n(T) \equiv \sigma(T)/\sigma(295\ K)$, also increases with increasing phenazine content in this temperature range.

The $\sigma(T)$ curves in Figure 4 are similar. We have previously shown that for (NMP)(TCNQ) (*26*) and numerous other systems (*27, 28*) that feature a broad weak maximum in $\sigma(T)$ at T_m, $\sigma(T)$ can be explained as a product of an activated carrier concentration, $n(T)$, and a temperature-dependent mobility, $\mu(T)$. We have found that we can

Table II. Conductivity Parameters for $(NMP)_x(Phen)_{1-x}(TCNQ)$

x	σ (295 K) ($ohm^{-1}\ cm^{-1}$)	$\sigma_n(T_m)$	T_m (K)	α	Δ (meV)
1.00	200	1.17	220	4.1	78
0.94	100	1.27	205	3.9	68
0.81	100	1.85	155	3.7	50
0.63	70	1.26	175	2.2	35

fit the $\sigma_n(T)$ data for $(NMP)_x(Phen)_{1-x}(TCNQ)$ for 60 K $< T <$ 400 K with

$$\sigma_n(T) = AT^{-\alpha}\left[\exp\frac{-\Delta(x)}{T}\right] \quad (1)$$

with $\Delta(x)$ (activation energy) constant for all samples of the same phenazine content (several for each phenazine concentration) and α sample-dependent constant in the ranges of 2 to 4 (Table II). The constant A is fixed by $\sigma_n(295\text{ K}) \equiv 1$.

The solid lines in Figures 4 and 5 show the fits obtained with these parameters in Equation 1. The good agreement above 65 K is particularly impressive in view of the large variation in $\sigma_n(T)$ with x. Below 65 K the observed conductivity is greater than that predicted by Equation 1. This suggests that another transport mechanism is dominating at low temperatures.

In Figure 6 the linear variation of the gap Δ with the square of the NMP content (band filling), x^2, is presented. This result is important in understanding the microscopic aspect of 1-D materials. The presence of a distortion of the underlying lattice with period $2a/x$, where a is the

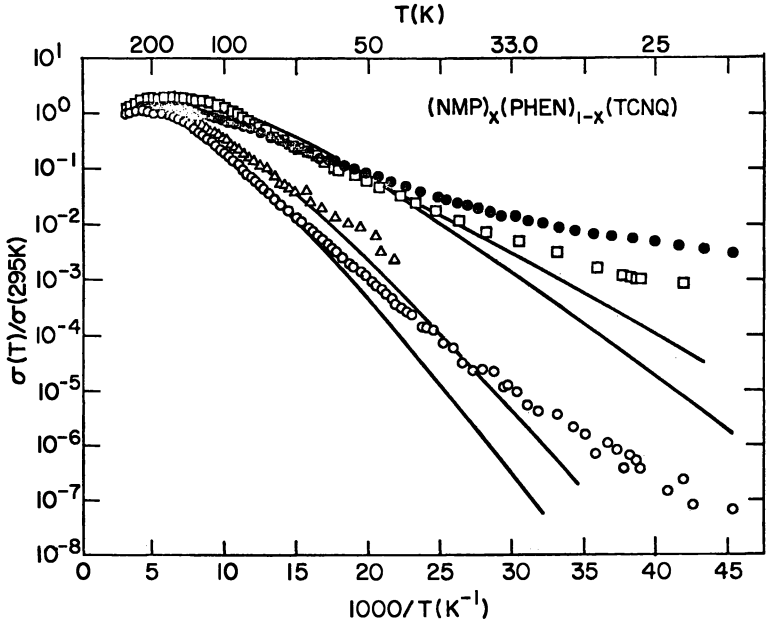

Figure 5. Experimental log σ(T)/σ(295 K) vs. inverse temperature for samples of Figure 4, and computer fits from Equation 1 with parameters given in Table II: (○), x = 1.00; (△), x = 0.94; (□), x = 0.81; (●), x = 0.63.

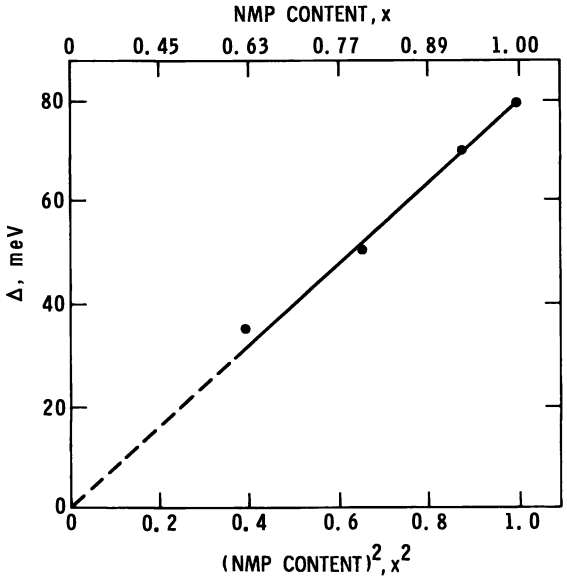

Figure 6. Variation of activation energy Δ obtained for T > 65 K with fraction x of NMP

average repeat unit along the TCNQ chain, would lead to an energy gap at the Fermi energy, E_F, for all band fillings. However, the experimental evidence for a Peirls type of distortion is not yet conclusive. Recent X-ray diffuse scattering studies of (NMP)(TCNQ) imply 0.67 charge transferred from NMP to TCNQ (*29, 30*). Earlier workers suggested a charge transfer of 0.91 based upon strong X-ray scattering to fifth order (*31*). A Mott–Hubbard gap due to on-site coulomb repulsion (*32*) would lead to a semiconductor gap for only $x = 1.0$. The addition of nearest-neighbor coulomb interactions (*33*) leads to a gap at the 1/4 band level as well, which is insufficient to explain the semiconducting behavior of the intermediate x systems. We point out that part (or even all) of Δ may be a mobility gap associated with localization of states at the band edges due to disorder. It has also been suggested that long-range intrachain coulomb interactions may lead to a gap at E_F for all x (*34*). However, none of these models as yet explain the observed variation of Δ with x^2.

A model based on the earlier work of Woynarovich et al. (*35*) is also attractive. In this model interchain electrostatic interaction between charge density waves stabilizes the charge density waves and leads to an energy gap at E_F for all band fillings. The magnitude of this gap depends roughly on the square of the charge density (that is, degree of charge transfer), in agreement with experimental data; *see* Figure 6. As formu-

lated, the ground state is nonmagnetic, although addition of on-site or intrachain coulomb repulsion would probably make the ground state magnetic. These results suggest that the observed activation energies in related systems are not solely due to on-site or near-neighbor coulomb interactions.

The question then arises as to whether a band semiconductor model is compatible with the disorder expected to exist in these crystals. What determines the nature of conduction is the length of the region for which the wave function is extended (*26–28*) l_a. At temperatures high enough for these states to be significantly occupied ($T > 65$ K in our samples), they will dominate the dc conductivity. At low enough temperatures (depending on the property being measured), electrons in localized states may dominate the behavior. Increasing the phenazine content increases the disorder and hence decreases l_a. Several groups have attempted to quantitatively model $\sigma(T)$ ($T > 65$ K) for TCNQ salts assuming that the electrons hop among the localized states. Bloch et al. (*36*) attributed σ at low temperatures to variable-range phonon-assisted hopping and at high temperatures to diffusive hopping. Gogolin et al. (*37*) quantitatively fit $\sigma(T)$ with a disorder model, utilizing intramolecular phonons for phonon-assisted hopping ($T < T_m$) and phonon localization ($T > T_m$). Attempts to apply these models to the $(NMP)_x(Phen)_{1-x}(TCNQ)$ system lead to a prediction of increasing T_m with increasing phenazine content, at variance with experimental findings. Shante (*38*) has also proposed a model for anisotropic hopping conduction in (NMP)(TCNQ) that suggests similar behavior for phenazine-substituted samples for $T <$ 100 K in contrast with experimental results.

In conclusion we have shown that $(NMP)_x(Phen)_{1-x}(TCNQ)$ forms a continuous series of materials with semiconducting behavior. Data analysis leads to $\Delta = (78 \text{ meV})x^2$ and a large, strongly temperature dependent mobility for $T > 65$ K. The major effect of increased disorder is to give rise to additional strongly localized states at the band edges (band tailing), increasing the low-temperature 1-D (hopping) conduction at low temperatures. This system has broad implications for understanding the source of energy gaps and the role of disorder in molecular conductors. Additional physical data, including magnetic susceptibility, electron spin resonance, and thermoelectric power, confirm this continuous behavior as a function of x between that characteristic of (NMP)(TCNQ) ($x = 1.0$) and that characteristic of the half-filled band case [for example, quinolinium $(TCNQ)_2$].

Glossary of Symbols

NMP^+ = *N*-methylphenazinium
$TCNQ^-$ = 7,7,8,8-tetracyano-*p*-quinodimethanide

1-D = one-dimensional
Phen = phenazine
DSC = differential-scanning calorimetry
σ = conductivity
T = temperature
T_m = temperature of maximum conductivity
n = carrier concentration
μ = mobility
σ_n = normalized conductivity
α = exponent for temperature dependence of mobility
Δ = activation energy
x = NMP fraction
E_F = Fermi energy
a = lattice period
A = constant
l_a = localization length
a = unit cell axis
b = unit cell axis
c = unit cell axis
V = unit cell volume

Acknowledgments

We thank E. M. Conwell and D. J. Sandman for stimulating discussions and P. Chaikin for providing laboratory facilities.

Literature Cited

1. "Synthesis and Properties of Low-Dimensional Materials"; Miller, J. S., Epstein, A. J., Eds.; *Ann. N.Y. Acad. Sci.* **1978**, 313.
2. Garito, A. F.; Heeger, A. J. *Acc. Chem. Res.* **1974**, *7*, 232.
3. Narita, M.; Pittman, C. U. *Synthesis* **1976**, *8*, 489.
4. Bespalov, B. P.; Titov, V. V. *Russ. Chem. Rev. (Engl. Trans.)* **1975**, *44*, 1091.
5. Andre, J. J.; Bieber, A.; Gaultier, F. *Ann. Phys. (Paris)* **1976**, *1*, 145.
6. Bloch, A. N.; Cowan, D. O.; Poehler, T. O. In "Energy and Charge Transfer in Organic Semiconductors"; Masuda, K., Silver, M., Eds.; Plenum: New York, 1974; 167–176.
7. Goodings, E. P. *Chem. Soc. Rev.* **1976**, *5*, 95.
8. Pal, L., Gruner, G., Janossy, A., Solyom, J., Eds.; *Lect. Notes Phys.* **1977**, 65.
9. Keller, H. J., Ed.; *NATO Adv. Study Inst. Ser., Ser. B*, *25*, **1977**.
10. Ibid., **1975**, *7*.
11. "Extended Interactions Between Metal Ions in Transition Metal Complexes," Interrante, L. V., Ed.; *ACS Symp. Ser.* **1975**, *5*.
12. Schuster, H. G., Ed.; *Lect. Notes Phys.* **1975**, *34*.
13. Miller, J. S.; Epstein, A. J. *Prog. Inorg. Chem.* **1976**, *20*, 1.
14. Thomas, T. W.; Undersill, A. E. *Chem. Soc. Rev.* **1972**, *1*, 99.

15. Shchegolev, I. F. *Phys. Status Solidi A* **1972**, *12*, 9.
16. Berlinsky, A. J. *Contemp. Phys.* **1976**, *17*, 331.
17. Zeller, H. R. *Festkoerperprobleme* **1973**, *13*, 31.
18. Miller, J. S.; Epstein, A. J. *J. Am. Chem. Soc.* **1978**, *100*, 1639.
19. Soos, Z. G. "Highly Conducting Organic Materials," personal communication.
20. Fritchie, C. J., Jr. *Acta Crystallogr.* **1966**, *20*, 892.
21. Morosin, B. *Phys. Lett. A* **1975**, *53*, 455.
22. Kobayashi, H. *Bull. Chem. Soc. Jpn.* **1975**, *48*, 1373.
23. Goldberg, I.; Shmueli, U. *Nature* **1971**, *234*, 36.
24. Melby, L. R. *Can. J. Chem.* **1965**, *43*, 1448.
25. Epstein, A. J.; Miller, J. S. *Solid State Commun.* **1978**, *27*, 325.
26. Epstein, A. J.; Conwell, E. M.; Sandman, D. J.; Miller. J. S. *Solid State Commun.* **1977**, *23*, 355.
27. Epstein, A. J.; Conwell, E. M. *Solid State Commun.* **1977**, *24*, 627.
28. Epstein, A. J.; Conwell, E. M.; Miller, J. S. *Ann. N.Y. Acad. Sci.* **1978**, *313*, 183.
29. Pouset, J. P.; Megtert, S.; Comés, R.; Epstein, A. J. *Phys. Rev. B* **1980**, *21*, 486.
30. Pouset, J. P.; Megtert, S.; Comés, R.; Epstein, A. J. *Bull. Am. Phys. Soc.* **1978**, *23*, 380.
31. Ukei, K.; Shirotani, I. *Commun. on Phys.* **1977**, *2*, 159.
32. Epstein, A. J.; Etemad, S.; Garito, A. F.; Heeger, A. J. *Phys. Rev. B* **1972**, *5*, 952.
33. Holczer, K.; Mihaly, C.; Janossy, A.; Grüner, R. *Mol. Cryst. Liq. Cryst.* **1976**, *32*, 199.
34. Grant, P.; Hubbard, J., personal communication.
35. Woynarovich, F.; Mihaly, L.; Grüner, G. *Solid State Commun.* **1976**, *19*, 1189.
36. Bloch, A. N.; Weisman, R. B.; Varma, C. M. *Phys. Rev. Lett.* **1972**, *28*, 753.
37. Gogolin, A. A.; Zolotukhin, S. P.; Melnikov, V. I.; Rashba, E. I.; Shchegolev, I. F. *JETP Lett. (Engl. Trans.)* **1975**, *22*, 278.
38. Shante, V. K. *Phys. Rev. B* **1977**, *16*, 2597.

RECEIVED September 13, 1978.

Hydrogen Absorption by Intermetallic Compounds

W. E. WALLACE, R. S. CRAIG, and V. U. S. RAO

Department of Chemistry, University of Pittsburgh, Pittsburgh, PA 15260

Many intermetallic compounds absorb hydrogen extensively, with volumetric capacities often exceeding that of liquid hydrogen. While the capacity of these materials is extraordinary, their most remarkable feature is the rapidity with which they dissolve and release hydrogen, the process often being 95% complete within about 200 sec at room temperature. Recent work dealing with structures, thermodynamics, kinetics, or sorption and a few aspects of the superconductivity of hydrogenated intermetallic compounds is reviewed. In hydrogenated rare earth intermetallics pressure increases, in a family of compounds, systematically with atomic number of the rare earth. In the series RET_3 (where RE is a rare earth and T = Fe, Co, or Ni), pressure increases in the sequence Fe to Co to Ni. Hydrogenation often significantly influences superconductivity.

The extensive solubility of hydrogen in palladium and other transition metals has been known for many years. Studies of these systems, particularly their magnetic properties, have engaged the attention of numerous investigators; this is because inferences can be drawn with regard to the electronic makeup of the host metal by establishing the effect of hydrogenation on the various physical properties of the system (*1*). Until recently, corresponding attention has not been paid to effects of hydrogenation on the properties of intermetallic compounds. This is now changed; studies of hydrogenated intermetallic compounds are currently the most active areas of inquiry in the general field of metal–hydrogen systems.

0–8412–0472–1/80/33–186–207$08.50/1

Interest in hydrogen-containing intermetallic compounds develops out of two rather separate concerns: (1) they present some striking features whose elucidation may improve our basic understanding of the solid state, and (2) they are of practical significance as a means for storing hydrogen, an issue that arises in efforts being made to develop hydrogen as a fuel. In regard to the first concern, the incorporation of hydrogen in the lattice can profoundly influence the electrical and magnetic behavior of the system. In certain systems the presence of hydrogen significantly affects the interactions that bring on superconductivity (*2–5*) or ferromagnetism (*6*). These interactions may be enhanced or diminished or even extinguished (*2–7*). Elucidation of these divergent behaviors should lead to an improvement in our understanding of the electronic makeup of the host metals. In regard to hydrogen storage it seems likely that the affinity of intermetallic compounds for hydrogen will be of pivotal significance in developing the fuel capability of hydrogen.

Since much has been written (*7, 8*) in recent years about hydrogen as a fuel and the so-called hydrogen economy, discussion of the various aspects of this issue is unwarranted. It is appropriate, however, to mention the problems that emerge when one considers the special issue of hydrogen storage, which is one aspect of the development of hydrogen as a fuel. There are three primary ways of storing hydrogen: (1) as a compressed gas, (2) as a liquid or solid, and (3) in the form of a metal hydride. Compressed hydrogen has low energy density and the containers required are bulky, heavy, and dangerous. Liquid or solid hydrogen entails cryogenic temperatures, 20 K or lower, and appears to lack the convenience and safety required for widescale, everyday usage. Metal hydrides are widely regarded as the only practical means for storing hydrogen for mobile use, as in powering an automobile, a bus,

Table I. Hydrogen Capacity Relative to Liquid Hydrogen[a]

Compound	*Capacity*
$REFe_3$[b]	0.9–1.3 (*9*)
$RECo_7$	0.9–1.4 (*10*)
$RECo_3$	1.4–1.5 (*10, 11*)
$LaNi_5$	1.4 (*12*)
$ErFe_{0.8}Mn_{1.2}$	1.7 (*13*)
Zr as ZrH_2	1.7[c]
U as UH_3	2.0[c]

[a] The volumetric capacity of liquid hydrogen is 4.2×10^{22} hydrogen atoms per cubic centimeter at 20 K. The volumetric capacities of the intermetallic compounds and of ZrH_2 and YH_3 are given for 1 atm and 25°C relative to liquid hydrogen at 20 K.

[b] RE represents the rare earths Gd, Tb, Dy, Ho, and Er.

[c] Computed from the known lattice parameter.

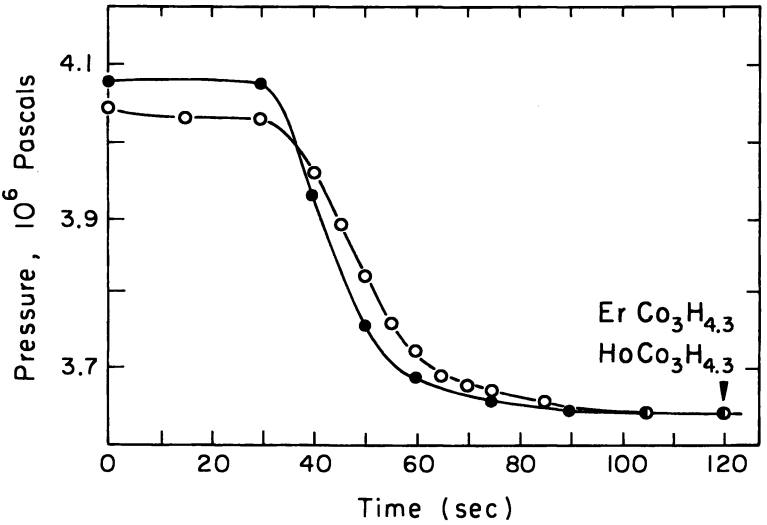

Figure 1. Hydrogen uptake by bulk specimens of $ErCo_3$ and $HoCo_3$ at room temperature: (●), $HoCo_3$; (○), $ErCo_3$.

or an airplane. Hence enormous attention is being focused on hydrogenated metals because of their significance from both a practical and fundamental point of view.

The hydrogen capacities of several intermetallics are listed in Table I, along with the capacities of two transition elements, Zr and Y. It seems that the binary hydrides ZrH_2 and UH_3 excel in regard to hydrogen capacity. In spite of this they are without significance as a practical means for storing hydrogen. This arises because they are too stable; for example, the pressure of hydrogen over ZrH_2 is about 10^{-14} torr at 25°C. Libowitz, Hayes, and Gibb (*14*) showed that when Zr is chemically united with Ni to form ZrNi, it hydrogenates to form $ZrNiH_3$, which has a 25°C vapor pressure of 5×10^{-4} torr. Although this is still too low for practical use, it has a vapor pressure nearly 10 orders of magnitude greater than ZrH_2. This early work illustrates one significant feature of hydrogenated intermetallics: they are often significantly less stable than the related binary hydride. This feature, while exceedingly important, is less significant than another aspect of intermetallic compounds—their kinetics. The rapidity with which appropriately chosen intermetallic compounds absorb and release hydrogen is illustrated (*15*) in Figures 1–3. This is the truly remarkable feature of intermetallic compounds, that which sets them apart from the metallic elements as hydrogen hosts and sets them apart as practical materials for the storage of hydrogen.

The literature dealing with hydrogenated intermetallic compounds is large and is growing at a substantial pace. Hence in a review of the

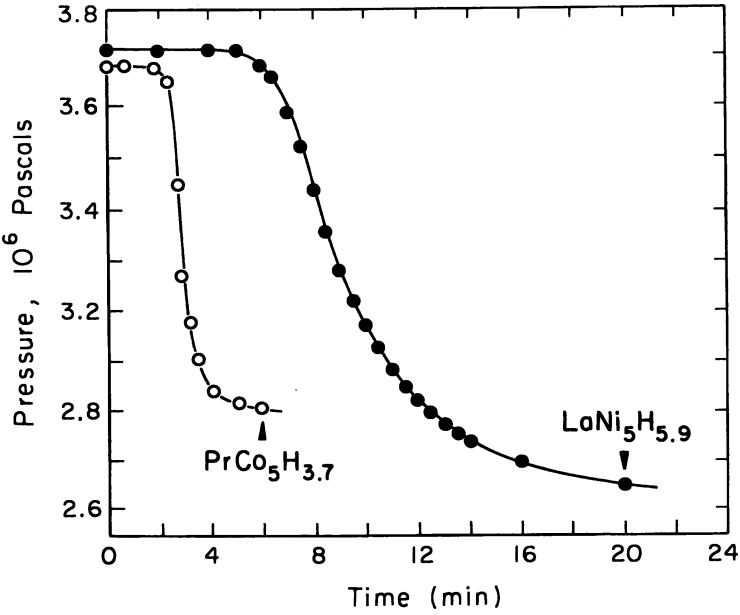

Figure 2. Hydrogen uptake by bulk specimens of $LaNi_5$ and $PrCo_5$ at room temperature: (●), $LaNi_5$; (○), $PrCo_5$.

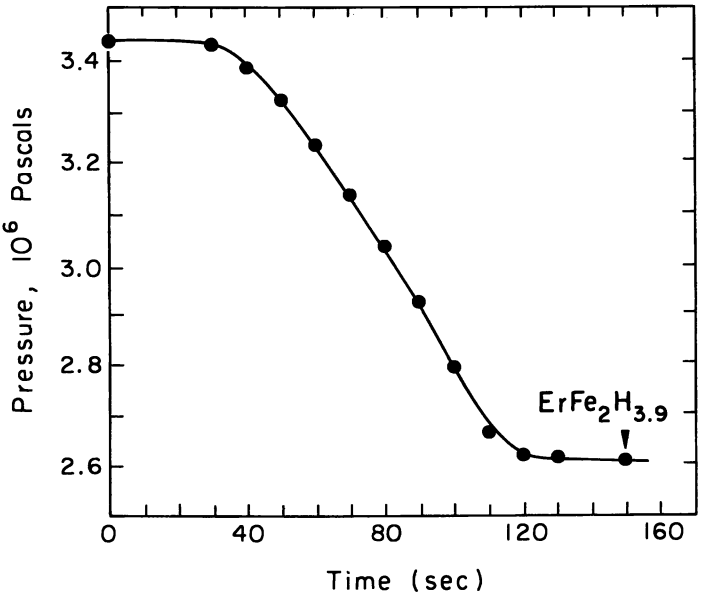

Figure 3. Hydrogen uptake by a bulk specimen of $ErFe_2$: (●), $ErFe_2$.

present nature, it is not feasible to cover all aspects of the field. The influence of hydrogenation on magnetic properties has been dealt with in two recent reviews (*16, 17*) and hence will not be included in the present discussion, although this represents one of the most active areas of the field. Attention will be limited to just four facets of the systems: structural features, thermodynamics, kinetics, and the effect of hydrogenation on superconductivity.

Structural Features

Evidence Gained from X-ray Diffraction. The influence of hydrogenation upon the host lattice is normally followed by X-ray diffraction measurements. But such measurements fail to give information about the positions of hydrogen. Hydrogen locations are normally established by neutron diffraction work. Almost without exception, entry of hydrogen into the host metal entails an expansion of the lattice. The expansions in $ErFe_2$ and in $Er(Fe,Mn)_2$ ternaries hydrogenated to saturation at 525 psi at room temperature are shown in Table II (*13*). These data are illustrative of the general trends observed. Volume increases of 30% are not uncommon for the hydrogen-saturated material. In $ErFe_2$ and in the $Er(Fe,Mn)_2$ ternaries, hydrogenation does not lead to a change in symmetry of the host lattice. This is exceptional. In the majority of cases hydrogenation does lead to a change in symmetry. For example, hydrogenation of $SmCo_5$, which has the hexagonal $CaCu_5$ structure, produces (*18*) a degradation of symmetry to orthorhombic. The same distortion is observed in deuterated $PrCo_5$, which has been investigated by using neutron diffraction techniques. Results obtained are discussed in the next section.

Neutron Diffraction Studies. When consideration is given to the absorption of hydrogen by a metal, one of the first concerns is the location of hydrogen in the host metal. Initially, attention was focused on transition metal hydrides. (Hydrides and deuterides are discussed interchangeably since their structural differences are almost always significant. The deuteride is usually used in neutron diffraction work instead of the hydride because of the large incoherent scattering of hydrogen.) UH_3 (*19*) and ThH_2 and ZrH_2 (*20*) were the earliest hydrides studied. Later,

Table II. Increase in Lattice Parameters in Hydrogenation of $Er(Fe,Mn)_2$ Alloys

x in $Er(Fe,Mn)_2H_x$	% Increase
3.8	8.1
4.2	8.0
4.6	10.0

many other hydrides were examined (*21*). General considerations suggested that hydrogen would be found in the interstices of the host metal at the tetrahedral or octahedral sites. Experiment confirmed these expectations in the majority of systems studied; for example, hydrogen is at the tetrahedral site in U and Zr and at the octahedral site in Pr (*22*) and Ni (*23*). This is not invariably the case. For example, Mansmann and Wallace observed that part of the hydrogen is in a site having three near neighbors in HoD_3 (*24*).

The earliest neutron diffraction work on hydrogenated intermetallic compounds appears to be that of Bergsma, Goedkoop, and Van Vucht on Th_2AlH_4 (*25*). They found that H in this material is in the tetrahedral interstices with four Th as nearest neighbors. In this respect the situation is identical with that in ThH_2. Later Peterson, Sadana, and Korst (*26*) examined $NiZrH_3$ and $NiZrD_3$ by neutron scattering. They found the material to contain two crystallographically inequivalent hydrogens. The unit cell contains eight H in tetrahedral sites, having three Zr and one Ni as near neighbors, and four H in what may be termed pseudooctahedral sites. The octahedral interstices are deformed, and the hydrogen is displaced so that it actually exists in fivefold coordination. The results for HoD_3 and $NiZrD_3$ are consistent with an observation made some years ago (*27*) that "structural evidence accumulated to date suggests that the ideal octahedral site is usually not a stable position for dissolved hydrogen."

As will become evident later, the large class of intermetallic compounds in which one component is a rare earth is presently the subject of intensive investigation by several research groups. Attention has been focused on the thermodynamics of these systems and the effects of hydrogen upon their magnetic properties. Surprisingly, until recently little attention has been paid to the structures of these interesting systems. However, this situation is changing rapidly. For example, in the past twelve months structural work has been published on hydrogenated $LaNi_5$ by three groups, from Norway, Switzerland, and Russia (*see* below).

The first work on hydrogenated rare earth intermetallics was carried out by Kuijpers and Loopstra (*28*). They established the structure of $PrCo_5D_{3.9}$ (D is used instead of of H because the incoherent scattering of D is smaller. This hydride will be discussed henceforth as $PrCo_5D_4$, on which it is structurally based and whose stoichiometry it closely approaches.) by using neutron diffraction techniques. The results obtained are shown in Figure 4. The D–D distances are such as to preclude the existence of molecular deuterium in the system. The D–D bond is ruptured at the surface of the metal, and the deuterium enters the lattice in monatomic form. (This is also true of the deuteride of $LaNi_5$, referred to below, and the other intermetallic hydrides.) In the unit

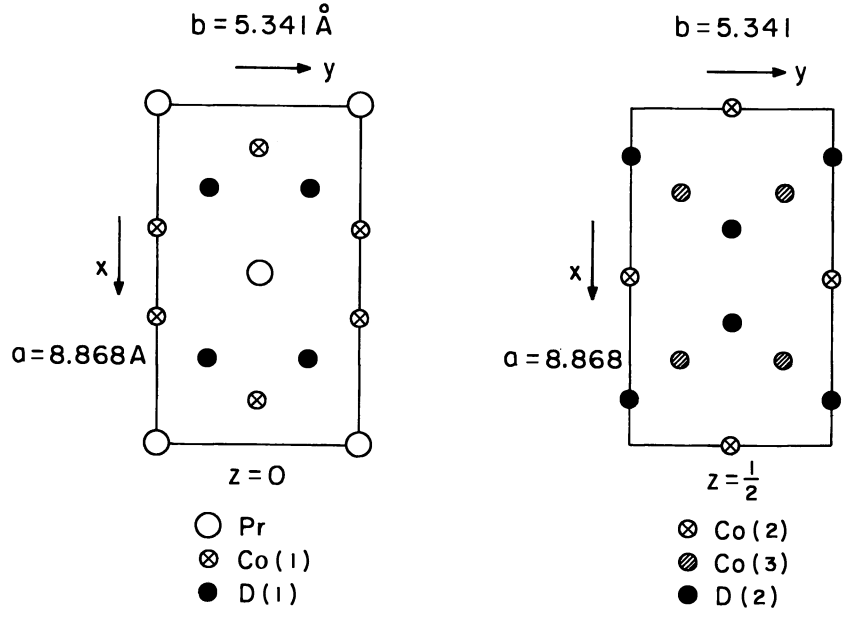

Figure 4. Structural arrangement in $PrCo_5D_4$ showing the atomic positions in planes at Z = 0 and Z = 1/2 in the unit cell. Upon deuteration, hexagonal $PrCo_5$ is transformed into an orthorhombic material.

cell there are 6 octahedral sites at Z = 0, 4 tetrahedral sites each at Z = ¼ and ¾, and 12 tetrahedral sites at Z = ½. The sites at Z = ¼ and ¾ have only Co as near neighbors, whereas all the others have two Pr among the near neighbors. Were all interstices having Pr near neighbors filled, the composition would be $PrCo_5H_9$. Steward (*29*) obtained, in isostructural $LaCo_5$, compositions tending toward $LaCo_5H_9$ at pressures exceeding 1000 atm.

The structure of $PrCo_5D_4$ (Figure 4) shows that the tetrahedral sites with only Co near neighbors are empty. D is found only in sites with two Pr near neighbors; the octahedral sites are two-thirds filled and the tetrahedral sites are one-third filled.

As a hydrogen host, $LaNi_5$ is the paradigm. Accordingly, there has been very considerable interest in ascertaining where hydrogen is situated in this material. Early structural efforts were unsuccessful (*30*). The structure was recently solved almost simultaneously by Andresen (*31*), Fischer et al. (*32*), and Burnasheva et al. (*33*). When examined by X-rays, hydrogenated $LaNi_5$ appears to retain the hexagonal symmetry of the metallic host. When examined by neutron diffraction, however, the symmetry is found to be degraded to rhombohedral. In the $LaNi_5D_6$ structure (see Figure 5) half of the hydrogen is in locations near the

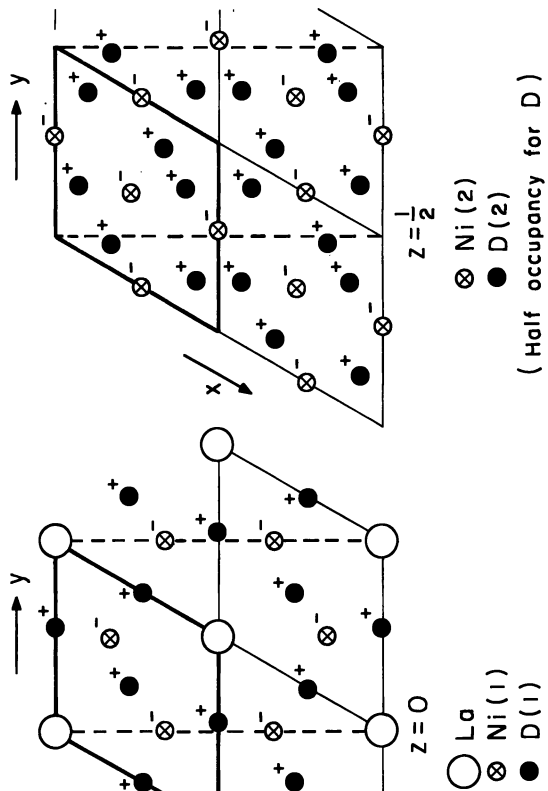

Figure 5. Structural arrangement in $LaNi_5D_6$ showing the atomic positions in planes at Z = 0 and Z = 1/2 in the unit cell. Upon deuteration, hexagonal $LaNi_5$ is transformed into a trigonal material. The dashed lines are drawn to facilitate comparison with $PrCo_5D_4$. D in the tetrahedral sites at Z = 1/2 is statistically distributed over the twofold more abundant sites.

Table III. Hydrogen Positions in $PrCo_5$ and $LaNi_5$[a]

	Octahedral Sites		*Tetrahedral Sites (Z = 1/4 and 3/4)*		*Tetrahedral Sites (Z = 1/2)*	
	$PrCo_5$	*$LaNi_5$*	*$PrCo_5$*	*$LaNi_5$*	*$PrCo_5$*	*$LaNi_5$*
Filled	4	6	0	0	4	12[b]
Empty	2	0	8	8	8	0
Total	6	6	8	8	12	12

[a] The unit cell for $PrCo_5D_4$ is the orthorhombic cell, which contains two formula units. To facilitate comparison of the two hydrides, $LaNi_5D_6$ is described in a hypothetical unit cell identical with that of $PrCo_5D_4$.
[b] These sites are occupied statistically by six D atoms.

ideal octahedral site positions in the $LaNi_5$. They are slightly displaced above the basal plane, and at the same time the Ni in the $Z = 0$ plane is displaced downward. There are additional displacements in the plane perpendicular to the *c*-axis, so that the system has a threefold rather than the sixfold axis of the host metal. These sites are completely occupied in $LaNi_5$, in contrast with the situation in $PrCo_5$ in which they are only two-thirds filled. The tetrahedral sites at $Z = ½$ are half filled instead of one-third filled as in $PrCo_5$, with hydrogen statistically occupying the sites. Here again there are slight displacements from the ideal positions.

The essential features of the hydrogen structure in these materials are summarized in Table III.

Thermodynamic Characteristics

General Comments. In this section attention will be focused primarily on four aspects of the thermodynamics of hydrogenated intermetallic compounds: (1) hydrogen capacity, (2) the number of hydrides formed, (3) the energetics of the hydrogenation process, and (4) certain systematics noted in the behavior of hydrogenated rare earth intermetallics. As regards hydrogen capacity this is, of course, pressure-dependent. However, the pressure generally rises very rapidly per unit increment of hydrogen beyond about 50 atm, and so, in practice, capacity information will be provided for applied pressures in the range of about 50 atm.

To date inferences in regard to the energetics of hydrogenation have been drawn from experimental determination of the dependence of hydrogen pressure (P) on temperature (T). ln P is observed to vary linearly with T^{-1} (see Figure 6 as an example), and the ΔH is obtained from the slope of the plot. This is thermodynamically valid only if the process is reversible. In certain instances, for example, TiFe–H, the process is not reversible (*34*); there is a large hysteresis between results obtained upon absorption and desorption. Consequently, ΔH values obtained by applying the van't Hoff equation to these systems are open to question.

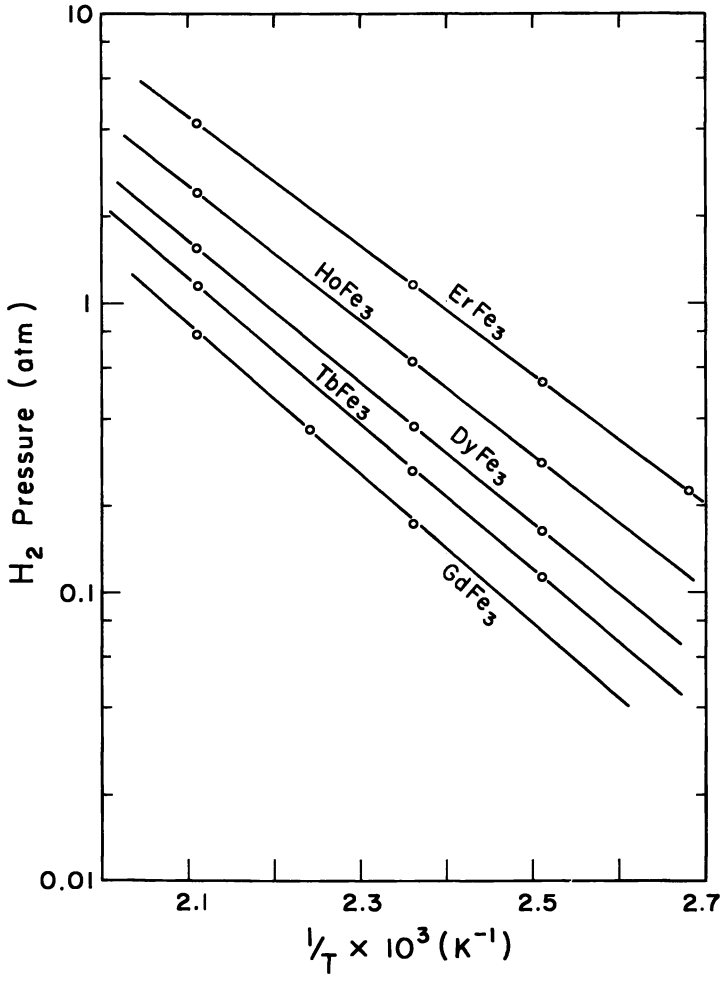

Figure 6. Plot showing the linear dependence of ln P_{Pl} on T^{-1} for several $REFe_3$–H systems; P_{Pl} is the plateau pressure.

The large variation in hydrogen vapor pressure between an element and a compound—Zr versus ZrNi—has been alluded to earlier. As noted, there is a difference of hydrogen pressure of 10 orders of magnitude between the element and the compound. There are also variations within families of compounds, for example, the $RECo_5$ or $RECo_3$ families. Interesting systematic trends are noted, and these are of significance from both a practical and fundamental point of view.

The number of phases is inferred from the pressure–composition isotherm (PCI). The two PCIs shown in Figure 7 illustrate this point.

It is customary to designate the several phases having progressively higher hydrogen contents as α, β, and γ hydrides.

Results obtained for TiFe are discussed in detail elsewhere (*34*). They are not elaborated upon in this review, despite the importance of this compound as a practical means for hydrogen storage, because of the irreversibility in this system. It is to be noted that the FeTi–H system forms two hydrides, $TiFeH_{\sim 1}$ and $TiFeH_{\sim 2}$, apart from a terminal α phase.

The systems $LaNi_5$–H and $SmCo_5$–H were among the first studied. Results shown in Figures 8 and 9 are taken from the doctoral thesis of F. A. Kuijpers, Delft University (*18*). Despite a detectable hysteresis,

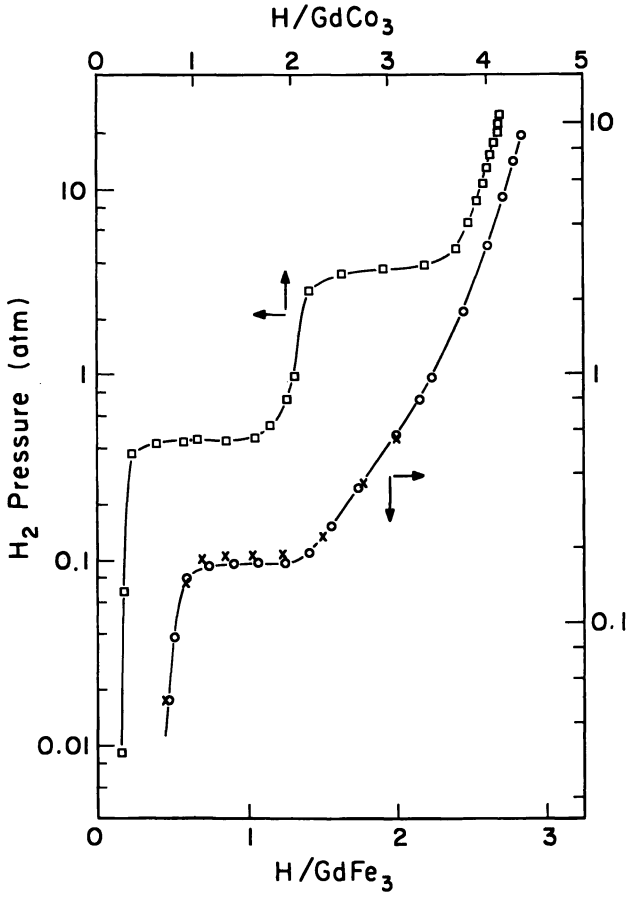

Figure 7. Pressure–composition isotherms for $GdFe_3$–H (150°C) and $GdCo_3$–H (150°C). The data points marked × represent absorption; the others represent desorption.

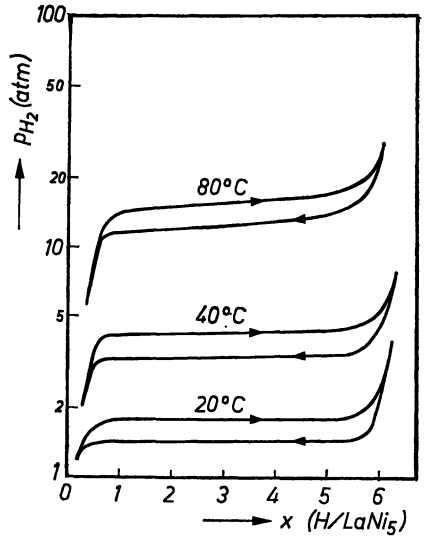

Figure 8. Pressure–composition isotherms for the $LaNi_5$–H system from Kuijpers for absorption (→) and desorption (←) (17)

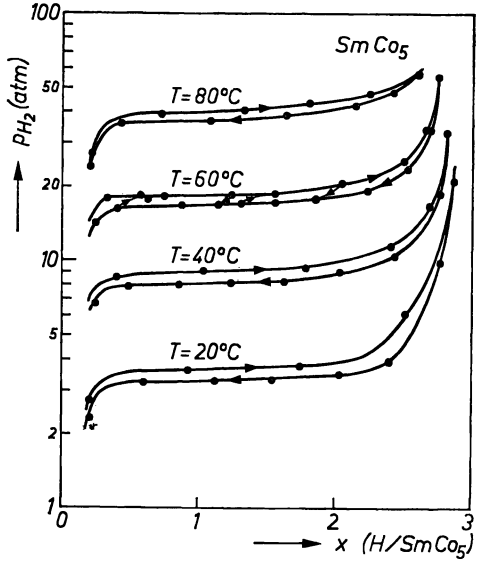

Figure 9. Pressure–composition isotherms for the $SmCo_5$–H system from Kuijpers for absorption (→) and desorption (←) (17)

the van't Hoff relationship was applied to these systems to obtain ΔH for the process. The ΔH of solution of hydrogen in $LaNi_5$ and $SmCo_5$ was observed to be -30 and -33 kJ·mol^{-1} H_2, respectively. This is the range of ΔH required to obtain a material having a vapor pressure of about 1 atm near room temperature. This follows because ΔS for the process is essentially the negative of the entropy of hydrogen gas, that is, ΔS is fixed by the loss in entropy of gaseous hydrogen when it condenses into a solid.

Hydrogen Capacity. The volumetric hydrogen capacities of FeTi, $LaNi_5$, and Mg_2Ni—the present prime candidates for hydrogen storage—are given in Table IV, along with those of several other materials. The metals in Table IV are restricted to binary systems that have the following characteristics: (1) appropriate hydrogen capacity and sufficiently rapid absorption and release of hydrogen to be of practical interest, and (2) known crystallographic characteristics so that the number of hydrogen

Table IV. Hydrogen Capacity of Several Metallic Hosts

Host	x *in (Host)* · H_x	r[a]
FeTi	1.9	1.41 (*34*)
$LaNi_5$	6.0	1.42 (*12*)
Mg_2Ni	4.0	1.30 (*35*)
$GdFe_3$	3.1	0.98 (*9*)
$TbFe_3$	4.2	1.32 (*9*)
$DyFe_3$	3.0	1.00 (*9*)
$HoFe_3$	3.6	1.19 (*9*)
$ErFe_3$	2.7	0.93 (*9*)
$GdCo_3$	4.6	1.48 (*9*)
$TbCo_3$	4.5	1.50 (*9*)
$DyCo_3$	4.3	1.48 (*9*)
$HoCo_3$	4.2	1.42 (*9*)
$ErCo_3$	4.2	1.43 (*9*)
Ce_2Co_7	5.3	1.40 (*10*)
Pr_2Co_7	5.8	0.88 (*10*)
Nd_2Co_7	6.2	1.00 (*10*)
Gd_2Co_7	5.9	0.93 (*10*)
Tb_2Co_7	6.6	1.05 (*10*)
Dy_2Co_7	6.4	1.02 (*10*)
$LaCo_5$	4.2	0.99 (*18*)
$CeCo_5$	2.6	0.67 (*18*)
$PrCo_5$	3.0	0.96 (*18*)
$NdCo_5$	2.7	0.69 (*18*)
$SmCo_5$	2.5	0.65 (*18*)

[a] r = number of hydrogen atoms per volume relative to 4.2×10^{22}, the number density in liquid hydrogen.

Table V. Hydrogen Capacity of Several Metallic Hosts

Host	x *in (Host)* · H_x	r^a
Y_3Ni	8.0	2.8 (*36*)
La_3Ni	8.8	3.1 (*36*)
Ce_3Ni	8.4	2.9 (*36*)
Th_7Ni_3	28.0	3.9 (*37*)
Y_3Ni_2	7.5	2.1 (*36*)
LaNi	3.6	2.5 (*36, 38*)
YNi	3.0	2.1 (*36*)
CeNi	2.7	1.9 (*36*)
La_2Ni_3	4.4	1.2 (*36*)
$LaNi_2$	4.5	2.1 (*38*)
YNi_2	3.7	1.7 (*36*)
$ThNi_2$	4.0	1.9 (*37*)
Pr_2Ni_7	9.5	1.3 (*39*)
$ErNi_3$	3.6	1.3 (*39*)
$CaNi_5$	4.8	1.1 (*40*)
Y_3Co	8.0	2.8 (*36*)
Y_4Co_3	11.6	2.3 (*36*)
YCo_2	4.2	1.9 (*36, 41*)
$GdCo_2$	4.1	1.9 (*36*)
Th_7Co_3	30.0	4.2 (*39*)
ThCo	4.0	2.8 (*37*)
$ThCo_5$	4.6	1.1 (*11, 37*)
YFe_2	4.2	1.9 (*36, 42, 43, 44*)
YFe_3	4.8	1.7 (*36, 43*)
Y_6Fe_{23}	20.0	1.0 (*36, 43, 45*)
$ThFe_3$	3.0	1.1 (*37, 46*)
Th_7Fe_3	28.0	3.9 (*37, 47*)
YMn_2	4.0	1.9 (*36, 38*)
Y_6Mn_{23}	25.0	1.2 (*36, 45, 48*)
Th_6Mn_{23}	25.0	1.2 (*6*)
YPd	3.1	2.1 (*36*)
ZrV_2	5.3	2.3 (*41*)
$ZrCr_2$	4.0	1.7 (*41*)
$ZrMn_2$	3.6	1.6 (*41*)

[a] r = number of hydrogen atoms per volume relative to 4.2×10^{22}, the number density in liquid hydrogen.

atoms per cubic centimeter can be accurately estimated. The metals listed in Table V can contain large amounts of hydrogen, but either their kinetic or crystallographic features, or both, are unknown. In view of the lack of the latter data, their volumetric hydrogen capacity has been calculated under the assumption that the volume per metal atom is the same as in $LaNi_5H_6$, that is, 1.69×10^{-23} cm^3. This is not wholly

unreasonable since the intermetallics included are from families known to be closely-packed, and the atomic volumes of the metals probably do not vary by more than 10 to 15%. The volumetric capacities are, accordingly, uncertain by approximately this amount. Despite this uncertainty, it is clear that the hydrogen capacity of many of these materials (for example, the 7:3Th compounds) is extraordinarily high.

The increase in hydrogen capacity in rare earth systems as the rare earth content increases is apparent from the data in Table IV. This is as expected since it is the chemical affinity of the rare earth component that draws the hydrogen into the lattice. Ti plays this role in TiFe, and Mg in Mg_2Ni.

Number of Phases. The data in Figure 7 indicate two plateau regions for the $GdCo_3$–H system but only one in the $GdFe_3$–H system. Since the plateau regions occur because of the coexistence of the two solid phases, there are two solid phases in the $GdFe_3$–H system and three (α, β, and γ) in the $GdCo_3$–H system. Goudy et al. (39) have concluded on the basis of crystallographic work that the two phases in the Fe system are α and γ. The features apparent in Figure 7 exemplify the behavior of the entire $RECo_3$–H and $REFe_3$–H families.

The number of phases indicated by the PCI for several systems of interest are summarized in Table VI. Present thinking is that the different hydride phases are characterized by different ways of arranging the hydrogen atoms (or ions) on the available interstitial sites. Consider, for example, $RECo_5$. It could be hydrogenated to $RECo_5H_{13}$ if all tetrahedral and octahedral sites were filled (see Table III) or to $RECo_5H_9$ if the tetrahedral sites having no RE near neighbors are left vacant. At the composition $RECo_5H_4$ less than half of the interstices are occupied. Thus there is the possibility of order–disorder phenomena and various superlattice formations involving different arrangements of the filled and empty interstices. This situation was encountered several years ago in Ta_2H and Ta_2D (*49, 50*). Ta with all tetrahedral and octahedral sites occupied would be represented by the formula Ta_2H_{18}. There are many ways to arrange the hydrogen atoms (or ions) on the 18-fold more abundant interstitial positions, and three or perhaps four polymorphic varieties of

Table VI. Number of Phases in Selected Hydrided Intermetallic Compounds

FeTi	3	$REFe_3$	3
Mg_2Ni	2	$RECo_3$	3
$LaNi_5$	2	RE_2Co_7	3
		$RECo_5$	3 (or 4) [a]

[a] Steward et al. (*29*) have observed a fourth phase in $LaCo_5$–H at very high pressures.

Table VII. Heats of Desorption of Hydrogen from Various Metals (kJ · mol^{-1} H_2)

	$\alpha+\beta$	$\beta+\gamma$
FeTi[a]	28	25
Mg_2Ni[b]	64	
$LaNi_5$[c]	30	

	$\alpha+\beta$	$\beta+\gamma$
$PrCo_3$[e]		54
$GdCo_3$[d]	51	45
$TbCo_3$	48.5	44
$DyCo_3$		42
$HoCo_3$		36
$ErCo_3$		38

	$\alpha+\beta$	$\beta+\gamma$
$CeCo_7$[d]	43.5	
Pr_2Co_7	64.5	55
Nd_2Co_7	72	57
Gd_2Co_7	57.5	40
Tb_2Co_7	48	40.5
Dy_2Co_7	46	36
Ho_2Co_7	42	37
Er_2Co_7	39	

	$\alpha+\beta$
$LaCo_5$[e]	45
$CeCo_5$	39
$PrCo_5$	38
$NdCo_5$	41
$SmCo_5$	31
YCo_5[e]	32

	$\alpha+\gamma$
$GdFe_3$[d]	50.5
$TbFe_3$	48
$DyFe_3$	47
$HoFe_3$	45
$ErFe_3$	43
ZrNi[f]	77

[a] Ref. *86*.
[b] Ref. *35*.
[c] Ref. *18*.
[d] $REFe_3$, $RECo_3$, and RE_2Co_7 data are taken from Ref. *10*.
[e] Ref. *11*.
[f] Ref. *14*.

Ta_2H were observed, differing in the way that hydrogen (or deuterium) populates the lattice sites. It seems likely that the structural differences between α, β, and γ rare earth intermetallic hydrides arise because of the different ways of arranging hydrogen in the energetically favored manyfold more abundant interstices.

The different α, β, and γ phases are characterized not only by different structures but also in some cases by strikingly different properties. For example, β and γ $GdCo_3$–H have a Curie temperature of about 600 and 28 K, respectively (*51*). $ErFe_2H_{3.6}$ and $ErFe_2H_4$ also have greatly differing Curie temperatures, about 300 and 2 K, respectively (*52*).

The concept advanced above to the effect that different phases are characterized by varying hydrogen arrangements is to date merely a plausible hypothesis. The necessary neutron diffraction work to support this postulate is yet to be carried out.

The Energetics of Hydride Formation. The slope of the plot of ln P versus $1/T$ has been used to establish ΔH for the formation of a number of hydrides. A compilation of results obtained is given in Table VII.

Entropies of absorption of hydrogen into the several metallic hosts studied are found (*18*) to be about -125 J · k^{-1} mol^{-1} H_2, which is approximately the negative of the molar entropy of hydrogen. This suggests that this loss is the major contribution to the ΔS associated with the entry of hydrogen into the metal. With this value for ΔS, the enthalpy of desorption must be in the range of 30–35 kJ · mol^{-1} H_2 to produce a vapor pressure of 1 to 10 atm at 25°C. Mg_2Ni has a considerably higher ΔH value, and it develops a pressure of 1 atm only at temperatures approaching 600 K. This is a disadvantage in using the substance as a practical storage material for hydrogen.

Systematic Trends. The hydrogenated rare earth intermetallics exhibit some very interesting systematic trends. These are exemplified

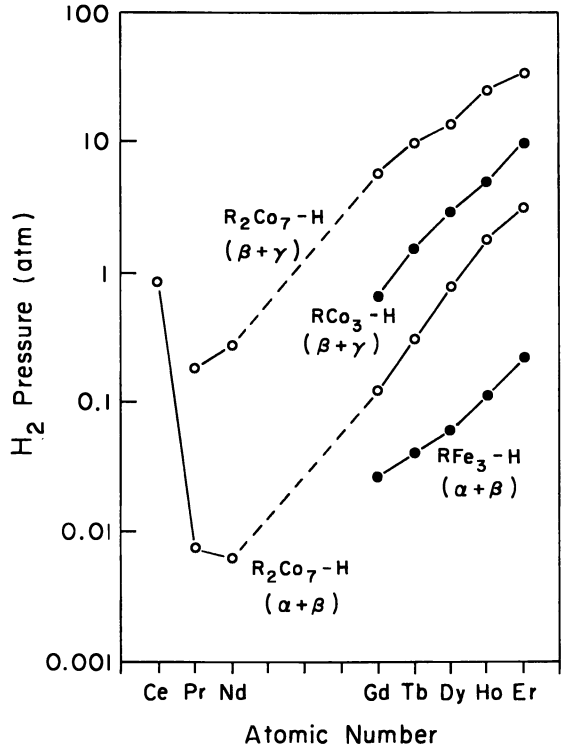

Figure 10. Variation of the measured plateau pressures (100°C) with nature of the rare earth for several families of rare earth intermetallic compounds

Table VIII. Plateau Pressures in Er Systems at 25°C

	P *(atm)*
$ErFe_3$	0.067
$ErCo_3$	0.48
$ErNi_3$	1.35

in Figure 10 and in Table VIII. The data in Figure 10 show a progressive rise in the plateau pressure at (arbitrarily selected) 100°C with atomic number of the rare earth constituent. Ce and Pr are exceptions to this trend because of an altered valence state. Ce exists as a quadripositive ion and Pr as a mixture of $+3$ and $+4$, whereas the other rare earths are tripositive. The data in Table VIII show that the plateau pressure in the sequence of three isomorphous Er compounds increases in the order Fe:Co:Ni.

The ultimate basis for the systematic trends noted undoubtedly lies in the band structure of the materials, which in the main remains to be elucidated. Proper band structure information has only been acquired for $SmCo_5$, $GdCo_5$, and YCo_5 (*53*), which is too restricted a coverage to permit one to interpret the trends observed.

The systematic trends noted empirically are of very considerable practical value in that systems can be chosen that have pressure–composition characteristics conforming to particular specifications, a feature of significance to design engineers.

Kinetic Features

As noted in the Introduction, the truly remarkable feature of the good hydrogen absorbers such as $LaNi_5$ is the rapidity with which they absorb and release hydrogen. This is the more remarkable when cognizance is taken of the complexity of the process. Upon absorption, molecular hydrogen must strike the surface, dissociate and possibly ionize, and then penetrate the lattice. Often the entry of hydrogen is accompanied by a phase transformation in the solid. Corresponding processes are involved in desorption.

Although many qualitative studies of the rates of hydrogen uptake or release have been made, few studies have been made in sufficient detail to permit establishment of the order of the process and the activation energy. Recently the kinetic features of the hydrogenation of several intermetallic compounds have been examined in some detail; these are all compounds in which one of the constituents is a rare earth. Results obtained in these studies will be summarized in this section.

The reason for the paucity of kinetic information is the difficulty in obtaining reproducible kinetic data. Surfaces are easily poisoned (*54*).

For example, Gualtieri et al. (*15*) showed that $LaNi_5$, $PrCo_5$, $ErCo_3$, $HoCo_3$, and $ErFe_2$, all of which normally absorb hydrogen with great rapidity, become inert to hydrogen after a brief exposure to an atmosphere containing about 0.1% SO_2. The rapidity of H_2 absorption by untreated $LaNi_5$ and $PrCo_5$ is illustrated in Figure 2. For the SO_2-treated materials there was no detectable H_2 absorption over a period of 20 hr.

As indicated above, absorption or desorption is a multistage process. For example, the following steps can be envisioned:

1. $H_2(g) \rightarrow H_2(surface)$
2. $H_2(surface) \rightarrow 2H(surface)$
3. $2H(surface) \rightarrow 2H(bulk)$

There may also be a phase change in the host metal accompanying step 3. The rate of collision with the surface is many orders of magnitude larger than the absorption rate, and so it can be excluded as the rate-determining step (RDS).

These three steps present but the barest outline of the total process. Other factors may be involved: for example, heat transfer effects, mass transport into the cracks and fissures of the pulverized material, migration on the surface to a low energy point of entry into the solid, and so on.

Studies of the $LaNi_5$–H System. This is the system that has received the greatest attention to date. It has been studied by Gualtieri, referred to earlier (*15, 54*), by Van Vucht et al. (*12*) who first demonstrated the rapid desorption, by Boser (*55*), and by Tanaka et al (*56, 57*).

Boser studied the absorption and desorption rates of hydrogen from $LaNi_5$ in the two-phase region. In his absorption experiments he exposed $LaNi_5$ to H_2 gas in a closed container and followed the decrease in pressure with time. In the desorption experiments the time dependence of the buildup in pressure was noted. For desorption and absorption Boser fit his measurements to an expression as follows:

$$\frac{P_0 - P_f}{P - P_f} = At + 1$$

where P_0 = initial pressure of hydrogen, P_f = final pressure of hydrogen, P = final pressure of hydrogen at time t, and A = a constant. For desorption, $(P_0 - P_f)/(P - P_f) = C_0/C$, where C_0 and C represent the concentrations of hydrogen in the metal at times 0 and t, respectively. Therefore, $1/C$ is linear with t, indicating that the process is second order with respect to hydrogen concentration. The absorption does not show a ln P or $1/P$ linear with time characteristic of first- and second-

order processes, respectively, confirming that the concentration in the gas phase is not rate controlling. Boser proposed that the rate of the phase transition was the RDS, a conclusion that is at variance with that of Tanaka et al. (*see* below).

Boser estimated an activation energy of 31 kJ · mol^{-1} for the activation energy of the process. In the early study of the hydrogenation and dehydrogenation of $LaNi_5$, Van Vucht et al. (*12*) found the process to be 90 to 95% complete at room temperature, and they estimated an activation energy of about 50 kJ · mol^{-1}. It is unlikely that the studies of hydrogen absorption into and desorption from $LaNi_5$ made prior to 1977 have anything more than qualitative significance. Probably the rate of the process was controlled by heat transfer.

The most careful study to date of $LaNi_5$ as a hydrogen host is that of Flanagan and his associates. In the first study (*56*) he and his associates have established the kinetics of absorption of hydrogen into a sphere 0.54 cm in diameter. This study involved only the α phase and was carried out at temperatures ranging from 353 to 423 K. In their second study (*57*) they performed measurements at 195 K in the two-phase region. The first study was carried out under conditions of nearly constant hydrogen pressure. They noted that the hydrogen uptake was linear with $(\text{time})^{1/2}$. Since the expression for diffusion into a sphere of radius r_0 reduces for small time to $C/C_\infty = 6(Dt/\pi r_0^2)^{1/2}$, where C and C_∞ are the concentrations at t and $t = \infty$ and D is the diffusion constant, Tanaka et al. concluded that the absorption into $LaNi_5$ is diffusion-controlled. They estimated an activation energy of 40 kJ · g-$atom^{-1}$ of H ($\pm$ 10%). This, of course, pertains to the α phase.

In the second experiment measurements were made at 195 K to suppress the rate of the process and hence to minimize the influence of heat transfer effects. Tanaka et al. (*57*) found that the initial rate of uptake of hydrogen varied as ΔP, where ΔP is the difference between the applied and equilibrium pressures. They concluded that the rate of the process is controlled by the rate at which hydrogen penetrates the cracks and fissures.

Gualtieri and Wallace (*54*) studied the absorption of H_2 by $LaNi_5$ over temperatures ranging from 77 to 300 K, using the change in ac resistance to monitor the hydrogen content of the sample. There was no absorption until the temperature reached about 150 K. Absorption proceeded at a measurable rate for all temperatures greater than 150 K. These observations are in general agreement with the findings of Halstead (*58*), who concluded from proton nuclear magnetic resonance (NMR) studies that hydrogen mobility in $LaNi_5$ essentially ceases for $T < 150$ K.

The rapidity with which hydrogen enters or leaves the lattice when the β phase is present suggests that hydrogen mobility is very much

larger in this phase than in the α phase. There is clear experimental evidence for this difference. The studies of Tanaka et al. (*56*) lead to a 25°C diffusion constant for hydrogen in the α phase of about 3×10^{-9} $cm^2 \cdot sec^{-1}$. Karlicek and Lowe (*59*) studied the β phase by the pulsed field gradient proton NMR technique and have obtained a value of about 1.3×10^{-8} $cm^2 \cdot sec^{-1}$.

The radically different diffusion rate in the α and β phases seems to provide an explanation for the rapidity of hydrogen uptake in $LaNi_5$ for $150 \leq T \leq 200$ K. Tanaka et al. (*56*) observed that about 100 min is required to achieve about 0.01% saturation at 195 K and 1 atm H_2 pressure. Gualtieri and Wallace (*54*) achieved 10% saturation at 175 K in 1 min but with an applied pressure of 20 atm. If the rate is proportional to P, as observed by Tanaka, Clewley, and Flanagan, 10% saturation at 1 atm would be achieved in about 20 min. The rapidity of this reaction suggests that at high pressures the β phase hydride is being formed directly from $LaNi_5$ without passing through the α phase as an intermediate. This occurs because of the hundredfold greater mobility in the β phase.

The differing kinetic features of the α and β phases is perhaps a consequence of the varying partial molal enthalpy of hydrogen in $LaNi_5$. Van Vucht et al. (*12*) found a heat of solution of -15 kJ $\cdot$ $g\text{-}atom^{-1}$ of hydrogen for an α–β mixture, whereas Tanaka et al. (*60*) observed -33.9 kJ $\cdot$ $g\text{-}atom^{-1}$ of hydrogen for the infinitely dilute solution. The lower energy of hydrogen in the α phase could give rise to a higher activation energy for diffusion and hence a lower mobility.

Studies of the $SmCo_5$–H System. Zijlstra and Westendorp (*61*) were studying the behavior of $SmCo_5$ in regard to its use as a magnetic material. While etching it for conventional metallographic examination, they observed that hydrogen entered the lattice. The extensive solvent capacity for hydrogen was confirmed by Van Vucht et al. (*11*) who observed that gaseous hydrogen rapidly entered $SmCo_5$ and was also rapidly released. In this case a phase change occurred, producing an orthorhombic material.

Raichlen and Doremus (*62*) studied the desorption process in the two-phase region. From the time dependence of desorption they concluded that diffusion was *not* rate controlling in the temperature range 0° to 30°C. They employed a model in which $SmCo_5$ was regarded as an assemblage of spherical particles of radius R. The phase boundary moved with a velocity v on desorption so that the radius of untransformed material is $R = R_0 - vt$, where R_0 is the radius at time t. They were able to fit their data reasonably well with $v = 1.6 \times 10^{-6}$ and 4.4×10^{-7} $cm \cdot sec^{-1}$ at 10° and 0°C, respectively. They derived an activation energy of about 50 kJ $\cdot$ mol^{-1}. However, the rapidity of hydrogen uptake

or release from $SmCo_5$ is such that the possibility of heat transfer being rate controlling cannot be excluded.

Studies of the $RECo_3$–H and $REFe_3$–H Systems. Goudy et al. (*10*) studied the kinetics of desorption of the hydrogenated $RECo_3$ and $REFe_3$ systems with RE = Dy and Er. Temperature ranges were chosen so as to restrain the rate of release of hydrogen, so that heat transfer was not rate limiting. (Also, the apparatus used was designed with this consideration in mind.) As noted above, three phases are found in the $RECo_3$–H systems. Desorption was studied in the γ and β phase regions and in both two-phase regions β–γ and α–β.

The rate of evolution of hydrogen was assumed to follow an expression of the following form:

$$\frac{dC}{dt} = -kC^n$$

where C is a measure of concentration, k is a rate constant, and n is a constant designating C reaction order. In the work cited it is the quantity of hydrogen remaining in the sample at time t measured as the volume that would be occupied if the hydrogen were a gas at 1 atm and 25°C. If $n = 1$, the reaction is first order and ln C is linear with time. Experiment was not in accord with first-order kinetics. For second-order kinetics (that is, $n = 2$), the expression above integrates to $1/C = kt +$ constant. This behavior was observed (*see* below) for all the systems studied by Goudy et al.

Results for the $ErCo_3$–H system given in Figure 11 are representative of the several systems studied. Initially, the hydrogen content was such as to put the system in the γ phase region, so that the initial rapid rate corresponded to the release of hydrogen from $\gamma ErCo_3$–H. The break in the curve corresponds to hydrogen release in the two-phase β–γ region. The slope is larger at smaller times, indicating that hydrogen release is more rapid from the pure γ phase.

The results obtained for the $ErCo_3$–H system in the β phase followed by desorption from the α–β region indicate a behavior generally similar to that described in the preceding paragraph for the γ and γ–β two-phase regions. In addition, the behavior of the $DyCo_3$–H system is very similar to that of the $ErCo_3$–H system. Data obtained for these systems are collected in Table IX. Rate constants and activation energies are shown only for desorption in the two-phase regions.

The $DyFe_3$–H and $ErFe_3$–H systems were studied by Goudy et al. (*10*) in the fashion used for the corresponding Co systems. Second-order kinetics were also observed for the release of hydrogen from these systems. The situation differs slightly in that for the Fe systems there

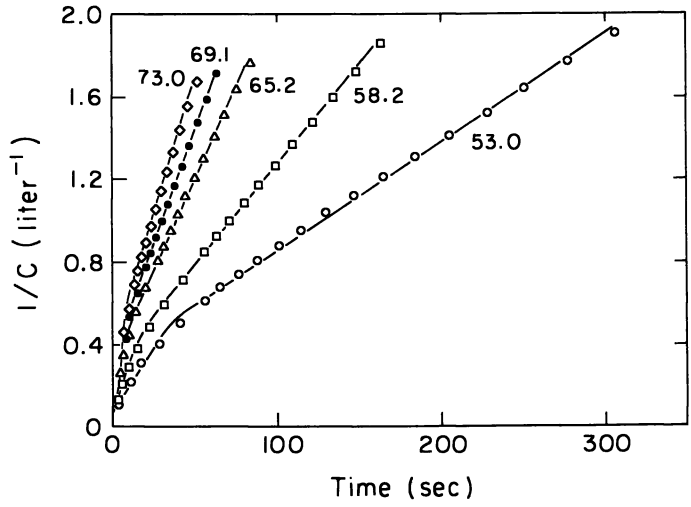

Figure 11. Plot showing the kinetic features of the release of hydrogen from the $ErCo_3$–H system at several temperatures. The sample is initially in the γ phase region. At the break the system enters the two-phase β–γ region. The concentration C is determined by the volume of gas released; hence C is proportional to volume.

are only two phases, termed α and γ. Hence the desorption involved initially the loss of hydrogen from the γ phase and later the loss of hydrogen and the γ–α phase transition. Data obtained are summarized in Table X.

Studies of the Gd_2Co_7–H and Dy_2Co_7–H Systems. The rare earths and cobalt form a compound having the stoichiometry RE_2Co_7, which is, of course, intermediate in composition between $RECo_3$ and $RECo_5$. Goudy et al. (*10*) examined two members of this series, RE = Gd and

Table IX. Kinetic Parameters for the Desorption of Hydrogen from $DyCo_3$ and $ErCo_3$

	Temperature Range (°C)	*10^5 k at 100°C (L^{-1} sec^{-1})*	E_a *(kJ · mol^{-1})*[a]
$ErCo_3$–H(γ)	53–73	2×10^5	110
$ErCo_3$–H(γ–β)	53–73	18.8	75
$ErCo_3$–H(β)	103–126	1.6×10^3	120
$ErCo_3$–H(β–α)	103–126	1.01	84
$DyCo_3$–H(γ)	79–107	4.6×10^3	70
$DyCo_3$–H(γ–β)	79–107	2.54	67
$DyCo_3$–H(β)	139–161	22	150
$DyCo_3$–H(β–α)	139–161	0.055	105

[a] E_a = activation energy.

Table X. Kinetic Parameters for the Desorption of Hydrogen from $DyFe_3$ and $ErFe_3$

	Temperature Range (°C)	*10^5 k at 100°C (L^{-1} sec^{-1})*	E_a *(kJ · mol^{-1})*[a]
$DyFe_3$–H(γ–α)	194–216	0.0032	105
$ErFe_3$–H(γ)	159–186	4.7	150
$ErFe_3$–H(γ–α)	159–186	0.109	96

[a] E_a = activation energy.

Dy, with regard to the kinetics of hydrogen desorption. In these systems, as with the $RECo_3$ and $REFe_3$ systems, the release of hydrogen obeyed second-order kinetics. Data for the two RE_2Co_7–H systems are presented in Table XI. Experiments were carried out in a slightly different fashion from that employed in studying the $REFe_3$–H and $RECo_3$–H systems. The initial composition was fixed by choice of hydrogen pressure to lie in the two-phase region γ–β or β–α. During the course of the reaction, the process changed from hydrogen evolution from a two-phase system to evolution from a single phase, β or α. However, in the case of Dy_2Co_7–H, the α phase was not reached because a pressure less than 1 atm would have been required, and all experiments were performed under conditions such that hydrogen was evolved under a constant pressure of 1 atm.

The kinetic results obtained on the $RECo_3$, $REFe_3$, and RE_2Co_7 systems merit two comments. First, the activation energies satisfy the criterion for an endothermal process in that they exceed the ΔH of process. Second, the observation of second-order kinetics gives strong indication that in the particular systems studied recombination of atoms at the surface is the rate-determining step. It should be emphasized that the evidence pertains to only a few systems, and it would be inappropriate to regard this as general for all intermetallic compounds or even for those involving the rare earths.

Table XI. Kinetic Parameters for the Desorption of Hydrogen from Gd_2Co_7 and Dy_2Co_7

	Temperature Range (°C)	*10^5 k at 100°C (L^{-1} sec^{-1})*	E_a *(kJ · mol^{-1})*[a]
Gd_2Co_7–H(γ–β)	68–99	60.0	75
Gd_2Co_7–H(β)	68–99	$\approx 2 \times 10^5$	85
Gd_2Co_7–H(β–α)	160–186	0.0083	150
Gd_2Co_7–H(α)	160–186	1.4	210
Dy_2Co_7–H(γ–β)	43–68	174	63
Dy_2Co_7–H(β)	43–68	$\approx 3 \times 10^5$	60
Dy_2Co_7–H(β–α)	122–143	1.65	96

[a] E_a = activation energy.

Effect of Hydrogenation on Superconductivity

General Comments. Another interesting feature of metal–hydrogen systems is the effect of hydrogenation on superconductivity. The discovery of superconductivity in $Th_4H(D)_{15}$ at 8.3 K (*63*), in Pd–H(D) alloys at 9 K (*64, 65*), and in Pd–Cu–H alloys at 16.6 K (*66*) (in each case the host metal being a nonsuperconductor) has stimulated the investigation of the superconductivity of the hydrides and deuterides of intermetallic compounds. The superconductivity of the Pd–H(I) alloys is interesting since the isotope effect is reversed from that normally encountered (*65*), that is, the higher-mass alloy has the higher superconducting transition temperature, T_s. Recent studies by Duffer et al. (*67*) of the hydrides and deuterides of the known superconductor HfV_2 (T_s = 9.2 K) have revealed a large but normal isotope effect, with T_s decreasing sharply with H(D) concentration (Figure 12).

Previous investigations (*68*) on the hydrogen absorption characteristics of ZrV_2 had revealed a large intake of hydrogen (up to 1.7 H atoms per metal atom) at moderate pressures. The ternary systems $Hf_{1-x}Zr_xV_2$ have been found to behave similarly. Results obtained in the investigation of the superconducting properties of the hydrides and deuterides of $Hf_{0.5}Zr_{0.5}V_2$ are presented in the following section. This alloy composition exhibits the highest T_s among the ternaries $Hf_{1-x}Zr_xV_2$ (Figure 13) and has hence been chosen for examination.

Studies of Hydrogenated $Hf_{0.5}Zr_{0.5}V_2$. For the superconductivity studies alloy buttons of $Hf_{0.5}Zr_{0.5}V_2$ were prepared by induction melting, followed by heat treatment at 800°C for 7 days. X-ray examination revealed single-phase materials with the cubic Laves structure and lattice parameter a_0 = 7.310 Å. The materials were then alloyed with high-

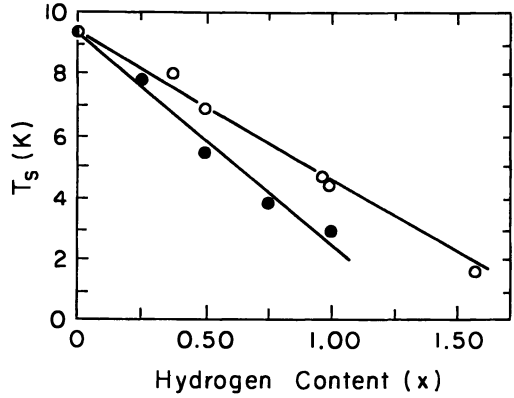

Figure 12. Variation of superconducting transition temperature (T_s) with x in HfV_2H_x (○) and HfV_2D_x (●)

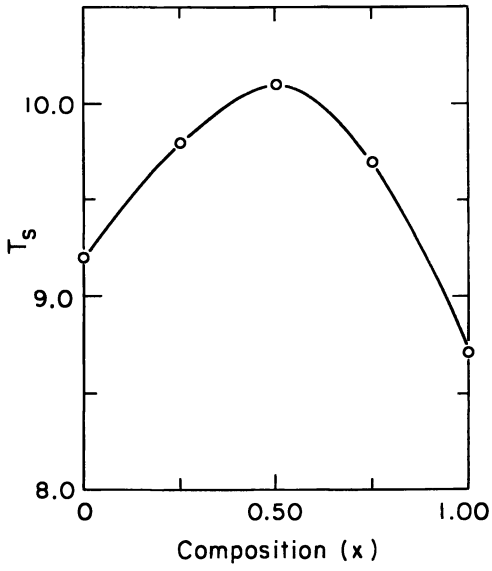

Figure 13. Variation of T_s with composition x in the parent alloys $Hf_{1-x}Zr_xV_2$

purity hydrogen or deuterium at room temperature and 2.5×10^6 Pa. Absorption of H(D) under these conditions resulted in an alloy of composition $Hf_{0.5}Zr_{0.5}V_2H(D)_{5.12 \pm 0.05}$. Within the limits of error, the amounts of H and D absorbed were identical. X-ray measurements revealed the cubic Laves structure with lattice parameter $a_0 = 7.910$ Å for each.

A range of H and D concentrations was produced by equilibrating various ratios of the fully hydrided or fully deuterided alloys with pure $Hf_{0.5}Zr_{0.5}V_2$ in quartz tubes under 2×10^4 Pa hydrogen (or deuterium) at 450°C for 48 to 72 hr. The resulting samples were approximately 0.5 g in weight. X-ray measurements of the samples indicated that complete equilibrium was achieved under these conditions, with the lattice parameter increasing linearly with H(D) concentration. All the hydrides and deuterides maintained the C15 Laves structure of the parent material.

Absorption of H(D) results in a disintegration of the parent ingots into a fine powder. The superconducting transition was detected by using an inductance bridge circuit as described earlier (*69*). The transition widths of the hydride and deuteride specimens were about 1 K.

As shown in Figure 14, the effect of hydrogen and deuterium absorption by $Hf_{0.5}Zr_{0.5}V_2$ is to first increase, then decrease, the transition tem-

perature. T_s is increased from 10.1 K for the parent material, $Hf_{0.5}Zr_{0.5}V_2$, to 11.8 K for $Hf_{0.5}Zr_{0.5}V_2D_{0.4}$. A normal isotope effect was found at all compositions. A surprising result of the investigation was the sudden depression of T_s beyond $x = 1.25$ for the hydride and beyond $x = 0.6$ for the deuteride. At higher concentrations investigated, up to $x = 1.5$, no superconductivity could be detected above 1.2 K for both hydrides and deuterides.

Several investigators have devoted attention recently to the effect of hydrogenation upon superconductivity. The ideas emerging can be applied to the systems described above. As shown by Ganguly (*70*) and by Papaconstantopoulos and Klein (*71*), the high-frequency H or D vibrational modes play an important role in influencing the T_s of hydride materials. In the case of the Pd–H(D) alloys, the enhancement of T_s by addition of H or D is related (*70, 71*) to the unusual softness of the vibrational modes detected by tunneling (*72*) and neutron inelastic scattering (*73, 74*) experiments. The rapid variation of T_s with x in PdH_x and PdD_x in the composition range $0.8 < x < 1.0$ has been shown by Klein et al. (*75*) to arise from the increase in the electronic density of states at the Fermi level for components associated with the H or D sites. The reverse isotope effect in PdH(D) has been attributed (*70,*

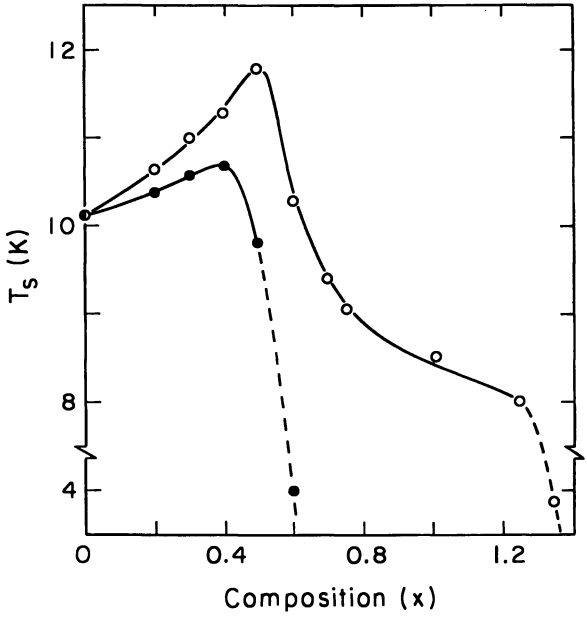

Figure 14. Influence of the addition of hydrogen and deuterium on the superconducting transition temperature of $Hf_{0.5}Zr_{0.5}V_2$: (○), $Hf_{0.5}Zr_{0.5}V_2H_x$; (●), $Hf_{0.5}Zr_{0.5}V_2D_x$.

75, 76) to the anharmonicity of the H(D) vibrations seen in the tunneling (*72*) and the neutron inelastic scattering (*74*) studies.

The McMillan expression (*77*) for T_s as modified by Dynes (*78*) may be written as

$$T_s = \frac{<\omega>}{1.2} \exp\left[\frac{-1.04(1+\lambda)}{\lambda - \mu^*(1+0.62\lambda)}\right]$$

where $<\omega>$ is an average phonon frequency as defined by McMillan (*77*), μ^* is the Coulomb (repulsive) pseudopotential, and λ is the electron–phonon mass enhancement factor. For a pure metal λ can be written (*77*) as

$$\lambda = \frac{N(E_o) < I^2 >}{M < \omega^2 >}$$

where M is the atomic mass, $<\omega^2>$ is the average of the square of the phonon frequency as defined by McMillan (*76*), $<I^2>$ is the average of the square of the electron–phonon matrix elements, and $N(E)$ is the electronic density of states at the fermi level. In alloys consisting of elements of vastly differing masses, such as metal hydrides (for example, PdH), λ can be written (*71, 79*) as the sum of contributions arising from the heavy and light atom vibrations. However, in the present case, since the concentration x of H or D in $Hf_{0.5}Zr_{0.5}V_2H(D)_x$ is small, in the range of concentration studied, such a separation will not be attempted.

Low-temperature heat capacity measurements on HfH_2 and ZrV_2 have been performed by Rapp and Vieland (*80*) and on HfV_2 and $Hf_{0.5}Zr_{0.5}V_2$ by Inoue and Tachikawa (*81*). The former reported the values of the electronic specific heat coefficient γ and the Debye temperature θ_D, whereas the latter reported only the values of γ. The results are summarized in Table XII.

Examination of these data suggests that the broad maximum (*82*) in T_s near $y = 0.5$ in the ternary system $Hf_yZr_{1-y}V_2$ is the result of the maximum in γ, and hence $N(E_o)$, at that composition.

Table XII. γ and θ_D Obtained from the Low-Temperature Specific Heat Measurements[a]

Compound	T_s *(K)*	$\gamma \times 10^{-4}$ *(erg · cm³ · K²)*	θ_D *(K)*
HfV_2	9.2	1.89	190
$Hf_{0.5}Zr_{0.5}V_2$	10.1	2.80	
ZrV_2	8.5	1.60	219

[a] Data from Refs. *80* and *81*.

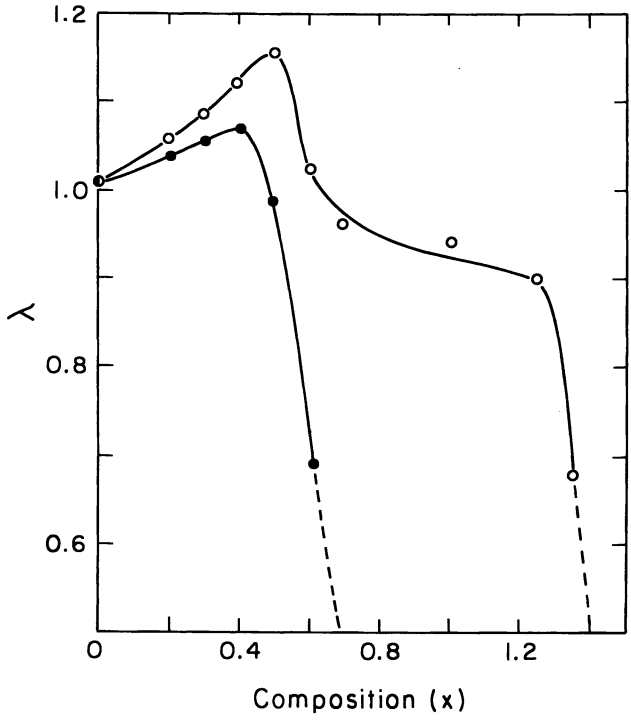

Figure 15. Variation of electron–photon mass enhancement factor λ with composition in $Hf_{0.5}Zr_{0.5}V_2H(D)_x$: (○), $Hf_{0.5}Zr_{0.5}V_2H_x$; (●) $Hf_{0.5}Zr_{0.5}V_2D_x$.

For the system $Hf_{0.5}Zr_{0.5}V_2H(D)_x$ values of θ_D or $<\omega>$ are not available because of the absence of heat capacity or neutron inelastic scattering data. Because of the relatively small H(D) concentration, $0 < x < 1$, one may expect $<\omega>$ to be not drastically altered in comparison to the parent compound $Hf_{0.5}Zr_{0.5}V_2$, since the number of H(D) modes introduced is proportionately small. For a rough estimate of λ, we will therefore assume $<\omega>$ for $Hf_{0.5}Zr_{0.5}V_2H(D)_x$ with small values of x to be nearly the same as that for $Hf_{0.5}Zr_{0.5}V_2$. Further, one has the approximate relation (77) $\theta_D \approx 1.2<\omega>$.

The data in Table XII suggest that $\theta_D \approx 200$ K for $Hf_{0.5}Zr_{0.5}V_2$. One may reasonably choose $\mu^* \approx 0.13$ for transition metals (77, 83). With these assumptions and the observed values of T_s, the values of λ have been calculated for $Hf_{0.5}Zr_{0.5}V_2H(D)_x$ as shown in Figure 15. It can be seen that the value of λ is raised from $\lambda = 1.015$ (for $Hf_{0.5}Zr_{0.5}V_2$) to $\lambda = 1.115$ (for $Hf_{0.5}Zr_{0.5}V_2H_{0.5}$) with the initial addition of hydrogen. This enhancement in λ may be caused by a moderate increase of $N(O)$

or by a slight decrease of the denominator in the expression above for λ because of the H mode being relatively soft.

The large depression in T_s at higher concentrations of H and D is rather surprising. For $T_s < 1.5$ K it is necessary to have $\lambda < 0.51$. It is unlikely that a twofold decrease in λ from the value for the nonhydrided alloy could have occurred from a corresponding increase in the denominator of the expression for λ for the relatively low concentrations of H(D) studied. It is more probable that there has been a decrease in $N(E_0)$ at these higher concentrations that has caused a reduction in λ.

It should also be mentioned that in the cubic Laves structure (C15) alloys, such as $Hf_{0.5}Zr_{0.5}V_2$, the unit cell has eight formula units of $Hf_{0.5}Zr_{0.5}V_2$ and the following (*67*) tetrahedral sites:

5 α sites formed by four V

20 β sites formed by two Hf(Zr) and three V

16 γ sites formed by two Hf(Zr) and two V

It appears that all the available sites are filled at the highest H(D) concentrations. At lower concentrations there may be preferential filling of the various sites, which may give rise to the maximum in the T_s versus x curve through a possible soft mode of H vibration at one of the sites. Resolution of these questions will necessitate neutron diffraction and inelastic neutron scattering measurements.

It is evident from this brief study of one selected system that the entry of hydrogen can significantly modify the superconducting properties of metals. The system Th_7Fe_3 is another example in this vein. The metal is a superconductor (*84*) with $T_s \approx 2$ K. When hydrogenated to $Th_7Fe_3H_{30}$, it loses its superconductivity and becomes a ferromagnet (*85*). The explanation advanced by Malik, Takeshita, and Wallace (*85*) for this surprising change is that Th donates electrons and H and Fe compete for these electrons. In the H-free material the Fe d band is filled by absorption of electrons donated by Th, and the material is a Pauli paramagnet; it transforms into a superconductor at sufficiently low temperatures. With the entry of hydrogen there is competition between H and Fe for the electrons donated by Th. Because of this competition, the Fe d band is no longer filled, Fe becomes magnetic, and the system develops ferromagnetism.

Acknowledgments

This work was assisted by a grant from the Army Research Office.

Glossary of Symbols

RE = rare earth
r = no. of hydrogen atoms per unit volume relative to that for liquid hydrogen
P_0 = initial pressure of hydrogen
P_f = final pressure of hydrogen
P = pressure of hydrogen at time t
C_0 = concentration of hydrogen in metal initially
C = concentration of hydrogen in metal at time t
C_∞ = concentration of hydrogen in metal at $t = \infty$
D = diffusion constant
r_0 = radius of sphere
A = constant
R_0 = radius of transformed $SmCo_5$ initially
R = radius of transformed $SmCo_5$ at time t
v = velocity ($cm \cdot sec^{-1}$)
k = rate constant
n = constant, reaction order
E_a = activation energy
a_0 = lattice parameter
$<\omega>$ = average phonon frequency
μ^* = Coulomb (repulsive) pseudopotential
λ = electron–phonon mass enhancement factor
$<I^2>$ = average of the square of the electron–phonon matrix elements
$N(E)$ = electronic density of states at the Fermi level
T_s = superconducting transition temperature
θ_D = Debye temperature
T = Fe, Co, or Ni
Z = coordinate in unit cell
D = deuterium
T = temperature
T_c = Curie temperature
H = hydrogen
PCI = pressure–composition isotherm
α, β, γ = hydrides with progressively higher hydrogen content
ΔS = entropy change
RDS = rate-determining step
NMR = nuclear magnetic resonance
M = atomic mass
γ = electronic
λ = specific heat coefficient

Literature Cited

1. Wallace, W. E. In "Topics in Applied Physics; Hydrogen in Metals I: Basic Properties"; Alefeld, G.; Völkl, J., Eds.; Springer–Verlag: New York, Vol. 28.
2. Satterthwaite, C. B.; Toepke, I. L. *Phys. Rev. Lett.* **1970**, *25*, 741.
3. Skoskiewicz, T. *Phys. Status Solidi A* **1972**, *11*, K123.
4. Duffer, P.; Gualtieri, D. M.; Rao, V. U. S. *AIP Conf. Proc.* **1976**, *34*, 72.
5. Duffer, P.; Gualtieri, D. M.; Rao, V. U. S. *Phys. Rev. Lett.* **1976**, *37*, 1410.
6. Malik, S. K.; Takeshita, T.; Wallace, W. E. *Solid State Commun.* **1977**, *23*, 599.
7. Winsche, W. E.; Hoffman, K. C.; Salzano, F. J. *Science* **1973**, *180*, 1325.
8. Gregory, D. P. *Sci. Am.* **1973**, *228*, 13.
9. Bechman, C. A.; Goudy, A.; Takeshita, T.; Wallace, W. E.; Craig, R. S. *Inorg. Chem.* **1976**, *15*, 2184.
10. Goudy, A.; Wallace, W. E.; Craig, R. S.; Takeshita, T. In "Transition Metal Hydrides," *Adv. Chem. Ser.* **1978**, *168*, 312.
11. Takeshita, T.; Wallace, W. E.; Craig, R. S. *Inorg. Chem.* **1974**, *13*, 2282.
12. Van Vucht, J. H. N.; Kuijpers, F. A.; Bruning, H. C. A. M. *Philips Res. Rpt.* **1970**, *25*, 133.
13. Gualtieri, D. M.; Wallace, W. E. *J. Less-Common Met.* **1977**, *55*, 53.
14. Libowitz, G. G.; Hayes, H. F.; Gibb, T. R. P., Jr. *J. Phys. Chem.* **1958**, *62*, 76.
15. Gualtieri, D. M.; Narasimhan, K. S. V. L.; Takeshita, T. *J. Appl. Phys.* **1976**, *47*, 3432.
16. Wallace, W. E. In "Hydrides for Energy Storage;" Anderson, A. F.; Maeland, A. J., Eds.; Pergamon Press, Inc., 1978, p. 217.
17. Wallace, W. E.; Malik, S. K.; Takeshita, T.; Sankar, S. G.; Gualtieri, D. M. *J. Appl. Phys.* **1978**, *49*, 1486.
18. Kuijpers, F. A. "RCo_5–H and Related Systems," Ph.D. Thesis, Technische Hogeschool, Delft, 1973.
19. Rundle, R. E. *J. Am. Chem. Soc.* **1951**, *73*, 4172.
20. Rundle, R. E.; Shull, C. G.; Wollan, E. O. *Acta Crystallogr.* **1952**, *5*, 22.
21. Wallace, W. E.; Malik, S. K. In "Hydrides for Energy Storage;" Andresen, A. F.; Maeland, A. J., Eds.; Pergamon Press, Inc., 1978, p. 33.
22. Worsham, J. E., Jr.; Wilkinson, M. K.; Shull, C. G. *J. Phys. Chem. Solids* **1957**, *3*, 303.
23. Cable, J. W.; Wollan, E. O.; Koehler, W. O. "Int. Colloq. on Diffraction Diffusion Neutrons," *Colloq. Int. CNRS* **1964**, *12t*, 36.
24. Mansmann, M.; Wallace, W. E. *J. Phys. (Paris)* **1964**, *25*, 454.
25. Bergsma, J.; Goedkoop, J. A.; Van Vucht, J. H. N. *Acta Crystallogr.* **1961**, *14*, 233.
26. Peterson, S. W.; Sadana, V. N.; Korst, W. L. *J. Phys.* **1964**, *25*, 451.
27. Wallace, W. E., presented at the 1963 Pittsburgh Diffraction Conf., unpublished.
28. Kuijper, F. A.; Loopstra, B. A. *J. Phys. (Paris), Suppl.* **1971**, *32*, C1–657.
29. Steward, S. A.; Lakner, J. F.; Uribe, F. *Adv. Chem. Ser.* **1977**, *163*, 284.
30. Bowman, A. L.; Anderson, J. L.; Nereson, N. G. *Proc. Rare Earth Res. Conf., 10th* **1973**, 485.
31. Andresen, A. F. In "Hydrides for Energy Storage;" Andresen, A. F.; Maeland, A. J., Eds.; Pergamon Press, Inc., 1978, p. 61.
32. Fischer, P.; Furrer, A.; Busch, G.; Schlapbech, L. *Helv. Phys. Acta* **1977**, *50*, 421.
33. Burnasheva, V. V.; Yartys, V. A.; Padeeva, N. V.; Solovlev, S. P.; Somenko, K. N. *Dokl. Acad. Nauk SSSR* **1978**, *238*, 844.
34. Reilly, J. J.; Wiswall, R. H., Jr. *Inorg. Chem.* **1974**, *13*, 218.
35. Ibid. **1968**, *7*, 2254.

36. Van Mal, H. V.; Buschow, K. H. J.; Miedema, A. R. *J. Less-Common Met.* **1976,** *49,* 473.
37. Buschow, K. H. J.; Van Mal, H. H.; Miedema, A. R. *J. Less-Common Met.* **1975,** *42,* 163.
38. Oesterreicher, H.; Clinton, J.; Bittner, H. *Mater. Res. Bull.* **1976,** *11,* 1241.
39. Goudy, A. Ph.D. Dissertation, University of Pittsburgh, 1976.
40. Sandrock, G. D. *Proc. of the 12th Intersociety Energy Conversion Engineering Conf., Am. Nuclear Soc., 1977,* **1,** 951.
41. Shaltiel, D.; Jaacov, J.; Davidow, D. *J. Less-Common Met.* **1977,** *53,* 117.
42. Buschow, K. H. J. *J. Less-Common Met.* **1977,** *51,* 173.
43. Buschow, K. H. J. *Solid State Commun.* **1976,** *19,* 421.
44. Buschow, K. H. J.; van Diepen, A. M. *Solid State Commun.* **1976,** *19,* 79.
45. Oesterreicher, H.; Bittner, H. *Phys. Status Solidi A* **1977,** *41,* K101.
46. van Diepen, A. M.; Buschow, K. H. J. *Solid State Commun.* **1977,** *22,* 113.
47. Malik, S. K.; Wallace, W. E., unpublished data.
48. Buschow, K. H. J. *Solid State Commun.* **1977,** *21,* 1031.
49. Wallace, W. E. *J. Chem. Phys.* **1964,** *41,* 3261.
50. Saba, W. G.; Wallace, W. E.; Sandmo, H.; Craig, R. S. *J. Chem. Phys.* **1961,** *35,* 2148.
51. Malik, S. K.; Wallace, W. E. *Solid State Commun.* **1978,** *28,* 977.
52. Shenoy, G. K., private communication.
53. Malik, S. K.; Arlinghaus, F.; Wallace, W. E. *Phys. Rev. B* **1977,** *16,* 1242.
54. Gualtieri, D. M.; Wallace, W. E. *J. Less-Common Met.* **1978,** *61,* 261.
55. Boser, O. *J. Less-Common Met.* **1976,** *46,* 91.
56. Tanaka, S.; Clewley, J. D.; Flanagan, T. B. *J. Phys. Chem.* **1977,** *81,* 17.
57. Tanaka, S.; Clewley, J. D.; Flanagan, T. B. *J. Less-Common Met.* **1977,** *56,* 137.
58. Halstead, T. K. *J. Solid State Chem.* **1974,** *11,* 114.
59. Karlicek, Jr., R.; Lowe, I. *Solid State Commun.* **1979,** *31,* 163.
60. Tanaka, S.; Flanagan, T. B. *J. Less-Common Met.* **1976,** *51,* 79.
61. Zijlstra, H.; Westendorp, F. S. *Solid State Commun.* **1969,** *7,* 857.
62. Raichlen, J. S.; Doremus, R. H. *J. Appl. Phys.* **1971,** *42,* 3166.
63. Satterthwaite, C. B.; Toepke, J. L. *Phys. Rev. Lett.* **1970,** *25,* 741.
64. Skoskiewicz, T. *Phys. Status Solidi A* **1972,** *11,* K123.
65. Stritzker, B.; Buckel, W. *Z. Phys.* **1972,** *257,* 1.
66. Stritzker, B. *Z. Phys.* **1974,** *268,* 261.
67. Duffer, P.; Gualtieri, D. M.; Rao, V. U. S. *Phys. Rev. Lett.* **1976,** *37,* 1410.
68. Pebler, A.; Gulbransen, E. A. *A.I.M.E.* **1967,** *239,* 1593.
69. Duffer, P.; Gualtieri, D. M.; Rao, V. U. S. *AIP Conf. Proc.* **1976,** *34,* 72.
70. Ganguly, B. N. *Z. Phys.* **1973,** *265,* 433.
71. Papaconstantopoulos, D. A.; Klein, B. M. *Phys. Rev. Lett.* **1975,** *15,* 110.
72. Dynes, R. C.; Garno, J. P. *Bull. Am. Phys. Soc.* **1975,** *20,* 422.
73. Rowe, J. M.; Rush, J. J.; Smith, H. G.; Mostoller, M.; Flotow, H. *Phys. Rev. Lett.* **1974,** *33,* 1297.
74. Rahman, A.; Skold, K.; Pelizzari, C.; Sinha, S. K.; Flotow, H. *Phys. Rev.* **1976,** *814,* 3630.
75. Klein, B. M.; Economou, E. M.; Papaconstantopoulos, D. S. *Phys. Rev. Lett.* **1977,** *39,* 574.
76. Ganguly, B. N. *Phys. Rev. B* **1976,** *14,* 3848.
77. McMillan, W. L. *Phys. Rev.* **1968,** *167,* 331.
78. Dynes, R. C. *Solid State Commun.* **1972,** *10,* 615.
79. Phillips, J. C. *AIP Conf. Proc.* **1972,** *4,* 339.
80. Rapp, O.; Vieland, L. J. *Phys. Lett.* **1971,** *36A,* 369.
81. Inoue, K.; Tachikawa, D. *Proc. Int. Conf. Low Temp. Phys., 21st,* **1971,** 483.
82. Inoue, K.; Tachikawa, K.; Iwasa, Y. *Appl. Phys. Lett.* **1971,** *18,* 235.
83. Gomersall, J. R.; Gyorffy, B. L. *Phys. Rev. Lett.* **1974,** *33,* 1286.

84. Matthias, B. T.; Compton, V. B.; Corenzwit, E. *J. Phys. Chem. Solids* **1961,** *17,* 130.
85. Malik, S. K.; Takeshita, T.; Wallace, W. E. *Solid State Commun.* **1978,** *28,* 359.
86. Pick, M. A.; Wenzel, H. 1st World Hydrogen Energy Conference, Miami Beach, FL, 1976.
87. Clinton, J.; Bittner, H.; Oesterreicher, H. *J. Less-Common Met.* **1975,** *11,* 187.

RECEIVED September 13, 1978.

13

Crystal Growth by the Electrolysis of Molten Salts

R. S. FEIGELSON

Center for Materials Research, Stanford University, Stanford, CA 94305

One of the unique features of electrodeposition is that it is an electrically driven process capable of precise control. Applied to the growth of single crystals it would provide a potentially significant advantage over more conventional crystal growth techniques, which utilize a thermal driving force to achieve crystallization. Discussed in this paper is some recent work concerning the application of electrodeposition to the growth of large single crystals and epitaxial films of various materials. Included is a brief discussion of the principles of electrochemical crystal growth, theoretical and experimental crystal growth studies, and the electrochemical synthesis and preparation of thin films of technologically useful semiconductors such as Si, GaP, InP, and GaAs.

Electrodeposition is an old technology that dates back to the early part of the 19th century. Two branches soon emerged, namely, low-temperature aqueous electrochemistry and molten salt electrochemistry (MSE). By far the largest concentration of effort was devoted to the low-temperature process for the obvious reasons that these are simple systems to construct and operate and that aqueous solution chemistry is much better understood than that for complex molten salts.

In spite of the fact that molten salt technology lagged far behind, both with regard to theoretical understanding and technological sophistication, two processes of significant commercial importance were developed: (1) the Hall process for refining aluminum from bauxite ore and (2) the alkali metal separation process. A brief history of MSE is given in Table I.

0-8412-0472-1/80/33-186-243$08.25/1

Table I. Historical Highlights of the Field of MSE

Year	*Event*	*Investigator*
1807	potassium from KOH	Davy
1833	decomposition of KI, $PbCl_2$, PbI_2, AgCl, SnI_2, PbO, Sb_2O_3, Sb_2S_3 and borax	Faraday
1852	alkaline earth metals from fused salts	Bunsen
1855	decomposition of $MgCl_2$	Bunsen and Matthisen
1861	synthesis of sodium–tungsten bronze (Na_xWO_3)	Scheibler
1898	beryllium from fused salts	Lebeau
1929	synthesis of borides	Andrieaux
1936	aluminum from fused salts	Hall
1936 to present	various antimonides, arsenides, borides, intermetallics, oxides, phosphides, refractory metals, silicides, and sulfides	

In addition to the development of the Hall process in the 1930s, workers, principally in France, started to explore the use of MSE for the synthesis of novel compounds whose preparation by other techniques was complicated by high melting temperatures and high dissociation pressures. These included many of the transition, refractory, and rare earth metal

Table II. Examples of Materials Produced by Molten

Borides		*Phosphides*		*Silicides*
BaB_6	MnB	Fe_2P	MnP	$TiSi_2$
CaB_6	Mn_3B_4	FeP	CrP	$ZrSi_2$
CeB_6	MnB_4	FeP_2	V_2P	$CrSi_2$
LaB_6	MnB_{12}	Fe_3P	VP	Mn_2SI
NdB_6	NbB_2	Ni_3P	Cu_3P	Mn_2Si
GdB_6	TaB_2	Ni_5P_2	Cu_2P	Cr_3Si
YB_6	TiB_2	Ni_2P	NbP	Fe_2Si
BrB_6	VB_2	Ni_6P_5	TaP	$TiSi_2$
YbB_6	VB_4	Co_2P	Zn_3P_2	Li_6Si_2
SrB_6	Zr_3B_4	CoP	Cd_3P_2	$CaSi_2$
ThB_6	ZrB_2	CoP_2	GaP	$CeSi_2$
CrB	Mo_2B	Mo_3P	InP	$LaSi_2$
Cr_2B	MoB	MoP		
CrB_2	WB	W_2P		
Cr_3B_2	SmB_6	WP		
Cr_3B_4	PrB_6	Mn_2P		

borides, carbides, and silicides, as shown in Table II. Excellent review articles on the subject of MSE were written by Kunnmann (*1*), Wold and Bellavance (*2*), and Elwell (*3*).

Since a variety of potentially useful materials can be synthesized by MSE, the development of techniques to produce large high-quality single crystals would be very desirable. The application of this technology to crystal growth, however, has so far been negligible. This is indeed surprising since it is relatively easy to produce electrodeposits with small, well-formed single crystals. Few studies, however, have been directed toward controlling the electrochemical parameters necessary to improve crystal size and quality. According to Kunnmann (*1*), "Materials electrochemically precipitated from fused melts can almost always be obtained in the form of reasonably large crystals when sufficiently low current densities are employed." While this is clearly an oversimplification, it does suggest, as implied by low current densities, that crystals can be grown if conditions of growth are carefully controlled. It has only been in the last few years, however, that crystal growth technologists have recognized that electrodeposition offers several unique advantages over conventional crystal processing techniques and have begun to study the conditions necessary to grow large single crystals and epitaxial layers with useful properties.

The potential advantages of molten salt electrocrystallization for crystal growth are as follows: (1) it is a relatively low-temperature technique that avoids thermal decomposition and excessive vapor pressure; (2) it is an isothermal process—temperature gradients are not

Electrocrystallization in Elevated-Temperature Salt Systems

Carbides	*Arsenides*	*Sulfides*	*Other Groups*
Fe_3C	MoAs	MoS_2	antimonides
MoC	WAs	WS_2	oxides
Mo_2C	FeAs		refractory metals
WC	$FeAs_2$		intermetallic compounds
W_2C	GaAs		

needed for growth; (3) it is relatively temperature-insensitive and small changes in temperature do not affect growth rate; (4) a congruently melting system is not required; (5) deposition can be controlled very accurately by controlling electrochemical parameters alone; (6) solutions can be purified by unique electrochemical techniques; and (7) growth features can be studied quantitatively by carefully varying electrochemical parameters [for example, *see* Bostanov (*4*)].

From the standpoint of crystal growth the most important potential advantage is that the control of the growth process can be achieved by controlling cell potential or current density. The precision with which this can be accomplished is orders of magnitudes better than that possible with temperature control, where 0.1°C is considered excellent temperature stability. Also, electrochemical purification, which will be discussed later, can be used to enhance the purity of the electrodeposits and in some cases would permit the use of more economical starting materials.

Among the several disadvantages to the MSE method are that (1) the depositing material has to be electrically conducting, (2) growth rates tend to be low since growth is from solution, and (3) selection of suitable solvent–solute systems is difficult.

In this paper some recent work at the Center for Materials Research, Stanford University, concerning the extension of electrodeposition to the growth of large single crystals of various types is discussed. Also discussed is the preparation of technologically useful semiconductors under conditions uniquely different from conventional techniques. The following topics will be covered:

1. Principles of electrochemical crystal growth
2. Crystal growth studies
   a. Comparison of electrocrystallization with thermal crystallization processes
   b. Seeded growth (static growth)
   c. Electrochemical Czochralski technique (dynamic growth)
3. Material preparation
   a. Si
   b. GaP and InP
   c. GaAs

It should be recognized at the outset that although MSE is a very old technology the state of the art for growing useful crystals for device applications is still very primitive, and its competitiveness with other, more classical approaches is still uncertain.

Principles of Electrochemical Crystal Growth

In MSE the passage of current through a molten salt electrolyte provides the driving force for the deposition of a desired material on an

electrode of an electrolytic cell. The passage of current is the result of an oxidation–reduction reaction in which electrochemically active species are reduced at the cathode and oxidized at the anode.

$$\text{Anode reaction: } A^{-y} \rightarrow A + ye^- \tag{1}$$

$$\text{Cathode reaction: } C^{+z} + ze^- \rightarrow C \tag{2}$$

where the overall reaction can be written as

$$zA^{-y} + yC^{+z} \rightarrow zA + yC \tag{3}$$

These reactions occur when the cell potential exceeds the decomposition potential (E_d) for the crystallizing species. The equilibrium potential E can be described by the Nernst equation:

$$E = E^0 - \left(\frac{RT}{zyF}\right) \ln \left(\frac{[A]^z[C]^y}{[A^{-y}]^z[C^{+z}]^y}\right) \tag{4}$$

where E^0 is the standard cell potential, R is the gas constant, T is the temperature (K), F is Faraday's constant, and [ ] indicates concentration or activity of the reacting species. The potential just in excess of this equilibrium potential is E_d and is used to drive the kinetic and diffusion processes in the melt and at the electrodes.

When voltage is applied to inert (nondissolving) electrodes of an electrolytic cell, the current behavior is as shown in Figure 1. In this idealized case E_d represents the decomposition potential for the deposition of the desired species. In real systems there is more than one set of

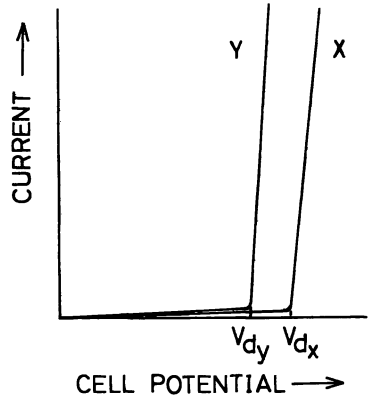

Figure 1. Idealized current vs. voltage curves for deposition of two species

reacting species that can plate out at the electrodes. Even in a very pure simple molten salt system, other species are present that can deposit under nonideal conditions. For example, the solvents themselves are capable of being dissociated.

If impurities are present, they also may deposit in a number of forms, depending upon the operating conditions. Species whose decomposition potentials are lower than those of the desired species ($E \leq E_d$) will electrodeposit at cell potentials less than E_d and will codeposit when the cell potential is equal to or greater than E_d. If the decomposition potential for a species is significantly greater than that of the desired species, it should stay in solution and not electrodeposit. It is particularly important, therefore, to choose a solvent system that has a high decomposition potential, such as alkali metal fluorides.

Those impurities in the system that deposit at potentials less than E_d can be removed from the melt by a preelectrolysis technique. After deposition for some period of time at $E < E_d$, the electrode containing the deposited impurities can be removed and replaced by a fresh one, and the crystal growth run started at $E > E_d$. When the impurity species has a decomposition potential equal to that of the species desired, then codeposition will occur.

The segregation phenomenon observed in electrodeposition is similar to the normal segregation of impurities during conventional recrystallization from solution. In these techniques the distribution coefficient (k) ($k = C_S/C_L$, where C_S is the concentration of solute in the solid and C_L is the concentration of solute in the liquid) describes the segregation behavior of the solute or an impurity in solution. When $k = 1$, there is no impurity segregation, and this corresponds to the case in electrodeposition where $E_{d(imp)} = E_{d(cmpd)}$. If $E_{d(imp)} > E_{d(cmpd)}$, then it is similar to having $k < 1$, where the impurity is rejected from the crystal and segregates in the melt (or solution). When $E_{d(imp)} < E_{d(cmpd)}$, the impurity is incorporated into the growing crystal, which is similar to having $k > 1$. The dependence of impurity incorporation on cell potential and decomposition potential is the basis for both electrochemical purification and doping control. Neither process, however, has been thoroughly studied yet. The decomposition potential is, as can be seen from the Nernst equation, a function of both temperature and concentration. Of particular importance is the solute or impurity concentration in solution.

Crystal Growth Studies

Comparison of Electrocrystallization with Thermal Crystallization Techniques. Electrodeposition has in common with other crystallization techniques, such as the solidification of melts, sublimation, recrystallization from solution, and chemical vapor reactions, that both nucleation and

growth phenomena are involved in the deposition process. To use MSE for crystal growth, therefore, it is very important to control both the nucleation process and the growth rate. The process of electrochemical crystallization can be thought of as analogous to normal crystal growth, where the supersaturation (or temperature gradient) is replaced by the electrical potential in excess of $E_d(\Delta E)$ as the driving force.

Elwell et al. (*5*) have suggested an analogy between normal crystal growth from solution and the flow of current in an electrolyte cell. They considered the various stages of growth as having the character of an impedance to the flow of crystallizing material and, by measuring the resistance in the circuit and its dependence on experimental parameters, were able to study crystal growth mechanisms and the nature of the rate-controlling process.

The linear growth rate (v) equation for a thermally driven solution growth process has been derived by Gilmer et al. (*6*) as follows:

$$v = \sigma D \eta_e \Omega \left[\Lambda + \delta + \Lambda \Lambda_s l \lambda^{-2} + \Lambda \left(\frac{l}{2\lambda} \coth \frac{l}{2\lambda} - 1 \right) \right]^{-1} \tag{5}$$

where σ is the relative supersaturation, D is the solute diffusion coefficient, η_e is the equilibrium concentration of solute, Ω is the molar volume, Λ is an adsorption parameter, D/Λ is the drift velocity of molecules entering the adsorption layer and boundary layer width, Λ_s is a surface diffusion parameter, l is the step spacing, and λ is the mean distance traveled by an adsorbed molecule. The impedances represented by the terms in the bracket relate to the various crystal growth steps, that is, volume diffusion and interface attachment kinetics (adsorption, surface diffusion, and incorporation). Therefore, the linear growth rate is proportional to the driving force (σ) and inversely proportional to the bracketed impedance terms (R).

$$v \propto \sigma [R]^{-1} \tag{6}$$

The growth rate equation for electrodeposition is

$$v = \frac{\epsilon I \Omega}{zFA} \tag{7}$$

where I is the cell current, F is Faraday's constant, A is the area of electrode, z is the number of electrons transferred per molecule, and ϵ is the deposition efficiency ($\epsilon \leq 1.0$). The growth therefore is directly proportional to i, the current density (I/A).

Looking back to Figure 1, we may write

$$E = E_d + IR \tag{8}$$

or

$$\Delta E = IR \tag{9}$$

In general, R is nonohmic since the dependence of current on potential may be extremely complex. Equation 9 can be rewritten as follows:

$$I = \frac{\Delta E \text{ (driving force)}}{R} = \eta[R]^{-1} \tag{10}$$

where η is the overpotential for a single electrode.

The similarity between Equations 6 and 10 is apparent. Furthermore, one can define for the case of solution growth with a thermal driving force:

$$R_{\text{solution}} = R_{\text{vd}} + R_{\text{ik}} \tag{11}$$

where R_{vd} and R_{ik} are the impedances to flow due to volume diffusion and interface attachment kinetics, respectively. In electrocrystallization, R contains an additional term, R_{ct}, due to charge transfer processes:

$$R_{\text{electrodeposition}} = R_{\text{vd}} + R_{\text{ik}} + R_{\text{ct}} \tag{12}$$

and therefore

$$I = \eta[R_{\text{vd}} + R_{\text{ik}} + R_{\text{ct}}]^{-1}$$

The dependence of crystal growth rate on supersaturation, Equation 6, in the limit where the interface kinetic stage is rate determining is normally written as

$$v = \frac{C\sigma^2}{\sigma_1} \tanh\left(\frac{\sigma_1}{\sigma}\right) \tag{13}$$

where C and σ_1 are surface structure and energy parameters:

$$\text{At low } \sigma: \qquad v = \frac{C\sigma^2}{\sigma_1} \tag{14}$$

$$\text{At high } \sigma (\sigma >> \sigma_1): \qquad v = C\sigma \tag{15}$$

The interface kinetic stage, therefore, may be either linear or nonlinear depending on the material and the effective supersaturation. In

crystal growth from thermally driven molten salt solutions, both a linear and a quadratic dependence of v on σ has been reported. The linear dependence is usually related to volume diffusion as the rate-determining step, and the quadratic dependence with growth on screw dislocations.

Using the guidelines above, Elwell et al. (5) showed that by plotting I versus η for electrolytic growth, the nature of the crystallization process could be postulated. They compared the electrolytic growth and dissolution of two materials, Na_xWO_3, where there is a high solute content and a low z, and LaB_6, which has a low solute content and a very high z. Plots of I versus η for both systems are shown in Figure 2. In the case of Na_xWO_3 the linear variation in anodic current with η could be due to either charge transfer or to low-volume diffusion. It was demonstrated, by measuring the variation of R with the rotation rate of the crystal, that volume diffusion was the rate-determining step. The nonohmic growth behavior is determined partly by volume diffusion and partly by interface attachment kinetics.

For the case of LaB_6 neither growth nor dissolution exhibit ohmic behavior, and therefore the crystal growth of LaB_6 does not depend on volume diffusion but on interface kinetics and charge transfer processes.

One can rewrite Equation 7 in the form

$$v = Ki \tag{16}$$

where K ($K = \Omega/zF$) is the growth rate constant. The maximum allowable growth rate will depend on the properties of the material to be electrodeposited. The influence of K on electrochemical crystal growth will be discussed later.

Seeded Growth (Static)

While some materials, such as the sodium–tungsten bronzes, can be electrodeposited easily in the form of large single crystals, this is not the case for most compounds that have been synthesized electrochemically. It was an important first step, therefore, to develop a thorough understanding of the experimental electrochemical parameters necessary for the growth of large single crystals. Both the nucleation characteristics of the system under investigation as well as the factors influencing growth stability are of importance.

Let us consider at this point what is required to generate an effective molten salt system for the electrodeposition of a specific compound. The first problem is to select an appropriate solvent system that will (1) dissolve the solute in reasonable concentrations, (2) keep the liquidus temperature low, (3) have low volatility, (4) have a low viscosity, and (5) have constituents whose decomposition potentials are large compared

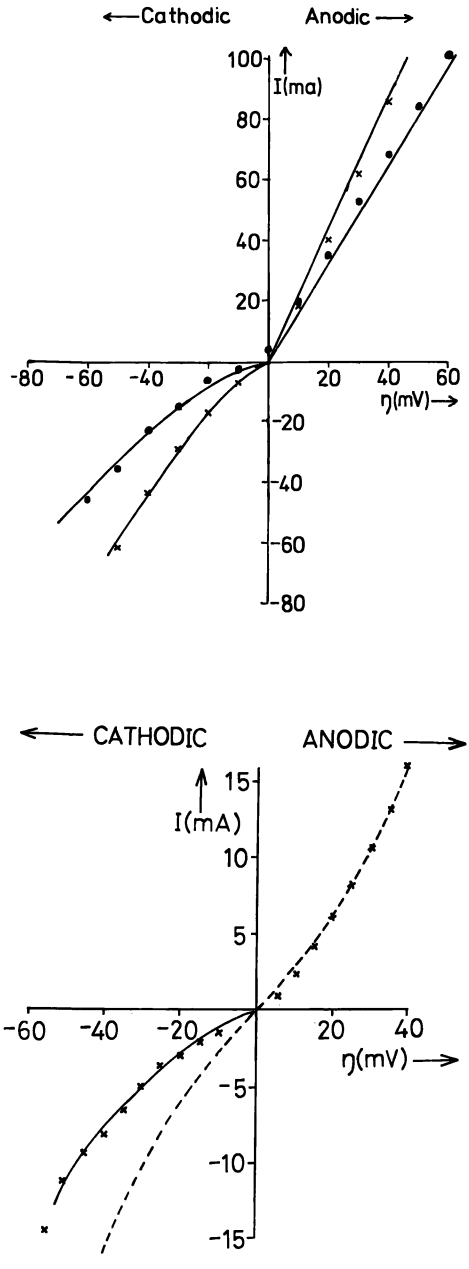

Journal of Crystal Growth

Figure 2. (a) Current vs. overpotential for tungsten bronzes: (○), $Na_{0.61}WO_3$; (×), $Na_{0.73}WO_3$. Cathodic curves calculated using $R = 0.612 + 0.164I^{1/2}\ \Omega$ *and* $R = 0.458 + 0.0931I^{-1/2}\Omega$, *respectively. (b) Current vs. overpotential for* LaB_6 *(5).*

to the species to be deposited. Many such solute–solvent systems are listed in the literature and can form the basic starting point for an investigation. Of particular importance in MSE have been the mixed alkali metal fluorides and mixed fluoride–oxide solvents.

Having chosen an appropriate solvent in which the species to be deposited can be dissolved in reasonable concentration and having chosen a suitable solute that has a low volatility and provides a large fraction of electrically active species, one must next solve the problem of compatibility between this molten salt solution and the crucible and electrode materials. Also, one must remember that the crucible and electrodes must be nonreactive with the electrodeposit and must be capable of withstanding the necessary operating temperature of the system. A wide range of electrode and crucible materials have been used in various MSE cells.

Since it is usually necessary to use two different solute species to electrodeposit a binary compound, the relative concentration of solute species in solution is important. Using stoichiometric ratios is not common since it is more important to match the decomposition potential of the two species. If the appropriate composition is not used, then one or the other species may plate out preferentially and an excess of one component will result.

The anode byproduct can also present some problems. In some cases (usually when O_2 is formed at the anode) this product must be kept away from the deposited materials since a chemical reaction might take place.

Zubeck et al. (7) chose lanthanum hexaboride (LaB_6), a member of the refractory rare earth borides, as a model material to study the problem of controlled nucleation and crystal growth. Lanthanum hexaboride is a good electron emitter and is currently being used as a replacement for conventional electron microscope filaments. It has a cubic metallic structure and exists over a wide stoichiometry range. Andrieux (8) first electrodeposited LaB_6 from a mixture of oxide and fluoride salts. The deposition product was in the form of submillimeter-sized crystallites. It is an example in which the solute–solvent ratio is very low, making growth particularly difficult both by electrochemical techniques and other solution growth techniques.

The emphasis of the LaB_6 work by Zubeck et al. (7) was controlled electrodeposition leading to the production of large single crystals. The electrolysis cell used is shown in Figure 3. Growth was accomplished under an inert He atmosphere. The bath used for electrodeposition contained 2.2 mol % La_2O_3, 33.5 mol % B_2O_3, 31.2 mol % Li_2O, and 33.1 mol % LiF. The B_2O_3 was used both as a fluxing agent and as the source of boron. LiF was used to dissolve the oxides and lower melt viscosity and the Li_2O was part of the low-temperature solvent.

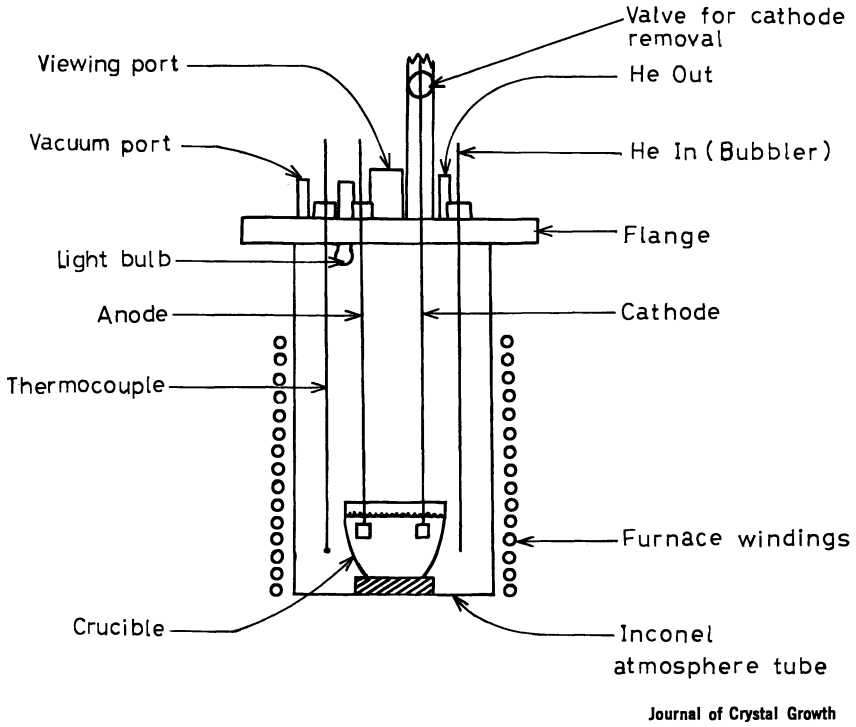

Figure 3. Molten salt electrolysis system (7)

The cell reactions are as follows:

$$2La_2O_3 + 12B_2O_3 \rightarrow 4LaB_6 + 21O_2 \quad (17)$$

$$\text{Anode: } 42O^{2-} \rightarrow 21O_2 + 84e^- \quad (18)$$

$$\text{Cathode: } 4La^{3+} + 24B^{3+} + 84e^- \rightarrow 4LaB_6 \quad (19)$$

Note that for each molecule of LaB_6 electrodeposited, 21 electrons have to be transferred. A large number of electrode materials were investigated, few of which were compatible with the molten salt solutions. Gold was found to be the most suitable both for the anode and cathode. Cell current could be adjusted by choosing an appropriate electrode area (20–50-mil-diameter wire for the cathode, 1.1-cm-wide foil for the anode). All compounds used were in the form of reagent-grade chemicals, but the baths were purified by preelectrolysis at a cell potential near E_d for LaB_6 and the cathodes subsequently replaced with new ones prior to the start of growth.

Under the cell conditions described, E_d for LaB_6 was 1.85 V. Deposition, therefore, was accomplished with cell potentials in the range 1.85–2.1 V. It is possible to drive the growth process in either a constant current or voltage mode or by varying either parameter in a controlled manner. Figure 4 shows the current behavior as a function of time for a constant cell potential. The initial current rise is due to the nucleation of small crystallites that form on the cathode, increasing substantially the surface area of the electrode and thereby lowering the cell potential. The current levels off as the crystals become larger and the rate of surface area change decreases substantially. Normally in a constant current mode the surface area increase due to deposition will result in a drop in cell potential, which can thereby fall below E_d. Under those conditions the deposit will start to dissolve or dissociate, as evidenced by etch pitting. In fact, the range of cell potentials possible for deposition is very narrow and is a major factor to be controlled during deposition, along with the current density (which, as stated before, is equivalent to the growth rate). The best results, therefore, were obtained with constant or programmed cell potential.

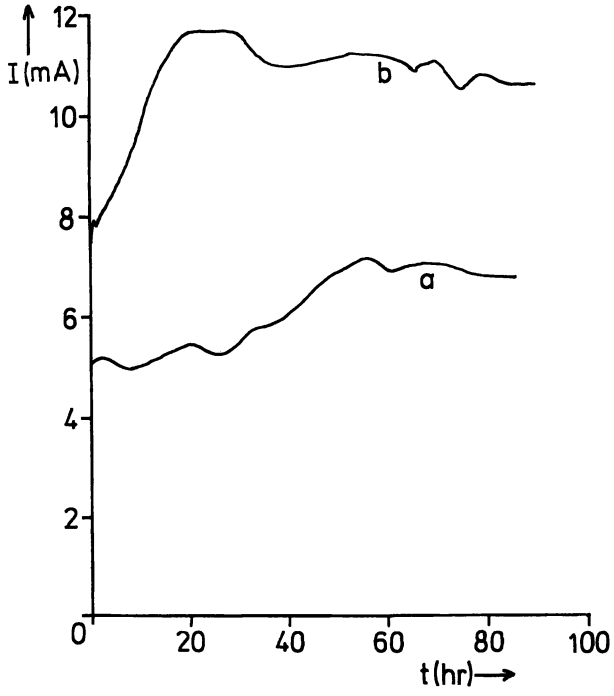

Figure 4. Current vs. time for LaB_6 growth (7)

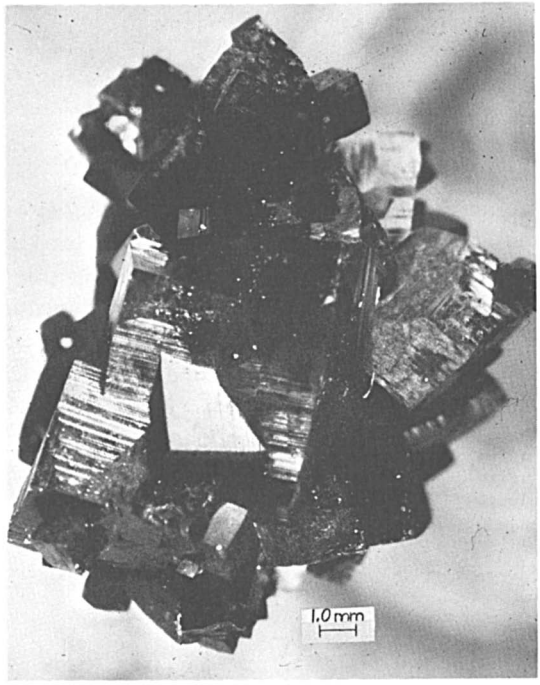

Journal of Crystal Growth

Figure 5. LaB_6 electrodeposit after 100 hr of unseeded growth (7)

The stable growth rate range for LaB_6 crystals was found to be between 20 and 40 mA · $(cm^2)^{-1}$. After 300 hr, clusters of crystallites up to 4 mm in diameter were produced, as shown in Figure 5. Observations of the growth morphology, reported by Elwell et al. (9), showed that at less than 25 mA · $(cm^2)^{-1}$ crystals grow as layers formed at pyramidal active sites at the center of crystal faces, with propagation outward in all directions. As the current density is increased to 30–50 mA · $(cm^2)^{-1}$, the active sites become located at the corners and edges of the crystallites, which are closest to the source of nutrient, and the layers propagate inward across the crystal face. This condition is the precursor of hopper growth often seen in solution growth. At current densities greater than 100 mA · $(cm^2)^{-1}$, dendrites grow from the corners along the [111].

The electrodeposit shown in Figure 5 clearly illustrates that nucleation of LaB_6 is difficult to control even at low current densities. Not only is primary nucleation a problem but so, too, is secondary nucleation which results from perturbations in the growth rate.

To avoid or minimize primary nucleation problems, one should use a seed crystal. In the study by Zubeck et al. (7) LaB_6 seed crystals

($2 \times 3 \times 3$ mm) were obtained from a zone-refined boule and used in place of the gold wire cathode. The seed had to be entirely submerged; otherwise, the exposed portion deteriorated rapidly. After 200 hr the crystal size had increased to $6 \times 6 \times 5$ mm, as shown in Figure 6. By estimating the surface area of the seed crystal, the cell voltage could be adjusted to give a current density of 20 mA · $(cm^2)^{-1}$. Small periodic adjustments in cell potential were made to control the shape of the current-versus-time curve.

Secondary nucleation problems were eliminated through the maintenance of stable operating conditions (cell voltage, current, and tempera-

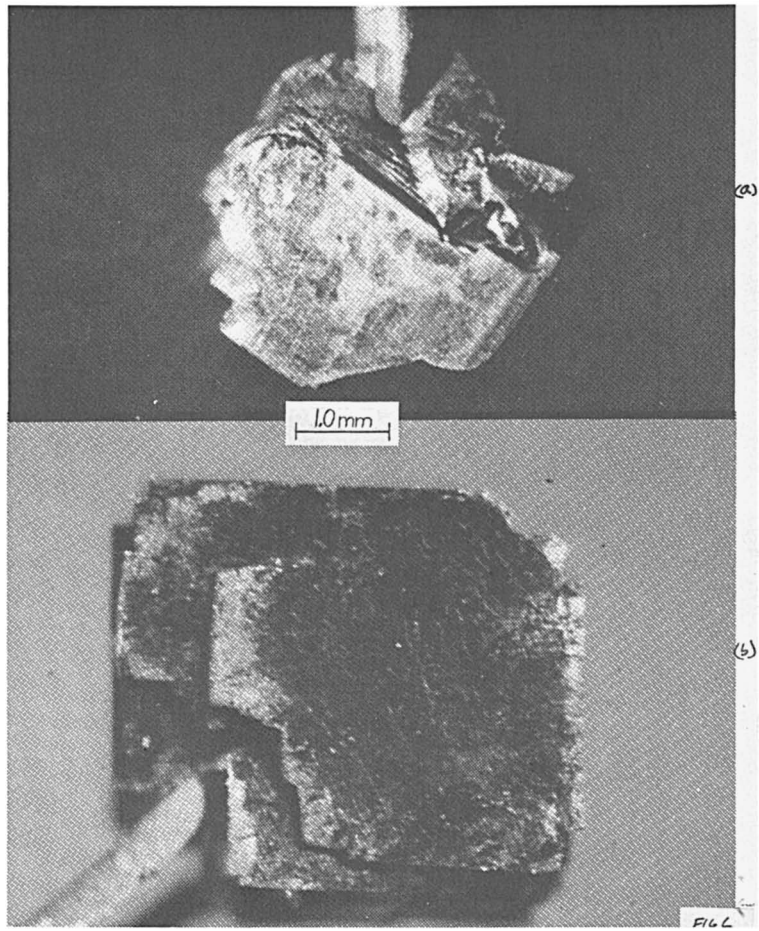

Figure 6. Seeded growth of LaB_6 suspended on gold wire cathode: (top) *after 87 hr of growth;* (bottom) *after 200 hr of growth (7).*

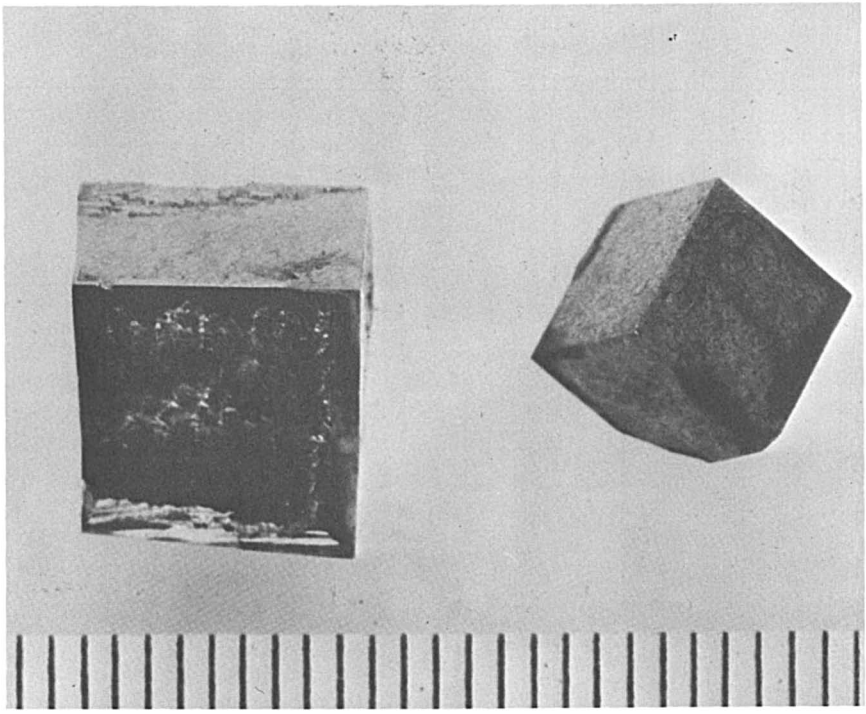

Journal of Crystal Growth

Figure 7. Crystals of Na_xWO_3 grown by standard MSE techniques for use as seeds in electrochemical Czochralski technique (10)

ture). After longer growth periods even larger crystals should be possible. For the growth of very large crystals, the size of the crucible and the quantity of the solution would have to be increased to minimize the effects of solute depletion as the crystals grow. Also, E_d changes as a result of the change in solution composition as the crystal grows (unless a dissolving anode is used), and in the growth of very large crystals, the cell potential might have to be adjusted accordingly.

Seeded Growth (Dynamic): The Electrochemical Czochralski Technique

One of the most important crystal growth techniques is the Czochralski method (crystal pulling). It is widely used commercially to grow large, near-perfect crystals such as silicon and gadolinium gallium garnet. De Mattei et al. (*10*) studied the possibility of adapting the concept of crystal pulling to electrodeposition. Sodium–tungsten bronze was used

as a model growth system because of the ease with which large single crystals can be grown by conventional static growth techniques, using a Na_2WO_4–WO_3 molten salt solution (Figure 7). The Na_xWO_3 system is an example of a system with a high solute content and a low z. The apparatus used is shown in Figure 8. It contains a growth chamber similar to the LaB_6 electrolytic cell except that now the cathode rod is attached to a Czochralski pulling system. The cathode could be rotated

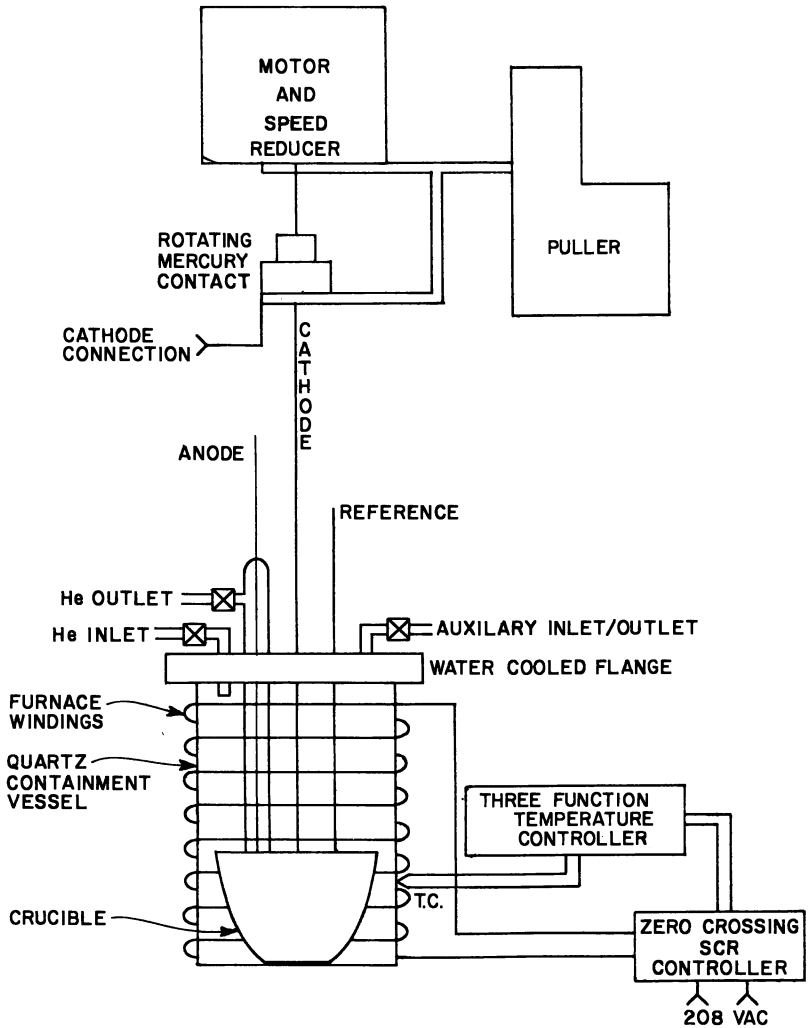

Journal of Crystal Growth

Figure 8. Schematic of electrochemical Czochralski crystal-pulling and rotation mechanism, growth furnace, and temperature controller (10)

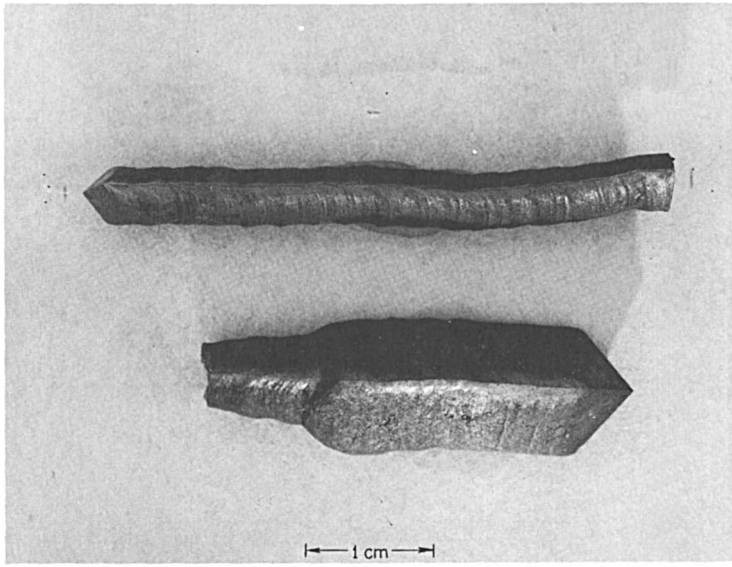

Journal of Crystal Growth

Figure 9. Electrochemical Czochralski crystals grown in [111] direction at two different current–pull rate combinations: (top) *constant pull rate, constant current;* (bottom) *constant pull rate, current increase of four times after initial growth period* (10).

as in standard Czochralski growth. Since the crystal has to be pulled above the surface of the melt during growth, it was found necessary to keep the oxygen generated at the anode from traveling either through the gas phase or across the melt surface to the crystal, which results in the chemical reaction

$$Na_xWO_3 + O_2 \rightarrow Na_2WO_4 \qquad (20)$$

Na_2WO_4 melts at the operating cell temperature (750°C). To accomplish this the anode was placed in a separate compartment such that He gas flushed the O_2 generated away from the cathode and out of the system.

The melt composition used was 25 mol % WO_3 and 75 mol % Na_2WO_4, and at this composition cubic Na_xWO_3 is produced. The first experiments were performed using [111]-oriented seeds obtained from statically grown crystals. Crystals of up to 11 cm in length and 2.5 cm in diameter were grown by the electrochemical Czochralski technique, a typical example of which is shown in Figure 9. Since there are no thermal constraints to fix the shape of the interface or diameter of the crystal, both the interface and sides of the crystals were highly faceted.

The crystal and interface morphology are a function of the growth direction.

In Figure 10 the variation of maximum stable pulling rate with seed rotation rate is shown. For any given rotation rate a pull rate greater than the maximum gave rise to dendrites growing at the growth interface. Based in Levich's equation for the limiting current density for a rotating electrode (*11*), the maximum allowable pull rate dy/dt was calculated to be

$$\frac{dy}{dt} = 2.25 + k'w^{1.17} \tag{21}$$

where k' is a constant and w is the rotation rate.

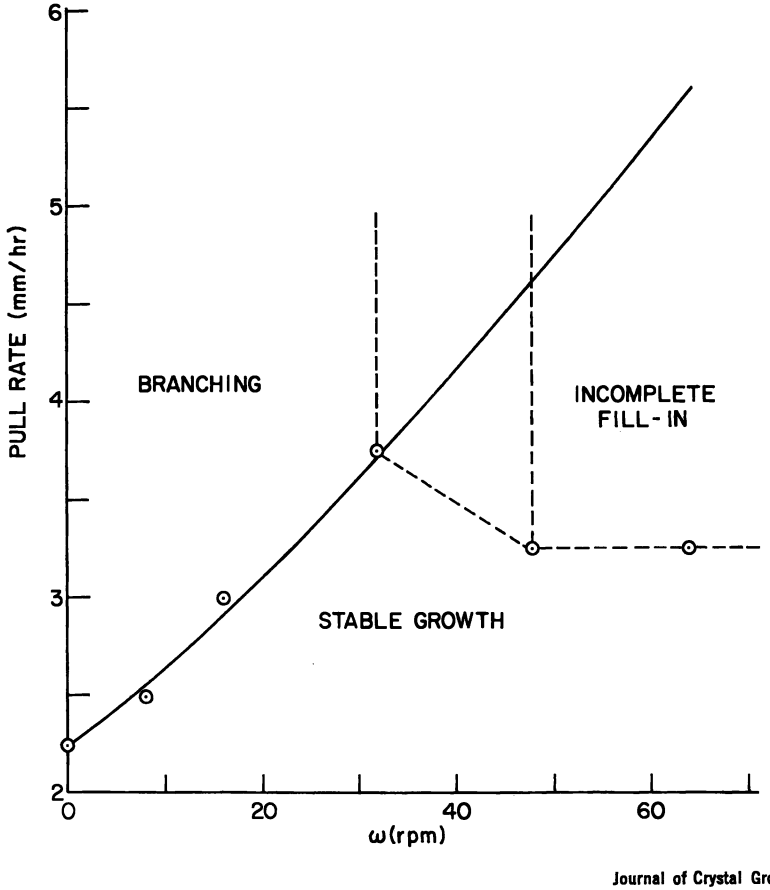

Figure 10. Maximum stable pull rate vs. crystal rotation rate for electrochemical Czochralski growth of Na_xWO_3: (⊙), experimental points; (——), calculated; $\sigma = \pm 0.06$ (10).

The solid curve in Figure 10 was derived from values calculated by using Equation 18 and the experimental data points, up to a seed rotation rate of 30 revolutions per minute (rpm), were in excellent agreement with the calculated values. Above 30 rpm the grown crystals exhibited a depleted zone at the growth facets. This was believed to be caused by flow separation at the apex of the interface.

In normal Czochralski growth automated techniques for diameter control have been recently developed. These techniques are based on either measuring the weight change of the crystal or melt during growth or monitoring the meniscus at the growing interface, either with respect to temperature or position.

In the electrochemical Czochralski technique, however, diameter control is an intrinsic feature. The volume (V) of material deposited electrochemically is

$$V = \left(\frac{M\epsilon}{nF\rho}\right) Q \tag{22}$$

where M is the molecular weight, Q is the total charge in coulombs, and ρ is the density of the material and n is the number of electrons transferred per unit of material deposited. Differentiating with respect to time t gives

$$\frac{dV}{dt} = K\epsilon I \tag{23}$$

where $K = (M/\rho nF)$ is the growth rate constant. Since the volume of material grown is equal to $A(dy/dt)$, it was shown that

$$d_{[111]} = \left(\frac{K\epsilon I}{0.75} \cdot \frac{1}{dy/dt}\right)^{1/2} \tag{24}$$

It is, therefore, possible to control crystal diameter d in the [111] direction by controlling only the pull rate dy/dt and the current I. This can be accomplished in principle with great accuracy.

The tungsten bronzes exhibit anisotropic growth behavior, with the [111] direction the fastest growth direction. The length and diameter of [111]-oriented crystals, therefore, were found to be easy to control. Growth on other axes, however, proved more difficult. During the growth of either [100]- or [110]-oriented crystals, the crystals pulled out of the melt after several centimeters had been grown. In the [111] direction there is no tendency for lateral growth, but in the [100] or [110] growth the fast-growth direction is inclined to the pull direction,

and in the absence of thermal constraints the crystal diameter widens out, as shown in Figure 11. Since material is deposited at a constant rate, the increased area of the growth interface causes the axial growth rate to drop below the pull rate and the crystal will not stay in the melt.

In the normal Czochralski method the crystal diameter is controlled by the freezing isotherm at the melt surface, which is created by the radial temperature gradient. In the electrochemical Czochralski technique, since no such thermal constraint exists, a mechanical constraint such as a cylindrical die or ring on the melt surface would help restrain unlimited growth of the crystal diameter in the fast-growth directions.

DeMattei and Feigelson (*12*) looked at the electrochemical Czochralski technique for growth of materials that exhibit isotropic growth behavior. For the two crystals chosen for growth, metallic Nb and Fe, the maximum allowable pull rate was exceedingly slow. Since pull rate is proportional to $K_e I$, it was important, therefore, to study the significance of the growth rate constant K on electrochemical Czochralski growth. For Na_xWO_3, K equals 2.136 $cm^3 \cdot (A \cdot hr)^{-1}$ and growth is relatively fast. For the case of most metals, however, K lies between 0.08 and 0.38 $cm^3 \cdot (A \cdot hr)^{-1}$. In general, De Mattei and Feigelson concluded that the growth rate constant K had a critical value near $K = 1$. If K is greater than 1.0, then growth rates greater than 0.5 mm $\cdot$ $(hr)^{-1}$ are possible. If the value is less than 1.0, then either a slow growth must be tolerated or the growth rate must be optimized by varying process parameters such as composition, stirring, and cell potential (application of electropolishing techniques).

Material Preparation

Once the techniques discussed above for growing large single crystals of some model materials were developed, the logical next step was to apply this technology to the growth of materials that are in the mainstream of device interest and whose properties are not yet well controlled by conventional techniques. The area of III–V epitaxial layers and bulk single crystals was chosen for this purpose. The main advantages of MSE in this case are the precise electronic control of the growth process compared to thermally driven systems, the low growth temperatures used, the insensitivity to temperature fluctuations, and the possibility for electrochemically controlled purification and doping.

One important problem area involves finding a suitable substrate material (cathode) that is compatible with the molten salt bath and has the appropriate crystallographic, chemical, and electronic properties for the electrodeposit.

Published on June 1, 1980 on http://pubs.acs.org | doi: 10.1021/ba-1970-0186.ch013

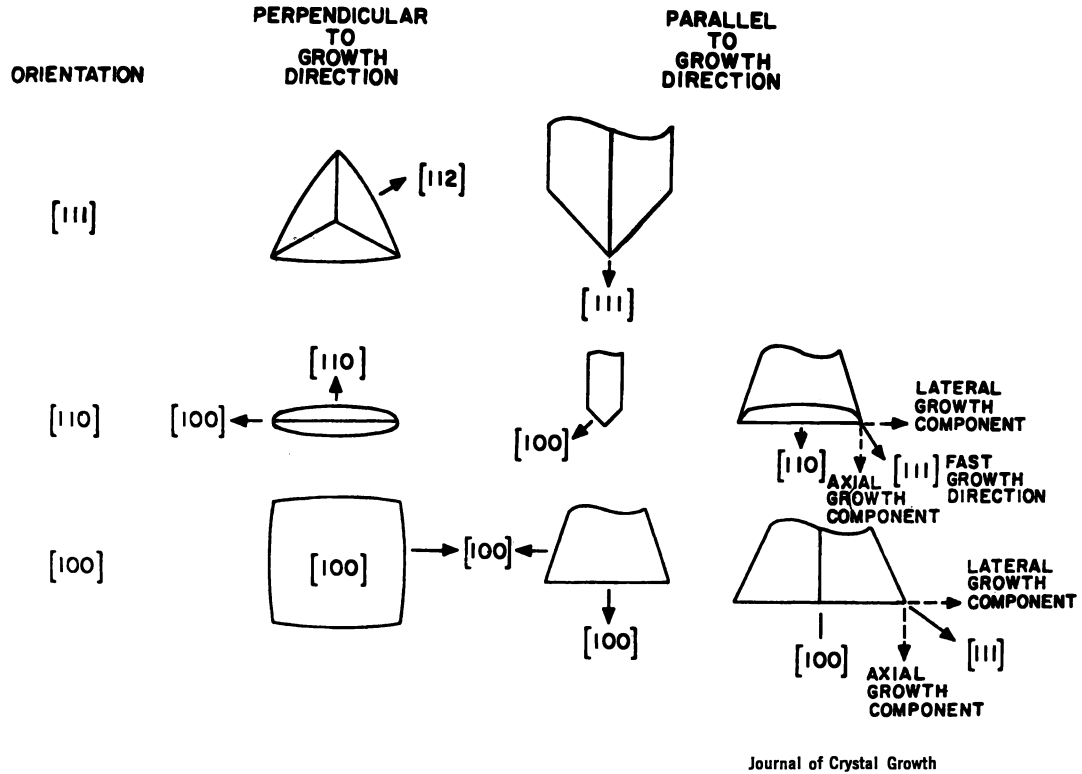

Figure 11. Diagrams of interface morphologies found for electrochemical Czochralski crystals grown in the [111], [110], and [100] directions and their relationship to the fast-growth [111] direction (10)

Silicon

Silicon was first deposited electrochemically in 1854 from a $NaAlCl_4$–Si molten salt bath by Deville (*13*) and later by Ullik (*14*) from K_2SiF_6 in KF. Since then only a few additional studies were undertaken. The basic electrodeposition process for Si deposition involves converting Si^{4+} ions in a molten salt bath to elemental Si on a suitable cathode. The overall reaction can be written as

$$SiO_2 \rightarrow Si + O_2\uparrow \tag{25}$$

Grojtheim and co-workers (*15, 16*) preferred the use of cryolite solutions at about 1000°C with 5 wt % SiO_2 as the solute. Cook (*17*) deposited Si at 800°C onto several refractory metals from a solution of K_2SiF_6 in an alkali fluoride mixture (particularly the LiF/NaF/KF eutectic known as Flinak). Flinak can also be used as a solvent for SiO_2, and electrodeposition below 1000°C is possible. Most of the Si produced in these early experiments was powdery or dendritic in character. Cohen and Huggins (*18*) produced coherent epitaxial and polycrystalline layers by using a salt mixture containing 5 mol % K_2SiF_6, 10 mol % KHF_2, and 85 mol % LiF–KF (47.5–37.5 mol %), using an apparatus similar to that shown in Figure 3. The KHF_2 dissociates to KF and HF, and the HF reacts with any oxygen in the system to produce H_2O vapor, which presumably is flushed out of the system when evacuated. Their baths were purified by preelectrolysis, using a sacrificial molybdenum strip cathode. The anode used was high-purity Si, which dissolves and is then transported to the cathode. The cathodes were either [111] Si substrates for epitaxial growth or W, Ag, Mo, Nb, and a Ag/Ni alloy for polycrystalline layers. Unintentionally doped films were p-type, with resistivities in the range 0.05–0.1 Ω · cm. In polycrystalline films grain size was 40–50 μm in diameter. Growth rates, and therefore layer morphology, were improved by using an alternating square wave pulse technique. Coherent Si deposits were obtained at current pulses up to 40 mA · $(cm^2)^{-1}$. Without this technique the allowable range was 1–10 mA · $(cm^2)^{-1}$.

III–V Semiconductors

The gallium phosphide (GaP) investigation by Cuomo and Gambino (*19*) was the pioneering effort on the epitaxial growth of III–V compounds by molten salt electrolysis. The layers of GaP and InP produced (details on InP electrodeposition were very sketchy) were on Si, Ge, and C substrates from melts containing $NaPO_3$, Ga_2O_3, or In_2O_3, and either mixed chloride or fluoride fluxes. The electrical characteristics of a GaP p–n junction diode were measured. Their work strongly indicated

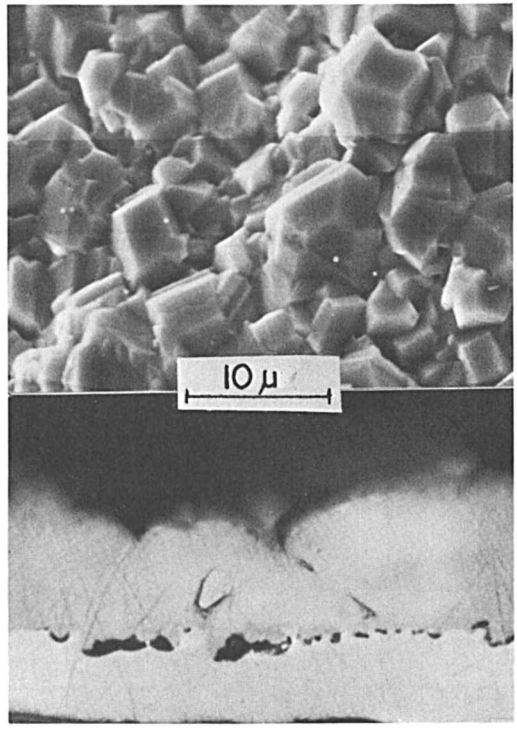

Journal of Crystal Growth

Figure 12. A GaP electrodeposit on a silicon substrate: (top) *surface;* (bottom) *cross-sectional view* (21).

that the GaP epitaxial layers were relatively easy to prepare but fell short of providing a sufficiently refined process to allow adequate comparison of the properties of electrochemically produced material to that produced in conventional processes. Several years later Yamamoto and Yamaguchi (*20*) developed a technique for electrodepositing ZnSe from a molten salt bath containing $NaSeO_3$ and ZnO.

De Mattei et al. (*21*) recently identified the variables that critically determine the morphology and uniformity of electrodeposited GaP layers. Using a molten salt composition containing 75.1 wt % sodium metaphosphate ($NaPO_3$), 7.7% sodium fluoride (NaF), and 17.2% gallium oxide (Ga_2O_3), GaP was electrodeposited in the 750°–900°C range by the following reactions:

$$\text{Cathode: } 16e^- + Ga_2O_3 + 8PO_3^- \rightarrow 2GaP + 3O^{2-} + 6PO_4^{3-}$$
$$16e^- + Ga_2O_3 + 2PO_3^- \rightarrow 2GaP + 9O^{2-} \qquad (26)$$

Anode: $2O^{2-} \rightarrow O_2 + 4e^-$

$$2PO_4^{3-} \rightarrow 2PO_3^- + O_2 + 4e^- \quad (27)$$

The apparatus used was similar to that shown in Figure 3. The crucible used was graphite, which also served as the anode to help scavenge the O_2 in the system by the reaction

$$C + O_2 \rightarrow CO_2\uparrow \quad (28)$$

Growths were attempted on three different substrate materials: (1) graphite, (2) phosphorus-doped *n*-type (100) silicon (0.3 Ω · cm), and (3) sulfur-doped *n*-type (111) GaP single-crystal wafers.

Figure 12 shows a GaP layer electrodeposited on an Si substrate at 900°C and 20 mA · $(cm^2)^{-1}$. The minimum decomposition potential was 0.5 V. The layer is similar in appearance to GaP layers produced on silicon by organometallic chemical vapor deposition (22). Silicon was chosen because of its availability and close lattice match with GaP. Si, however, appeared to react slightly with the melt to form SiO_2, and since there is also a large thermal expansion mismatch between Si and GaP, the use of Si as a useful substrate material is limited.

GaP substrates were also found to react with the melt at temperatures of 900°C or greater. At 800°C, however, the reaction is reduced to a

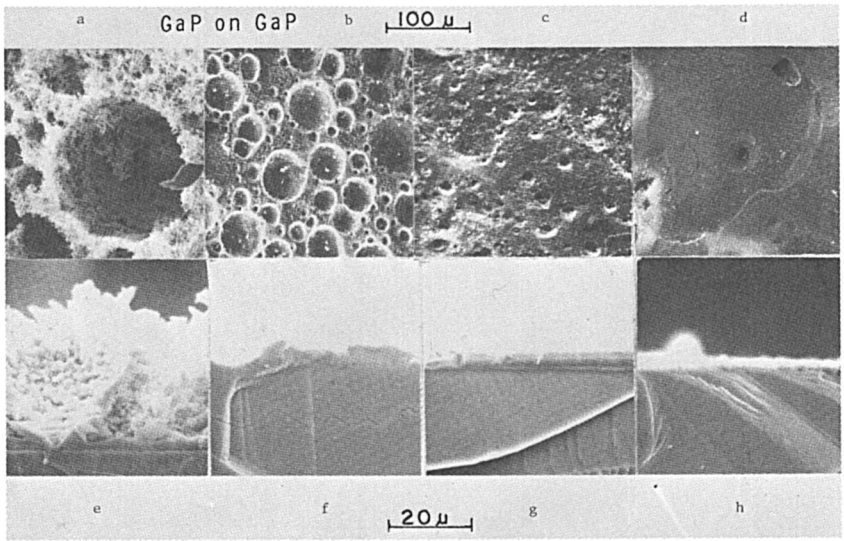

Journal of Crystal Growth

Figure 13. GaP electrodeposits on GaP substrates for a deposition time of 20 min at current densities of 48 mA · $(cm^2)^{-1}$ (a and c); 24 mA · $(cm^2)^{-1}$ (b and f); 12 mA · $(cm^2)^{-1}$ (c and g); and 6 mA · $(cm^2)^{-1}$ (d and h) (21).

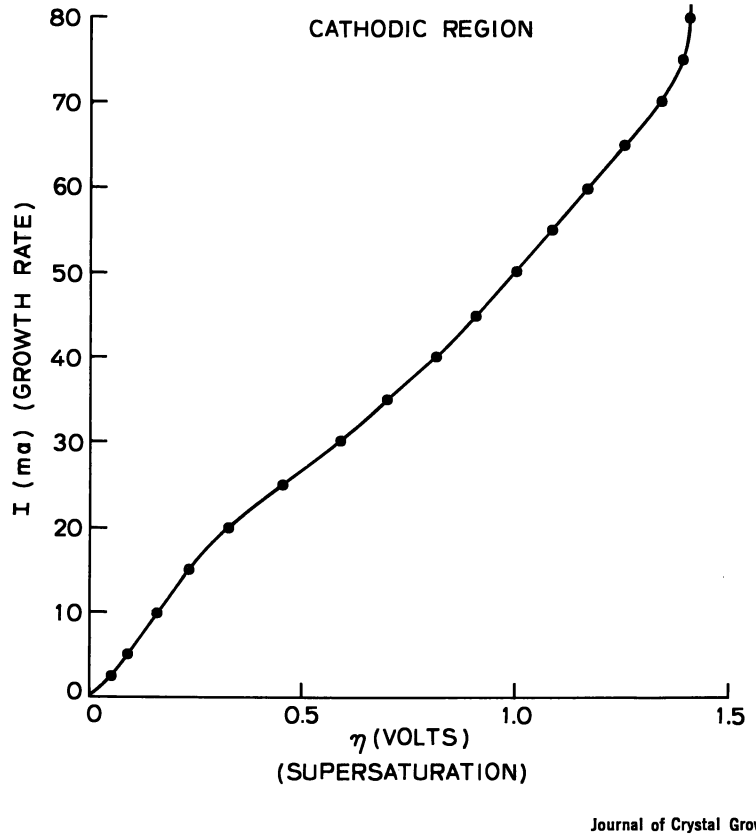

Figure 14. Plot of current (I) versus overpotential (η) for the deposition of GaP on GaP (21)

point where etching is not serious. The minimum decomposition potential was 1.16 V. To increase the conductivity of the electrodeposit and avoid dendritic growth, the researchers added 0.1% ZnO to the melt, giving a Zn-doped layer. Figure 13 shows a series of experiments run with a systematic variation in cathodic current density [6–48 mA · $(cm^2)^{-1}$]. The cross sections of the deposits prepared at the lower current density show the formation of coherent layers of uniform thickness. There was no evidence of dendrites or polycrystals. At 12 mA · $(cm^2)^{-1}$ and greater, craters appeared at the surface, and they increase in size and depth as the current density increases. These craters are related to the formation of excess phosphorus (gas bubbles) at the cathode. The formation of small GaP dendrites adjacent to the bubbles is quite visible. It was clear from this study that current densities below 10–20 mA · $(cm^2)^{-1}$ are necessary for stable growth conditions and the preparation of uniform layers of controlled thickness.

In order to understand the influence of growth rate (current density) on the growth process, the researchers plotted I against η (using a GaP reference electrode), as shown in Figure 14. The curve consisted of (1) an initial linear region, which is postulated to represent a region where growth is controlled by volume diffusion of solute ions; (2) a transition region; and (3) a second linear region at high current densities, which is also volume-diffusion-controlled and where the growth is highly dendritic.

Figure 15 shows two GaP layers grown at 800°C and at 10 mA · $(cm^2)^{-1}$. The layer on the left was deposited in 20 min, on the right in 3 hr. Note that the surface features are relatively smooth.

No property measurements were made in this study, nor was there any attempt to improve the purity of the deposit by starting with ultra-high purity chemicals or by preelectrolysis of the molten salt bath.

InP

InP has become, in recent years, a potentially important material for electronic device applications. It has been traditionally difficult to grow high-quality single crystals of this material because the high vapor pressure of P makes stoichiometry, and therefore the electronic properties, difficult to control. InP is subject to thermal decomposition by loss of P. Conventional methods utilize temperatures near the melting point (1062°C), where the equilibrium pressure is 27.5 atm. The apparatus

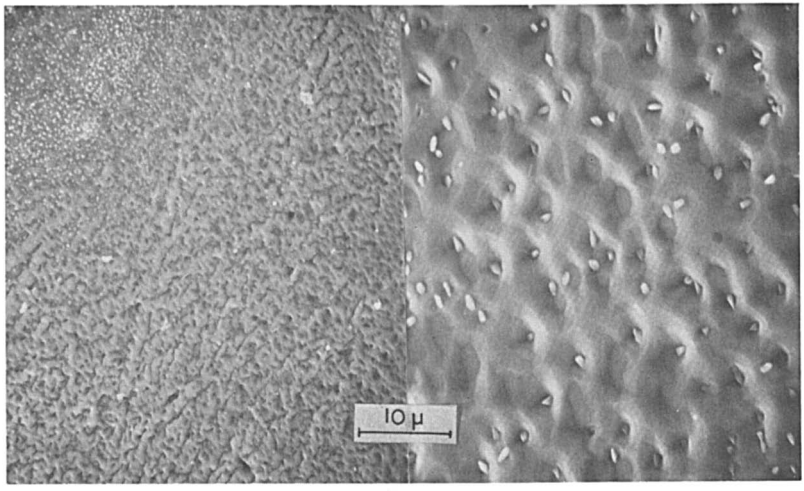

Journal of Crystal Growth

Figure 15. GaP layers electrodeposited at 800°C and 10 mA · $(cm^2)^{-1}$ for 20 min (left) *and 3 hr (right)* (21)

Table III. Solvent Systems Studied for InP Electrodeposition

Solvent	*Major Advantages*	*Major Disadvantages*
LiCl–KCl	Low melting point eutectic (328°C). High solubility for In_2O_3 and InF_3	High volatility. Reactivity with nickel. No InP deposits.
$NaPO_3$–NaF	Used for electrodeposition of GaP	High viscosity. Rather high mp (490°C). Low solubility of In_2O_3 at ~ 600°C.
LiF–NaF–KF	Oxygen-free. Low mp eutectic (454°C). Low viscosity. Has given InP deposits.	Low solubility for In_2O_3 and InF_3. KPF_6 as source of phosphorus is very hygroscopic.
Li_2O–B_2O_3–LiF	Used widely in electrocrystallization e.g. for LaB_6. Quite low viscosity and volatility.	Very low solubility for In_2O_3
$NaPO_3$–NaF–KPO_3–KF	Lower mp eutectic (~ 439°C). Gives good InP deposits. Low volatility	Rather high viscosity
$LiPO_3$–LiF–KPO_3–KF	Lower viscosity than $NaPO_3$–NaF–KPO_3–KF	Lower solubility for In_2O_3 than $NaPO_3$–NaF–KPO_3–KF — (≲ 1m/o). LiF is insoluble in water.
$LiPO_3$–LiF–$NaPO_3$–NaF	Very low melting point (300°C)	Has not given InP deposits. LiF is insoluble in water.

used is expensive and under a high ambient pressure, which is potentially dangerous.

Elwell and Feigelson (*23*) have recently started a program to investigate the conditions necessary to prepare high-quality InP epitaxial layers and crystals by MSE and to study their electronic properties. Electrochemical synthesis can provide control over stoichiometry and impurities, as stated before. Use of a low melting solvent and operation under a slightly positive pressure should help to control P evaporation. Generally, the defect concentration would be expected to be lower in materials prepared under these conditions, and the electrochemical equipment is inexpensive and easy to assemble.

While it was expected that InP would electroplate as readily as GaP from a similar bath composition by simply substituting In_2O_3 for Ga_2O_3, as suggested by Cuomo and Gambino (*19*), this was found not to be the case because of significant chemical dissimilarities between In and Ga salts. In compounds were less soluble in the melts studied and had higher vapor pressures than similar Ga compounds.

Table III gives an idea of the various molten salts studied for the electrodeposition of the InP. The attractiveness of a completely nonoxide system such as the Flinak (LiF, NaF, KF eutectic) + InF_3 + KPF_6 is obvious, but so far a suitable, stable melt composition has not been found from which InP could be deposited.

The most suitable bath found to date for InP electrodeposition is a quaternary solvent composition containing $NaPO_3/KPO_3/NaF/KF$ (Pofnak) and In_2O_3 as the source of In. The In_2O_3 solubility was greater in this melt than in a comparable melt of $LiPO_3/KPO_3/LiF/KF$, which had a lower viscosity and melting temperature. The InP deposits from Pofnak were of better quality. The Pofnak melt, therefore, has received the most attention to date. Table IV shows the suitability of various electrode materials for InP deposition in this melt. Of the metal cathodes studied, only nickel was reasonably compatible with the melt and the InP deposit. Two other cathode materials were found to be very good substrate materials, InP and CdS single crystals. The CdS_3InP heterojunction is a potentially important structure for solar cell application, and the electrodeposition method provides a low-cost process for producing such a material.

Table IV. Cathode Materials Studied for InP Electrodeposition

Material	*Adhesion of InP Deposit*
Graphite (rod)	Poor; adheres in small, isolated regions.
Germanium (single crystal)	Poor; adheres in isolated patches only.
Pyrolytic graphite	Fairly poor; only little better than normal graphite.
Tungsten (sheet)	Very poor; no trace of InP shown by microscope.
Indium phosphide (single crystal)	Very good
Molybdenum (sheet)	Very poor
Gold (foil)	Attacked by phosphate melts
Niobium (sheet)	Poor
Platinum (foil)	Attacked by phosphate melts
Cadmium sulfide (single crystal)	Very good
Nickel (sheet)	Good
Tantalum (sheet)	Very poor

Figure 16. InP layer electrodeposited on a CdS substrate

Many InP deposits have been put down on CdS substrates, one of which is shown in Figure 16. Thicknesses range from 1–10 μm depending upon deposition time. At present, an analysis of surface morphology, chemical composition, impurity content, and electrical properties is underway. The effectiveness of electrochemical purification techniques is also being studied in these experiments.

The general conditions used to electrodeposit InP on CdS from the Pofnak melt are as follows: (1) melt composition 60.9% $NaPO_3$, 14.0% KPO_3, 20.5% NaF, 4.7% KF, 3% In_2O_3 (mol %); (2) cell temperature 600°C; (3) cell potential 0.90 V ($E_d \approx 0.80$ V); (4 current density about 5 mA · $(cm^2)^{-1}$; (5) deposition time 1 hr.

GaAs

A few arsenides (*see* Table II) had been previously electrodeposited. De Mattei et al. (*24*) investigated the possibility of electrodepositing the most important of III–V semiconductors, GaAs. As a starting point, they attempted simply to substitute $NaAsO_3$ (sodium meta arsenate) for $NaPO_3$ in the previously described GaP growth solution. Since the meta arsenate is easily reduced, with conversion of As^{5+} to As^{3+} or elemental As in the presence of carbon, metals, or GaAs, they found $NaAsO_2$ (sodium arsenite) to be a more suitable source of As for GaAs electrodeposition. The melt composition that gave the best results consisted of 67.4% B_2O_3, 20.3% NaF, 4.2% Ga_2O_3, and 8.1% $NaAsO_2$, by weight. The molar concentrations of $NaAsO_2$ and Ga_2O_3 were 4.1% and 1.4%, respectively.

The B_2O_3 was used to reduce the melt temperature and thereby the volatility of $NaAsO_2$ at the electrodeposition temperatures, which were in the range 720°–760°C. The decomposition potential for deposition on a GaAs substrate was 1.7 V, and it was 2.4 V on nickel. An epitaxial 10-μm-thick layer of GaAs was deposited on a GaAs substrate.

Conclusions

Molten salt electrochemistry is an old technology that has just recently begun to be considered seriously for use in crystal growth. While conventional techniques utilize a thermal driving force, electrodeposition is an electronically driven process, and, as such, the growth process in principle can be very precisely controlled. Recent work has concentrated on understanding the electrodeposition processes with respect to both nucleation and growth phenomena, to permit the controlled growth of large high-quality single crystals. The application of this knowledge to the preparation of important semiconductor materials such as Si, InP, GaAs, and SiC has just started, and the competitiveness of molten salt electrochemical crystal growth with conventional processes will be evaluated over the next few years.

Glossary of Symbols

A = area of electrode
C_L = concentration of solute in liquid
C_S = concentration of solute in solid
D = solute diffusion coefficient
D/Λ = drift velocity
d = crystal diameter
dy/dt = maximum allowable pull rate
E^0 = standard cell potential
E_d = decomposition potential
F = Faraday's constant
i = current density (I/A)
I = cell current
K = growth rate constant
k = distribution coefficient
k' = constant
l = step spacing
M = molecular weight
MSE = molten salt electrochemistry
Q = total charge
R = gas constant or impedance
R_{ct} = impedance due to charge transfer

R_{ik} = impedance due to interface attachment kinetics
R_{vd} = impedance due to volume diffusion
T = temperature (K)
V = volume
v = linear growth rate
w = rotation rate
z = number of electrons transferred
[ ] = concentration or activity of reacting species
A = anode species (electrochemically oxidized)
C = cathode species (electrochemically reduced)
C = constant
E = equilibrium potential
$E_{d(imp)}$ = decomposition potential of impurity
$E_{d(cmpd)}$ = decomposition potential of compound
n = number of electrons transferred uer unit of material deposited
y = ionization state for anode species
z = ionization state for cathods species
Δ = relative supersaturation
ϵ = deposition efficiency
η = overpotential
η_e = equilibrium concentration of solute
Λ = adsorption parameter
Λ_s = surface diffusion parameter
λ = mean distance traveled by an adsorbed molecule
ρ = density
Ω = molar volume
δ = boundary layer width
σ = relative supersaturation
σ_1 = constant

Literature Cited

1. Kunnmann, W. "Preparation and Properties of Solid State Materials"; Lefever, R. A., Ed.; Dekker: New York, 1971; p. 1.
2. Wold, A.; Bellavance, D. "Preparative Methods in Solid State Chemistry"; Hagenmuller, P., Ed.; Academic: New York, 1972; p. 279.
3. Elwell, D. "Crystal Growth and Materials"; Kaldis, E.; Scheel, H. J., Eds.; North Holland: Amsterdam, 1976; p. 606.
4. Bostanov, V. *J. Cryst. Growth* **1977**, *42*, 194.
5. Elwell, D.; De Mattei, R. C.; Zubeck, I. V.; Feigelson, R. S.; Huggins, R. A. *J. Cryst. Growth* **1976**, *33*, 232.
6. Gilmer, G. H.; Ghez, R.; Cabrera, N. *J. Cryst. Growth* **1971**, *8*, 79.
7. Zubeck, I. V.; Feigelson, R. S.; Huggins, R. A.; Pettit, P. A. *J. Cryst. Growth* **1976**, *34*, 85.
8. Andrieux, L. *Ann. Chim.* (Paris) **1929**, *12*, 423.
9. Elwell, D.; Zubeck, I. V.; Feigelson, R. S.; Huggins, R. A. *J. Cryst. Growth* **1975**, *29*, 65.

10. De Mattei, R. C.; Huggins, R. A.; Feigelson, R. S. *J. Cryst. Growth* **1976,** *34,* 1.
11. Levich, V. C. "Physiochemical Hydrodynamics"; Prentice-Hall: Englewood Cliffs, NJ, 1962.
12. De Mattei, R. C.; Feigelson, R. S. *J. Cryst. Growth,* in press.
13. Deville, H. St. C. *Compt. Rend.* **1854,** *39,* 323.
14. Ullik, F. *Ber. Akad. Wien* **1865,** *52,* 115.
15. Grjotheim, K.; Matiasovsky, K.; Fellner, P. *Can. Met.* **1971,** *Q10,* 19.
16. Boe, G.; Grjotheim, K.; Matiasovsky, K.; Fellner, P. *Can. Met.* **1971,** *Q10,* 179.
17. Cook, N. C. U.S. Patent Re. 25 630 1964; *Sci. Am.* **1969,** 38.
18. Cohen, U.; Huggins, R. A. *J. Electrochem. Soc.* **1976,** *123,* 381.
19. Cuomo, J. J.; Gambino, R. J. *J. Electrochem. Soc.* **1968,** *115,* 755.
20. Yamamoto, A.; Yamaguchi, M. *Jpn. J. Appl. Phys.* **1975,** *14,* 561.
21. De Mattei, R. C.; Elwell, D.; Feigelson, R. S., submitted for publication in *J. Cryst. Growth.*
22. André, J. P.; Hallais, J.; Schiller, C. *J. Cryst. Growth* **1975,** *31,* 147.
23. Elwell, D.; Feigelson, R. S., private communication.
24. De Mattei, R. C.; Elwell, D.; Feigelson, R. S. *J. Cryst. Growth* **1978,** *43,* 643.

RECEIVED September 29, 1978.

14

Rare Earth Gallium Garnet Crystal Growth and Related Chemistry

M. A. DIGIUSEPPE

Corporate Research Center, Allied Chemical Corporation, Morristown, NJ 07960

The chemistry of rare earth gallium garnets ($RE_3Ga_5O_{12}$, where RE = rare earth ion) is discussed. These materials, in the form of large, high-quality, single crystals, serve as substrates for magnetic-bubble memory devices. The Czochralski technique, which is used to grow rare earth gallium garnet single crystals weighing several kilograms, is reviewed. The relationship between melt composition, phase stability, and the growth of high-quality crystals is described. The phase separation of samarium–gallium garnet and gadolinium–gallium garnet to orthorhombic distorted perovskite and beta-gallium oxide is discussed.

The term garnet refers to a class of compounds crystallizing in the Ia3d space group. The garnet crystal structure was first reported for $\{Ca_3\}[Al_2](Si_3)O_{12}$ by Menzer (*1, 2*). The structure was refined later by several investigators (*3, 4, 5, 6*) using synthetic $\{Y_3\}[Fe_2](Fe_3)O_{12}$ crystals (*7*). The unit cell consists of 8 formula units with 24 ions occupying dodecahedral $\{c\}$ sites, 16 ions occupying octahedral $[a]$ sites, and 24 ions on tetrahedral (d) sites ({ }, [ ], and ( ) denote dodecahedral, octahedral, and tetrahedral sites, respectively). Since the structure is capable of accepting a large number of different ions, there are numerous ways of varying the physical properties of the resulting compounds (*8*).

The simplest chemical formula for a synthetic rare earth garnet can be represented as $\{RE_3\}[B_2](B_3)O_{12}$ (abbreviated $RE_3B_5O_{12}$) where RE is a rare earth ion and B is most commonly Al^{3+}, Ga^{3+}, or Fe^{3+}. The magnetic rare earth garnets contain rare earth ions on the $\{c\}$ site and

0-8412-0472-1/80/33-186-277$05.00/1

Fe^{3+} ions on the [a] and (d) sites. These garnets are ferromagnetic (*3, 4, 9*), with the net rare earth magnetic moments and the iron moments on the [a] site aligned in one direction, opposite to the direction of the iron moments on the (d) site. Since the discovery of growth-induced uniaxial magnetic anisotropy in these garnets (*10*), they have become the principal material used in magnetic-bubble memory devices. Magnetic bubbles are small cylindrical domains in which the direction of magnetization is opposite to that of the surrounding material. Under certain conditions these domains can be moved through the material and used to store information.

As a result of the incongruent melting nature of the $RE_3Fe_5O_{12}$ garnets, early investigations of garnet bubble materials were carried out on bulk single crystals grown in molten fluxes of PbO and B_2O_3. Unfortunately, it is usually difficult to obtain large defect-free crystals with this technique. This problem can be overcome by the use of liquid phase epitaxial (LPE) growth. This process can produce defect-free magnetic garnet films suitable for device applications on paramagnetic ⟨111⟩ oriented garnet substrates (*11, 12, 13*). The success of the LPE process, however, is dependent on the availability of high-quality, single-crystal substrate material.

Synthetic Rare Earth Garnets

It is important that the lattice parameter (a_0) of the substrate equal that of the film, since a lattice parameter mismatch can influence the magnetic properties of the film (*14, 15, 16, 17*). As seen in Table I, the $RE_3Ga_5O_{12}$ garnets (the 3:5 mole ratio of RE_2O_3 to Ga_2O_3 is used for simplicity; actual compositions can vary from this stoichiometry) have

Table I. Lattice Parameter (a_0) Range of Polycrystalline Yttrium and Rare Earth Aluminum, Iron, and Gallium Garnets

$RE_3Al_5O_{12}$

RE = Y^{3+}; a_0 = 12.01 Å
RE = $Lu^{3+} \rightarrow Gd^{3+}$; a_0 range is 11.91 Å–12.11 Å

$RE_3Fe_5O_{12}$

RE = Y^{3+}; a_0 = 12.38 Å
RE = $Lu^{3+} \rightarrow Sm^{3+}$; a_0 range is 12.28 Å–12.53Å

$RE_3Ga_5O_{12}$

RE = Y^{3+}; a_0 = 12.28 Å
RE = $Lu^{3+} \rightarrow Pr^{3+}$; a_0 range is 12.18 Å–12.56 Å

the same a_0 range as do the $RE_3Fe_5O_{12}$ garnets and therefore can be used as substrates for these garnet films.

The substrate material with the largest available lattice parameter in the $RE_3Ga_5O_{12}$ system is $Nd_3Ga_5O_{12}$ (a_0 = 12.509 Å) since $Pr_3Ga_5O_{12}$ melts incongruently and both Ce^{3+} and La^{3+} do not form a garnet phase due to the size restriction placed on the {*c*} site ion by the presence of the Ga^{3+} ion on the [*a*] site. Other substrate materials are available at discrete lattice parameter values between 12.509 Å and 12.28 Å (for example, $Sm_3Ga_5O_{12}$ at 12.439 Å and $Gd_3Ga_5O_{12}$ at 12.383 Å). This limited availability of substrate material adds to the difficulty of tailoring the magnetic properties of the film to the desired specifications since adjustments must be made in such a way as to keep the lattice parameter of the film equal to that of the available substrate.

Interest in obtaining a more extensive choice of substrate lattice parameters prompted the synthesis of substituted and mixed rare earth gallium garnets. Substitutions into the gallium garnet structure of various ions like Sc^{3+}, Ca^{2+}, Mg^{2+}, and Zr^{4+} offers ways of varying the lattice parameter of the substrate. Complex garnets such as $\{Nd_{3-y}RE_y\}[RE_x\text{-}Ga_{2-x}](Ga_3)O_{12}$, $\{La_{3-y}RE_y\}[RE_2](Ga_3)O_{12}$, and $\{RE_{3-y}Sc_y\}[Sc_2](Ga_3)\text{-}O_{12}$ have been obtained as single-phase polycrystalline materials and extensively characterized (*18, 19, 20, 21*). Many of these compounds exhibit lattice parameters greater than 12.509 Å; for example, in the $\{La_{3-y}RE_y\}[RE_2](Ga_3)O_{12}$ system a_0 exceeds 13.0 Å.

Czochralski Crystal Growth

The Czochralski technique (*22*) is the most widely accepted method for growing large, defect-free garnet crystals. The growth chamber is illustrated in Figure 1. A typical furnace is constructed of stabilized ZrO_2 tubing and granular ZrO_2, which insulate an rf-heated crucible. A glass bell jar is placed around the furnace assembly to control atmosphere. This is necessary because the crucible material (usually iridium) is susceptible to oxidation at high temperatures. The presence of a small amount of oxygen is necessary, however, to suppress the loss of Ga_2O_3. A rotating seed crystal oriented in the ⟨111⟩ crystallographic direction is dipped into the melt and slowly withdrawn. Crystal diameter is automatically controlled by either optical- or weight-sensing methods (*23, 24, 25*).

Most of the $RE_3Ga_5O_{12}$ garnets can be easily grown as single crystals by this technique. Crystals of $Gd_3Ga_5O_{12}$, which are used as substrate material for commercial garnet bubble films, are routinely grown at 3 mm · hr^{-1} with diameters to 7.6 cm and weights of 10 kg. These crystals usually contain less than one defect per square centimeter (*26*).

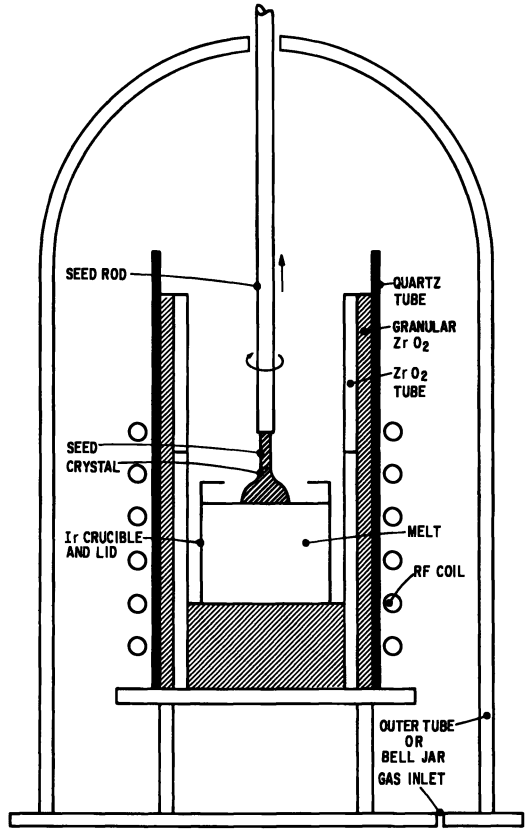

Figure 1. Czochralski furnace used for garnet crystal growth

The single-crystal growth of substituted garnets, on the other hand, has been achieved with only limited success. The solid solutions of $\{Nd_{3-x}Sm_x\}Ga_5O_{12}$, $\{Sm_{3-x}Gd_x\}Ga_5O_{12}$, and $\{Gd_{3-x}Dy_x\}Ga_5O_{12}$ have been grown as single crystals for $x = 0.25$, 0.5, and 0.75 (*27, 28*). The substitution of Sc^{3+} for Ga^{3+} on the [*a*] site in both $Y_3Ga_5O_{12}$ and $Gd_3Ga_5O_{12}$ produces single crystals with lattice parameters around 12.40 Å and 12.55 Å, respectively (*29*). Recent interest in garnet films with high Faraday rotation (*30, 31*) produced a need for substrates with $a_0 \approx$ 12.48 Å. This led to the crystal growth of $\{Gd_{3-x}Ca_x\}Ga_{5-y-z}Zr_yGd_zO_{12}$ and $Gd_3Ga_{5-x-y}Mg_xZr_yO_{12}$ (*31, 32*). Crystals in these systems exhibit some lattice parameter variation along the length of the crystal due to compositional nonuniformity. Variations in composition appear to be a chronic problem in many substituted systems, although they can be minimized with the utilization of very slow growth rates.

Czochralski Growth of High-Quality Crystals

Another important requirement for the substrate is crystalline perfection. Any defects that intersect the surface of the substrate can be propagated into the film. The presence of a large number of crystalline imperfections in the film will impair bubble mobility due to the pinning of the bubbles at the defect site. Defects can be introduced either during crystal growth or during fabrication (cutting, grinding, or polishing) of the boule into substrate wafers. During the substrate growth process, dislocations can initiate from the seed–crystal junction, inclusions, strain, or instability at the crystal growth interface.

The propagation of dislocations from the seed–crystal junction can be eliminated, or at least reduced, by reducing the seed diameter after it is inserted into the melt. Inclusions in garnet crystals (primarily iridium, Ga_2O_3 or RE_2O_3) occur from changes in the melt composition during growth. This can result from improper growth or atmospheric conditions as well as from the use of an incongruent-melting nominal composition. Czochralski-grown rare earth gallium garnet crystals exhibit lattice parameters larger than those of the corresponding $RE_3Ga_5O_{12}$ polycrystalline compositions (*see* Figure 2). This results from the partial occupation of [*a*] sites by the rare earth ion in the single crystal (*34, 35*). The general formula for the congruent-melting gallium garnet compositions can be represented as $\{RE_3\}[RE_xGa_{2-x}](Ga_3)O_{12}$, with the degree of rare earth [*a*] site substitution dependent upon the ionic radius of the rare earth ion. The congruent-melting composition for gadolinium gallium garnet is $\{Gd_3\}[Gd_{0.05}Ga_{1.95}](Ga_3)O_{12}$ (*36, 37*). Crystals grown from this composition have lattice parameters of 12.3835 Å and show no significant lattice

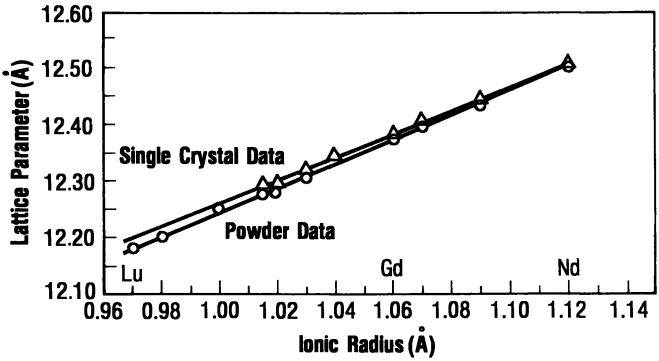

Figure 2. Lattice parameters of rare earth gallium garnet single crystals grown from $RE_3Ga_5O_{12}$ melts and polycrystalline $RE_3Ga_5O_{12}$ data versus rare earth dodecahedral ionic radius (34)

parameter variation (±0.0005 Å) along the length of the boule. Lattice parameters are determined with great accuracy [to a few parts per million (ppm) on nearly perfect single crystals] by using the Bond method (*38*). Other techniques using X-ray diffraction from two lattice planes also can be used but with less accuracy (*39*).

The shape of the solid–liquid interface during crystal growth also can influence crystal quality. The interface shape is determined by the convection pattern of the melt, which depends on temperature gradient, melt height, surface tension, melt viscosity, crucible diameter, crystal diameter, and crystal rotation rate. A detailed discussion of the melt growth process with respect to fluid dynamics can be found in the literature (*40*). Qualitatively, melt flow can be described in terms of natural and counterflow convection, the former being primarily dependent on temperature gradient and the latter on the diameter and rotation rate of the crystal (*40, 41*). The interface shape is convex toward the melt if natural convection predominates, Figure 3(a), and concave if the counterflow predominates, Figure 3(c). It becomes flat when there is a balance between the two flow patterns, Figure 3(b). For a fixed crystal diameter the interface shape will change from convex to flat and finally become concave as the rotation rate is increased (*42*).

The best-quality crystals are obtained with a flat solid–liquid growth interface. Garnet crystals oriented in the ⟨111⟩ crystallographic direction, grown with a convex solid–liquid interface contain (211) and (110) facets on the growth interface. These facets produce a macroscopic strain pattern (or core) in the crystal, as shown in Figure 4. Lattice parameter measurements on faceted and nonfaceted regions of $Gd_3Ga_5O_{12}$ have been made by using the Bond technique (*43*). These results, seen in Table II, show a variation in lattice parameter, possibly suggesting a variation in composition between these regions. Thus the presence of this type of strain in the substrate could adversely affect film properties. These facets and the strain associated with them are no longer present when a flat growth interface is achieved. This is accomplished with the proper choice of crystal diameter and rotation rate. Thus the crystal

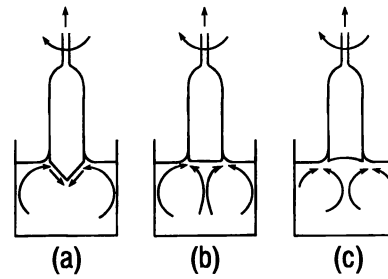

Figure 3. Crystal growth interface and a simplified representation of the convection flow pattern in the melt: (a) convex growth interface, natural convection predominates at slow rotation rates; (b) flat growth interface, natural and counterflow convections are balanced; (c) concave growth interface, counterflow convection predominates at excessive rotation rates.

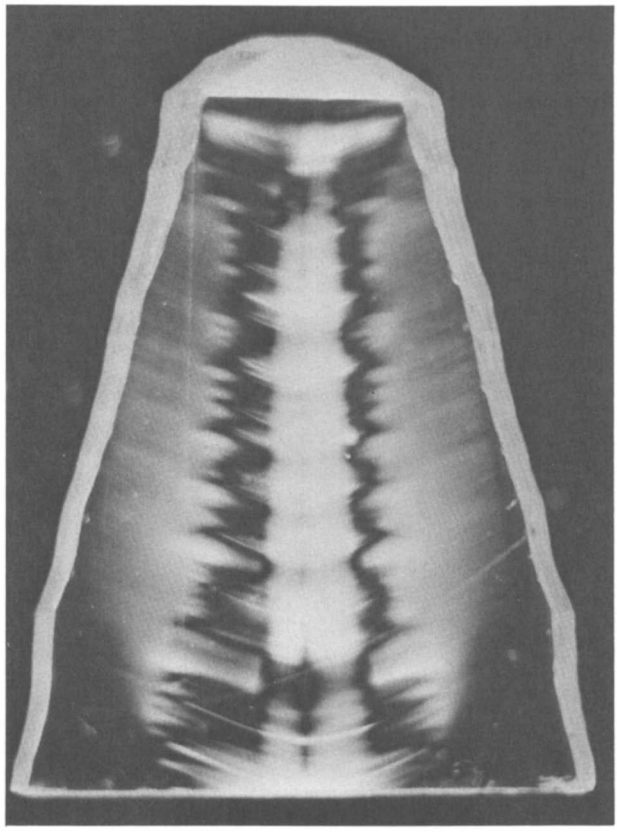

Figure 4. Strain field, viewed with polarized light, in a longitudinal cross section of the top of a <111> samarium gallium garnet crystal

grows initially with a convex interface until the final diameter is achieved, where an abrupt transition to a planar interface occurs. This transition and the (211) and (110) facet symmetry about the ⟨111⟩ growth axis are illustrated in Figure 5. The convex growth interface is useful, however, in the elimination of dislocations. Facets tend to be free of

Table II. Lattice Parameters for (211) and (110) Facets in $Gd_3Ga_5O_{12}$ (43)

	(211) Facets	*(110) Facets*	*Nonfaceted Region*
Lattice parameter a_0 (Å)	12.3841_4	12.3838_8	12.3824_0
Δa_0	0.0017	0.0014	

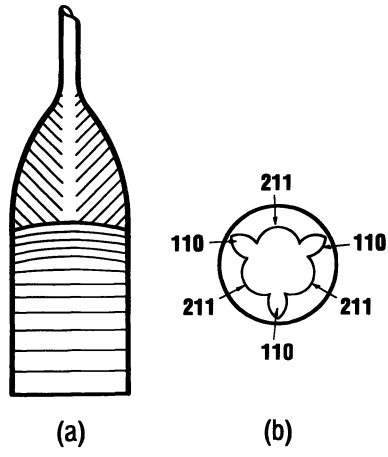

Figure 5. (a) Representation of strain pattern observed with polarized light in a longitudinal section of a garnet crystal. (b) Representation of facet strain pattern in a transverse section of a garnet crystal grown with a convex interface.

dislocations (*44*), so the faceted region between the seed and the final diameter of the crystal can be used to block the formation of dislocations and propagate existing defects towards the crystal edge.

Melt Chemistry

As mentioned previously, the growth atmosphere is an important factor in composition control and in the elimination of inclusions (*45*). An inert atmosphere is necessary, since iridium reacts with oxygen according to the following reactions (*46*):

$$Ir(s) + O_2 \overset{< 1100°C}{\rightarrow} IrO_2(s) \quad (1)$$

$$2IrO_2(s) + O_2 \overset{< 1100°C}{\rightleftarrows} 2IrO_3(g) \quad (2)$$

$$2Ir(s) + 3O_2 \overset{> 1100°C}{\rightleftarrows} 2IrO_3(g) \quad (3)$$

The presence of an inert atmosphere over the gallium garnet melt, on the other hand, results in the loss of Ga_2O_3 from the melt. This occurs through the formation of the volatile oxide $Ga_2O(g)$ as represented by the following equilibrium:

$$Ga_2O_3 \rightleftarrows Ga_2O(g) + O_2 \quad (4)$$

This equilibrium at ambient pressure depends on the partial pressure of oxygen and to some extent the type of crucible material used to contain the melt (*35*). With available pressure and temperature data (*47*) for

Equation 4, it is possible to achieve an acceptable balance between these two competing processes through the use of N_2 or Ar with a small partial pressure of oxygen.

The chemical reactions that take place when gallium oxide is lost from rare earth gallium garnet melts by vaporization at elevated temperatures, as illustrated by Reaction 4, can be represented by the following equations:

$$RE_3Ga_5O_{12} \rightarrow 3REGaO_3 + Ga_2O_3 \quad (5)$$

$$4REGaO_3 \rightarrow RE_4Ga_2O_9 + Ga_2O_3 \quad (6)$$

$$RE_4Ga_2O_9 \rightarrow 2RE_2O_3 + Ga_2O_3 \quad (7)$$

We have found that when gallium oxide loss is prevented and the maximum temperature of the melt exceeds a critical value, phase separation of garnet to distorted perovskite and beta-gallium oxide occurs (*48*):

$$RE_3Ga_5O_{12} \rightleftarrows 3REGaO_3 + Ga_2O_3 \quad (8)$$

It was observed in some instances after the Czochralski crystal growth of $Sm_3Ga_5O_{12}$ or $Gd_3Ga_5O_{12}$ that the residual melt crystallized as a perovskite and beta-gallium oxide mixture. When this mixture, which was stable at room temperature, was reheated to the respective garnet melting

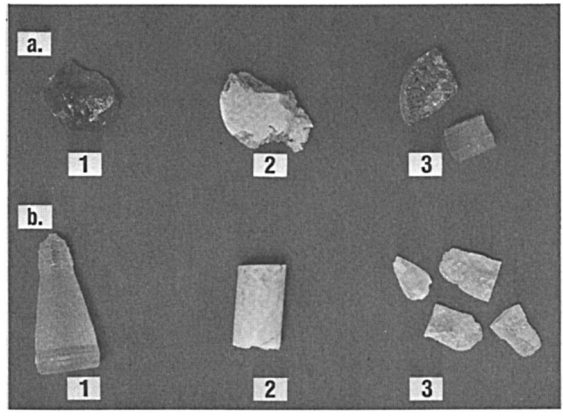

Figure 6. (a) (1) $Sm_3Ga_5O_{12}$; (2) after phase separation $Sm_3Ga_5O_{12} \rightarrow 3SmGaO_3 + Ga_2O_3$; (3) after reverse reaction $3SmGaO_3 + Ga_2O_3 \rightarrow Sm_3Ga_5O_{12}$ when perovskite–gallium oxide mixture is heated to the garnet melting point. (b) (1) $Gd_3Ga_5O_{12}$; (2) after phase separation $Gd_3Ga_5O_{12} \rightarrow 3GdGaO_3 + Ga_2O_3$; (3) after reverse reaction $3GdGaO_3 + Ga_2O_3 \rightarrow Gd_3Ga_5O_{12}$ when perovskite–gallium oxide mixture is heated to the garnet melting point (48).

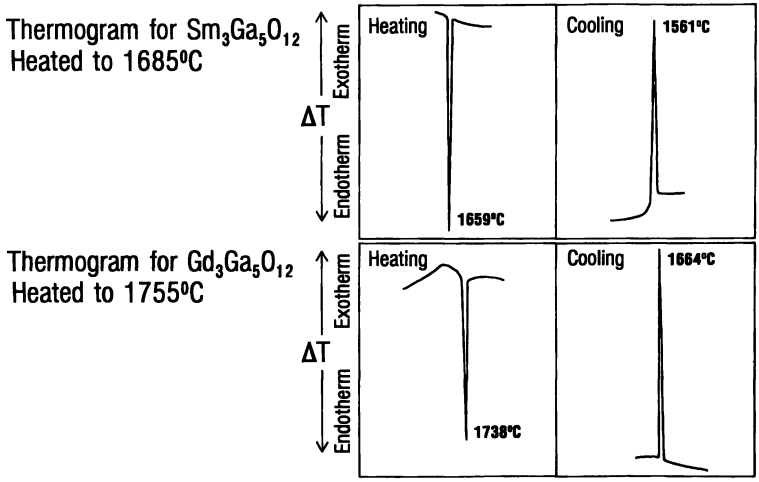

Figure 7. Thermograms for $Sm_3Ga_5O_{12}$ and $Gd_3Ga_5O_{12}$ heated to within 25°C above their respective melting points

point (T_m of $Sm_3Ga_5O_{12} \approx 1664$°C; T_m of $Gd_3Ga_5O_{12} \approx 1735$°C), monophase garnet reformed on cooling. These garnet and perovskite–gallium oxide mixtures are shown in Figure 6.

Differential thermal analysis (DTA) studies have shown Reaction 8 to be temperature-dependent and reversible. During cooling from 25°C above the garnet melting point, a single exotherm appeared, as shown

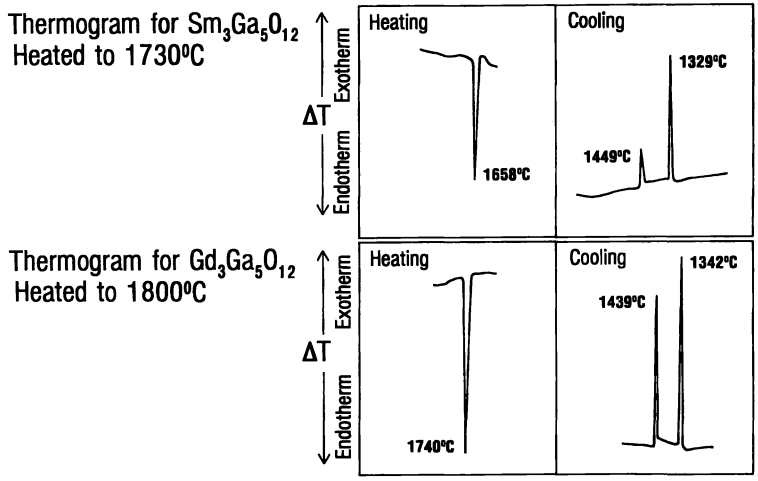

Figure 8. Thermograms for $Sm_3Ga_5O_{12}$ and $Gd_3Ga_5O_{12}$ heated to ≈ 70°C above their respective melting points

in Figure 7. The crystallized phase was identified as garnet. When maximum heating temperatures exceeded the melting point by more than 70°C, two exothermic transitions occurred on cooling corresponding to the crystallization of both $REGaO_3$ and Ga_2O_3 (*see* Figure 8). Upon repeated heating of the perovskite and gallium oxide mixture to 25°C above the garnet melting point, reversion to the garnet phase occurred. In most instances four or more heating cycles were necessary to achieve this reverse transformation (*see* Figure 9).

The garnet phase appears to be thermodynamically more stable than the perovskite phase in the solid state. Garnet can be prepared by direct solid state reaction of rare earth and gallium sesquioxides; however, attempts to prepare perovskite in an analogous manner during this work

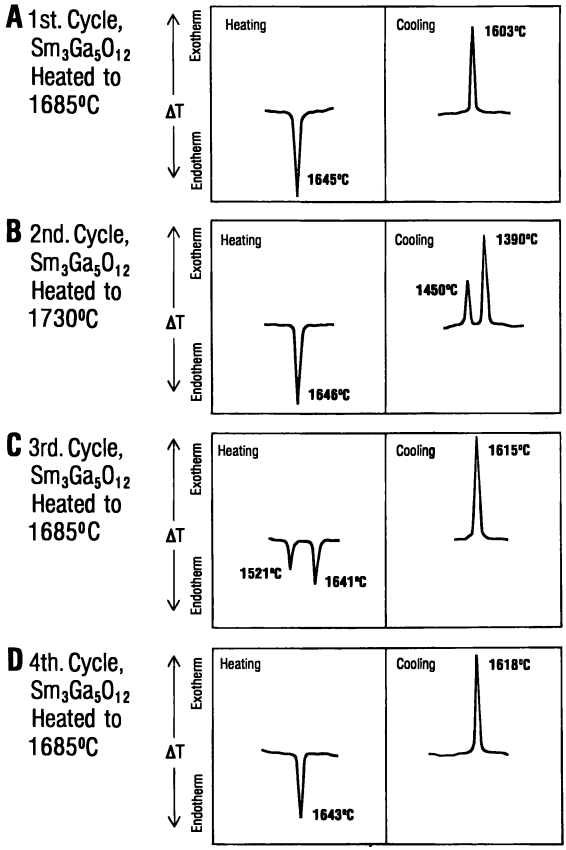

Figure 9. Thermograms showing the reversible nature of Reaction 8 for $Sm_3Ga_5O_{12}$: (a) first cycle, $Sm_3Ga_5O_{12}$ heated to 1685°C; (b) second cycle, $Sm_3Ga_5O_{12}$ heated to 1730°C; (c) third cycle, $Sm_3Ga_5O_{12}$ heated to 1685°C; (d) fourth cycle, $Sm_3Ga_5O_{12}$ heated to 1685°C.

and also by other investigators (*49*) were unsuccessful, with the resulting products consisting of garnet plus another phase. This behavior could be related to the stabilizing influence that the tetrahedral site provides for gallium in the garnet structure. The perovskite, however, can be prepared only by cooling molten samples of equimolar mixtures of sesquioxides. Consequently, the crystallization process has an important influence on the formation of the perovskite phase.

A qualitative estimation of the crystallization activation energies obtained from the shape of the garnet and perovskite crystallization exotherms (*50*) indicates that perovskite has a lower crystallization activation energy than garnet and is kinetically favored over garnet in the crystallization process. It is possible that the observed phase separation results from structural changes in the liquid as the temperature of the liquid is increased. Similar structural changes have been found to occur in Al_2O_3 (*51*).

Summary

The Czochralski technique can be used to grow large, high-quality, rare earth gallium garnet single crystals for use as substrates in magnetic-bubble memory devices. Some limited success has been achieved also with the crystal growth of both substituted and mixed rare earth gallium garnets. The crystal quality of these materials can be controlled by the growth conditions. Defects caused by iridium oxidation and the loss of Ga_2O_3 can be eliminated with the appropriate temperature gradient and growth atmosphere. The phase separation of garnet to distorted perovskite and gallium oxide, which could have a detrimental effect on the crystal growth process, can be prevented by proper thermal treatment.

Acknowledgments

The author thanks P. F. Tumelty for helpful discussions and S. L. Soled for relevant comments.

Literature Cited

1. Menzer, G. *Z. Kristallogr.* **1926**, *63*, 157–158.
2. Menzer, G. *Z. Kristallogr.* **1928**, *69*, 300–396.
3. Geller, S.; Gilleo, M. A. *Acta. Crystallogr.* **1957**, *10*, 239.
4. Geller, S.; Gilleo, M. A. *J. Phys. Chem. Solids* **1957**, *3*, 30–36.
5. Euler, F.; Bruce. J. A. *Acta. Crystallogr.* **1962**, *15*, 1268–1270.
6. Ibid. **1965**, *19*, 971–978.
7. Nielsen, J. W.; Dearborn, E. F. *J. Phys. Chem. Solids* **1958**, *5*, 202–207.
8. Geller, S. *Z. Kristallogr.* **1967**, *125*, 1.
9. Bertaut, F.; Forrat, F.; Herpin, A.; Mériel, P. *C. R. Hebd. Seances Acad. Sci.* **1956**, *243*, 898–901.

10. Bobeck, A. H.; Spencer, E. G.; Van Uitert, L. G.; Abrahams, S. C.; Barnes, R. L.; Grodkiewitz, W. H.; Sherwood, R. C.; Schmidt, P. H.; Smith, D. H.; Walters, E. N. *Appl. Phys. Lett.* **1970**, *17*, 131.
11. Linares, R. C. *J. Cryst. Growth* **1968**, *3*, *4*, 443–466.
12. Shick, L. K.; Nielson, J. W.; Bobeck, A. H.; Kurtzig, A. J.; Michaelis, P. C.; Reekstin, J. P. *Appl. Phys. Lett.* **1971**, *18*, 89
13. Levenstien, H. J.; Licht, S.; Landorf, R. W.; Blank, S. L. *Appl. Phys. Lett.* **1971**, *19*, 486.
14. Gianola, U. F.; Smith, D. H.; Thiele, A. A.; Van Uitert, L. G. *IEEE Trans. Magn.* **1969**, *MAG-5*, 558.
15. Bobeck, A. H. *Bell System Tech. J.* **1967**, *46*, 1901.
16. Thiele, A. A. *Bell System Tech. J.* **1971**, *50*, 725.
17. Mee, J. E.; Besser, P. J.; Elkins, P. E.; Glass, H. L.; Whitcomb, E. C. NASA Report CR-112012, February 1972.
18. Suchow, L.; Kokta, M.; Flynn, V. *J. Solid State Chem.* **1970**, *2*, 137–143.
19. Suchow, L.; Kokta, M. *J. Solid State Chem.* **1972**, *5*, 85–92.
20. Kokta, M.; Grasso, M. *J. Solid State Chem.* **1973**, *8*, 357–359.
21. Mondegarian, R.; Kokta, M.; Suchow, L. *J. Solid State Chem.* **1976**, *18*, 369–375.
22. Czochralski, J. *Z. Phys. Chem.* **1918**, *92*, 219.
23. Kyle, T. R.; Zydzik, G. *Mater. Res. Bull.* **1973**, *8*, 443–450.
24. Reinert, R. C.; Yatsko, M. A. *J. Cryst. Growth* **1974**, *21*, 283.
25. Digges, T. G., Jr.; Hopkins, R. H.; Seidensticker, R. G. *J. Cryst. Growth* **1975**, *28*, *29* 326.
26. Brandle, C. D. *J. Appl. Phys.* **1978**, *49*(3), 1855–1858.
27. Brandle, C. D.; Valentino, A. J. *J. Cryst. Growth* **1972**, *12*, 3–8.
28. Moudy, L. A.; Austerman, S. B. *Advances in X-Ray Anal.* **1973**, *16*, 177–185.
29. Chow, K.; Keig, G. A.; Hawley, A. M. *J. Cryst. Growth* **1974**, *23*, 58–64.
30. Daval, J.; Ferrand, B.; Geynet, J.; Challeton, D.; Peuzin, J. C. *Mater. Res. Bull.* **1975**, *10*, 95–102.
31. Kestigian, M.; Bekebrede, W. R.; Smith, A. B. *J. Cryst. Growth* **1977**, *42*, 343–344.
32. Mateika, D.; Herrnring, J.; Rath, R.; Rusche, Ch. *J. Cryst. Growth* **1975**, *30*, 311–316.
33. Mateika, D.; Rusche, Ch. *J. Cryst. Growth* **1977**, *42*, 440–444.
34. Brandle, C. D.; Barns, R. L. *J. Cryst. Growth* **1974**, *26*, 169–170.
35. Carruthers, J. R.; Kokta, M.; Barns, R. L.; Grasso, M. *J. Cryst. Growth* **1973**, *19*, 204–208.
36. Makino, H.; Nakamura, S.; Matsumi, K. *Jpn. J. Appl. Phys.* **1976**, *15*(3), 415–419.
37. Allibert, M.; Chatillon, C.; Mareschal, J.; Lessalde, F. *J. Cryst. Growth* **1974**, *23*, 289.
38. Bond, W. L. *Acta Crystallogr.* **1960**, *13*, 814.
39. Isomae, S.; Kishino, S.; Takagi, K.; Ishi, M.; Maki, M. *J. Appl. Crystallogr.* **1976**, *9*, 342.
40. Carruthers, J. R. "Treatise on Solid State Chemistry"; Hannay, N. B., Ed.; Plenum: New York, 1975; Vol. 5, pp. 325–406.
41. Takagi, K.; Fukazawa, T.; Ishii, M. *J. Cryst. Growth* **1976**, *32*, 89–94.
42. Cockayne, B.; Lent, B.; Rosington, J. M. *J. Mater. Sci.* **1976**, *11*, 259–263.
43. Cockayne, B.; Roslington, J. M.; Vere, A. W. *J. Mater. Sci.* **1973**, *8*, 382–384.
44. Cockayne, B.; Roslington, J. M. *J. Mater. Sci.* **1973**, *8*, 601–605.
45. Brandle, C. D.; Miller, D. C.; Nielsen, J. W. *J. Cryst. Growth* **1972**, *12*, 195–200.
46. Cordfunke, E. H. P.; Meyer, G. *Recl. Trav. Chim. Pays-Bas* **1962**, *81*, 495–504.
47. Shchukarev, S. A.; Semenov, G. A.; Rat'kovskii, I. A. *Russ. J. Inorg. Chem. (Engl. Transl.)* **1969**, *14*(1), 1–5.

48. DiGiuseppe, M. A.; Soled, S. L. *J. Solid State Chem.* **1979**, *30*, 203–208.
49. Geller, S.; Curlander, P. J.; Ruse, G. F. *Mater. Res. Bull.* **1974**, *9*, 637.
50. Baró, M. D.; Clavaguera, N.; Bordas, S.; Clavaguera-Mora, M. T.; Casas-Vázquez, J. *Therm. Anal.* **1977**, *11*, 271.
51. Nukui, A.; Tagai, H.; Morikawa, H.; Iwai, S. I. *J. Am. Ceram. Soc.* **1976**, *59*(11–12), 534.

RECEIVED November 10, 1978.

15

Rare Earth Intermetallics for Magnetostrictive Devices

JOSEPH B. MILSTEIN[1]

Naval Research Laboratory, Washington, D.C. 20375

A discussion of methods of preparation of single crystals of cubic Laves phase compounds, $REFe_2$, and their solid solutions is given. Motivation for the preparative methods studied and an explanation of how the materials prepared might be utilized in magnetostrictive devices are provided by a review of the unusual physical properties of the materials. Fundamental experimental results obtained in measuring these physical properties lead to the explanation of the interatomic magnetic interactions of rare-earth and iron atoms in $REFe_2$ crystals, confirmation of the single-ion model as appropriate to these systems, elucidation of the nature of the magnetocrystalline anisotropy, and a demonstration of the potential for and preferred mode of application of the materials in both bulk and surface wave magnetoacoustic devices.

Magnetostrictive materials have the property that their physical dimensions are changed during the process of magnetization. The magnetostrictive effect is used, for example, in certain sonar devices such as the free-flooded nickel scroll magnetoacoustic transducer. The magnetostrictive strain available in cube-textured oxide-annealed nickel is only 35 parts per million (ppm), however. Larger strains, available at room temperature and small magnetic fields, would be highly desirable for device applications.

The lanthanide rare earth metals exhibit large magnetostriction, up to 10,000 ppm, but at cryogenic temperatures. The metals iron, cobalt,

[1] Current address: Photovoltaic Advanced Silicon Branch, Solar Energy Research Institute, 1617 Cole Boulevard, Golden, CO 80401.

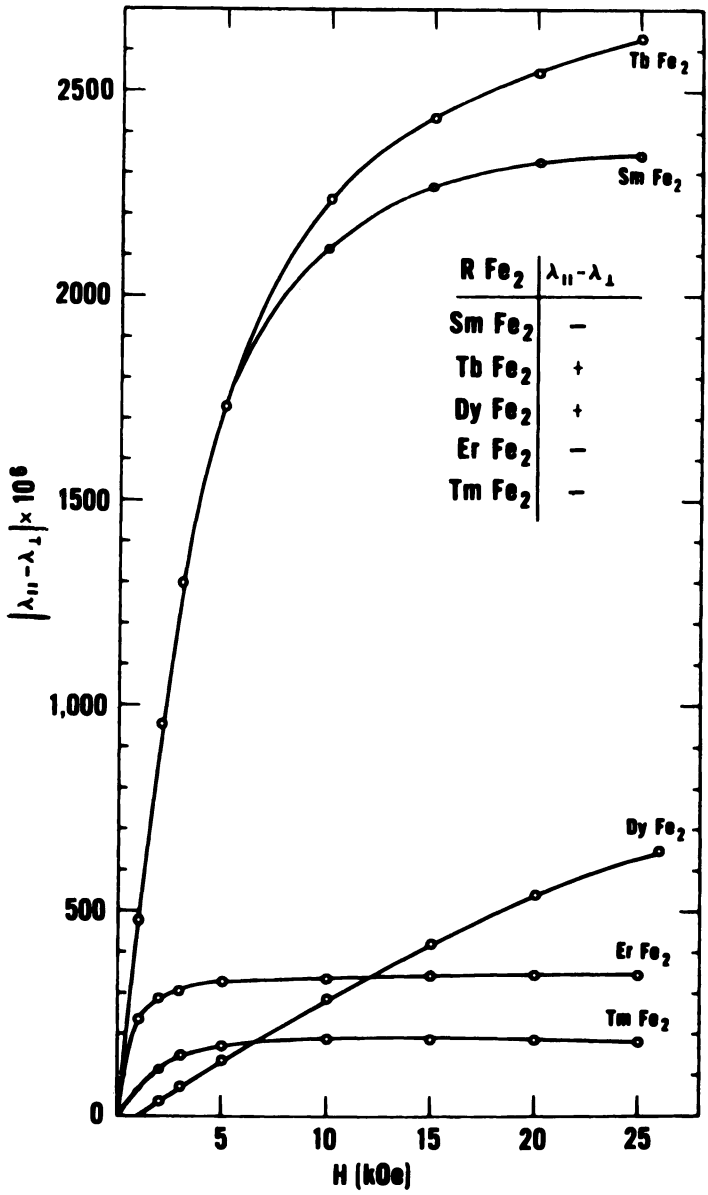

Figure 1. Room-temperature magnetostrictive strain and strain polarity as a function of magnetic field (5)

and nickel are good ferromagnets at room temperature. One therefore might expect that combinations of these metals, as alloys or intermetallic compounds, could exhibit large magnetostrictive strains at room temperature. The discovery of large, room-temperature magnetostrictive strains in the class of cubic Laves-phase (*1*) intermetallic compounds, $REFe_2$, where RE represents a lanthanide rare earth metal, was made at the Naval Research Laboratory (NRL) (*2*) and the Naval Surface Weapons Center (NSWC) (*3*). Examples of the strain as a function of field relationship are shown in Figure 1 for a number of compositions.

Pure binary $REFe_2$ compounds suffer from a number of problems, however. Large magnetic fields, of the order of several tesla, are required to produce the large magnetostrictions. This is impractical from a device standpoint. In certain cases magnetic saturation is not obtained even at 12T. The magnetostrictive strains vary as a function of rare-earth elements, temperature, and crystallographic orientation. The materials are brittle in polycrystalline form. The rare earth metals are extremely reactive at elevated temperatures, which poses serious fabrication problems. Lastly, the rare earth metals are expensive at this time. These problems will be addressed in the following sections.

The Physics of Magnetostriction in $REFe_2$ Compounds

The structure of the cubic Laves-phase $REFe_2$ compounds is shown in Figure 2. The lattice parameter for the Tb, Dy, Ho, and Er binary compounds are approximately 7.34, 7.32, 7.30, and 7.28 Å, respectively (*4*). From an examination of the structure, and from the lattice parameter, one sees that the shortest rare earth–rare earth distance is approximately 3.2 Å, roughly the same or slightly shorter than that in pure rare-earth metals. This distance will be discussed in a later section.

How, then, does one obtain a material that has large magnetostrictive strain at low fields? The pure binary compositions have, depending on the rare-earth metal, either positive or negative magnetostriction (λ) and either positive or negative anisotropy constants (K_1, K_2). These are presented in Table I and are based on observed values and theoretical estimates by Clark (*5*). The anisotropy of the $REFe_2$ phases is dominated by the rare-earth metal.

To have the best magnetostrictive response a material should have as large a magnetostriction (λ) and as small a total anisotropy (K) as possible, as the figure of merit used, which is proportional to λ^2/K, will be maximized. Examining the table entries, one sees that some combination of Tb, Dy, Ho, and Fe will yield positive magnetostriction and, in principle, zero K_1 and K_2, assuming that the parameters λ, K_1, and K_2 may be combined in a linear manner.

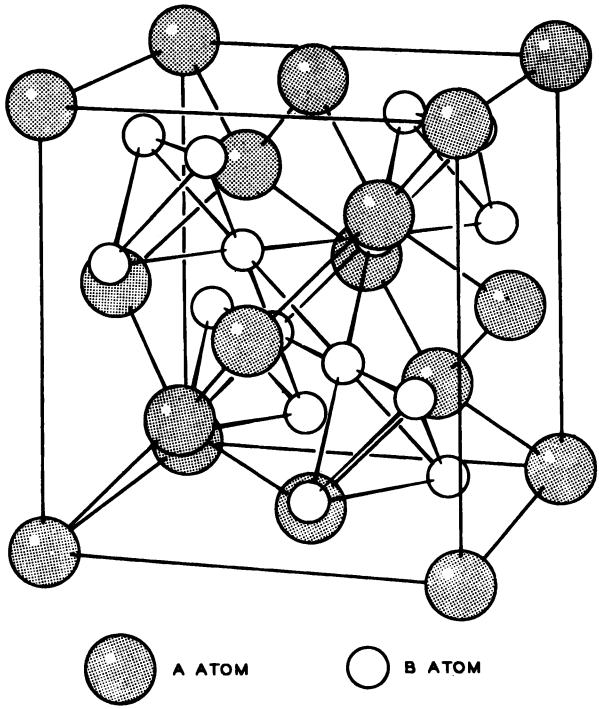

Figure 2. Crystallographic structure of the cubic (C-15) Laves phase. A atoms are large (RE) atoms; B atoms are small (Fe) atoms.

The study of the magnetostriction and anisotropy constants as a function of composition is carried out best on homogeneous single-crystal specimens in order to obtain the composition and crystallographic orientation dependences as accurately as possible. Magnetic anisotropy measurements on $REFe_2$ materials have been carried out by using the magnetic torque (*6*) and magnetization (*7*) techniques. In the former technique one measures directly the energy required to rotate the magnetization from one crystallographic direction to another. In the latter method one must calculate the anisotropy based on the magnetization behavior in selected crystallographic directions.

Table I. Polarity of λ, K_1, and K_2

	$TbFe_2$	$DyFe_2$	$HoFe_2$
λ	+	+	+
K_1	−	+	+
K_2	+	−	+

If suitable single crystals are available, one may wish to study other physical properties as well.

Crystal Growth

Three methods have been used for growing $REFe_2$ crystals. These are the Triarc Czochralski method (*8, 9*), the radiofrequency (rf) levitation Czochralski (*10*) method, and the rf levitation horizontal-zoning method (*11*). In all cases one must observe certain precautions because of the extreme reactivity of rare-earth metals. Titanium-gettered argon can be used as a protective atmosphere to prevent the contamination of the melt by oxygen, in particular.

One should exclude foreign materials to the greatest extent possible, particularly from objects that contact the melt, such as seed wires and crucibles. One should use the most rapid growth method available in order to reduce the time during which contamination may occur. Additionally, one may wish to have the possibility of using a seed in order to prepare crystals of selected orientation. One should use starting materials of the best purity available, especially where high-quality crystals are desired. For commercial production of $REFe_2$ materials, however, the cost of starting materials may limit the purity of the rare earth that can be used profitably.

The starting composition that should be used to prepare a given compound frequently can be determined by consulting a suitable phase diagram. Unfortunately, for most rare earth intermetallics, such phase diagrams do not exist or are of questionable accuracy. Some systems, such as Er–Fe, have been investigated by a number of workers, with varying results (*12, 13, 14*). One then must work empirically, using various starting compositions; by correlating the results obtained under the appropriate thermodynamic regime, one can deduce certain features of the phase diagram of interest. In this way $HoFe_2$ and $ErFe_2$ have been shown to behave as congruently melting materials (*9*). For these materials, as well as ternaries and quaternaries based on $HoFe_2$, it is useful to start with a 1% rare earth-rich composition, that is, $REFe_{1.98}$, in order to prevent the formation of second-phase material. The starting composition chosen implies that for a congruently melting material the rare earth should contain no more than 1% atomic oxygen, or roughly 10^3 ppm oxygen by weight. If the oxygen concentration is larger than this, one runs the risk of growing a crystal contaminated with ever increasing quantities of $REFe_3$ phase material. For peritectic materials, such as $DyFe_2$ or $TbFe_2$, the rare-earth concentration must exceed 33% atomic by an amoun sufficient to compensate for both oxygen concentration and the rare-earth excess required by thermodynamic considerations. It may

prove necessary to try several starting compositions in order to grow a desired material, because the oxygen concentration by weight in pure commercial rare earths is somewhat variable and may reach 10^4 ppm, although 10^3 ppm may be found more commonly in the more expensive distilled grades of the heavy rare-earth metals.

A convenient and straightforward method for preparing starting melts is the rf levitation melting of ingots of the metals in the desired proportions. Reaction takes place quickly, producing a homogeneous melt in minutes.

The application of the Czochralski method requires a seed, which is dipped into the molten starting charge and withdrawn at a selected rate under controlled thermal conditions, leading to the growth of a boule. In the absence of a single crystal from which an oriented seed may be obtained, one may cut a section of a polycrystalline ingot such that a small number of grains, ideally only one, will contact the melt upon seeding. After growing a boule, one may repeat the process until a seed of the desired orientation is obtained.

The quality of the grown crystal will be determined in part by the presence or absence of contact by foreign solids with the crystal or the crystal–melt interface as growth proceeds. A solid that contacts the crystal may introduce defects by a mechanical or a thermal stress mechanism as the crystal cools from the melting point to room temperature. The presence of a solid at the crystal–melt interface can result in the spurious nucleation of second grains or other defects. Such a solid can be either a container for the melt, as in the Bridgman method, or particles of dross or dirt that lie on the surface of the melt. Dark, apparently oxidic drosses are produced frequently upon alloying rare earths with transition metals.

Arc-Powered Czochralski Crystal Growth. No single-crystal growth apparatus or technique is the best for the growth of all crystals. The application of a given technique using certain apparatus to a selected crystal growth problem must be made on the basis of the properties of the desired material and the capabilities of the technique and apparatus.

The use by the author of an electric arc-powered Czochralski method (8) for the growth of crystals of rare earth intermetallic compounds was based on several criteria. The compounds are arc compatible and are prepared frequently by arc melting on a water-cooled copper hearth. Preliminary data on arc-melted materials suggested that the desired cubic compounds crystallized readily, making the Czochralski technique a natural choice for rapid crystal growth. The high reactivity of rare earth metals suggested further that crucibles be avoided if at all possible.

Approximately 25 g of polycrystalline material is transferred to the crystal growth furnace. The material is melted on a rotatable, cooled

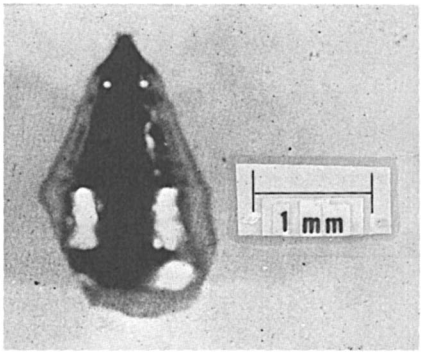

Figure 3. A crystal of $Ho_{0.88}Tb_{0.12}Fe_2$ grown by the triarc Czochralski method, which was studied by inelastic neutron diffraction methods (20)

copper hearth by the action of three electric arcs directed at it from thoriated tungsten electrodes. Gettered argon at an overpressure of several pounds per square inch is used as protective atmosphere. Once a pool of liquid has been established, a seed crystal is dipped into the melt and Czochralski growth commences.

In order to minimize radial thermal gradients in the system, the melt and growing crystal are rotated. Rotation of the melt effectively causes the localized arcs to sweep the surface of the melt, providing more uniform heating, electromagnetic stirring, and the efficient removal of dross from the growth region.

A crystal of $Ho_{0.88}Tb_{0.12}Fe_2$ grown by this method and examined by neutron diffraction by Nicklow et al. (*15*) is shown in Figure 3.

Radiofrequency Levitation Czochralski Crystal Growth. Crystals also have been grown from a water-cooled Hukin crucible (*16*), using rf induction melting with electromagnetic levitation of the melt.

Approximately 150 g of charge material is prepared. Dross that appears upon compounding may be removed by etching in aqueous HNO_3, followed by repeated washing with anhydrous methanol. The charge is melted in the crucible, which is housed in an A. D. Little model MP crystal-growing furnace under an overpressure of gettered argon. A seed crystal is dipped into the melt and Czochralski growth commences.

In this system the top portion of the melt is apparently the coolest region. Whatever dross is still present frequently appears as a thin skin or patch on the upper surface of the melt. There appears to be no mechanism for its removal. The crystal therefore grows from a system that has particulate matter at the crystal–melt interface. If extremely pure starting materials were used, the dross might be absent. In the author's experience, using commercial rare-earth metals, a completely dross-free melt surface has not been achieved.

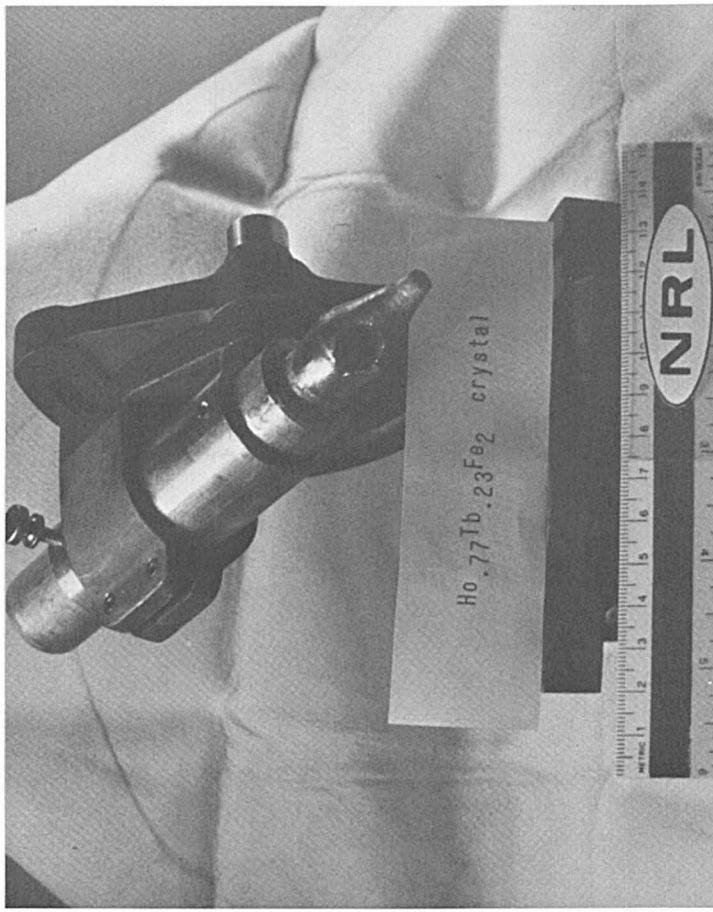

Figure 4. A 70-g boule of $Ho_{0.77}Tb_{0.23}Fe_2$ grown by the rf levitation method after being x-ray-oriented and cored. The cylindrical specimen removed (dark circle) was oriented along [111] (27).

A crystal of $Ho_{0.77}Tb_{0.23}Fe_2$ grown by this method, from which a [111]-oriented cylinder was prepared for magnetoacoustic study by Timme and Meeks (*17*), is shown in Figure 4.

Radiofrequency Horizontal Levitation Zone Crystal Growth. In a recent paper McMasters et al. (*11*) reported the growth of a number of $REFe_2$ compositions by using an rf induction-heated horizontal levitation zone melting method. As is well known, zone melting is a technique very well suited to materials that do not melt congruently (*18*), such as $TbFe_2$ and $DyFe_2$.

From the description given it would appear that this method presents two severe problems from the crystal grower's point of view. First, an extremely large temperature gradient must exist vertically along the crystal–melt interface, since the top of the charge, which is cooled principally by radiation, is very near the melting point (of the order of 1000°C), while the lower surface of the solidified boule, roughly 1 cm away, rests on a surface maintained at approximately room temperature by water cooling. Second, a solid surface, that of the crucible, is present at the growth interface. These circumstances may contribute to the generation of defects by thermal stress or by the nucleation of second grains, or to thermally induced compositional variations across the crystal diameter in the case of ternary or higher-order systems. Zoning in the vertical direction, as has been applied to RE_2Co_{17} systems by Miller and D'Silva (*19*), would eliminate both of these difficulties but would be more difficult to perform.

A comparison of the results obtained by the three methods appears in Table II.

Although the Czochralski methods described have produced the largest- and the highest- (crystallographic) quality $REFe_2$ crystals to date, it should be noted in fairness that the materials studied are congruently melting.

Table II. Properties of Crystals Grown by Various Methods

	Arc Czochralski	*RF Levitation Czochralski*	*RF Levitation Horizontal*
Size (typical)	~ 1-cm diameter × 1–2-cm length (~ 1.5 cm^3)	~ 1-cm diameter × ~ 9-cm length (~ 7 cm^3)	~ 1-cm diameter × 1–2-cm length (~ 1 cm^3)
Homogeneity	Homogeneous by microprobe and magnetic torque measurements	—	—
Perfection	Mosaic spread of about 0.1° (bulk, neutron-rocking curve)	Mosaic spread about 1° to 3° (bulk, neutron-rocking curve)	—

Physical Measurements

Single crystals of compositions in the Ho–Tb–Dy–Fe_2 system produced by the Czochralski methods described above have been examined by a variety of physical techniques, including measurements of elastic and inelastic magnetostriction, magnetic anisotropy, neutron diffraction, surface acoustic wave (SAW) velocity, and magnetoacoustic transduction. A brief description of these measurements is given below; for a more complete discussion, the original references should be consulted.

In the Ho–Tb–Dy–Fe_2 system the easy direction of magnetization is observed to vary as a function of temperature and composition. At room temperature the Ho–Tb system exhibits [111] → [110] → [100] as easy directions as the Ho content increases, while the Dy–Tb system exhibits [111] → [100] reorientation only. The spin reorientation diagrams (*20*) for these systems are shown in Figure 5. The solid lines, which delineate the easy direction regions, are obtained by theoretical calculations. The hatched areas correspond to easy directions of magnetization in the (100) plane between [110] and [100]. The circles and squares are data points. This behavior is consistent with the assumption of $K_2 > 0$ for the Ho–Tb system and $K_2 < 0$ for the Dy–Tb system, with $K \approx 0$ in the neighborhood of the reorientations. Thus a combination of Tb, Dy, and Ho in the proper amounts should lead to $K_1 = K_2 = 0$ at room temperature. In such a case the magnetic field necessary to saturate the magnetostriction will be small. However, since the magnetostriction is quite anisotropic, with $\lambda_{111} >> \lambda_{100}$, as shown in Table III (*21*), it will be necessary to have a textured polycrystalline material or, if possible, a single-crystal material to obtain the best efficiency.

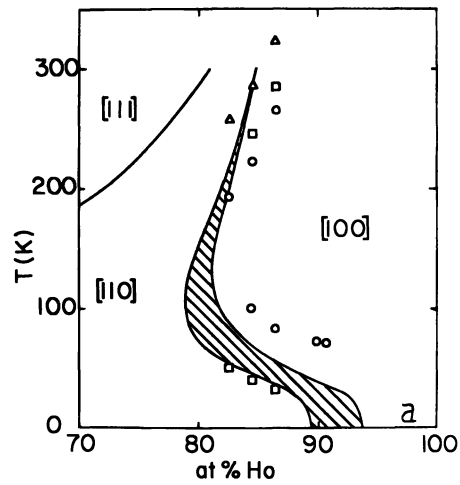

Journal of Applied Physics

Figure 5a. Spin reorientation diagram for the Ho–Tb–Fe_2 system as a function of rare-earth content and temperature (18)

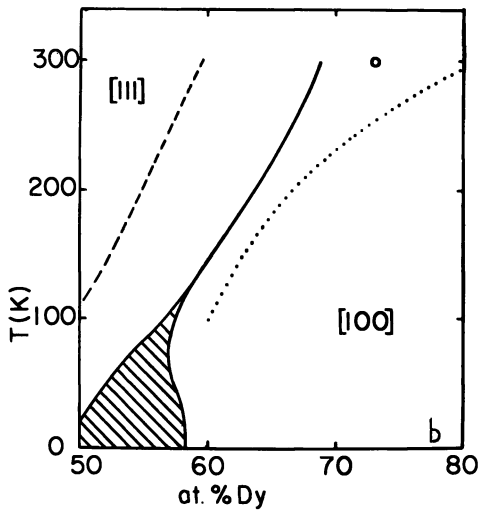

Figure 5b. Spin reorientation diagram for the Dy–Tb–Fe_2 system as a function of rare-earth content and temperature (18)

Neutron diffraction methods have provided several interesting data. The crystallographic quality of Czochralski-grown crystals has been determined (*10*). Triarc-grown crystals produce rocking curve peak widths one-tenth that of levitation-grown crystals. These data are presented in Figures 6(a) and 6(b). One sees conclusively the appreciable difference in quality, the triarc-grown crystals being systematically more perfect. The difference in quality is ascribed to the absence of dross at the growth interface in the arc-powered method and to the presence of dross in the levitation method. Triarc-grown crystals thus are suited better for more detailed and precise measurements than are levitation-grown specimens.

Neutron inelastic scattering measurements have been performed on $Ho_{0.88}Tb_{0.12}Fe_2$, $ErFe_2$, and $HoFe_2$ (*15, 22, 23*). Although there are variations in the detailed results obtained from these specimens, several features are quite systematic. The exchange interactions occur as

$$\text{Fe–Fe} \approx \text{tens of millielectronvolts}$$

$$\text{RE–Fe} \approx 1 \text{ meV}$$

$$\text{RE–RE} = 0.00 \pm 0.01 \text{ meV}$$

Thus the Fe–Fe interaction is roughly equivalent to that in pure iron metal.

Table III. Room-Temperature Magnetostrictive Constants

	$TbFe_2$	$DyFe_2$	$HoFe_2$
λ 111 ($\times 10^{-6}$)	2460	1060 ± 150	185 ± 20
λ 100 ($\times 10^{-6}$)	300 ± 100	0 ± 4	−59 ± 6

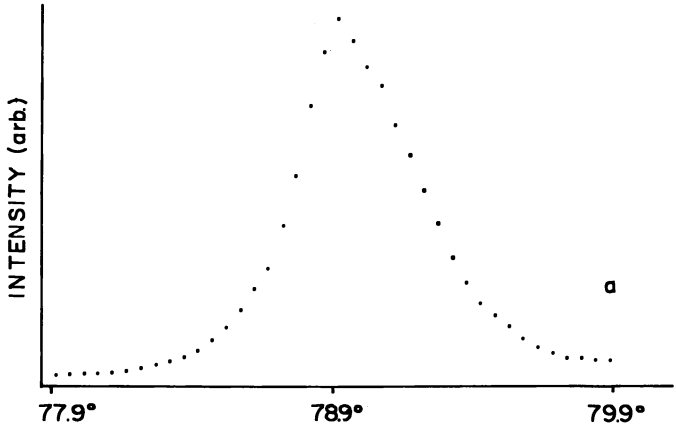

Plenum Publishing Corporation

Figure 6a. Neutron diffraction rocking curves for triarc-Czochralski-grown $REFe_2$ crystals. The angular values are arbitrary and merely serve to indicate the rocking-curve width (10).

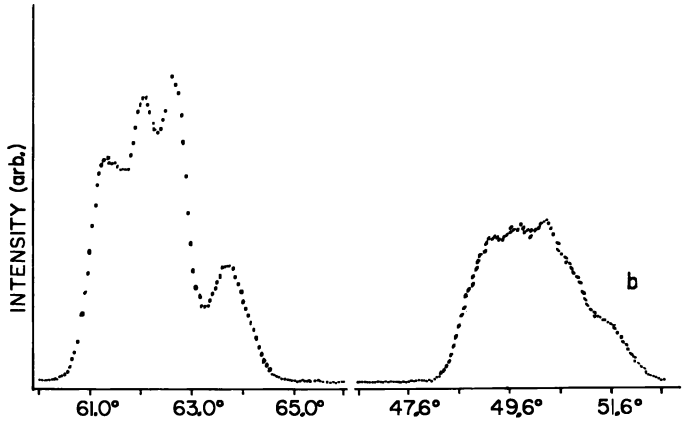

Plenum Publishing Company

Figure 6b. Neutron diffraction rocking curves for rf levitation Czochralski-grown $REFe_2$ crystals. The angular values are arbitrary and merely serve to indicate the rocking-curve width (10).

The rare earths order by coupling via the iron sublattice. The rare earth's nearest neighbors, although at about the same distance as in pure rare-earth metals, do not interact in any measurable way. These facts are rather firm confirmation of the single-ion model, which has been involved in calculations of various properties of these systems. The inelastic neutron diffraction results for $ErFe_2$ at room temperature are shown in Figure 7 and are typical of the results found for all of the $REFe_2$ systems studied to date.

SAW studies (*24*) have been carried out by using several single crystals in the Ho–Tb–Dy–Fe_2 system. The wave velocity could be altered from about 1.75 to 2.15 $\times$ 10^5 cm $\cdot$ sec^{-1}, for propagation of waves having $f \approx 85$ MHz, along the [001] direction of a [110]-cut

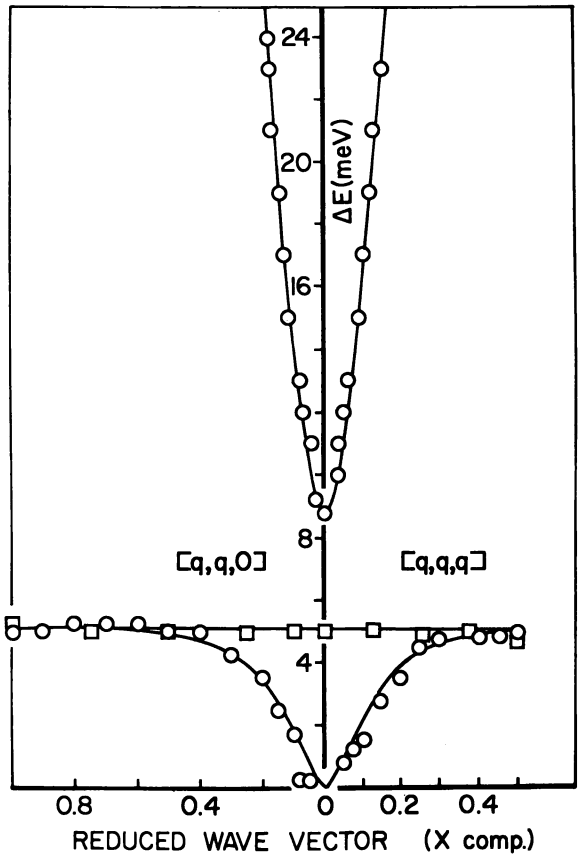

Figure 7. Room-temperature inelastic neutron diffraction data for $ErFe_2$ with fit curves and fitting parameters (21): $ErFe_2$, 295 K; $\langle J \rangle_{Er} = 3.6$; $\langle S_Z \rangle_{Fe} = 0.66$; $\partial_{Fe-Fe} = 30$ meV; $\partial_{Fe-Er} = -0.32$ meV; $\partial_{Er-Er} = 0$. Experimental, (○); model, (——).

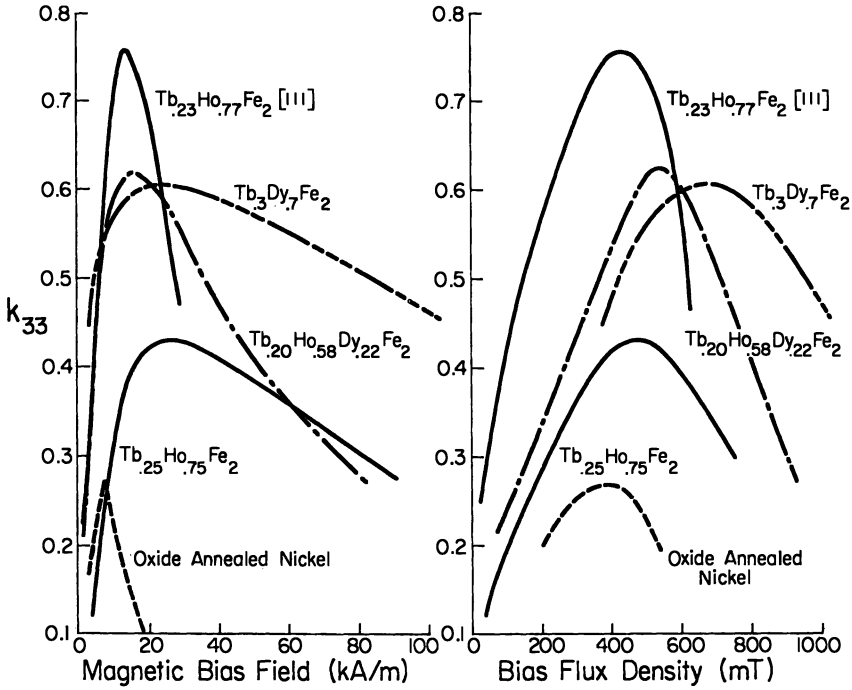

Figure 8. Room-temperature coupling coefficient K_{33} for several $REFe_2$ materials in polycrystalline and oriented form as a function of magnetic field (27)

crystal, with a magnetic field of 8.6 KOe whose direction was varied from [001] to [110]. This velocity change of approximately 20% is apparently the largest continuously variable surface velocity change reported to date.

Examination of $REFe_2$ polycrystalline and single-crystal materials for use in magnetoacoustic transducers has been carried out by groups at NRL and NSWC (*17, 25, 26*). Data obtained on the same materials by different techniques are in good agreement.

The parameter that is most commonly taken as a measure of the quality of a magnetoacoustic transducer element is K_{33}, the magneto-mechanical coupling coefficient. This quantity is a measure of the efficiency with which magnetic energy supplied to the transducer element is converted to mechanical (or acoustic) energy. Another important parameter is the strain developed in the transducer element. The larger the available strain, the higher is the attainable sound pressure for a given geometrical configuration of the transducer. Sound pressure and efficiency are parameters of some consequence to designers of sonar equipment.

Figure 8 depicts the relationship between K_{33} and magnetic bias field for polycrystalline and oriented $REFe_2$ specimens, with nickel included as a reference value (*27*). The coupling coefficient for [111]-oriented $Tb_{0.23}Ho_{0.77}Fe_2$ is approximately 0.75, which is appreciably greater than the values for the polycrystalline specimens. This value is among the largest coupling coefficients ever reported. Typical values for piezoelectric ceramic transducer elements, the most widely used type, are about 0.6.

The strain as a function of bias field (*27*) for the same materials is shown in Figure 9. Two features are noticed readily. The first is that [111]-oriented $Tb_{0.23}Ho_{0.77}Fe_2$ saturates, while polycrystalline $Tb_{0.25}Ho_{0.75}Fe_2$ does not saturate in the low fields applied. The second is that saturation occurs rapidly in the oriented specimen. Thus the oriented specimen yields far higher strain with a high rate of change in the low-field region. The implications of these properties is that the use of

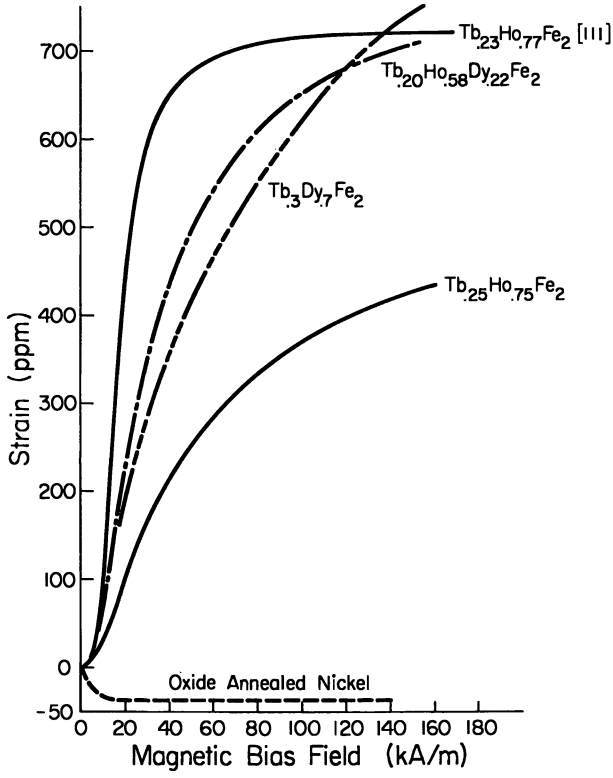

Figure 9. Room-temperature magnetostrictive strain as a function of magnetic field for several $REFe_2$ materials in polycrystalline and oriented form (25)

oriented material results in a superior magnetoacoustic device. The designer would like to use oriented material, which places a constraint on the fabricator of the magnetostrictive elements. The device would be operated by magnetically biasing the elements to a point roughly halfway up the steep rise in strain and by applying an oscillating magnetic field to drive the elements over the full dynamic strain range. This mode of operation would allow the greatest economy in required power supplies, coils, volume, and mass, all of which are factors in the potential application of such systems.

Conclusions

The efforts of several workers have led to the ability to prepare materials that exhibit improved magnetostrictive behavior at room temperature. Major advances have been made in our understanding of the basic magnetic interactions in the $REFe_2$ intermetallic compounds.

Areas that require additional effort include the examination of additional intermetallic systems—for example, those based on Sm rather than Tb—and the design of transducer devices that utilize the unusual characteristics of these materials.

Literature Cited

1. Nassau, K.; Cherry, L. V.; Wallace, W. E. *J. Phys. Chem. Solids* **1960**, *16*, 131.
2. Koon, N. C.; Schindler, A. I.; Carter, F. L. *Phys. Lett. A* **1971**, *37*, 413.
3. Clark, A. E.; Belson, H. S. *Phys. Rev. B* **1972**, *5*, 3642.
4. Ray, A. E. *Proc. Rare Earth Res. Conf.* **1968**, *2*, 473.
5. Clark, A. E. *AIP Conf. Proc.* **1974**, *18*, 1015.
6. Williams, C. M.; Koon, N. C.; Milstein, J. B. *AIP Conf. Proc.* **1976**, *29*, 191.
7. Clark, A. E.; Belson, H. S.; Tamagawa, N. *Phys. Lett. A* **1972**, *42*, 160.
8. Milstein, J. B.; Koon, N. C.; Johnson, L. R.; Williams, C. M. *Mater. Res. Bull.* **1974**, *9*, 1617.
9. Milstein, J. B. *AIP Conf. Proc.* **1976**, *29*, 592.
10. Milstein, J. B. "Crystallographic Quality of RFe_2 Crystals Containing Ho," In "Rare Earths in Modern Science and Technology"; McCarthy, G. J.; Rhyne, J. J.; Eds.; Plenum: New York, 1978; p. 315.
11. McMasters, O. D.; Holland, G. E.; Gschneider, K. A., Jr. *J. Cryst. Growth* **1978**, *43*, 577.
12. Buschow, K. H. J.; van der Goot, A. S. *Phys. Stat. Sol.* **1969**, *35*, 515.
13. Meyer, A. *J. Less-Common Metals* **1969**, *18*, 41.
14. Kolesnikov, V. E.; Trekhova, V. F.; Savitskii, E. M. *Izv. Akad. Nauk SSSR, Neorg. Mat.* **1971**, *7*, 495.
15. Nicklow, R. M.; Koon, N. C.; Williams, C. M.; Milstein, J. B. *Phys. Rev. Lett.* **1976**, *36*, 532.
16. Hukin, D. A.; Jones, D. W. *Proc. Rare Earth Res. Conf.* **1976**, 891.
17. Meeks, S. W.; Timme, R. W. *J. Accoust. Soc. Am.* **1977**, *62*, 1158.
18. Pfann, W. G. "Zone Melting"; Wiley: New York, 1966.
19. Miller, A. E.; D'Silva, T.; Rodrigues, H. *IEEE Trans. Mag.* **1976**, *MAG-12*, 1006.

20. Koon, N. C.; Williams, C. M. *J. Appl. Phys.* **1978**, *49*, 1948.
21. Koon, N. C.; Williams, C. M. *U.S. Navy Journal of Underwater Acoustics* **1977**, *27*, 127.
22. Rhyne, J. J.; Koon, N. C.; Milstein, J. B.; Alperin, H. A. *Proc. Conf. Neutron Scattering* **1976**, CONF-760601-P2, 783.
23. Rhyne, J. J.; Koon, N. C. *J. Appl. Phys.* **1978**, *49*, 2133.
24. Ganguly, A. K.; Webb, D. C.; Davis, K. L.; Koon, N. C.; Milstein, J. B. *Proc. IEEE Ultrasonics Symposium, Phoenix, 1977*, p. 785.
25. Timme, R. W. *J. Acoust. Soc. Am.* **1976**, *59*, 459.
26. Savage, H. T.; Abbundi, R.; Clark, A. E.; McMasters, O. D. *Proc. Conf. on Magnetism and Magnetic Materials*, Cleveland, OH, 1978, in press.
27. Timme, R. W.; Meeks, S. *J. de Physique*, in press.

RECEIVED November 3, 1978.

Phase and High-Temperature Thermodynamic Studies in the Lutetium–Sulfur System

HUGO F. FRANZEN and ALLEPPEY V. HARIHARAN

Ames Laboratory, DOE and Department of Chemistry, Iowa State University, Ames, IA 50011

The lutetium–sulfur system was investigated to determine the extended nonstoichiometry of the monosulfide, intermediate phase(s), and thermodynamic properties. The homogeneity range of the cubic monosulfide extends from $LuS_{0.75}$–$LuS_{1.30}$. A new intermediate line phase, Lu_3S_4, with a superstructure derived from the parent face-centered cubic (fccub) sublattice, was identified between the sulfur-rich end of the monosulfide homogeneity range and Lu_2S_3. The high-temperature thermodynamic properties of the congruently vaporizing Lu_3S_4 and LuS are reported.

The lanthanide monosulfides, except SmS, EuS, and YbS, exhibit nonstoichiometry towards metal-rich compositions. The homogeneity range extends down to a composition corresponding to $LuS_{0.75}$ for yttrium and the heavy lanthanides; this range is much smaller for the light lanthanides (*1, 2, 3, 4*). Lutetium monosulfide is unique in that the nonstoichiometric composition extends significantly to the metal-rich and sulfur-rich regions while maintaining the fccub rock salt structure. In the hyperstoichiometry of the monosulfide, and in the general crystal chemistry of chalcogenides, lutetium compounds tend to be similar to those of scandium. The phase and high-temperature behavior of the Lu–S system was of interest especially in view of the observation that in the Sc–S system the congruently vaporizing composition is $ScS_{1.24}$ (*5*).

The purpose of the present study was to establish the extent of nonstoichiometry of LuS, identify intermediate and terminal phase(s) and the congruently vaporizing composition, and obtain pertinent thermodynamic data in the system.

0–8412–0472–1/80/33–186–309$05.00/1

Phase Studies

Lutetium sulfides in the composition range of S/Lu 0.6–1.5 were synthesized by the direct combination of the elements contained in outgassed, evacuated, and sealed quartz tubes at 870°C. The as-reacted materials were subsequently homogenized at 1500°C in tungsten crucibles in high vacuum. Since the weight losses of the samples during homogenization were negligible, the final product compositions were taken as essentially the same as the initial compositions. X-ray diffraction patterns of the powdered samples were obtained in a Hagg-type Guinier camera (radius 50 mm; Cu $K\alpha_1$ radiation; silicon internal standard).

The homogeneity range of lutetium monosulfide is established as $LuS_{0.75}$–$LuS_{1.30}$. The cubic lattice parameter increases sharply from 5.316(1) Å at $LuS_{0.71}$ (in equilibrium with Lu metal) to 5.356(1) Å at $LuS_{1.03}$ and thereafter less rapidly to 5.364(1) Å at $LuS_{1.29}$ (Figure 1). The trend in the lattice parameter indicates that the extended homogeneity results from the presence of random vacancies in the sulfur and lutetium sublattices, respectively, on either side of the true monosulfide composition. The lattice parameter of stoichiometric $LuS_{1.0}$ is interpolated to 5.355(1) Å. The composition S/Lu = 1.5 forms pure Lu_2S_3 [rhombohedral–hexagonal: $a = 6.722(2)$ Å; $c = 18.141(7)$ Å].

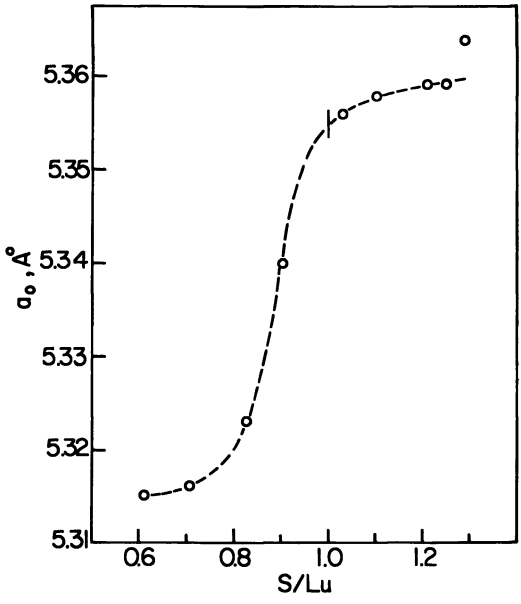

Figure 1. Cubic cell lattice parameters (±0.001 Å) of LuS_x versus composition

A significant result of this study is the identification of a new intermediate line phase, Lu_3S_4, between the sulfur-rich end of the monosulfide homogeneity range and Lu_2S_3. The structure of Lu_3S_4, tentatively established from the Guinier powder diffraction, is closely related to the defect Sc_2S_3 type (*6*) and is a superstructure derived from the parent fccub sublattice. The sulfur lattice is completely filled, and vacancies occur in the cation sublattice sites (ordered in the case of the Sc_2S_3 structure type but partly occupied in Lu_3S_4). A substructure of the compound is orthorhombic, space group Fddd, with $a = 10.764(3)$ Å; $b = 7.708(3)$ Å; $c = 22.861(8)$ Å. Single-crystal refinement of the structure is in progress.

X-ray photoelectron spectra of lutetium sulfide compositions $LuS_{0.8}$–$LuS_{1.2}$, Lu_3S_4, and Lu_2S_3 have also been studied (*7*). The most significant information about the cation–anion interaction in these compounds is obtained from the S 2p binding energies. This value, 162.7 ± 0.2 eV in $LuS_{0.8}$–$LuS_{1.2}$ and Lu_3S_4, is very close to the binding energy in neutral sulfur, whereas in Lu_2S_3 it is appreciably shifted, to 161.8 eV, typical of relatively ionic sulfides. The data indicate very low charge transfer from the metal to sulfur, or, alternatively, appreciable back bonding from the anion to the metal in the nonstoichiometric monosulfides and the structurally related Lu_3S_4, while in Lu_2S_3 conventional ionic bonding becomes predominant. The Lu 4d core-binding energies also show a parallel trend in these compounds.

Thermodynamic Studies

The intermediate phase, Lu_3S_4, is established as the congruently vaporizing composition in the Lu–S system at high temperature. The vaporization of this phase was studied by mass spectrometric and target collection Knudsen effusion techniques in the temperature range of 1927–2216 K. Lu_3S_4 vaporizes according to

$$LuS_{1.33}(s) = Lu(g) + 1.33S(g) \quad (1)$$

$$LuS_{1.33}(s) = LuS(g) + 0.33S(g) \quad (2)$$

From the slopes of the log I^+T versus $(1/T)$ data for Lu and LuS vapor species, and a corresponding slope for sulfur gas consistent with the congruency of the vaporization reactions (1) and (2), the dissociation energy of LuS(g) is computed as $D_0°[LuS(g) = Lu(g) + S(g)] = 120.6 \pm 3.2$ kcal · mol^{-1}. The effusion data have been reduced to obtain the following second-law thermodynamic values (eu represents entropy unit):

Reaction (1): $\Delta H°_{298} = 317.6 \pm 2.3$ kcal

$\Delta S°_{298} = 79.6 \pm 1.1$ eu

Reaction (2): $\Delta H°_{298} = 196.9 \pm 3.1$ kcal

$\Delta S°_{298} = 55.9 \pm 1.5$ eu

These thermal data, appropriately combined, yield, for the condensed phase, $LuS_{1.33}$, $\Delta H°_{f,298}[LuS_{1.33}(s)] = -126.5 \pm 2.3$ kcal · mol^{-1} and $S°_{298}[LuS_{1.33}(s)] = 18.0 \pm 1.1$ eu.

The monophasic compositions $LuS_{0.75}$–$LuS_{1.30}$ decompose on heating in vacuum with loss of Lu and eventually form Lu_3S_4. In order to calculate the thermodynamic properties of stoichiometric lutetium monosulfide, $LuS_{1.0}$, the activity of Lu in the cubic phase region was measured at 2026 K by the Knudsen effusion method. Gibbs–Duhem integration of the data yielded the activity of sulfur across the single-phase region with respect to the congruently vaporizing composition of Lu_3S_4. From the combined data the following thermodynamic values for $LuS_{1.0}$ are calculated:

$$\Delta H°_{\text{atomization, 298}}[LuS(s) = Lu(g) + S(g)] = 268.5 \pm 3.0 \text{ kcal} \cdot \text{mol}^{-1}$$

$$\Delta H°_{\text{sublimation, 298}}[LuS(s) = LuS(g)] = 147.7 \pm 3.0 \text{ kcal} \cdot \text{mol}^{-1}$$

$$\Delta H°_{f,298}[LuS(s)] = -99.6 \pm 3.1 \text{ kcal} \cdot \text{mol}^{-1}$$

Glossary of Symbols

fccub = face-centered cubic
T = temperature in kelvin
I^+ = mass spectrometric ion intensity (arbitrary units)
eu = entropy unit, calories per degree per mole
(s) = solid
(g) = gas
$D°_8$ = dissociation energy
$\Delta H°_{298}$ = standard enthalpy change at 298 K
$\Delta S°_{298}$ = standard entropy change at 298 K
$\Delta H°_{f,298}$ = standard enthalpy of formation at 298 K
$S°_{298}$ = standard entropy at 298 K

Acknowledgment

This work was supported by the U.S. Department of Energy, Office of Basic Energy Sciences, Materials Sciences Division.

Literature Cited

1. Flahaut, J.; Laruelle, P. "Progress in the Science and Technololgy of the Rare Earths"; Eyring, L., Ed.; Pergamon: New York, 1968; Vol. 3, p. 149.

2. Flahaut, J.; Guittard, M.; Gonchov, O.; Winterberger, M. In "Proprietes Thermodynamiques, Physiques et Structurales des Derives Semimetalliques"; Colloque Orsay: Paris, 1967; No. 157, p. 431.
3. Bruzzone, G.; Olcese, G. L. In "Properties Thermodynamiques, Physiques of Structurales des Derives Semimetalliques"; Colloque Orsay: Paris, 1967; No. 157, p. 387.
4. Guittard, M. *Compt. Rend.* **1965**, *261*, 2109.
5. Tuenge, R. T.; Laabs, F.; Franzen, H. F. *J. Chem. Phys.* **1976**, *65*, 2400.
6. Dismukes, J. P.; White, J. G. *Inorg. Chem.* **1964**, *3*, 1220.
7. Franzen, H. F.; Hariharan, A. V. *J. Solid State Chem.* **1978**, *26*, 189.

RECEIVED September 13, 1978.

Some Structural and Magnetic Properties of $A_xV^{II}{}_xV^{III}{}_{1-x}F_3$ Compounds

Y. F. LEE, R. F. WILLIAMSON, and W. O. J. BOO[1]

Department of Chemistry, The University of Mississippi, University, MS 38677

Tungsten bronze-like $A_xV^{II}{}_xV^{III}{}_{1-x}F_3$ compounds were studied in order to determine the effects of small composition changes on structure and magnetic properties. Pseudo-hexagonal K_xVF_3 (x = 0.19–0.27) does not change lattice dimensions with composition but a superstructure was observed to be optimum for small x. *Hexagonal Cs_xVF_3 (x = 0.19–0.31) and tetragonal K_xVF_3 (x = 0.450–0.558) have lattice dimensions that change smoothly with composition. All of the compounds reported displayed antiferro or ferrimagnetic ordering above 4.2 K. In each of the three systems, spontaneous magnetic moments were composition dependent. A single crystal of $K_{0.20}VF_3$ revealed a small spontaneous moment only when its* c *axis was aligned parallel with the field.*

Phase diagrams of mixed-valence systems often are reported to have single phased regions that extend over broad composition ranges. Within these regions, the ratios of mixed-valence ions, as well as compositions of other components, may change. The hexagonal K_xVF_3 (x = 0.19–0.27) and Cs_xVF_3 (x = 0.19–0.31) systems (*1, 2*) and the tetragonal K_xVF_3 (x = 0.450–0.558) system (*3, 4*) are reportedly related structurally to the tungsten bronzes. Although the structures are similar, differences exist in the A_xVF_3 compounds such as superlattices, lattice distortions, and even space groups.

[1] Author to whom correspondence should be addressed.

0–8412–0472–1/80/33–186–315$05.00/1

The purpose of this chapter is to report subtle, but interesting, structural and magnetic properties of the $A_xV^{II}_xV^{III}_{1-x}F_3$ phase systems. It emphasizes the fact that physical changes which often accompany composition changes within an apparent single phase provide an interesting area of investigation for the solid state chemist.

Experimental

Stoichiometric mixtures of KF or CsF, VF_2, and VF_3 were mixed thoroughly inside an inert atmosphere glove box. Samples of these mixtures were vacuum encapsulated in molybdenum by electron-beam welding techniques. The capsules were fired at 800°C for 30 days in an evacuated stainless steel tube inside a Hevi Duty furnace. VF_2 and VF_3 were prepared in this laboratory but optical-grade KF and CsF were obtained commercially. Chemical analyses of products were in agreement with calculated values within experimental error. Small quantities of impurity phases were separated from bulk samples by Pasteur's method under an American Optics stereoscopic microscope. Final products were inspected under a Leitz Dialux polarizing microscope. Single crystals of composition $K_{0.20}VF_3$, suitable for magnetic susceptibility measurements, were obtained from an independent experiment by the following procedure: a mixture of KF, VF_2, and VF_3 was heated to 1000°C inside a graphite-lined nickel furnace tube under a controlled gas flow of HF, H_2, and Ar. Several large single crystals, which had grown from the vapor phase, were deposited downstream in the cooler portion of the furnace. From these, one single crystal elongated along its *c* axis and weighing 5.0 mg was chosen for magnetic anisotropy measurements.

The samples were characterized by X-ray diffraction methods. Both Debye–Scherrer and Guinier–Hägg techniques were used on powder samples. Single crystals, where available, were studied by Weissenberg methods for superstructures, domain structures, and other structural anomalies.

A PAR vibrating sample magnetometer equipped with a liquid helium dewar and gallium arsenide thermometer was used for magnetic susceptibilities from 2.8–300 K at a constant field of 10,000 G on randomly oriented powder samples, as well as on a single crystal of hexagonal $K_{0.20}VF_3$ oriented with its *c* axis parallel and perpendicular to the field. Spontaneous moments were determined at constant temperatures in fields ranging from 10,000–1,000 G and extrapolated to zero field. In every experiment, samples were cooled in a field of 10,000 G.

Slopes on plots of X_M^{-1} versus T were obtained by linear regression. A Dec-10 computer was used to reduce the X-ray data.

Results and Discussion

Pseudohexagonal K_xVF_3. A hexagonal lattice can be described easily by a set of orthorhombic base vectors. If these vectors are chosen such that $\mathbf{a}_o = 1/2\ \mathbf{a}_h + \mathbf{b}_h$, $\mathbf{b}_o = 1/2\ \mathbf{a}_h$, and $\mathbf{c}_o = \mathbf{c}_h$; then $|\mathbf{a}_h| = 2/\sqrt{3}\ |\mathbf{a}_o| = 2|\mathbf{b}_o|$ and $|\mathbf{a}_o|/\sqrt{3}|\mathbf{b}_o| = 1.000$. There are two simple possibilities

for distortion from hexagonal symmetry by which the lattice remains orthorhombic. For the first kind, $|a_o|/\sqrt{3}\,|b_o|$ is greater than unity, and for the second kind it is less than unity. For distortions of either kind, the hexagonal Miller indicies are transformed to orthorhombic indicies by the matricies

$$\begin{vmatrix} \frac{1}{2} & 1 & 0 \\ \frac{1}{2} & 0 & 0 \\ 0 & 0 & 1 \end{vmatrix}, \quad \begin{vmatrix} \bar{\frac{1}{2}} & \frac{1}{2} & 0 \\ \frac{1}{2} & \frac{1}{2} & 0 \\ 0 & 0 & 1 \end{vmatrix}, \text{ and } \quad \begin{vmatrix} \bar{1} & \bar{\frac{1}{2}} & 0 \\ 0 & \frac{1}{2} & 0 \\ 0 & 0 & 1 \end{vmatrix}.$$

The hexagonal $(h0\bar{h}l)$ reflections are transformed into three orthorhombic reflections $(h/2, h/2, l)$, $(\bar{h}/2, h/2, l)$, and $(\bar{h}0l)$. The $(hh2\bar{h}l)$ reflections are transformed into $(3/2h, h/2, l)$ $(0hl)$, and $(\bar{3}/2h, h/2, l)$. In both cases, two of the three orthorhombic reflections are degenerate and, in powder diffraction experiments, one observes a doublet of which one reflection is twice the intensity of the other. For a distortion of the first kind, the $(h0\bar{h}l)$ reflections split into doublets of which the first reflection (larger d) is half as intense as the second, and the $(hh2\bar{h}l)$ reflections split into doublets of which the first reflection is twice as intense as the second. For a distortion of the second kind, the order of intensities obviously would be reversed.

Guinier–Hägg photographs show that the lattices of $K_{0.20}VF_3$ and $K_{0.25}VF_3$ are distorted to an orthorhombic structure of the first kind. Table I shows X-ray powder data of $K_{0.25}VF_3$. The hexagonal Miller indicies in the first column were those assigned to low-angle Debye–Scherrer data. One superlattice reflection indexed as $(21\bar{3}3)$ makes the hexagonal a value appear to double. The second column in Table I gives Miller indicies of the multiple orthorhombic reflections which are generated from the hexagonal reflections. The observed d values from Guinier–Hägg films are shown in the third column and are in good agreement with the calculated values. All of the hexagonal $(h0\bar{h}l)$ reflections that were resolvable are observed to split into doublets of intensity 1:2, whereas, all $(hh2\bar{h}l)$ reflections are split into doublets of intensity 2:1. A detailed analysis of this system is published elsewhere (2).

Figure 1 displays the inverse susceptibility versus temperature of a single crystal of $K_{0.20}VF_3$ oriented parallel and perpendicular to a magnetic field of 10,000 G over the 4.2–100 K temperature range. The insert of Figure 1 is a plot of spontaneous moments extrapolated to zero field at fixed temperatures. These measurements reveal a spontaneous moment only when the crystal is oriented with its c axis parallel to the field.

The inverse susceptibility and spontaneous magnetic moment versus temperature of a randomly oriented powder sample of $K_{0.20}VF_3$ is shown in Figure 2, and that of $K_{0.25}VF_3$ in Figure 3. Small corrections for

Table I. Guinier–Hägg Data for $K_{0.25}VF_3$: $a = 12.88 \pm 0.01$; $b = 7.39 \pm 0.01$; $c = 7.52 \pm 0.01$

Hexagonal (hkil)	*Orthorhombic* (hkl)	$d_{observed}$	$I_{observed}$	$d_{calculated}$
$(20\bar{2}0)$	(200)	6.448	W	6.438
	(110)	6.419	W^+	6.409
$(00\bar{0}2)$	(002)	3.763	M	3.760
$(22\bar{4}0)$	(310)	3.715	W^{-1}	3.711
	(020)	3.698	W^{-2}	3.694
$(20\bar{2}2)$	(202)	3.246	W	3.247
	(112)			3.243
$(40\bar{4}0)$	(400)	3.224	W^+	3.219
	(220)	3.205	M	3.204
$(22\bar{4}2)$	(312)	2.643	W^{-1}	2.641
	(022)	2.638	W^{-2}	2.635
$(42\bar{6}0)$	(510)	2.438	W^{-2}	2.432
	(420)			2.427
	(130)			2.419
$(33\bar{6}1)$	(031)	2.339	W^{-3}	2.341
$(20\bar{2}3)$	(203)	2.335	W^{-3}	2.336
	(113)			2.334
$(42\bar{6}1)$	(511)	2.314	W^{-3}	2.314
	(421)			2.310
	(131)			2.303
$(21\bar{3}3)$	(213)	2.229	W^{-4}	2.227
$(60\bar{6}0)$	(600)	2.146	W^{-3}	2.146
	(330)	2.136	W^{-2}	2.136
$(22\bar{4}3)$	(313)	2.075	W^{-3}	2.077
	(023)			2.074
$(00\bar{0}4)$	(004)	1.880	W	1.880
$(60\bar{6}2)$	(602)	1.865	W^{-4}	1.864
	(332)	1.856	M	1.857
$(44\bar{8}0)$	(620)			1.855
	(040)	1.847	W^{-2}	1.847
$(20\bar{2}4)$	(204)	1.805	W^{-3}	1.805
	(114)			1.804
$(62\bar{8}0)$	(710)	1.787	W^{-4}	1.785
	(530)			1.780
	(240)			1.776

Table I. Continued

Hexagonal (hkil)	*Orthorhombic* (hkl)	$d_{observed}$	$I_{observed}$	$d_{calculated}$
$(22\bar{4}4)$	(314) (024)	1.677	W^{-4}	1.677 1.676
$(44\bar{8}2)$	(622) (042)	1.664 1.658	W^{-1} W^{-2}	1.664 1.658
$(40\bar{4}4)$	(404) (224)	1.622	W^{+}	1.623 1.622
$(80\bar{8}0)$	(800) (440)	1.610 1.602	W^{-2} W^{-2}	1.610 1.602
$(80\bar{8}2)$	(802) (442)	1.479 1.474	W^{-3} W^{-1}	1.480 1.474
$(64\bar{10}2)$	(822) (732) (152)	1.374	W^{-4}	1.374 1.372 1.368
$(44\bar{8}4)$	(624) (044)	1.321 1.319	W^{-2} W^{-3}	1.321 1.318

temperature-independent orbital paramagnetism of V^{+3} were made on all hexagonal samples. The value 6×10^{-4} emu/(mol V^{+3}) used by Gossard et al. (5) on VF_3 when applied to our data gave linearity to the paramagnetic region of X_M^{-1} vs. T plots of all of the hexagonal A_xVF_3 compounds.

For mixed-valence compounds of the type $A_xV^{II}_xV^{III}_{1-x}F_3$, the molar Curie constant can be expressed as the sum of components from V^{+2} and V^{+3} by the equation

$$C_M = x\,C_{(+2)} + (1 - x)\,C_{(+3)}$$

For V^{+2}, which is a spin only system,

$$C_{(+2)} = \frac{N g_{(+2)}^2 \mu_B^2\,(3/2)\,(3/2 + 1)}{3k}$$

and for V^{+3} in which the orbital moment is quenched,

$$C_{(+3)} = \frac{N g_{(+3)}^2 \mu_B^2\,(1)\,(1 + 1)}{3k}$$

where N is Avogadros number, $g_{(+2)}$ and $g_{(+3)}$ are average values of the Lande spliting factors for V^{+2} and V^{+3}, respectively, μ_B is the Bohr

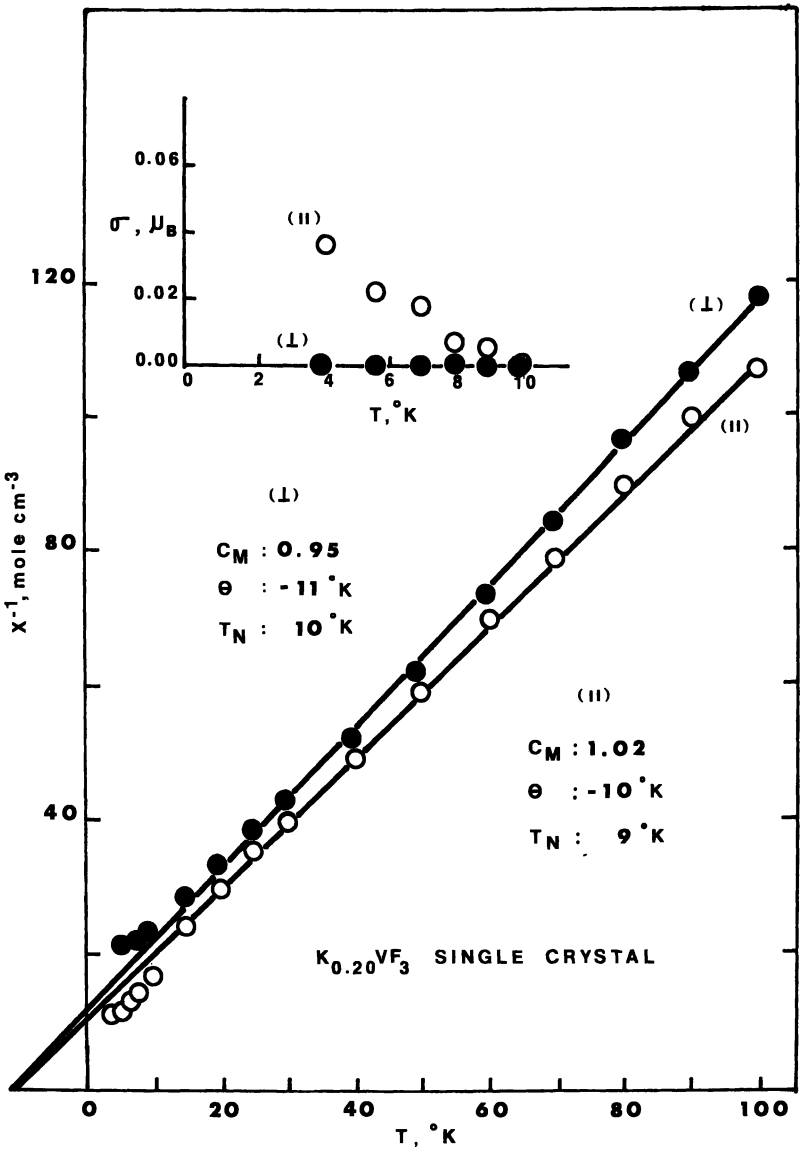

Figure 1. Inverse molar susceptibilities and spontaneous moments versus temperature of a single crystal of $K_{0.20}VF_3$ oriented parallel and perpendicular to the field

magneton, and k is the Boltzmann constant. It has been established that $g_{(+2)}$ is isotropic and has a value of 1.97 in an octahedral fluoride environment (*6, 7*). For VF_3, the average value of $g_{(+3)}$ is 1.80 (*5*). From the single-crystal data of $K_{0.20}VF_3$, an average value of $g_{(+3)}$ was calculated

to be 1.75. Curie constants for powdered samples of $K_{0.20}VF_3$, $K_{0.25}VF_3$, $Cs_{0.25}VF_3$, and $Cs_{0.31}VF_3$, calculated with $g_{(+2)} = 1.97$ and $g_{(+3)} = 1.75$, are in excellent agreement with measured values as seen in Table II. This evidence strongly supports the conclusion that the orbital moment of V^{+3} is quenched largely in the hexagonal A_xVF_3 compounds as is typical of transition metal ions in solids. However, some orbital contribution reduces the effective g value below 2.0 owing to spin–orbit coupling.

Hexagonal Cs_xVF_3. Debye–Scherrer and Guinier–Hägg X-ray powder data reveal that $Cs_{0.25}VF_3$ and $Cs_{0.31}VF_3$ retain hexagonal symmetry but have lattice constants that increase slightly with x. These are: $a =$

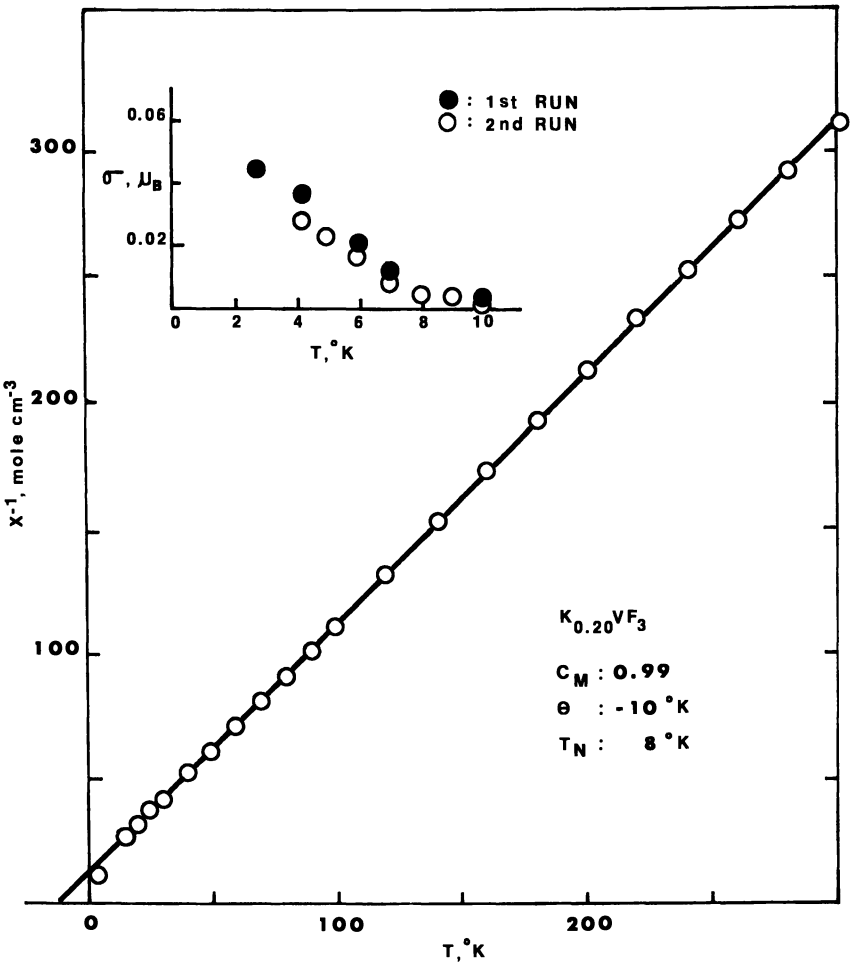

Figure 2. Inverse molar susceptibility and spontaneous moments versus temperature of a powder sample of $K_{0.20}VF_3$

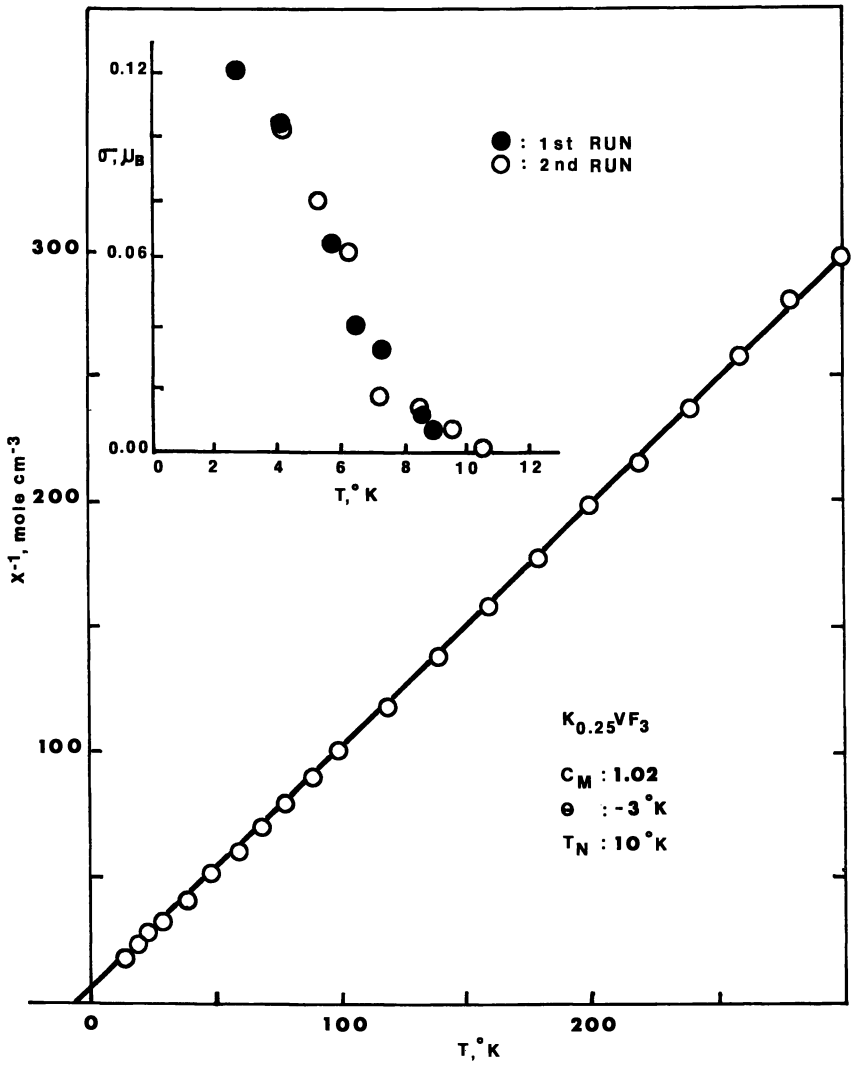

Figure 3. Inverse molar susceptibility and spontaneous moments versus temperature of a powder sample of $K_{0.25}VF_3$

7.50 ± 0.01 Å, c = 7.67 ± 0.01 Å and a = 7.51 ± 0.01 Å, c = 7.69 ± 0.01 Å, respectively. The inverse magnetic susceptibility versus temperature of $Cs_{0.25}VF_3$, shown in Figure 4, indicates an antiferromagnetic transition at 22 K. No spontaneous moment was observed for this material. Like $K_{0.20}VF_3$ and $K_{0.25}VF_3$, the inverse susceptibility of $Cs_{0.31}VF_3$, shown in Figure 5, indicates no magnetic ordering transition. (Materials that order ferrimagnetically usually do not display maxima

Table II. Magnetic Constants of A_xVF_3 Compounds

Compound	C_M *(observed)*	C_M *(calculated)*	Θ *K*	T_N *K*	σ μ_B
	(cm^3 deg mol^{-1})				
$K_{0.20}VF_3$	0.99	0.98	−10	8	0.05
$K_{0.25}VF_3$	1.02	1.03	−3	10	0.13
$Cs_{0.25}VF_3$	1.02	1.03	−20	22	0.00
$Cs_{0.31}VF_3$	1.09	1.10	−11	12	0.06
$K_{0.450}VF_3$	1.39	—	−65	48	0.28
$K_{0.498}VF_3$	1.49	—	−75	47	0.010
$K_{0.558}VF_3$	1.51	—	−78	45	0.004

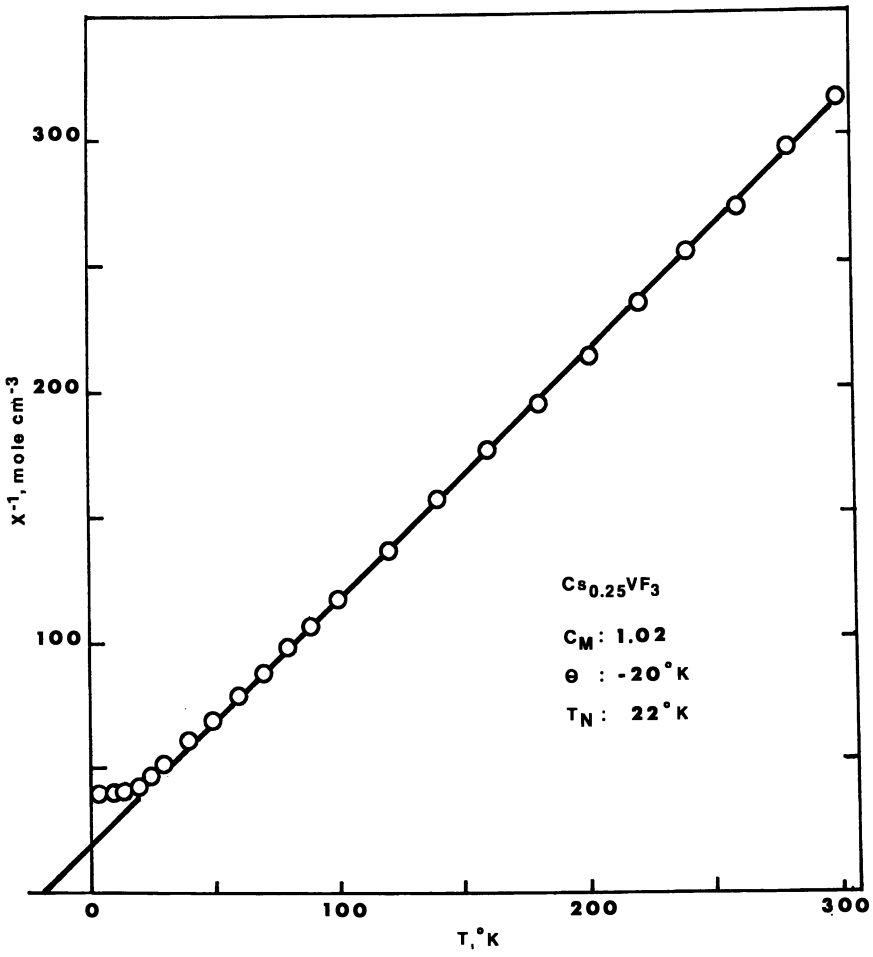

Figure 4. Inverse susceptibility versus temperature of a powder sample of $Cs_{0.25}VF_3$

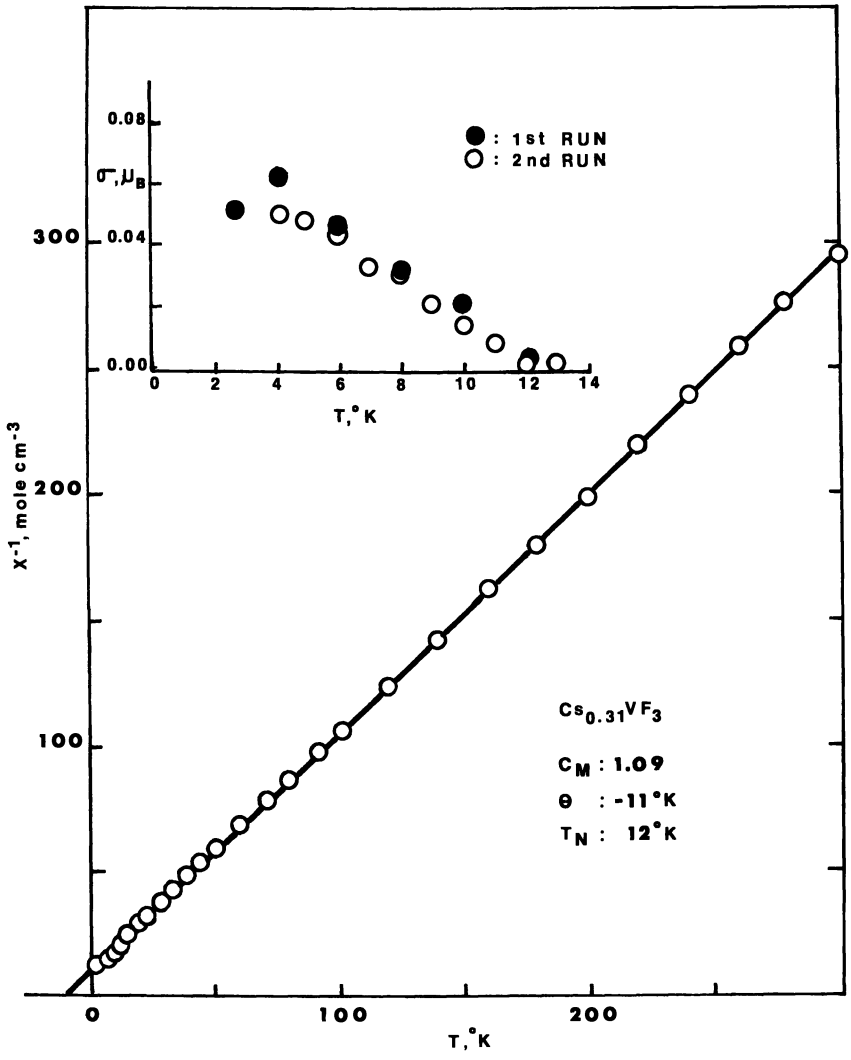

Figure 5. Inverse susceptibility and spontaneous moments versus temperature of a powder sample of $Cs_{0.31}VF_3$

in x.) However, a remnant magnetic moment which appears below T_N, and disappears above T_N, gives evidence of magnetic ordering and defines the ordering temperature very well. A summary of the magnetic constants is given in Table II.

Tetragonal K_xVF_3. The lattice constants of the tetragonal K_xVF_3 phase reportedly change smoothly with x (*4*) and a superstructure with dimensions $|a_{super}| = 2\sqrt{2}|a_{sub}|$; $c'_{super} = 2\ c_{sub}$ was observed for the composition $x = 0.558$. The inverse magnetic susceptibility of tetragonal K_xVF_3 indicated long-range magnetic ordering near 45 K (*4*). The

dependence of spontaneous moment on composition, displayed in Figure 6, is an important effect that has not been reported previously. The dimensions $|a_{super}| = 2 \quad 2|a_{sub}|$; $c_{super} = 2\ c_{sub}$ was observed for the com- remnant moments on randomly oriented powder samples of composition $x = 0.558$ and 0.498 are small, but for $x = 0.450$ the magnitude of the moment per vanadium atom is 0.28 μ_B. A summary of the magnetic constants of tetragonal K_xVF_3 is included in Table II.

Conclusions

The bronze-like A_xVF_3 structures are perovskite-like, as V–F–V bond angles are all close to 180°. They are unlike perovskites, however, in

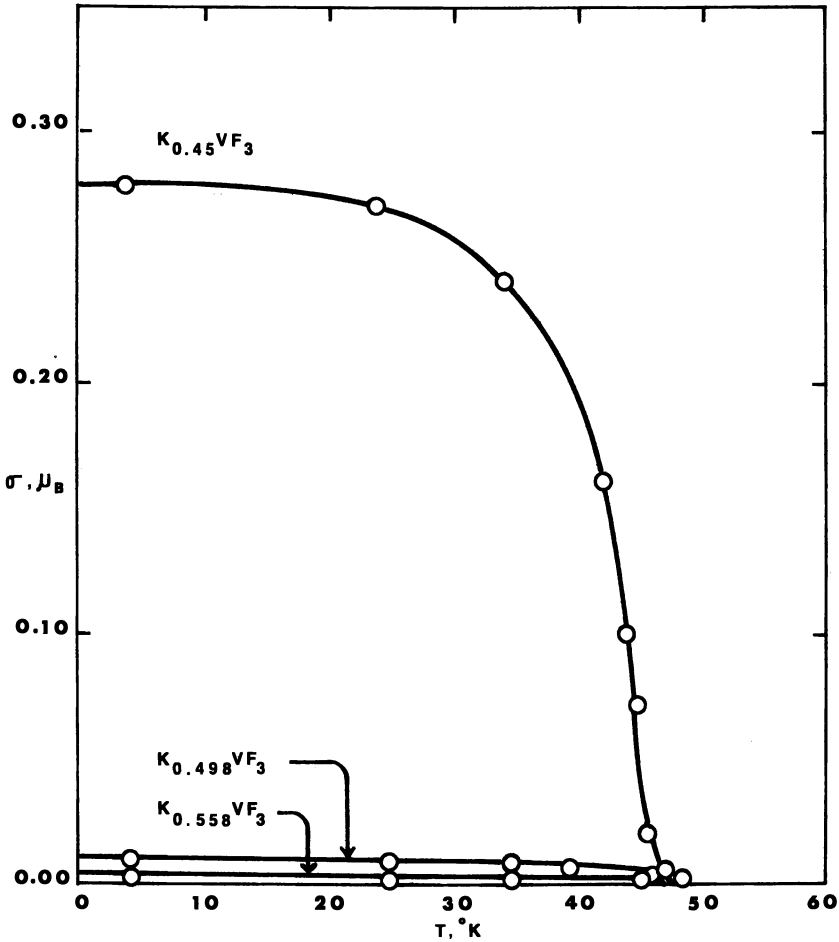

Figure 6. Spontaneous magnetic moments versus temperature of tetragonal K_xVF_3 for x = 0.450, 0.498, and 0.558

that the nearest neighboring vanadium ions in the *a–b* planes also have common nearest neighbors. The rules of Goodenough (*8*) and Kanamori (*9*) predict that these V–F–V interactions should be antiferromagnetic; however, the triangular grouping of vanadium atoms causes a constraint to this antiferromagnetic ordering. In KVF_3 (*7*) (T_N = 130 K, Θ = large), tetragonal $K_{0.498}VF_3$ (T_N = 47 K, Θ = − 75 K), and pseudohexagonal $K_{0.25}VF_3$ (T_N = 10 K, Θ = 3 K) have 0, 0.4, and 0.67 constraints per vanadium atom, respectively. Although the decrease in V^{+2}/V^{+3} would lower T_N and the magnitude of Θ, the primary cause is the increase in the number of constraints.

More subtle differences in magnetic properties within a so-called single-phase region are also significant. The important feature is that spontaneous magnetic moments change with composition. The tetragonal K_xVF_3 phase changes from ferrimagnetic (x = 0.450) to antiferromagnetic (x = 0.498 and 0.558); hexagonal Cs_xVF_3 changes from antiferromagnetic (x = 0.25) to weak ferrimagnetic (x = 0.31); and pseudohexagonal K_xVF_3 increases its ferrimagnetic moment as x increases from 0.20 to 0.25. The main reason for changes in the spontaneous moments of these compounds is probably the result of differences in atomic ordering within an apparent single phase. This ordering occurs at high temperatures and is apparent by superlattice reflections and differences in intensity of other Bragg reflections. In the case of the tetragonal K_xVF_3 compounds, weak superlattice reflections suggest V^{+2} — V^{+3} ordering. For pseudohexagonal K_xVF_3, the (031 and (213) reflections indexed as orthorhombic increase as x decreases. The lattice constants do not change with x and neither does the distortion ratio $|\mathbf{a}|/\sqrt{3}|\mathbf{b}|$ which is 1.006. This suggests K^+ ordering which is optimized with composition. The change in spontaneous magnetic moment implies that some V^{+2} — V^{+3} ordering occurs simultaneously. In the hexagonal Cs_xVF_3 phase, the X-ray data suggests little ordering of the large Cs^+ ion, and the reduced magnitude of spontaneous moments is explained best as a more random distribution of the dilute V^{+2} ion.

It is significant that all of the hexagonal and tetragonal A_xVF_3 compounds order antiferromagnetically or ferrimagnetically above 4.2 K. Most of these materials display spontaneous magnetic moments, which give a more accurate determination of T_N. All of the materials which have spontaneous moments display hysteresis effects. The magnitude of the moment depends primarily upon composition and the magnitude of the field in which the sample is cooled. Measurements made on a single crystal of $K_{0.20}VF_3$ not only substantiated anisotropy in the susceptibility but also revealed a spontaneous moment only when the c axis was parallel with the field. This suggests that the ordered spins

lie parallel to the *c* axis. Further studies of the effects of concentration on structural and magnetic properties of these phases are in progress.

Acknowledgment

The authors gratefully acknowledge the National Science Foundation (Grant No. DMR 76–83360). They thank E. Catalano for electron-beam welding services and the NASA Langley Research Center for the loan of an electromagnet and power supply. Appreciation is expressed to the University of Mississippi Computer Center for providing the time necessary for data reduction.

Literature Cited

1. Cros, C.; Feurer, R.; Pouchard, M.; Hagenmuller, P. *Mater. Res. Bull.* **1975**, *10*, 383.
2. Hong, Y. S.; Williamson, R. F.; Boo, W. O. J. *Inorg. Chem.* **1979**, *18*, 2123.
3. Cros, C.; Feurer, R.; Pouchard, M.; Hagenmuller, P. *Rev. Chim. Miner.* **1974**, *11*, 585.
4. Williamson, R. F.; Boo, W. O. J. *Inorg. Chem.* **1977**, *16*, 649.
5. Gossard, A. C.; Guggenheim, H. J.; Hsu, F. S. L.; Sherwood, R. C. *Proceedings of the Annual Conference on Magnetism and Magnetic Materials, 17th, 1971*, p. 302.
6. Stout, J. W.; Lau, H. Y. *J. Appl. Phy.* **1967**, *38*, 1472.
7. Williamson, R. F.; Boo, W. O. J. *Inorg. Chem* **1977**, *16*, 646.
8. Goodenough, J. B. "Magnetism and the Chemical Bond"; Interscience: New York, 1963; pp. 165–185.
9. Kanamori, J. *J. Phys. Chem. Solids* **1959**, *10*, 87.

RECEIVED September 15, 1978.

Extended Metal–Metal Interactions in Binary Halides of the Early Transition Metals: A New Structural Chemistry

JOHN D. CORBETT

Ames Laboratory, DOE and the Department of Chemistry, Iowa State University, Ames, IA 50011

Two distinct types of reduced halides occur for these elements: (1) metallic diiodides (for example, LaI_2) in structure types common for sulfides and silicides (single metal layers), and (2) structurally novel chlorides and bromides ($1 \leq X{:}M < 2$, X = halogen and M = metal) with halide-capped metal octahedra condensed into infinite chains, double chains, and double metal layers (for example, Gd_2Cl_3, Sc_7Cl_{10}, ZrCl). Iodine appears important in band formation and delocalization in (1). Structures in (2) are evidently governed principally by the X:M ratio and the need to bind halogen and less by electron concentration, which may remain relatively constant on condensation. Nearly all the halide structures in (2) are significantly more anisotropic than are related chalcides, which is attributed to a lower halogen participation in band formation and the resulting dominance of metal–metal bonding.

Until recently, structures known for binary transition metal halides in low oxidation states exhibited very little in the way of extended metal–metal interactions; witness the plethora of common structure types associated with these reduced phases (NaCl, CdX_2, BiI_3, UCl_3, and so on) and the contrast with the diverse structures and properties found with reduced oxides (TiO, NbO, Na_xWO_3) and metal-rich sulfides (Hf_2S, $Zr_{21}S_8$, Ta_6S) (*1*, *2*). Well-characterized examples of halides involving extensive metal–metal bonding have been limited to phases containing

0–8412–0472–1/80/33–186–329$05.00/1

the localized M_6X_n clusters of Ta, Nb, Mo, and W (X = Cl, Br, I) save for the novel, infinite chain structure of Gd_2Cl_3 (*3*) and the recent discoveries discussed in this paper. In fact, kinetic limitations have been the principal reason for this lack, although no particularly obvious reasons why this should have been suspected come to mind. In simple terms one associates fairly decent volatilities and atom mobilities with halides and thereby infers that metal halide reactions at high temperatures should reach thermodynamic equilibria with some facility relative to chalcides. Thus in metal–molten halide systems, which do appear to come to rapid equilibrium at 600°–900°C, the absence of reduction beyond the dihalide stage has been taken as compelling evidence for the absence of lower phases (*4, 5, 6*). This conclusion is already known to be wrong for the Sc–$ScCl_3$, Y–YCl_3, and Tb–$TbCl_3$ systems and will doubtlessly prove so for others. Metal–metal halide reactions can be amazingly slow when extended metal–metal bonding must be formed in the product and good transport conditions do not pertain. Also, the region of the periodic table where extended metal–metal bonding predominates appears to lie significantly to the left of elements forming either the well-known halide clusters or the complex chalcides. It is the purpose of this paper to describe the unique aspects of reduced halide chemistry, particularly structural, and to point out some of the contrasts–and, in a few cases, similarities—with chalcides and to offer some rationale for these. Much of the classification and explanation is based on structural comparisons, since a limited number of other physical characterizations are available for many of these new compounds.

Background

Except for the enigmatic Ag_2F (anti-$CdCl_2$ type), the traditional examples of metal–metal bonding in transition metal halides have all involved only the localized bonding in what are known as clusters, that is, isolated groups of up to six metal atoms together with strongly bound halogen. Although some have a significant solution chemistry, we will consider only their solid state structural properties. Well-established halide clusters that contain three or more metal atoms have all involved metals from transition groups V, VI, and VII. All classes of these have been known for a decade or more and will be itemized solely for comparison with the newer examples of extended clusters.

Niobium in phases M_3X_8, as well as Re_3Cl_9, contains well-bound triangular metal groups basically occupying neighboring interstices between close-packed halide layers. Pairs of triangles sharing a common edge are found in $CsNb_4Cl_{11}$ and closely related phases. But the best-known and most relevant examples involve the stoichiometries $MX_{2.33}$

and $MX_{2.50}$ for M = Nb, Ta and $M'X_2$ for M' = Mo, W (plus $NbI_{1.83}$). Without being totally specific or comprehensive, these involve two classes of hexametal clusters, respectively:

$M_6X_{12}^{2,3+}$: octahedra of metal atoms *edge*-capped by halogen

$M_6'X_8^{4+}$: octahedra of metal atoms *face*-capped by halogen (*1*)

These clusters evidently all possess low-energy orbitals that are exo or outward pointing from each metal atom, judging from the fact that these positions are always occupied either in the ternary systems by ligands or anions (as $M_6X_{12}{}^{n+}Y_6$) or in the binary halides in the solid state by halogens that are, for example, edge bridging in one cluster and exo in another. According to the standard description scheme (*7*), where *i* refers to inner and *a* to outer or exo positions, Ta_6Cl_{15} and Nb_6I_{11} are $Ta_6Cl^i{}_{12}Cl^a{}_{6/2}$ and $Nb_6I^i{}_8I^a{}_{6/2}$, with three halide anions bridging between clusters and occupying all six axial positions. Similarly, Nb_6Cl_{14} (or $Nb_6Cl_{12}Cl_2$) is better described as $Nb_6Cl^i{}_{10}Cl^{i-a}{}_{4/2}$, the middle type of chloride being both edge bridging in one cluster and exo to another. Similar characteristics or orbital requirements can be discerned in the extended structures described here as well. Molecular orbital approximations for bonding in these six-metal clusters are available (*8, 9*), though results to be considered later suggest that the electron count in the condensed clusters is not as critical for stability as once thought.

The chalcides, particularly the sulfides, constitute the best-studied area of solid state chemistry with which to compare halide properties, in particular, for chloride relative to the isoelectronic sulfide and, to a lesser degree, telluride versus iodide. On the other hand, oxide versus fluoride is relatively sterile because of the paucity of fluoride examples; evidently, the small size, high lattice energy, hard anion, small covalency, and higher anion:cation ratio for the same oxidation state all favor higher oxidation states and insulating products with fluoride. The remarkable TiO, ZrO, NbO, and so forth seem to have no analogy in fluoride chemistry, Ag_2F being a noteworthy exception.

The organization of the following derives from the character of the conclusions, namely, that the closest analogies between halides and chalcides come when the iodides are considered, a fact that can be attributed to the greater covalency of the iodides. In contrast, the bromides and chlorides provide numerous examples of a new and novel structural chemistry (and presumably new phenomena as well) that are not known or recognized elsewhere. Future discoveries may of course diffuse what now appear to be sharp boundaries.

The Metallic Diiodides

Reduced iodides of the active metals as a class appear to form a unique class of metallic diiodides; that is, iodides that are saltlike in the usual sense but that also exhibit a metal-like electronic conduction. A typical example can thus be formulated $La^{3+}(I^-)_2e^-$. Although some of these have been known for some time (*10*), recent structural work on the rare earth examples, especially by Bärnighausen and co-workers (*11, 12*), has made the classification emphatic. Table I lists the known examples together with structural types and some properties. All these occur in layered structures, either in the unusual eight-coordinate and almost alloylike $MoSi_2$ type or in well-known dichalcide (MoS_2, NbS_2) types of structures. These in all cases involve single, infinite metal sheets between double iodine sheets in which the distances between metal and iodine closely approximate the sum of those for iodide and normal-valent cations (La^{3+}, Th^{4+}, and so on), consistent with delocalization of (and poor screening by) the differentiating electron(s).

Table I. The Metallic Diiodides

Compounds	*Structure Type*[a]	*Properties*
LaI_2, CeI_2	$MoSi_2$[b] (*12*)	$\sigma_{300} \approx 15{,}600\ \Omega^{-1} \cdot cm^{-1}$; pauli paramagnetic ($LaI_2$) (*10*)
PrI_2	$MoSi_2$, 2MoSBr–, 2R–MoS_2 $CdCl_2$ (*10, 11, 12*)	
NdI_2	$MoSi_2$ (high P) (*13*)	
GdI_2	2H_1–MoS_2 (*14*)	high σ (*15*)
ThI_2	4H–NbS_2 (*16*)	Pauli paramagnetic, high σ (*17*)
$ScI_{2.16}$	about CdI_2[c]	$\sigma_{300} \approx 800\ \Omega^{-1} \cdot cm^{-1}$, weak paramagnet (*18*)

[a] H = hexagonal, R = rhombohedral structures.
[b] Also referred to as $CuTi_2$-type structure.
[c] No evidence of superstructure by Debye-Scherrer Techniques.

The following summarize significant factors for this type of compound:

1. Metallic binary halides, which involve single metal sheets, have to date been found only with iodides. Such phases have not been found in the bromide or chloride systems of the same metals even though most of these have been studied.
2. These are with very few exceptions the only metal–metal-bonded halides which occur in structure types also found with the chalcides. [Another example is α-ZrI_2, a semiconductor that occurs in the β-$MoTe_2$ structure with infinite metal chains (*19*).]

3. A significant covalence and participation of iodide in the conduction band is probably involved, paralleling the recognized covalence with the chalcides.

The contrast with other iodides are rather sharp; TiI_2 (CdI_2 type) is a semiconductor with localized spins and $T_N \approx 200$ K, while VI_2 is described as an insulator. The metallic examples would appear to require parent cations that have ground or low-lying d states, meaning that diiodides of the divalent rare earth metal ions with f^n states are either saltlike (for example, NdI_2 at ambient pressure, SmI_2, DyI_2, TmI_2) or nonexistent. A substantial participation of the iodide in formation of the conduction band (in energy and in overlap) seems likely in view of the fact that such compounds are not known for the smaller chloride and bromide where overlap within a cation sublattice would be more favorable. Evidently only with the large and polarizable iodide does this overlap and covalency become significant relative to that generally recognized with the higher-charged sulfide. In the terms of Goodenough (*20*), a π^* conduction band would appear to be a useful representation for these iodides. The absence of a dominant mixing with the more tightly bound valence electrons in chloride and bromide is probably the most significant factor for the appearance of a contrasting novel chemistry with the lighter halide anions. On the other hand, there is a good possibility that more highly reduced iodides (I:M < 2) can be prepared for some of these elements and that these compounds may exhibit something of the novel low dimensionality and interconnectivity of the lighter halides described in the following section.

Extended Metal Structures

Present examples of extensive metal–metal bonding in halides where this feature appears to be of major importance if not structure determining are presently limited to the chlorides and bromides of transition groups III and IV together with related rare earth elements. The metals involved thus occur in the periodic table at least one group further to the left of those where extended metal–metal bonding occurs with chalcides. As will be detailed later, the structures found with these halides are nearly always more anisotropic than the corresponding chalcides.

The halide examples encompass the doubly metal-layered ZrCl (*21*) [and the isostructural GdCl and TbCl (*22*)], the closely related ZrBr (*23*) [plus HfCl and ScCl (*24*)], and three structure types involving chains of metal octahedra, Gd_2Cl_3 (*3*), Sc_5Cl_8 (*25*), and Sc_7Cl_{10} (*26*). In all cases the distances observed between metal and halide on the outside of the sheet or chain are again quite close to the sum of those for halide and normally valent Sc^{3+}, Zr^{4+}, and so on, emphasizing the distribution of reduction electrons *within* the metal-bonded array.

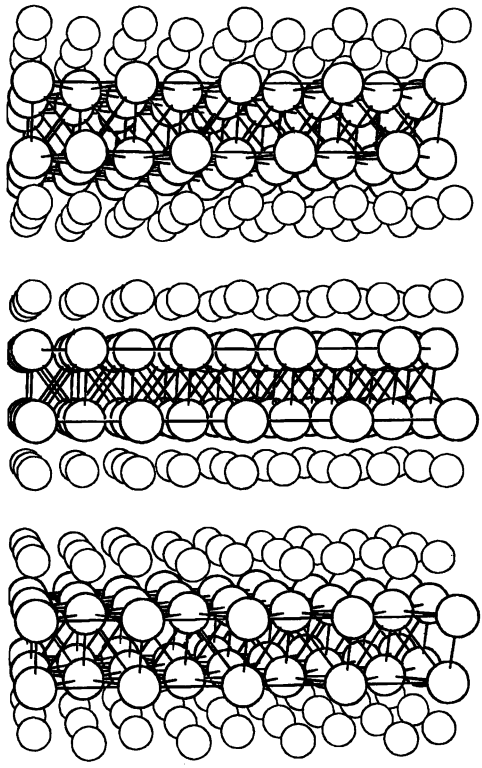

Figure 1. The four-layer slabs Cl—Zr—Zr—Cl in the structure of ZrCl. The larger and heavier spheres depict zirconium. [Arbitrary-size spheres and field view; the cell is R3m, a = 3423, c = 26.69 Å (21)]

The structure of ZrCl, Figure 1, consists of three slabs differing only in orientation, with each slab containing four closely packed layers, sequenced Cl-Zr-Zr-Cl. Each metal atom has six like neighbors in the sheet at 3.42 Å, plus three in the other sheet at 3.09 Å, which compare with 3.19 Å in thet close-packed metal. The structure provides an interesting alternative to that of the isoelectronic NbO, a three-dimensional condensed cluster $Nb^{i}_{6/2}O^{i}_{12/4}$, where all inner atoms are shared between clusters (d_{Nb-Nb} = 2.98 Å) (*8*). This condition is not feasible geometrically with the large chloride, as the metal–metal bonds would have to be lengthened to an unreasonable 3.7 Å. X-ray photoelectron spectroscopy (XPS) data (*23*) for ZrCl show a well-defined Zr 4d valence peak at 1.2 eV below E_F (the Fermi energy), with an appreciable density of occupied states at E_F. Band calculations (*27*) agree with this conclusion and confirm that the highest valence band is primarily zirconium in character, chlorine 3p being significantly more tightly bound at 6.4 eV

(by XPS). Conductivities have been reported (*28*) (without much detail) as 55 and 1.5×10^{-3} $\Omega^{-1} \cdot cm^{-1}$ for $\sigma_{||}$ (parallel) and $\sigma_{\perp}$ perpendicular), respectively. Weak bonding between the slabs is responsible for numerous defects in the crystals and graphite-like damage on grinding. Attempts at intercalation reactions so well known for layered sulfides have all been unsuccessful (*23*).

The structure of ZrBr is achieved by interchanging the top two four-layer slabs shown for ZrCl, thereby achieving some greater binding and hardness through the gain of additional second-nearest neighbors of the other kind across the van der Waals gap (comparable to $CdCl_2$ versus CdI_2). The XPS and theory results are quite similar to those for ZrCl, as expected. The formation of ScCl, as well as GdCl and TbCl, in these structures is rather surprising, as they presumably involve only two rather than three electrons in binding the metal sheets together, though this presents no difficulty with the band calculation results.

Both zirconium monohalides react readily with hydrogen to form the compounds $ZrXH_{0.5}$ and $ZrXH_{1.0}$ (*29*). These show significant hydrogen mobility just above room temperature according to nuclear magnetic resonance (NMR) studies (*30*), with the hydrogen most probably located in the tetrahedral holes between the metal layers, where it experiences an exceedingly large shielding anisotropy appropriate to its location in a two-dimensional metal sheet. Values of $(T_{1e}T)^{-1/2}$, where T is temperature and T_{1e} is spin lattice relaxation time, for these phases in the rigid region indicate densities of occupied states at E_F that are comparable to those found in (α) TaH_x and NbH_x (*31*).

The remarkable chain structure of Gd_2Cl_3—the so-called eighth wonder of the rare earth world—is depicted in Figure 2. In this structure,

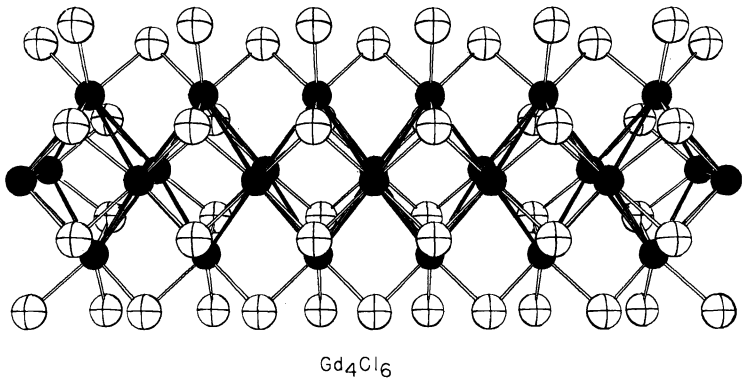

Figure 2. A portion of the infinite chain in Gd_2Cl_3: (●), gadolinium; (○), chlorine; both of arbitrary size. Duplicate rows of chlorine atoms at the top and the bottom bridge between parallel chains of metal (3).

elongated metal octahedra share short (3.35 Å) trans-edges to form infinite chains. The repeat distance along the chain (the *b*-axis) is 3.90 Å; apex atoms are 3.71–3.78 Å from the waist atoms. These distances compare with 3.60 Å in the 12-coordinate metal. Each outward-facing triangle of metal atoms in the chain is capped by a chlorine atom, so that the chain can be viewed as the product of the condensation of face-capped M_6Cl_8 types of clusters cited earlier. Two additional chlorides (shown duplicated at the top and bottom of the figure) bridge to parallel neighboring chains so as to generate sheets, and these in turn pack so that face-capping chlorides in one sheet occupy exo positions of gadolinium atoms in the shared edges in other sheets, and vice versa. The phases Gd_2Br_3 and Tb_2Cl_3 also occur in this structure (32).

The scandium chloride system contains in addition to ScCl several more reduced phases in the range $1.0 < Cl:Sc < 2.0$, and two of these have been shown to contain infinite chains of shared octahedra, Sc_5Cl_8, Figure 3, and Sc_7Cl_{10}, Figure 4. Both illustrate a new feature of metal halide chemistry (which is also found in the cluster compound Sc_7Cl_{12}), the incorporation of isolated scandium(III) cations that in turn make the metal chains *anionic*, a logical circumstance for the relatively electron-poor scandium. Thus Sc_5Cl_8 is formulated simply as $(ScCl_2^+)_\infty(Sc_4Cl_6^-)_\infty$. The latter part represents the chain of elongated metal octahedra that again share very short trans-edges (3.02 versus 3.26 Å in the metal), and this chain is in turn edge-capped by six chlorine atoms per repeating unit. The cationic part consists of octahedra of chlorine that also share trans-edges and contain the isolated scandium atoms. The apices of these chlorine octahedra are edge-bridging chlorines in other metal chains (not shown). The chlorine atoms thus sheath the anionic chain as well as stabilize the isolated cations in a very regular and sensible fashion. The compound does not give an electron spin resonance (ESR) signal (compare Sc_7Cl_{10} below) and is a presumed but not proven metallic conductor. Conceptually, the chain again comes from condensation of clusters, this time *edge*-bridged, as found in the compound $Sc^{3+}(Sc_6Cl_{12}^{3-})$ (33) as

$$Sc^{3+}(Sc_6Cl_{12}^{3-})\,(s) \rightarrow (ScCl_2^+)\,(Sc_4Cl_6^-)\,(s) + 2ScCl_2(g)$$

Finally, the most complex of the known series, Sc_7Cl_{10}, can be cataloged as the product of condensation of two parallel chains of the sort just described to give $(ScCl_2^+)_\infty(Sc_6Cl_8^-)_\infty$ (*see* Figure 4), namely

$$2(ScCl_2^+)\,(Sc_4Cl_6^-)\,(s) \rightarrow (ScCl^+{}_2)\,(Sc_6Cl_8^-)\,(s) + 3ScCl_2(g)$$

the hypothetical process being accompanied by conversion from edge- to face-capping of the outward-facing triangles of the metal chain by chloride. (This, of course, does not represent a mechanism, although

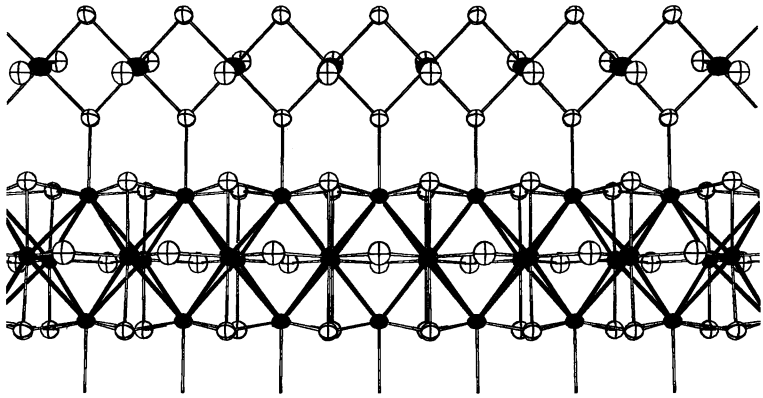

Figure 3. Sc_5Cl_8 *or* $(ScCl_2^+)(Sc_4Cl_6^-)$*: A section of the infinite parallel chains of chlorine octahedra containing scandium(III)* (top) *and of metal octahedra (solid atoms) capped by chlorine* (bottom)*. Dangling bonds at the bottom go to chlorine atoms shown at the top in other chains, while the apices of chlorine octahedra at the top are also exo to metal chains in other sheets. (Thermal ellipsoids are drawn at the 90% probability level.)* (25)

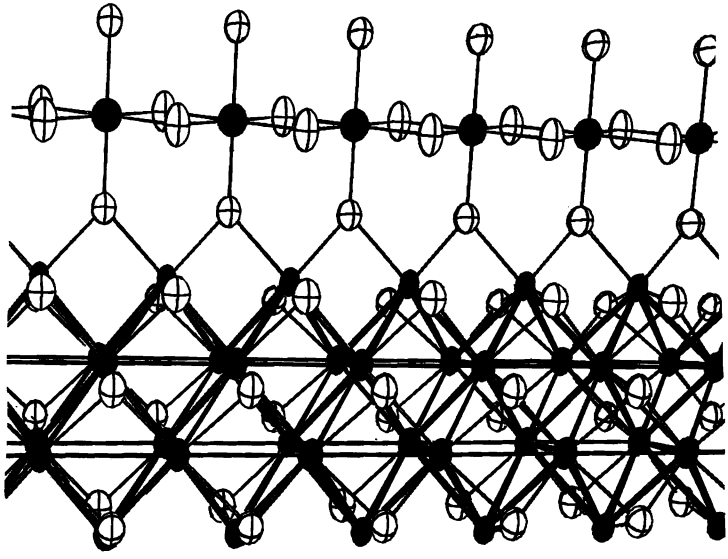

Figure 4. Sc_7Cl_{10} *or* $(ScCl_2^+)(Sc_6Cl_8^-)$*. Side view of the double octahedra of scandium metal* (bottom) *and parallel chain of chlorine octahedra containing scandium(III)* (top) *(90% thermal ellipsoids)* (26).

$ScCl_2$ is thought to be the active species in the gas phase transport reaction.) Again, similar chlorine octahedra surround the isolated scandium(III) ions in a parallel chain, all of these chlorides also being exo to more distant metal atoms in the anion chain. All three of the shared edges of the metal structure are moderately short, 3.15 Å; all other scandium–scandium distances in the compounds that have not already been cited are in the range of 3.20 to 3.55 Å, the longer distances arising from distortion of the shared metal octahedra.

This compound is most remarkable in giving a very sharp ESR signal (g = 1.97, 50g fwhm, for g = gyromagnetic ratio and fwhm = full width at half-maximum) and a substantial magnetic susceptibility. If the latter data are assumed to follow the Curie–Weiss law, the resulting moment corresponds very closely to that expected for two isolated d^1 ions per repeating unit in the chain. Since the signal suggests these are weakly interacting at room temperature, they have been speculated to be localized at the relatively isolated apices of the double metal chain, which would leave 9 of the 11 electrons per repeating unit delocalized. The onset of some magnetic ordering is evident near 80 K (*26*).

Continued condensation of the scandium chains of octahedra via edge-sharing and chlorine elimination, proceeding approximately vertically in Figure 4, will ultimately yield the face-capped double metal sheets of ScCl (*see* Figure 1), and condensation of these in the third direction will lead directly to the close-packed metal.

The high reactivity and small yields of some of these compounds have made further characterization limited and difficult. However, good-quality XPS and ultraviolet photoelectron spectroscopy (UPS) results for Sc_7Cl_{10} have been obtained by taking the precaution of opening the reaction container only in the dry box attached to the spectrometer. The results offer some pleasing confirmation of the structure above via both the apparent resolution of the Sc $2p_{3/2}$ and $2p_{1/2}$ peaks for atoms in the chain from those from the isolated scandium(III) atom at several-volts-higher binding energy and the appearance of a broad valence band with a sharp edge at E_F indicative of metallic conduction (*34*).

Synthetic Problems and Techniques

Significant kinetic limitations in the formation of many of these reduced scandium and zirconium halide systems are evident when one considers the sizable number of phases now known and the extent to which they have escaped detection in earlier studies. Apparently reactions of excess metal with a liquid halide in a higher oxidation state often become ineffective after only a thin layer of product forms on the metal surface, yielding little or nothing in the way of meaningful results from

a conventional phase study. Thus Sc_2Cl_3 (*5*), the first product to form on the metal when either liquid or gaseous $ScCl_3$ is the oxidant, gives a coating thereon which persists in metastable equilibrium up to the decomposition point of Sc_2Cl_3 (877°C) (*26*) in spite of the thermodynamic stability of at least three lower phases. [The more oxidized Sc (Sc_6Cl_{12}) and Sc_5Cl_8 have not been detected in the direct reaction either.] On heating to about 960°C, all intermediate phases decompose and the product is ScCl. Intermediate temperatures allow the production of intermediate phases via disproportionation but often in mixtures and therefore not in equilibrium.

Synthesis with chemical transport, when possible, has turned out to be the most useful, though the yields are characteristically low. For this situation a sealed tantalum tube is heated under a temperature gradient, with metal strips in the hot end or throughout the length of the tube and with $ScCl_x(s)$ as a reservoir in the cool end. For example, at about 850°C a partial pressure of $ScCl_3$ is generated by a disproportionation such as $ScCl_x(s) \rightarrow Sc(s) + ScCl_3(g)$, after which the trichloride diffuses to the hottest end of the tube (about 1000°C), where reaction with the metal produces a small partial pressure of a reduced species, probably $ScCl_2$, via the endothermic reaction

$$2ScCl_3(g) + Sc(s) \xrightarrow{1000^\circ} 3ScCl_2(g)$$

Diffusion of this product toward the cool end reverses the foregoing reaction and deposits not the metal but an equilibrium phase via

$$7ScCl_2(g) \xrightarrow{900^\circ} Sc_5Cl_8(s) + 2ScCl_3(g)$$

and the process with $ScCl_3$ repeats. The products are often deposited in bands, with the oxidation state increasing [increasing $P(ScCl_3)$ at constant T] with decreasing temperature.

All the above require that tantalum or other similarity inert and refractory containers be used for containment; glass is naturally very unsuitable because of the high stability of the oxides and silicides of the elements of interest.

New Clusters

Although this article is largely concerned with extended and not localized examples of metal–metal bonding, considerations of stability and electron count require that we note some new localized examples that have also been synthesized via transport reactions and that effectively

extend the known existence of clusters two groups to the left in the periodic table (33). Materials characterized structurally include gem crystals of $Zr_6Cl^{i-i}{}_{12}Cl^{a-a}{}_{6/2}$, which is isostructural with TaT_6Cl_{15}, the new Zr_6Cl_{12} and Zr_6I_{12} ($Zr_6X^i{}_6X^{i-a}{}_{12/2}$ with half of the bridging halides exo to metal in other clusters), and $Sc^{3+}(Sc_6Cl_{12}{}^{3-})$, where the cluster itself is isoelectronic in valence electrons with that in $(Zr_6Cl_{12}{}^{3+})(Cl^-)_3$. The distribution of bridging chlorine is neglected in the last two formulations.

Electron Count and Stability

Chemists tend to associate stability with certain electron configurations, particularly in molecules. Comparable relationships sometimes pertain in the extended solid state, but one surprising contrast has already been noted: a change from ZrBr or ZrCl, with three electrons per metal in the band, to ScCl or GdCl, with two electrons per metal, occurs within the same respective structure type. Even the localized examples of isolated clusters are surprisingly variable in their electronic structure. In fact, a comparison suggests that, at least for the relatively electron-deficient examples, the anion:cation ratio may be more important than electron count in determining structure and thence the degree of metal–metal bonding. On the other hand, an electronic (rather than geometric) reason for, or a difference arising from, edge versus face capping is not apparent.

Table II summarizes the electron count per six metal atoms for all halides with octahedral metal groupings in discrete or extended clusters.

Table II. Electron Counts for Discrete and Extended-Cluster Halides (Electrons per six metal atoms)

		Halide-Capping Mode	*e/6M*
Traditional Clusters:[a]	$Mo_6X_8{}^{4+}$	face	24
	$Nb_6I_8{}^{3+}$	face	19
	$Nb_6X_{12}{}^{2,3,4+}$	edge	14–16
New Clusters:	Zr_6X_{12}	edge	12
	$Zr_6Cl_{12}{}^{3+}$, $Sc_6Cl_{12}{}^{3-}$	edge	9
Chains:	Gd_2Cl_3	face	9
	$(ScCl_2^+)(Sc_4Cl_6^-)$[b]	edge	10.5
	$(ScCl_2^+)(Sc_6Cl_8^-)$[b]	face	9–11[c]
Double Sheets:	ScCl, GdCl	face	12
	ZrCl, ZrBr	face	18

[a] Tantalum is comparable to niobium and, to a lesser extent, tungsten to molybdenum.
[b] Electron count per six metal atoms in metal–metal-bonded chains.
[c] Count depends on interpretation of magnetic properties (*see* text) (*26*).

The new examples of isolated clusters for group III and IV naturally extend by a fair amount the lower limit of what has been supposed necessary for cluster stability. This is naturally accompanied by a lengthening of the metal–metal bonds, those in $Zr_6Cl_{12}^{3+}$ being about 0.3 Å longer than in analogous niobium clusters, an effect that is presumably also emphasized by larger orbitals in the earlier element.

The significant role of halide is particularly apparent on progressing from clusters to chains (*see* Table II). Here condensation of the normally trivalent elements is found to take place with almost no change in electron concentration and solely by reduction in the halide:metal ratio. Thus there is a basically isoelectronic series from X:M $\approx$ 2 to 1.25–1.5 in the chains themselves, or 1.4–1.6 in overall composition, the latter including halide necessary to occupy to exo positions as well as to sheath the isolated cations. Further reduction and condensation to double sheets is accomplished with no more electrons than in the chain compounds in the case of trivalent elements or with a 50% gain in electron count for zirconium. The electron concentration in the zirconium cases is now in the range found with traditional isolated clusters. Given adequate metal–metal bonding, the structure with a more electropositive element appears to be determined principally by the X:M ratio, extended metal–metal bonding taking place to the extent allowed by the number of halide ions, with the requirements that exposed metal edges or faces be capped by halide and that exposed exo positions be occupied through secondary interaction with otherwise bound halides. These factors are of necessity deduced from these present examples and may be subject to appreciable modification in the future. The new features already discerned, particularly the presence of anionic chains, raise even more questions; for example, whether the neutral Sc_4Cl_6 chain, Figure 3, would be stable and obtain adequate packing by itself. [A compound with this composition is known (5) but its structure is not.] The idea of going to ternary systems so that different cations may either replace the function of the homometallic scandium(III) in the examples in Figures 3 and 4 or provide other structural arrangements indeed seems pregnant with possibilities. Also, it is not at all obvious why the features of these new structures, especially the idea of anionic chains, should not also be found in reduced halides of elements further to the right in the periodic table than discussed here.

Some subtleties of electron count versus distance are already discernible within the scandium compounds, the Pauling bond orders summed over all metal–metal bonds in each structure varying smoothly with the number of electrons per metal. Thus the ionic chains $Sc_4Cl_6^-$ reasonably exhibit relative shortening of the metal–metal bonds when compared with those in Gd_4Cl_6 (25).

Table III. Contrasts in Structural Types Between Metal–Metal-Bonded Halides and Related Chalcides with Isoelectronic Anions[a]

Same Formula Type, Same Metal

ScCl	(ZrBr)		ScS	(NaCl)
ZrCl	(ZrCl)	vs.	$Zr_{1-x}S$	(defect NaSl)
GdCl	(ZrCl)		GdS	(NaCl)
ZrBr	(ZrBr)		$Zr_{1-x}Se$	(defect NaSl)

Same Formula Type, Isoelectronic

ScCl	(ZrBr)		TiS	(NiAs)
ZrCl	(ZrCl)	vs.	NbS	(MnP $\approx$ NiAs)
ZrBr	(ZrBr)		NbS[b]	(MnP)

Same Metal and Oxidation State

ZrCl	(ZrCl)		Zr_2S	(Ta_2P)
HfCl[c]	(ZrBr)		Hf_2S[d]	(Hf_2S)
ZrBr	(ZrBr	vs.	Zr_2Se	(Ta_2P)
LaI_2	($MoSi_2$)		LaTe	(NaCl)
ThI_2	(4H–NbS_2)		Hf_2S[c]	(CsCl)

[a] Sources for halide structures are cited elsewhere in this article; for chalcide structures, *see 1, 2.*
[b] The isoelectronic NbSe is unknown.
[c] Both contain the structural feature of double metal layers, but the number of nonmetal layers differs.

Structural Comparisons with Sulfides

An earlier section noted that only with the heaviest iodide does one obtain metallic halides that exhibit sulfide-like types of structures (among others), a feature that could be attributed to roughly comparable participation of the polarizable iodide anion in bonding and band formation. On the other hand, the situation with lighter isoelectronic anions—that is, chloride versus sulfide, bromide versus selenide—is one of structural contrast, as summarized in Table III. For such purposes one might compare (A), compounds of the same nonmetal:metal ratio and for same metals, such as ScCl versus ScS, on the basis of the evidence cited in the previous section; (B), completely isoelectronic compounds of the same formula type but of necessity with different elements (ScCl versus TiS); or (C), compounds of the same metal in the same oxidation state but necessarily of a different formula type (ZrCl versus Zr_2S). In fact, the basis for the comparison does not make much difference in the principal conclusion; the highly reduced chlorides and bromides inevitably exhibit structures of lower dimensionality and greater anisotropy than

those for the chalcides with isoelectronic anions. The only similarity perceived in the whole list (as long as we restrict ourselves to metallic compounds) is the presence of double metal layers both in Hf_2S and in the isoelectronic HfCl, the nonmetal layers between them being single and double, respectively, although some extended but highly shared metal structures can be discerned in the Ta_2P examples. Other than this, the structural relationships are ones of contrast rather than similitude.

The foregoing comparisons and the results of the previous section on extended structures lead to the following generalities:

1. Relative to sulfides or selenides, the corresponding chloride or bromide ions possess lower charges, lower polarizabilities, and higher ionization energies and therefore bring about less metal–nonmetal covalency or mixing. This means that there is less halide participation in bonding and in band formation, which in turn leads to more contracted d orbitals on the metal (nephelauxetic effect) and to less direct metal–metal overlap at the same distance.
2. As a consequence of the factors in item 1, strong metal–metal bonding in the presence of halide, relative to chalcide,
   a. will be found further to the left in the periodic table;
   b. occurs in anisotropic structures more dominated by metal–metal interactions;
   c. is found to occur in structure types where the nonmetal:metal ratio is the principal determining factor, much more so than the actual electron count for metal–metal bonding; and
   d. will at the same nonmetal:metal ratio contain stronger (or more) metal–metal bonding in the halide because of the increased number of electrons (presuming the change in structure type is interpretable).

Although the foregoing generalities fit the facts pleasingly well, there are opposing changes in some comparisons that are difficult to sort out. Thus the increase in both nuclear charge and probable covalency on going from the halide to the isoelectronic chalcide (for example, ZrCl to NbS) affects orbital size in opposite directions, thus making distance comparisons difficult to fathom even after the change in structure type is allowed for. The problem also comes up with $ZrCl_2$ versus MoS_2, below.

Some Halide Puzzles

Finally, included for completeness are a few structures that at first glance appear to be favorable for metal–metal bonding but that do not exhibit the expected conduction.

Four compounds that occur in the β-$ZrCl_3$ (or β-$TiCl_3$) structure have received significant amounts of attention: $ZrCl_3$, $ZrBr_3$, ZrI_3, and

HfI_3. This conceptually simple structure consists of hexagonal, close-packed halide layers in which metal atoms occupy one-third of the octahedral interstices so as to form infinite metal chains parallel to the *c*-axis, the remaining octahedra presumably being vacant (*35*). The ideal metal–metal distances along these chains are quite short relative to those with lower oxidation states: 3.067 Å in $ZrCl_3$ and 3.156 Å in $ZrBr_3$, versus 3.09 Å and 3.13 Å between the metal sheets in ZrCl and ZrBr, 3.38 Å in 3R–$ZrCl_2$ (below), and 3.18 Å for the shortest distance in α-zirconium. The four trihalides listed above are also significantly nonstoichiometric, increasingly so with heavier halide. The iodides develop a recognizable superstructure toward the upper composition limit, while the chloride at the lower limit ($ZrCl_{2.94}$) exhibits a diffuse 001 reflection suggestive of distortions of the chains (*36*). But even with the stoichiometric compounds, only semiconduction can be detected ($\sigma \approx 10^{-5}\ \Omega^{-1} \cdot cm^{-1}$, $E_g \approx 0.25$ eV, where E_g = energy gap) and an appreciable paramagnetism is present (*37*).

Both this magnetism and the absence of abnormal thermal ellipsoids according to a single-crystal structure study of $ZrBr_3$ (*38*) mitigate against distortions leading to pairing of the metal atoms. Although the initial modeling for this structure concluded that conduction would result from a half-filled d_{z^2} band (*39*), the observed trigonal elongation of the MX_6 octahedra strongly suggests the crystal field therefrom places the e_g level lower, thereby putting the odd electron in an orbit normal to the *z*-axis. Defects from displacement of some metal atoms into the other two strongs of octahedra that are normally vacant and reduced overlap from contraction and tighter binding of the 4d orbitals on oxidation to zirconium(III) (*40*) may also be important.

Zirconium(II) chloride is novel in that it represents the only halide known that exhibits solely trigonal prismatic coordination of metal by halide, being isostructural (and isoelectronic) with the slab structure 3R–MoS_2. The phase is a semiconductor according to both XPS and conductivity data (*40*). The large metal separation (6 neighbors at 3.38 Å versus 12 at 3.18–3.19 Å in the metal) is consistent with the narrow valence band observed at 1.1 eV, presumably comprised of Zr 4d. MoS_2 is well known to have a filled d^2 valence band well removed from E_F with substantial overlap and mixing of metal and nonmetal states. The properties of other dihalides that occur in layered (CdX_2) structures, such as $TiCl_2$, VCl_2, $FeCl_2$, and $NiCl_2$ (but excluding the metallic $ScI_{2.16}$; Table I), all indicate only relatively weak interactions between metal centers.

Chalcide Clusters

This article has already made note of both the well-known layered and the highly reduced (metal-rich) chalcides, both the simple and

relatively complex structures in the latter being isotropic compared with some halides. These extremes should be balanced by a brief note that some intermediate phases do exhibit well-defined clusters. In Mo_6Se_8 (*41*) trigonally distorted metal octahedra are face-capped by selenium, analogous to the dichloride, and these are connected by selenium bridging to exo positions in neighboring metal octahedra. In many respects the structure appears to be the face-capped equivalent of the edge-bridged Zr_6I_{12} (*33*). Mixed chalcide–halide derivatives, as well as the $M^{II}Mo_6S_8$ Chevrel phases, are well known (*42*). Metal tetrahedra that are face-capped by sulfur are found in $Mo_4S_4Br_4$ (*43*) and in the isostructural Pr_4I_8 (*12*). An extended cluster in Ti_5Te_4, V_5Se_4, and related phases consists of chains of metal octahedra sharing opposite vertices and face-capped by bridging nonmetal (*44*). Future work may be expected to bring about a bridging between these types and the halide structures already discussed in both an experimental and a conceptual sense. (Added in proof: Many more examples of extended and localized metal–metal-bonded structures now are being found for the rare earth metal halides (*45*).)

Glossary of Symbols

a = outer or exo binding halide
d = distance
E_F = Fermi level
E_g = energy gap
e^- = electron
σ = electrical conductivity
$\sigma_{||}$ = electrical conductivity, parallel
$\sigma_\perp$ = electrical conductivity, perpendicular
g = gyromagnetic ratio
(g) = gas state
fwhm = full width at half-maximum
i = inner bridging halide
M = metal
T_{1e} = spin lattice relaxation time
T = temperature
T_N = Néel temperature
X = Cl, Br, I
(s) = solid state

Acknowledgments

The author is indebted to H. Bärnighausen for the preliminary information on many of the structures cited in Table I and to H. F. Franzen for several valuable discussions on chalcide structures. The author also

gratefully acknowledges past and present students who have contributed in a major way to the accumulation of much of the evidence considered here, as is clear from the references cited. Many of the new developments come from the recent Ph.D. theses of Douglas Adolphson, Richard Daake, Alan Cisar, and Kenneth Poeppelmeier. All the work has been supported by the U.S. Department of Energy, Office of Basic Energy Sciences, Materials Sciences Division.

Literature Cited

1. Wells, A. F. "Structural Inorganic Chemistry," 4th ed.; Clarendon Press: Oxford, 1975.
2. Franzen, H. F. *Prog. Solid State Chem.* **1978**, *12*, 1.
3. Lokken, D. A.; Corbett, J. D. *Inorg. Chem.* **1973**, *12*, 556.
4. Corbett, J. D.; Pollard, D. L.; Mee, J. E. *Inorg. Chem.* **1966**, *5*, 761.
5. McCollum, B. C.; Camp, M. J.; Corbett, J. D. *Inorg. Chem.* **1973**, *12*, 778.
6. Corbett, J. D. *Rev. Chim. Miner.* **1973**, *10*, 239.
7. Schäfer, H.; Schnering, H.–G. *Angew. Chem.* **1964**, *76*, 833.
8. Cotton, F. A.; Haas, T. E. *Inorg. Chem.* **1964**, *3*, 10.
9. Robbins, D. J.; Thomson, A. *J. Chem. Soc., Dalton Trans.* **1972**, 2350.
10. Corbett, J. D.; Sallach, R. A.; Lokken ,D. A. In "Lanthanide-Actinide Chemistry," *Adv. Chem. Ser.* **1967**, *71*, 56.
11. Warkentin, E.; Bärnighausen, H. *Third European Crystallographic Meeting, Zürich, Switzerland, Abstract M 05 O, 1976*, p. 354.
12. Warkentin, E.; Bärnighousen, H. *Z. Anorg. Allg. Chem.* **1979**, *459*, 187.
13. Beck, H. P. *Z. Naturforsch.* **1976**, *31B*, 1548.
14. Bärnighausen, H., personal communication, 1978.
15. Mee, J. E.; Corbett, J. D. *Inorg. Chem.* **1965**, *4*, 88.
16. Guggenberger, L. J.; Jacobson, R. A. *Inorg. Chem.* **1968**, *7*, 2257.
17. Clark, R. J.; Corbett, J. D. *Inorg. Chem.* **1963**, *2*, 460.
18. McCollum, B. C.; Corbett, J. D. *J. Chem. Soc., Chem. Commun.* **1968**, 1666.
19. Guthrie, D. H.; Corbett, J. D., unpublished data.
20. Goodenough, J. B. *J. Appl. Phys.* **1966**, *37*, 1415.
21. Adolphson, D. G.; Corbett, J. D. *Inorg. Chem.* **1976**, *15*, 1820.
22. Simon, A.; Mattausch, Hj; Holzer, N. *Angew. Chem., Int. Ed. Engl.* **1976**, *15*, 624.
23. Daake, R. L.; Corbett, J. D. *Inorg. Chem.* **1977**, *16*, 2029.
24. Poeppelmeier, K. R.; Corbett, J. D. *Inorg. Chem.* **1977**, *16*, 294.
25. Poeppelmeier, K. R.; Corbett, J. D. *J. Am. Chem. Soc.* **1978**, *100*, 5039.
26. Poeppelmeier, K. R.; Corbett, J. D. *Inorg. Chem.* **1977**, *16*, 1107
27. Marchiando, J.; Harmon, B. N.; Liu, S. H. *Physica* **1980**, *in press.* .....
28. Troyanov, S. I. *Vestn. Mosk. Univ., Khim.* **1973**, *28*, 369.
29. Struss, A. W.; Corbett, J. D. *Inorg. Chem.* **1977**, *16*, 360.
30. Hwang, T. Y.; Torgeson, D. R.; Barnes, R. G. *Phys. Lett. A* **1978**, *66*, 137.
31. Barnes, R. G., personal communication, 1978.
32. Simon, A.; Holzer, N.; Mattausch, Hj. *Z. Anorg. Allg. Chem.* **1979**, *456*, 207.
33. Corbett, J. D.; Daake, R. L.; Poeppelmeier, K. R.; Guthrie, D. H. *J. Am. Chem. Soc.* **1978**, *100*, 652.
34. Poeppelmeier, K. R. Ph.D. Dissertation, Iowa State University, Ames, IA, 1978.
35. Dahl, L. F.; Chiang, T.; Seabaugh, P. W.; Larsen, E. M. *Inorg. Chem.* **1964**, *3*, 1236.

36. Daake, R. L.; Corbett, J. D. *Inorg. Chem.* **1978**, *17*, 1192.
37. Clemmer, R. G. *Diss. Abstr. B* **1977**, *38*, 674.
38. Kleppinger, J.; Calabrese, J. C.; Larsen, E. M. *Inorg. Chem.* **1975**, *14*, 3128.
39. Dahl, L. F.; Chiang, T.; Seabaugh, P. W.; Larsen, E. M. *Inorg. Chem.* **1964**, *3*, 1236.
40. Cisar, A.; Corbett, J. D.; Daake, R. L. *Inorg. Chem.* **1979**, *18*, 836.
41. Bars, O.; Guillevic, J.; Grandjean, D. *J. Solid State Chem.* **1973**, *6*, 48.
42. Chevrel, R.; Sergent, M.; Prigent, J. *J. Solid State Chem.* **1971**, *3*, 515.
43. Perrin, C.; Chevrel, R.; Sergent, M. *C. R. Acad. Sci., Ser. C* **1975**, *280*, 949.
44. Grønvold, F.; Kjekshus, A.; Raam, F. *Acta Crystallogr.* **1961**, *14*, 930.
45. Simon, A., private communication, 1979.

RECEIVED September 13, 1978.

Hydrothermal Stability of Simulated Radioactive Waste Glass

GREGORY J. McCARTHY[1], BARRY E. SCHEETZ, SRIDHAR KOMARNENI, DEANE K. SMITH, and WILLIAM B. WHITE

Materials Research Laboratory, Pennsylvania State University, University Park, PA 16802

A study of stability of a typical simulated high-level waste glass in contact with pressurized water at 300°C in a closed system has shown that extensive reaction occurred within a few weeks. The water acted as a catalyst–solvent in devitrification of the glass and in dissolution, transport, and recrystallization of some of its constituents, and as a reactant in forming hydrated and hydroxylated phases. Solid glass was converted into fragmented and partially dispersed masses of crystalline and noncrystalline material plus dissolved species. The crystalline reaction products were found to be analogues of minerals. Much of the Na, Mo, and B in the original glass were identified in the product solutions. Of the elements or analogues of long-lived, hazardous, radionuclides, only Cs was observed in the solutions in substantial amounts.

Solid state chemistry plays an important role in modern energy research (*1*). Many energy research problems are characterized by exceedingly complex chemical systems in which solid substances must be in contact with liquids, gases, or plasmas under extreme conditions of temperature and pressure. Some examples include MHD electrode degradation, first-wall stability in fusion reactors, chemical reactions in oil shales during retorting, reactions of geothermal waters with rocks, pumps, and plumbing, performance of refractories in coal gasification reactors, and many problems associated with nuclear reactors and nuclear waste disposal.

[1] Author to whom correspondence should be sent. Current address: Department of Chemistry, North Dakota State University, Fargo, ND 58105.

0–8412–0472–1/80/33–186–349$10.25/1

Such complex problems are more often studied by manipulation and detailed examination of solid–liquid–gas–fluid–plasma reactions followed by combined inductive–deductive analyses based on experience with simpler systems rather than by exact thermodynamic and kinetic calculations.

The record for chemical complexity may well be held by problems involving the stability of radioactive wastes. When these wastes are introduced into underground disposal sites (repositories), the potential waste–rock–water interactions (2) involve more than half the elements in the periodic table. What follows is a report of original research into the reactions of a complex, simulated (nonradioactive) nuclear waste product with water under one moderately severe set of pressure–temperature (P–T) conditions postulated for a nuclear waste repository (2, 3). The tools and methodology to be described could just as well be applied to any of the problems involving chemically complex systems that were cited earlier.

Disposal of high-level radioactive waste (radwaste) produced by nuclear power plants requires three steps: (1) the preparation of a suitable waste form; (2) the packaging of the waste form for handling, transport, and storage; and (3) the final disposal of the waste form. The research discussed in this paper concerns borosilicate glasses as a reprocessing waste form and geological repositories as the disposal sites. Clearly these are only two of many options, depending on policy decisions concerning whether spent reactor fuel will be reprocessed to recover uranium and plutonium or disposed of directly, whether the spent fuel or reprocessing wastes will be stored for long times (10 to 100 years) to allow for decay of short-lived isotopes, whether there should be a few national respositories (which require long-distance transport) or many small repositories nearer to the sources of the wastes, whether to perform separations among the complex wastes and burn the long-lived actinide fraction in reactors or dispose of it in space, and so on.

The borosilicate glass waste form is one of the most intensively developed concepts. It is presupposed that the reactor fuel rods have been reprocessed and that a high-level waste stream containing most of the fission products plus some corrosion products and reprocessing chemicals is the source material for the waste form. These materials are transported in solutions that are evaporated, dried, and fired to produce a calcine that is mixed with a frit in an in-can melter to produce a low-viscosity borosilicate glass. The glass is made, in the form of a massive ingot, directly in the stainless steel canister, which then serves as the handling unit and also as an additional barrier in final storage (4). The ratio of high-level waste calcine to frit can be controlled. The waste canisters produced in this manner are initially thermally hot with surface

temperatures ranging up to 400°C depending on the age of the wastes, the waste loading (waste-to-frit ratio), and the thermal properties of the repository (*3*). The surface temperature drops to nearly ambient over a period of several hundred years (the thermal period) as short-lived, heat-emitting, radionuclide decay (*2, 3*).

Geological repositories are conceived as mined-out chambers at depths in the range of 500–1000 m. Bedded salt, basalt, granite, and shale have all been considered as candidate rock types. The repository is usually conceived as remaining open for a number of years to permit insertion of additional canisters and to permit retrieving of canisters should that be desirable. Ultimately, however, the repository would be back-filled and the wastes would be in permanent storage. The waste form itself, the canister, and the geological formation act as barriers to prevent migration of dangerous radioactive elements to the biosphere.

A major factor in the transport of radionuclides from the repository to the biosphere is water. Some water occurs in the host rock, and it could be mobilized by the thermal heat of the canisters. Although repository rocks are selected with low permeability as an important criterion, there is always some percolation of groundwater. There is also the possibility, remote but real, of accidental flooding of the repository. Providing that the canister remains intact, circulation of water is of little importance, but should the canister be breached, the reaction of water with the waste form becomes a key element in the analysis of repository behavior. Thus the present research is addressed to the problem of the stability of the borosilicate glass waste form if it comes in contact with water during the thermal period.

Glass has been advocated as a waste form because it is chemically inert, has a low leach rate with respect to radionuclides, and can be fabricated in remotely operated facilities (*4*). Experiments on the stability and insolubility of glasses, however, have mainly been restricted to a temperature regime of 25° to 100°C. Leaching evaluation, for example, is mainly done with the Paige test (*5*), which involves soaking the glass in frequently replaced water at 25°C, or with the Soxhlet test (*5*), which bathes the glass in continuously distilled water at 100°C. Water coming into contact with the glass during the thermal period will be much hotter than water used in previous test conditions, and it was not clear that the same optimistic conclusions concerning stability and insolubility would obtain. The present research was initiated to evaluate the stability of a typical radwaste glass under conditions more representative of the repository environment.

The experiments described here were carried out at 300°C and 300 bar total pressure. The pressure corresponds roughly to the load pressure in a back-filled repository at a depth of 1000 m. The temperature is in

the range expected from young waste (10 years out of the reactor) at a level of waste loading corresponding to 3.2 kW per 6-in.-diameter by 8-ft-high canister (3). Under these conditions water exists as a liquid, although conditions are rather close to the critical point, 215 bar and 373°C.

Borrowing a concept from experimental geochemistry, we define reactions involving hot aqueous solutions confined under pressure as "hydrothermal" reactions, although the pressure–temperature conditions are not supercritical. In a strict sense geochemists concerned with the transport of ores by aqueous fluids have divided the temperature scale into "epithermal," "mesothermal," and "hydrothermal," to mean roughly hot water, superheated water, and supercritical water, respectively. This terminology has not yet penetrated the nuclear waste management literature.

The experiments were closed systems. Glass plus water was sealed into gold capsules, and these capsules were placed in pressure vessels for reaction. This method allows an easy examination of the solid phases, because the total mass of the system is conserved. Water was present in excess so that all phase assemblages included a liquid phase. Analysis of the final solutions permitted an evaluation of elements extracted by aqueous solutions but, because the volume of fluid was limited, cannot be used to determine transport rates.

Experimental

Simulated High-Level Waste Glass. The simulated high-level waste glass used in these experiments was Pacific Northwest Laboratory (PNL) formulation 76-68 (5). It was supplied by PNL. The glass was formulated according to the projected reprocessing flow sheet of the Nuclear Fuel Services plant in West Valley, N.Y., and is sometimes referred to as "NFS glass." The composition of PNL-76-68 glass (6) is given in Table I. One notable compositional feature is that the glass contains 62 wt % (Na_2O + Fe_2O_3 + SiO_2). The glass was colored green black in massive pieces, but in thin fragments it had an amber brown coloration. It contained numerous vesicles (bubbles), some up to several hundred micrometers in diameter. Also incorporated in the glass were clusters of dull to metallic black crystallites. Studies at PNL (7) have shown that these crystallites consist both of crystalline phases that never dissolved in the molten glass plus phases that crystallize on cooling. In work specific to PNL-76-68, it was shown that the crystalline phases were RuO_2 and a ferrite spinel in the as-prepared glass, with fluorite structure phase, chiefly CeO_2, formed on heat treatment (7). A small amount of this fluorite phase, along with RuO_2, ferrite spinel, and perhaps Pd metal, was identified in diffractograms of the slow-cooled glass received from PNL. The total amount of crystalline products in the glass was reported to be less than 10 wt % (7).

The glass was received from PNL as several large fragments. The typical specimen used in the present study was a single shard broken

from one of these fragments and weighing about 30 mg. Figure 1 is a photograph of one of these shards. The opaque regions are the crystalline inclusions. It should be noted that the ratio of these crystalline phases to glass was not constant from specimen to specimen. Because of the variability of the amounts of these inclusions, it is estimated that the actual composition of an element in a particular specimen could vary by as much as 10–20% of the nominal composition given in Table I. Several of the specimens used in the early stages of this study were made into spheroidal shapes by an abrasion technique.

Hydrothermal Treatment. The inert container chosen for these experiments was fashioned from 5-mm-diameter gold tubing. A length of tubing was cut and sealed at one end by electric arc welding or cold welding with a crimping tool. A weighed glass specimen was placed in the capsule along with either deionized water or artificial Hanford groundwater (nominal concentration in micrograms per milliliter: 168 Na, 0.5 Ca, 0.1 Mg, 90 Cl, 14 (SO_4), 56 (HCO_3), 87 (CO_3), 4 K; pH = 10; water was in contact with amorphous SiO_2) in a water-to-solid ratio of 10:1 or 30:1, and the capsule was welded shut. The sealed capsules were then weighed, heated for several hours in a vacuum oven, and reweighed. Any leaks in the welds would show up as weight losses due to evaporation of the water through the leak.

The experiments were performed in conventional 0.5-in. (12.7-mm) sealed gold capsules. The vessel was inserted into a resistance-heated cold-seal pressure vessels (*8*), using water as the pressurizing medium. In a typical experiment each vessel contained three to six individual sealed gold capsules. The vessel was inserted into a resistance-heated tube furnace having a solid state controller–power supply. Temperature was measured with a chromel-alumel thermocouple inserted into a well in the vessel near the level of the gold capsules and was displayed continuously on a digital readout. The temperature was nominally 300°C, but over the course of the typical experiment it varied between 294°C and 306°C. Pressure, measured continuously with a Bourdon gauge, was

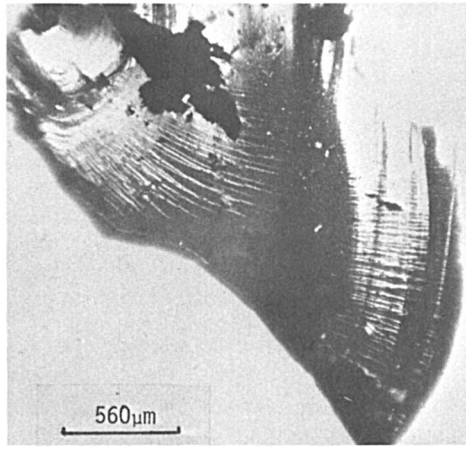

Figure 1. Typical specimen of PNL-76-68 before hydrothermal treatment

Table I. Composition of PNL-76-68 Glass[a]

Oxide[b] (waste oxides)	*Wt %*	*Oxide*	*Wt %*
		Pr_6O_{11}	0.53
Rb_2O	0.13	Nd_2O_3	1.67
SrO	0.38	Sm_2O_3	0.33
Y_2O_3	0.21	Eu_2O_3	0.07
ZrO_2	1.77	Gd_2O_3	0.05
MoO_3	2.28	U_3O_8	4.58
RuO_2	1.07	Fe_2O_3	9.77
Rh_2O_3	0.17	Cr_2O_3	0.41
PdO	0.53	NiO	0.20
Ag_2O	0.03	P_2O_5	0.48
CdO	0.03	Na_2O	5.02[c]
TeO_2	0.26	(glass-forming additives)	
Cs_2O	1.03	Na_2O	7.49[c]
BaO	0.56	SiO_2	39.80
La_2O_3	0.53	B_2O_3	9.47
CeO_2	1.19	CaO	2.00
		ZnO	4.97
		TiO_2	2.97

[a] After Ref. *6*; waste loading 33 wt %; fission product loading 12.8 wt %.
[b] Composition normalized to these oxides by PNL; the oxide compositions do not necessarily reflect the actual cation valences in the glass.
[c] Total $Na_2O = 12.51$ wt %.

300 ± 10 bar. Run durations were 7, 14, 21, and 28 days. At least two runs were made at each duration to evaluate reproducibility of the solid and solution products.

Combined temperature–pressure cooling in air was used at the end of each run. The cooling rate was approximately 10°C · min^{-1} from 300°C to 200°C, 8°C · min^{-1} from 200°C to 150°C, and 2°C · min^{-1} to 90°C. The capsules were removed and reweighed. Any breach of closure would show up as a weight change. The capsules were also examined microscopically for signs of pinholes or stains from leaked contents. Any run that had leaked was repeated.

The gold capsule was cut open at one end, and the liquid was poured into a plastic beaker. The outside of the capsule, as well as the scissors, were gently washed with deionized water, using a wash bottle. The capsule was next opened longitudinally and placed in the beaker for about 10 min to equilibrate in about 20 mL of water. The solution from the beaker was then quantitatively transferred to a 25-mL volumetric flask. The beaker, the sample, and the gold capsule were rinsed, and this solution was also added to the volumetric flasks. Next, 186 mg of KCl was added to make the solution 0.1*N* in KCl when made up to volume. The use of 0.1*N* KCl serves two purposes: first, it helps in the flocculation of the sample, if any, during centrifugation and second, it removes the ionization interference during atomic absorption spectrophotometric analysis for cesium, rubidium, and sodium. The solution was next centri-

fuged in polycarbonate tubes at 2500 revolutions per minute (rpm) to sediment any fine particles in the solution and then pipetted from the polycarbonate tubes into polyethylene bottles without disturbing any sediment at the bottom. A drop of toluene was added to the solution to prevent bacteria from growing.

Characterization of Solid Products. The solid products, still contained in the open gold capsule, were initially examined under a binocular microscope at up to 40 times magnification. The extent of hydrothermal alteration was first estimated at this stage. Because in all cases material had been transported from the original glass specimen onto the inside walls of the gold capsule, solid products characterization was necessary throughout the capsule.

X-ray diffraction was used for crystalline phase identification. Individual clusters of crystals or apparently homogeneous alteration zones were examined by the Gandolfi camera technique (*9*) and the bulk product was then ground and studied by conventional X-ray diffractometry. For the Gandolfi studies individual fragments or crystals were extracted by using a sharpened needle and transferred to the tip of a hollow thin glass fiber that had already been mounted in the normal camera specimen holder. They were cemented to the fiber by various media. Where a cluster of crystals or several fragments of the same material were available, the crystals were crushed between microscope slides and the powder carefully collected into a ball at the tip of the glass fiber. It was important to keep the sample size small and spherical in order to obtain sharp diffraction lines and good line resolution. Having several individual crystals on the fiber was also important so that all observed Debye–Scherrer reflections of low-symmetry crystals would be included on the film.

Qualitative elemental analysis for elements above neon was obtained by energy-dispersive X-ray spectrometry (EDX) on a scanning electron microscope (SEM). The microstructures of the alteration zone or microcrystalline products were observed simultaneously by SEM. Quantitative elemental analysis and elemental distributions were studied on a computer-controlled electron microprobe.

X-ray powder data read from the Gandolfi films, plus chemistry from the SEM/EDX, allowed crystalline phase identification to be made by reference to the JCPDS Powder Diffraction File (PDF) (*10*). The Mineral Subfile of the *PDF* was especially useful in this work.

Chemical Analyses of Solutions. Solutions were analyzed for eighteen of the elements in PNL-76-68. All the elements except Cs, Rb, Na, Zn, and U were analyzed with a computer-interfaced atomic emission spectrometer (AES). The elements Cs, Rb, Na and Zn were analyzed by atomic absorption spectrophotometry (AAS). Uranium was determined by a fluorometric method. Results of duplicate chemical analyses of the same solution had a mean deviation of $\pm 2\%$.

The objective of the analyses is to determine what proportion of the elements from the glass are present in the product solutions. Because the product solutions are always diluted to a 25-mL analytical solution, the sensitivity of the analyses to glass dissolution is a function only of specimen weight and the instrumental detection limits. The level of sensitivity is illustrated by the data in Table II. Detection limits are

Table II. Comparison of Solution Analysis Detection Limits with the Maximum Solution Concentration[a] for One Specimen

Element in Glass	*Maximum Solution Concentration for a 19.5-mg Specimen ($\mu g \cdot mL^{-1}$)*	*Detection Limits ($\mu g \cdot mL^{-1}$)*		
		Atomic Absorption Spectrophotometry	*Atomic Emission Spectrometry*	*Fluorimetry*
Na	73.3	0.002	—	—
B	23.2	—	0.05	—
Si	146.8	0.08	0.2	—
Mo	12.0	0.03	—	—
Cs	7.67	0.05	—	—
Rb	0.94	0.005	—	—
Sr	2.54	0.01	0.01	—
Ba	3.92	—	0.2	—
Ca	11.3	—	0.002	—
Zn	31.5	0.002	—	—
Ni	1.24	—	0.003	—
Cr	2.22	—	0.003	—
Fe	48.5	—	0.005	—
La	3.56	—	0.07	—
Nd	11.3	—	not available	—
Ti	14.1	—	0.08	—
Zr	10.3	—	0.3	—
U	29.2	—	—	0.001

[a] The concentration that would be present in the 25-mL analytical solution if the specimen had completely dissolved during hydrothermal treatment.

compared to the concentration of selected elements that would be present in the 25-mL analytical solution of a particular glass specimen if it had totally dissolved during the hydrothermal run and there were no insoluble solid phases formed on cooling. For example, the data in Table II indicate that, for this weight of specimen, it would be possible to detect dissolution of 0.003% of the Na, 0.25% of the Mo, 0.4% of the Sr, 0.6% of the Cs, or 0.003% of the U present in the original glass. The typical specimen was twice as heavy, so the typical analysis was twice as sensitive to the presence of an element from the glass in the solutions.

Results

Twenty individual experiments were performed at 300°C and 300 bar. The experimental variables and run numbers are listed in Table III. The results of the hydrothermal treatments of the glass will be described first for the solid products and then for the solutions extracted from the reaction capsules.

Table III. Experimental Parameters and Run Numbers of the 300°C, 300-Bar Hydrothermal Treatments

Run Duration (days)	*Run Number*	*Water Type*[a]	*Water-to-Solids Ratio*
7	GD 59[b]	DW	10:1
	GD 113	DW	10:1
	GH 112	HGW	10:1
	GD 121	DW	30:1
	GD 126	DW	30:1
14	GD 68[b]	DW	10:1
	GD 88	DW	10:1
	GD 124	DW	10:1
	GD 127	DW	10:1
	GH 150	HGW	10:1
	GD 123	DW	30:1
	GD 143	DW	30:1
21	GD 80	DW	10:1
	GD 81	DW	10:1
28	GD 78	DW	10:1
	GD 79	DW	10:1
	GD 89	DW	10:1
	GD 90	DW	10:1
	GH 111	HGW	10:1
	GD 122	DW	30:1

[a] DW = Deionized water; HGW = artificial Hanford groundwater.
[b] These specimens were spheroids; all others were shards.

The Solid Reaction Products. Reconnaissance experiments described elsewhere (*11*) had shown that powdered PNL-76-68 glass would be altered by hydrothermal solutions at 200°–400°C and would form crystalline phases. More massive specimens were used in this study to enable us to follow the alteration of the glass as a function of time. Spheroidal specimens were chosen for the first few experiments in the expectation that the hydrothermal alteration front might extend only into a small portion of the glass and thus that measurements of weight and volume changes as a function of time could be obtained. However, upon opening of the first capsule, it became obvious that, even for times as short as 7 days, the alteration of the glass was too extensive, and it would not be possible to employ these techniques. After 7 days (run GD 59) the alteration had proceeded into approximately one-third of the specimen and material had been transported from the glass and onto the inside walls of the gold reaction capsule. Figure 2 shows a portion of the cross section of this product mounted in plastic and photographed in

Figure 2. Cross section of a spheroidal specimen of PNL-76-68 glass after hydrothermal treatment with deionized water at 300°C and 300 bars for 7 days (approximate dimensions: 2 mm × 4 mm)

reflected light. The white and light gray zones are altered glass; the black interior zone is apparently unaltered glass. The oval-shaped gray and white features near the interior of the glass could be traced to cracks that permitted access by the solutions. These cracks might have been introduced during the mechanical treatment to form the spheroids. The product from the 14-day experiment (GD 68) had fragmented and was thus not recoverable in its original spheroidal shape. Because of the possibility of mechanical damage from fabrication of the spheroids, it was decided to use the less damaged glass shards in all further experiments.

The typical appearance of the products from the other 18 experiments is illustrated in Figure 3. This photograph was taken after the liquid had been removed from the gold capsule and the capsule had been cut open. In all cases the first observations with the binocular microscope showed abundant, yellow needlelike crystals measuring 0.2–2 mm along the needle axis that had grown throughout the capsule and in fissures in the altered shard, plus a light-colored coating covering the inside wall of the capsule.

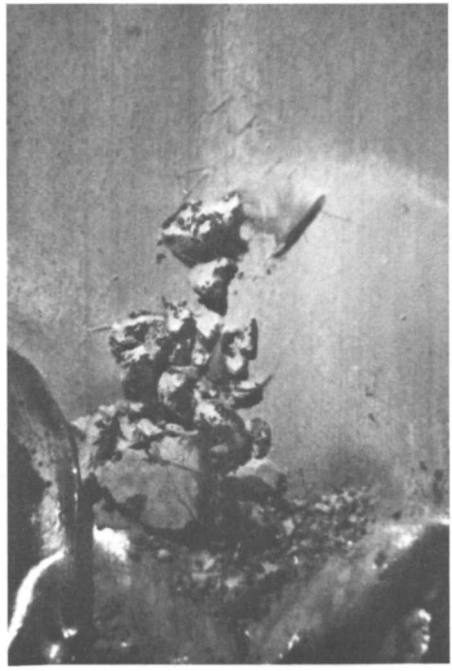

Figure 3. Typical solid products after treatment of PNL-76-68 at 300°C and 300 bar (the background is a cut-open gold capsule)

The product was always fragmented. In some cases a relatively large remnant of the original shard was present, but it was nested in other fragments that had spalled off during the treatment, cooling, or opening steps.

The yellow crystals were studied by SEM/EDX and found to contain U, Si, Na, Cs, and minor Rb. Figure 4 is a photomicrograph of clusters of these crystals growing on the walls of the capsule. They were rectangular in cross section and had either a pinacoid or a dome for a termination. X-ray examination by the Gandolfi method yielded powder data that gave a very good match to the data of the mineral weeksite, $K_2(UO_2)_2(Si_2O_5)_3 \cdot 4H_2O$, pattern 12-462 in the PDF (*10*). Table IV is a list of the X-ray powder data for these crystals and for the mineral weeksite. The combination of elemental chemistry and X-ray data served to identify these crystals as a weeksite structure phase with Na, Cs, and Rb substituting for the K in the prototype mineral. Sodium weeksite, $Na_2(UO_2)_2(Si_2O_5)_3 \cdot 4H_2O$, is known (12), but this is the first report of a weeksite structure phase with the large alkali ions Cs and Rb

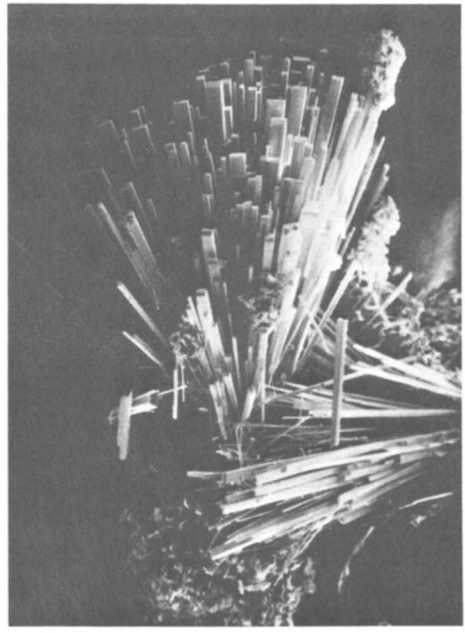

Figure 4. Clusters of yellow needlelike crystals (length along needle axis is typically 1–2 mm)

substituting for K. The weeksites (henceforth, the Na-Cs-Rb-weeksite structure phase will be simply referred to as "weeksite") observed in *every* experiment, whether for 7 or 28 days, with deionized water or simulated Hanford groundwater, and with water-to-solids ratios of 10:1 or 30:1. In the longer-duration runs the weeksite crystals appeared to be coated or etched and were often nearly colorless near their tips. The X-ray pattern and EDX chemistry were virtually identical for yellow as well as these lighter regions of the crystals. However, these observations suggest that the original alteration product weeksites may be metastable and would themselves alter in much longer duration experiments.

The cream- or tan-colored phase covering the inside of the gold capsule proved to be made up of 2–10-μm bladelike crystals. Figure 5 is an SEM photomicrograph of these crystals on the gold capsule. Their radiating habit suggests nucleation and growth from solution on to flaws on the surface of the gold. The EDX chemistry of these crystals consisted of primary Si, Fe, and Na, with very minor Ti, Zn, and perhaps several other elements. X-ray powder data obtained with the Gandolfi camera showed a quite good interplanar spacing (d) match and a fair intensity (I) match to the data for the mineral acmite, $NaFeSi_2O_6$, *PDF* 18-1222. This identification is fully consistent with the EDX chemistry. Table V gives

Table IV. X-ray Powder Data for the Yellow Needlelike Crystals and for the Mineral Weeksite

Yellow Crystals		*Weeksite (PDF 12-462)*	
d^a	I^a	d^a	I^a
8.94	ms	8.98	90
7.14	ms	7.11	100
5.58	s	5.57	90
4.85	vw	4.83	30
4.57	m	4.58	40
		4.48	30
3.84	m	3.84	40
3.57	mw	3.55	70
3.32	m	3.34	40B
		3.30	70
3.20	mw	3.20	50
3.00	vw	2.99	40
2.93	s	2.91	60
2.81	vvw	2.80	30
2.52	vvw	2.51	30
2.41	w	2.41	40
2.38	w	2.37	50
2.30	w	2.28	50
2.24	w	2.29	40
2.18	vvw	2.20	30
2.15	vvw	2.13	40
2.11	vw	2.11	40
2.00	vw	1.994	40
1.982	vw	1.973	30
1.936	vw	1.922	30
1.905	vw	1.905	40

[a] Symbols: s = strong; m = medium; w = weak; v = very; B = broad reflection; d = interplanar spacing; I = relative intensity.

the Gandolfi X-ray data and the *PDF* data for acmite. It is possible that the very small size of the crystals and the potential for some orientation with the mounting fiber could account for the only fair agreement of the I data.

The very light color of the acmite crystal coating was somewhat surprising. In nature, acmite is usually green or brown due to minor solid solution substitutions and the partial reduction of Fe^{3+} to Fe^{2+}. The light color requires that the composition be close to stoichiometric $NaFeSi_2O_6$ and that the Fe be trivalent. The presence of an Fe^{3+} phase suggests oxidizing conditions inside the sealed capsule. The universal occurrence of the uranyl phase, weeksite, also supports oxidizing conditions. Apparently PNL-76-68 was an oxidized glass. The color of the acmite crystal coating turns brown after several weeks of exposure to air.

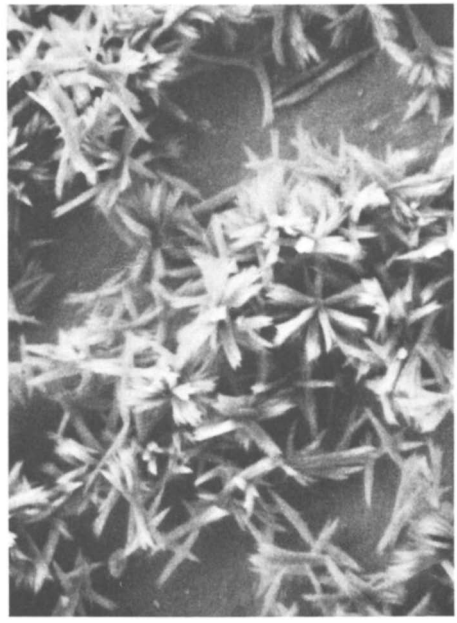

Figure 5. SEM photomicrograph of the crystals coating the inside of the gold capsule

MICROSTRUCTURE AND MICROCHEMISTRY. The microstructure and microchemistry of the bulk products from a 7-day, 14-day, and 28-day hydrothermal treatment were studied by SEM and electron microprobe analysis. The 7- and 14-day specimens were from the two runs where glass spheroids had been used. Although they were cracked, these products were not as fragmented as the products from glass shards. Thus they could be handled, mounted in the plastic, sectioned, and polished with less damage to the specimen.

Figure 6 is a secondary electron image (SEI) of the cross-sectioned spheroid shown in Figure 2. The brightness of the SEI can be correlated to the mean atomic number of a material and to density. Thus the apparently unaltered glass core is bright, with still further brightness for the crystalline inclusions in this glass. The altered portions of the product give a dull gray SEI. Cracks in the product are black. Note the correlation of the gray white oval-shaped alteration features in Figure 2 with the gray zones in the bright core in Figure 6. Similarly, the residual crystalline inclusions in the altered glass zone that were dark gray in Figure 2 are brighter than their matrix in Figure 6.

A thin skin or rind not evident in Figure 2 is observed in Figure 6. This was a characteristic feature in *all* products. Under the binocular

Table V. X-ray Powder Data for the Crystalline Coating and for the Mineral Acmite

Coating		*Acmite (PDF 18-1222)*	
d	*I*	*d*	*I*
6.37	50	6.369	90
4.42	50	4.416	80
3.62	10	3.614	10
3.20	2	3.188	50
2.998	100	2.983	70
2.912	20	2.900	100
2.536	30	2.5408	50
2.475	20	2.4701	60
2.201	10	2.1995	10
2.122	10	2.1200	30
2.032	10	2.0162	20
1.937	10	1.9350	10
1.834	2	1.8263	5
1.731	5	1.7293	60
1.687	2		
1.664	2	1.6590	5
1.637	5	1.6341	5
1.613	5	1.6210	50
1.598	5	1.5920	50
1.533	2	1.5377	10
1.506	5	1.5290	10
1.475	5	1.4671	20
1.400	5	1.3975	60
1.379	2		
1.328	2	1.3283	20
1.302	5	1.3021	40
1.271	2	1.2687	30
1.230	5	1.2289	20

microscope this skin was seen to consist of at least two bands, an outer band of white and almost spherical material covering an orange brown inner band. Figure 7 is an electron backscatter (EBS) image with accompanying Na, Si, and Fe X-ray maps for a near-surface portion of a 2-week run, GD-68. Two features are notable. First, the skin is enriched in Fe and second, there is a bright area to the right that has Na, Fe, and Si concentrations. This area is probably unaltered or only partially altered glass. A cross section of the skin is shown under higher magnification in Figure 8, along with Sr, Fe, and Ca X-ray maps. It is clear from this figure that the outer band of the skin is rich in Ca and Sr, while the adjoining band is Fe-rich. The X-ray emission traces across this banded skin, shown in Figure 9, confirm the enrichment of Ca and Sr in the outer band and indicate that Si is associated with Fe in the adjoining band.

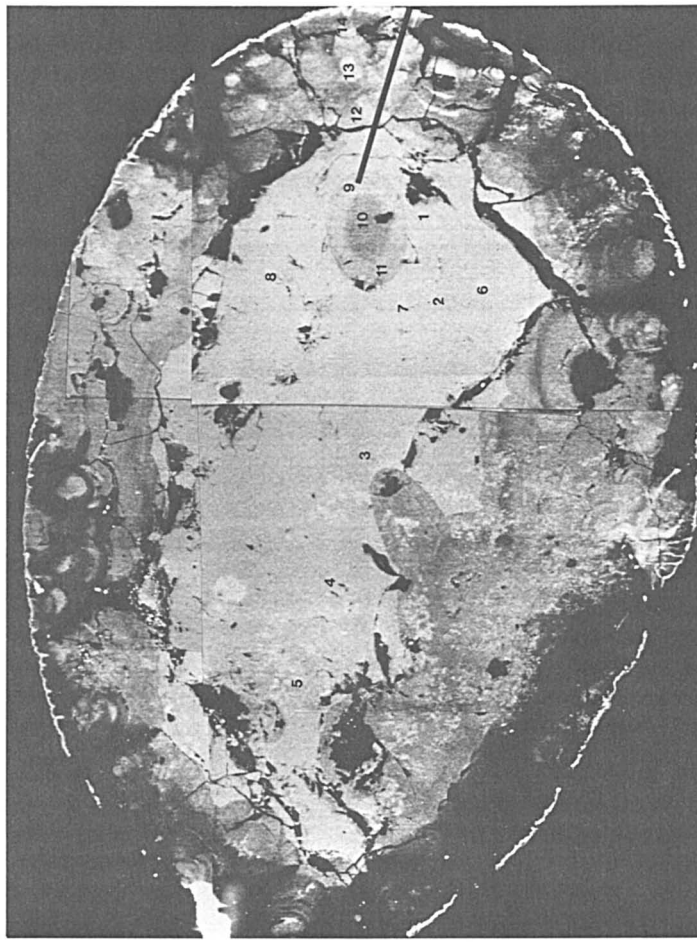

Figure 6. SEM-SEI photomicrograph of a section through the product from a 7-day hydrothermal treatment (run GD 59)

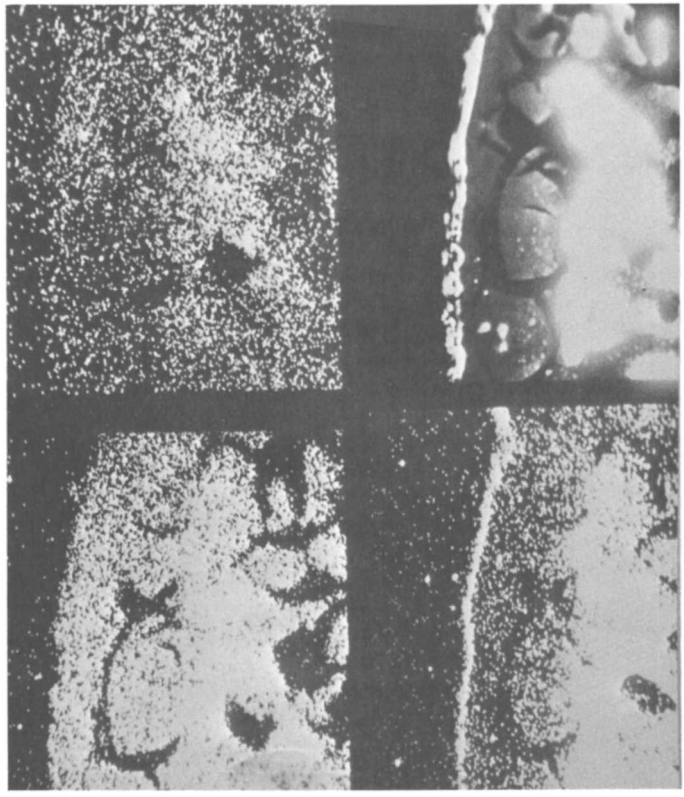

Figure 7. X-ray maps of the near-surface zone of the product from run GD 68 (160 times magnification): Top left, *Na;* top right, *EBS;* bottom left, *Fe;* bottom right, *Si.*

Samples of each band were examined by Gandolfi X-ray diffraction, and crystal structure types for these phases were obtained. The outermost band of white material had the apatite structure type. [This phase identification was based on crystals obtained from the surface of the products from longer-duration (3 to 4 weeks) treatments. It is not certain that the apatite structure band in the 1- and 2-week products were crystalline.] X-ray data for this phase and for hydroxyapatite, $Ca_5(PO_4)_3OH$, are given in Table VI. A U X-ray map of the EBS image in Figure 8 showed that U was crystallizing in this apatite phase. Examination of the material in the SEM showed these spheroids to be actually made up of aggregates of randomly oriented fibrous crystals. Their EDX chemistry was quite complex, with Ca, Sr, Ba, rare earths (Ln), Si, U, and P as the primary elements. Thus the material should be assigned to the generalized solid solution formula

$$(Ca,Sr,Ba,Ln,U)_5[(Si,P)O_4]_3OH$$

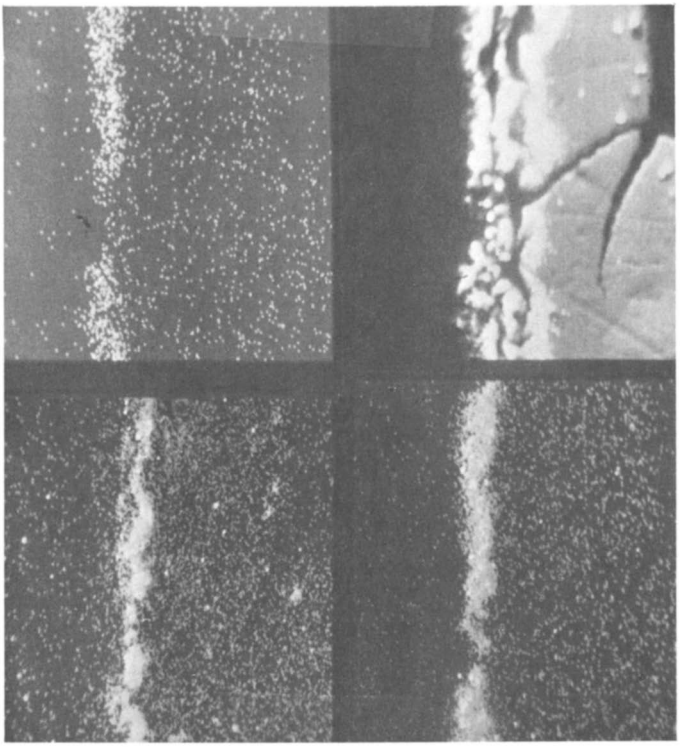

Figure 8. X-ray maps of a portion of Figure 7 (800 times magnification): top left, *Sr;* top right, *EBS;* bottom right, *Ca;* bottom left, *Fe.*

The orange brown band gave X-ray data typical of a pyroxene (single-chain silicate) near the acmite–augite, $(Na,Ca)(Fe,Mn,Zn,Mg,Ti)(Al,Si)_2O_6$, composition (see *PDF* 18-1221 and 19-1). In Figures 8 and 9 it was demonstrated that this band had high-Fe concentration, and in X-ray emission traces the presence of Na, Zn, and Ti was observed. A generalized solid solution formula for this phase is

$$(Na,Ca)(Fe,Ti,Zn)Si_2O_6$$

In the EBS image from Figure 8 it is seen that there is a third, innermost band to the skin. Both X-ray maps and X-ray traces across the skin (Figure 9) indicated that this band was especially enriched in U relative to the adjoining altered glass zone. This U concentration was higher than that in the apatite phase constituting the outermost band. Titanium also appeared to be concentrated in this high-U band. No phase identification has as yet been made for this innermost band.

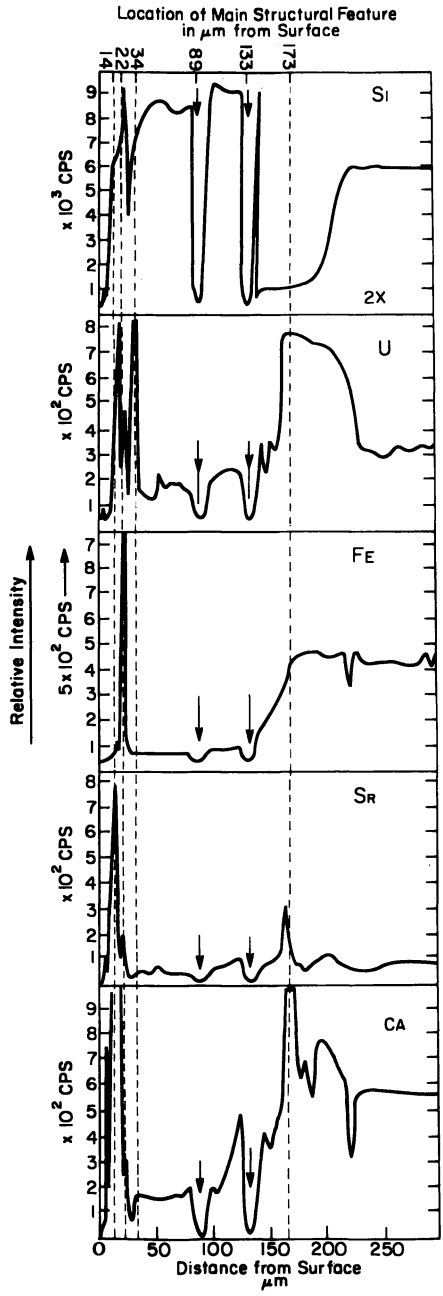

Figure 9. X-ray emission profiles of the near-surface zone of the product from run GD 68. Arrows indicate the positions of cracks. Dashed lines at the left mark the approximate boundaries of the three bands of the skin, and the line near the center marks the boundary between less altered and more altered glass.

Table VI. X-ray Powder Data for the White Outer Band and for Hydroxyapatite

White Band		*Hydroxyapatite (PDF 9-432)*	
d	*I*	*d*	*I*
3.45	60	3.44	40
3.18	10	3.17	12
2.814	100	2.814	100
		2.778	60
2.714	20	2.720	60
2.637	10	2.631	25
2.522	5	2.528	6
2.276	10	2.262	20
2.071	10	2.065	8
2.006	5	2.000	6
1.949	10	1.943	30
1.903	5	1.890	16
1.848	10	1.841	40
1.725	10	1.722	20

Element distributions among the various altered and unaltered glass regions were further characterized by electron microprobe analysis. Results were obtained in the form of characteristic X-ray emission traces through these regions and quantitative elemental analyses at selected spots on the product. In Figure 6 the traverse of a microprobe scan is marked by the black line starting at the banded skin and passing through a region of generally altered glass, then into the unaltered core, and terminating in the oval-shaped alteration feature. X-ray emission traces for 19 elements monitored during this scan are shown in Figures 10, 11, and 12.

The enrichments in Na, Ca, Sr, Fe, Ti, and U in the banded skin have already been discussed. Except for Mo and Na, the X-ray traces did not display further major fluctuations (the sharp dips that occur in all traces in the same place are due to cracks). The broad maximum in Mo and the sharp fluctuations in Na occurring between 500 and 700 μm correlate with the traverse of the beam out of an altered zone, into unaltered glass, and then back into the oval-shaped alteration feature. This correlation suggested the use of Mo and Na as marker elements for the presence of alteration.

The numbers in Figure 6 mark individual point analyses with the computer-interfaced microprobe. Calibration standards were those available in the university's Mineral Constitution Laboratory for silicate rock and mineral analyses. The results presented in Table VII are for 13 of the elements in the glass (plus K, which was not reported to be a

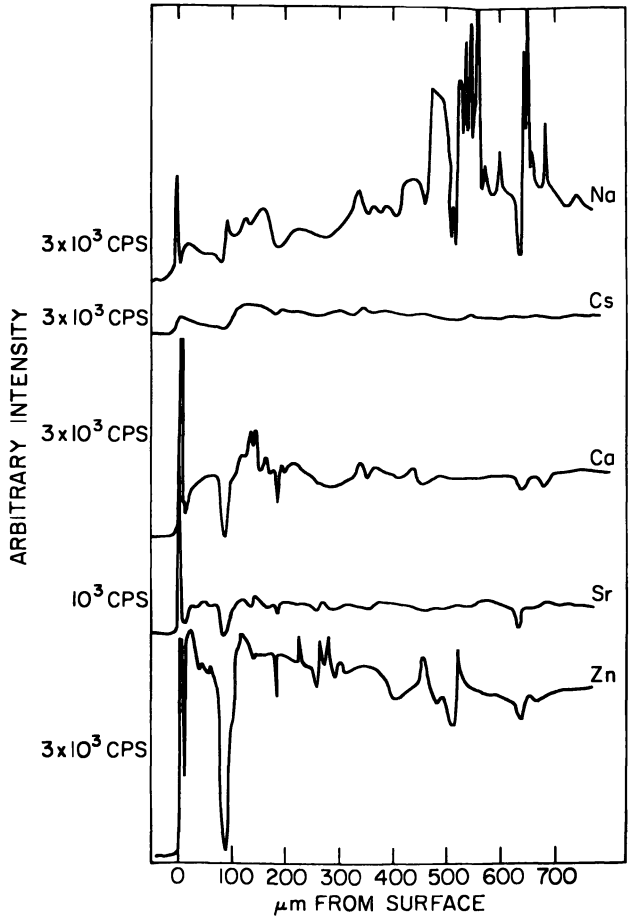

Figure 10. X-ray emission traces for Na, Cs, Ca, Sr, and Zn along the traverse shown in Figure 6

constituent of the glass). Note that the available computer code calculated concentrations as oxides. The U analyses were suspect because a U standard with a suitably high U concentration in an appropriation matrix was not available. There also appeared to be a problem with the Na analyses, perhaps due to the familiar difficulty with Na vaporization in the electron beam. Analyses for the 13 elements for a specimen of the as-received PNL-76-68 glass were within 5% of the compositions reported by PNL for Ca, Ti, Nd, Fe, Zn, Si, and Mo. Analyses differed by greater amounts for Cs, Ce, Sr, and Zr, as well as for the previously discussed U and Na. The importance of these compositional variations is not known because the glass is an inherently inhomogeneous product and the PNL composition is nominal (that is, based on the starting batch) rather than the result of an actual chemical analysis.

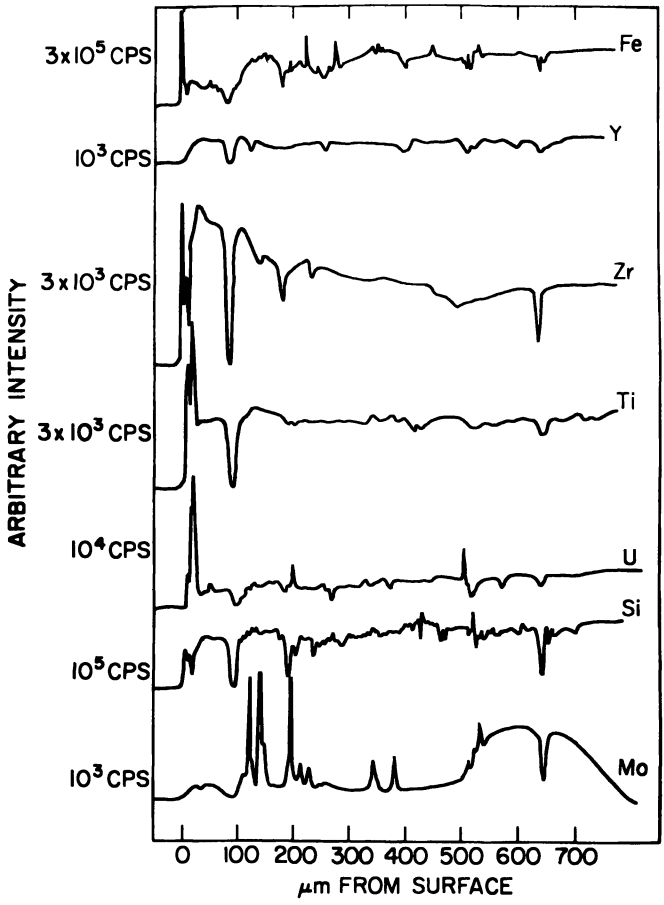

Figure 11. X-ray emission traces for Fe, Y, Zr, Ti, U, Si, and Mo along the traverse shown in Figure 6

The microprobe data for the various zones in the product are averages of multiple analyses. The core of apparently unaltered glass gave an analysis averaged from eight points that compares moderately well to that of the original glass specimen. Note their correspondence in Mo concentrations. In alteration zones I and II the Mo and Na concentrations were appreciably lower. The data for zone I were averaged from three analyses in the oval-shaped feature in Figures 2 and 6. Three analyses from the more heavily altered outer region occurring between the skin and the core constitute zone II. Here somewhat lower Fe, Si, and U concentrations were noted in addition to the heavy depletion in Mo and Na. One of the most consistent and useful observations from the study of this specimen was that Mo and Na appear to be early and sensitive indicators of hydrothermal alteration in the glass.

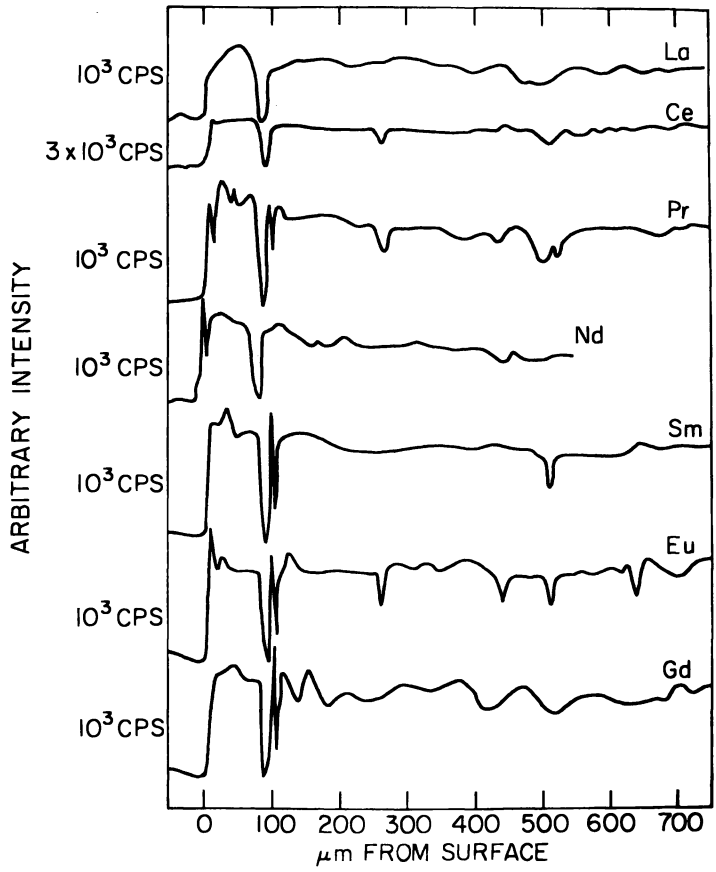

Figure 12. X-ray emission traces for the lanthanides along the traverse shown in Figure 6

The partially altered product just described for the 1-week treatment differed markedly from the products from longer treatments. For specimens treated for 2 to 4 weeks, there appeared to be at least partial alteration throughout the solid. One of the 4-week products was sufficiently intact after the treatment that a partial cross section could be prepared for examination by SEM and the microprobe. In Figure 13 it can be seen that major fragments of the product had separated and parts of the surface had spalled off prior to specimen preparation. Yet enough of the product was retained that all the typical alteration features were displayed in one cross section. The alteration has been divided into four zones and microprobe analyses (*see* Table VIII) have been obtained from each of them.

The least altered of the zones was the core. In reflected light it retained its original green black coloration and it appeared to have

Table VII. Electron Microprobe Analyses of the Product Shown in Figure 6 (Run GD 50)

	Weight Percent				
	PNL-76-68 Nominal Composition[a]	*PNL-76-68 Microprobe Analysis*	*Unaltered Glass*[b]	*Alteration Zones*	
Oxide				*I*[c]	*II*[d]
CaO	2.0	2.0	1.9	2.0	2.0
Cs_2O	1.0	1.3	1.0	1.0	0.9
TiO_2	3.0	3.2	2.9	2.9	3.0
CeO_2	1.2	1.6	2.3	2.3	2.9
Nd_2O_3	1.7	1.8	1.7	1.5	2.0
FeO	8.9	9.3	8.9	8.8	5.8
ZnO	5.0	4.8	5.5	5.3	5.2
SiO_2	40.3	39.0	38.2	42.1	34.2
SrO	0.4	0.2	0.1	0.1	0.1
ZrO_2	1.8	2.3	2.0	1.9	2.7
MoO_3	2.3	2.4	2.4	0.2	0.8
UO_2	4.5	7.2[f]	5.4[f]	5.8[f]	4.3
K_2O	0.0[e]	0.1	0.1	0.3	0.1
Na_2O	12.7	8.6	10.5	3.1	2.1
	84.8	83.8	82.9	77.3	66.1

[a] Modified from Table I to show Fe as FeO and U as UO_2.
[b] Averaged from points 1–8 in Figure 6.
[c] Averaged from points 9–11, the oval-shaped alteration zone, in Figure 6.
[d] Averaged from points 12–14 in Figure 6.
[e] No K was reported in the composition of PNL-76-68.
[f] The U standards were designed for lower U concentrations, so these values may be in error.

become more transparent as a result of the treatment. The core zone had the bright secondary electron image typical of unaltered glass in Figure 6, but the microprobe analyses (Table VIII) indicated that this zone was heavily depleted in Mo and Na. An exterior core zone differed only slightly from the core in optical and SEM image characteristics, but microprobe analysis indicated almost total depletion in Mo and a distinct enrichment in Cs compared to the adjoining alteration zones. The outer core zone was at least partially crystalline because an X-ray diffraction pattern consisting of broad reflections was obtained from it. The data, listed in Table IX, have not been matched to any phase or mixture of phases in the *PDF*.

In reflected light the region labeled "interior zone" in Figure 13 was cream white, porous, and rich in opaque microcrystalline inclusions. These inclusions were dull black and were often surrounded by a purple hue. They were less abundant in the core and outer zones. Also their orientation in the interior zone seemed to be related to the external

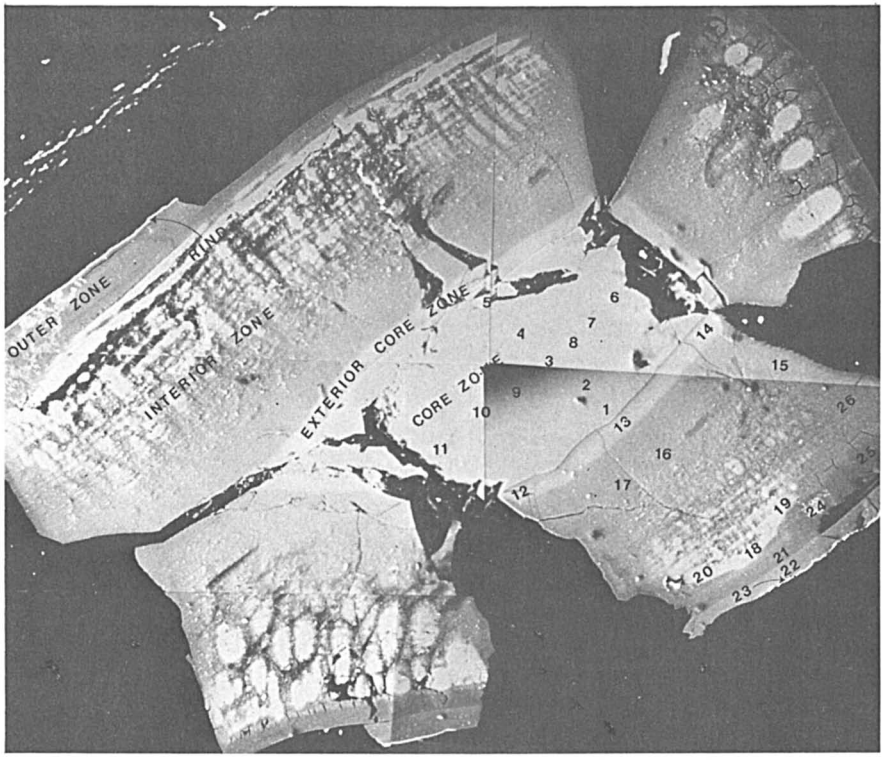

Figure 13. SEM photomicrograph of a section through the product of a 4-week hydrothermal treatment

morphology of the original glass shard. These two observations suggest transport and recrystallization of the opaque phases. X-ray diffraction analyses indicated that the opaques consisted of several phases, a Fe-rich spinel, $(RuO_2)_{ss}$, and usually $(Pd)_{ss}$ (the subscript ss refers to solid solution). The spinel had a unit cell parameter of 8.40 Å, and its powder data correspond closely to those of the Fe-spinel magnetite Fe_3O_4, *PDF* 19-629. The Ru-rich phase has been designated as $(RuO_2)_{ss}$, a solid solution phase, because its powder data indicated a slightly larger unit cell than is found for pure RuO_2, *PDF* 21-1172. Similarly, in those products where Pd-rich crystalline inclusions were identified, the unit cell parameter, 3.92 Å, was larger than the 3.89-Å parameter of pure Pd, *PDF* 5-681. No fluorite structure CeO_2-rich phase was detected in any products.

The microprobe data for the interior zone indicated a depletion of Cs, Zr, and lanthanides, and enrichment in Na, Ca, Fe, Ti, Zn, and Si, in comparison to adjoining zones. The enrichment was most pronounced

Table VIII. Electron Microprobe Analyses of the Product Shown in Figure 13 (Run GD 78)

	Weight Percent				
		Alteration Zones			
Oxide	*PNL-76-68 Microprobe Analysis*	*Core Zone*[a]	*Exterior Core Zone*[b]	*Interior Zone*[c]	*Outer Zone*[d]
CaO	2.0	2.1	2.1	2.5	1.6
Cs_2O	1.3	1.4	3.1	0.4	1.5
TiO_2	3.2	3.1	2.9	4.3	2.6
CeO_2	1.6	1.4	1.4	0.9	2.0
Nd_2O_3	1.8	2.1	1.9	1.2	3.2
FeO	9.3	9.6	8.7	13.2	3.7
ZnO	4.8	4.3	4.5	5.3	3.8
SiO_2	39.0	39.1	38.9	46.3	28.0
SrO	0.2	0.4	0.3	0.4	0.4
ZrO_2	2.3	2.2	2.1	1.5	3.1
MoO_3	2.4	1.1	0.1	0.0	0.1
UO_2	7.2	6.1	5.3	5.5	2.0
Na_2O	8.6	2.0	2.4	5.2	0.7
	83.6	74.9	73.7	86.8	52.7

[a] Averaged from points 1–11 in Figure 13.
[b] Averaged from points 12–14 in Figure 13.
[c] Averaged from points 18–20 in Figure 13.
[d] Averaged from points 15, 21, 22, and 26 in Figure 13.

in those features in the interior zone that are brighter in Figure 13. X-ray analysis of these features gave a pyroxenelike pattern, with moderately broad reflections corresponding to those of the acmite augites described earlier. The microprobe and X-ray powder data are consistent with a pyroxene structure phase having a generalized solid solution formula, $(Na,Ca)(Fe,Ti,Zn)Si_2O_6$. X-ray patterns of representative samples from the interior zone showed that there was a considerable amount of an X-ray amorphous phase mixed with the pyroxene and opaque crystalline phases.

The region labeled "outer zone" in Figure 13 consisted of light-colored translucent material lying just below the skin. In reflected light this material has distinct opalescence. With the typical product much of this zone and the skin were found to have spalled off. X-ray examination of random samples from this zone indicated that it was generally noncrystalline. A few broad pyroxenelike reflections were noted. Microprobe data (Table VIII) indicated major depletion of Na, Fe, Si, and U. These are the key elements of the skin and the two phases crystallized after transport, acmite and weeksite. Note that the analyses of the oxides listed in the table sum only to about 56%. This fact, when combined with

the characteristic opalescence of this zone, suggests that hydrated or hydroxylated, perhaps gellike, material has been formed in this zone by the hydrothermal treatment of the glass.

The skin, seen as a thin, bright layer on some of the more intact segments in Figure 13, was again made up of a white crust of small spheres overlying an orange band. X-ray diffraction confirmed that here also the orange band was a pyroxene phase and, with one exception, the white crust was an apatite phase. In that one exception, aggregates looking very much like the apatite phase (the spheres were even made up of tiny needle crystals), had quite dissimilar X-ray powder data (*see* Table IX).

Table IX. X-ray Powder Data for Additional Alteration Zones or Phases

Outer Core Zone		*Orange Vesicle Crust*[a]		*White Spherical Aggregates*[b]	
d	*I*	*d*	*I*	*d*	*I*
4.11	m[c]	4.13	50	7.03	80
3.99	m	3.68	5	6.56	30
3.75	ms	3.47	20	5.13	50
3.49	w	3.18	20	4.82	10
3.24	w	2.978	20	4.53	5
2.998	ms	2.940	20	4.15	100
2.894	m	2.84	10	3.90	5
2.629	vs	2.515	60	3.75	10
2.543	m	2.259	100	3.58	5
2.455	m	1.961	50	3.45	10
2.380	m	1.684	5	3.24	50
		1.637	10	3.18	20
		1.480	20	3.11	50
		1.388	10	2.940	30
		1.182	10	2.814	30
		1.130	5	2.652	20
		1.088	5	2.536	20
		0.9022	5	2.380	10
				2.067	10
				1.892	5
				1.852	5
				1.734	5
				1.578	5

[a] Noted only in products of 2-week treatments.
[b] Noted only in one product of a 4-week treatment; morphologically similar to the apatite phase.
[c] Symbols: s = strong; m = medium; w = weak; v = very.

Two other alteration features were noted. Often, fissures or veins in the altered glass were filled with a translucent pale yellow material. This phase had both the elemental chemistry and characteristic (although broad) X-ray reflections of the pyroxene phase. Another feature was an orange crust lining one of the vesicles from the original glass. It looked quite like the orange pyroxene band observed on the skin, but its X-ray data, given in Table IX, were distinctly different.

The white spherical aggregates and orange vesicle crust features were two examples of the need for utilizing multiple methods of characterization in this work. If visual or SEM appearance had been used alone, then the phases would have been misidentified as apatite and pyroxene, respectively.

Bulk X-ray Diffraction. At least one product treated at each different set of conditions (time, water type, water-to-solid ratio) was studied in bulk specimens by routine X-ray diffractometry. All the solids were collected from inside the gold capsules and were ground together to make up the diffractometer specimen. The resulting diffraction patterns were remarkably similar to each other and to patterns of products from other hydrothermal experiments involving PNL-76-68 glass. The diffractogram of the original glass specimen is compared to that of the products of a typical alteration product (run GH 111) in Figure 14. The glass is X-ray amorphous except for a few weak reflections of $(RuO_2)_{ss}$, $(CeO_2)_{ss}$, and the Fe spinel(s), while the alteration product has strong reflections from crystalline phases. The broad hatched reflections are due to the various acmite and acmite–augite pyroxene phases and all but a few of the remaining reflections are those of the weeksitelike phase. One of these extra reflections is consistent with the strongest apatite phase reflection, but, in general, the other phases that were so clearly discernible as tiny crystals by the Gandolfi technique are apparently below the level of detection by bulk X-ray diffraction.

The same basic diffractogram was obtained for six other run products where a 10:1 water-to-solids ratio had been used. The major difference between 1 and 4 weeks of treatment was in the sharper and more intense pyroxene reflections observed for the longer treatments. In the diffractograms of the 4-week, 30:1 water-to-solid-ratio product, the weeksite reflections were just as evident, but those of the pyroxenes were much less intense. There was also a larger diffuse scattering halo, which suggested a higher proportion of X-ray amorphous phases in this product.

The weeksite plus pyroxenes phase assemblage was also observed in another set of hydrothermal treatments described elsewhere (*11*). In these a 200-mesh powder of PNL-76-68 glass had been treated at 300°C and 300 bar for an extended period of time. The water-to-solid ratio was 0.5:1 rather than 10:1 or 30:1. Diffractograms of 4-, 8-, and 24-week products were very similar to that of the altered glass in Figure 14.

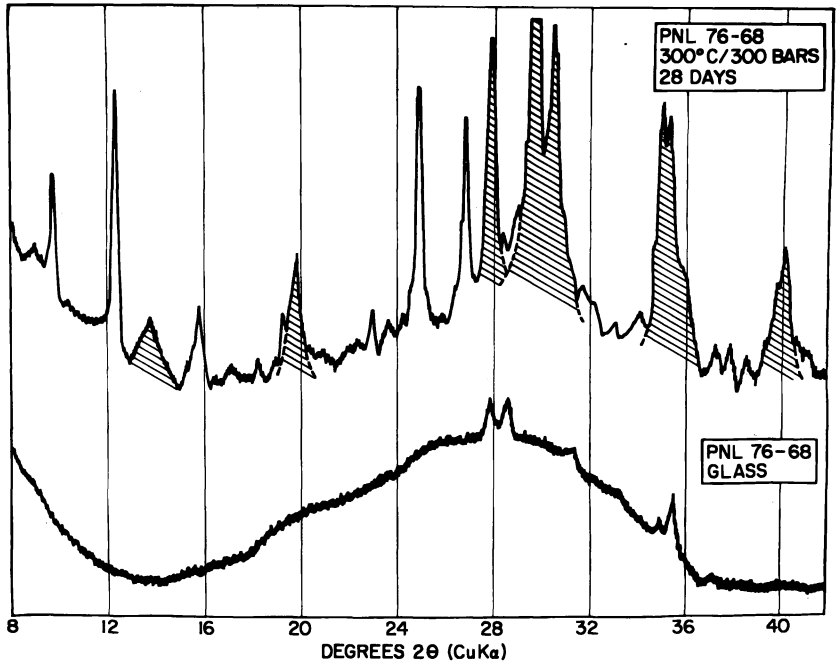

Figure 14. Portions of the X-ray diffractograms for PNL-76-68 before hydrothermal treatment and after treatment with artificial Hanford groundwater at 300°C and 300 bar for 28 days (run GH 111)

In another series of experiments with the powdered glass and the 0.5:1 ratio, the weeksite-plus-pyroxenes assemblage was well crystallized after only 2.5 days at 400°C and 300 bar, and it was seen to be starting to crystallize after the same 2.5-day treatment at 200°C and 300 bar (*13*).

Chemical Analyses of Solutions. The product solutions from each gold capsule were analyzed for 18 of the elements present in PNL 76-68 by the techniques described above. These analyses covered all the elements whose oxides were present at greater than 1 wt % except Ru (*see* Tables I and II). More than 96 wt % of the oxide composition of the glass was included.

There are two potential contributions to these solutions. First, there are the elements that had been extracted from the glass during the hydrothermal treatment and had remained in solution during the cooling of the run. A second contribution could come from any solid products that were sufficiently soluble to have dissolved during either the 10-min equilibration of the capsule in 20 mL of water or the subsequent washing of the solid products. This second contribution might include such salts as sodium molybdates or borates that either had formed as solids at

temperature because the solution was already saturated or had precipitated from solution during the cooling of the run. In the discussion that follows both contributions will be considered under the "solutions" portion of the products.

Solutions From Runs Using Deionized Water. The analyses of the solutions from 12 of the runs using deionized water are given in Table X. Because every specimen had a different weight, the concentrations have been normalized to a specimen weight of 0.1 g to facilitate comparisons among runs. The elements present in the solutions in the greatest concentrations were Na, B, and Mo. Reproducibility among replicate runs that used glass shard specimens (that is, all but GD 59 and GD 68) was within 10% of the amount present for these three elements. This was about that expected from the variation in specimen composition due to variable content of crystalline inclusions. Note, for example, the Cr analyses in the 2-week runs. In GD 124 there was none detected, while in GD 127 there were 42 $\mu g \cdot mL$ of Cr in solution. Chromium is thought to be present in PNL-76-68 in the spinel(s) (5, 7), so GD 124 may have contained less of this crystalline inclusion than GD 127. Other important constituents of the solutions were Si and Cs. Reproducibility, among replicate analyses for these elements, was only within a factor of two to three times the amount present.

Table X. Solution Concentrations[a]

	1 Week		*2 Weeks*			
	GD 59[b]	*GD 113*	*GD 68*[b]	*GD 88*	*GD 124*	*GD 127*
Na	1800	4300	3900	3900	3900	4700
B	1300	2500	3000	2500	2500	2800
Si	750	510	710	1070	430	620
Mo	1300	1100	1100	1100	1100	1100
Cs	19	42	110	58	33	74
Rb	ND[c]	ND	6	3	2	ND
Sr	0.8	2.0	ND	0.3	2.4	2.8
Ba	0.7	7.4	—	0.5	11.6	13.1
Ca	2.4	7.4	ND	2.8	9.8	10.9
Zn	ND	0.8	7.8	0.7	1.5	0.9
Ni	—	1.5	29.0	2.5	2.6	3.1
Cr	ND	66	—	—	ND	42
Fe	ND	3	ND	—	3	4
La	ND	4	ND	ND	4	ND
Nd	—	ND	ND	ND	ND	ND
Ti	ND	ND	ND	ND	ND	ND
Zr	ND	ND	ND	ND	ND	ND
U	2.6	5.6	4.8	1.1	0.6	6.2

[a] In micrograms per milliliter.
[b] These specimens were in the form of spheroids.

The most notable aspect of the data in Table X is that (with the exception of GD 59, discussed later) the concentrations are roughly the same for the four run durations. This aspect becomes even more evident when analyses from the replicated runs are averaged. In Table XI these averaged concentrations are given along with the percentage of the particular element from the original glass represented by these concentrations. It should be noted that this percentage is only the amount of an element detected in the analytical solution and not the total percentage of an element extracted or leached from the glass. The latter would include at least the components of the weeksite and acmite phases that were dissolved, transported, and crystallized on the inside walls of the gold capsule. The concentrations of Na, Mo, and Cs in solution were nearly constant for all four durations at about 45%, 70%, and 5% of the amount available in the glass. The B and Rb concentrations increased gradually with time of treatment. Some Si, about 4%, was observed. Very little of the available alkaline earths, Ca, Sr, and Ba, was found in the solutions. There was virtually no detectable Ti, Zn, Zr, La, or Nd in the solutions. Only a very small percentage of the available U was present in solution and that percentage decreased with longer treatment times.

It is instructive to consider the total concentration of the elements in solution as a percentage of the available concentrations of the 18 elements

(10:1 Deionized Water to Glass)

3 Weeks		*4 Weeks*			
GD 80	*GD 81*	*GD 78*	*GD 79*	*GD 89*	*GD 90*
4000	4300	4300	4400	4200	3900
2500	2800	2600	2900	2800	2700
1280	1140	1180	1290	450	550
1100	1000	1100	1200	—	—
50	40	50	48	—	—
5	3	10	11	—	—
0.6	0.8	ND	ND	1.2	0.7
0.4	0.1	0.8	ND	0.6	0.4
15.4	2.4	9.0	10.0	30.5	20.3
1.0	1.0	ND	ND	0.8	0.1
ND	2.3	12.4	9.8	1.3	1.9
47	53	—	—	73	80
ND	ND	—	—	1	1
ND	ND	ND	ND	3	3
—	—	—	—	ND	ND
ND	ND	ND	ND	ND	ND
ND	ND	ND	ND	ND	ND
0.9	1.5	0.6	0.9	1.8	0.9

[a] ND = none detected.

Table XI. Average Solution Concentration and Percentage

	1 Week[a]		*2 Weeks*[a]	
	$\mu g \cdot mL^{-1}$	%	$\mu g \cdot mL^{-1}$	%
Na	4300	46	4200	45
B	2500	84	2600	87
Si	510	2.7	700	3.7
Mo	1100	72	1100	72
Cs	42	4.3	55	5.6
Rb	ND[b]	—	2	1.4
Sr	2.0	0.62	1.8	0.55
Ba	7.4	1.47	8.4	1.67
Ca	7.4	0.51	7.9	0.55
Zn	0.8	0.02	1.0	0.02
Ni	1.5	0.94	2.8	1.76
Cr	66	23	21	8
Fe	3	0.05	4	0.06
La	4	0.88	1	0.24
Nd	ND	—	ND	—
Ti	ND	—	ND	—
Zr	ND	—	ND	—
U	5.6	0.15	2.6	0.07

[a] Glass spheroid runs GD 59 and GD 68 were not included in the average.

from the glass that were included in the chemical analyses. After first converting elemental into oxide concentrations, we found that 17–19 wt % of the glass was observed in solution after any one of the four hydrothermal treatments. [Note that the elements included in the chemical analyses accounted for only for only 96.2 wt % of the glass. This percentage might change by 0.5–1 wt % if, at some later time, the remaining elements in PNL-76-68 (Ru, Y, Rh, Pd, Ag, Cd, Te, Pr, Sm, Eu, Gd, P) were included in the chemical analyses.] There was a small increase in percentage with time of treatment:

1 week	16.8%
2 weeks	17.2%
3 weeks	18.5%
4 weeks	18.5%

The results of the analyses from GD 59, the 1-week run that used a spheroidal specimen, appeared to be anomalous when compared to the trend of the other analyses. The concentrations of Na, B, and Cs were only half those found for the runs with the glass shard specimens. Also, the Cs analysis in GD 68, the other glass spheroid run, was high. Although the possibility of a systematic analytical error cannot be ruled

of Element in Solution (10:1 Deionized Water to Glass)

3 Weeks		*4 Weeks*	
$\mu g \cdot mL^{-1}$	%	$\mu g \cdot mL^{-1}$	%
4100	44	4200	45
2700	89	2800	93
1210	6.4	870	4.6
1100	72	1100	72
45	4.6	49	5.0
4	3.4	11	8.7
0.7	0.22	0.5	0.15
0.2	0.04	0.5	0.1
8.9	0.62	17.4	1.20
1.0	0.02	0.2	0.005
1.1	0.69	6.3	3.96
50	18	77	27
ND	—	1	0.02
ND	—	2	0.48
—	—	ND	—
ND	—	ND	—
ND	—	ND	—
1.2	0.03	1.0	0.03

[b] ND = none detected.

out, it seems likely that the radical difference in the surface condition between the two types of specimens was responsible for different amounts of alteration and thus the apparently anomalous solution analyses.

One explanation for the approximate constancy of solution concentrations after only one week of treatment might be that the solutions simply have become saturated in various elements. In order to test this explanation, five runs were made where the deionized water-to-glass ratio was incrased to 30:1. If the solutions became saturated in 10:1 water-to-solid ratio experiments, the percents of elements extracted in 30:1 water-to-solid ratio experiments when equilibrium was attained should be three times as much as in 10:1 water-to-solid ratio experiments. Analytical results from these runs are listed in Table XII. The Si content in solution increased substantially while Na increased slightly, B remained about the same, and Mo showed a substantial decrease. These results indicate that in the 10:1 water-to-solid ratio experiments the solution might have become saturated only with respect to Si.

Solutions From Runs Using Artificial Hanford Groundwater. All the experiments discussed so far have utilized deionized water (DW). At first it would appear that to make the experiment more relevant, Hanford groundwater (HGW) should have been used. However, it can

Table XII. Percent of Element in Solution (30:1 Deionized Water to Glass)

	1 Week[a]	*2 Weeks*[a]	*4 Weeks*
Na	55	55	67
B	81	91	91
Si	11.5	8.3	7.8
Mo	52	59	46
Cs	2.6	5.1	3.6
Rb	—[b]	—	—
Sr	0.6	—	—
Ba	1.8	—	0.4
Ca	0.4	—	—
Zn	0.03	0.06	0.13
Ni	0.8	0	1.6
Cr	20	28	13
Fe	0.01	—	—
La	—	—	—
Nd	—	—	—
Ti	—	—	—
Zr	—	—	—
U	0.20	0.11	0.22

[a] Average of duplicates.
[b] Indiactes that element was below the level of detection.

be shown that groundwaters typical of those beneath the Hanford site are so low in total dissolved solids (TDS) that, in these *closed-system* hydrothermal experiments, soon after the experiment begins the solutions would contain far greater concentrations of TDS released from the glass than were present in the original HGW. For example, when a 0.1-g specimen of glass releases 17% of its constituents into 1.0 mL of solution, that solution would contain 17,000 $\mu g \cdot mL^{-1}$ of total dissolved solids. This compares to the 420 $\mu g \cdot mL^{-1}$ of TDS in the artificial HGW described in the experimental procedures section. The HGW would make a contribution of less than 3% to the TDS in such a run. Three experiments were performed to test the validity of this argument.

The results of chemical analyses for solutions from 1-, 2-, and 4-week treatments of the glass with an artificial HGW are given in Table XIII. Footnote *b* to this table gives the results of a concurrent cation analysis of the HGW. After subtracting the contribution of Na from the HGW, it is evident that the range of Na concentrations duplicates the results of the comparable DW experiments. Similarly, with the other major constituents of the solutions, B, Mo, and Cs, the concentration ranges were in good agreement with the corresponding DW experiments. Among the minor elements, Cs and Cr concentrations were somewhat higher and Si was lower. In general, these results support the position that

Table XIII. Solution Concentrations[a] (10:1 Artificial Hanford Groundwater[b] to Glass)

	1 Week GH 112	*2 Weeks GH 150*	*4 Weeks GH 111*
Na	4600	4100	4400
B	2600	2800	2700
Si	430	350	190
Mo	1200	1200	1200
Cs	86	85	44
Rb	2	ND[c]	ND
Sr	2.0	ND	ND
Ba	8.4	2.2	6.1
Ca	7.5	ND	32.2
Zn	ND	ND	0.4
Ni	0.9	ND	ND
Cr	149	126	132
Fe	ND	ND	ND
La	5	ND	ND
Nd	ND	ND	ND
Ti	ND	ND	ND
Zr	ND	ND	ND
U	4.6	3.5	ND

[a] In micrograms per milliliter.
[b] Analyzed concentrations ($\mu g \cdot mL^{-1}$): 170 Na, 60 Si, 6.8 K, 0.4 Mg; no Ca detected.
[c] ND = none detected.

deionized water is a quite satisfactory generic stand-in for low-TDS groundwaters *in closed-system experiments.*

Discussion and Conclusions

The results presented show that, in the laboratory, the radwaste glass reacts with water under the temperature–pressure regime of 300°C and 300 bar. Reaction for times on the order of weeks resulted in the conversion of a solid shard of glass into a fragmented and partially dispersed mass of crystalline and noncrystalline material plus dissolved species. The more massive solid products were compositionally banded and zoned, which is a common indication of the nonattainment of equilibrium. Yet the solid crystalline products and the species retained in the solutions did not vary greatly over the four reaction times used. It appears that there is a rapid initial reaction of the water with the glass to form a variety of recrystallization products, followed by a much longer time of nearly steady state conditions. Although final thermodynamic equilibrium was not reached for the system as a whole, many of the crystalline phases are likely to be stable under the *P-T* conditions of the experiments.

Water plays three distinct and important roles in the degradation of the glass: as a solvent and catalyst for glass recrystallization [long known to geochemists who use glasses as reactive starting materials for hydrothermal phase equilibrium experiments (*8*)]; as a transport medium carrying elements extracted from the solids to different parts of the capsule and redepositing them at temperature or during cooling as the observed crystalline capsule-lining phases; and as a component for the formation of hydrated or hydroxylated phases such as weeksite and apatite.

Occurrence of Key Elements in Solid and Solution Products. The key elements are those that have potentially hazardous and relatively long-lived radionuclides. In high-level nuclear wastes from light-water reactors, these elements (radionuclides) would include Cs(^{137}Cs), Sr(^{90}Sr), Np (^{273}Np), Pu (^{239}Pu), Am (^{241,243}Am), Cm (^{243,244}Cm), I (^{129}I), and Tc (^{99}Tc). Only two of these elements, Cs and Sr, are present in the simulated high-level waste glass used in this investigation. However, there is considerable (though certainly not complete) analogy between the crystal chemistry and solution speciation of Np and Pu with U, and Am and Cm with the lanthanides (Ln). Thus U and the Ln's will be included among the key elements discussed below.

Concerning the solutions, it should be noted again that only those elements remaining in solution or forming in readily soluble solid phases during the cool down from 300°C would be observable in the product solutions. There were certainly other species in solution at temperature that either grew into crystals during the course of the run or precipitated on cooling to form phases that were not dissolved during the subsequent procedures used to separate solids from solutions. The weeksite and acmite phases and, probably, the multiphase banded skin are examples of such solid phases.

Table XIV is a compilation of the occurrences of each PNL-76-68 element in solid alteration products and in solutions of the 10:1 water-(DW or HGW) to-solid-ratio experiments. The occurrences in solids are based on SEM/EDX observations and microprobe X-ray maps and X-ray emission traces. The assignment of structure types and generalized solid solution formulas resulted from X-ray diffraction studies. The key elements are in italic.

Cesium was observed in weeksite and in certain of the noncrystalline solid (NCS) alteration zones. Some 4–9% of the Cs available in the glass was found in the product solutions. Only traces of Sr were found in solution, and its occurrences in the solid products were in the apatite band of the skin and in various NCS alteration zones. Uranium was found in many of the solids but only in trace quantities in solutions. X-ray emission traces of the lanthanides showed that they were relatively well distributed among the NCS alteration zones. The only crystalline

Table XIV. Occurrence of Elements in Solids and Solutions

Element	*Solids*	*Solutions*[a] *(%)*
Na	acmite,[b] acmite augites,[c] weeksite,[d] NCS[e]	44–47
Si	acmite, acmite augites, weeksite, apatite[f]	1–6
B		84–93
Ca	acmite augites, apatites, NCS	0.5–2
Zn	acmite augites, NCS	0.2–0.05
Ti	acmite augites, NCS	ND[g]
Rb	weeksite	ND–9
Sr	apatite, NCS	0.2–0.6
Zr	NCS	ND
Mo	NCS	68–78
Ru	$(RuO_2)_{ss}$	—
Pd	$(Pd)_{ss}$	—
Cs	weeksite, NCS	4–9
Ba	apatite, NCS	0.04–2
Ln[h]	apatite, NCS	0.2–0.9 (La, Nd)
U	weeksite, apatite, NCS	0.03–0.15
Fe	acmite, acmite augite, spinel,[i] NCS	ND–0.06
Cr	spinel	18–54
P	apatite	—
Ni	spinel	0.7–4
Te, Rh, Ag, Cd[j]	—	—

[a] Percentage of the amount of the element present in PNL-76-68 that was detected in solutions from the 10:1 water-to-solid-ratio runs.
[b] Acmite = $NaFeSi_2O_6$.
[c] Acmite augite = $(Na,Ca)(Fe,Zn,Ti)Si_2O_6$.
[d] Weeksite = $(Na,Cs,Rb)_2(UO_2)_2(Si_2O_5)_3 \cdot 4H_2O$.
[e] NCS = noncrystalline solids; general designation of the X-ray amorphous alteration zones.
[f] Apatite = $(Ca,Sr,Ba,Ln,U)_5[(Si,P)O_4]_3(OH)$.
[g] ND = none detected.
[h] Ln = Y,La,Ce,Pr,Nd,Sm,Eu,Gd.
[i] Spinel = $(Zn,Ni,Fe)(Fe,Cr)_2O_4$.
[j] Not included in any of the analyses.

host for the Ln elements was the apatite structure phase that made up the outermost band of the skin. Less than 1% of (La + Nd) was observed in any of the various solution analyses. Thus of the key elements, only Cs occurs in the product solutions in substantial amounts.

It is interesting to look at the behavior of some of the other elements. Approximately 62 wt % of PNL-76-68 glass consisted of ($Na_2O + Fe_2O_3 + SiO_2$), so it was not surprising to find that the major crystalline phases in the 10:1 water-to-solid-ratio experiments were Na–Fe-rich pyroxenes. Note that nearly half the available Na was observed in the product solutions. When the amount of water was tripled, the Na in solution increased to as much as 67% in the 4-week run, while the amount of

pyroxenes in the solid products decreased. Apparently Na is a key constituent of these high-Fe^{3+} pyroxenes, and with more Na going into solution, less was available to form the pyroxenes. This trend suggests that when water-to-solid ratios are less than 10:1, less Na would go into the solutions and the formation of crystalline pyroxenes in the altered products would be greater.

Boron is apparently extracted from the glass as one or more species of borate ions and molybdenum as the molybdate ion. When the solutions extracted from PNL-76-68 glass are allowed to evaporate to dryness at room temperature, SEM/EDX and X-ray diffraction characterization of the residual solids revealed the presence of a hydrated sodium molybdate and the borate mineral tincalconite, $Na_2B_4O_7 \cdot 5H_2O$ (*13*).

The occurrence of the other major constituent of the glass, Fe, was almost completely confined to the solid products. It was found in the pyroxene, NCS, and spinel phases. A substantial portion of the original spinel crystalline inclusions interacted with the hydrothermal solutions. Much of the Fe content of the glass originally present in these inclusions was recrystallized in the pyroxene phases. This mechanism may also account for the large amounts of Cr in solution. Chromium occurs with Fe in the spinels. When the spinel is altered and Fe is recrystallized in the pyroxenes, the Cr might remain behind in solution.

The preceding discussion illustrates that with the multiple-tool characterization used in this study, it is possible to describe alteration of this complex glass in near-mass-balance detail for many of its elements.

Glass Crystallization and Repository Design. Solution and recrystallization of the prototype radwaste glass takes place so readily that some cognizance of the potential for this effect must be taken during the repository design. Because many of the observed reactions require only water as a catalyst, some of the recrystallization and transport could be expected in the presence of only small amounts of water. One can either view the hydrothermal reactions as a problem in need of a solution, or one can simply incorporate the potential for hydrothermal reactions as part of the overall waste storage concept. There are some fairly obvious engineering solutions to the problem and also some potentially interesting ways of incorporating the reactions as a positive benefit, although data are too sparse at present to make definitive statements about the latter.

First, an obvious requirement for hydrothermal conditions is a certain amount of heat. The heat output of the canisters can be adjusted by adjusting the waste loading. Loadings could be adjusted downward until the skin temperature of the canister was below the temperature at which the reactions would be a problem. The cost of this approach to the problem is that much larger volumes of material would be created for the disposal of a given volume of waste.

Second, it may be remembered that heat comes from the decay of mostly short-lived isotopes. The thermal period of the repository is short, a few hundred years at most. One expedient is to retain the canisters in controlled and cooled surface storage for a few tens of years before removal of the material to the repository. Temperatures fall rapidly with time out of the reactor, and even a few years of storage improves the thermal heat output greatly. Alternatively, the canister design could be improved in such a way that breaching of the canister during the thermal period became unlikely.

A completely different approach is to examine the implications of waste, rock, and water as a chemical system (*2*). The results reported in this paper dealt with a glass waste form in a closed system in the presence of water only. This situation would surely obtain if invading waters came into contact with the surface of the glass ingot or penetrated into cracks and flaws in the material. The initial chemical reactions would be completely dominated by the composition of the glass. As the solutions carrying dissolved species or the solid reaction products themselves came into contact with the surrounding rock of the wall, the chemistry would come to be dominated by the rock. If the rock were of basalt, granite, or shale, new reactions would take place that would greatly modify the final phase assemblage. It is the final assemblage, when the waste has come into steady state conditions with the rock, that must be regarded as the source term for further transport and dispersal of the waste elements by slow processes over the functional life of the repository (*2*). The paragraphs below outline some of the possibilities based on new but not final experimental results from current waste rock interaction studies at Pennsylvania State University (*11, 13*).

STRONTIUM AND LANTHANIDES. Much of the Sr and Ln in the original glass was found with the NCS alteration products. Equilibration with hydrothermal solutions could well result in crystallization of apatite phases similar to that identified as one of the skin phases. Apatites are a common accessory mineral in basalts and other igneous rocks and, once formed, they may remain in, or close to, thermodynamic stability with the rock throughout the thermal period. Mixed phosphate–silicate apatites of Ca, Sr, Ln, and U (britholite), such as those formed on the product skin, are known.

URANIUM. Small amounts of the U in PNL-76-68 crystallized in the apatite phase as has already been noted. The other well-characterized crystalline host for U was weeksite. Uranium in weeksite is in the hexavalent state. Host rocks containing Fe^{++}, sulfides, and organic materials would buffer the oxygen activity well into the reducing range where the U^{6+} would not be stable. In one of a series of experiments designed to explore this stability question, the authors have treated weeksite

crystals gathered from glass alteration product with HGW in contact with a sixtyfold excess by weight of crushed Columbia River basalt. The water-to-solids ratio was 30:1, and the experimental conditions were 300°C, 300 bar, and 4 weeks. The resultant crystals had turned black and gave an X-ray powder pattern of uraninite, UO_{2+x}, with a cubic cell parameter typical of a composition near $UO_{2.25}$. As long as the conditions remain reducing, uraninite should remain a stable and insoluble phase (*14*). It is possible that the U in the NCS alteration zones would be converted to uraninite through long-term equilibration with basalt-saturated hydrothermal solutions.

Cesium. This element was observed in alteration product solutions, in weeksite, and in various NCS alteration zones. (Note that the Cs would be released from weeksite by the decomposition mechanism just described.) The authors have completed numerous experiments in which solutions containing Cs were reacted with Columbia River basalts, with individual basalt phases, and with shales and constituent clay minerals (*14*). Under conditions of 200°–300°C and 300 bar, virtually all the Cs was removed from the solutions. Intense reflections analogous to those of the mineral pollucite, $(Cs,Na)AlSi_2O_6 \cdot nH_2O$, were present in X-ray diffractograms of many reaction products. Pollucite occurs in hydrothermally formed pegmatites and may be stable in contact with basalt and shale under hydrothermal conditions. Results to date indicate that Cs would react with alumino-silicate minerals and become immobilized as pollucite.

Glossary of Symbols

AAS = atomic absorption spectrophotometry
AES = atomic emission spectrometer
d = interplanar spacing (in X-ray data)
DW = deionized water
EBS = electron backscatter
EDX = energy-dispersive X-ray spectrometry
HGW = Hanford groundwater
I = intensity (in X-ray data)
Ln = lanthanides
NCS = noncrystalline solids
PDF = Powder Diffraction File
PNL = Pacific Northwest Laboratories of Battelle Memorial Institute
P–T = pressure–temperature
SEI = secondary electron image
SEM = scanning electron microscopy

ss = solid solution
TDS = total dissolved solids
rad waste = radioactive waste

Acknowledgments

This research is supported by the U.S. Department of Energy through Rockwell Hanford Operations and the Office of Nuclear Waste Isolation. J. E. Mendel provided the specimen of PNL-76-68. C. A. Smith assisted with the hydrothermal experimentation.

Literature Cited

1. Goodenough, J. B.; Whittingham, M. S., Eds.; In "Solid State Chemistry of Energy Conversion and Storage," *Adv. Chem. Ser.* **1977**, *163*.
2. McCarthy, G. J.; White, W. B.; Roy, R.; Scheetz, B. E.; Komarneni, S.; Smith, D. K.; Roy, D. M. "Interactions Between Nuclear Waste and Surrounding Rock," *Nature* **1978**, *273*, 217–219.
3. Jenks, G. J. "*NWTS Program Conference on Waste-Rock Interactions*"; Y/OWI/SUB-77/14268; Roy, D. M., Ed.; Pennsylvania State University: University Park, PA, July 1977; 5–17.
4. Mendel, J. E.; McElroy, J. L.; Platt, A. M. In "High-Level Radioactive Waste Management," *Adv. Chem. Ser.* **1976**, *153*, 93–107.
5. Mendel, J. E.; Ross, W. A.; Roberts, F. P. "Annual Report on the Characteristics of High-Level Waste Glasses"; BNWL-2252; Battelle Pacific Northwest Laboratories: Richland, WA, 1977.
6. McElroy, J. L. "Quarterly Progress Report, Research and Development Activities, Waste Fixation Program"; PNL-2264; Battelle Pacific Northwest Laboratory: Richland, WA, 1977.
7. Ross, W. A.; Bradley, D. J.; Bunnell, L. R. "Annual Report on the Characterization of High-Level Waste Glasses"; PNL-2625; Battelle Pacific Northwest Laboratory: Richland, WA, 1978.
8. Roy, R.; Tuttle, O. F. In "Physics and Chemistry of the Earth"; Pergamon: New York, 1956; Vol. 1, 138–180.
9. Gandolfi, G. "Discussions Upon Methods to Obtain X-Ray Powder Patterns from a Single Crystal," *Mineral. Petrogr. Acta* **1967**, *13*, 67.
10. "*Powder Diffraction File*"; McClune, W. F., Ed.; JCPDS, (International Centre for Diffraction Data): Swarthmore, PA.
11. McCarthy, G. J.; Scheetz, B. E.; Komarneni, S. "Simulated High-Level Waste-Basalt Interaction Experiments—First Interim Progress"; Rockwell Hanford Operations Report; University Park, PA, March 1978.
12. Outerbridge, W. F.; Staatz, M. H.; Meyrowitz, R. "Weeksite, a New Uranium Mineral from the Thomas Range, Juab County Utah;" *Am. Mineral.* **1960**, *45*, 39–52.
13. McCarthy, G. J.; Scheetz, B. E.; Komarneni, S.; Barnes, M. W.; Smith, C. A.; Smith, D. K.; Lewis, J. F. "Simulated High-Level Waste-Basalt Interaction Experiments. Second Interim Progress Report"; Rockwell Hanford Operations Report; University Park, PA, June 1978.
14. McCarthy, G. J.; Komarneni, S.; Scheetz, B. E.; White, W. B. In "Scientific Basis for Nuclear Waste Management," McCarthy, G. J., Ed.; Plenum: 1979; Vol. 1, 329–340.

RECEIVED November 6, 1978.

20

Phase Equilibria Research in Portions of the System K_2O–MgO–Fe_2O_3–Al_2O_3–SiO_2

ROBERT S. ROTH

National Bureau of Standards, Washington, DC 20234

Preliminary phase equilibria diagrams are given for some binary and ternary joins and cuts through the five-component system K_2O–MgO–Fe_2O_3–Al_2O_3–SiO_2. The diagrams are those that are most pertinent to the chemical reactions taking place between potassium seed and the four-component synthetic slag of importance in corrosion studies of a magnetohydrodynamics system. Although the systems $KAlO_2$–SiO_2, $KFeO_2$–SiO_2, and K_2MgSiO_4–SiO_2 are apparently true binary joins, other pseudobinary cuts involving only kalsilite types of end members are generally not binary. The phase $K_2MgSi_3O_8$ dissociates at low temperatures into a second kalsilite-like phase plus leucite. Thus leucite is a major component even just below liquidus temperatures of magnesia containing ternary and quaternary compositions that might be expected to exhibit only kalsilite-like phases.

The development of new materials with useful properties for applications in the area of electronic ceramics, catalysts, electrolytes, electrodes, and so on is strongly dependent on a knowledge of the chemistry of many unusual oxide systems. A better understanding of the mechanisms of corrosion, wear, fracture, and the general behavior of materials under use conditions of severe environments is also dependent on a knowledge of chemical compatibility. The prediction of physical and chemical properties of materials is limited by our knowledge or ability to predict chemical reactions and general crystal chemical relations. A detailed experimental study of a few selected systems often enables us to predict the crystal chemical principles governing the chemical reactions in more complex industrial systems.

In a study of the phase equilibria relations of a model system, it is always desirable to prepare single crystals of all the previously unknown phases to be certain of having identified all the reactions. Even a knowledge of the crystal structure of many of the phases is needed to understand the mechanisms involved in the chemical reactions. A study of phase equilibria, crystal growth, and crystal chemistry is currently being conducted in portions of the system K_2O–MgO–Fe_2O_3–Al_2O_3–SiO_2 to understand the chemical corrosion of refractory components by seed/slag in a coal-fueled magnetohydrodynamics system.

Previous studies in this complex system have been confined mainly to the ternary systems. The most important of these (*1–5*) have been concerned mainly with the high-silica portions of the system because of the obvious geological interest. However, the main object of the present study is to understand the reaction between molten coal slag and potassium oxide, used to enhance the conductivity of the plasma in a MHD channel. Therefore, our major interest is in those phases in equilibrium with the higher K_2O compositions and the minerals kalsilite and leucite, which have the compositions $KAlSiO_4$ and $KAlSi_2O_6$, respectively. Iron and/or magnesium containing analogues also can be formulated. The first results of these studies, involving the join $KAlO_2$–SiO_2, were published recently (*6*), as well as several abstracts (*7, 8, 9*) on other portions of the system. Some of the other data mentioned in this paper have been previously reported only in project reports to sponsors, if at all.

Much of the work reported in the present paper is preliminary in nature, and important portions of the phase diagrams may be changed in future publications. All the experimental points are shown in the diagrams, so that the reader can judge where further work may be needed to unambiguously understand the nature of the equilibrium reactions. As all corrosion and stability problems in a working MHD system necessarily involve relations with the K_2O-containing compound added as seed (such as K_2CO_3 and K_2SO_4), only those portions of the system containing K_2O are discussed.

Experimental

All specimens for this study were prepared from reagent-grade materials, of nominal 99% purity or better. Starting materials used were K_2CO_3, α — Fe_2O_3 (hematite, —0.5 μm), $MgCO_3$, γ — Al_2O_3 (0.05 μm), and SiO_2 (quartz, less than 5 μm). Batches were weighed to the nearest 0.01 mg, mixed, and calcined several times before final heat treatments. Many experiments were duplicated by approaching equilibrium in the solid state only and by annealing a premelted glass. Specimens were annealed for periods varying from several hours to several months until

equilibrium was achieved. Most specimens heated above about 900°C were enclosed in sealed Pt tubes in order to minimize K_2O volatilization and generally quenched after the heat treatment.

All specimens were examined after each heat treatment by X-ray powder diffraction analyses using a high-angle diffractometer equipped with a graphite single-crystal monochromator using CuKα radiation. In general, equilibrium was believed to have been achieved when further heat treatment at the same (and/or higher) temperatures caused no change in the X-ray diffraction pattern. Due to the very sluggish rate of reaction in silicate systems, specimens were held at temperature for much longer times than is common for most solid state chemistry phase equilibria experiments.

For proper interpretation of the X-ray diffraction powder patterns, it is extremely important that *every* peak in the pattern be mathematically accounted for by indexing all the single-phase patterns. It is not sufficient to simply assign peaks to a kalsilite-like phase without knowing the true unit cell, as small peaks in the pattern often may represent a small amount of a previously unknown second phase. Consequently, attempts were made to grow small, single crystals, sufficient for the X-ray diffraction precession technique, for every unknown phase in the system. By adhering to this principle, we found a new compound with tetragonal symmetry in the $KAlO_2$–SiO_2 system, referred to as $K_{1+x}Al_{1+x}Si_{1-x}O_4$ by Cook et al. (*6*).

Most of the single crystals prepared to study these silicate systems were made by H. S. Parker (*10*), using the flux technique. The flux used was generally either KF as in Cook et al. (*6*) or K_2MoO_4 with or without additions of either V_2O_5 or KVO_3 in various proportions. The full details of the crystal growth of each of the phases will be found in later publications. Many of the crystals were examined in a scanning electron microscope equipped with X-ray dispersive analysis and a windowless detector, enabling semiquantitative determination of elements down to atomic number 6. Neither molybdenum [atomic number 42] nor fluorine [atomic number 9] was found in the crystals, although a strong oxygen peak was always seen with the window open. The detection limit for fluorine was about 1.4 wt % F, and the $KAlSiO_4$ and related compounds contained less than 0.2 units of F when described as $K_{1+x}AlSiO_{4-x}F_x$. However, it should be remembered that it is very difficult to determine F by this technique in the presence of Fe because of the overlap of the major peaks of the characteristic spectra. In order to be certain that the type of unit cell in the single crystals grown was not biased by impurities from the flux, both KF- and K_2MoO_4-based fluxes were often used to grow crystals of the same phase. In general, the size (less than 0.2 mm in diameter) and total amount of the crystals were insufficient for any wet chemical analysis.

Single-crystal X-ray structure determination is presently underway on most of the phases in these systems. Neutron diffraction total profile analysis will be attempted to determine the nature of the nonstoichiometry but must await some previous X-ray structure determination. High-resolution, electron microscope lattice-imaging techniques would be very valuable to study the nature of the ordering of alkali and vacancies in the kalsilite-like polymorphs.

The Quaternary System K_2O–Al_2O_3–Fe_2O_3–SiO_2

The Ternary System K_2O–Al_2O_3–SiO_2. The latest version of this ternary system was published by Schairer and Bowen in 1955 (*2*), and a composite diagram was published as one of a series of large-scale phase diagrams by the American Ceramic Society and as Figure 407 in the book "Phase Diagrams for Ceramists" (*11*). This diagram is now in need of revision, especially in the region containing β-Al_2O_3 as an equilibrium phase and in the high-K_2O portion of the system.

The binary join K_2O–SiO_2 was studied by Kracek (*12*), and the latest version of the system Al_2O_3–SiO_2 is that of Aksay and Pask (*13*). Unfortunately, no experimental study of the system K_2O–Al_2O_3 has appeared in the literature. The present investigation has established the limits of solid solution of the β-Al_2O_3 phase as varying from about 15% K_2O to about 10% K_2O from 1000° to 1600°C, decreasing slightly at the higher temperatures. The melting point of $KAlO_2$ has not yet been established, but preliminary data obtained by using an unsealed Ir crucible indicate a value greater than 2100°C, and a value of 2150 ± 100°C is our best estimated at this time. (Experiments have been performed now to determine the melting point of $KAlO_2$ in sealed Mo tubes (OD, 3.0 mm; ID, 1.5 mm) and the temperature at which the internal pressure from the $KAlO_2$ exceeded the rupture strength of the tubes was found to be ~ 2260°C.) The eutectic between $KAlO_2$ and β-Al_2O_3 was found to occur at about 1910°C, but the composition has not yet been established.

$KAlO_2$–SiO_2. An investigation of the crystal chemistry of the system $KAlO_2$–$KAlSiO_4$ was reported by Cook et al. (*6*) as the first part of the present study. The main contributions of this work were the discovery of the high-temperature form of $KAlSiO_4$, orthorhombic, with unit-cell parameters $a = 18.110$ Å, $b = 15.600$ Å, and $c = 8.560$ Å, the tetragonal phase $K_{1+x}Al_{1+x}Si_{1-x}O_4$ ($x \approx 0.1$) $a = 8.943$ Å and $c = 5.5221$ Å, and the investigation of the solid solution of SiO_2 in $KAlO_2$, stabilizing the pseudocubic modification of this structure.

Since the submission of the manuscript of Cook et al. (*6*), a considerable amount of experimental data has been accumulated on this binary join. The information interpreted from these experiments is summarized in Figure 1 as the system $KAlO_2$–$KAlSi_2O_6$. A more complete description of this system will be published, when completed, by J. L. Waring et al. (*14*). In this diagram the new tetragonal phase is found to occur at a ratio very close to the composition $4KAlO_2$:$3SiO_2$. However, it seems doubtful that this ratio has any significance with respect to Al/Si ordering when compared with the small size of the unit cell. Immediately after publication of the paper by Cook et al. (*6*), J. V. Smith brought to

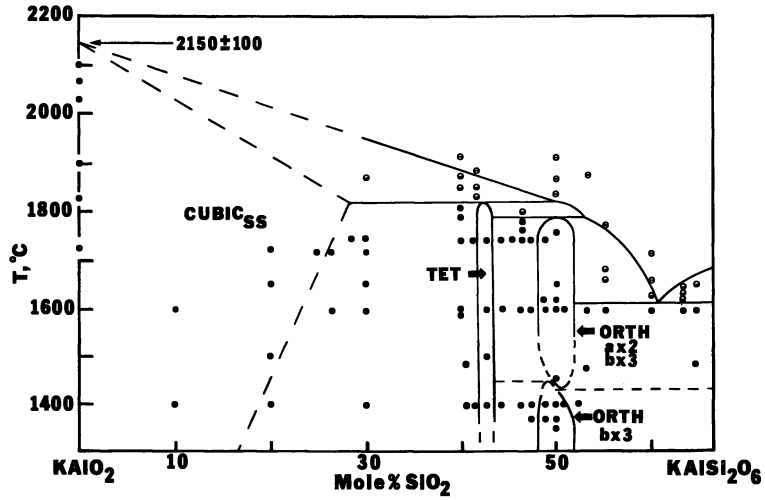

Figure 1. Preliminary phase equilibria diagram of the system $KAlO_2$–$KAlSi_2O_6$: (●), no melting; (◒), partially melted; (⊖), completely melted. TET = tetragonal phase; ORTH b × 3 = low-temperature orthorhombic form of $KAlSiO_4$; ORTH a × 2, b × 3 = high-temperature orthorhombic form of $KAlSiO_4$.

our attention a classification of framework silicates describing possible linkages from a simple hexagonal net, published a short time earlier (*15*). He pointed out that this tetragonal phase could correspond to his possible structure designated SCCSCC. Indeed, it seems likely that the structure of this phase may correspond to this form, which is composed of double tetrahedral units, as shown in Figures 2(a) and 2(b). A structural refinement of this phase is currently underway along with a crystal structure analysis of the two orthorhombic polymorphs of $KAlSiO_4$, previously reported by Cook et al. (*6*), in an attempt to learn more about the possible Al/Si ordering as well as the K vacancy ordering in the kalsilite-like phases.

The Ternary System K_2O–Fe_2O_3–SiO_2. This ternary system has not been previously studied in any great detail. Faust (*16*) reported the presence of compounds equivalent to kalsilite, leucite, and feldspar, but all were located only in the presence of glass on the join $K_2O{:}6SiO_2$–Fe_2O_3. Potassium–iron feldspar, $KFeSi_3O_8$, was synthesized hydrothermally and structurally analyzed by Wones and Appleman (*17*).

The system Fe_2O_3–SiO_2 contains no binary compounds unless accompanied by reduction of $Fe^{3+} \rightarrow Fe^{2+}$. However, the system K_2O–Fe_2O_3 studied by Takahashi et al. (*18*) contains $KFeO_2$ and a β-Al_2O_3 type of phase. An unknown phase reported on the high-Fe_2O_3 end of the system has been found in the present work to actually be a β'''-type of compound,

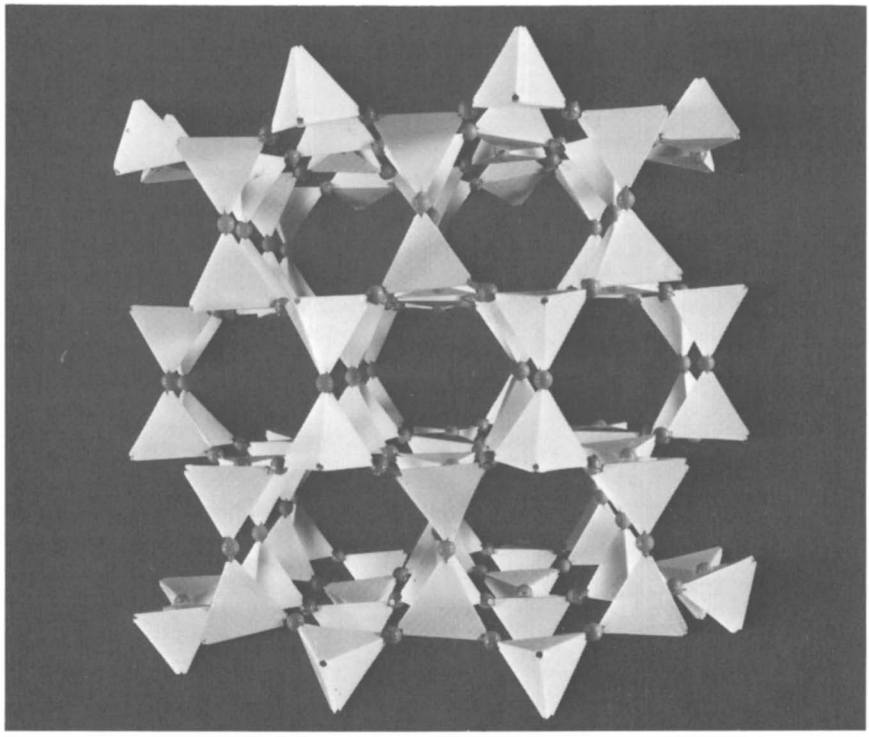

Figure 2a. Tetrahedral model of the structure of the phase designated SCCSCC (15). View looking down one of the a-axes showing pseudo-hexagonal symmetry.

that is, six spinel-like layers between the alkali layers, with hexagonal symmetry $a = 5.927$ Å and $c = 33.45$ Å. This phase undoubtedly has some Fe^{2+} ions as an integral part of the structure. Indeed, the regular β-Al_2O_3 type of compound probably also contains some Fe^{2+}, the Fe^{3+}/Fe^{2+} ratio depending on the heat treatment. The current study indicates that the composition of the β phase occurs at the 1/5.75 K/Fe ratio at 800°C, widening slightly with increasing temperature. The complete experimental data and phase equilibrium diagram will be published eventually by Parker et al. (*19*).

$KFeO_2$–SiO_2. The system $KFeO_2$–SiO_2 has been examined in the present study (*8*), and the interpretation of the experimental data is shown in Figure 3. The hexagonal kalsilite-like phase, $KFeSiO_4$, $a = 5.278$ Å and $c = 8.824$ Å, was found to exist below 945°C and to transform reversibly to an orthorhombic form with a c-axis seven times the size of the pseudoorthorhombic cell, $a = 9.115$ Å, $b = 5.433$ Å, and $c = 59.61$ (7×8.516) Å. The large superstructure cannot be seen in

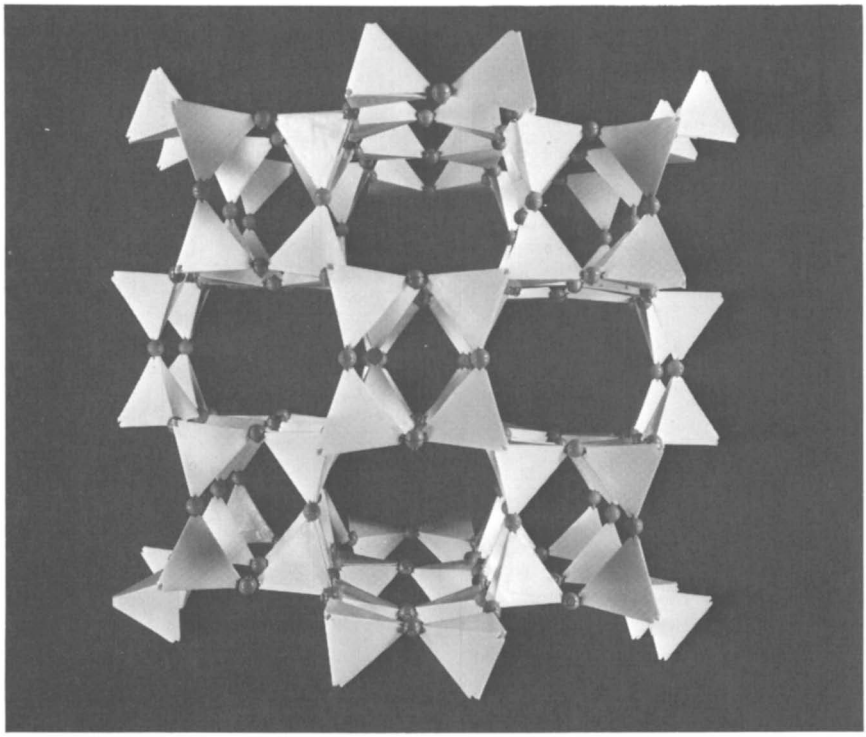

Figure 2b. Tetrahedral model of the structure of the phase designated SCCSCC (15). View looking down the c-axis showing the real body-centered tetragonal nature of the unit cell.

X-ray diffraction powder patterns, and it is necessary to examine single crystals (*10*) to see the large cell. The kalsilite-like polymorphs accept 2 to 5 mol % SiO_2 in solid solution depending on the temperature. A body-centered tetragonal phase, $a = 9.09$ Å and $c = 5.33$ Å, apparently isostructural with that in the alumina system, occurs at approximately the same silica content near $4KFeO_2{:}3SiO_2$. It should be noted that a feldspar type of phase can be formed by annealing a glass of composition $KFeSi_3O_8$ below the solidus at atmospheric pressure. Single crystals of the tetragonal phase, of both polymorphs of kalsilite, with and without excess silica, and of $KFeSi_2O_6$, the iron leucite-like phase, were produced in sealed Pt tubes using both KF and $K_2MoO_4{:}KVO_3$ as fluxes (*10*). The high-temperature orthorhombic kalsilite polymorph containing 2–4 mol % excess silica, when first treated with KF in an attempt to increase the grain size, formed a new phase on attempts to reverse the equilibria at 850°C. Pure $KFeSiO_4$, whether or not treated with KF, and the solid solutions not treated with KF showed no such anomaly. No single crystals

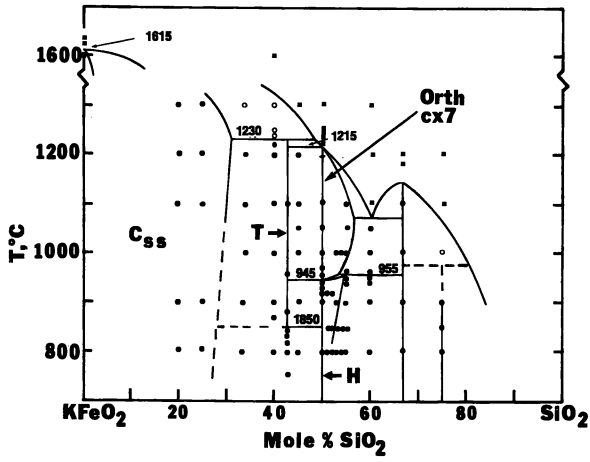

Figure 3. Preliminary phase equilibria diagram of the system $KFeO_2$–SiO_2: (●), no melting; (○), partial melting; (■), completely melted. C_{ss} = cubic $KFeO_2$ solid solution; T = tetragonal phase; H = hexagonal kalsilite-like phase; ORTH c × 7 = high-temperature orthorhombic form of $KFeSiO_4$.

have yet been synthesized with this new unknown structure. (This phase now has been identified as isostructural with the kalsilite-like polymorphs of $KFeGeO_4$ and $RbAlGeO_4$, hevagonal with $a \approx \sqrt{3}$ times the value in the low-temperature form.) The complete experimental data and final version of this phase diagram will be published in another paper (*20*).

The Ternary System K_2O–Al_2O_3–Fe_2O_3. No compositions were studied in the present work that did not contain silica as one of the ingredients. However, several compositions in the quaternary system established that solid solutions are formed between the $KAlO_2$–$KFeO_2$ phases and between the β-Al_2O_3 types of phases in the aluminum and iron oxide systems. No three phase regions were identified.

$KAlSiO_4$–$KFeSiO_4$. Three compositions at 3:1, 1:1, and 1:3 ratios of $KAlSiO_4$–$KFeSiO_4$ were initially prepared to check the solid solution expected in these kalsilite-like phases. The experimental results are interpreted in Figure 4. A few more compositions are being prepared and examined in order to check the phase boundaries. A new stable phase was found to occur at 75$KFeSiO_4$:25$KAlSiO_4$ ($KFe_{0.75}Al_{0.25}SiO_4$). Single crystals of this phase (*10*) proved to be isostructural, with a metastable variety of $KAlSiO_4$ produced by ion exchange from $RbAlSiO_4$ (*21*), and are monoclinic with a pseudoorthorhombic C-centered cell, with a = 18.45 Å, b = 10.73 Å, and c = 8.55 Å. Attempts to reverse the phase transition of the high temperature polymorphs at 800°C were successful, but reversal experiments at 850°C produced the new phase

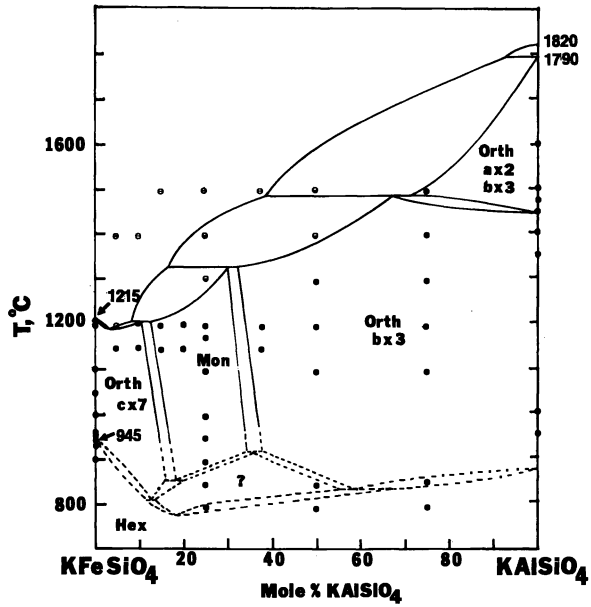

Figure 4. Preliminary phase equilibria diagram of the system $KFeSiO_4$–$KAlSiO_4$: (●), no melting; (◒), partial melting; (⊖), completely melted. HEX = hexagonal kalsilitelike phase; ORTH c × 7 = orthorhombic $KFeSiO_4$ type of phase; MON = monoclinic distortion of the kalsilite-like phase; ORTH b × 3 = low-temperature orthorhombic kalsilite-like phase; ORTH a × 2, b × 3= high-temperature orthorhombic kalsilite-like phase; ? = kalsilite-like phase of unknown symmetry.

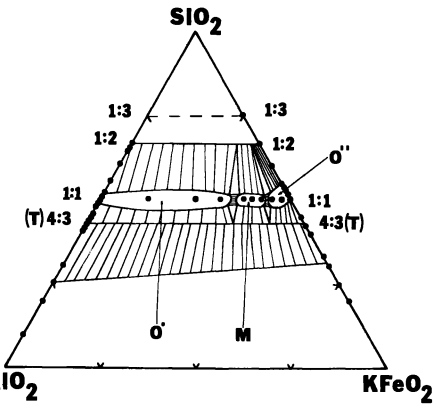

Figure 5. Preliminary phase equilibria diagram of the system $KAlO_2$–$KFeO_2$–SiO_2 representing an isotherm at about 1050°C: (●), compositions studied. O' = low-temperature orthorhombic b × 3 kalsilite-like phase; M = monoclinic distortion of the kalsilite-like phase; O'' = orthorhombic c × 7 $KFeSiO_4$ type o fphase; T = tetragonal kalsilite-like phase.

found for $KFeSiO_4$ with excess silica in solid solution prereacted with KF (*see* section titled "$KFeO_2$–SiO_2"). As this phase apparently forms only during reversal from the high-temperature forms, it may be metastable only with respect to the orthorhombic form. The exact nature of this phase must await examination of single crystals that have gone through the same reversal attempts.

$KAlO_2$–$KFeO_2$–SiO_2. Although many experimental compositions have been studied on each binary containing SiO_2 as one end member, no compositions in the ternary field have been studied except those on the join $KAlSiO_4$–$KFeSiO_4$. Nevertheless, a subsolidus ternary phase diagram can be hypothesized by comparison with known reactions in the binary systems, as shown in Figure 5. This diagram needs experimental verification and probably will be modified considerably in the near future.

The Quaternary System K_2O–MgO–Fe_2O_3–SiO_2

The Ternary System K_2O–MgO–SiO_2. The K_2O–MgO–SiO_2 system was studied by Roedder (*3*, *4*). He reported the existence of several ternary compounds and noted that no phases appeared on the join K_2O–MgO. However, he found that several ternary compounds existed that were essentially isostructural with the phases on the join $KAlO_2$–SiO_2. Apparently a structural substitution of $2Al \longleftrightarrow MgSi$ can take place, so that a compound is formed essentially isostructural with $KAlO_2$ at the composition $K[Mg_{0.5}Si_{0.5}]O_2$ or K_2MgSiO_4. In addition to the phases on the join K_2MgSiO_4–SiO_2, a ternary compound was reported with the composition $K_2Mg_5Si_{12}O_{30}$.

THE SYSTEM K_2MgSiO_4–SiO_2. Many experiments were conducted on the join K_2MgSiO_4–SiO_2. The results of these experiments are interpreted and shown in Figure 6, plotted as the system $K[Mg_{0.5}Si_{0.5}]O_2$–SiO_2 to show the analogy to the system $KAlO_2$–SiO_2 (Figure 1) and $KFeO_2$–SiO_2 (Figure 3). The solidus and liquidus values determined by Roedder (*3*) are indicated on the diagram.

The present data differ from that of Roedder (*3*, *4*) in several important details. First of all, the kalsilite-like composition represented by the formula $K[Mg_{0.5}Si_{0.5}]SiO_4$ or $K_2MgSi_3O_8$ does not melt congruently as suggested in Roedder (*3*). Instead, it melts incongruently to another kalsilite-like phase deficient in silica. There is apparently a congruent type of composition represented by a monotectic (The term "monotectic" is used when there is insufficient experimental evidence to determine if the compound melts just slightly incongruently or congruently or really represents the limiting case between the two) at about the ratio $4K[Mg_{0.5}Si_{0.5}]O_2{:}3SiO_2$ or $2K_2O \cdot 2MgO \cdot 5SiO_2$. Single crystals have been grown (*10*) of the low-temperature form of the kalsilite-like composition, which is hexagonal, just as for the compounds $KAlSiO_4$ and $KFeSiO_4$. The high-

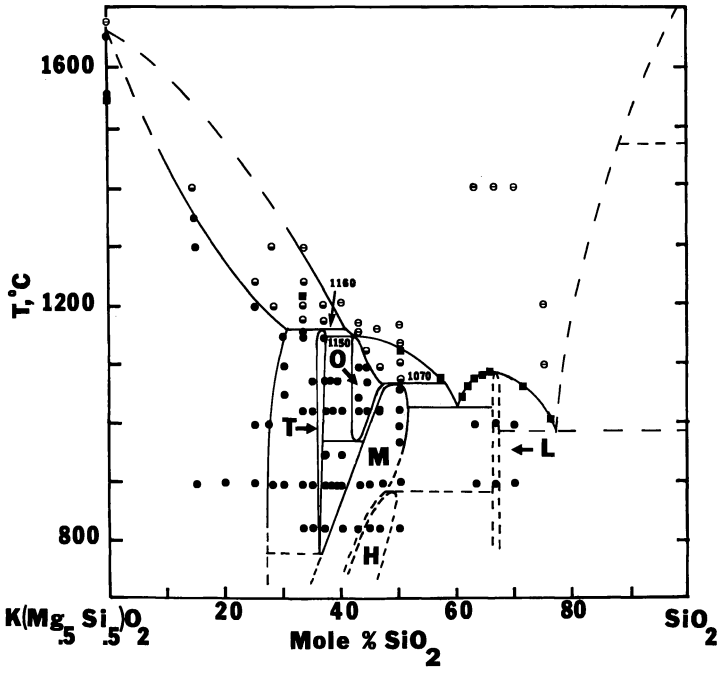

Figure 6. Preliminary phase equilibria diagram of the system K[$Mg_{0.5}$-$Si_{0.5}$]O_2–SiO_2: (●), no melting; (◒), partial melting; (⊖), completely melted; (■), liquidus values of Roedder (3). T = tetragonal kalsilite-like phase; O = orthorhombic kalsilite-like phase; M = monoclinic kalsilite-like phase; H = hexagonal kalsilite-like phase; L = leucite-like phase.

temperature form existing between about 900°C and 1070°C has an X-ray diffraction powder pattern essentially identical to that of 75$KFeSiO_4$:25$KAlSiO_4$ [*see* section titled "$KAlSiO_4$–$KFeSiO_4$" and Minor et al. (*21*)]. It therefore is referred to as a monoclinic phase, although no single crystals have yet been grown (*10*). The powder pattern of the phase occurring at the 4:3 ratio strongly resembles that of $KFeSiO_4$ and is labeled orthorhombic, although again no single crystals are available and it is very doubtful that this phase has the same $c \times 7$ superstructure found in $KFeSiO_4$ (*8, 20*). All these kalsilite-like phases exist as solid solutions having small but experimentally determinable ranges of stoichiometry. It is interesting to note in the phase diagram in Figure 6 that the composition corresponding to $K[Mg_{0.5}Si_{0.5}]SiO_4$ or $K_2O \cdot MgO \cdot 3SiO_2$ is not quite single phase at temperatures below about 950°C. A single-phase specimen prepared at higher temperatures actually exsolves a small amount of leucite when heated at lower temperature. This instability of the kalsilite-like composition in the MgO system becomes very important in the equilibrium relations of more complex systems (*see* section titled "The Quaternary System K_2O–MgO–Al_2O_3–SiO_2").

The tetragonal phase first found by Cook et al. (*6*, *7*) in the system $KAlO_2$–SiO_2 [*see* Figures 1, 2(a), and 2(b)] and in the system $KFeO_2$–SiO_2 (Figure 3) also occurs in this system, except that it occurs at the ratio $5K[Mg_{0.5}Si_{0.5}]O_2{:}3SiO_2$ ($5K_2O{:}5MgO{:}11SiO_2$) instead of at 4:3 as in the alumina and iron oxide systems. The complete experimental details of this system will be published elsewhere in the near future (*22*).

$K_2MgSi_3O_8$–$KFeSiO_4$. It can be seen from Figure 7 that the $K[Mg_{0.5}Si_{0.5}]SiO_4$–$KFeSiO_4$ system is almost a binary join. The small amount of leucite that occurs at temperatures below about 950°C for $K_2MgSi_3O_8$ apparently disappears when a small amount of $KFeSiO_4$ is added in solid solution. However, the instability of the magnesia phase is reflected in the nonbinary nature of the melting relations in the region up to about 20–25 mol % $KFeSiO_4$. The low-temperature hexagonal phase is stabilized by the addition of $KFeSiO_4$ and the orthorhombic and monoclinic polymorphs found in the $K[Mg_{0.5}Si_{0.5}]O_2$–SiO_2 system are eliminated. Thus the hexagonal phase is stable up to the solidus from about 5 mol % to about 30 mol % $KFeSiO_4$. On the other side, the adidtion of $K[Mg_{0.5}Si_{0.5}]SiO_4$ to $KFeSiO_4$ causes both the hexagonal and high-temperature orthorhombic ($c \times 7$) forms to be eliminated from the diagram. Instead, a new phase appears with an X-ray diffraction powder pattern very similar to the low-temperature orthorhombic form of $KAlSiO_4$. However, there are a few extra lines in the pattern, and it can-

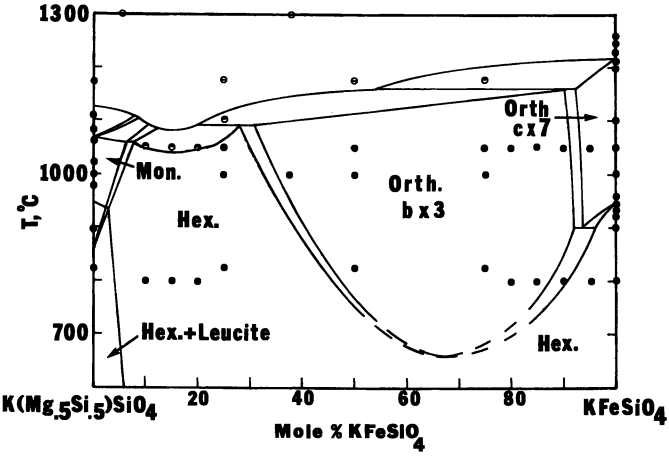

Figure 7. Preliminary phase equilibria diagram of the system $K[Mg_{0.5}Si_{0.5}]SiO_4$–$KFeSiO_4$. Note nonbinary nature of this system up to about 30% $KFeSiO_4$. (●), no melting; (◒), partially melted; (⊖), completely melted. HEX = hexagonal kalsilitelike phase; MON = monoclinic kalsilite-like phase; ORTH b × 3 = orthorhombic phase similar to the low-temperature b × 3 *phase of $KAlSiO_4$; ORTH* c × 7 = *orthorhombic $KFeSiO_4$ type of phase.*

not be completely indexed on the basis of the orthorhombic cell with $b \times 3$. Single crystals of this phase have not yet been prepared (*10*), as the MgO apparently does not enter easily into the structure, with all experiments resulting in either $KFeSi_2O_6$ or $KFeSiO_4$. Complete details will be published later (*22*).

K_2MgSiO_4–$KFeO_2$–SiO_2. Examination of specimens in the system $K[Mg_{0.5}Si_{0.5}]O_2$–$KFeO_2$–SiO_2 thus far have been limited to the join illustrated in Figure 7. Nevertheless, it is possible from the data already determined to make a good guess as to the general nature of an isothermal section just below the solidus (about 1050°C), as shown in Figure 8. It should be remembered that this diagram is very preliminary in nature and boundaries may change considerably as more experimental data is obtained. Further details will be reported in the near future (*22*).

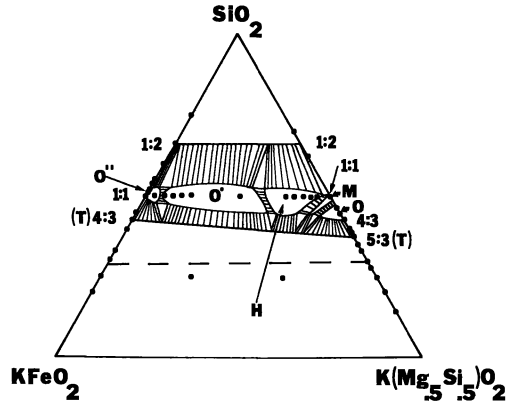

Figure 8. Preliminary phase equilibria diagram of the system $K[Mg_{0.5}Si_{0.5}]O_2$–$KFeO_2$–SiO_2. Isothermal section at about 1000°C. (●), compositions studied. T = tetragonal kalsilite-like phase; O'' = orthorhombic $KFeSiO_4$ type of phase; O' = orthorhombic phase similar to the low-temperature b × 3 phase of $KAlSiO_4$; H = hexagonal kalsilite-like phase; M = monoclinic kalsilite-like phase; O = orthorhombic kalsilite-like phase.

The Quaternary System K_2O–MgO–Al_2O_3–SiO_2

The high-silica portion of this quaternary system was discussed in detail by Schairer (*5*). However, the higher-K_2O-containing phases have not been examined in any detail in previous papers.

The Ternary System K_2O–MgO–Al_2O_3. This ternary system has not been reported in any detail even in reports to sponsors. A few preliminary experiments, however, have shown that this system is analogous to the Na_2O–MgO–Al_2O_3 system in its compound formation. All the ternary βAl_2O_3-related phases labeled β'', β''', and β^{iv} can be found in the

system, but their exact compositional limits have not been accurately determined. It has also been established by T. Negas (*23*) that $MgAl_2O_4 + K_2O \rightarrow MgO + 2KAlO_2$. This has been found to be the mechanism for degradation of $MgAl_2O_4$ insulation in an MHD system.

$K_2MgSi_3O_8$–$KAlSiO_4$. The system $K[Mg_{0.5}Si_{0.5}]SiO_4$–$KAlSiO_4$ shown in Figure 9 is not a binary join. The tendency for instability in the kalsilite-like hexagonal form of $K[Mg_{0.5}Si_{0.5}]SiO_4$ is enhanced by the addition of $KAlSiO_4$. All compositions that have been examined so far show some leucite both above and below the solidus. Although this was a completely unexpected result, it should not be surprising in view of the statement made by Roedder in footnote number 42, page 236:

> ". . . the system $K_2O \cdot MgO \cdot 3SiO_2$–$K_2O \cdot Al_2O_3 \cdot 2SiO_2$ is only partially binary at liquidus temperatures, forming leucite over c considerable range of temperatures" (*4*).

As a matter of fact, the amount of leucite present in these specimens actually increases with increasing $KAlSiO_4$ content, varying from about 5% leucite with no $KAlSiO_4$ to about 50% leucite at the composition $25K[Mg_{0.5}Si_{0.5}]SiO_4$:$75KAlSiO_4$. Of course, it must decrease again with further addition of $KAlSiO_4$ as that end member shows no leucite. There is no evidence in the present data to indicate any new kalsilite-like phases in this system.

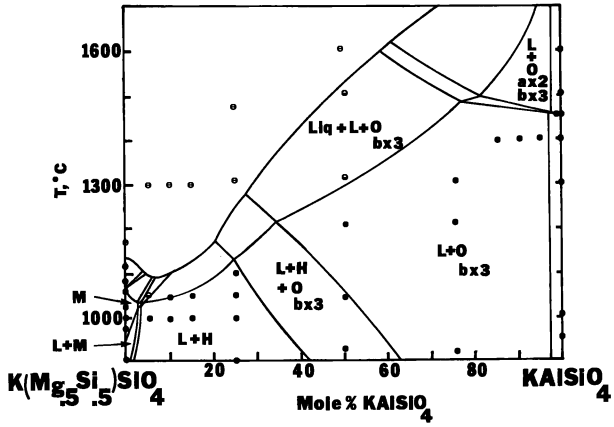

Figure 9. Preliminary phase equilibria diagram of the system $K[Mg_{0.5}Si_{0.5}]SiO_4$–$KAlSiO_4$. Note that this is not a binary join, as a leucite-like phase exists at all compositions studied. (●), no melting; (◒), partially melted; (⊖), completely melted. L = leucite type of phase; M = monoclinic kalsilite-like phase; H = hexagonal kalsilite-like phase; O b × 3 = low-temperature orthorhombic $KAlSiO_4$ type of phase; O a × 2, b × 3 = high-temperature orthorhombic $KAlSiO_4$ type of phase; Liq = liquid.

K_2MgSiO_4–$KAlO_2$–SiO_2. The system $K[Mg_{0.5}Si_{0.5}]O_2$–$KAlO_2$–SiO_2, shown in Figure 10, is much more complex than the corresponding system containing iron oxide instead of alumina. This complexity is caused by the large deviation of the join, shown in Figure 9, from binary equilibria. Many compositions in the ternary must be examined before this diagram can be considered determined even approximately. From the data accumulated so far, no conclusions can be drawn as to the reason for the large amount of leucite occurring in compositions on the join $K_2MgSi_3O_8$–$KAlSiO_4$.

K_2O:MgO–$KAlO_2$–SiO_2. One logical reason for the kalsilite-like compositions discussed earlier to show leucite is to assume that the $KAlSiO_4$ structure will not tolerate much excess silica. The true solid solution may exist in the direction $K_{1+x}Al_{1-x}Mg_xSiO_4$ instead of $KAl_{1-2x}Mg_xSi_{1+x}O_4$, or at least in some compromise between these two alternates. If the previous diagram, Figure 10, is redrawn so that *all* the silica is plotted at one apex, as shown in Figure 11, then the right-hand corner becomes $KMg_{0.5}O$ or 1/2[K_2O:MgO]. If the true solid solution is really $K_{1+x}Al_{1-x}Mg_xSiO_4$, the diagrams in Figures 10 and 11 would still not illustrate these compositions. Nevertheless, Figure 11 does show that the observed compositions may well be single phase when the total silica content is no more than 50% of the total number of small cation oxides. Much more work remains to be done on solid solutions in the kalsilite-like phases involving MgO.

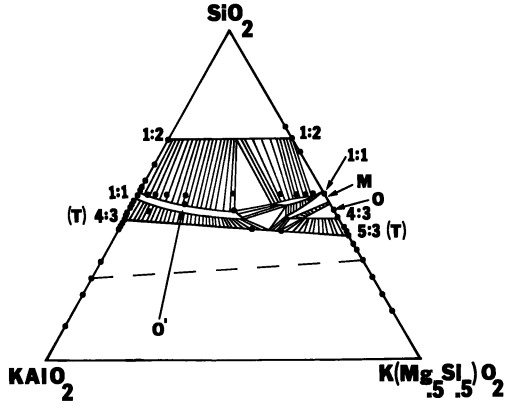

Figure 10. Preliminary phase equilibria diagram of the system $K[Mg_{0.5}Si_{0.5}]O_2$–$KAlO_2$–SiO_2. Isotherm section at about 1000°C. (●), compositions studied. T = tetragonal kalsilite?like phase; O′ = low-temperature orthorhombic b × 3 kalsilite-like phase; M = monoclinic kalsilite-like phase; O = orthorhombic kalsilite-like phase.

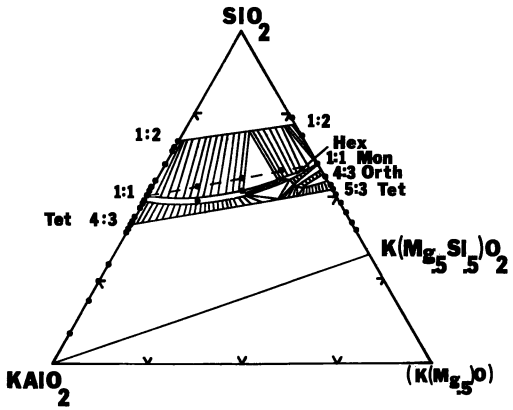

Figure 11. The same system as illustrated in Figure 10 except redrawn to show total SiO_2 content at upper apex of the diagram: HEX = hexagonal kalsilite-like phase; MON = monoclinic kalsilite-like phase; ORTH = orthorhombic kalsilite-like phase; TET = tetragonal kalsilite-like phase.

The Five-Component System K_2O–MgO–Al_2O_3–Fe_2O_3–SiO_2

This five-component system has not been studied in detail as yet. In the present study no attempt has been made to study systematically the effect of the possible reduction of iron from Fe^{3+} to Fe^{2+}. Previous preliminary studies were made by Roedder in the system K_2O:FeO:SiO_2

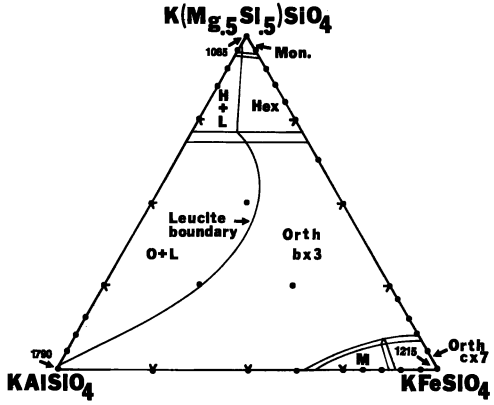

Figure 12. Preliminary phase equilibria diagram of the system $K[Mg_{0.5}Si_{0.5}]SiO_4$–$KAlSiO_4$–$KFeSiO_4$. Isotherm at about 1000°C. Note that a leucite-like phase extends into the ternary system. MON = monoclinic kalsilite-like phase; H and HEX = hexagonal kalsilite-like phase; L = leucite-like phase; O and OTH b × 3 = low-temperature orthorhombic $KAlSiO_4$ type of phase; M = monoclinic kalsilite-like phase; ORTH c × 7 = orthorhombic $KFeSiO_4$ type of phase.

(*24*) and K_2O:FeO:Al_2O_3:SiO_2 (*25*). He indicated that equilibrium involving FeO, at least in compound formation, was similar to that of the systems involving MgO.

$KAlSiO_4$–$KFeSiO_4$–$K_2MgSi_3O_8$. Three compositions were prepared in this system, and the interpretation of the data is shown in Figure 12. It should be noted that the leucite field extends into this pseudoternary, but the major area of kalsilite-like compositions is that of the $KAlSiO_4$ type of ($b \times 3$) orthorhombic phase. The presence of the hexagonal kalsilite phase, stabilized between 5% and 30% additions of $KAlSiO_4$–$KFeSiO_4$, cuts off the field of monoclinic $K[Mg_{0.5}Si_{0.5}]SiO_4$ from its apparently isostructural analogue in the low-MgO-containing compositions.

Other Studies. It is presently planned to study portions of the system $KAlO_2$–$KFeO_2$–$K[Mg_{0.5}Si_{0.5}]O_2$–SiO_2 by looking at diagrams containing equal silica content (when plotted as written). The past work has been confined to the diagram containing 50% SiO_2. A series of compositions containing 25% SiO_2 are currently being examined to check the boundaries of the cubic solid solution found to be about 25–30% in each of the binary systems. In view of the unexpected occurrence of leucite in much of the system at 50% silica, it is possible that some surprises may occur in other portions of these systems.

Additional studies are presently underway to study the system K_2O–CaO–Al_2O_3–SiO_2. It is also planned to study the effect of lower P_{O_2} (partial pressure of oxygen) on the phase assemblages in the system K_2O:FeO:Fe_2O_3:SiO_2 and in the more complex systems involving MgO, CaO, and Al_2O_3.

These experiments have already proven useful in understanding the complex chemical reactions occurring in the MHD channel. For example, in test runs on MHD power generation utilizing coal as the heat source and running in a slagging mode, the major crystalline product is a kalsilite-related phase. The phase transition in kalsilite at about 1450°C is useful therefore as a tool to determine the temperature of the wall at the point where the molten slag crystallized. This transition thus acts as an internal thermocouple. However, it is important to understand the effect of moderate additions of MgO and Fe_2O_3/FeO on the transition temperature.

Acknowledgments

This paper is a review of studies being conducted in the author's laboratory by members of the Solid State Chemistry group of the Division of Ceramis, Glass and Solid State Sciences. Those who have contributed substantially to these studies are L. P. Cook, C. L. McDaniel, D. B. Minor, T. Negas, H. S. Parker, R. S. Roth, and J. L. Waring. Others who made contributions either in the form of specimen preparation and ex-

periments or consultation are M. Austin, W. S. Brower, C. A. Harding, C. D. Olson, and C. Skarda. The author is especially grateful for the assistance of M. Clevinger in the preparation of the manuscript.

Portions of this work were sponsored by DOE [Contract No. E(49-1)-3800] and NASA (Contract No. H-27954B).

Literature Cited

1. Bowen, N. L. *Am. J. Sci.* **1917**, *43*, 115–132.
2. Schairer, J. F.; Bowen, N. L. *Am. J. Sci.* **1955**, *253*, 681–746.
3. Roedder, E. W. *Am. J. Sci.* **1951**, *249*, 81–130.
4. Roedder, E. W. *Am. J. Sci.* **1951**, *249*, 224–248.
5. Schairer, J. F. *J. Am. Ceram. Soc.* **1954**, *37*, 501–533.
6. Cook, L. P.; Roth, R. S.; Parker, H. S.; Negas, T. *Am. Mineral.* **1977**, *62*, 1180–1190.
7. Cook, L. P.; Roth, R. S.; Parker, H. S.; Negas, T. *Geol. Soc. Am., Abstracts* **1976**, *8*(6), 819–820.
8. Roth, R. S.; McDaniel, C. L.; Parker, H. S.; Cook, L. P.; Negas, T.; Minor, D. B. *Geol. Soc. Am., Abstracts* **1977**, *9*(7), 1149.
9. Roth, R. S. *Bull. Am. Ceram. Soc.* **1978**, *58*(3), 379.
10. Parker, H. S. Fourth American Conf. on Crystal Growth, Abstracts, submitted for publication in *J. Cryst. Growth.*
11. Levin, E. M.; Robbins, C. R.; McMurdie, H. F. "Phase Diagrams for Ceramists"; American Ceramic Society: Columbus, 1964.
12. Kracek, F. C.; Bowen, N. L.; Morey, G. W. *J. Phys. Chem.* **1937**, *41*, 1183–1193.
13. Aksay, I. A.; Pask, J. A. *J. Am. Ceram. Soc.* **1975**, *58*, 507–512.
14. Waring, J. L., unpublished data.
15. Smith, J. V. *Am. Mineral.* **1977**, *62*, 703–709.
16. Faust, G. T. *Am. Mineral.* **1936**, *21*, 735–763.
17. Wones, D. R.; Appleman, D. E. *J. Petrol.* **1963**, *4*, 131–137.
18. Takahashi, T.; Kuwabara, J.; Kase, Y. *Denki Kagaku* **1975**, *43*, 273–277.
19. Parker, H. S., unpublished data.
20. McDaniel, C. L., unpublished data.
21. Minor, D. B.; Roth, R. S.; Brower, W. S.; McDaniel, C. L. *Mater. Res. Bull.* **1978**, *13*, 575–581.
22. Roth, R. S., unpublished data.
23. Negas, T., personal communication.
24. Roedder, E. W. *Am. J. Sci., Bowen volume* **1952**, 435–456.
25. Roedder, E. W. *Am. Mineral.* **1951**, *36*, 282–286.

RECEIVED September 13, 1978.

21

Mixed Valence States of Iron in the Ba–Fe–S System

HUGO STEINFINK

Department of Chemical Engineering, University of Texas at Austin, Austin, TX 78712

Compounds in the Ba–Fe–S system exhibit complex stoichiometries, containing mixed valence states of Fe^{2+} and Fe^{3+} that strongly influence the physical properties. Results from crystal structure analysis and Mössbauer spectroscopy are used to predict electrical conductivity and magnetic susceptibility behavior and to distinguish between effects due to the delocalization of d *electrons or due to the promotion of electrons from the valence to the conduction band. The crystal chemical architecture is primarily a function of BaS_6 trigonal prism linkages, but the physical properties depend on FeS_4 tetrahedral arrays. The Fe–Fe distances are critical parameters in determining the delocalization of* d *electrons. Delocalization can occur within tetrahedral polynuclear clusters or over the complete structure.*

Interest in the chemistry and physics of mixed-valence compounds can be dated back almost 275 years, to the synthesis of Prussian blue, $KFe_2(CN)_6$. The development of solid state technology over the past three decades has brought about a renaissance of inorganic chemistry and a renewed interest in mixed valence compounds. They have received intensive scrutiny because of the intimate connection between their chemistry and physical properties. Mixed valence compounds are substances in which an ion of the same element, usually a transition metal, exists in two different formal oxidation states, as exemplified in Prussian blue or magnetite, or in which an exchange of electrons can take place, creating oscillating valence states between two different ions, as in the mixed oxide Ce_2UO_6 or in rare earth compounds. One of the earliest

0–8412–0472–1/80/33–186–409$05.00/1

inferences made was that a correlation exists between the color of a compound and the presence of the mixed oxidation state, but other effects—for example, magnetic and electrical transitions—can be linked to the presence of mixed oxidation states. Thus the study of the interrelationships among electronic structure, molecular structure, crystal structure, electronic spectra, electronic conduction, magnetism, and mixed valence states in crystals contributes to the fundamental understanding of the solid state and to the advancement of technology.

An extensive review, "Mixed Valence Chemistry—A Survey and Classification," has been published by Robin and Day (*1*); it deals primarily with oxides of the transition metals. The unique physical properties of many rare earth compounds have been shown to be due to the presence of mixed, or oscillating, valence states (*2*). Robin and Day limited themselves to oxides because the presence of mixed valence states can be uniquely studied in these materials. In sulfides, arsenides, and other compounds in which the ligand is strongly covalently bonded to the metal, electron delocalization frequently occurs because of the small value of the band gap. It becomes difficult, therefore, to ascribe the origin of a given physical effect—for example, electrical conductivity —to the promotion of electrons from the valence band to the conduction band or to electron delocalization caused by mixed valence states. We concentrated our investigation of the interrelationship between structure and properties on compounds formed in the ternary Ba–Fe–S system because Mössbauer spectroscopy is a unique and easily used tool for studying the oxidation state of iron. It permits, in conjunction with structural results, the differentiation between effects due to valence band–conduction band transitions and *d* electron delocalization due to mixed valence states.

The determination of the precise stoichiometry of a compound is a prerequisite for the study of mixed valence states. The classical analytical techniques for the determination of elemental constituents are not sufficiently precise. Error limits in these determinations could imply the presence of mixed valence states when none are required, or give incorrect ratios for mixed valence states. Furthermore, the possibility of polyanion formation, such as S_2^{2-} and S_3^{2-}, could raise doubts about the assignment of formal valence states on the basis of chemical analysis alone. Again, preparations of new phases frequently contain admixtures of small amounts of impurities not detectable by X-ray powder diffraction or other means, and a bulk determination of composition would be misleading. The complete crystal structure determination is a necessity for the correct determination of stoichiometry and anion type, although the presence of disorder and partial site occupancies can, and does, create difficulties.

In the compounds we studied, evidence for the presence of homogenous or inhomogeneous mixed valence states can be deduced from structural and Mössbauer observations. If high-spin divalent and trivalent iron in tetrahedral coordination occupies distinct, separate crystallographic sites, designated as the class II case by Robin and Day (*1*) or as inhomogeneously mixed valence by Varma (*2*), then the respective bond distances to sulfur will have characteristic values of 2.37 Å and 2.23 Å, respectively, and the Mössbauer spectrum will consist of distinct absorption lines from the two types of iron. If the metal ions are randomly distributed over the crystallographic sites, an intermediate value for the Fe–S bond will be obtained from a crystal structure determination. The question of the existence of localized versus itinerant electrons in the compound cannot be resolved from such a result, but distinct Mössbauer absorption spectra for the two Fe oxidation states will be observed and unambiguously indicate the presence of localized *d* electrons. Delocalization of the *d* electrons, a class III compound (*1*), or a homogeneous mixed valence state (*2*) would give rise to Fe–S bonds of intermediate value and only a single, quadrupole split Mössbauer absorption spectrum. We have observed in these compounds that delocalization occurs when Fe–Fe distances are less than 3 Å, permitting the overlap of d_{z^2} orbitals and the formation of narrow *d* bands in the solid. The determinativeness of metal–metal distances on the physical properties of many crystalline solids has been extensively discussed by Goodenough and others (*3*).

Structure–Property Relations

The structural chemistry of the Ba–Fe–S compounds is based principally on the articulation of BaS_6 trigonal prisms, although tetragonal prisms, bisdisphenoids, and square antiprisms are other coordination polyhedra observed around the barium ion. The importance of trigonal prism building blocks in crystal chemistry and physics is well known (*4*). Many ternary Ba–M–X (M = transition metal, X = chalcogen) chalcogenides exhibit common features of columns of base-sharing trigonal prisms formed by the chalcogen element whose centers are occupied by barium ions. These columns can be free standing or articulate laterally by edge and face sharing into two- or three-dimensional networks. Tetrahedral voids are created by the chalcogen packing, and these can be filled to various extents by the transition metal. These structures can be considered as stuffed derivatives of simpler types. Figure 1 illustrates the development of the $BaFe_2S_3$ structure from a slight distortion of the $SnNi_3$ type of structure with subsequent filling of tetrahedral sites by Fe. An extensive discussion of these relationships has been given by Shoemaker (*5*) and Iglesias and Steinfink (*6*).

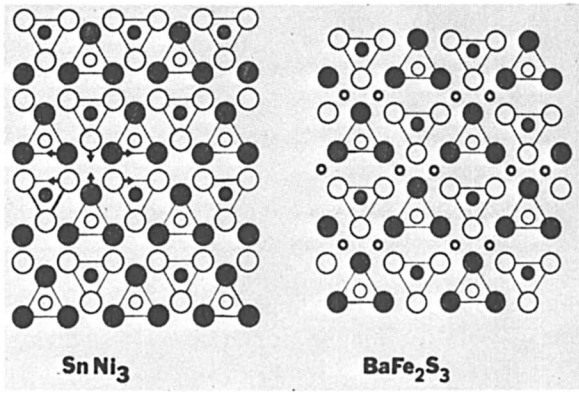

Figure 1. Development of the crystal structure of $BaFe_2S_3$ from a distortion of the $SnNi_3$ type of structure. The arrows point along the motion of the atoms. The shaded and open circles represent atoms that are in planes separated by 1/2 of the projection axis. The small circles are Fe.

The physical behavior of these compounds is best understood in terms of the FeS_4 tetrahedral articulations, and Figure 2 illustrates the various arrangements that have been encountered in this system. Many compounds contain tetrahedral linkages that form one-dimensional infinite chains or columns that are separated laterally by more than 6 Å from each other. Thus the physical properties that arise from the presence of the transition metal are highly anisotropic. Table I lists the crystallographic data for the phases that have been characterized to date.

Ba_2FeS_3. The articulations of the trigonal prismatic units create tetrahedral interstices that are filled by iron in such a way as to give rise to infinite, one-dimensional chains of corner-sharing tetrahedra; *see* Figure 2. The stoichiometry implies the presence of ferrous iron only. Within the chain the Fe–Fe distances are greater than 4 Å, and the average Fe–S bond length is 2.38 Å (7). The measured effective magnetic moment, 5.3 BM (8), and the Mössbauer isomer shift, 0.62 mm · sec^{-1} (relative to α-Fe) (9), are consistent with the presence of Fe^{2+}. No Fe–Fe bonding is expected, and the *d* electrons should be localized in this compound. The relatively high room temperature electrical resistivity of about 10^4 Ω · cm (9) is in agreement with expectations. The formal valence state of +2, expected on the basis of stoichiometry, is confirmed.

$BaFe_2S_3$. Based on stoichiometry, this compound similarly should contain only ferrous iron. The crystal structure can be considered as a stuffed derivative of slightly distorted $SnNi_3$, Figure 1, and the filling of the tetrahedral interstices gives rise to isolated, infinite, linear double chains in which each tetrahedron shares three edges. Fe–Fe distances

are approximately 2.7 Å, and direct metal–metal bonding through the b_{1g} electron orbitals can be expected. The Fe–S bond is 2.28 Å. The Mössbauer isomer shift of 0.41 mm · sec^{-1} (*9*) indicates an intermediate oxidation state for iron, and the very low room temperature electrical resistivity, 0.5 Ω · cm, confirms that electron delocalization has occurred. A homogeneously mixed valence state of about 2.5 for iron exists in this compound.

$Ba_7Fe_6S_{14}$. On the basis of stoichiometry this compound contains two Fe^{2+} and one Fe^{3+} ion. The crystal structure consists of a complex three-dimensional network of BaS_6 trigonal prisms, and the filling of tetrahedral interstices by iron creates infinite chains in which a linear trinuclear unit, formed by edge sharing of three tetrahedra, propagates with the next unit by corner sharing, Figure 2 (*10*). The trinuclear unit thus could accommodate two Fe^{2+} and one Fe^{3+} with the ions in fixed sites, a model corresponding to an inhomogeneously mixed valence state. The Fe–Fe distances within the trinuclear, edge-sharing unit are 2.8 Å

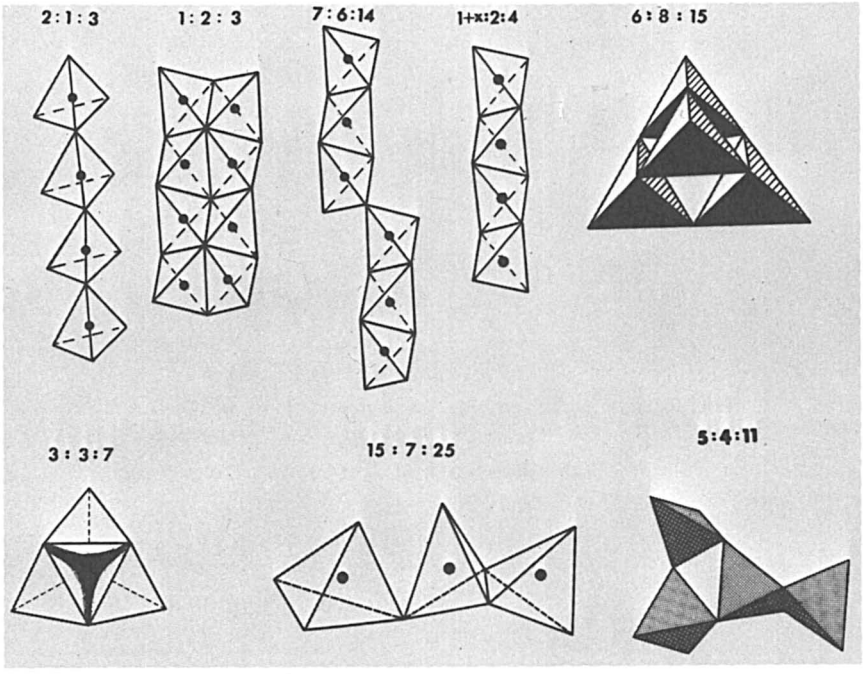

Figure 2. Tetrahedral articulations in phases in the Ba–Fe–S system. The stoichiometric ratios shown above the configurations are Ba:Fe:S.

Table I. Crystallographic Data for

Compound	Specific Gravity	a (Å)[a]
$BaFe_2S_3$	Cmcm	8.7835
$BaFe_2Se_3$	Pnma	11.878
Ba_2FeS_3	Pnma	12.087
$Ba_6Fe_8S_{15}$	I4/m	11.408
$Ba_7Fe_6S_{14}$	C2/c	25.490
$Ba_3Fe_3Se_7$	$P6_3mc$	10.843
$Ba_9Fe_{16}S_{32}$[b]	P4/mnc	7.7758
$Ba_5Fe_4S_{11}$	$Pmn2_1$	16.060
Ba_3FeS_5[c,d]	Pnma	12.405
β-$Ba_9Fe_4S_{15}$[c]	Pnma	25.212
$Ba_{15}Fe_7S_{25}$[c]	Pnma	41.91
α-$Ba_9Fe_4S_{15}$	$I4_1/a$	9.634
$Ba_{12}Fe_6S_{20}(S_2)$	$A\bar{1}$	9.003
$Ba_9Fe_3S_{11}(S_2)_2$[d,e]	$P\bar{6}c2$	9.218

[a] a, b, and c are lattice constants; α, β, and γ are angles of unit cell.
[b] Member of infinitely adaptive series $Ba_{1+x}Fe_2S_4$.
[c] Member of infinitely adaptive series $Ba_3Fe_{1+x}S_5$.

and are 3.7 Å across corner-shared tetrahedra. If the deductions concerning the interrelationships of the structural and physical parameters from the two previous examples are applied to this case, it would be expected that electron delocalization should occur within the trinuclear unit but that the electrical resistivity should be high because the larger Fe–Fe distance caused by the corner-sharing tetrahedral linkages prevents the formation of a continuous d band in the solid. The anion environment around the three crystallographically distinct iron atoms in the trinuclear unit is not identical, since the central tetrahedron shares two edges while the outside tetrahedra share one edge and one corner, and the complex Mössbauer spectrum is interpreted as being caused by three different iron ions with isomer shifts of 0.49, 0.36, and 0.36 mm · sec^{-1} (9), indicative of intermediate oxidation states for Fe within the trinuclear unit. Table II gives the calculated valence values and isomer shifts for the three iron ions. Fe(3), located in the middle tetrahedron, has a valence of 2.32 and a calculated isomer shift of 0.47 mm · sec^{-1} (*see* the section titled "Bond Distance—Mössbauer Isomer Shift" for the calculations), indicating that the outside iron ions have a more trivalent character than does the middle one and are separated by the maximum distance. The magnetic susceptibility, 5.3 BM, and the high room temperature electrical resistivity of 10^3 Ω · cm are in accord with expectations. This compound could be classified as belonging to class IIIA.

$Ba_9Fe_{16}S_{32}$. The behavior of $Ba_9Fe_{16}S_{32}$ ($Fe^{3+}/Fe^{2+} = 7$), in which the FeS_4 tetrahedral articulations form infinite chains of edge-sharing

Phases in the Ba–Fe–S (Se) System

b (Å)[a]	c (Å)[a]	α (degrees)[a]	β (degrees)[a]	γ (degrees)[a]
11.219	5.2860			
5.447	9.160			
4.246	12.359			
	10.256			
8.244	14.949		118.85	
	7.384			
	44.409			
7.260	8.863			
9.516	8.5212			
9.549	12.575			
9.572	12.654			
	34.311			
6.7086	24.658	91.49	105.10	90.74
	18.042			

[a] High-pressure phase.
[b] Octahedrally coordinated Fe.

tetrahedra (Figure 2), can be predicted with confidence. This compound is a member of the infinitely adaptive series $Ba_{1+x}Fe_2S_4$, with $x = 0.125$ (*11, 12*). The Fe–Fe distances are approximately 2.8 Å and the average Fe–S distance is 2.25 Å. Delocalization of electrons is expected, and, indeed, the Mössbauer spectrum shows only a single quadrupole and an isomer shift of 0.20 mm · sec^{-1}, a value characteristic of Fe^{3+} (9), and the room temperature resistivity is about 1 Ω · cm.

$Ba_6Fe_8S_{15}$. Predicting the physical behavior of $Ba_6Fe_8S_{15}$ requires a more subtle analysis of the relationship between structure and properties. Stoichiometry requires the presence of three Fe^{2+} and one Fe^{3+}. The structure consists of infinite columns formed by a tetranuclear unit of FeS_4 tetrahedra (Figure 2), with the clusters propagating by mirror reflection operations across two opposite edges of the tetranuclear unit. The Fe–Fe distance within a cluster is about 3.6 Å, but it is 2.8 Å across the shared edges between clusters (7). The arrangement appears similar to that in $Ba_7Fe_6S_{14}$. However, only one crystallographic iron is present in $Ba_6Fe_8S_{15}$. This equivalence is achieved by π bonding between Fe and S through overlap of the *e* and *t* electron orbitals with empty *d* orbitals of sulfur. The π bonding gives rise to delocalization of electrons within the cluster, and short Fe–Fe bonds between clusters should cause this material to exhibit a relatively low room temperature resistivity. The Mössbauer spectrum shows only one quadrupole split doublet with an isomer shift of 0.47 mm · sec^{-1}; the effective magnetic moment is 5.57 BM; and the room temperature resistivity is about 1 Ω · cm; all

Table II. Calculated and Observed

Compound		V_{calcd}		V_{obsd}	δ_{calcd}[a] ($mm \cdot sec^{-1}$)
Ba_2FeS_3		1.90		2.00	0.64
$BaFe_2S_3$		2.64		2.00	0.34
$Ba_7Fe_6S_{14}$	1[c]	2.59			0.36
	2	2.56	< 2.49 >	2.33	0.38
	3	2.32			0.47
$Ba_6Fe_8S_{15}$		2.43		2.25	0.43
$B_9Fe_{16}S_{32}$	1	2.8			0.28
	2	3.0			0.20
	3	2.54	< 2.89 >	2.88	0.38
	4	3.2			0.12
$Ba_{15}Fe_7S_{25}$	1	2.76			0.29
	2	2.72			0.31
	3	2.98			0.21
	4	2.84	< 2.81 >	2.86	0.27
	5	2.90			0.24
	6	2.64			0.34
	7	2.80			0.28

[a] Isomer shifts relative to α-Fe.
[b] Symbols: μ = effective magnetic moment; ρ = resistivity in BM (Bohr magnetons).

these values are in expectation with the results obtained from structural considerations.

$Ba_{15}Fe_7S_{25}$. The discussion of one other compound will illustrate the case in which isolated tetrahedral units are present. The compound $Ba_{15}Fe_7S_{25}$ is one member of the infinitely adaptive series with the general formula $Ba_3Fe_{1+x}S_5$ (*13, 14*) . The BaS_6 framework forms distorted hexagonal rings, and some of the tetrahedral interstices in these rings are occupied by Fe. An isolated trinuclear unit is observed in which the central tetrahedron shares one edge and one corner (Figure 2); also, isolated single tetrahedra are present. Six Fe^{3+} and one Fe^{2+} are required by stoichiometry, and two trinuclear units and one tetrahedron exist per formula unit. An obvious and tempting distribution for the seven crystallographically independent metal ions would be the placement of Fe^{3+} in the trinuclear units and Fe^{2+} in the single tetrahedron, to yield an inhomogeneously mixed valence state compound. However, the Fe–S distances in the single tetrahedron are 2.23 Å, and the average Fe–S distance in the trinuclear unit is 2.26 Å, so that either a disordered Fe^{2+}–Fe^{3+} state is possible or all Fe have essentially the same valence state. Only one broad quadrupole split Mössbauer absorption spectrum is observed, with an isomer shift of 0.20 mm · sec^{-1} indicative of Fe^{3+}. The broadening is due to the overlapping of seven quadrupole split doublets corresponding to the seven crystallographically independent iron

Parameters for Phases in the Ba–Fe–S System

	δ_{obsd}[a] ($mm \cdot sec^{-1}$)	μ_{calcd} μ_B	μ_{obsd} μ_B	ρ[b] ($\Omega \cdot cm$)	*Fe–Fe* (Å)
	0.62	4.8	5.3	10^4	4.3
	0.41	5.5		0.5	2.7
	0.36				
	0.36	5.4	5.3	10^3	2.8
	0.49				3.7
	0.47	5.3	5.6	1	2.8
					3.5
	0.20			1	2.7–2.9
< 0.25 >	0.20				
	0.22				2.7
					4.0
< 0.28 >	0.22				

[a] Crystallographically separate Fe sites in the crystal structure.

atoms. The Fe^{2+} ion is located in one of the edge-sharing tetrahedral sites, and electron delocalization occurs because of the short Fe–Fe distance (2.7 Å) to produce an overall effective charge distribution of $5Fe^{3+}$ and $2Fe^{2.5+}$. This occurs randomly over the two edge-sharing units. A theoretical Mössbauer spectrum based on these mixed states was consistent with the observed spectrum. This arrangement must represent an energetically more favorable case than valence state ordering (*1*).

Bond Distance—Mössbauer Isomer Shift

If the assumption is made that a linear variation exists between the electron density at the nucleus of an atom and its valence, then the Mössbauer isomer shift δ can be related to the valence of high-spin iron in a tetrahedral sulfur environment by

$$\delta = 1.4 - 0.4V$$

where V is the valence of Fe. Further, the valence can be related to the cation–anion bond lengths by the equation

$$V = 178.2 \sum_i R_i^{-6.81}$$

where R_i represents the observed Fe–S distances (*15*).

Thus the valence of Fe can be calculated from the observed Fe–S distances and can be used to predict the Mössbauer isomer shift, which, in turn, has implications with regard to localized or itinerant electrons in the solid. These two equations were applied to the compounds synthesized in this system. Table II shows the calculated and observed values for several parameters, and the agreement among them is quite satisfactory. The same approach was used for the correlation of properties and valence states for many other iron chalcogenides taken from the literature, and a summary of those results can be found in Hoggins and Steinfink (*15*).

Infinitely Adaptive Series of Compounds

Anderson (*16*) has defined a category of compounds as "infinitely adaptive" if "within certain composition limits, every possible composition can attain a unique, fully ordered structure. . . ." Two such series have been found in the Ba–Fe–S system with general formulas $Ba_{1+x}Fe_2S_4$ (*11, 12*) and $Ba_3Fe_{1+x}S_5$ (*14*). In the former series the FeS_4 tetrahedra share edges to form infinite, one-dimensional chains (Figure 2), and the previous discussion of $Ba_{1.125}Fe_2S_4$ ($Ba_9Fe_{16}S_{32}$) has pointed out that delocalization of electrons occurs with a resultant low electrical resistivity. The preparation of compounds with different values of x is strongly dependent on the sulfur activity (*17*); in particular, the preparation of the end member $BaFe_2S_4$ has proven to be difficult. Boller (*18*) has prepared a fibrous material with this composition from $KFeS_2$ by ion exchange techniques and has analyzed the crystal structure from the X-ray fiber diagrams. He confirms the predicted space group, I4/m (*12*), but proposes a somewhat different structure, which requires Ba to have a 50% statistical site occupancy. We have prepared excellent single crystals about 15 × 230 μm and have analyzed the crystal structure from three-dimensional X-ray diffraction intensities (*17*). The structure is indeed as proposed in Hoggins and Steinfink (*12*), with the exception that S parameters are $x = 0.301$, $y = 0.120$, $z = \frac{1}{2}$, i.e. the chain of edge-sharing tetrahedra is rotated by 90° from the previous model. The cell parameters are $a = 7.678(2)$ Å, $c = 5.292(4)$ Å, and the structure was refined to $R = 0.031$ for 108 observed reflections. We expect that the electrical conductivity should be comparable to that of $KFeS_2$, 10^3 Ω · cm, because all the iron should be trivalent.

The second series contains only isolated polynuclear tetrahedral units or single tetrahedra. The previous discussion of the behavior of $Ba_3Fe_{1.4}S_5$ ($Ba_{15}Fe_7S_{25}$) should be typical for the other compounds of the series. It should be pointed out that the end member, Ba_3FeS_5, can be prepared only at very high pressure (*13*) and that the formal Fe^{4+} state is reduced to an effective trivalent state by back-donation of an electron from sulfur (*15, 19*).

High-Pressure Phases

High pressure stabilizes high valence states and high coordination numbers because of the increased densities that can be realized. In all the compounds that have been synthesized, iron was in tetrahedral coordination. The high valence state indeed is observed in the high-pressure phase Ba_3FeS_5. We have synthesized a polymorph of Ba_3FeS_5, $Ba_9Fe_3S_{11}(S_2)_2$, in which iron is in octahedral coordination, and the structure consists of limited regions of closely packed layers formed by Ba^{2+} and S^{2-} ions. The FeS_6 octahedra share faces to form isolated, infinite chains in which the Fe–Fe distances are 3 Å (*20*). The Mössbauer spectrum shows two quadrupole split lines with isomer shifts of 0.30 and 0.83 mm · sec^{-1}, respectively, and their area ratios are 2:1. Stoichiometry requires a formal valence of two Fe^{3+} and one Fe^{2+}, and the Mössbauer results are interpreted as indicating the presence of high-spin trivalent and divalent iron (*21*). This implies that a 3-Å Fe–Fe distance is longer than the critical distance, R_c (*3*), for direct Fe–Fe overlap to occur, and a high electrical resistivity would be predicted for this material. The physical properties of this compound are under investigation.

Summary

The intimate relationship between the existence of mixed valence states in a solid with its physical properties has been explored for a series of compounds in the Ba–Fe–S system. The stoichiometries of the phases were determined by solving the crystal structures. From the knowledge of Fe–S and Fe–Fe distances, inferences can be drawn with regard to the oxidation state of iron, that is, whether homogeneous or heterogeneous mixed valence states are likely. The Mössbauer isomer shift provides additional, essential information to confirm the type of mixed valence present. These results can be combined to allow the prediction of the electrical conductivity and magnetic susceptibility of the phases.

Acknowledgment

The author acknowledges with gratitude the contributions that have been made by numerous graduate students and postdoctoral investigators. The references to the published papers shall serve to credit the individual efforts. Gratitude is expressed to the R. A. Welch Foundation, Houston, Texas, and to the National Science Foundation for their support of this research.

Glossary of Symbols

δ = Mössbauer chemical isomer shift
V = valence
a, b, c = lattice constants
α, β, γ = angles of unit cell
μ = effective magnetic moment
ρ = resistivity
M = transition metal
X = chalcogen
R_i = observed Fe–S distances
R_c = critical distance

Literature Cited

1. Robin, Melvin B.; Day, Peter. *Advances Inorg. Chem. and Radiochem.* **1967**, *10*, 247.
2. Varma, C. M. *Rev. Mod. Phys.* **1976**, *48*, 219.
3. Goodenough, John B. "Magnetism and the Chemical Bond"; Interscience Publishers: New York–London, 1963.
4. Pearson, W. B. "The Crystal Chemistry and Physics of Metals and Alloys"; Wiley: New York, 1972; pp. 477–555.
5. Shoemaker, C. B. *Z. Kristallogr.* **1973**, *137*, 225.
6. Iglesias, J. E.; Steinfink, H. *Z. Kristallogr.* **1975**, *142*, 398.
7. Hong, H. Y.; Steinfink, H. *J. Solid State Chem.* **1972**, *5*, 93.
8. Steinfink, H.; Hong, H. Y.; Grey, I. E. "Solid State Chemistry, Proceedings of the 5th Materials Research Symposium," *Nat. Bur. Stand. (U.S.), Spec. Publ.* **1972**, *364*, 681.
9. Reiff, W. M.; Grey, I. E.; Fan, A.; Eliezer, A.; Steinfink, H. *J. Solid State Chem.* **1975**, *13*, 32.
10. Grey, I. E.; Hong, H.; Steinfink, H. *Inorg. Chem.* **1971**, *10*, 340.
11. Grey, I. E. *J. Solid State Chem.* **1974**, *11*, 128.
12. Hoggins, J. T.; Steinfink, H. *Acta Crystallogr. Sect. B* **1977**, *33*, 673.
13. Lemley, J. T.; Jenks, J. M.; Hoggins, J. T.; Eliezer, Z.; Steinfink, H. *J. Solid State Chem.* **1976**, *16*, 117.
14. Cohen, S.; Rendon–DiazMiron, L. E.; Steinfink, H. *J. Solid State Chem.* **1978**, *25*, 179.
15. Hoggins, J. T.; Steinfink, H. *Inorg. Chem.* **1976**, *15*, 1682.
16. Anderson, J. S. *J. Chem. Soc., Dalton Trans.* **1973**, 1107.
17. Swinnea, J. S.; Steinfink, H. *J. Solid State Chem.*, in press.
18. Boller, H. *Monatsh. Chem.* **1978**, *109*, 975.
19. Norman, J. G.; Jackels, S. C. *J. Am. Chem. Soc.* **1975**, *97*, 3833.
20. Jenks, J. M.; Hoggins, J. T.; Rendon–DiazMiron, L. E.; Cohen, S.; Steinfink, H. *Inorg. Chem.* **1978**, *17*, 1773.

RECEIVED October 2, 1978.

INDEX

C

D

E

F

G

I

J

K

N

O

P

Q

T

U

V

Jacket design by Carol Conway.

Editing by Carol Beal.

Production by Candace Deren.

The book was composed by Service Composition Co., Baltimore, MD, printed and bound by The Maple Press Co., York, PA.